AN ABSTRACT OF THE DISSERTATION OF

Qiang Li for the degree of Doctor of Philosophy in Civil Engineering presented on November 21, 2017.

Title: Investigation of Drilled Shafts under Axial, Lateral, and Torsional Loading

Abstract approved:

____

Armin W. Stuedlein

Drilled shaft foundations provide significant geotechnical resistance for support of structures, such as highway bridges, traffic sign, and signal pole structures, and are used widely to meet their structural foundation requirements. The amount of steel reinforcement in drilled shaft foundations has increased over the past several decades to account for anticipated seismic hazards. Increased reinforcement may lead to increased possibilities of anomalies within shafts due to the increased difficulty for concrete to flow through reduced clearance between the reinforcement. High-strength steel reinforcement and permanent steel casing may be used to mitigate the concreting concern. However, the comparison of axial and lateral load transfer between drilled shafts with and without permanent steel casing and high-strength reinforcement has not been previously investigated, raising questions regarding the suitability of existing analytical approaches for the evaluation of axial and lateral load transfer. In addition to axial and lateral loading, deep foundations may need to resist torsional loads, resulting from wind loading on traffic sign and signal pole structures, or seismic loading on curved or skewed bridges. However, the

understanding of the actual resistance to torsion provided by deep foundation elements is not well established. The design methods for deep foundations in torsion at the ultimate limit states need to be evaluated and their accuracy needs to be quantified with loading test data. Furthermore, the accuracy of existing load transfer-based torsion-rotation methods to predict the full-scale, in-service rotation performance that considers state-dependence of the soil needs to be quantified.

Two uncased instrumented drilled shafts were constructed and used to evaluate the torsional capacity and load transfer at full-scale. The quasi-static monotonic and cyclic torsional loading tests were conducted. Based on the results of the torsional loading tests, design methods to predict ultimate resistance were proposed. To facilitate the serviceability and ultimate limit state design of geometrically-variable deep foundations constructed in multi-layered soils, a torsional load transfer method was presented using a finite difference model (FDM) framework. Simplified state-dependent spring models, relating the unit torsional resistance to the magnitude of relative displacement, were developed in consideration of soil-structure interface shear test results. Parametric studies illustrated the significant effect of nonlinear soil responses and nonlinear structural response on the torsional behavior of deep foundations.

The axial and lateral load transfer of drilled shaft foundations were studied using four instrumented drilled shafts at full-scale: two uncased and two cased drilled shafts, reinforced with either mild or high strength steel reinforcement. Based on the results of axial loading tests, selected axial load transfer models were evaluated and modified to produce region-specific axial load transfer models to aid the design of drilled shaft bridge foundations for similar soils in the Willamette Valley. The effects of permanent casing on axial load transfer were summarized to provide an up-to-date reference on the reductions expected based on construction sequencing and installation methods. The lateral responses of the test drilled shaft foundations indicated that the high-strength reinforcement could be used without detriment to the lateral performance of drilled shafts; and the cased shafts responded in a more resilient manner than uncased shafts at the same nominal diameter due to their significantly greater flexural rigidity. Based on the empirical soil reaction-displacement (*p*-*y*) curves, a region-specific *p*-*y* curve model was proposed with recommendations to account for pseudo-scale effects due to the increasing contribution of shaft resistance to lateral resistance with increased diameter.

INVESTIGATION OF DRILLED SHAFTS UNDER AXIAL, LATERAL, AND TORSIONAL LOADING

by
Qiang Li

A DISSERTATION

Submitted to

Oregon State University

in partial fulfillment of
the requirements for the
degree of

Doctor of Philosophy

Presented November 21, 2017
Commencement June 2018

Doctor of Philosophy dissertation of Qiang Li presented on November 21, 2017

APPROVED:

Major Professor, representing Civil Engineering

Head of the School of Civil and Construction Engineering

Dean of the Graduate School

I understand that my dissertation will become part of the permanent collection of Oregon State University libraries. My signature below authorizes release of my dissertation to any reader upon request.

Qiang Li, Author

ACKNOWLEDGEMENTS

I wish to acknowledge the many agencies, firms, and individuals who have contributed to this research effort. First and foremost, I would like to thank God for giving me the wisdom and the perseverance to complete this research. I would like to express my gratitude to my advisor, Dr. Armin Stuedlein, who has been a friend and mentor, for offering support and direction on this research. I would also like to express my sincere appreciation to the members of my research committee, including Dr. Andre Barbosa, Dr. Ben Leshchinsky, Dr. Brian Fronk, and Dr. T. Matthew Evans, for the thoughtful comments and guidance in this research.

I want to thank my family, including my father and mother, Yuanlu Li and Donghua Niu, my father- and mother-in-law, Yujie Yang and Jianrong Chai, for their full support and endless encouragement during this process. I would like to specifically acknowledge my wife Ting Yang, for her love, patience, and support on my research, for listening to my concerns and offering guidance, and for taking care of the whole family.

This research was funded by Grant SPR 304-701 and SPR 765 through the Oregon Department of Transportation and Grant DTRT13-G-UTC4O and DTRT12-UTC10 through the Pacific Northwest Transportation Consortium (PacTrans). PLI Systems, Inc., of Hillsboro, Oregon, donated materials, equipment and labor to construct the test shafts for the full-scale torsional loading tests. For the full-scale axial and lateral loading tests, the West Coast Chapter (WCC) of the ADSC contributed funds to help offset material costs associated with the construction of the test shafts, with critical coordination efforts and guidance provided by John Starcevich (Malcolm Drilling, Inc.), Becky Patterson (WCC

ADSC), and Rick Walsh (Hayward Baker, Inc.). Malcolm Drilling, Inc. constructed the test shafts for axial and lateral loading tests; Pacific Foundation, Inc. installed the reaction piles for axial loading tests; and Ralph's Concrete donated the concrete pumping services. The Grade 80 solid and hollow steel reinforcement bars were donated by ConTech Systems, whereas the Grade 60 steel reinforcement bars and all cage fabrication was donated by PJ's Rebar. The permanent steel casing was donated by Skyline Steel, and the Grade 150 steel reinforcement bars for the reaction anchors were contributed by Williams Form, Inc. Spacers and bar boots were provided by Foundation Technologies. Crosshole sonic logging service was donated by GEI Consultants; and Thermal Integrity Profiling Thermal Wires® and logging services were provided by Pile Dynamics, Inc. I would also like to thank James Batti for his help with the setup of the data acquisition system used in the loading tests. Helpful assistance with the test setup and execution was provided by Andrew Strahler, David Bailey, Eric North, Jeff Gent, John Martin, Robert Leaf, Tygh Gianella, Xiaomin (Jacky) Chen, and Youssef Bougataya. Without the support of all of these individuals, firms, and organizations, this research would not have been completed.

TABLE OF CONTENTS

Page

TABLE OF CONTENTS (Continued)

Page

TABLE OF CONTENTS (Continued)

Page

TABLE OF CONTENTS (Continued)

Page

TABLE OF CONTENTS (Continued)

Page

TABLE OF CONTENTS (Continued)

Page

LIST OF FIGURES

Figure Page

LIST OF FIGURES (Continued)

Figure Page

LIST OF FIGURES (Continued)

Figure Page

LIST OF FIGURES (Continued)

Figure | Page

LIST OF FIGURES (Continued)

Figure | Page

LIST OF FIGURES (Continued)

Figure Page

LIST OF FIGURES (Continued)

LIST OF TABLES

LIST OF TABLES (Continued)

DEDICATION

This dissertation is dedicated to my father, Yuanlu Li, and mother, Donghua Niu, my father and –mother-in-law, Yujie Yang and Jianrong Chai, respectively.

I also dedicate this work to my wife, Ting Yang, my sister Wen Li, and my children, Lydia, Luke, and Gabriel.

1. INTRODUCTION

1.1 Statement of Problem

Drilled shafts provide significant geotechnical resistance for support of highway bridges and are used widely to meet their structural foundation requirements. Due to changes in construction methods and poor near-surface soils, the use of permanent steel casing for drilled shaft installation has increased. However, geotechnical design models for axial and lateral resistance of drilled shafts are largely based on soil-concrete interfaces, not soil-steel interfaces associated with large diameter steel casing. Owing to the improved understanding of our regional seismic hazards, the amount of steel reinforcement used in drilled shaft construction has increased over the past several decades, creating a new construction concern for engineers: the greater steel area results in a reduced clearance between adjacent reinforcement bars in the steel cage, such that concrete has an increased difficulty in flowing through the cage and likelihood for voids and defects within the shaft, which can lead to poor structural and geotechnical performance. The use of high-strength reinforcement steel can lead to improved clearance within the steel cage, mitigating concreting issues. The use of steel casing, the amount of steel area, and the corresponding yield stress control the axial and lateral resistance of the shaft. However, depending on the method of construction, the steel casing may result in reduced axial load transfer to the surrounding soil. Thus, existing analytical approaches need to be evaluated for modern construction methods and new approaches developed if necessary to ensure desired performance criteria are met.

In addition to axial and lateral loading, drilled shaft foundations commonly experience torsional loads. Such cases include loads on mast arm traffic sign and signal poles, or seismically-induced inertial loading of foundations supporting skewed or curved bridges. In the former case, foundation loading includes moments due to cantilevered dead loads, which may be represented as a lateral shear, and torsional loads that arise from wind gusts. Often, torsional loads can control the design length of the foundation, particularly in storm-prone regions that can produce significant wind speeds. For example, observations of storm-induced winds along the Oregon and Washington coast in 2007 indicated a maximum wind gust of 237 km/h (Reiter 2008). Despite the prevalence of drilled shafts for the support of traffic sign and signals in practice, the understanding of the actual torsional load transfer provided by deep foundations is not well established..

1.2 Purpose and Scope

This study is based on an investigation of two research projects on the shared subject of load transfer of drilled shaft foundations. The purpose of the first project is to study the impact of steel casing and high-strength steel reinforcement on the axial and lateral performance of full-scale drilled shaft foundations and to evaluate the appropriateness of existing load transfer models. In-situ tests, including cone penetration and shear wave velocity tests were conducted to establish the relevant soil properties at the Oregon State University (OSU) Geotechnical Engineering Field Research Site (GEFRS). Four full-scale, instrumented test shafts and twelve continuous flight auger reaction piles were constructed. Axial and lateral loading tests were conducted to determine the effect of high strength steel reinforcement bars on lateral resistance, steel casing on axial and lateral resistance, and steel casing without internal reinforcement on lateral resistance. The second project forming the basis for this study is conducted to gain an understanding of the load transfer of and torsionally loaded drilled shafts at full-scale and to develop a nonlinear numerical simulation methodology to aid in the design of deep foundations under torsional loading. Two full-scale, instrumented test shafts were constructed at GEFRS in order to evaluate the torsional load transfer of typical drilled shafts with and without a “frictionless base”. To facilitate the serviceability and ultimate limit state design of geometrically-variable deep foundations constructed in multi-layered soils, a torsional load transfer method was presented using a finite difference model (FDM) framework. Simplified state-dependent spring models, relating the unit torsional resistance to the magnitude of relative displacement, were developed in consideration of soil-structure interface shear test results.

1.3 Organization of this Document

Chapter 2 of this report presents a brief literature review. Technical details regarding the engineering and construction of drilled shaft foundations are discussed, as well as the limited studies on the effect of high-strength reinforcement and permanent casing on performance. Efforts are made to describe shortcomings and data gaps in these studies. The literature review also describes some previous studies on the response of drilled shafts loaded in torsion, focusing on the available experimental investigations. The literature review concludes with a brief discussion of some experimental and analytical design methods for drilled shafts in axial, lateral, and torsional loads and a summary of those critical issues that require further study as addressed in this research.

Chapter 3 presents the research objectives and program established to improve the understanding of load transfer of drilled shaft foundations under axial, lateral, and torsional loading.

Chapter 4 presents the characterization of the test site used to perform the full-scale loading tests, including the geotechnical explorations, stratigraphy, and corresponding subsurface conditions.

Chapter 5 describes the full-scale torsional loading tests conducted on two instrumented drilled shafts used for support of mast-arm traffic signs and signals. The results of quasi-static monotonic and cyclic torsional loading tests on drilled shafts are presented. Based on the test data, the torsional load transfer along the test shafts is evaluated. Design procedures for the calculation of the ultimate total and unit torsional resistances of drilled shafts are proposed and resulting estimates compared against the resistances observed in this from the testing program and other studies reported in the literature.

Chapter 6 presents the development of a numerical framework for the simulation of torsionally-loaded, geometrically-variable deep foundations in multi-layered soils. Simplified torsional load transfer models are developed using torsional loading test data and available interface shear tests that account for hardening and softening as function of the state of the soil relative to its critical state and the surface roughness of the interface. Finally, parametric studies illustrate the role of various design parameters and demonstrate significant effects of nonlinear soil-structure response on the torsional behavior of deep foundations, including the effects of pressure-dependent softening at the soil-structure interface.

Chapter 7 describes the experimental setup used to conduct the full-scale axial and lateral loading tests, including a discussion of the shaft construction and the instrumentation used to monitor the performance of the test shafts.

Chapter 8 presents the results of the axial loading tests, including the axial load-displacement curves, the axial load transfer distributions, and the back-calculated *t-z* and *q-z* curves. Then, selected axial load transfer models are evaluated and modified to produce region-specific axial load transfer models for uncased drilled shafts. Finally, the effect of permanent casing on the axial response is discussed, and recommendations for axial shaft reduction with casing are developed based on available test data, soil conditions, and construction sequencing.

Chapter 9 describes the results of the lateral loading tests, including the performance at the head of each shaft, lateral displacement profiles, and the back-calculated curvature, moment, and soil reaction-displacement (*p-y*) curves. Back-calculated *p-y* curves for each shaft are compared and used, along with widely-available *p-y* curve models, to simulate the lateral response of each shaft to form a basis for the evaluation of model suitability and differences in interface friction.

Chapter 10 presents the interface and diameter effects on the *p-y* curves. Recommendations are made to account for these effects, set within the framework of a newly-developed, region-specific lateral load transfer model that can be implemented in commonly-used software.

Finally, Chapter 11 summarizes the results and findings of the completed work, and the proposal for the future work.

1.4 References

Reiter, M. (2008). *December 1–4, 2007 storm events summary*. Prepared for Weyerhaeuser Western Timberlands, Weyerhaeuser Company, Federal Way, WA.

2. LITERATURE REVIEW

2.1 An Introduction to Drilled Shaft Foundations

Drilled shaft foundations, also known as drilled piers, drilled caissons, caissons, cast-in-drilled-hole piles, bored piles, among other terms, are cast-in-place, reinforced concrete deep foundations constructed in a stabilized drilled borehole (Kulhawy 1991). Drilled shafts are capable of transferring loads from bridge or building superstructures to a competent bearing stratum; as such, they are designed to provide significant axial and lateral resistance, and for certain superstructures, torsional resistance. Drilled shafts have been used for a wide array of applications, including support for highway bridges, mast arm traffic sign and signal pole structures, landslide stabilization, and to support retaining walls and sound barriers.

Drilled shafts are distinguished from other types of deep foundations employed in transportation works, such as driven piles, micropiles, continuous flight auger piles and drilled displacement piles in that: (1) they are often significantly larger in size; (2) a single shaft is frequently used to support a single column without a pile cap; (3) they are frequently installed into a strong, stiff bearing layer to achieve adequate geotechnical resistance (Brown et al. 2010).

Drilled shafts can be used in urban settings where vibration tolerances are stringent or where shallow foundations could not provide sufficient bearing capacity (Gunaratne 2006). A convenient and cost-saving design feature of drilled shafts is the possibility of omitting the construction of pile caps for new foundations constructed near existing structures (Brown et al. 2010).

2.2 Studies of Drilled Shafts with Steel Casing

Permanent steel casing can be left in place in caving ground conditions, and also be utilized to provide additional stiffness (or rigidity) to the reinforced concrete drilled shaft. Steel casing provides significant flexural resistance and confinement to the concrete in-filled concrete, which leads to an increase of inelastic deformation capacity and better seismic performance (Roeder and Lehman 2012). This type of deep foundation is called as Cast-In-Steel-Shell (CISS) pile foundation or concrete filled steel tubes (CFT) and has been commonly used by the Departments of Transportation in Washington, California, and Alaska (Gebman et al. 2006, Roeder and Lehman 2012, Yang et al. 2012).

2.2.1 Impact of Permanent Steel Casing on Axial Capacity of Drilled Shafts

Limited axial loading tests have been conducted to study the impact of casing on axial capacity of drilled shafts and subsequently reported in the literature. The two studies available are summarized here. Owens and Reese (1982) conducted full-scale tests to investigate the effect of permanent steel casing on the axial capacity of drilled shafts. Six drilled shafts were tested. Four of them, designated G-1, G-2, G-3, and G-4, were constructed at a site in Galveston, Texas. Two shafts, designated E-1 and E-2, were constructed at an undisclosed site in eastern Texas. The soil profiles at the Galveston site and the eastern Texas site are shown in Figure 2-1 and Figure 2-2, respectively. In this section, only the comparisons for the uncased shafts G-1 and E-2, the partially cased shaft G-3, and the fully cased shaft E-1 are presented. Shaft G-1, which was 1.21 m (48 inches) and 18.3 m (60 ft) in diameter and length, respectively, was an uncased shaft. A 1.22-m (48-inch) casing was driven into a depth of 15.8 m (52 ft); then, an auger of 1.17-m (46-inch) diameter was used to excavate the soil inside the casing and to advance the hole to the depth of 18.3 m (60 ft). The steel casing was pulled out during placement of concrete. Shaft G-3, which was 0.91 m (36 inches) and 18.3 m (60 ft) in diameter and length, respectively, was constructed with diameter permanent casing installed to a depth of 12.2 m (40 ft). Inside a 1.07-m (42-inch) surface casing extended to a depth of 3 m (10 ft), a 0.91-m (36-inch) hole was augured to a depth of 10.7 m (35 ft); then the casing was screed into a depth of 12.2 m (40 ft). The excavation was continued with 0.83-m (34-inch) auger to the depth of 18.3 m (60 ft). Axial loads were applied in equal increments of 150 kN (15 ton). Figure 2-3 compares the maximum load transfer in shaft resistance versus depth for shaft G-1 and G-3. The maximum load transfer in the region 0 to 12 m (40 ft) for G-3 is much smaller than that for G-1.

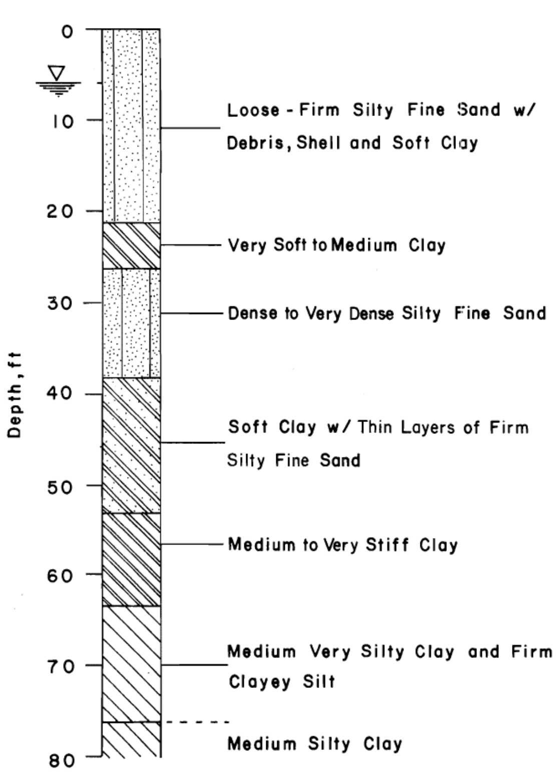

Figure 2-1 Soil profile at the Galveston site (after Owens and Reese 1982)

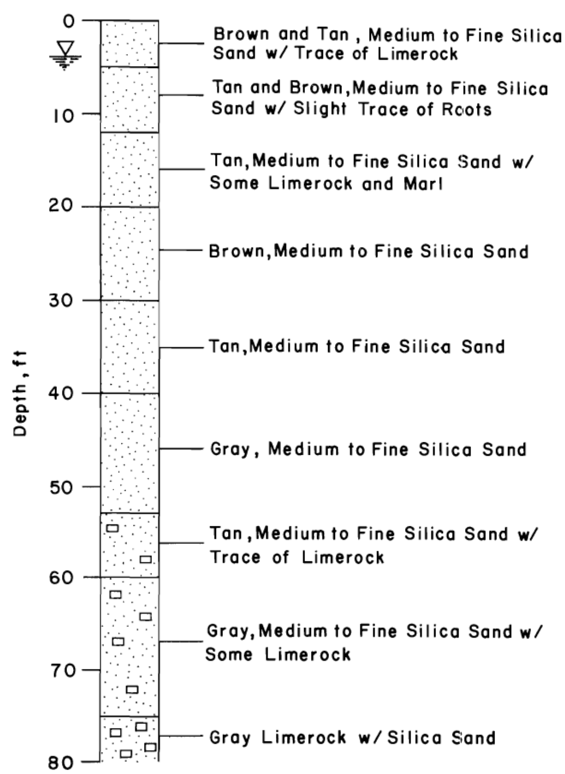

Figure 2-2 Soil profile at the Eastern site (after Owens and Reese 1982)

Comparison of the axial performance of shafts E-1 and shaft E-2 was also conducted; both of these shafts were constructed with a 0.91 m (36 inches) and 18.3 m (60 ft) diameter and length, respectively. Shaft E-1 was constructed with full-length casing. The casing was driven into ground and excavation was performed inside the casing. Shaft E-2 was installed without casing. In these tests, shaft E-1 carried a total load of 2,450 kN (246 tones) in shaft resistance; and 4,435 kN (445 tones) was carried by shaft E-2 in shaft resistance. A comparison of the ultimate load transfer in shaft resistance versus depth is shown in Figure 2-4. It reveals that the overall load transfer of the shaft E-2 is higher than that of the shaft E-1. Owens and Reese (1982) concluded that the capacity of the test shaft was significantly lower if the casing was left in place irrespective of whether the casing was driven or installed in an over-sized borehole. To mitigate the effects of the casing on the reduced shaft resistance, Owens and Reese (1982) recommended grouting of annular spaces that may develop in an over-drilled borehole. As shown in Figure 2-3, after grouting of the top 12 m of shaft G-3, the load transfer increased significantly in the grouted region. If the casing was installed using impact of vibratory driving, then grouting is not feasible. Drilled shafts with driven casing may require larger diameters, longer lengths, or installation in groups in the event the axial capacity is not sufficient for a given substructure element.

Camp et al. (2002) conducted axial loading tests on a total of 12 instrumented drilled shafts at three different test sites in Charleston, South Carolina. The test shafts were either 1.8 or 2.4 m (corresponding to 5.9 or 7.9 ft) in diameter with embedded length of either 30 or 46 m (corresponding to 98 or 151 ft). Eight of the drilled shafts were constructed with permanent casing, which was driven though loose sands and/or soft clays into Cooper Marl. The length of casing varied from 17.7 to 23.3 m (corresponding to 58 or 76 ft). Unit shaft resistances for both cased and uncased portion of the test shafts into the Cooper Marl were reported for three of the test shafts (designated MP1, MP3, and MP4) and summarized in Table 2-1. It was found that for the Cooper Marl, a stiff calcareous clay or silt (CH/MH), the unit shaft resistance developed for the cased portion was substantially lower than that for the uncased portion.

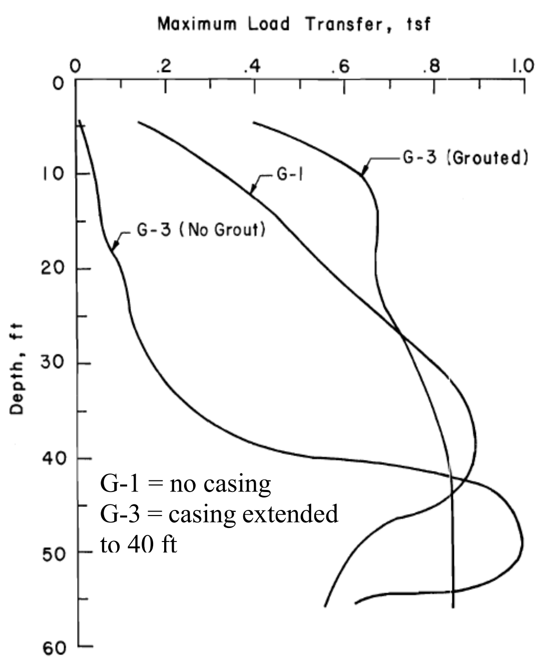

Figure 2-3 Load transfer versus depth (after Owens and Reese 1982)

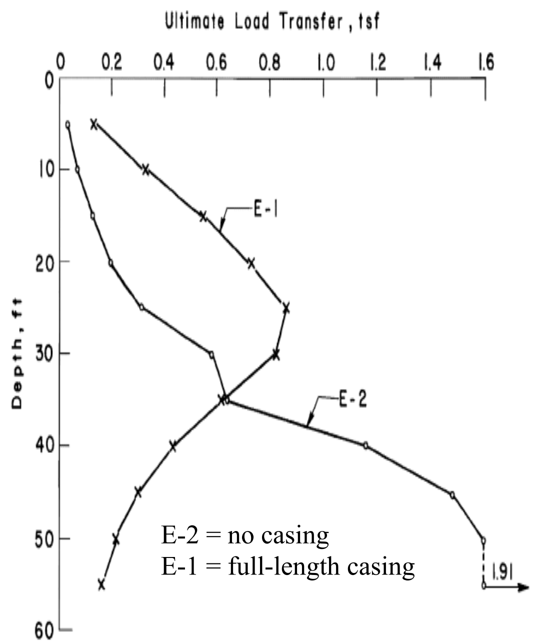

Figure 2-4 Load transfer versus depth (after Owens and Reese 1982)

Table 2-1 Comparison of the unit shaft resistance at cased portion and uncased portion for the axial loading test conducted by Camp et al. (2002).

Shaft	Unit Shaft Resistance, kPa (psf)		Ratio of Unit Shaft Resistance at Cased Portion over uncased Portion
	Cased Portion	Uncased Portion	
MP1	32 (668)	163 (3,404)	20%
MP3	100 (2,089)	172 (3,592)	58%
MP4	47 (982)	192 (4,010)	24%

2.2.2 Impact of Permanent Steel Casing on Lateral Capacity of Drilled Shafts

A number of lateral loading tests and lateral load transfer studies have been performed on drilled shafts with and without permanent casing (e.g., Welch and Reese 1972; Bierschwale et al. 1981; Davidson et al. 1982; Mayne et al. 1992; Duncan et al. 1994;.Wallace et al. 2001; Hulsey et al. 2011). Brown and Camp (2002) describe some lateral loading test results of drilled shafts with and without casing, and showed that the uncased shaft exhibited greater flexural strains and at shallower depths than the cased shaft; however, no detailed load transfer analyses were presented. The lateral performance of drilled shafts with and without permanent casing in similar soil conditions needs to be further studied.

2.2.3 Design Methods for Concrete Filled Steel Tubes (CFTs)

Few guidelines on the design of concrete filled tubes (CFTs) are available, particularly regarding the calculations of the strength and stiffness of these members (Roeder and Lehman 2012). The American Institute of Steel Construction (AISC) LRFD (AISC 2005), the American Concrete Institute (ACI) 318 Specifications (ACI 2008), and the American

Association of State Highway and Transportation Officials (AASHTO) LRFD Specifications and the Seismic Design Guidelines (AASHTO 2009, 2007) provide three approaches to estimate the strength and stiffness of CFT members. Roeder and Lehman (2012) compared these three codes in term of estimation of flexural resistance, stability limits, and effective stiffness; a review of their findings follows.

2.2.3.1 Estimation of Flexural Resistance

The AISC Specification (2005) allows using the plastic stress distribution (Figure 2-5a) or the strain compatibility methods (Figure 2-5b) to predict the flexural and axial resistance of circular CFT elements. The plastic distribution method assumes that: (1) each component of the section (i.e., the concrete and longitudinal steel), has reached the maximum plastic stress, and (2) no slip occurs between the steel and the concrete. As shown in Figure 2-5a, the uniform compressive stress of concrete is $0.95f'_c$ which is higher than the typical value of $0.85\,f'_c$ due to the confinement provided by steel casing to the concrete, and the tensile and compressive stresses of the steel are F_y. Then, the axial loading and flexural capacity can be estimated by equaling the stresses over the cross-section.

The strain compatibility method assumes that (1) no slip occurs between the concrete components and the steel components, and (2) the strain distribution is linear, as show in Figure 2-5b. The commonly used material model for the steel is elastic-perfectly plastic model and a parabolic curve for the concrete. The axial stress and flexural strength is for a maximum compressive strain in the concrete of 0.003.

The ACI (2008) method (Figure 2-5c) is similar to the AISC strain compatibility method. In this method, the compressive stress of concrete is assumed to be $0.95f'_c$ and acting along a depth $\beta_1 dc$, where dc is the depth from the neutral axis to the maximum compressive strain and β_1 is a function of concrete strength.

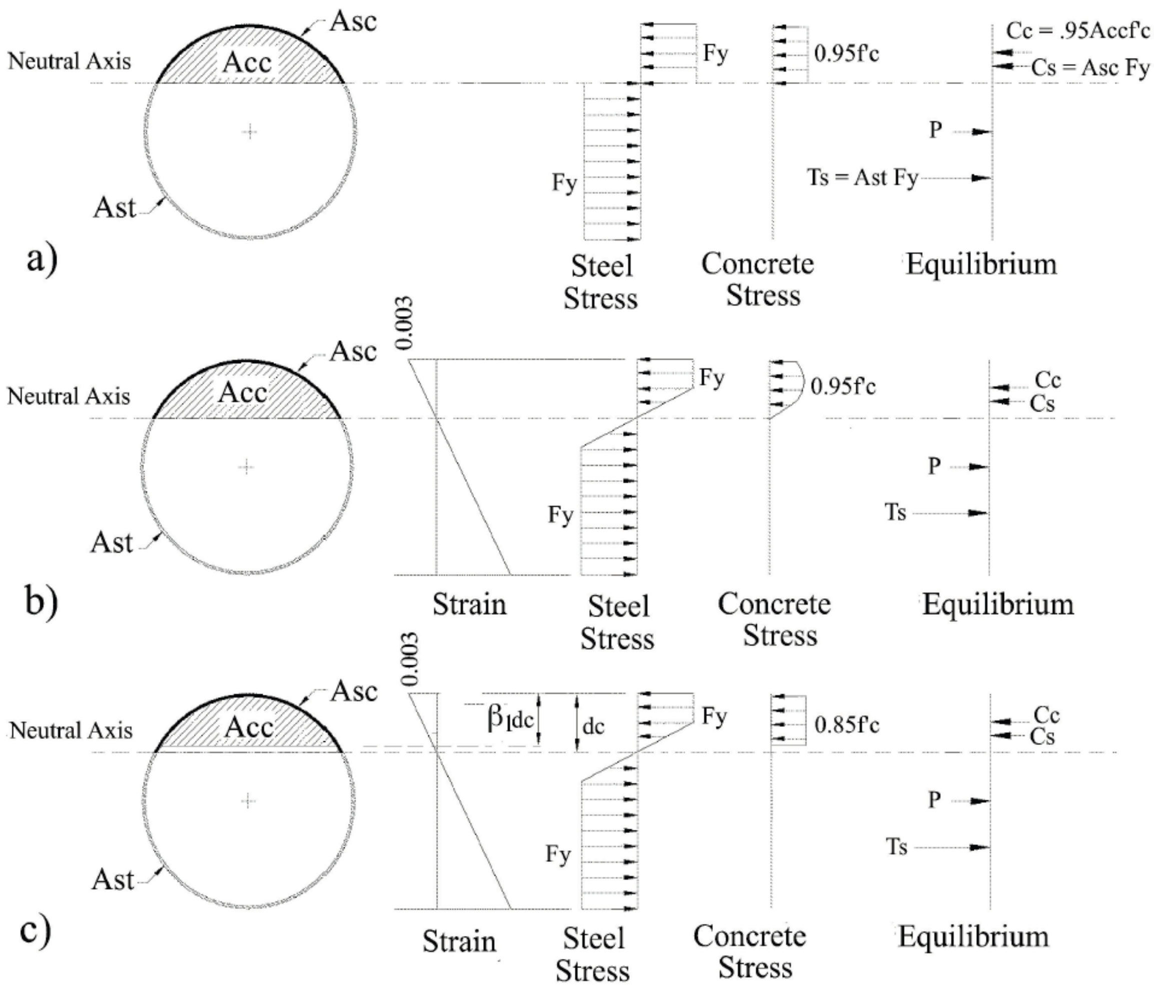

Figure 2-5 Approaches for estimating of resistance of CFT; a) AISC plastic stress distribution method, b) AISC strain compatibility method, and c) ACI method (after Roeder and Lehman 2012).

The AASHTO LRFD Specification (2009) assumes that the axial load capacity is determined by the concrete compressive stress of $0.85f'_c$ and the yield stress of steel. The AISC axial load-bending moment interaction curves, as shown in Figure 2-6, can be used for CFT. The AASHTO Guide Specification for LRFD Seismic Bridge Design provides a similar design method as the AISC plastic stress distribution method.

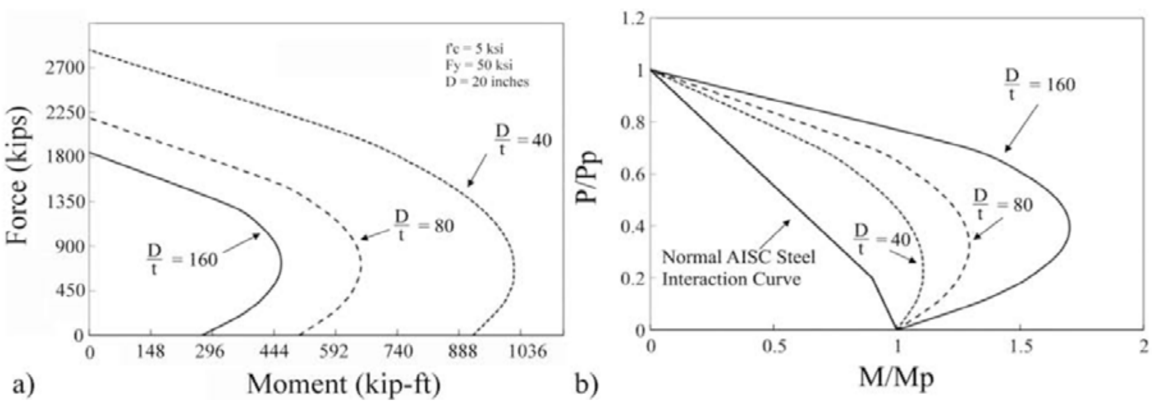

Figure 2-6 Axial load-bending moment interaction curves for CFT: (a) plastic stress distribution, (b) normalized (after Roeder and Lehman 2012).

2.2.3.2 Stability Limits

The AISC, ACI, and AASHTO LRFD Specifications provide expressions to limit local buckling of the tube through use of Eqs. (2.1), (2.2), and (2.3), respectively.

$$\frac{D}{t} \le 0.15\frac{E}{F_y} \tag{2.1}$$

$$\frac{D}{t} \le \sqrt{8\frac{E}{F_y}} \tag{2.2}$$

$$\frac{D}{t} \le 2\sqrt{\frac{E}{F_y}} \tag{2.3}$$

where D = diameter of the tube, t = thickness of the tube, E = composite elastic modulus of the CFT, and F_y equals the yield strength of the steel. Additionally, the AISC and AASHTO provisions suggest that calculation of column buckling may be performed using:

$$P_{cr} = 0.658^{P_o/P_e} P_o \qquad \text{for stocky columns,} \qquad P_e < 44P_o \tag{2.4}$$

$$P_{cr} = 0.877 P_e \qquad \text{for slender columns,} \qquad P_e > 44P_o \tag{2.5}$$

where P_e = the Euler buckling load, and P_o= ultimate axial crushing load, given by:

$$P_o = 0.95 f_c^{'} \cdot A_c + F_y \cdot A_s \tag{2.6}$$

where A_c and A_s = areas of concrete and steel, respectively. For circular CFT columns, the resistance factor is 0.75; and the axial load ratio P/P_o in interaction curves (i.e., Figure 2-6) is limited to 0.75 in provisions (Roeder and Lehman 2012).

2.2.3.3 Effective Stiffness

The AISC, ACI, and AASHTO LRFD Specifications describe different methods to estimate the effective member flexural rigidity (EI_{eff}) of CFT, given by Eqs.(2.7), (2.8), and (2.9), respectively:

$$EI_{eff} = E_s I_s + E_c I_c \left(0.6 + \frac{A_s}{A_s + A_c} \right) \tag{2.7}$$

$$EI_{eff} = E_s I_s + \frac{0.2 E_c I_g}{1 + \beta_d} \tag{2.8}$$

$$EI_{eff} = E_s I_s + 0.4 \frac{E_c A_c}{A_s} I_s \tag{2.9}$$

where E_s and E_c = the elastic modulus of the steel and concrete, respectively, I_s and I_c = the moment of inertia of the section for the steel and concrete, respectively, I_g = moment of inertia of the gross concrete section, and β_d = a parameter that is usually approximately 1.0.

2.3 Related Studies on High-Strength Reinforcement

Commonly used types of reinforcing steels for drilled shaft foundations are summarized in Table 2-2. The yield strength of the steel used in the reinforcement cages ranges from 280 MPa (40 ksi) to 420 MPa (60 ksi). In order to fulfil structure requirements, the number and section area of the steel reinforcement can be great, which leads to reduced rebar spacing and difficulty for concrete to flow through the reinforcement. This may cause voids in the shaft and can result in poor structural and geotechnical performance, depending on a given loading case (serviceability vs. strength limit) or location. In cases where a significant number of bars are required, high strength steel may be used to substitute the lower strength steel which can in turn reduce the number or size of the steel reinforcement bar and increase the rebar spacing.

Table 2-2 Reinforcing steel recommended for drilled shaft (Brown et al. 2010).

Designation	Description	Yield Strength, f_y, MPa (ksi)
AASHTO: M31 ASTM: A615	Deformed and plain billet-steel bars	280/420 (40/60)
AASHTO: M42 ASTM: A616	Deformed and plain rail-steel bars	350/420 (50/60)
ASTM: A706	Deformed low-alloy steel bars	420 (60)

For the design of reinforced concrete structures, the yield strength values of steel are limited to 550 MPa (80 ksi) and 515 MPa (75 ksi) by the ACI edition of ACI 318 (2008) and the AASHTO LRFD Bridge Design Specification (2007), respectively. The use of 690 MPa (100 ksi) steel yield strength is permitted only for the spiral transverse reinforcement in compression members (ACI 318 2008). These limits were developed in consideration of the limiting strain in the concrete and considerations for crack development and limitation of crack width under service loads; the limitation of the maximum stress in steel members to a strain of 0.3% is thought to facilitate the limitation of strain in the concrete (Shahrooz et al. 2011). Of note, both ACI 318 (2008) and AASHTO LRFD Bridge design Specification (2007) limit only the value of the yield strength that may be used in design; these codes do not exclude the used of higher strength grades of steel (Zeno 2009).

For a beam or column, using of high-strength rebar may increase the structural performance. Hassan et al. (2008) conducted tests with six large-size reinforced concrete beams with either conventional steel of Grade 60 (f_y = 420 MPa) or high-strength steel microcomposite multistructural formable (MMFX) steel (f_y = 827 MPa) and found that the beams with high-strength steel had higher shear strength (which increased as much as 80%) and less stress area (40% less). Trejo et al. (2014) and Barbosa et al. (2015) studied the seismic performance of 0.6-m (24-inch) diameter circular reinforced concrete bridge columns using ASTM A706 Grade 60 and Grade 80 reinforcement and found that comparing with Grade 60 columns, Grade 80 columns had equal or greater maximum drift ratio, and that both grades exhibited similar column drift (i.e., lateral displacement) and ductility. However, no axial or lateral loading test data have been found in the literature for drilled shafts constructed with high-strength internal reinforcement.

2.4 Torsional Loading Tests Reported in the Literature

Compared to the axial and lateral loading tests on deep foundations, the availability of torsional loading tests is relatively limited. The available torsional loading tests on full-scale driven piles and drilled shafts, as well as scaled single- and multi-*g* piles and shafts are described in this literature review.

2.4.1 Torsional Loading Tests on Small-Size Model Piles and Drilled Shafts

Poulos (1975) performed a series of torsional loading tests on four solid aluminum piles driven in Kaolin clay. The diameter and length of each pile were 25.4 mm and 502 mm, 25.4 mm and 254 mm, 19 mm and 527 mm, and 19 mm and 298 mm (corresponding to 1.0 in and 19.75 in, 1.0 in and 10 in, 0.75 in and 20.75 in, and 0.75 in and 11.75, respectively). All piles were driven into the soil to full embedment. The rotation of the test piles and applied torque were monitored. Relationship between the applied torque and rotation from test was reported, as shown in Figure 2-7. Although all of the piles were rotated 2° (0.035 radians), Poulos (1975) reported test results for smaller rotations. As shown in Figure 2-7, no definitive peak was observed for the torque-rotation curves.

Dutt (1976) and Dutt and O'Neill (1983) performed torsional loading tests using two circular aluminum piles of 48 mm (1.9 in) external diameter and 2.5 mm (0.1 in) wall thickness and two square piles of 51 mm (2.0 in) outside dimensions and 3.2 mm (0.125 in) wall thickness. The total length of each pile was 1.7 m (5.5 ft) with 0.15 m (6 in) above ground surface. Owing to the focus on drilled shafts in this report, only the results of the test on the circular pile are summarized. The test piles were installed by placing the air-dried sand around the piles. Both loose and dense sand conditions were considered with relative density of 21 and 88%, respectively. After the torsional loading tests on the model piles were concluded, the same model piles were removed and then driven into the soil, and torque applied so as to assess the differences in the torque-rotation response due to the construction method.

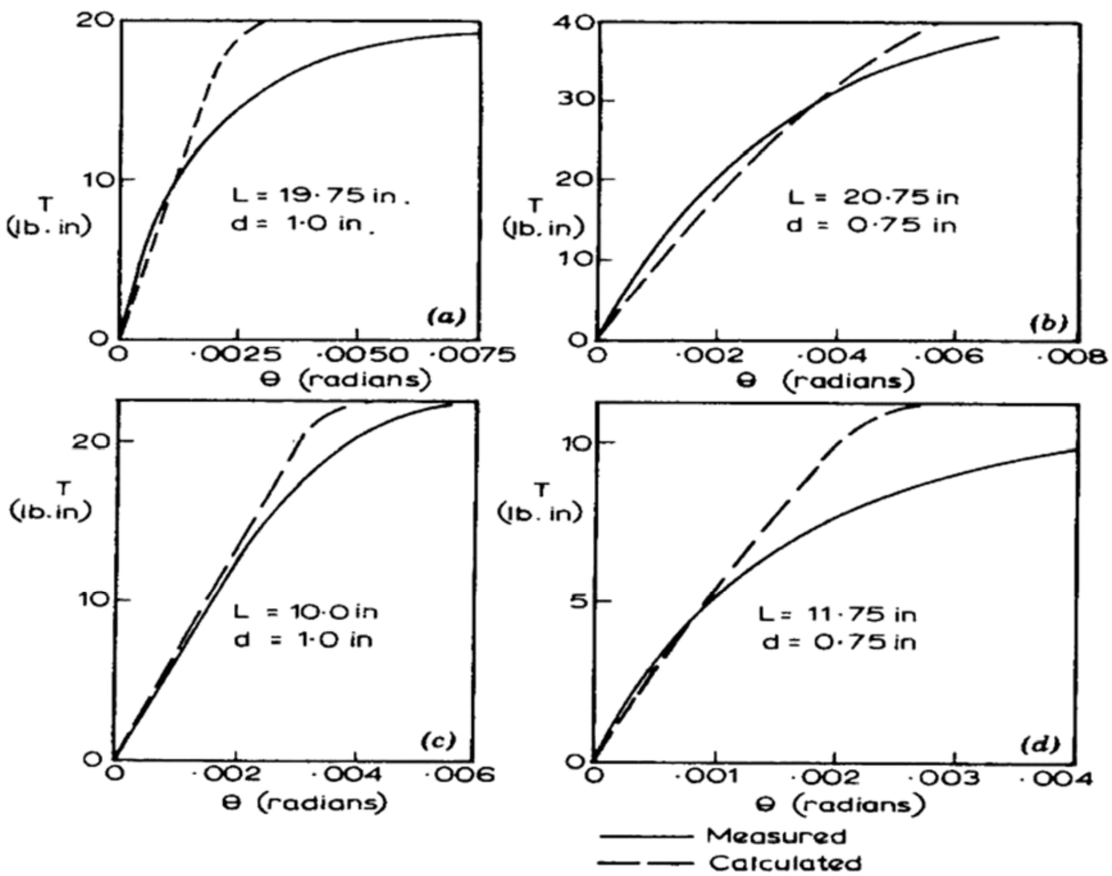

Figure 2-7 Relationship between torque and rotation (after Poulos 1975). Note: 0.005 radians equals 0.29 degrees.

Resistance strain gauges were installed at four different elevations of the circular pile to measure the shear strains. However, valid data was only obtained from the pile that was embedded (as opposed to driven) in the dense sand. The relationship between torque and pile head twist (Figure 2-8) indicated that: (1) an increase of approximately four-fold in relative density from the loose to the dense state led to a less than a two-fold increase in the apparent pile head torque for the circular pile at failure, and (2) the torsional resistance for the driven pile was slightly larger than that for the embedded condition, which was due to the vibration-induced densification caused by driving. Based on the torque distribution for circular pile embedded in dense sand, the torsional resistance offered by the base of the pile was insignificant, if not zero. Relationship between the torsion transfer and twist at different depths, as shown in Figure 2-9, were computed for circular pile embedded in dense sand. From this figure, the apparent ultimate torque transferred to the soil increased with depth, indicating the torque transferred to the soil is a function of the effective stresses.

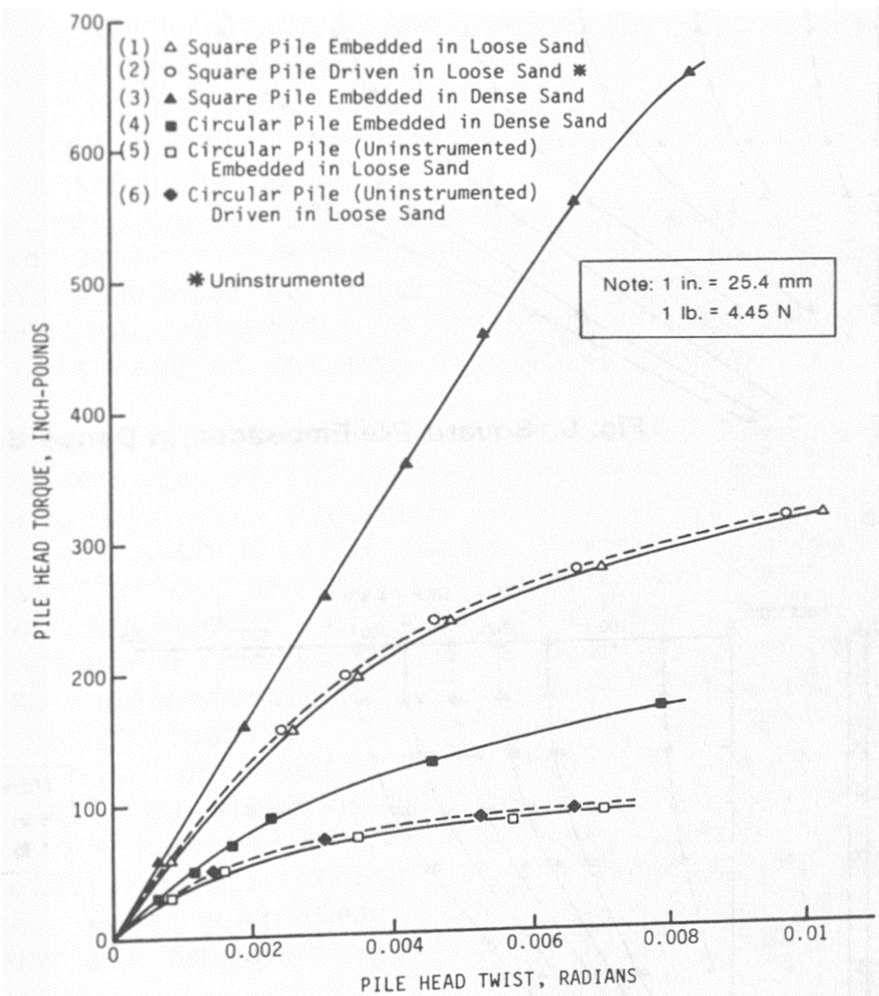

Figure 2-8 Pile-head torque-twist curves (after Dutt and O'Neill 1983)

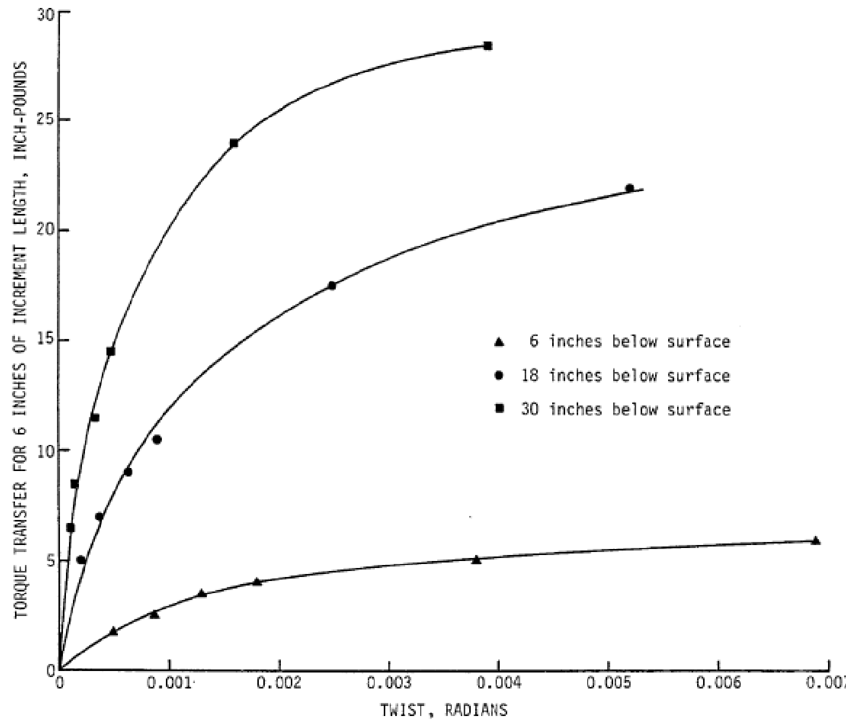

Figure 2-9 Shear stress-strain curves at different depth for circular pile embedded in dense sands (after Dutt and O'Neill 1983)

Randolph (1983) described torsional loading tests on a steel pile of 10.6 mm (0.42 in) diameter and a polypropylene pile of 11.2 mm (0.44 in) diameter jacked 300 mm (11.8 in) into normally consolidated Kaolin clay to study the effect of the flexibility of a pile on its performance under monotonic and cyclic loading. The shear modulus of the polypropylene pile was between 0.30 and 0.44 GPa (44 to 64 ksi), whereas the shear modulus of the steel pile was about 77 GPa (11×10^3 ksi). To achieve a consistent surface texture for the different piles, both piles were coated with thin layer of araldite (an adhesive) and fine sand. Monotonic loading was applied on the piles followed by cyclic loading. Cyclic loading tests were performed between 2 and 50% (point A in Figure 2-10a) and between 2 and 63% (point B in Figure 2-10a) of the peak capacity for the steel pile. For the polypropylene pile, the cyclic loading tests were conducted between 3 and 53 (point A in Figure 2-10b), 3 and

73% (point B in Figure 2-10b), and 3 and 93% (point C in Figure 2-10b) of the peak capacity.

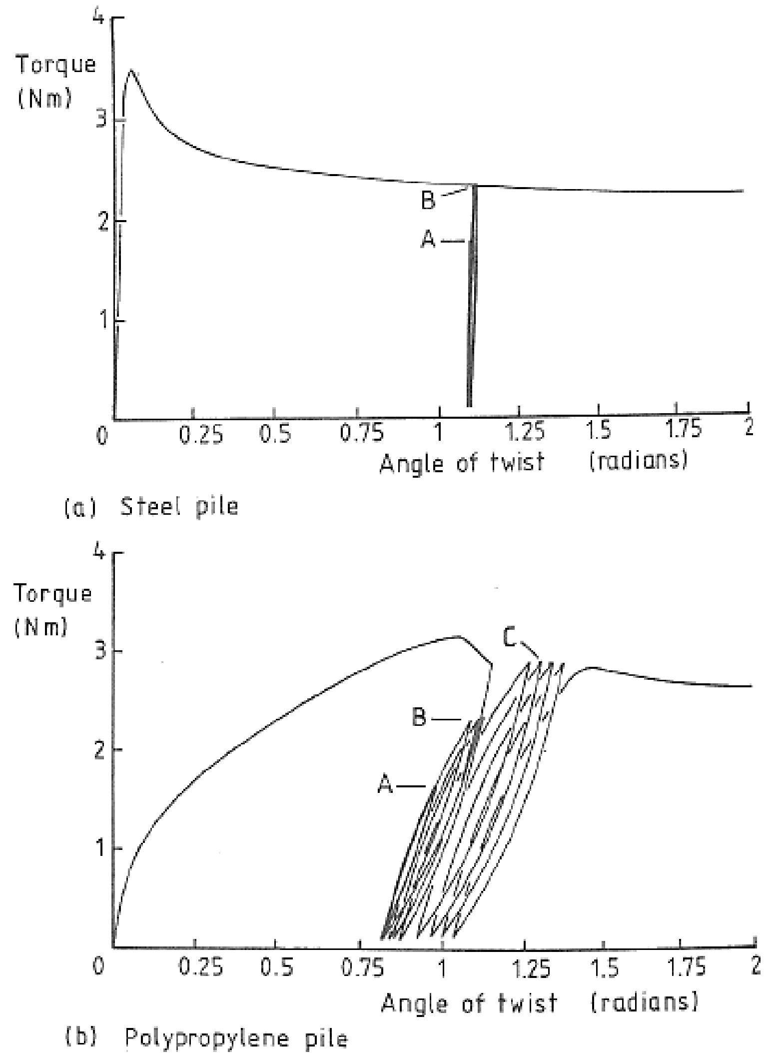

Figure 2-10 Torque-twist relationship for (a) steel pile and (b) polypropylene pile (after Randolph 1983)

The torque-twist relationships for both test piles are shown in Figure 2-10. The steel pile, which had higher stiffness, reached its peak at the rotation of about 0.05 radians (3°). However, the torsional response was softer for the polypropylene pile, which achieved its peak value at the rotation of about 1.05 radians (60°). A reduction in torsional resistance was observed beyond the peak capacity. During the cyclic loading, no obvious degradation of torsional resistance was observed for the steel pile. For the polypropylene pile, the initial stiffness seemed constant during the cyclic loading; and permanent rotation was developed during every loading cycle.

Tawfiq (2000) used a 1.2 m (4 ft) diameter and 1.5 m (5 ft) deep steel chamber to perform torsion tests for a small-scale shaft model in sand. The shaft, which was made of plain concrete, was 508 mm (20 in) long with a diameter of 102 mm (4 in). Two sets of loading tests were conducted: the first consisted of a set of tests that allowed the development of both toe and shaft resistance, whereas the second set of tests was conducted to evaluate base and shaft resistance separately. The toe resistance was eliminated by placing two greased metal plates at the shaft bottom; and the side friction was eliminated by enlarging the borehole so that the shaft surface was separated from the surrounding soil. As shown in Figure 2-11, the tests by Tawfiq (2000) indicated that the shaft resistance comprised about 91 percent of the total available torsional resistance (~27 ft-lbs or 0.04 kN-m) at approximately two radians (approximately 115 degrees). On the other hand, the toe resistance was not observed to be larger than 5 ft-lbs (0.007 kN-m) when evaluated alone, and about 2.5 to 3 ft-lbs (0.0034 to 0.004 kN-m) when evaluated with shaft resistance.

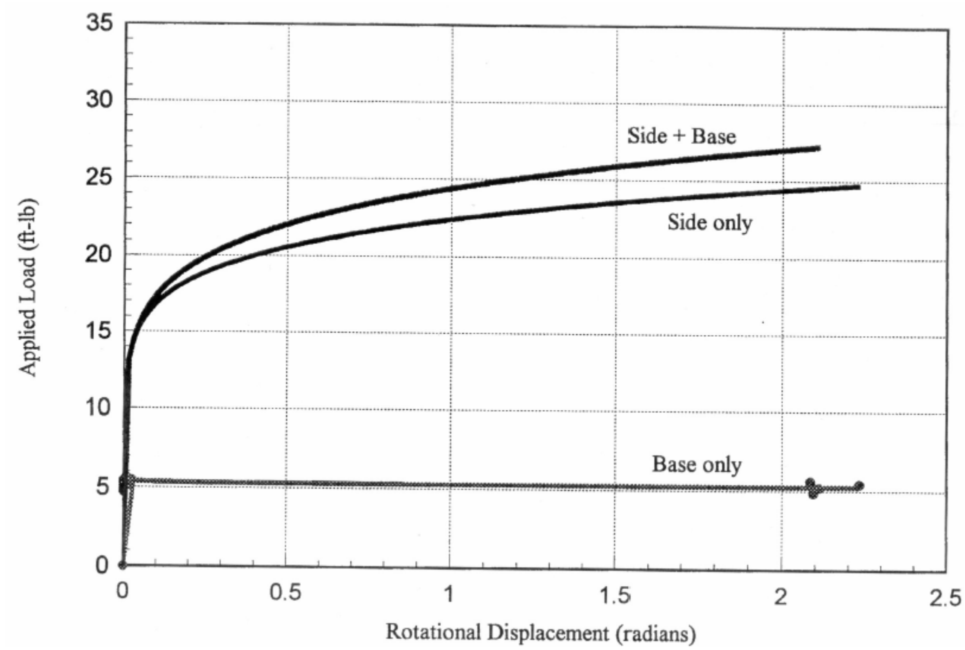

Figure 2-11 Relationship between torque and rotation (after Tawfiq 2000)

2.4.2 Torsional Loading Tests on Centrifuge Model Piles and Shafts

Bizaliele (1992) conducted static and cyclic torsion tests on aluminum model piles of 21 mm (0.83 in) diameter, 1 mm (0.04 in) wall thickness, and 340 mm (13.4 in) embedded length in sands. The total length of the model pile was 380 mm (15 in). With the chosen acceleration level of 50*g*, the model piles simulated prototype piles of 1.05 m (41 in) diameter and 17.0 m (56 ft) embedded length. Strain gauges were mounted at 45° to the axis of the pile at five levels. The sand used in this test was uniformly-graded with an effective grain size D_{10} of 0.12 mm and angle of internal friction of 38°. The maximum and minimum dry density was 1.69 and 1.42 g/cm^3, respectively. The static pile head torque-twist behavior is depicted in Figure 2-12. A linear response was observed for applied torque up to 8 N-m (6 lb-ft); the response transitioned to nonlinear for greater torsion. The maximum torque was approximately 28 N-m (24 lb-ft) at approximately 0.07

radians of pile head twist, followed by softening. The shaft resistance at each level was calculated using the measured shear strain. Figure 2-13 shows the magnitude of torsional shaft resistance at different depths (*n.b.*, L = depth and r = shaft radius) as a function of the number of cycles. Results indicated that a small change in shaft resistance was observed for the first 10 cycles. After that, little variation of the shaft resistance with additional cycling was observed.

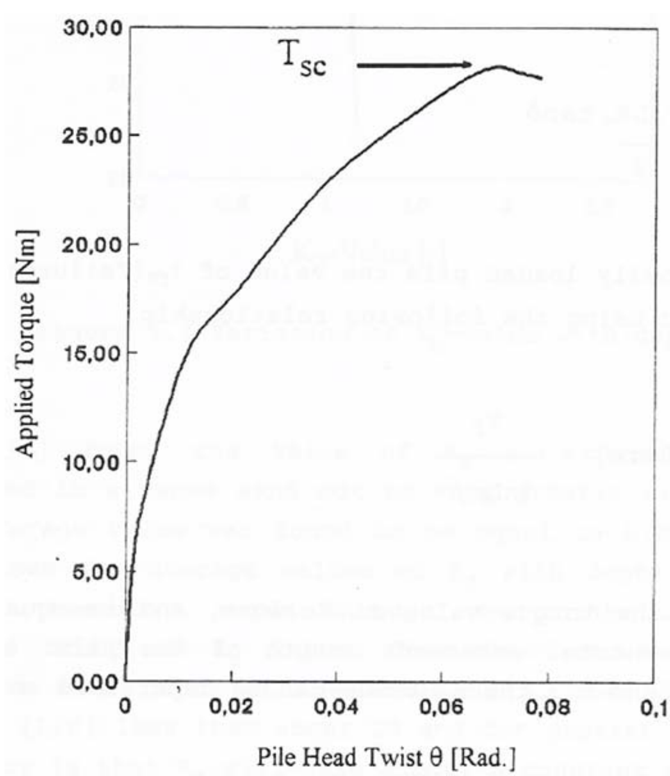

Figure 2-12 Static pile head torque-twist behavior in model scale (after Bizaliele 1992)

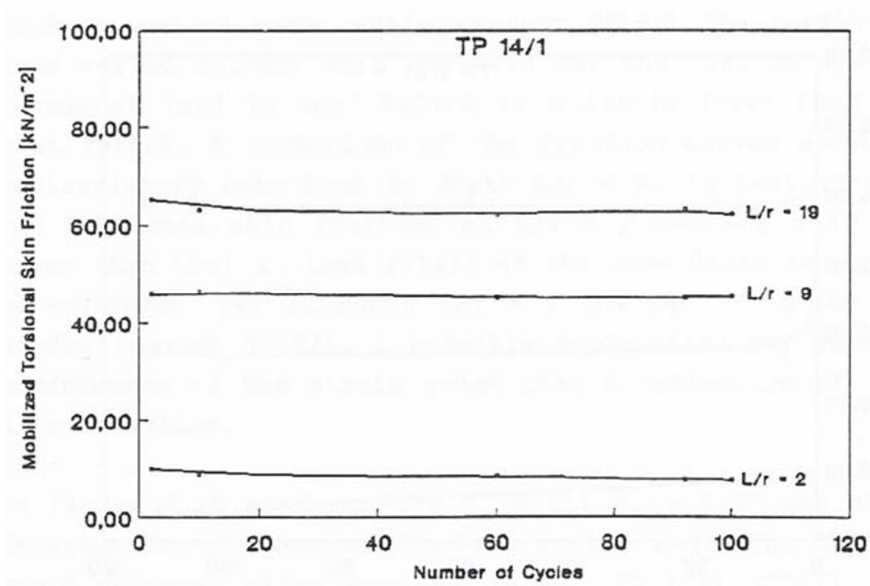

Figure 2-13 A typical distribution of torsional shaft resistance at different depth as a function of the number of cycles (after Bizaliele 1992)

Laue and Sonntag (1998) performed torsion tests on hollow aluminum model piles with a diameter of 15 mm (0.6 in) and a length of 170 mm (6.7 in) in sand. The acceleration level was 100*g*, and the model piles represent prototype piles of 1.5 m (5 ft) diameter and 17.0 m (56 ft) length. Two types of sand in a dense state were used: Normsand (angle of internal friction = 38°) and fine Fontainebleau sand (angle of internal friction = 37°). Figure 2-14 shows the torque-rotation response under different soil-shaft interface and soil conditions as summarized in Table 2-3. The torque-rotation response of smooth-shaft TP 2.1 was consistent with a hyperbolic relationship, whereas the rough-shaft TP 3.2 exhibited a near-linear perfectly-plastic response; neither pile exhibited post-peak softening. The torque-rotation response of the smooth-shaft pile TP 6.1 was also consistent with a hyperbolic curve, requiring significant rotation to achieve the peak resistance. However, the rough-shaft TP 6.2 achieved a peak torsional load at approximately 1° of rotation, as a result of the rough interface being modeled. The results show that the relative value of roughness and gradation influenced the torsional resistance of pile. Tests with combined axial and torsional loads were performed and found that the existing axial loads increased the torsional capacity for the smooth pile in Normsand from about 1.8 N-m (1.3 lb-ft) to 2.8 N-m (2.1 lb-ft). A cyclic loading test was also performed. Figure 2-15 shows the results of the first four cycles; the initial stiffness and post-yield slope for each loading cycle were quite similar.

Table 2-3 Summary of test conditions evaluated by Laue and Sonntag (1998).

Test Designation	Shaft Interface Condition	Soil Evaluated
TP 2.1	Smooth	Normsand
TP 3.2	Rough	Normsand
TP 6.1	Smooth	Fine Fontainebleau sand
TP 6.2	Rough	Fine Fontainebleau sand

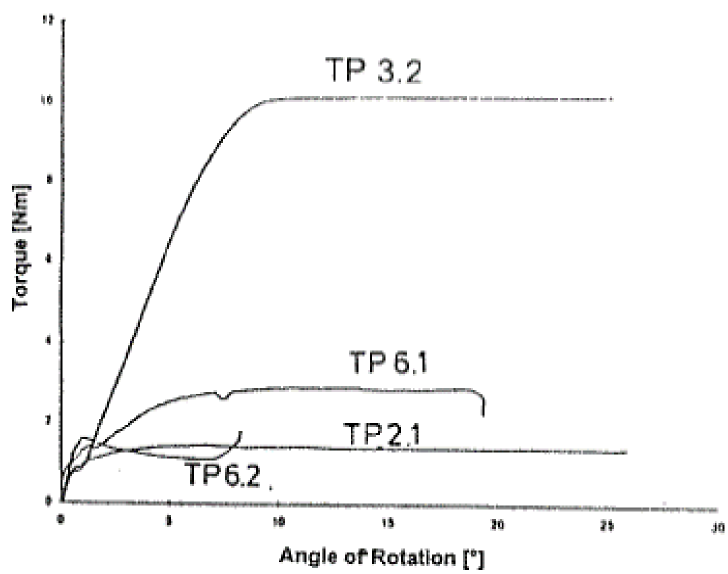

Figure 2-14 Comparison on the torque-rotation response (after Laue and Sonntag 1998)

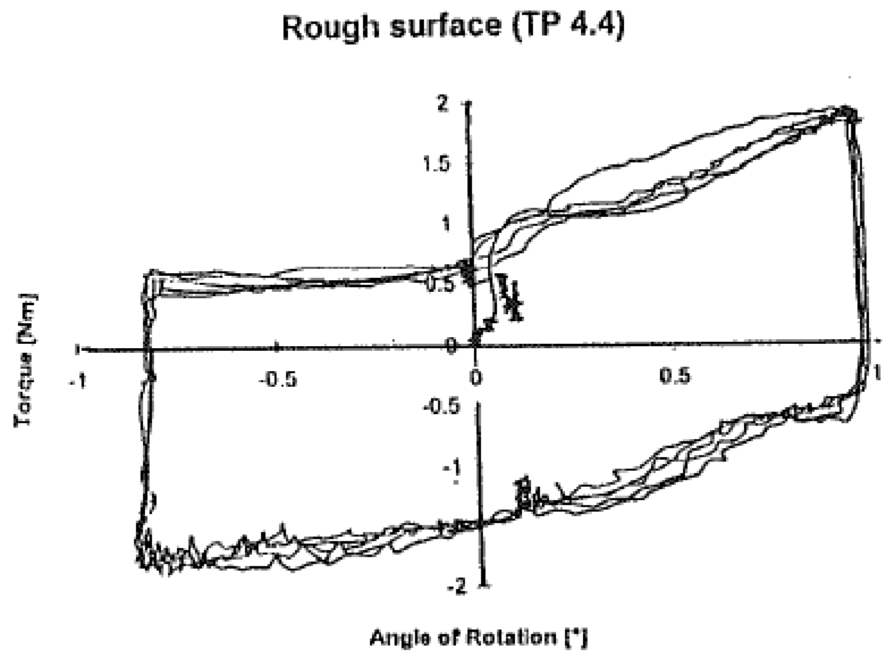

Figure 2-15 Pile under cyclic torsional loading (after Laue and Sonntag 1998)

A number of centrifuge tests on high mast sign/signal structures (mast arm, pole, and drilled shaft) were conducted in University of Florida to determine the optimum depth of drilled shafts subjected to combined torsion and lateral loads (McVay et al. 2003, McVay and Hu 2003, and Hu 2003). The prototype shaft diameter was 1.5 m (5 ft), and the prototype embedment length ranged from 4.6 m (15 ft) to 10.7 m (35 ft). The shafts were constructed in dry and saturated silica-quartz sand from Edgar, FL, compacted to loose, medium dense, and dense conditions. To investigate the effect of various construction methods, steel casings and wet methods, using bentonite slurry and KB polymer slurry produced by KB Technologies Ltd. (http://www.kbtech.com), were evaluated. Table 2-4 summarizes the centrifuge tests. Torque and lateral load were applied simultaneously. Some typical test results of the relationship between torque and shaft rotation from Hu

(2003) are shown in Figure 2-16. No definitive peak was observed for the shafts constructed using both types of slurries. The results of the centrifuge tests indicated that the magnitude of lateral loads had little effects on the torsional capacity; and the construction method exhibited significant effects on the torsional response of the test shafts.

Table 2-4 Summary of the centrifuge tests conducted in University of Florida.

	McVay et al. (2003)	McVay and Hu (2003)	Hu (2003)
Construction Method	Steel casings and wet methods using bentonite slurry	Wet methods using polymer slurry	Wet methods using bentonite and polymer slurry
Soil state with relative density	Loose (29%), medium dense (51%) and dense (64%)	Loose (34%) and dense (69%)	Loose (34%) and dense (69%)
Prototype embedment length m (ft)	4.6, 7.6, and 10.7 (15, 25, and 35)	7.6 and 10.7 (25 and 35)	7.6 and 10.7 (25 and 35)

Zhang and Kong (2006) studied torsional load transfer using aluminum tubes of 300 mm (1 ft) in length, 15.7 mm (0.6 in) in outside diameter, and 0.9 mm (0.035 in) in wall thickness under 40*g* acceleration. The prototype length, outside diameter, and wall thickness for this level of acceleration was equal to 12 m (39 ft), 628 mm (24 in), and 36 mm (1.4 in), respectively. A quartz-based uniform sand with D_{50} = 0.14 mm was used. The relative densities evaluated were 32% and 75% to represent the loos and dense condition, respectively. The test piles were instrumented with strain gauges along the length of model piles. The test piles were pushed into the sand bed after the centrifuge was spun to 40 *g* and the ground settlement ceased to develop. The embedded length of the prototype pile was 10.8 m (35 ft). Six tests were performed with various loading rates (i.e., 1, 3, and 8 degree/s)

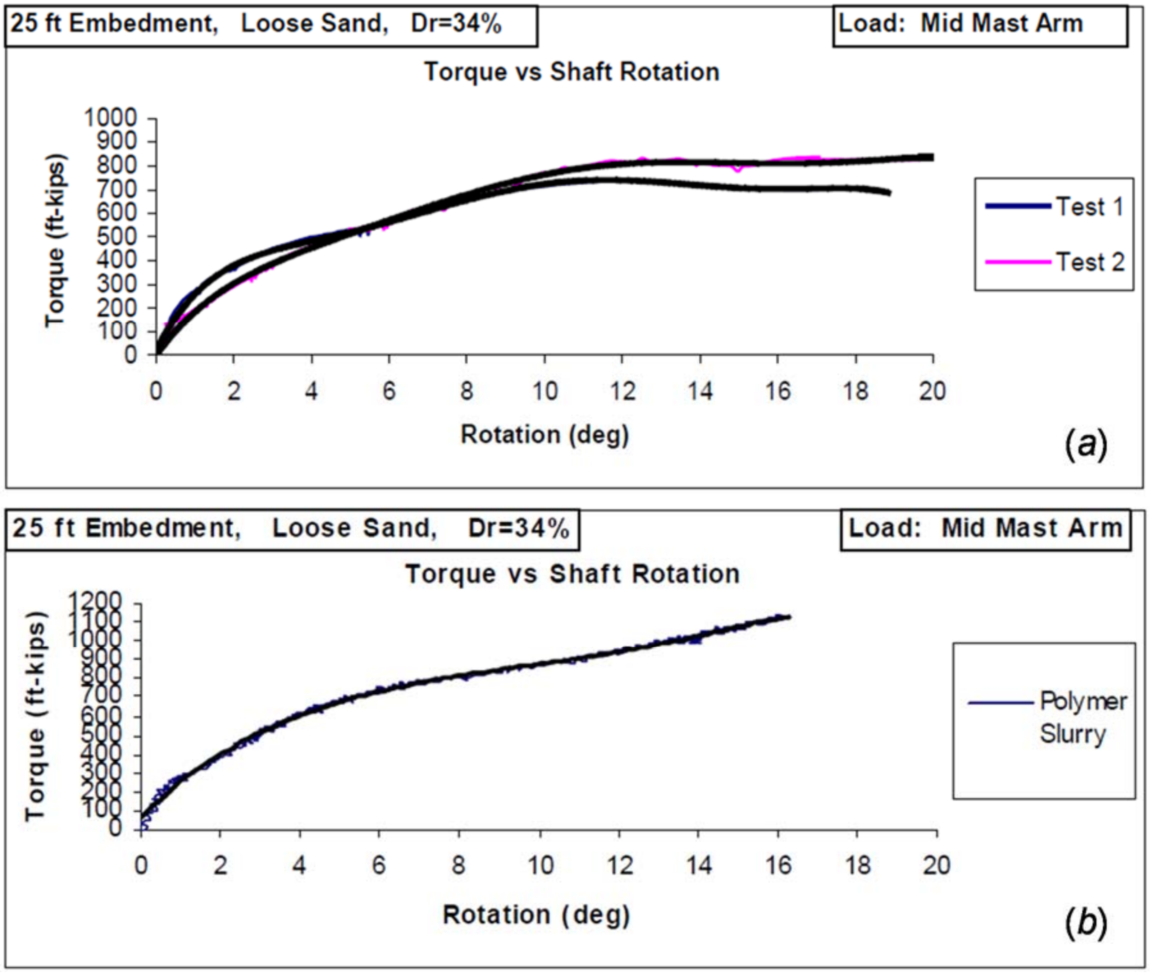

Figure 2-16 Torque-shaft head rotation response for shafts constructed using (a) bentonite and (b) polymer slurry with 25 ft embedment length in loose sand (after Hu 2003)

for each of the two relative densities, for a total of 12 tests. The torque-twist curves are shown in Figure 2-17, and indicate an approximately hyperbolic relationship. With a rotation of 1°, the applied torque was about 75% and 57% of the torsional capacity in the loose and dense sand, respectively. The torsional resistance was almost fully mobilized at approximately 4° for all of the cases. As expected, the relative density of the sand had a significant influence on the torsional resistance. Figure 2-18 displays the torque distribution along pile shaft at the loading rate of 1.0 degree/second. For this case, the toe resistance contributed 23% and 40% of the total torsional resistance in the loose and dense sands, respectively. However, this finding is not consistent with the results from Tawfiq (2000) and Dutt and O'Neill (1983), in which the contribution of toe resistance was less than 10%. The manifestation of the toe resistance in the centrifuge test could be a result of the downward acceleration of the sand deposit, which possibly imparted a drag load due to downward movement relative to the shaft.

2.4.3 Torsion Tests on Full-scale Driven Piles and Drilled Shafts

In what may be the first reported test of torsional capacity, Stoll (1972) applied torque to two driven steel pipe piles filled with concrete, designated Pile A-3 and Pile V-4. The steel piles are of 0.27 m (10.75 in) external diameter and 6.3 mm (0.25 in) wall thickness. Figure 2-19 shows the setup of the loading test. The soil profiles and driving logs for each test pile are shown in Figure 2-20, and indicates the piles were driven in heterogeneous soil conditions. The test piles were driven to a final penetration resistance of 50 to 60 blows/foot. The resulting embedded length of Pile A-3 and Pile V-4 were 17.4 m (57 ft) and 20.7 m (68 ft), respectively. The length of pile above ground surface for Pile A-3 and Pile V-4 were 1.0 m (3 ft) and 0.7 m (2 ft), respectively. The rotation at the top of each test pile and applied torque were monitored and are shown in Figure 2-21. The torsional resistance of both piles increased with the increase of pile rotation until failure at approximately 0.055 radians (3.2°). No definitive peak was observed for either of the test piles.

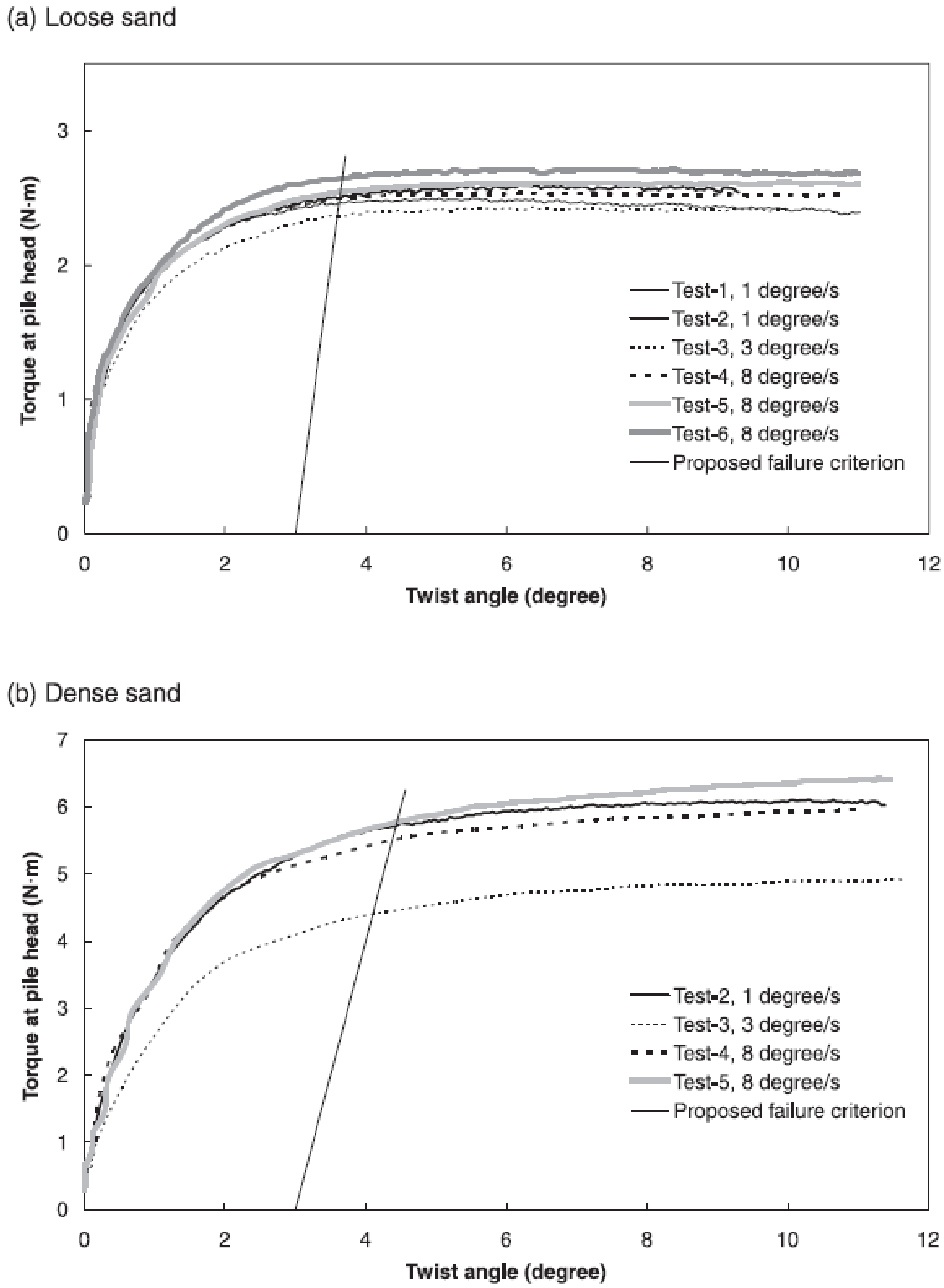

Figure 2-17 Torque-twist curves (after Zhang and Kong 2006)

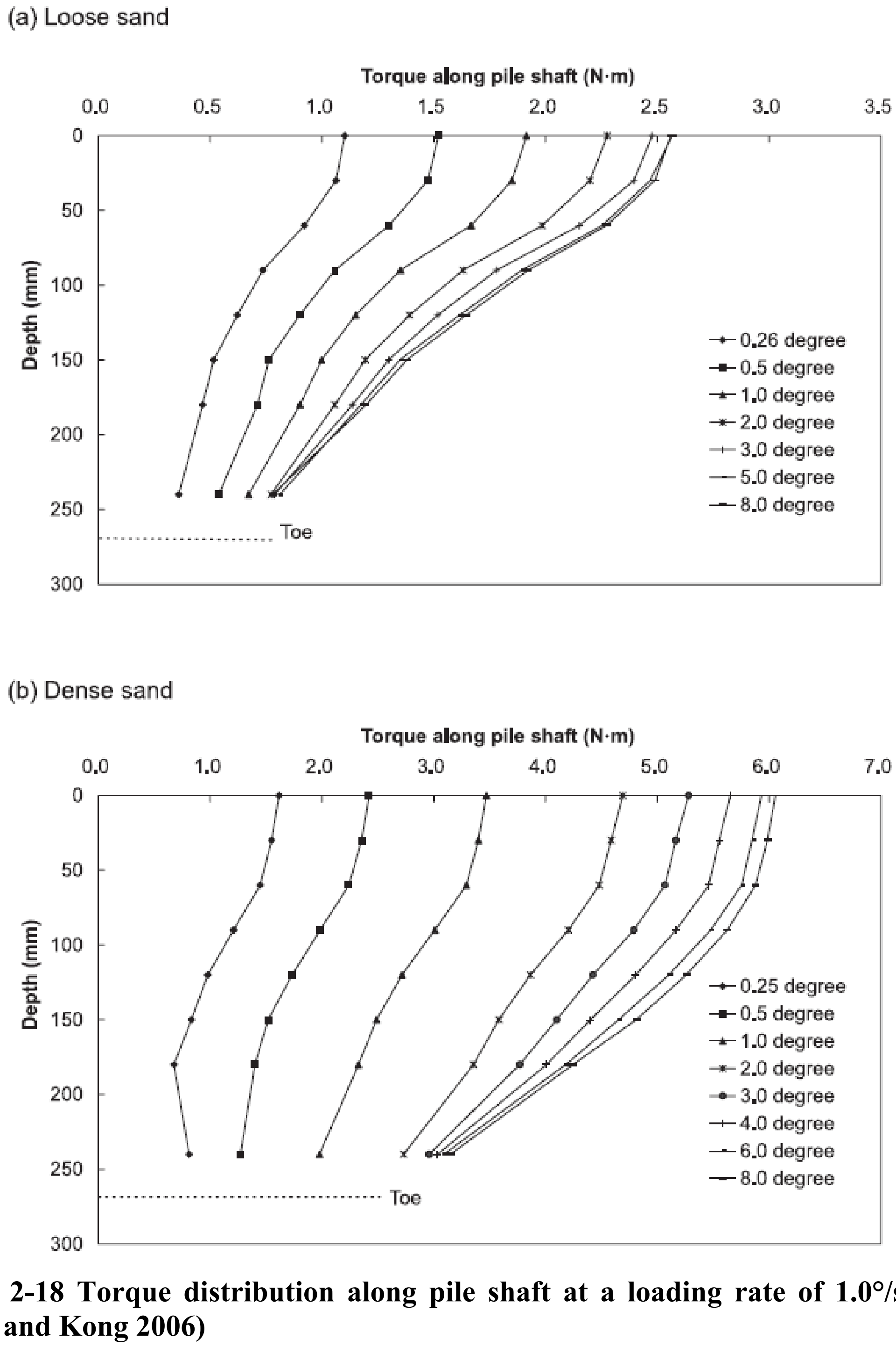

Figure 2-18 Torque distribution along pile shaft at a loading rate of 1.0°/s (after Zhang and Kong 2006)

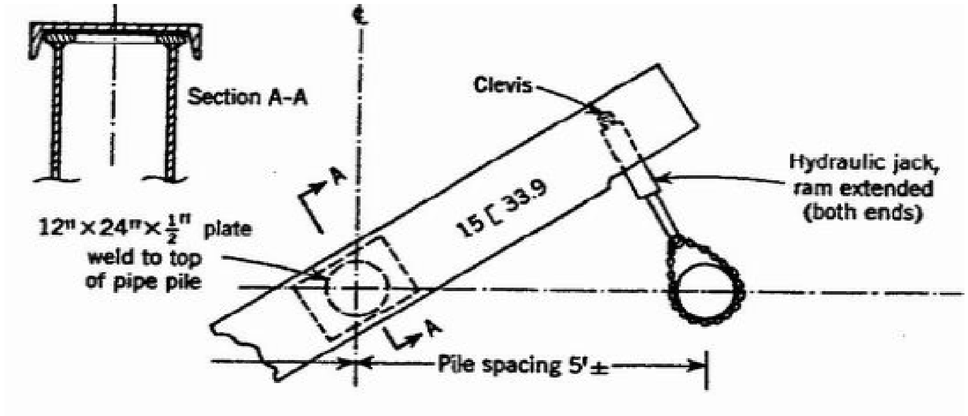

Figure 2-19 Pile torque shear test setup (after Stoll 1972)

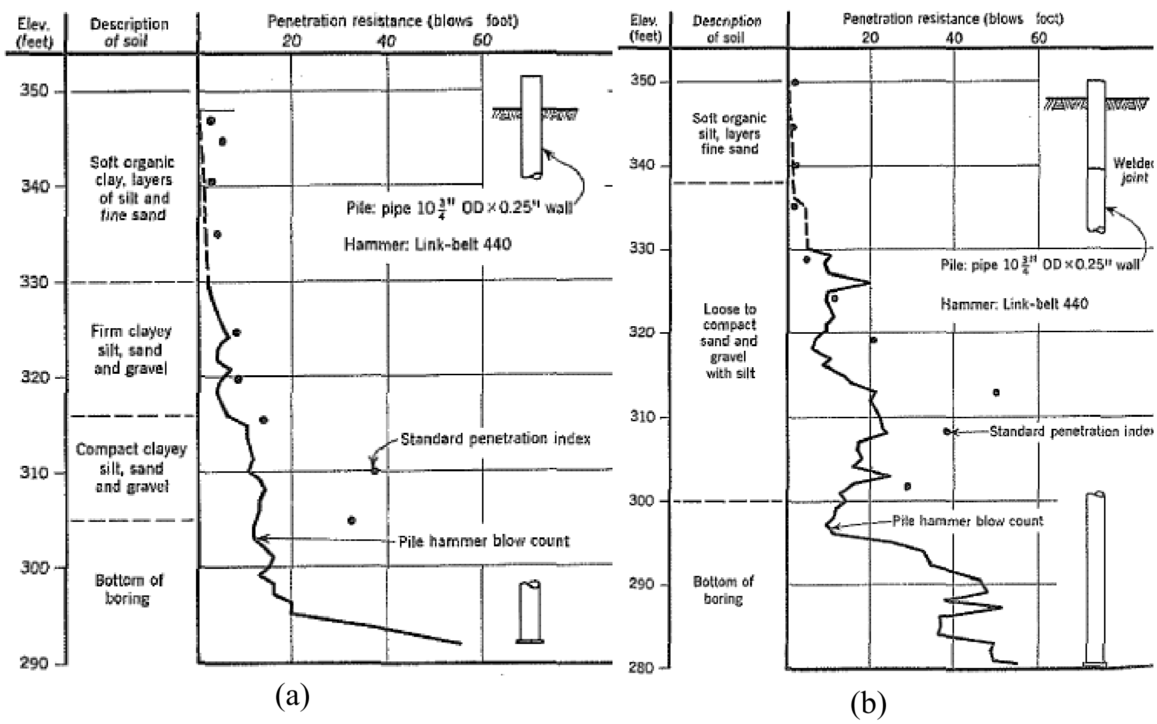

Figure 2-20 Soil profile and driving log for (a) Pile A-3 (b) Pile V-4 (after Stoll 1972)

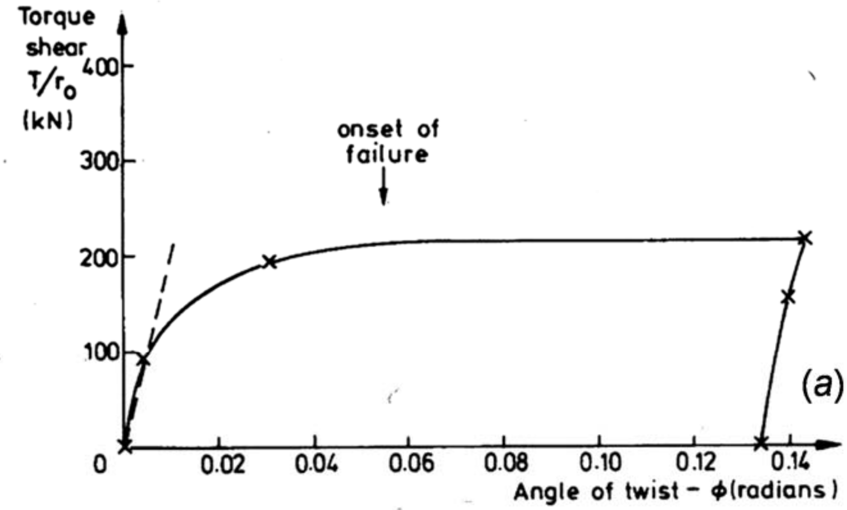

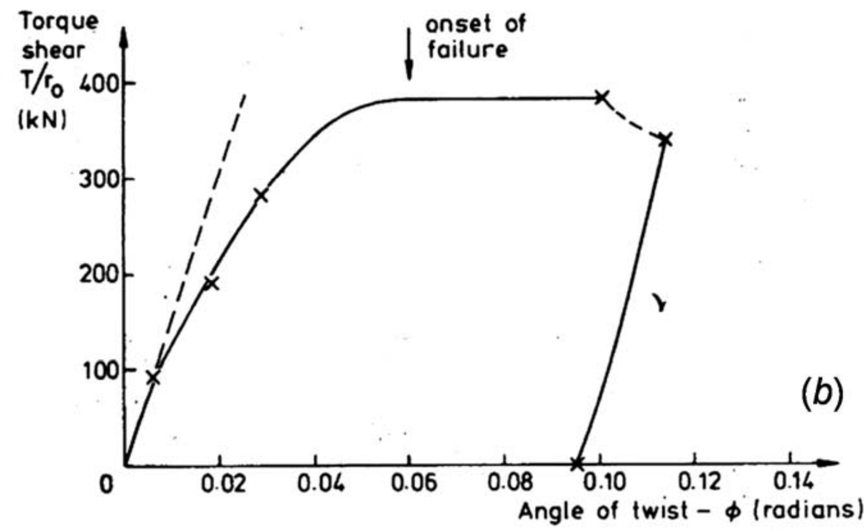

Figure 2-21 Results from torsional load tests: (a) Pile A-3 (b) Pile V-4 (after Randolph 1981, originally from Stoll 1972). Note: 0.1 radians = 5.7 degrees.

In addition to the model tests, Tawfiq (2000) performed full-scale field tests on three 1.2 m (4 ft) diameter by 6.1 m (20 ft) depth drilled shafts constructed in Tallahassee FL. As shown in Figure 2-22, load was applied using a 3.1 m (10 ft) steel cantilever beam. One shaft was constructed with dry method (no slurry). The other two shafts were constructed using the wet method, with one supporting the drill cavity with a bentonite slurry and the other with a polymer slurry. Generally, a layer of silty sandy was encountered from ground surface to a depth of 0.3 m (1 ft), underlain by a layer of clayey sand or sandy clay to a depth arranging from 2.7 to 5.0 m (9 to 16 ft). Below this layer is a stratum of clayey, silty, fine sand underlain by a layer of sand with silt for the dry shaft (constructed with no slurry) or sandy clay for the shaft using polymer slurry. The groundwater table was below the depth of the base of the foundation (over 20 ft).

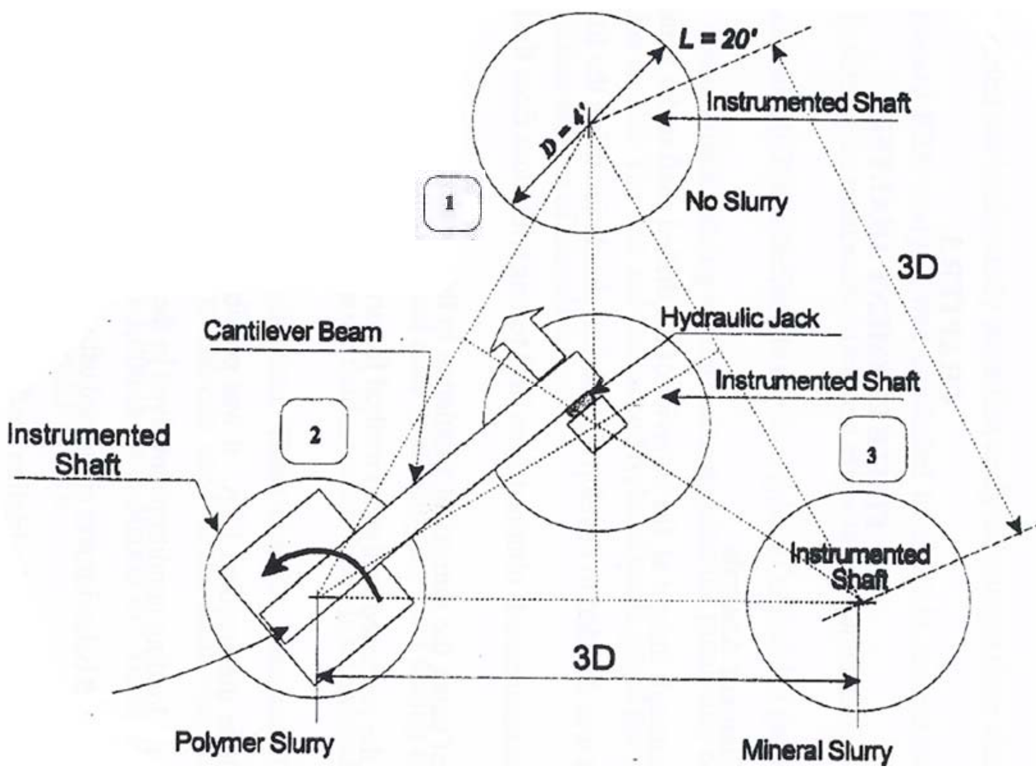

Figure 2-22 Full-scale test setup (after Tawfiq 2000)

The test results for the shafts constructed using dry method and bentonite slurry are shown in Figure 2-23. The load-rotation response for the shaft constructed using polymer slurry was not provided by the author. The induced rotation of the dry shaft was limited to 0.45°, with corresponding maximum torque of 664 kN-m (490 kip-ft), as the shaft experienced structural failure. The maximum applied torque for the shaft constructed using

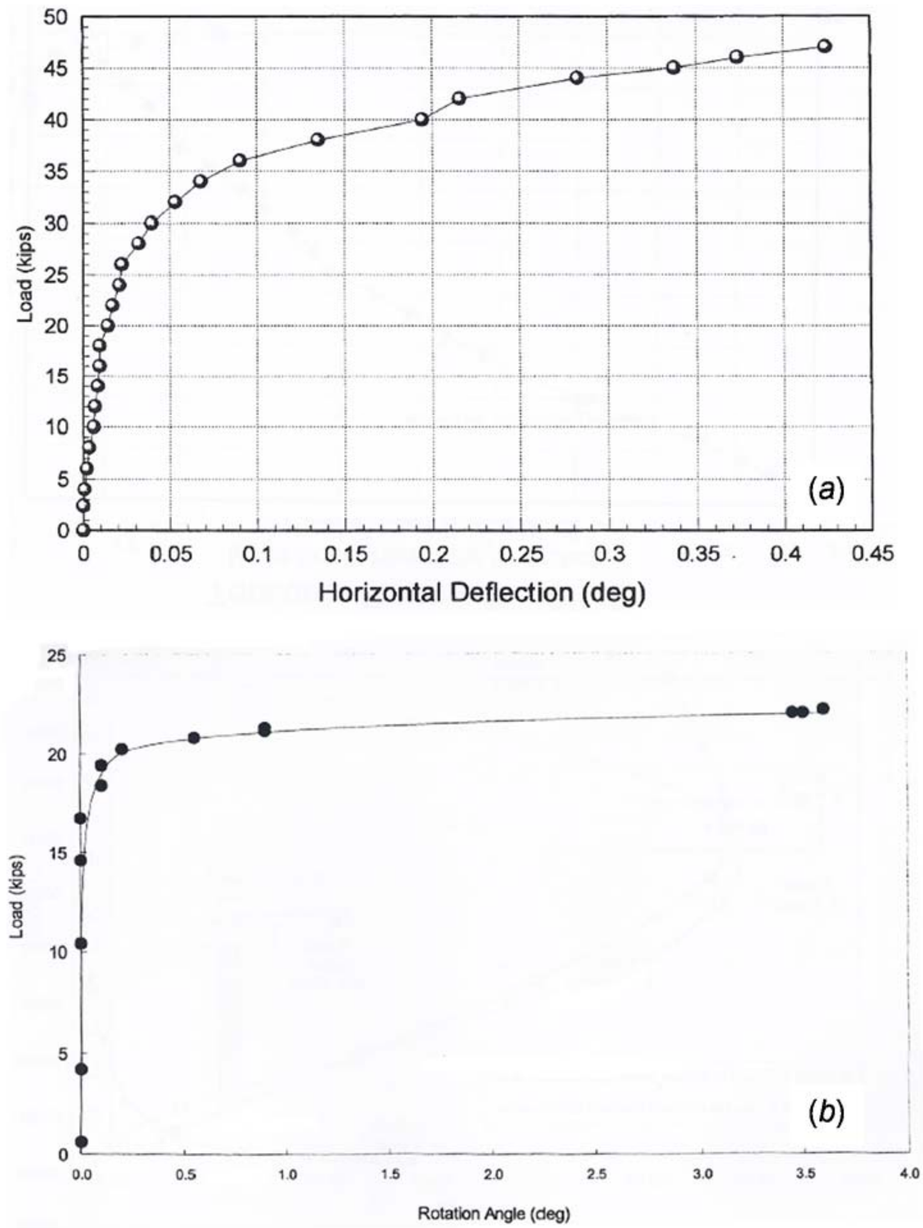

Figure 2-23 Test results of shafts constructed using (a) dry method and (b) bentonite slurry (after Tawfiq 2000)

bentonite slurry was 380 kN-m (280 kip-ft), which was 43% less than the maximum applied torque of the dry shaft, as shown in Figure 2-23b. For the torsional loading test on the shaft constructed using polymer slurry, Tawfiq (2000) reported that the performance of the shaft was similar to the dry shaft at the torque of 380 kN-m (280 kip-ft). Owing to the experience with dry shaft, the upper 1.5 m (5 ft) of soil around the polymer slurry-constructed shaft was removed during loading to avoid structural failure. The maximum applied torque for the shaft constructed using polymer slurry was 569 kN-m (420 kip-ft). Considering that the final embedded length for the shaft constructed using polymer slurry was 4.6 m (15 ft), the torsional capacity for this shaft with same embedded length may be larger than the dry shaft. Note that there is a concern regarding the setup of the test: the center-to-center distance from the reaction shaft to each test shaft was only about 2.1 m (7 ft) and the clear span between shafts was only 0.9 m (3 ft). Therefore, the effect of shaft-to-shaft interaction should have been investigated. Since the torsional load transfer was not studied in this test, the effect of interaction between the shafts could not be explored.

McVay et al. (2014) performed a series of full-scale torsional loading tests on three drilled shafts in Keystone Heights, FL. The drilled shafts included one with a 1.2 m (4 ft) diameter and 3.7 m (12 ft) embedded length (designated TS1), and the other two shafts were constructed with a 1.2 m (4 ft) diameter and 5.5 m (18 ft) embedded length (designated TS2 and TS3). All of the shaft heads were 0.46 m (1.5 ft) above ground surface. The soil profile for each test shaft is shown in Figure 2-24. No temporary casing was used during excavation of the test shafts. The shaft cavities were drilled using the dry method to a depth of about 1.8 m (6 ft), and then bentonite slurry was used to support the cavity for the remainder of the shaft excavation. After installation of the test shafts, Mast arm-pole assemblies were attached to the test shafts. The lengths of pole and arm were 6.7 and 12.2 m (22 and 40 ft), respectively. Lateral loading was applied with increments of 0.5 kips on the mast arm at an offset distance of 10.7 m (35 ft), as shown in Figure 2-25, to supply the torque to the test shaft. A load cell was installed between the mast arm and a crane-mounted winch cable to measure the load associated with the applied load. Upon the observation of failure for shafts TS2 and TS3, the shafts were unloaded. Three types of instrumentation were used to measure the rotation of the test shafts, including two total stations and survey monitoring, two sets of string potentiometers (four potentiometers in each set), and a set of four dial gauges. The water table was about 3 m (10 ft) below ground surface.

Figure 2-26 displays the relationship between applied torque and rotation for each test shaft. The torsional resistances were fully mobilized at 95, 285, and 232 kN-m (corresponding to 70, 210, and 171 kip-ft) for TS1, TS2, and TS3, respectively. The difference of torsional capacity between TS2 and TS3 can be attributed to the difference in soil profile. TS2 was constructed with a greater length in the sand layer, which provided more torsional resistance.

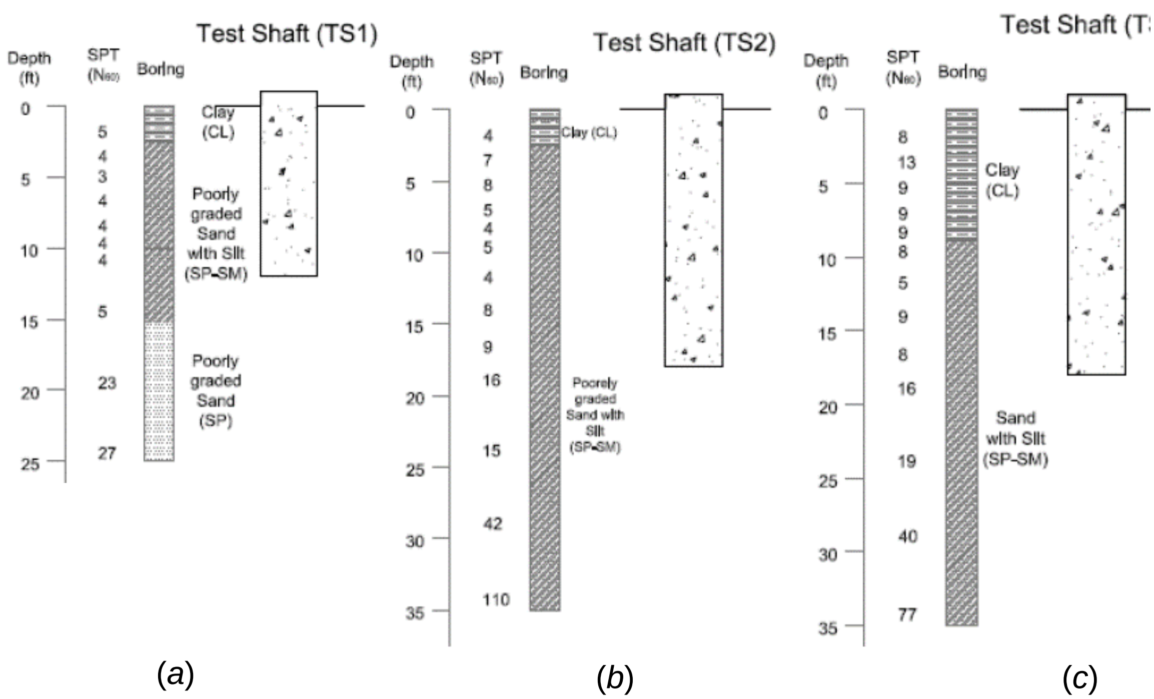

Figure 2-24 Soil profile at the location test drilled shafts (after McVay et al. 2014)

Figure 2-25 Combined torsion and lateral loading (after McVay et al. 2014)

2.5 Design Methods for Drilled Shafts

2.5.1 Design Methods for Axially Loaded Shafts

Axial loads are supported by toe resistance and shaft resistance along the shaft length (Poulos and Davis 1980, Salgado 2008), as shown in Figure 2-27. Kulhawy (2004) summarized the formulation to compute the axial capacity (Q_c) of a drilled shaft in compression as:

$$Q_c = Q_{sc} + Q_{tc} - W \tag{2.10}$$

where Q_s = shaft resistance, Q_t = toe resistance, and W = shaft weight, which is the effective weight for drained loading or the total weight for undrained loading.

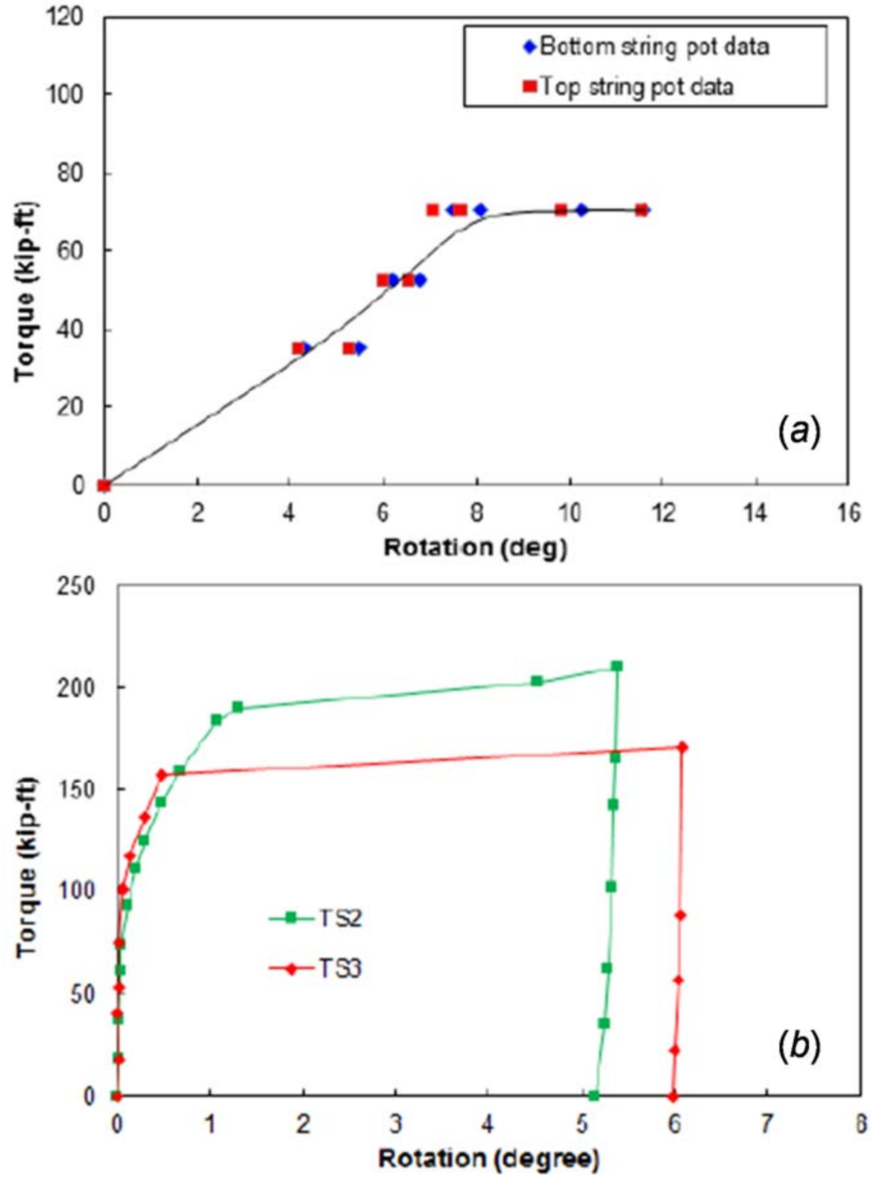

Figure 2-26 Torque vs. rotation response of (a) TS1 and (b) TS2 and TS3 (after McVay et al. 2014)

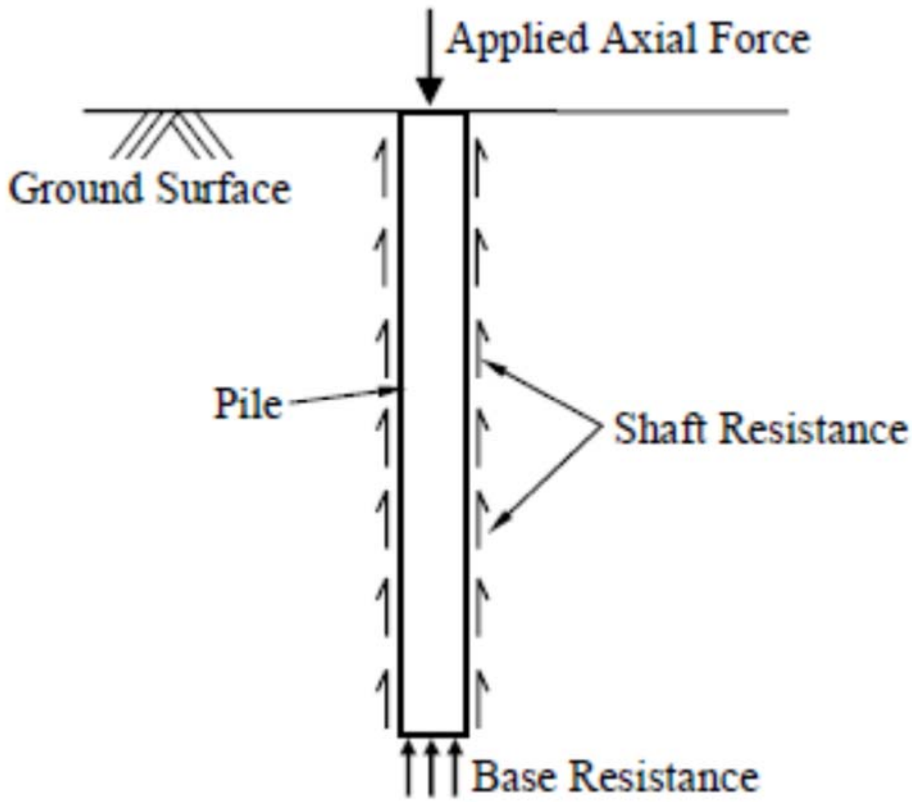

Figure 2-27 Load Transfer Mechanism of Axially Loaded Piles (after Salgado 2008)

A number of researchers (e.g., O'Neill and Reese 1978; Reese and O'Neill 1988; Poulos 1989; Kulhawy 1991, Mayne and Harris 1993, Chen and Kulhawy 1994; O'Neill and Reese 1999; Chen and Kulhawy 2002, Jamiolkowski 2003; Kulhawy 2004; Kulhawy and Chen 2007; Brown et al. 2010) have established procedures to calculate the axial capacity of deep foundations with consideration of a soil's stress history (preconsolidation stress and overconsolidation ratio), the in-situ lateral stresses and coefficient of earth pressure, undrained shear strength (total stress approach), effective friction angle (effective stress approach). The shaft resistance of a drilled shaft can also be estimated directly by scaling up cone penetration test (CPT) and standard penetration test (SPT) data (Niazi et al. 2010). A number of methods are proposed to evaluate the unit shaft resistance and toe capacity of drilled shafts directly based on CPT, including the Laboratoire Central des Ponts et Chaussées (LCPC) method (Bustamante and Gianeselli 1982; Alsamman 1995), the Politecnico di Torino (PT) method (Fioravante et al. 1995), the Unicone method (Eslami and Fellenius 1997, Eslami 2006), and the Kajima Technical Research Institute (KTRI) method (Takesue et al. 1998).

The methods discussed above are useful for estimating the capacity of a drilled shaft; however, they do not provide information regarding the magnitude of displacement required to achieve a given axial resistance. The load transfer method has been developed to address this gap. In this method, the soil reaction around the shaft and under the tip can be represented by discrete nonlinear springs distributed along the shaft (*t-z* curves), and at the shaft tip (*q-z* curves), respectively, where t = unit axial shaft resistance, z = is relative displacement, q = bearing stress at toe. The approach to develop load-transfer curves includes empirical procedures based on experimental data (e.g., Coyle and Reese 1966, Coyle and Sulaiman 1967, Holmquist and Matlock 1976, and Grosch and Reese 1980), numerical techniques (e.g., Poulos and Davis 1968, Butterfield and Banerjee 1971), and theoretical methods (e.g., Chin 1970, Kraft et al. 1981, Chow 1986, McVay, et al., 1989, Randolph 1994, and Poulos 2001).

For drilled shafts constructed with permanent steel casing, AASHTO (2007) and Brown el. (2010) states that a reduction in the axial capacity should be considered. AASHTO (2007) states that no specific data are available and that reduction factors of 0.6 to 0.75 are commonly used. However, as reported by Camp et al. (2002), the reduction factor can be as low as 0.20. Therefore, more axial loading tests on both cased and uncased drilled shafts embedded in similar soil conditions would be helpful to address this issue.

2.5.2 Design Methods for Laterally Loaded Piles

Pushover analysis is commonly used to develop the lateral load-deflection relationship for drilled shafts. Several models have been developed to evaluate the lateral response of a soil-shaft system include the elastic pile and soil model (e.g., Hetenyi 1946; Polous and Davis 1980), the finite element (FE) or continuum soil model (e.g., Yegian and Wright 1973; Thompson 1977; Kuhlemeyer 1979; Kooijman 1989; Brown et al. 1989), rigid pile and plastic soil model (Broms 1964a, 1964b), the load transfer approach using *p*-*y* curves (e.g., Matlock 1970; Cox et al. 1974; Reese et al. 1975; Reese and Welch 1975; API 1993; Ismael 1990; Georgiadis and Georgiadis 2010), and the strain wedge (SW) approach (Norris 1986; Ashour et al. 1998).

The limitation of the elastic pile and soil model is that it is not suitable for assessing the large deformation response of a pile in soil (Wallace et al. 2001). The FM method can produce good representation of soil nonlinearity, but may be computationally intensive and time consuming. The rigid pile and plastic soil model is only suitable for short piles or drilled shafts that do not exhibit significant flexure and are constructed in a uniform deposit of soil. The SW model is developed based on a passive wedge of soil in front of the pile. However, the stress–strain relationship was developed with on the basis of limited experimental data (Xu et al. 2013).

The load transfer method is a popular design method used in practice owing to its use and familiarity in practice and basis in full-scale experiments. However, the commonly used *p*-*y* models for laterally loaded deep foundations were developed from specific loading tests in specific soil deposits and with small diameter piles. Accordingly, these p-y curves may not be suitable for a large diameter deep foundations, which are known to exhibit scale effects (Stevens and Audibert 1979, O'Neill and Gazioglu 1984, and Lam 2013). In addition, the effects of soil-structure interface conditions (e.g., soil-concrete versus soil-steel interface) is not explicitly considered; *p-y* curves developed for steel interfaces may not be suitable for concrete interfaces, a possibility that would increase in significance with increases in diameter owing to the role of shaft resistance in resisting lateral loads (Lam 2013). Therefore, full-scale lateral loading tests on the drilled shafts with and without permanent casing in similar soil condition would help to address the gap in knowledge regarding the role of interface roughness on lateral resistance.

2.5.3 Design Methods for Torsionally Loaded Piles

In general, the torsional capacity or ultimate torsional resistance of drilled shafts, defined as the maximum torsional resistance possible independent of the magnitude of rotation, consists of the sum of the ultimate shaft and toe resistance, given by:

$$T = T_s + T_t \tag{2.11}$$

where T_s = shaft resistance, and T_t = toe resistance.

Design methods available to estimate the torsional capacity of drilled shaft foundations include the Florida Structural Design Office method, the District 5 method, and District 7 method developed by Florida Department of Transportation (e.g. Tawfiq 2000 and Hu 2003) and the Colorado Department of Transportation (CDOT) design method (Nusairat et al. 2004).

For estimating the torsional shaft resistance, the Florida Structural Design Office method consider the deep foundation as a rigid body and the soil behaves as a rigid plastic material. The District 5 method employs the β method (O'Neill and Reese 1999) for drilled shaft in granular soils. The District 7 method combines the β method for granular soils and α method (Brown et al. 2010) for plastic, fine-grained soils in a single equation so that it can be used in both cohesive and cohesionless soils. For the CDOT method, the unit shaft resistance for drilled shafts in plastic, fine-grained soils is assumed equal to the undrained shear strength, which may cause overpredicted torsional shaft resistance. The CDOT method proposed a function for lateral earth pressure coefficient for granular soil without physical basis provided.

For torsional toe resistance, the Florida District 7 method assumes the mobilized unit torsional toe resistance distributes linearly with distance away from the center of the toe, whereas the Florida Structural Design Office and CDOT method assume that is uniformly distributed. In granular soils, the Florida District 7 method assumes the normal force giving rise to the frictional toe resistance is the sum of shaft weight and axial dead load applied to the drilled shaft, whereas the CDOT design method assumes the normal force is equal to shaft weight. However, the normal force at the toe should actually equal the sum of the shaft weight, and axial dead load applied to the drilled shaft, minus the mobilized axial shaft resistance.

Analytical and numerical methods to model the torsional response of deep foundations have been proposed assuming variously that the shear modulus of the soil is constant or varies with depth. Linear elastic or linear elastic-perfectly plastic solutions for torsionally loaded deep foundations have been developed by O'Neill (1964), Poulos (1975), Randolph

(1981) Chow (1985), Hache and Valsangkar (1988), Guo and Randolph (1996), Guo et al. (2007), and Zhang (2010). O'Neill (1964) developed closed-form differential equations for piles in a homogenous soil. Poulos (1975) and Randolph (1981) developed boundary element solution and closed form solution, respectively, for piles in a homogeneous or linearly varying soil. Chow (1985) proposed discrete element approach for piles with varying sections in nonhomogeneous soil. Hache and Valsangkar (1988) provided non-dimensional charts for piles in layered soils. Guo and Randolph (1996) proposed analytical and numerical solutions for piles in a layer of nonhomogeneous soils with stiffness profile following a simple power law with depth. Zhang (2010) developed an analytical method for piles in a two-layer soil profile assuming the shear modulus of soil of each layer varies linearly. Guo et al. (2007) established closed-form solutions for a pile in a two-layer nonhomogeneous soil deposits assuming stiffness profile for each layer increasing as a simple power law of depth. These methods can only produce reasonable results for small rotations and cannot account for the reality of nonlinear soil response.

Load transfer models have been proposed for the study of torsionally-loaded deep foundations using nonlinear springs to model the soil-structure interaction (SSI). Georgiadis (1987) and Georgiadis and Saflekou (1990) used elasto-plastic and exponential torsional springs, respectively, along the shaft with the relationship of pile rotation, θ, and torsional shaft resistance, T, to study the influence of torque on axial pile response. However, the torsional toe resistance was not considered in these models. In addition, the model from Georgiadis and Saflekou (1990) was only validated on the axial response, in terms of axial load and pile head settlement relationship, with model tests; and no validation was performed on predicting torsional behavior of deep foundations. Guo et al.

(2007) presented a logarithmic relationship between pile rotation, θ, and unit torsional shaft resistance, τ_s for the torsional springs. Again, no torsional toe resistance was explicitly considered; nonetheless the results of the analyses compared well with those from continuum-based numerical approaches and finite element models for elastic soil response. However, none of the load transfer methodologies described above were validated using empirically derived load transfer data.

2.6 Summary

This chapter reviewed the relevant studies on the use of steel casing and high-strength reinforcement in drilled shafts, including available axial loading tests and selected structural tests on concrete beams or columns using high-strength reinforcement and casings (i.e., steel tubes). The torsional loading tests in the literature were also described. This chapter concluded with a discussion of design methods for axially-, laterally-, and torsionally-loaded drilled shafts.

Owing to the increased understanding of the regional seismic hazards in the Pacific Northwest, the amount of steel reinforcement used in drilled shaft construction has increased over the past several decades. This may lead to a reduced rebar spacing and increased difficulty for concrete to flow through the reinforcement, such that it may cause voids and defects within the shaft and result in poor structural and geotechnical performance. To mitigate this problem, high strength steel can be employed in design to reduce the amount of steel and increase the rebar spacing, or the contribution of steel casing to flexure can be considered avoiding the use of congested reinforcement cages. Concrete filled tubes (CFTs) have been widely used in some states due to the large inelastic deformation capacity and better seismic performance. However, little information is available on the efficient design of CFTs and the effect of high-strength steel on the performance of drilled shafts. For example, no full-scale experiments have been conducted to study the difference in the lateral response between cased and uncased shafts in the same soil conditions, and no studies have been found in the literature that evaluate the effect of high-strength reinforcement on the geotechnical performance of drilled shafts. Therefore, full-scale loading tests on the drilled shafts with permanent casing and high-strength reinforcement would help to address the gap.

For both axially- and laterally- loaded shafts, the load transfer approach for estimating the deflection associated with a given load are well established. However, few lateral load transfer models have been developed specifically for drilled shaft foundations with concrete interfaces. Additionally, the commonly used load transfer models for laterally-loaded deep foundations were developed from loading tests of small diameter piles Therefore, accurate load transfer models for cased and uncased drilled foundations should be developed from axial and lateral loading tests with relatively larger diameter, drilled, cast-in-place deep foundations.

With regard to the literature on torsionally-loaded deep foundations, torsional load transfer has been previously investigated using scale models and centrifuge loading tests by measuring the shear strains along the test shafts. However, only three full-scale torsional loading tests were found in the literature. Unfortunately, no load transfer observations were reported for any of the full-scale tests, limiting our understanding of the contributions of shaft and toe resistance in torsion. Therefore, full-scale tests on drilled shafts instrumented to measure load transfer in torsion would address a major need for engineers concerned with the design of deep foundations that may experience torsional loads.

To evaluate ultimate torsional resistance, design methods have been proposed by Florida Department of Transportation (FDOT) and Colorado Department of Transportation (CDOT). Analytical and numerical methods have been developed assuming that the shear modulus of soil follows a certain type of variation with depth and linear-elastic or linear-elastic perfectly-plastic soil-structure interaction. The load transfer method has been used for deep foundations loaded in torsion with nonlinear torsional springs. However, the contribution of torsional resistance by the toe of the foundation was not considered in these models. In addition, none of these approaches have been validated using observed load transfer data. Therefore, a methodology for and implementation of load transfer models that have been validated against experimental interface shear data and full-scale loading tests would be helpful to improve our understanding of the torsional response of deep foundations.

2.7 References

AASHTO, (2007). *LRFD Bridge Design Specifications*. 4th edition and 2008–2009 interims, American Association of State Highway and Transportation Officials, Washington, D.C.

AASHTO (2009) *AASHTO LRFD Bridge Design Specification*. American Association of State Highway and Transportation Officials, Washington, D.C.

ACI Committee 318, (2008). *ACI 318-08/ACI 318R-08 Building Code Requirements for Reinforced Concrete and Commentary*, American Concrete Institute, Farmington Hills, MI.

AISC (2005) *Specifications for Structural Steel Buildings*. ANSI/AISC Standard 360-05, American Institute of Steel Construction, Chicago, IL.

Alsamman, O. M. (1995). “The use of CPT for calculating axial capacity of drilled shafts.” *Ph.D. Dissertation*, University of Illinois at Urbana-Champaign, IL.

American Petroleum Institute (API). (1993). “Recommended Practice for Planning, Designing and Constructing Fixed Offshore Platforms-Working Stress Design.”. *20th Ed., API RP2A-WSD*, Washington, D.C.

Ashour, M., Norris, G., and Pilling, P. (1998). "Lateral loading of a pile in layered soil using the strain wedge model." *Journal of geotechnical and geoenvironmental engineering*, *124*(4), 303-315.

Barbosa, A. R., Link, T., and Trejo, D. (2015). "Seismic Performance of High-Strength Steel RC Bridge Columns." *ASCE J. Bridge Eng*., 10.1061/(ASCE)BE.1943-5592.0000769, http://ascelibrary.org/doi/abs/10.1061/(ASCE)BE.1943-5592.0000769

Bierschwale, M. W. Coyle, H. M., and Bartoskewitz, R. E. (1981). "Lateral load tests on drilled shafts founded in clay." *Drilled piers and caissons*, M. W. O'Neill, ed., ASCE, New York, N.Y., 98-113.

Bizaliele, M. M. (1992). "Torsional cyclic loading response of a single pile in sand." Dissertation, Schriftenreihe des Instituts fur Grundbau, Ruhr-Univ., Bochum, Germany.

Broms, B. B. (1964a). "Lateral resistance of piles in cohesive soil". *Journal of Soil Mechanics and Foundation Division*, 90(2), pp. 27-64.

Broms, B.B. (1964b). "Lateral resistance of piles in cohesionless soil," *Journal for Soil Mechanics and Foundation Division*, 90(SM3), pp. 123-156.

Brown, D., Shie, C., and Kumar, M. (1989). "P-y curves for laterally loaded piles derived from three dimensional finite element model," *Proc. 3rd Intl. Symposium on Numerical Models in Geomechanics*, Niagara Falls, 683-690.

Brown, D. A., Turner, J. P., and Castelli, R. J. (2010). "Drilled shafts: Construction procedures and LRFD design methods." *Report No. FHWA-NHI-10-016.* US Department of Transportation, Federal Highway Administration, Washington, D.C.

Brown, D.A. and Camp, W.M. (2002). "Lateral load testing program for the Cooper River Bridge, Charleston, SC," *Deep Foundations 2002*, ASCE, Reston, VA, pp. 95-109

Bustamante, M. and Gianeselli, L. (1982). "Pile bearing capacity prediction by means of static penetrometer." *Proc., European Symp. on Penetration Testing*. Vol. 2, Amsterdam: 493-500.

Butterfield, R., and Banerjee, P. K. (1971). "The elastic analysis of compressible piles and pile groups." *Geotechnique*, London, England, *21*(1), 43-60.

Camp, W.M., Brown, D.A., and Mayne, P.W. (2002). "Construction methods effects on drilled shaft axial performance." *Deep foundations 2002*, Geotechnical Special Publication No. 116, M.W. O'Neil and F.C. Townsend, eds., ASCE, Reston, VA. 193-208.

Chen, Y.J. and Kulhawy, F.H. (1994). "Case history evaluation of the behavior of drilled shafts under axial and lateral loading." *Electric Power Research Institute TR-104601, ResearchProject*, *1493– 04*, Palo Alto.

Chen, Y.J. and Kulhawy, F. H. (2002). "Evaluation of drained axial capacity for drilled shafts." *Proc., Deep Foundations 2002, Geotech. Spec. Publication No. 116*, ASCE, Reston, Va., 2, 1200–1214.

Chin, T. K. (1970). “Estimation of the ultimate load of piles from tests not carried at failure.” *Proc., Second South East Asian Conf. Soil Mech. Found. Engrg.*, Singapore.

Chow, Y. K. (1985). “Torsional response of piles in nonhomogeneous soil.” *J. Geotech. Engrg.*, 111(7), 942–947.

Chow, Y.K. (1986). "Analysis of vertically loaded pile groups." *International Journal for Numerical and Analytical Methods in Geomechanics*, 10, pp. 59-72.

Coyle, H. M., and Reese, L. C. (1966). “Load transfer for axially loaded piles in clay.” *Journal of Soil Mechanics and Foundations Div*, *92*. SM2.

Coyle, H.M., and I.H. Sulaiman. (1967). “Skin friction for steel piles in sand.” *Journal of the Soil Mechanics and Foundation Division*, ASCE, 93(SM6), 261-278.

Cox, W.R., Reese, L.C., Grubbs B.R. (1974). “Field testing of laterally loaded piles in sand.” *Proc. 6th Offshore Technology Conf.,* OTC 2079, 2, 459-472.

Davidson, H. L., Cass, P. G., Khilji, K. H., and McQuade, P. V. (1982). "Laterally loaded drilled pier research." *Rep. EL-2197*, Electric Power Res. Inst., Palo Alto, CA

Duncan, M., Evans, L. T. and Ooi, P. S. K. (1994). “Lateral load analysis of single piles and drilled shafts.” *J. Geotech. Engng.*, *Am. Soc. Civ. Engrs.* **120**(5), 1018-1033.

Dutt, R. N. (1976). “Torsional response of piles in sand.” *Ph.D. thesis*, Univ. of Houston, Houston, Texas.

Dutt, R. N., and O’Neill, M. W. (1983). “Torsional behavior of model piles in sand.” *Geotechnical Practice in Offshore Engineering*, ASCE, New York, 315-334.

Eslami, A. (2006). “Bearing capacity of shallow and deep foundations from CPT resistance.” *Proc., GeoCongress* Atlanta, GA, ASCE, Reston, 6.

Eslami, A., and Fellenius, B. H. (1997). “Pile capacity by direct CPT and CPTu methods applied to 102 case histories.” *Canadian Geotechnical Journal*, *34*(6), 886-904.

Fioravante, V., Ghionna, V. N., Jamiolkowski, M., and Pedroni, S. (1995). “Load carrying capacity of large diameter bored piles in sand and gravel.” In *Proceedings of 10th Asian regional conference on soil mechanics and foundation engineering, Beijing*, Vol. 2, 3-15.

Gebman, M., Ashford, S. A, and Restrepo, J. I. (2006). “Axial force transfer mechanisms within cast-in-steel-shell piles”. *Report No. SSRP-94/10*, Department of Structural Engineering, University of California at San Diego, La Jolla, CA.

Georgiadis, M. (1987). “Interaction between torsional and axial pile response.” *Int. J. Numer. Analyt. Meth. Geomech.*, 11, 645–650.

Georgiadis, M., and Saflekou, S. (1990). “Piles under axial and torsional loads.” *Comput. Geotech*., 9, 291–305.

Georgiadis, K., and Georgiadis, M. (2010). “Undrained lateral pile response in sloping ground.” *Journal of geotechnical and geoenvironmental engineering*, *136*(11), 1489-1500.

Grosch, J., and Reese, L. (1980). “Field tests of small-scale pile segments in asoft clay deposit under repeated axial loading.” *Proceedings, 12th offshore Technology Conference*, Houston, TX, Vol. 4, 143-151.

Gunaratne, M. (2006). *The foundation engineering handbook*. CRC Press Boca Raton, Fla.

Guo, W. D., Chow, Y. K., and Randolph, M. F. (2007). “Torsional pile in two-layered nonhomogeneous soil.” *Int. J. Geomech.,* 7(6), 410–422.

Guo, W. D., and Randolph, M. F. (1996). “Torsional piles in nonhomogeneous media.” *Comput. Struct.*, 19(4), 265–287.

Hache, R. A. G., and Valsangkar, A. J. (1988). “Torsional resistance of single pile in layered soil.” *J. Geotech. Engrg.*, 114(2), 216–220.

Hassan, T.K., Seliem, H.M., Dwairi, H., Rizkalla, S.H., and Zia, P. (2008). “Shear Behavior of Large Concrete Beams Reinforced with High-Strength Steel,” *ACI Structural Journal*,105(2), 173–179.

Hetenyi, M. (1946). *Beams on Elastic Foundations*, University of Michigan Press, Ann Arbor.

Holmquist, D. V. and Matlock, H. (1976). “Resistance-Displacements Relationships for Axially Loaded Piles in Soft Clay.” *Proceedings, 8th offshore Technology Conference*, Houston, TX, Vol. 1, 553-569

Hu, Z. (2003). “Determining the optimum depth of drilled shafts subject to combined torsion and lateral loads in saturated sand from centrifuge testing.” Master’s dissertation, University of Florida, Gainesville, FL.

Hulsey, J. L., Horzdovsky, J. E., Davis, D., Yang, Z. J., and Li, Q. (2011). “Seasonally Frozen Soil Effects on the Seismic Performance of Highway Bridges.” *Final Report, Report No.: FHWA-AK-RD-12-15* Alaska University Transportation Center, Fairbanks, AK.

Ismael, N. F. (1990). “Behavior of laterally loaded bored piles in cemented sands.” *Journal of Geotechnical Engineering*, *116*(11), 1678-1699.

Jamiolkowski, M. (2003). “Deep foundations on bored and auger piles.” *Proc. 4th Intern.Geotechnical Seminar on Deep Foundations on Bored and Auger Piles*, Ghent: 83–100.

Koojiman, A. (1989). “Comparison of an Elastoplastic Quasi Three-Dimensional Model for Laterally Loaded Piles with Field Tests,” *Proc. 3rd Intl. Symposium on Numerical Models in Geomechanics*, Niagara Falls, 675-682.

Kraft, L. M., Kagawa, T., and Ray, R. P. (1981). “Theoretical t-z curves.” *Journal of the Geotechnical Engineering Division*, *107*(11), 1543-1561.

Kuhlemeyer (1979). “Vertical Vibration of Piles,” *J. Geotech. Eng.*, ASCE, 105(2), 273-287.

Kulhawy, F. H. (1991). Drilled shaft foundations.” *Foundation engineering handbook*, 2nd Ed., H. Y. Fang, ed., Van Nostrand-Reinhold, New York.

Kulhawy, F. H. (2004). “On the axial behavior of drilled foundations.” *Proc., GeoSupport 2004: Drilled Shafts, Micropiling, Deep Mixing, Remedial Methods, and Specialty Foundation Systems, GSP 124*, J. P. Turner and P. W. Mayne, eds., ASCE, Reston, Va., 34–51.

Kulhawy, F.H. and Chen, J.-R. (2007). “Discussion of ‘Drilled Shaft Side Resistance in Gravelly Soils’ by Kyle M. Rollins, Robert J. Clayton, Rodney C. Mikesell, and Bradford C. Blaise,” *Journal of Geotechnical and Geoenvironmental Engineering*, ASCE, 133(10), 1325-1328.

Lam, I.P.O. (2013). “Diameter Effects on p-y Curves,” *38th Annual Meeting of the Deep Foundations Institute*, Phoenix, AZ.

Laue, J., and Sonntag, T. (1998). “Pile subjected to torsion.” *Proc., Centrifuge ’98*, Balkema, Rotterdam, the Netherlands, 187–192.

Matlock, H. (1970). “Correlations for Design of Laterally Loaded Piles in Soft Clay.” *Proc., 2nd Annual Offshore Technology Conf.,* OTC 1204, Houston, Vol. 1, 577-594.

Mayne, P. W., Kulhawy, F. H., and Trautmann, C. H. (1992). "An experimental study of the behavior of drilled shaft foundations under static and cyclic lateral and moment loading." *Rep. TR-lO0221*, Electric Power Res. Inst., Palo Alto, CA

Mayne, P.W., and Harris, D.E. (1993). “Axial Load-Displacement Behavior of Drilled Shaft Foundations in Piedmont Residuum,” *FHWA Reference Number 41-30-2175*, Georgia Tech Research Corporation, Atlanta, GA.

McVay, M.C., F.C. Townsend, D.G. Bloomquist, M.O. O'Brien, and J.A. Caliendo. (1989). "Numerical analysis of vertically loaded pile groups." *Proceedings, Foundation Engineering Congress: Current Principles and Practices*, Evanston, IL, pp. 675-690.

McVay, M. C., Herrera, R., and Hu, Z. (2003). “Determine optimum depths of drilled shafts subject to combined torsion and lateral loads using centrifuge testing.” *Report Contract No. BC-354, RPWO #9*. Florida Department of Transportation, Tallahassee, FL.

McVay, M. C., and Hu, Z. (2003). “Determine optimum depths of drilled shafts subject to combined torsion and lateral loads from centrifuge testing (using KB polymer slurry)-supplemental research.” *Report Contract No. BC-545, WO #4*. Florida Department of Transportation, Tallahassee, FL.

McVay, M. C., Bloomquist, D., and Thiyyakkandi, S. (2014). “Field testing of jet-grouted piles and drilled shafts.” *Report BDK75-977-41, 91977.* Florida Department of Transportation, Tallahassee, FL.

Niazi, F. S., Mayne, P. W., and Woeller, D. J. (2010). “Drilled Shaft O-Cell Response at Golden Ears Bridge from Seismic Piezocone Tests.” *Art of Foundation Engineering Practice*, (198), 452.

Norris, G. M. (1986). “Theoretically based BEF laterally loaded pile analysis.” *Proc., Third Int. Conf. on Numerical Methods in Offshore Piling*, Editions Technip, Paris. France, 361-386.

Nusairat, J., Liang, R., Engel, R., Hanneman, D., AbuHejleh, N., and Yang, K. (2004). "Drilled shaft design for sound barrier walls, signs, and signals." *Report No. CDOT-DTD-R-2004-8*, Colorado Department of Transportation, Denver, CO.

O'Neill, M. W. (1964). "Determination of the pile-head torque-twist relationship for a circular pile embedded in a clay soil." *Master's thesis*, The Univ. of Texas at Austin, TX.

O'Neill, M.W. and Gazioglu, S.M. (1984). "An Evaluation of p-y Relationships in Clays," *Report to the American Petroleum Institute UHCE-84-3*, University of Houston, TX.

O'Neill, M. W., and Reese, L. C. (1978). "Load transfer in a slender drilled pier in sand" *Spring Convention and Exposition,* Pittsburgh, PA.

O'Neill, M. W., and Reese, L. C. (1999). "Drilled shafts: Construction procedures and design methods." *Publ. No. FHWA-IF-99-025*, Federal Highway Administration, Office of Implementation, McLean, VA

Owens, M. J., and Reese, L. C. (1982). "The influence of a steel casing on the axial capacity of a drilled shaft." *Report No. 255-1F*. Texas State Department of Highways and Public Transportation Center for Transportation Research, Bureau of Engineering Research, The University of Texas at Austin, Austin, TX.

Poulos, H. G. (1975). "Torsional response of piles." *Journal of the Geotechnical Engineering Division*, 101(10), 1019-1035.

Poulos, H. G., and Davis, E. H. (1968). "The settlement behaviour of single axially loaded incompressible piles and piers." *Geotechnique*, London, England, *18*(3), 351-371.

Poulos, H. G. and Davis, E. H. (1980). *Pile foundation analysis and design*. John Wiley and Sons, New York, N.Y.

Poulos, H. G. (1989). "Pile behaviour—theory and application." *Géotechnique, London, England*, 39 (3), 365–415.

Poulos, H.G. (2001). "Pile foundations." In *Geotechnical and Geoenvironmental Engineering Handbook*, Edited R.K. Rowe, Kluwer Academic Press.

Randolph, M. F. (1981). "Piles subjected to torsion." *J. Geotech. Engrg. Div.*, 107(8), 1095–1111.

Randolph, M. F. (1983). "Design consideration for offshore piles." *Geotechnical Practice in Offshore Engineering,* ASCE, New York, 422–439.

Randolph, M.F. (1994). "Design methods for pile groups and pile drafts." *Proceedings, XIII ICSMFE*, New Delhi, India , pp. 61-82.

Reese, L., Cox, W., and Koop, F. (1975). "Field Testing and Analysis of Laterally Loaded Piles in Stiff Clay." *Proc. 7th Offshore Technology Conf.*, OTC 2312, Houston, 2, 671-690.

Reese, L. C., and O'Neill, M. W. (1988). "Drilled shafts: Construction procedures and design methods." *Pub. No. FHWA-HI-88-042*, U.S. Dept. of Transportation, Washington, D.C., 564–564.

Reese, L., Welch, R. (1975). “Lateral loading of deep foundations in stiff clay.” *Journal of Geotechnical Engineering Div*., ASCE, 101(GT7), 633-649.

Roeder, C., and Lehman, D. (2012). “Initial Investigation of Reinforced Concrete Filled Tubes for Use in Bridge Foundations.” *Report No. WA-RD 776.1*. The State of Washington Department of Transportation, Olympia, Washington.

Salgado, R. (2008). *The engineering of foundations*. New York: McGraw Hill.

Shahrooz, B. M., Miller, R.A., Harries, K.A., and Russel, H.G. (2011). “Design of concrete structures using high-strength steel reinforcement.” *NCHRP Report 679*, Transportation Research Board, Washington, DC.

Stevens, J.B. and Audibert, J.M.E. (1979) “Re-examination of p-y Curve Formulations,” *Proceedings, 11th Annual Offshore Technology Conference*, Houston TX.

Stoll, U. W. (1972). “Torque shear test of cylindrical friction piles.” *Civil Engineering*, 42(4), 63-65.

Takesue, K., Sasao, H., and Matsumoto, T. (1998). “Correlation between ultimate pile skin friction and CPT data.” *Geotechnical Site Characterization*, *2*, 1177-1182.

Tawfiq, K. (2000). “Drilled shafts under torsional loading conditions.” *Report Contract No. B-9191*, Florida Department of Transportation, Tallahassee, FL.

Thompson, G. (1977). “Application of Finite Element Method to the Development of p-y Curves for Saturated Clays,” *Thesis*, University of Texas, Austin.

Trejo, D., Barbosa, A.R., and Link, T. (2014). “Seismic Performance of Circular Reinforced Concrete Bridge Columns Constructed with Grade 80 Reinforcement”. *Research SRS 500-610*. Oregon State University, Corvallis, OR.

Wallace, J. W., Fox, P. J., Stewart, J. P., Janoyan, K., Qiu, T., and Lermitte, S. (2001). “Cyclic large deflection testing of shaft bridges: Part I-Background and field test results.” *Report to California Department of Transportation*, University of California, Los Angeles, CA

Welch, R. C., and Reese, L. C. (1972). "Lateral load behavior of drilled shafts," *Res. Rep. 89-10*, Center for Highway Research, The University of Texas at Austin, Tex

Xu, L.Y., Cai, F., Wang, G., and Ugai, K. (2013). “Nonlinear analysis of laterally loaded single piles in sand using modified strain wedge model.” *Computers and Geotechnics*, 51: 60–71.

Yang, Z., Li, Q., Horazdovsky, J., Hulsey, J. L., and Marx, E. (2012). Analysis of laterally loaded piles in frozen soils. *State of the Art and Practice in Geotechnical Engineering (GeoCongress2012)*, Geotechnical Special Publication, (225), 215-224.

Yegian, M. and Wright, S. (1973). “Lateral Soil resistance - Displacement Relationships for Pile Foundations in Soft Clays,” *Proc. 5th Offshore Technology Conf*., OTC 1893, Houston, Vol. 2, 663-676.

Zeno, G. A. (2009). “Use of High-Strength Steel Reinforcement in Shear Friction Applications.” Doctoral dissertation, University of Pittsburgh ,PA.

Zhang, L. (2010). “Nonlinear analysis of torsionally loaded piles in a two layer soil profile.” *Int. J. Geomech.*, 10(2), 65–73.

Zhang, L. M., and Kong, L. G. (2006). “Centrifuge modeling of torsional response of piles in sand.” *Canadian Geotechnical Journal*, 43(5), 500-515.

3. RESEARCH OBJECTIVES AND PROGRAM

3.1 Research Objectives

The objective of this study is to improve the understanding of load transfer of drilled shaft foundations under axial, lateral, and torsional loading at full-scale using various and novel composite cross-sections. The objectives for this research are driven by gaps in knowledge regarding the use of high strength steel and steel casing in the performance of drilled shafts, and by the gaps in knowledge regarding the resistance of drilled shafts to torsional loading, as described in Chapter 2. The specific objectives of this dissertation are to:

1. Evaluate the effects of high strength steel reinforcement bars on lateral resistance, steel casing on axial and lateral resistance, and steel casing without internal reinforcement on lateral resistance;
2. Develop recommendations to account for the effects of casing on axial and lateral resistance;
3. Evaluate the appropriateness of existing axial and lateral load transfer models to predict the performance of and for use with typical and proposed (i.e., steel-cased) drilled shafts;
4. Develop region-specific axial and lateral load transfer models if available models prove incapable of sufficiently capturing the observed performance;
5. Investigate the effects of deep foundation diameter on the lateral resistance of deep foundations and to establish an approach to account for "scale effects";
6. Observe and characterize torsional load transfer at full-scale;

7. Develop a numerical framework for the simulation of torsionally-loaded, geometrically-variable deep foundations in multi-layered soils; and,

3.2 Research Program

The research program developed to accomplish the objectives of this study include the:

1. Characterization of the test sites used to conduct full scale tests, including geotechnical explorations and laboratory tests to establish the relevant soil properties;
2. Design and installation of six full-scale, instrumented test shafts, including two uncased shafts using mild and high strength steel reinforcement, two shafts with steel casing and with and without internal mild steel reinforcement, and two uncased shafts used for support of mast-arm traffic signs and signals;
3. Comparison of non-destructive tests used to evaluate potential for defects in shafts, with specific emphasis on the use of hollow bar for cross-hole sonic logging;
4. Full-scale testing of four shafts in axial and lateral loading, and two shafts in torsional loading;
5. Evaluation and comparison of the performance between the cased and uncased test shafts under axial and lateral loads to study the effects of steel casing on the relevant load transfer;
6. Evaluation and comparison of the performance between the uncased test shafts under lateral loads to study the effects of high strength reinforcement on the

mechanism and magnitude of lateral resistance (i.e., moment-curvature relationship);

7. Development of empirical load transfer curves, including *t*-*z* and *q*-*z* curves from axial loading tests, *p*-*y* curves from lateral loading tests, and τ-Δ curves from torsional loading tests where t = unit axial shaft resistance, z = is relative displacement, q = bearing stress at toe, p = lateral soil reaction, y = lateral displacement, τ = unit torsional shaft resistance, and Δ = relative circumferential soil-shaft displacement;
8. Formulation of region-specific axial and lateral load transfer models that are normalized using CPT and/or shear wave velocity measurements, in order to generalize the proposed models;
9. Establishing of a fundamentally correct and empirically-justified approach to commonly-used *p*-*y* curves to account for the apparent "scale effects" associated with
10. Development of simplified torsional load transfer models using torsional loading test data and available interface shear tests that account for hardening and softening as function of the state of the soil relative to its critical state and the surface roughness of the interface; and,
11. The development of a numerical framework to simulate the performance of torsionally-loaded geometrically-variable deep foundations in multi-layered soils.

4. SUBSURFACE CONDITIONS AT THE TEST SITE

4.1 Overview

The Geotechnical Engineering Field Research Site (GEFRS) at Oregon State University (OSU), the site where the experimental shafts were constructed and tested in this study, is located near the western edge of the main portion of the OSU campus, adjacent to the Hinsdale Wave Research Lab (Figure 4-1). This test site has been used for over twenty years to conduct geotechnical experiments at full-scale. The geotechnical explorations, stratigraphy, and corresponding subsurface conditions for the site, and specifically the location of the test shafts, are presented in this chapter.

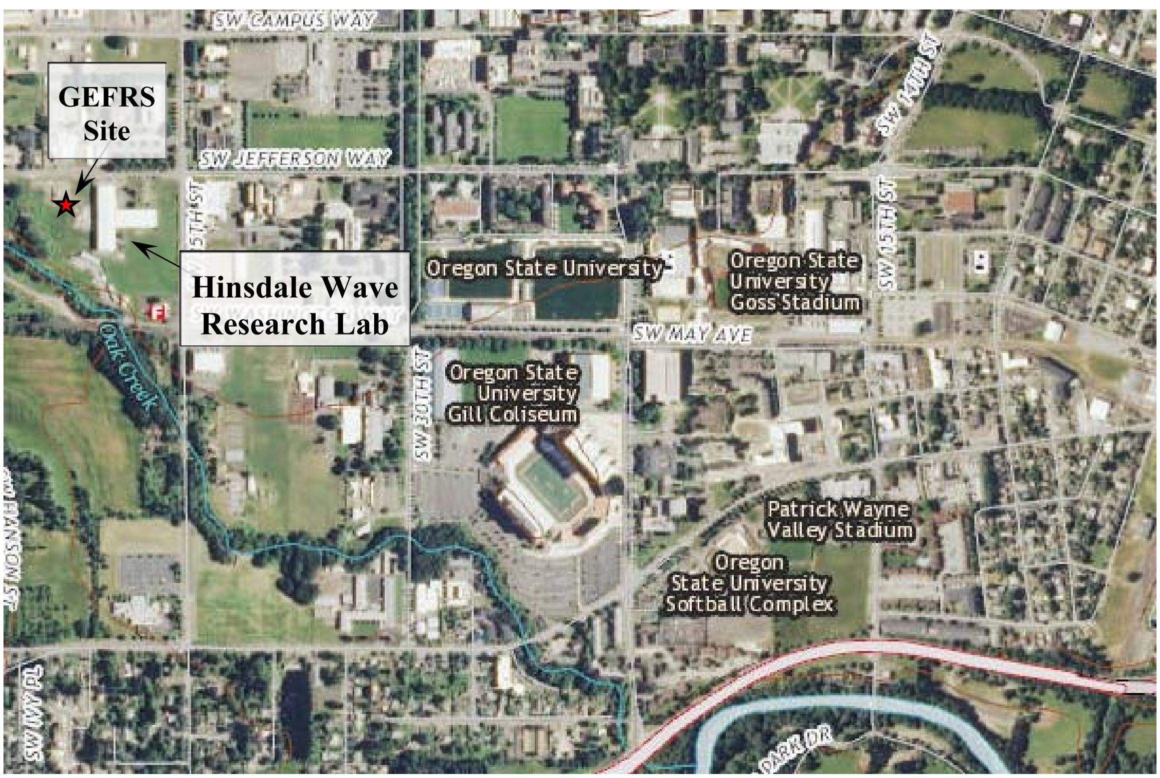

Figure 4-1. Project site (adapted from USGS National Map Viewer, 2015)

4.2 General Site at the GEFRS

Several geotechnical explorations have been conducted at the GEFRS with soil information summarized in Dickenson and Haines (2006), Nimityongskul (2010), and Martin (2018). Based on samples retrieved from borings distributed across the GEFRS, Dickenson and Haines (2006) summarized the general the range in water contents and Atterberg limits with depth as shown in Figure 4-2. Figure 4-3 shows the corrected standard penetration test (SPT) blow counts versus depth. Dickenson and Haines (2006) generally describe the stratigraphic sequence of GEFRS to consists of, beginning from the ground surface, the upper Willamette Silt, underlain by an intermittent lens of silty gravelly sand, followed by the lower Willamette Silt, underlain by a thicker lens of silty gravelly fine sand, and then a thick deposit of blue-gray clay (which actually consists of clayey silt). Based on the SPT results, the upper and lower Willamette Silt layer ranges from medium stiff to very stiff; in the experience of the authors, the consistency of the upper Willamette Silt layer depends upon the season and depth to groundwater. Figure 4-4 presents the Atterberg limits in the form of the plasticity chart for soil samples retrieved at the GEFRS, including those from Dickenson and Haines (2006) and from this study (as discussed subsequently). A wide range of liquid limits and plasticity indices was observed for Willamette Silt (both upper and lower Willamette Silt) from low plasticity silt (ML) to highly plastic clay (CH) across the entire GEFRS. The blue-grey clay can be classified as high plasticity clayey silt (MH).

Based on consolidation tests on soil samples retrieved from GEFRS, Dickenson and Haines (2006) constructed estimated profiles of the current (σ'_{v0}) and maximum past effective or preconsolidation stress (σ'_p), as shown in Figure 4-5, which indicates that the

Willamette Silt and blue-gray clay are moderately to highly overconsolidated with typical overconsolidation ratios (OCRs) from four to seven and with some values as high as fourteen.

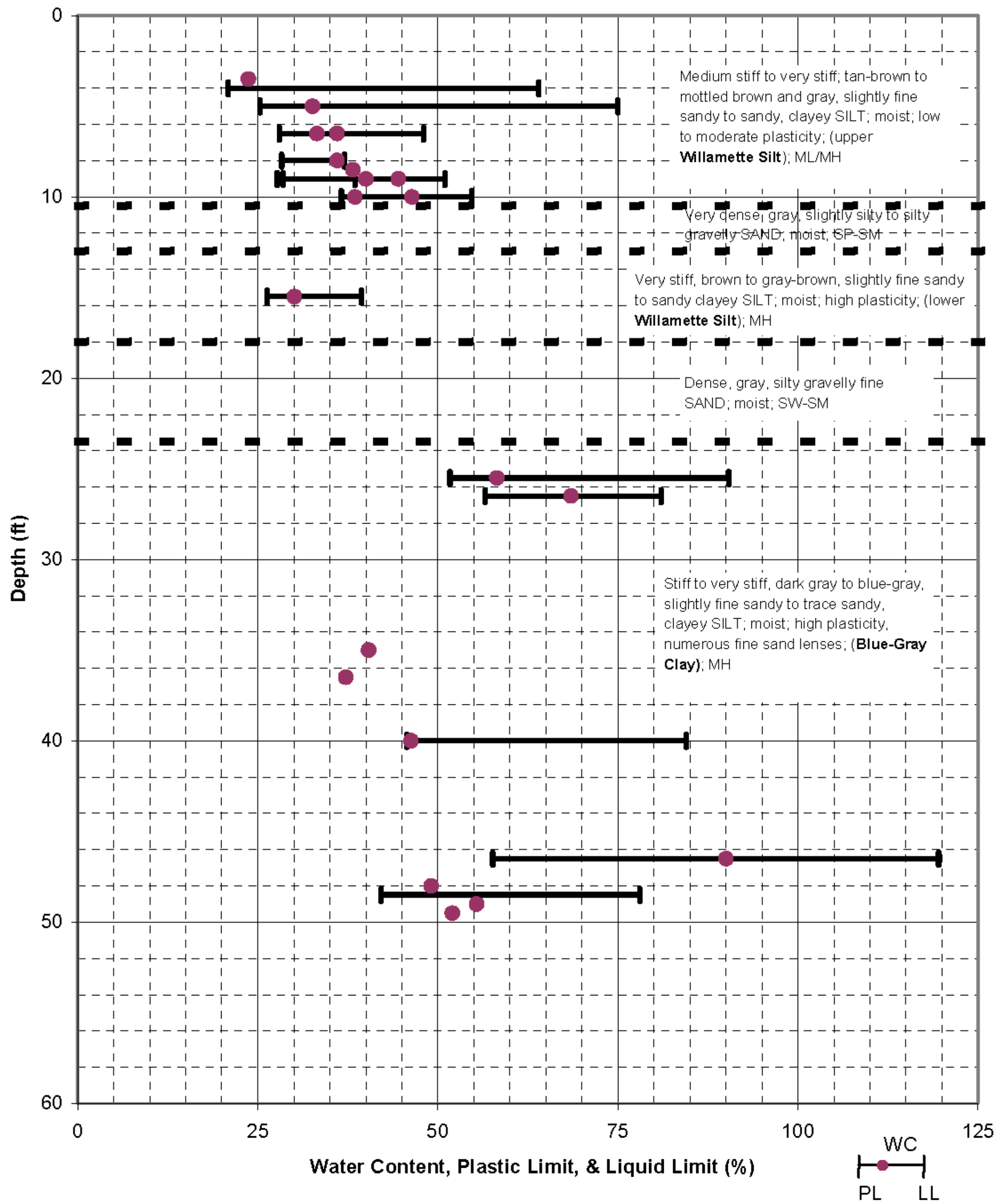

Figure 4-2. Water content and Atterberg limits at GEFRS (Dickenson and Haines 2006)

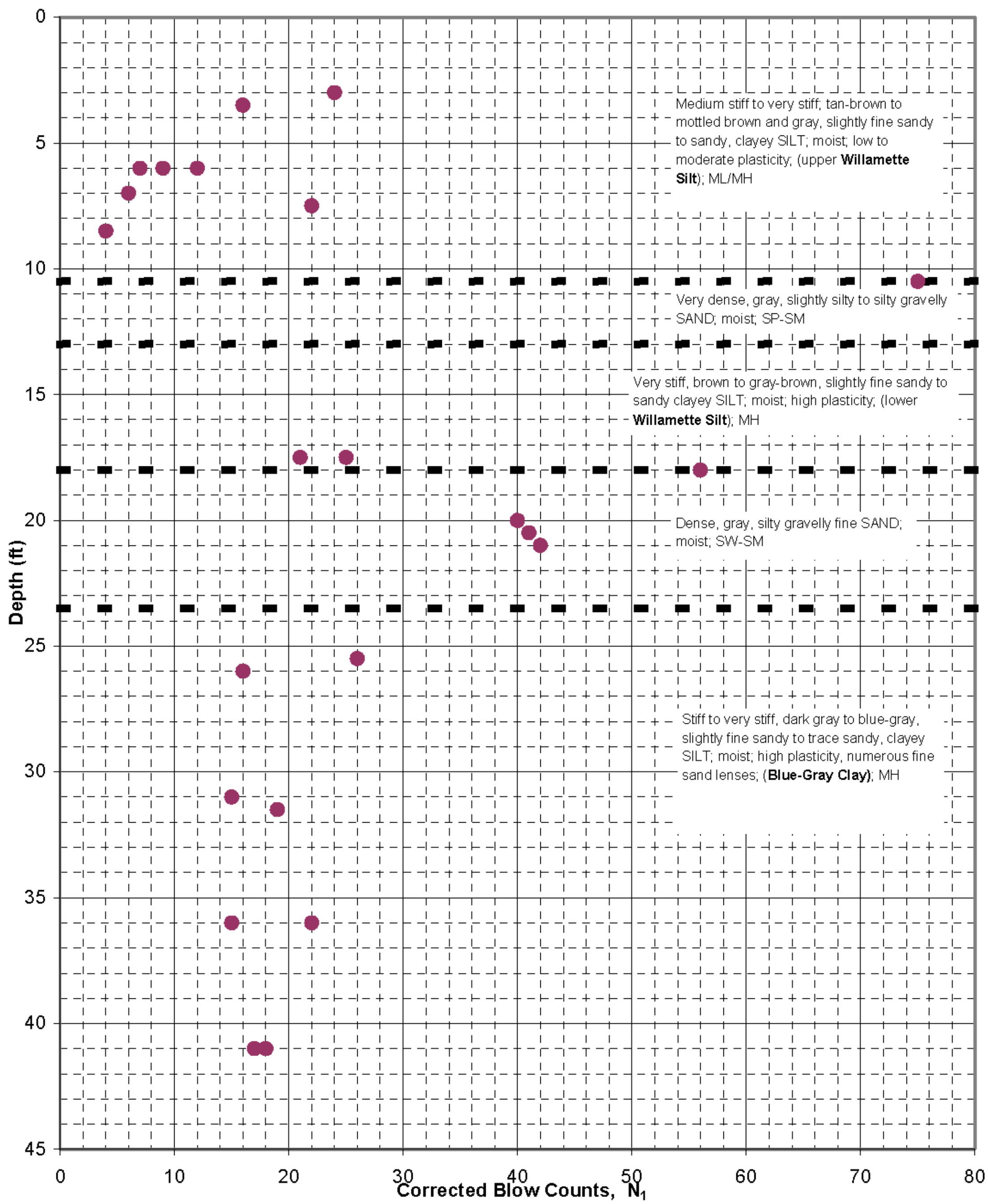

Figure 4-3. Corrected SPT blow count versus Depth at GEFRS (Dickenson and Haines 2006)

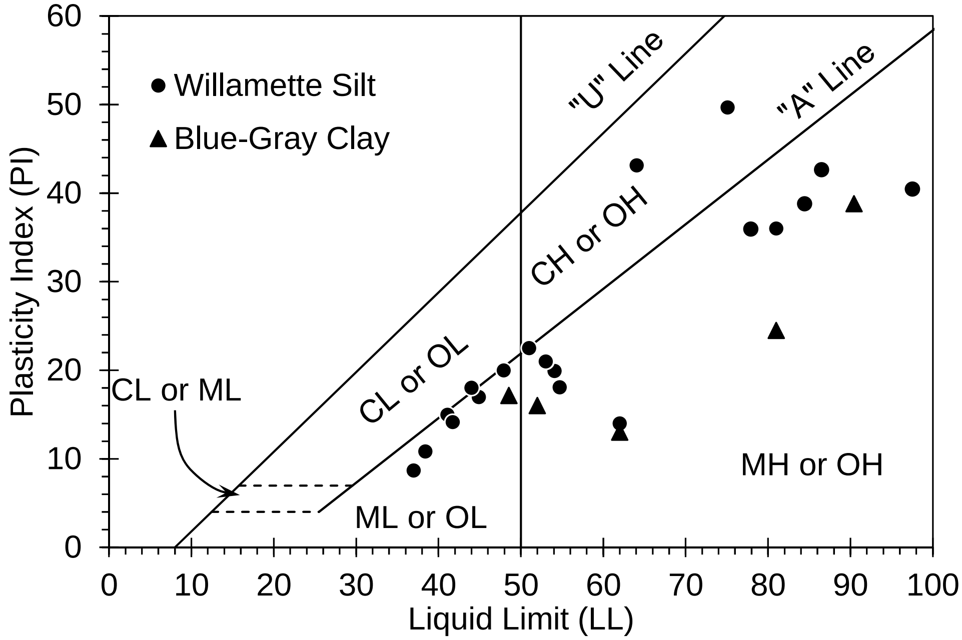

Figure 4-4. Soils classification using plasticity chart at GEFRS based on Dickenson and Haines (2006), Nimityongskul (2010), and soil samples obtained from this study.

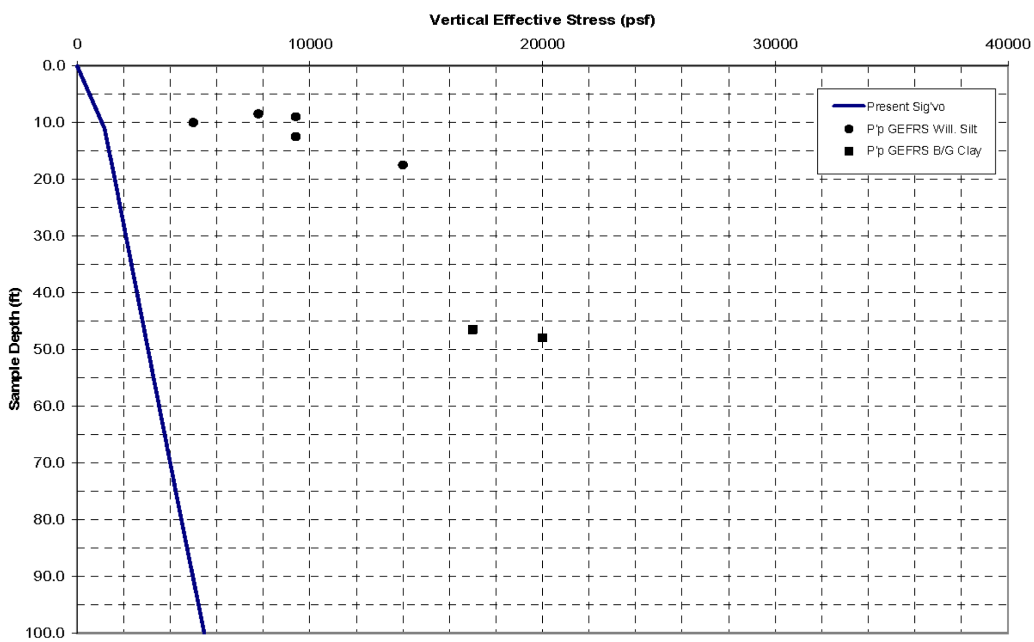

Figure 4-5. Current and maximum effective stress versus depth at GEFRS (Dickenson and Haines 2006). Note: *Sig'vo* = σ'_{v0} = current effective overburden stress, *P'p* = σ'_p maximum past effective stress

4.3 Site Specific Geotechnical Exploration for Torsional Loading Test

Figure 4-6 shows the site plan for torsional loading test, indicating the geotechnical explorations in relation to the experimental shafts. Two borings advanced for split-spoon and thin walled-tube sampling and standard penetration testing (SPT), two cone penetration tests (CPTs) and one seismic CPT (SCPT) were used to characterize the soil stratigraphy at the test site. Appendix A.1 through A.3 present all of the CPT and SCPT results for this site. The time of the first peak, t_{peak}, at each sampling depth, as shown in the Appendix A.2, was selected as the travel time with slant path from the source to the receiver. In this study, the corrected vertical travel time versus depth analysis method (Redpath 2007) was used to estimate the V_s. and then used in the following analyses. To consider the offset of the signal source to the collar of the borehole, the vertical travel time, t_v, from the ground surface down to the receiver was estimated by multiplying the travel time by the cosine of the angle (θ) between the slant path and vertical. The t_v were plotted against their respective depths; and the velocities were estimated by determining the slopes of the interpreted major straight-line segments of the plotted data. Figure 4-7 shows the determination of shear wave velocity, V_s, for SCPT-2.

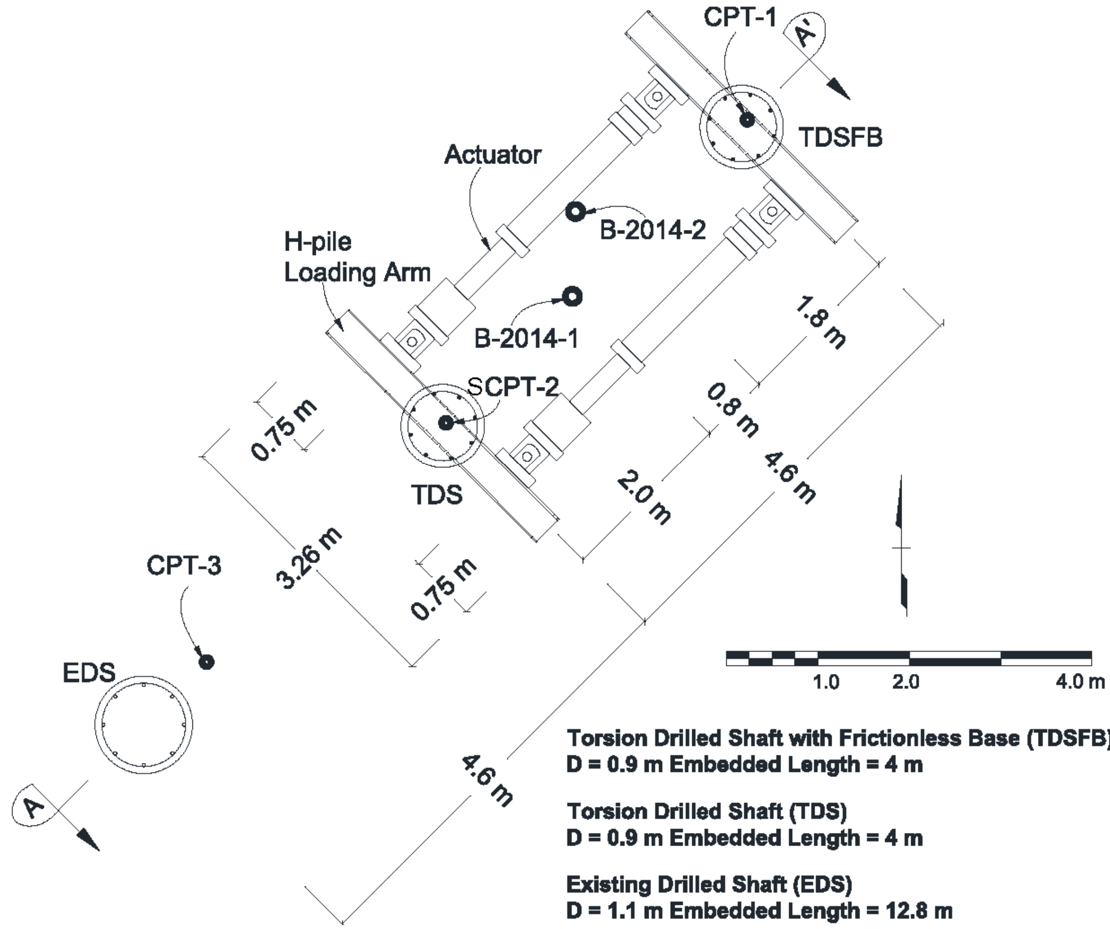

Figure 4-6 Test site layout, including the torsion drilled shaft with frictionless base, torsion drilled shaft, and existing drilled shaft (EDS), and exploration plan.

As shown in Figure 4-8, the subsurface consisted of overconsolidated silty clay to clayey silt to approximately 5.2 m depth, underlain by a layer of sand to silty sand. The near-surface soils were desiccated to a depth of 0.9 m and formed a very stiff to hard crust (when dry), as indicated by high q_t and SPT N conducted during a period of extended low groundwater levels, as is typical for the test site in general. From a depth of 0.9 m to approximately 5.2 m, the silty clay to clayey silt is of medium stiff to very stiff consistency. A 1.1 m thick layer of dense silty sand with gravel (SM) was encountered in CPT-2, in B-2014-1, and in the excavated spoils of the test shaft installed at this location. The toe of

TDS penetrated this sand lens to bear into the underlying clayey silt; as described subsequently, the sand lens resulted in significant differences in torsional loading performance. The average unit weight of the silty clay to clayey silt layer and the silty sand layer is 18 and 20 kN/m^3, respectively, based on the laboratory results described by Dickenson and Haines (2006) and Nimityongskul (2010). The relative density and friction angle of the sandy layer is approximately 75% and 40° estimated using correlations to SPT *N* (Gibbs and Holtz 1957, Meyerhof 1956) and CPT cone tip resistance, q_c (Meyerhof 1956). As shown in Figure 4-8, the piezometric surface varies between a depth of 0.6 and 2.5 m (2 to 8 ft) below the ground surface throughout the year and was located at 1.9 m depth during the torsional loading tests.

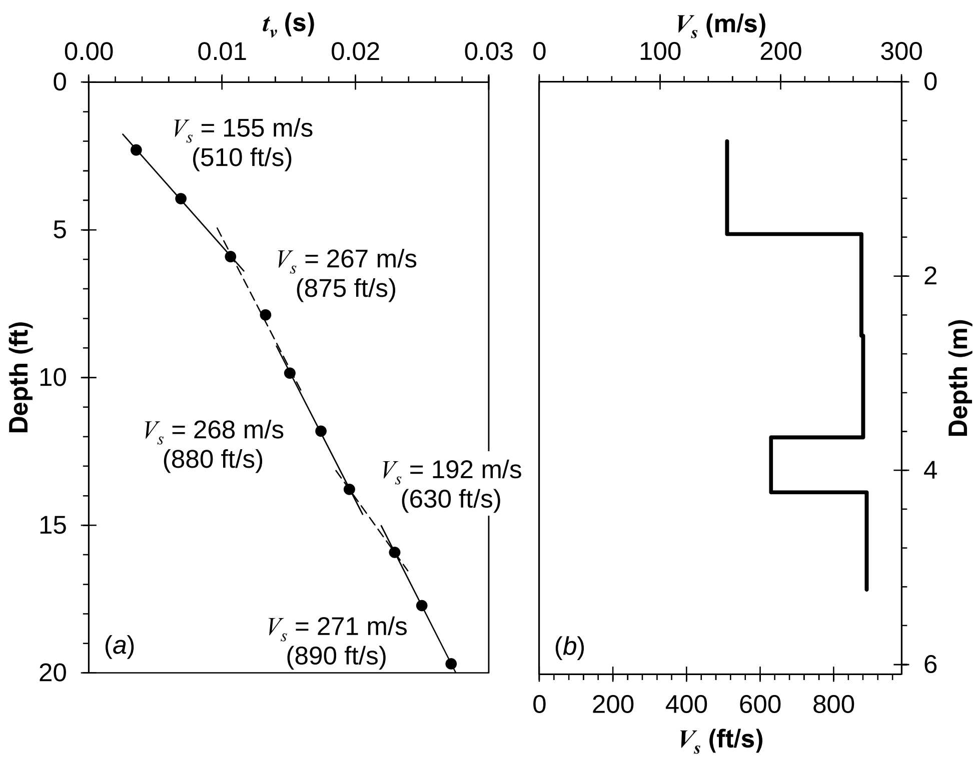

Figure 4-7 Determination of shear wave velocity, V_s, for SCPT-2 of torsional loading test, including (a) vertical travel time, t_v, versus depth and (b) V_s profile.

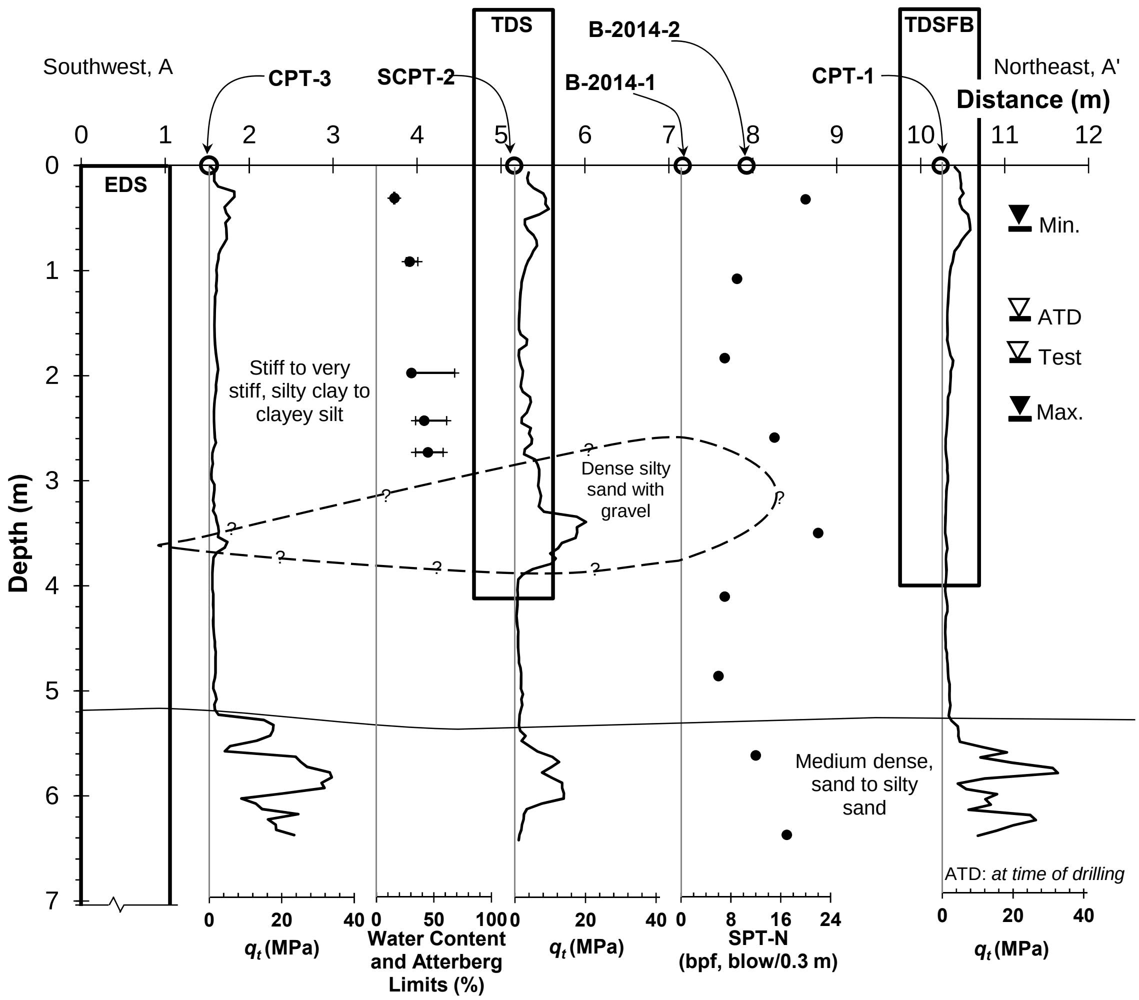

Figure 4-8. Subsurface profile at test site indicating the location of the test shafts.

4.4 Site Specific Geotechnical Exploration for Axial and Lateral Loading Tests

To obtain more geotechnical information of the specific testing area for the axial and lateral loading tests, site-specific explorations, including the cone penetration test (CPT) and six seismic CPTs (SCPTs), were made, as shown in Figure 4-9. Nearby borings conducted to support tests of drilled shafts in torsion were also considered. The specific testing footprint is approximately 20 m (66 ft) south of the area where the full-scale torsional response of drilled shafts was evaluated. Appendix A.4 through A.11 present all of the CPT and SCPT results for this test site. The shear wave velocity profile for SCPT-1, -2 and -3 was estimated, as shown in Figure 4-10, and used to estimate the maximum shear modulus, G_{max} for the cased and uncased shafts, respectively.

The testing area-specific soil profile, shown in Figure 4-11, was developed using the results of the CPTs, recent and historical nearby borings, and Atterberg limit tests on split-spoon and grab samples collected during drilling. The native soil profile consists of stiff to very stiff, plastic Willamette Silt to a depth of approximately 5.2 m (17 ft), with an intermittent, thin sand lens at a depth of approximately 3 m (10 ft). A layer of dense silty sand with gravel and intermittent seams of sandy silt follows, with an approximate thickness of 6.5 m (21.3 ft) separates the Willamette Silt deposits from a thick and deep deposit of plastic, stiff to very stiff sandy clayey silt with intermittent seams of silty sand that grades finer to silty clay to clayey silt (referred to as blue-grey clay by Dickenson and Haines 2006). The piezometric surface was located at a depth between 1.6 and 1.8 m (5 and 6 ft) during the axial loading tests of the test shafts, and was located at the depth of 1.9 and 2.0 m (6.3 and 6.6 ft) during the lateral loading tests of the uncased shafts and the cased shafts, respectively. Some groundwater flows through the thin sand lens at depth of about 3 m, but is generally concentrated in the silty sand and sandy silt layer at about 5 m depth below ground surface.

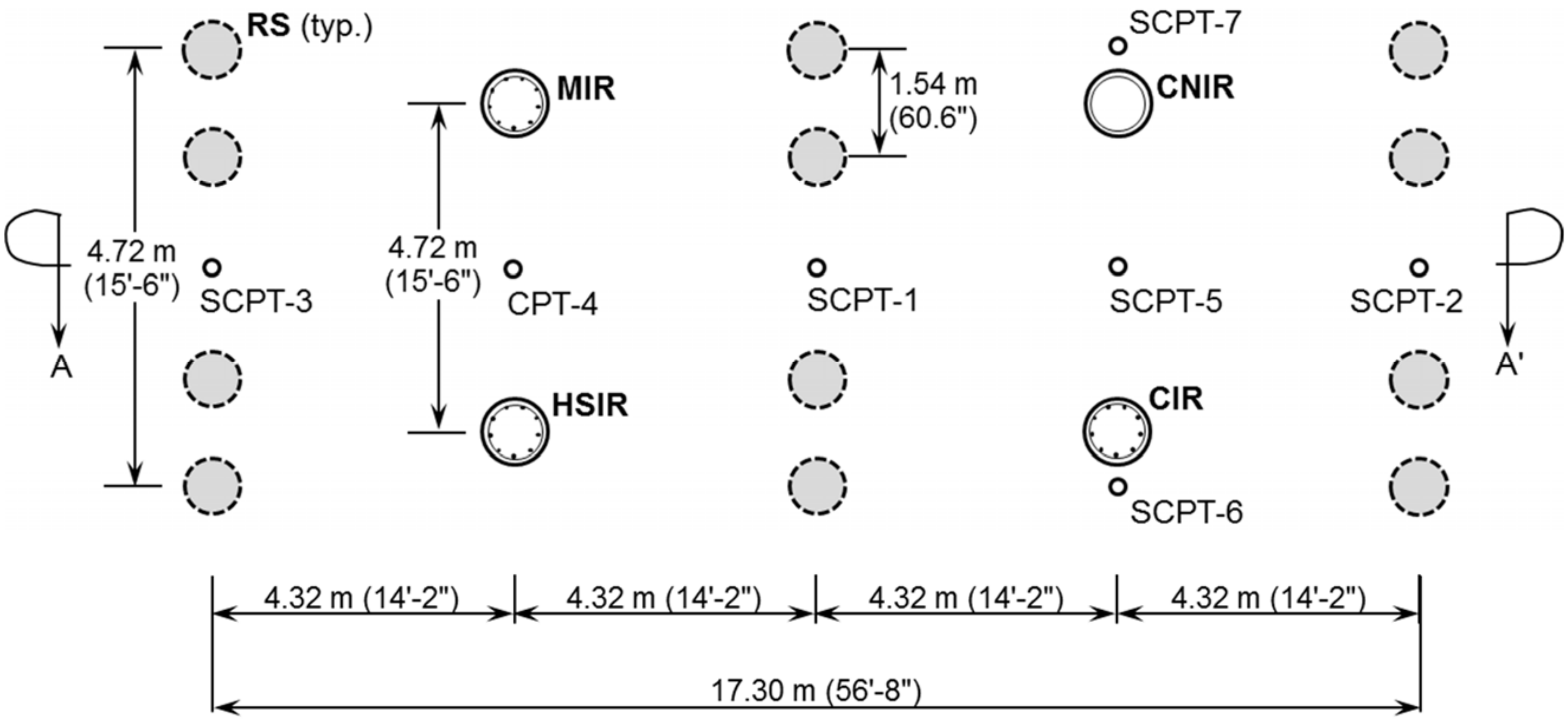

Figure 4-9. Test site layout, including test shafts for axial and lateral loading tests, reaction shafts (RS) and exploration plan. Note: MIR = drilled shaft with mild internal steel reinforcement, HSIR = drilled shaft with high-strength internal reinforcement, CIR = cased drilled shaft with mild internal steel reinforcement, and CNIR = cased drilled shaft with no internal steel reinforcement.

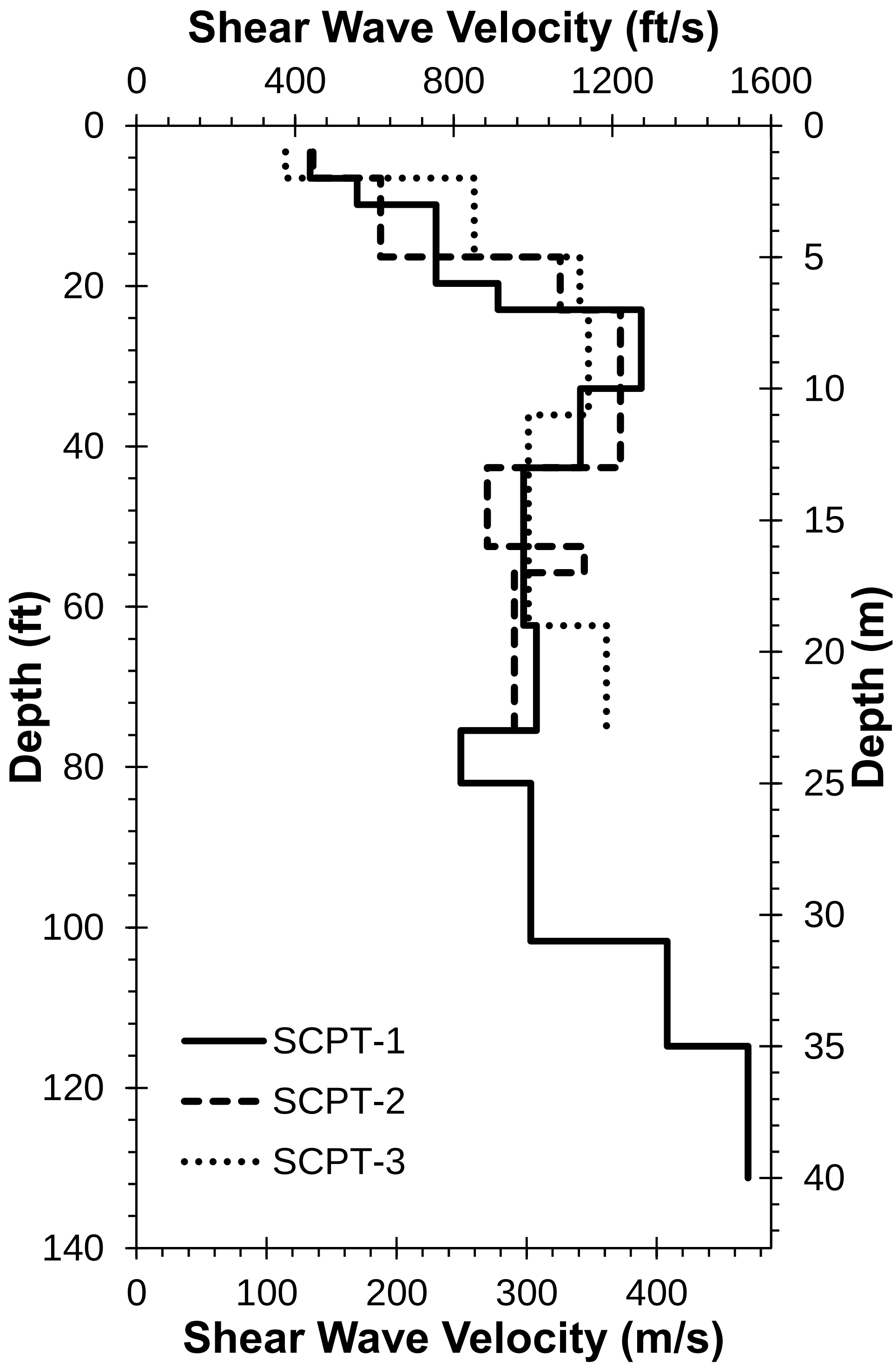

Figure 4-10 Profiles of shear wave velocity, V_s, for SCPT-1, -2 and -3 of axial and lateral loading tests

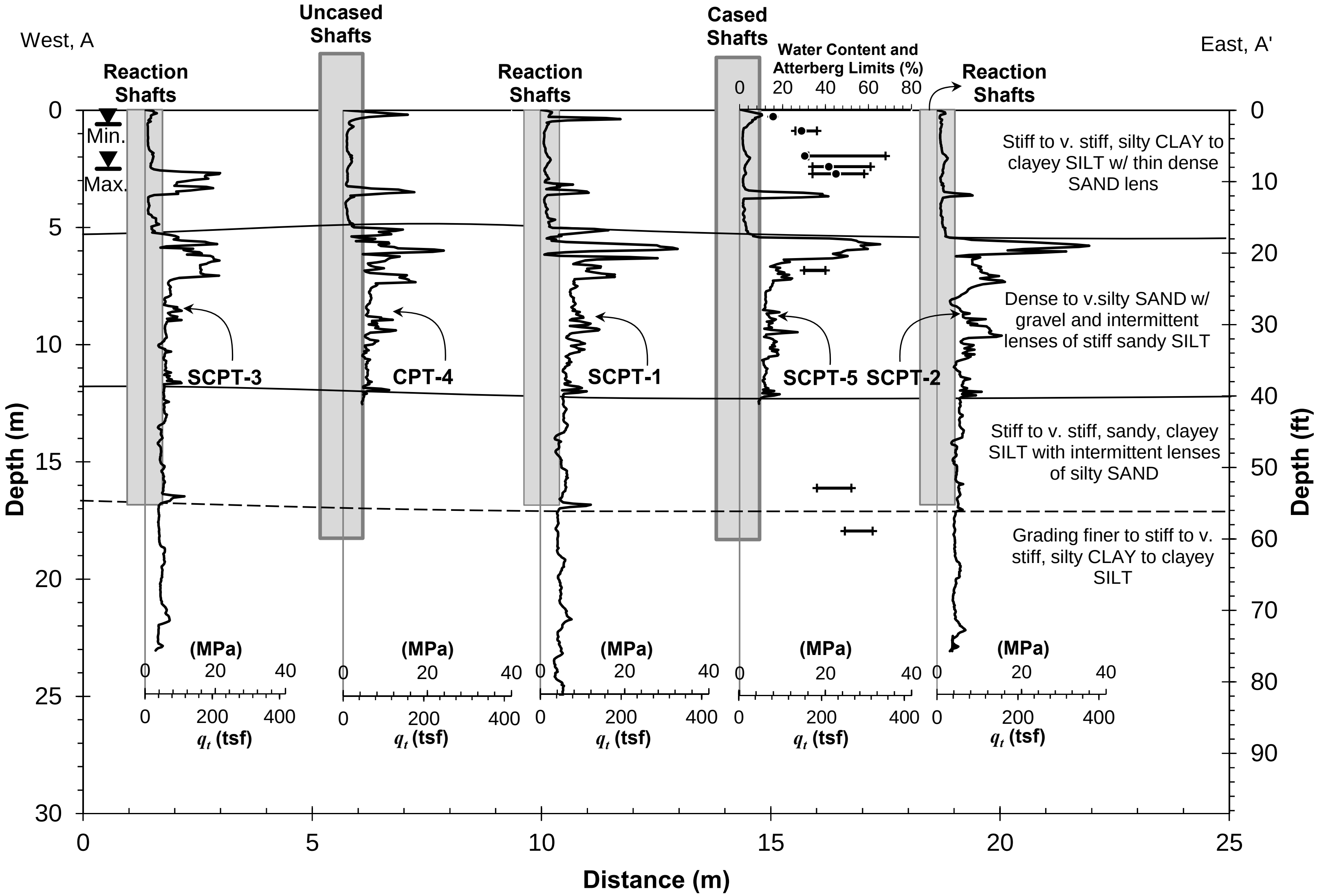

Figure 4-11: Subsurface profile at test site indicating the location of the test shafts, cone tip resistance, and Atterberg limits

4.5 References

Dickenson, S.E. and Haines, B.Z. (2006). *Characterization of the geotechnical engineering field research site at Oregon State University*, 3rd Ed., Oregon State Univ., Corvallis, OR.

Gibbs, H. J., and Holtz, W. G. (1957). "Research on determining the density of sands by spoon penetration testing". *Proceedings, 4th International Conference on Soil Mechanics and Foundation Engineering*, London, England, Vol. I, 35-39.

Martin, J.P. (2018). "Full-Scale Loading Tests of Shallow Foundations on Aggregate Pier-reinforced Clayey Silt," *MS Thesis*, Oregon State University, Under Development

Meyerhof, G. G. (1956). "Penetration tests and bearing capacity of cohesionless soils." *Journal of Soil Mechanics and Foundation Division.* 82(1), 1-19.

Nimityongskul, N. (2010). "Effects of soil slope on lateral capacity of piles in cohesive soils." *Ph.D. Dissertation*, Civil and Construction Engineering Department, Oregon State University, Corvallis, OR.

Redpath B. (2007). "Downhole Measurements of Shear- and Compression-Wave Velocities in Boreholes C4993, C4996, C4997, and C4998 at the Waste Treatment Plant, DOE Hanford Site." *PNNL-16559*, prepared by Redpath Geophysics, Murphys, California, for Pacific Northwest National Laboratory, Richland, Washington.

USGS. The National Map Viewer. Available: http://viewer.nationalmap.gov/viewer/. Accessed September 2, 2015.

5. TORSIONAL LOAD TRANSFER OF DRILLED SHAFT FOUNDATIONS

Authors:

Qiang Li, Armin W. Stuedlein, and Andre R. Barbosa

Journal:

Journal of Geotechnical and Geoenvironmental Engineering

Volume 143, Issue 8, August 2017

5.1 Abstract

Drilled shaft foundations commonly experience torsional loads, in addition to axial and lateral loading. Such cases include loads on mast arm traffic sign and signal poles, or seismically induced inertial loading of foundations supporting skewed or curved bridges. Despite the prevalence of drilled shafts, the understanding of the actual resistance to torsion provided by these deep foundation elements is not well established. To help address this gap in knowledge, two instrumented drilled shafts were constructed to evaluate the torsional capacity and load transfer at full scale. Both monotonic quasi-static and cyclic loading tests were performed. The imposed rotation and corresponding torque was monitored using string potentiometers and load cells, respectively. Strain gauges installed to measure shear strains facilitated computation of the torsional load transfer, which is described in detail. Design procedures for the calculation of the ultimate total and unit torsional resistances of drilled shafts are proposed and resulting estimates compared against the resistances observed in the testing program and other studies reported in the literature. The rational design methodology proposed herein overpredicts or underpredicts the torsional capacity, indicating the need for the development of improved methods for assessing the torsional resistance of drilled shaft foundations.

5.2 Introduction

Drilled shaft foundations are commonly selected by public transportation agencies to support mast arm traffic sign and signal pole structures along highway alignments and to support bridge column loads. In the former case, foundation loading includes moments due to cantilevered dead loads, which may be represented as a lateral shear, and torsional loads that arise from wind gusts. Often, torsional loads can control the design length of the foundation, particularly in storm-prone regions that can produce significant wind speeds. For example, observations of storm-induced winds along the Oregon and Washington coast in 2007 indicated a maximum wind gust of 237 km/h (Reiter 2008). Despite the prevalence of drilled shafts for the support of traffic sign and signals in practice, the understanding of the actual torsional load transfer provided by deep foundations is not well established, and there is no accepted national standard for the sizing of drilled shafts to resist design torsional loads. In addition to geotechnical torsional capacity, design guidance validated by full-scale load transfer data, presently lacking in the literature, may lead to an improvement in the design of transverse reinforcement in drilled shafts.

Despite the lack of design standards, some significant studies have been conducted on the prediction of the response of foundation elements subjected to torsion. For example, analytical and numerical models have been developed using boundary element methods (Poulos 1975; Basack and Sen 2014), discrete element analyses (Chow 1985), nonlinear spring models (Georgiadis 1987; Georgiadis and Saflekou 1990), and closed-form analytical solutions (e.g., Randolph 1981, Hache and Valsangkar 1988; Guo and Randolph 1996; Guo et al. 2007; Zhang 2010). Some design guidance for the ultimate resistance of torsionally-loaded foundations have been provided by several public agencies (e.g., Hu 2003), however, these design approaches do not provide any guidance on the amount of rotation, θ, that may be anticipated upon reaching the ultimate resistance (Nusairat et al. 2004). The lack of widespread adoption of these methods in state or national codes may stem in part from the lack of previously reported torsional load transfer data developed from physical experiments.

Torsional loading tests of physical models described in the literature may be categorized into three types: (1) tests on small-scale models of driven piles and drilled shafts at 1*g* (Poulos 1975; Dutt and O'Neill 1983; Randolph 1983; Tawfiq 2000), (2) multi-*g* centrifuge loading tests (Bizaliele 1992; Laue and Sonntag 1998; McVay et al. 2003; McVay and Hu 2003; Hu 2003; Zhang and Kong 2006), and (3) full-scale 1*g* loading tests (Stoll 1972; Tawfiq 2000; McVay et al. 2014). Among these tests, torsional load transfer was only investigated in one scale model test (Dutt and O'Neill 1983) and two centrifuge loading tests (Bizaliele 1992; Zhang and Kong 2006) by measuring the torsionally-induced shear strains along the test specimens. No load transfer observations were reported for any of the full-scale tests.

This study presents the results of quasi-static monotonic and cyclic torsional loading tests on drilled shafts tested to observe foundation load transfer at full-scale. Two drilled shafts, 0.9 m in diameter and embedded approximately 4 m below the ground surface, were constructed at the geotechnical field research site on the Oregon State University (OSU) campus in Corvallis, Oregon. The test shafts are designated herein as the test drilled shaft with production base (TDS; constructed using normal methods), and the test drilled shaft with frictionless base (TDSFB). Each shaft was instrumented to observe torsional shear and flexural strains, displacements and rotations, and loads (to compute the applied torque). In this chapter, first, the subsurface conditions at the test site are described and the experimental setup, including the instrumentation program, is presented. Second, loading test results described include applied torsion-shaft head rotation curves, and shear strain, torsion, and unit torsional shaft resistance distributions along the length of the shafts. Third, the back-calculated unit torsional shaft resistance-local rotation (τ-θ) curves are provided for each tributary instrumented area. Next, the results of the cyclic loading tests are described in the context of mobilized unit shaft resistance and cyclic stiffness. Finally, the ultimate resistance computed using proposed design methods are compared against that observed from the loading tests as well as other loading test data available in the literature to provide a preliminary baseline of design method accuracy and variability.

5.3 Experimental Program

5.3.1 Subsurface Conditions

The test shafts were constructed at the geotechnical engineering field research site at OSU. The site plan with the geotechnical explorations and the experimental shafts is shown in Figure 4-6. The detailed subsurface conditions for the torsional loading test are discussed in Section 4.3.

5.3.2 Construction and Experimental Details of the Test Shafts

The test shafts were designed to support Oregon Department of Transportation (ODOT) signal pole type SM3, which is specified in Standard Drawing TM651 (ODOT 2014). The standard maximum design base reactions for signal pole type SM3 includes an axial load of 15.5 kN, a shear load of 34.6 kN, a moment of 138.4 kN-m, and a torque of 82.9 kN-m. The diameter associated with signal pole type SM3 corresponded to a shaft diameter of 0.9 m based on ODOT Standard Drawing TM653 (ODOT 2014). The embedded length of the shaft, equal to 4.0 m, was determined by ODOT using the Broms (1964) method in consideration of lateral loading requirements only, as specified by the ODOT *Traffic Structures Design Manual* (ODOT 2015). This design approach assumes that the drilled shafts were embedded in a homogenous deposit of plastic, fine-grained soil, and applies an effective factor of safety of 2.15 to the lateral capacity. The torsional resistance was not explicitly considered. The required steel reinforcement consisted of eight #8 longitudinal bars and #4 hoops at 152 mm spacing with 457 mm hoop lap length. Figure 5-1a illustrates the details of the test shafts. The dry method of construction was used for both test shafts. To create a near-zero base shear condition for shaft TDSFB, bentonite chips were placed evenly across the bottom of the cavity and separated from the concrete with plywood. During the excavation of TDS, the hole was over-drilled by approximately 150 mm. The compressive strength of the concrete for TDS and TDSFB on the day of the test was 42 and 46 MPa, respectively. The shear modulus of the concrete was estimated to be 11.7 and 12.5 GPa for TDS and TDSFB, respectively, using the compressive strengths and the ACI 318-05 Model (ACI 318 2005).

Equal, but opposite, displacements were applied to the H-pile loading arm that were cast in the shaft, as shown in Figure 4-6. The total axial load transferred to the test shafts embedded in the ground consisted of the sum of the self-weight of the shafts above ground surface, loading arms, and actuators. For each shaft, the axial load was approximately 50 kN, or approximately three times larger than the typical design axial load for this standard foundation type (ODOT 2014).

5.3.3 Instrumentation and Interpretation of Torsional Load Transfer

Vibrating wire concrete embedment strain gauges (ESG) and resistance strain gauges (RSG) were installed on the steel cages at five elevations to measure torsionally induced shear strains and potential flexural strains, respectively, as shown in Figure 5-1a. The RSGs were fixed to longitudinal bars, whereas the ESGs were installed in between the longitudinal bars with a 45° inclination to the longitudinal axis. Each instrumented elevation consisted of two pairs of ESGs and two pairs of RSGs, for redundancy. Two string-potentiometers were attached to each end of the loading arms to monitor their displacement and determine the individual rotation of each shaft. Two sets of load cells were used to measure the forces that developed from the imposed displacements. The torque exerted at the shaft head was calculated as the product of the moment arm (0.88 m) and measured force. Appendix B.1 describes the procedure used to smooth the displacements observed using the string-potentiometers, whereas Appendix B.2 describes the methodology used to estimate the internal torque at the location of each ESG.

To produce the most accurate estimate of torsional load transfer, both of the shafts were exhumed (Figure 5-1b) after testing, cleaned, and as-built dimensions measured for use in the back-calculation of τ-θ curves. For shaft TDS, approximately 0.3 m of the concrete at the shaft toe appeared to have been contaminated with the silty sand that was encountered during excavation of this shaft that may have caved from the side walls of the excavation. The four ESGs that were located within 230 mm of the toe appeared to have been affected by the poor quality material encapsulating them, as confirmed in the data described subsequently. A portion of the base of shaft TDSFB also indicated poor concrete quality. Based on the inspection of that shaft, it appeared that some amount of bentonite traveled between the small-diameter holes in the plywood base to mix with the concrete, as the concrete showed signs of bentonite contamination. The concrete was soft and was easily chipped with hand tools; the effect of the softer base concrete was also apparent in the strain gauge data as described subsequently.

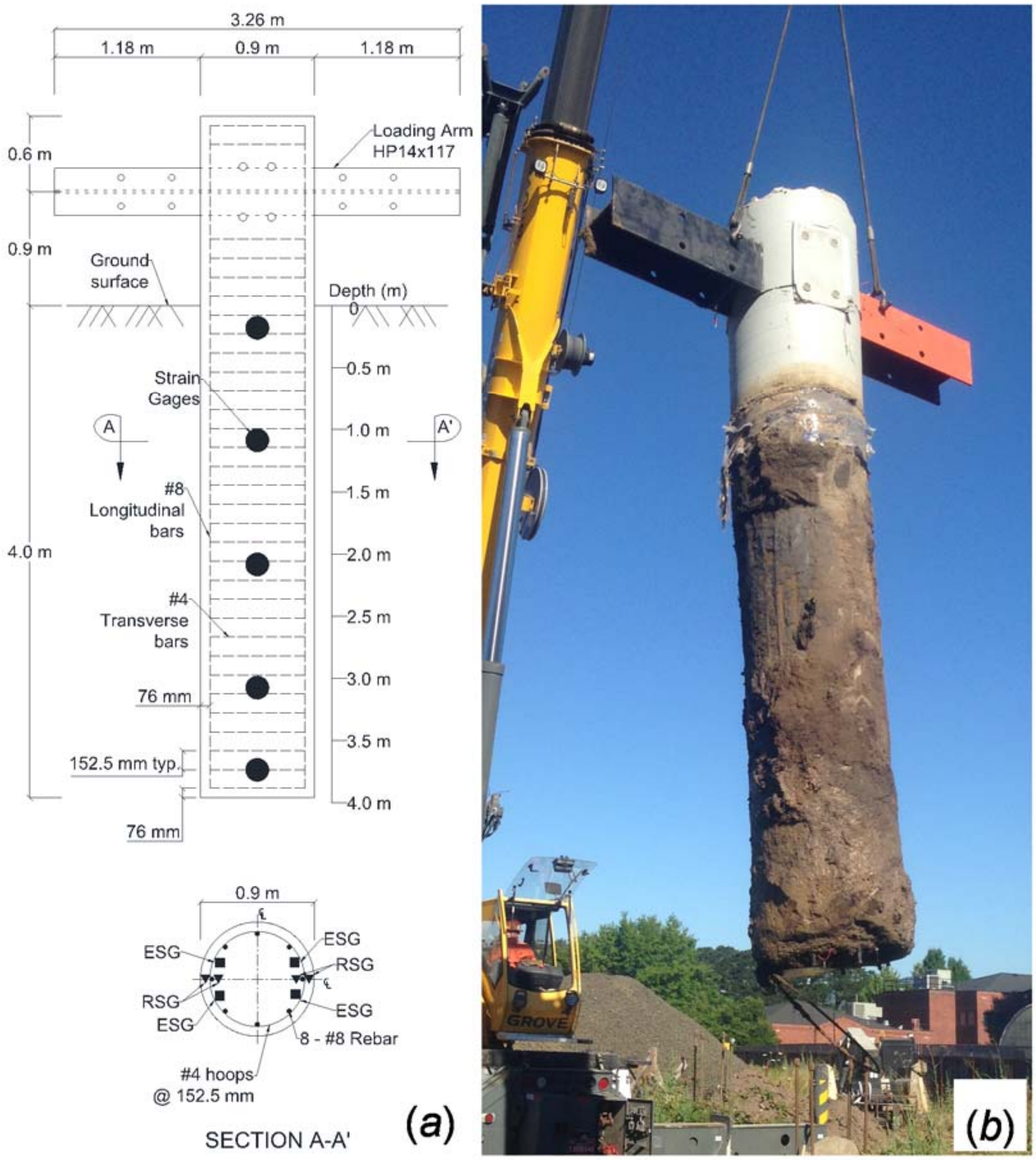

Figure 5-1. Construction details of test shafts: (a) schematic of drilled shaft elevation and cross-section of A-A', and (b) photograph of exhumed shaft. Note: ESG = embedded strain gauges and RSG = resistance strain gauges (image by Armin W. Stuedlein).

5.4 Loading Test Results and Discussion

The torsional loading test was conducted during a strong winter storm with significant precipitation, ideal (i.e., worst case) conditions for evaluating the performance of signal pole foundations in the moisture-sensitive fine-grained soils of Western Oregon. The planned torsion test protocol was initiated with quasi-static loading to very large target rotations. Thereafter, the shaft was unloaded and the zero-torsion state evaluated. The final stage of the loading protocol included twenty displacement-controlled loading-unloading cycles to observe changes in cyclic torsional stiffness. The results of this testing program are described in detail subsequently.

5.4.1 Quasi-Static Loading of the Test Shafts

The loading test commenced with a target incremental rotation of 0.1° at the loading arms. However, the lens of dense silty sand located near the base of shaft TDS prevented significant rotation of this shaft, and the rotation of shaft TDSFB was used to guide the loading procedure. After shaft TDSFB reached approximately 1.75° of applied rotation (corresponding to a rotation of 0.1° for TDS; Figure 5-2), the specified incremental rotation was increased to 0.5° until 5° of total rotation was reached. Then, the incremental rotation was increased to 1° until approximately 13° of total rotation was achieved. Differences between the prescribed rotation and the actual rotation of test shafts measured from the string potentiometers were observed because of differences in torsional stiffness and strength at the soil-structure interfaces. Displacements were held at 5-min time intervals at each target shaft rotation to allow sufficient sampling of ESG data (which required 3 s/sample). The applied shear strain rate along the soil-shaft interface during the quasi-static loading test, computed assuming $\gamma = 2\theta$ per Randolph (1981) and Dutt and O'Neill (1983) and where γ = shear strain, was 0.07, 0.35, and, 0.70% per minute when the incremental rotation was 0.1°, 0.5°, and 1°, respectively, and the initial fivefold increase in the shear strain rate appeared to produce an increase in torsional resistance of approximately 5%. Toward the end of the quasi-static loading test, spiral-type cracks up to 300 mm in length and 6 mm in width were observed at the ground surface next to TDSFB (Figure 5-2a), whereas diagonal shear cracks were observed in the concrete along the surface of TDS. At the end of the quasi-static loading, TDSFB rotated approximately 13°, whereas TDS only rotated 0.14° because of the layer of dense silty sand.

The torsional resistance for TDSFB transitioned from the initial stiff response to a softer response between rotations of approximately 0.2° to 0.5°, and became fully mobilized (i.e., achieved the ultimate resistance) with a resistance equal to approximately 185 kN-m at a rotation of approximately 1.0°, as shown in Figure 5-2a. The torsional resistance remained unchanged until 1.75°, where after increases in resistance resulting from increases in strain rate, as discussed previously, resulted in a maximum resistance of 199 kN-m. The inset of Figure 5-2b shows that for shaft TDS after approximately 0.1° of rotation (corresponding to 1.75° for TDSFB and just prior to increasing the strain rate), increases in rotation resulted in increases torsional resistance. Thereafter, the torque-rotation curve flattens to produce no further increases in resistance, as the experimental setup required that the two shafts remain in torsional equilibrium. Since shaft TDSFB failed, the ultimate resistance of TDS could not be achieved experimentally. Since no further torsional resistance could be generated by TDS, rotations greater than 0.1° indicate the development of soil creep under the sustained torsional resistance. Approximately 0.04° of creep-induced rotation occurred over a duration of approximately 75 minutes, a duration commensurate with sustained wind loads.

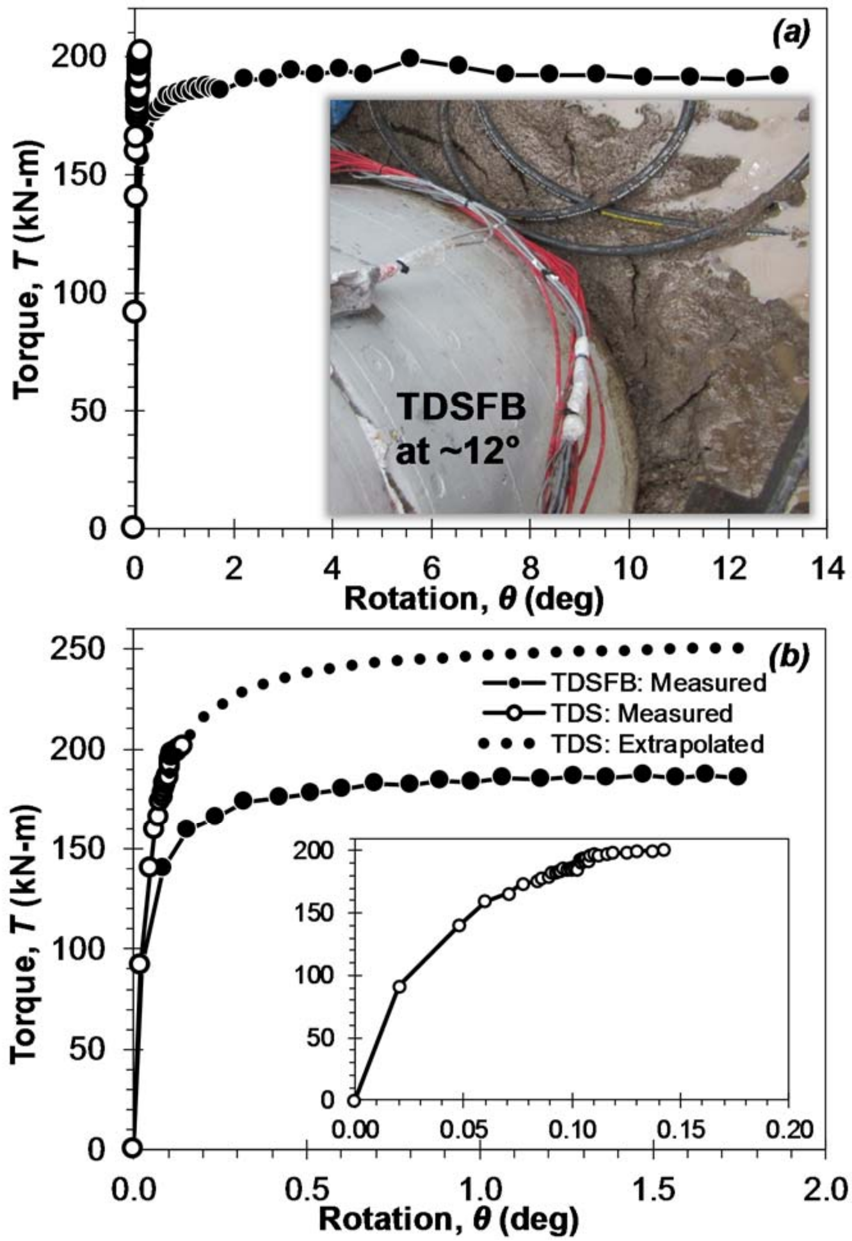

Figure 5-2. Relationship between torque and applied rotation for the test shafts under quasi-static loading: (a) full results to very large rotations of TDSFB with inset photo showing ground cracking (image by Armin W. Stuedlein), and (b) observed and extrapolated torque and applied rotations, with inset showing the small rotation response of TDS.

Because the relationship between torque, T, and rotation, θ, of shaft TDSFB was well modeled by a hyperbola, the hyperbolic model was used to model and extrapolate the torque-rotation response of shaft TDS for rotations up to 1.75° (creep-induced rotations were neglected in the model fitting). The hyperbolic model has been successfully used to represent the stress-strain response of cohesive soils (e.g. Kondner 1963), the load-settlement response of axially loaded piles (e.g. Chin 1970, 1971, Stuedlein and Reddy 2014) and footings (Huffman et al. 2015). The hyperbolic model is given by:

$$T = \frac{\theta}{C_1 + C_2 \cdot \theta} \tag{5.1}$$

where C_1 and C_2 are fitting parameters determined using ordinary least squares. The suitability of the hyperbolic model to represent the observed (θ, T) data is facilitated by transforming the data into hyperbolic (θ/T, θ) space, and assessing the goodness of fit of the presumed linear function, given by:

$$\frac{\theta}{T} = C_1 + C_2 \cdot \theta \tag{5.2}$$

to the transformed data. For the quasi-static test, the mean bias (i.e., the ratio of the measured and the predicted torque) of the observed shaft head response of TDSFB and the fitted hyperbolic model was 1.01, and the coefficient of variation of the sample bias was 0.9%. The mean and coefficient of variation of the sample bias for shaft TDS was 1.0 and 3.0%, respectively, for the fitted hyperbolic model. Appendix B.3 compares the observed torsion-rotation responses for shaft TDS and TDSFB at the shaft heads and the corresponding fitted hyperbolic models. The model fitted to the observed torque-rotation response of TDS allowed extrapolation of the observations from 0.1° to 1.75°, as shown in Figure 5-2b, and an estimate of the ultimate torsional resistance, equal to 250 kN-m. An independent assessment of the torque at the head of TDS was made using fitted τ-θ curves, as described subsequently, and produced an ultimate resistance of 257 kN-m, within 3% of that estimated using the global torque-rotation observations.

5.4.1.1. Torsional Load Transfer

Figure 5-3 shows the selected shear strain profiles for TDS up to 0.1° and TDSFB up to 1.75° with the corresponding profiles of shaft diameter. The strains reduce with depth, indicating the transfer of torsional loading to the soil with increasing depth. To better understand the torsional load transfer, the internal torque at each instrumented tributary area was estimated using the measured shear strains. The torsion transferred to the soil in shaft and toe resistance is shown in Figure 5-4. The corrected cone tip resistance is also shown for each shaft to illustrate the correlation between torsional load transfer and the corrected cone tip resistance, q_t. Figure 5-4a shows the measured and extrapolated torsion along shaft TDS when the head rotations of shaft TDS was 0.1° and 1.75°, respectively, whereas Figure 5-4b shows the measured torsion along shaft TDSFB at 1.75°. Based on the data observed from the bottom-most ESGs (Figure 5-3), as well as the condition of the concrete surrounding the gauges upon exhumation of the drilled shafts, it was determined that the ESG data recorded from the bottom-most locations were unreliable, as indicated in Figure 5-4. Owing to the construction of TDSFB with a bentonite base, the torsional resistance was assumed to be zero at the base. The toe resistance of shaft TDS was estimated using Eq. (5.13b), discussed subsequently, which indicates the low likely torsional toe resistance.

The torsional resistance of shaft TDS was negligible from the ground surface to a depth of 0.18 m. The estimated internal torque at the depth of 0.18 m was slightly larger than the torque developed at the shaft head, and this may be partially attributed to the use of a constant shear modulus for interpretation of the measured strains. Shear cracks were observed on shaft TDS during testing, and this suggests that the shear modulus may have decreased following cracking. The torsional resistance between 0.18 and 2.1 m was significantly less than for TDSFB for the same magnitude of torque at the shaft head owing to the differences in mobilized shear strain at the soil-shaft interface. However, considerable torsional resistance was provided by the clayey silt and sandy soil that were encountered from the depths of 2.1 to 4.1 m.

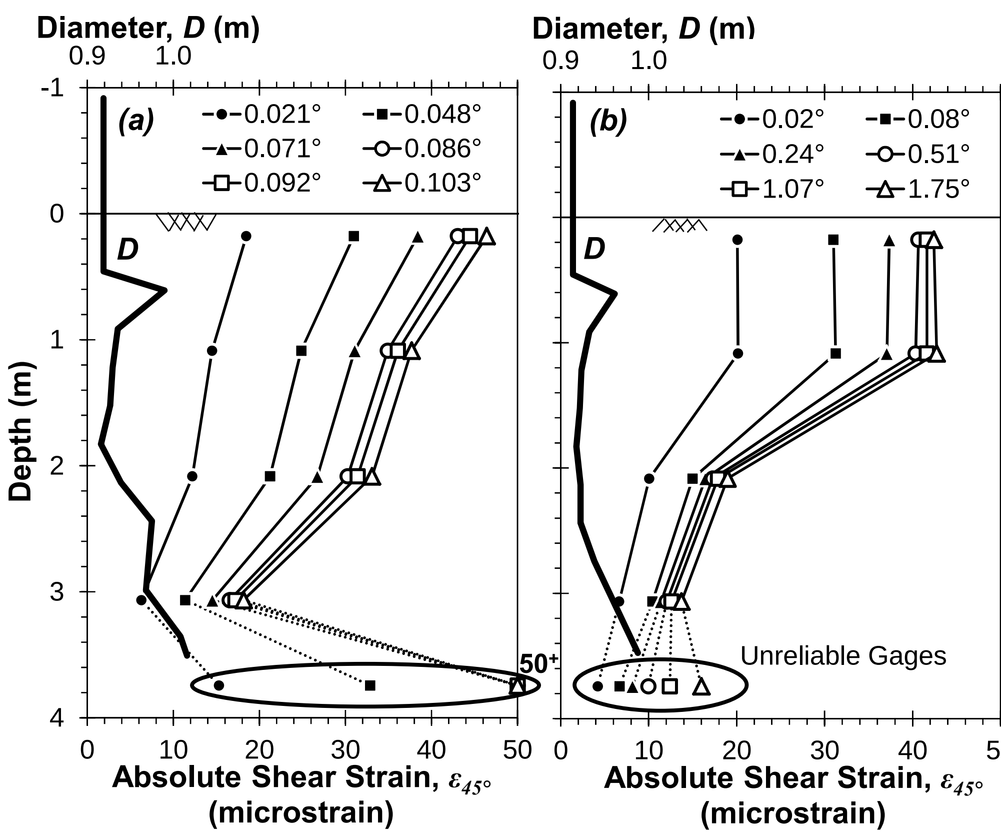

Figure 5-3. Strain profiles and diameter profiles for (a) shaft TDS up to 0.1° applied rotation; (b) shaft TDSFB up to 1.75° applied rotation.

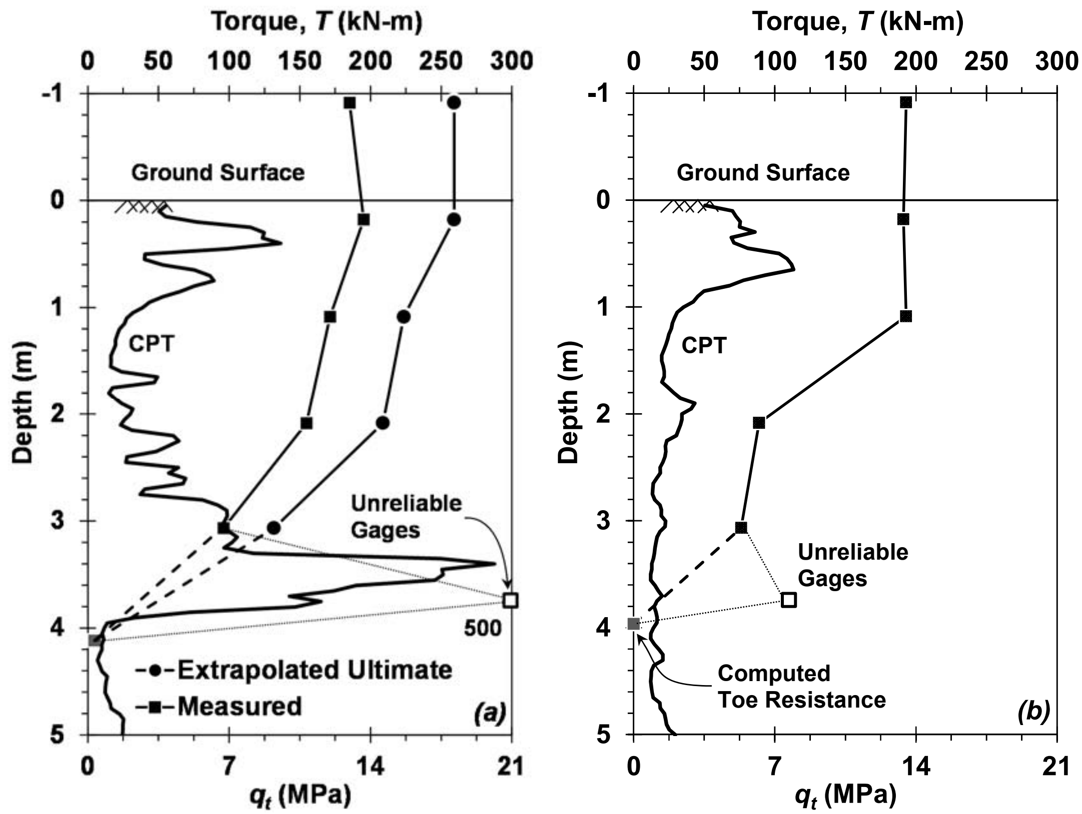

Figure 5-4. Torsional load transfer profiles with corrected cone-tip resistance, q_t, for (a) shaft TDS (observed to 0.1° rotation and extrapolated ultimate); (b) TDSFB to 1.75° rotation.

5.4.1.2. Unit Torsional Shaft Resistance and Rotation Relationships (τ-θ Curves)

The unit torsional shaft resistance, τ, was back-calculated by considering the representative tributary area for each portion of the instrumented shafts and the relative rotation at the soil-shaft interface for each tributary area. The relative rotation of a given section of shaft is affected by the torsional stiffness of the shaft and the degree of fixity or soil resistance along its shaft, and is computed by subtracting the internal twist from the rotation along the neighboring section. Specifically, the angle of twist, φ, under torsion is computed using:

$$\varphi = \frac{T \cdot \Delta L}{G \cdot J} \tag{5.3}$$

where T = average torque along the tributary area, ΔL = length of the tributary area, G = shear modulus of the shaft, and J = polar moment of inertia = $\pi D^4/32$. The as-built diameter (Figure 5-3) and the torque profile recorded at each instrumented level was incorporated in the evaluation of the angle of internal twist (see Appendix B.4) so as to develop the representative rotation at each elevation. The relationship between unit torsional shaft resistance and rotation, known as a τ–θ curve, was thus constructed and represents the mobilization of shearing resistance along a unit tributary area of a deep foundation element.

Figure 5-5 presents the mobilization of unit torsional shaft resistance with rotation for TDS and TDSFB. Because TDS did not experience large rotations owing to the dense sand layer at depth, an attempt was made to estimate the ultimate unit torsional shaft resistance by extrapolation. Figure 5-5a compares the small-rotation data in hyperbolic space against a fitted trend at selected observation intervals for the stiff silty clay to clayey silt (2.1 to 3.1 m) and dense silty sand (3.1 to 4.1 m) layers, and shows that the small-rotation data generally followed the fitted hyperbolic relationship. The hyperbolic model is justified across the full range in quasi-static rotation for the plastic fine-grained soils at the test site, as shown in Figure 5-5d, but may not be appropriate for the tributary area of shaft TDS in the sand layer, given its dilative state and tendency to soften at large relative displacements. Larger rotations than those imposed on shaft TDS would have been necessary to definitively evaluate the suitability of the hyperbolic model. However, the assumption appears tentatively reasonable given the agreement with the magnitude of extrapolated torque at the shaft head and the progressive mode of interface shear mobilization along the shaft with depth. Figure 5-5b shows the comparison of fitted and observed data in arithmetic space for comparison. Given the relatively good fit, the hyperbolic model was used to extrapolate the unit torsional resistance at larger rotations and for all tributary areas, as shown in Figure 5-5c for TDS. Figure 5-5c shows that the unit torsional shaft resistance for shaft TDS from the ground surface to a depth of 0.18 m was mobilized at the beginning of the quasi-static test and then decreased gradually to zero as the test proceeded. The unit torsional shaft resistance for the tributary areas from the depths of 0.18 to 2.1 m appeared nearly fully mobilized at the end of the quasi-static loading with the head rotation of approximately 0.1°. Based on the extrapolation for TDS, the soil resistance for the tributary areas from the depths of 2.1 to 4.1 m could have reached a fully mobilized condition at a rotation of approximately 0.5°. The unit shaft resistance for TDSFB from the ground surface to the depth of 1.1 m was negligible (Figure 5-5d); and the soil resistance for the remainder of the shaft produced significant resistance that became fully mobilized at rotations ranging from 0.2° to 0.5°. The observed ultimate unit torsional soil resistance for shaft TDSFB was in the range of 10 to 80 kPa; the extrapolated ultimate unit torsional soil resistance for shaft TDS was in the range of 18 to 100 kPa.

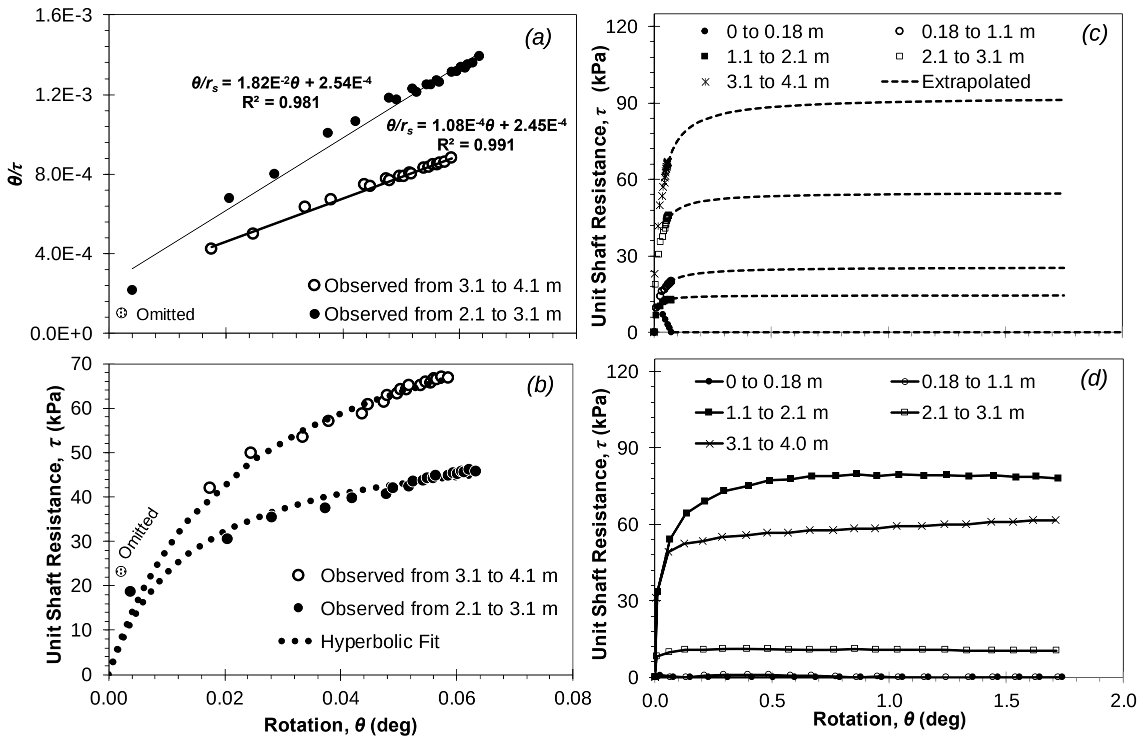

Figure 5-5. Unit torsional shaft resistance–local rotation (τ–θ) curves for the instrumented test shafts: (a) comparison of selected τ–θ data in hyperbolic space for shaft TDS; (b) comparison of fitted hyperbolic models and back-calculated τ–θ data corresponding to (a), (c) back-calculated and extrapolated τ–θ curves for shaft TDS, and (d) back-calculated τ–θ curves for shaft TDSFB.

5.4.1.3. Unit Torsional Shaft Resistance Profiles

The estimated and observed ultimate unit torsional shaft resistance profiles for TDS and TDSFB at a rotation of 1.75° as well as the undrained shear strength profile are shown in Figure 5-6. The undrained shear strength was correlated to cone tip resistance using (e.g., Kulhawy and Mayne 1990):

$$s_u = \frac{q_c - \sigma_{vo}}{N_k} \tag{5.4}$$

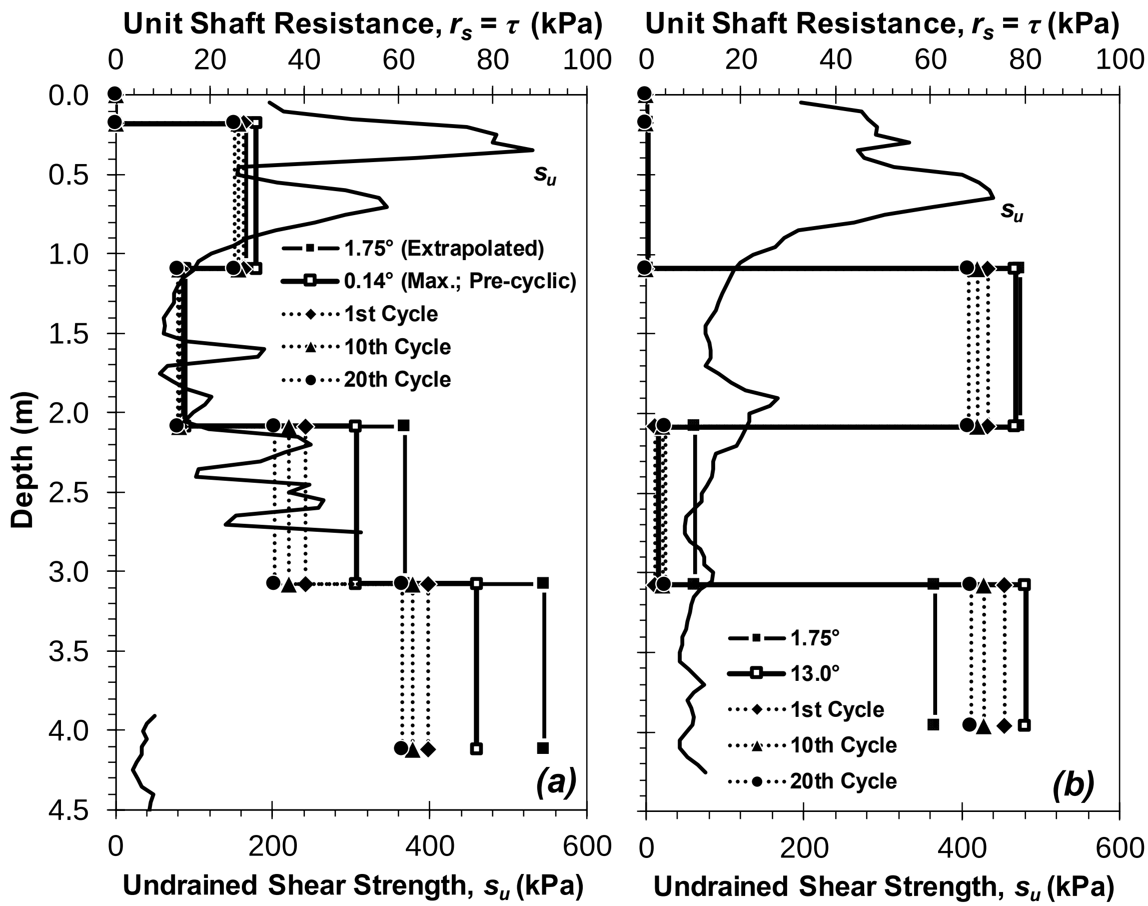

Figure 5-6. Unit torsional shaft resistance profile at 1.75° rotation and selected loading cycles with the undrained shear strength profile for (a) shaft TDS, and (b) shaft TDSFB; note: the undrained shear strength was correlated to CPT data collected under dryer conditions than those during the loading tests and the near surface values may not be representative.

where σ_{vo} = total overburden stress and N_k = cone factor, equal to 18 and back-calculated from the results of loading tests of embedded footings at the same site and soil conditions (Huffman et al. 2016). The estimated ultimate unit shaft resistance for TDS for each tributary area correlate to the undrained shear strength profile, whereas some differences between the observed undrained shear strength and the deeper tributary areas for TDSFB are noted. The unit torsional shaft resistance just prior to initiating the cyclic test is also plotted in Figure 5-6; this corresponds to a rotation of 13° for TDSFB and 0.14° for TDS.

Figure 5-6 shows that a portion of shaft TDSFB softened over the duration of the quasi-static test, whereas the deepest portion of the shaft continued to gain resistance as suggested by Figure 5-5.

It is common to reduce s_u using an adhesion factor α when estimating the load transfer for rapidly loaded foundation elements in plastic, fine-grained soils. Poulos (1975) found that α did not vary significantly between torsional and axial load transfer (exhibiting a mean bias of 0.96) for model piles in kaolinite, and thus it was of interest to evaluate the magnitude of α in this study. The adhesion factor was back-calculated for each tributary instrumented area embedded in the plastic, fine-grained soil for the observed and extrapolated unit shaft resistances at 1.75° and compared with the axial loading data from Chen and Kulhawy (1994) and the design model proposed by O'Neill and Reese (1999) in in Figure 5-7. In general, the mean and coefficient in variation in bias was 0.68 and 110%, respectively, indicative of the scatter typically associated with desiccated, clayey crust soils. However, it is noted that the design model proposed by O'Neill and Reese (1999) was based on the response of axially-loaded drilled shafts longer than 7 m, which are subjected to smaller percentage of near-surface seasonal effects on shaft resistance. Additionally, the deepest tributary area for TDSFB continued to harden beyond 1.75°, indicating that α increased beyond this selected rotation magnitude. Finally, cone tip resistance was measured during an extended dry period, and the near-surface undrained shear strength varies considerably with soil moisture; thus, much of the scatter in Figure 5-7 is likely associated with changes in matric suction following precipitation.

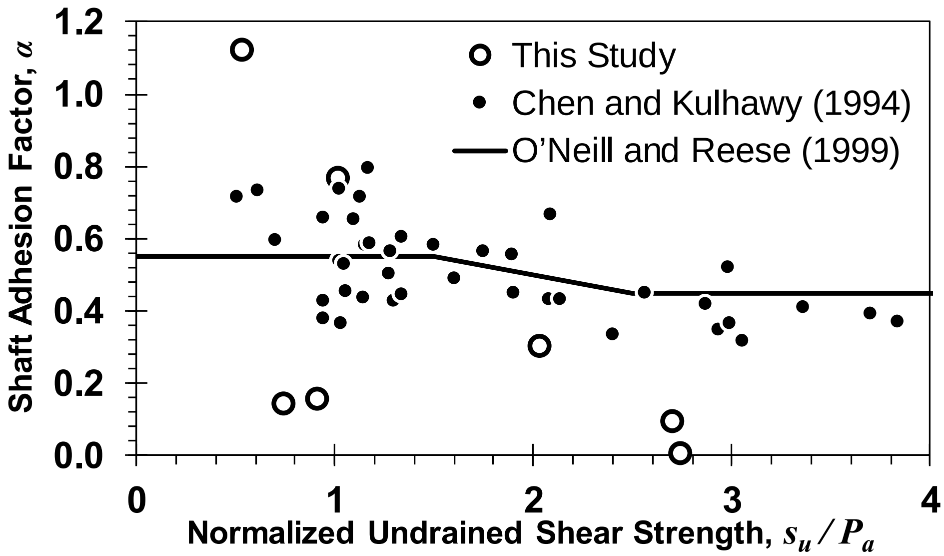

Figure 5-7. Comparison of back-calculated shaft adhesion factor, α, to those reported by Chen and Kulhawy (1994) and design line proposed by O'Neill and Reese (1999).

5.4.2 Cyclic Loading of the Test Shafts

Owing to the potential for wind gusts to repeatedly load traffic sign and signal structures, the cyclic response of the drilled shaft foundations at the soil-shaft interface was of interest, and therefore this aspect of performance was investigated. Figure 5-8a presents the actual displacement protocol applied to the loading arms of the shafts, which departed from the prescribed protocol (with displacements to range from d_0 to d_2) due to some actuator control problems that developed during the heavy precipitation. The difference of imposed displacements between the first cycle (d_1) and the remaining cycles (d_2) resulted in the difference in rotation between these cycles, as shown in Figure 5-8(b and c), respectively, for TDS and TDSFB. Although the overall rotation of shaft TDS after the quasi-static loading was quite small, the magnitude of cyclic change in rotation was similar between TDS and TDSFB. Differences in rotation may have developed owing to the ground cracking around TDSFB and the differential ability to resist lateral load, which developed over the course of the larger rotations.

The relationship between the torque and the applied rotation for TDS and TDSFB under the cyclic loading protocol is shown in Figure 5-9. The initial stiffness and postyield slope of each cycle is similar for each shaft, which is consistent with the observations made by Randolph (1983), indicating that no global degradation in the torsional response was observed. The post-yield slope of shaft TDS is stiffer than that of shaft TDSFB, a function of the granular layer present for shaft TDS. The average initial stiffness and postyield stiffness are 92 and 2.3 MN-m/deg, respectively, for TDSFB, and 96 and 4.1 MN-m/deg, respectively, for TDS.

Comparison of Figure 5-2 and Figure 5-9 indicates that the global torsional resistance produced during cyclic loading was smaller than the maximum resistance developed during quasi-static loading. Figure 5-6 compares the observed unit shaft resistance profiles for TDS and TDSFB after the 1st, 10th and 20th cycles to that at the end of the quasi-static loading. The cyclic unit shaft resistance for the upper 2.1 m of shaft TDS is similar to the estimated ultimate resistance and that at the end of the quasi-static loading. However, the unit shaft resistance from tributary areas ranging from 2.1 to 3.1 m, and 3.1 to 4.1 m, reduced to 83 and 84% of the extrapolated maximum quasi-static unit resistance at the end of the quasi-static loading, whereas it reduced to 55 and 67% by the 20th cycle. This observation suggests that either the unit shaft resistance for shaft TDS was not fully mobilized along these depths, and/or that the dense sand layer may have experienced friction fatigue during cycling. Because all soils initially contract upon shearing, the initial volume reduction produces a corresponding decrease in the lateral effective stress, a process that is exacerbated during load cycling (White and Bolton 2004; Basu et al. 2011, 2014).

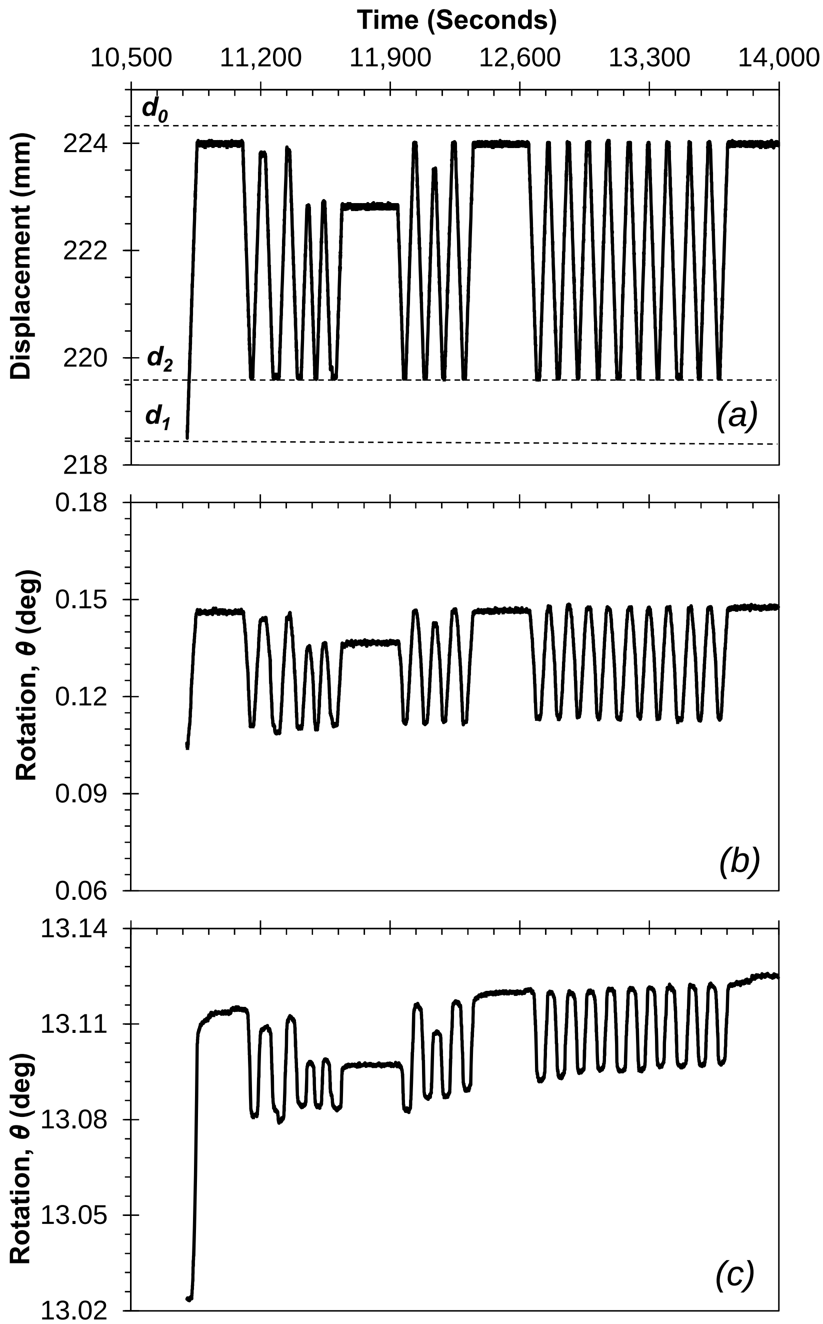

Figure 5-8. Cyclic loading test protocol implemented, including (a) the actual displacement time history prescribed, and the rotation time histories for (b) shaft TDS, and (c) shaft TDSFB.

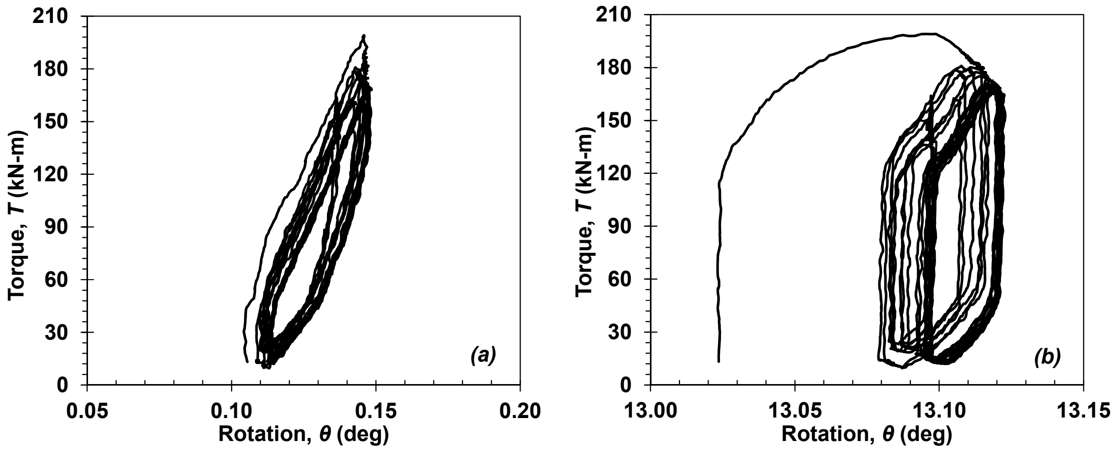

Figure 5-9. Torque-rotation hysteresis observed for (a) shaft TDS, and (b) shaft TDSFB.

The soil around shaft TDSFB provided negligible torsional resistance from the ground surface to a depth of 1.1 m during cyclic loading (Figure 5-6). The unit shaft resistance for the tributary area ranging from 1.1 to 2.1 m did not appear fully mobilized, whereas softening had occurred prior to cyclic loading for the depths of 2.1 to 3.1 m. The unit torsional shaft resistance for depths from 3.1 to 4.0 m did not appear fully mobilized during cyclic loading, with the observed resistance about 14% smaller than the pre-cyclic resistance at the 20th cycle. Based on these observations, it appears that investigation into the effect of cyclic torsional loading on the response of drilled shafts is warranted in future studies.

5.5 Assessment of Torsional Resistance of Drilled Shafts

5.5.1 Recommended Design Methodologies

Nusairat et al. (2004) provide a summary of design methodologies for torsional resistance of drilled shafts that are implemented in certain public agencies, and this report may provide some useful guidance. However, many of the design methods discussed lacked critical details and justifications regarding the assumptions invoked in the various methods. Design methodologies are thus proposed here to serve as an alternative for the estimation of the torsional capacity of drilled shafts. In general, the torsional capacity or ultimate torsional resistance of drilled shafts, defined as the maximum torsional resistance possible independent of the magnitude of rotation, consists of the sum of the ultimate shaft and toe resistance, given by:

$$T = T_s + T_t \tag{5.5}$$

where T_s = shaft resistance, and T_t = toe resistance.

For shafts in granular soils, the unit shaft resistance, r_s, can be estimated using the typical β method for use with drilled shafts under axial loading:

$$r_s = \beta \cdot \sigma'_{v0} \tag{5.6}$$

where β = shaft resistance coefficient; and σ'_{v0} = vertical effective stress at the midpoint of the layer of interest . Based on the method recommended by O'Neill and Reese (1999), the β coefficient may be correlated to depth and the energy-corrected SPT blow count, N_{60}:

$$\beta = 1.5 - 0.245\sqrt{z},\ 1.2 \geq \beta \geq 0.25 \qquad \text{for} \qquad N_{60} \geq 15 \tag{5.7a}$$

$$\beta = \frac{N_{60}}{15}(1.5 - 0.245\sqrt{z}) \qquad \text{for} \qquad N_{60} < 15 \tag{5.7b}$$

where z = depth from ground surface to the mid-point of the layer of interest in meters. The unit shaft resistances for gravelly sands and gravels may be designed using the depth-dependent correlations to the β coefficient proposed by Rollins et al (2005).

Another approach for estimating the β coefficient is recommended by Brown et al. (2010):

$$\beta = (1 - \sin\phi') \cdot \mathrm{OCR}^{\sin\phi'} \tan\phi' \leq K_p \tan\phi' \tag{5.8}$$

where OCR = overconsolidation ratio, computed using an empirical estimate of the normalized vertical effective preconsolidation stress, σ'_p:

$$\frac{\sigma'_p}{P_a} = 0.47 \cdot (N_{60})^m \tag{5.9}$$

where P_a = atmospheric pressure, m = 0.6 for clean quartzitic sands and m = 0.8 for silty sands to sandy silts, and K_p = Rankine coefficient of passive earth pressure. Brown et al. (2010) recommends that the β coefficient for depths shallower than 2.3 m be set to the value computed at that depth.

For drilled shafts in plastic, fine-grained soils, the unit shaft resistance, r_s, can be obtained using the α method recommended by O'Neill and Reese (1999) and Brown et al. (2010) for drilled shafts under axial loading:

$$r_s = \alpha \cdot s_u \tag{5.10}$$

where s_u = average undrained shear strength over the depth of interest and α given as a function of the average s_u for the stratum of interest (O'Neill and Reese 1999), as plotted in Figure 5-7):

$$\alpha = 0.55 \qquad \text{for} \qquad \frac{s_u}{P_a} \leq 1.5 \tag{5.11a}$$

$$\alpha = 0.55 - 0.1\left(\frac{s_u}{P_a} - 1.5\right) \qquad \text{for} \qquad 1.5 \leq \frac{s_u}{P_a} \leq 2.5 \tag{5.11b}$$

$$\alpha = 0.45 \qquad \text{for} \qquad \frac{s_u}{P_a} > 2.5 \tag{5.11c}$$

Based on Brown et al. (2010) and the results from this study, the shaft resistance from the ground surface to a depth z_n = 1.5 m, or to the depth of seasonal moisture change, should be neglected.

For a given rotation, the relative displacement between the soil and the base of the shaft increases linearly with distance away from the center of the toe. Because mobilized resistance is a function of relative displacement, and the mobilized unit torsional toe resistance is zero at the center of the shaft. However, the distribution of mobilized unit toe resistance between the center and edge of the shaft must be rather complicated, with the possibility of simultaneous softening at the shaft edge and hardening along inner portions depending on the soil state and magnitude of rotation. For simplicity, and with regard to the lack of available, measured unit torsional toe resistance and their distributions, it may be assumed that the mobilized unit torsional toe resistance is distributed uniformly or linearly with distance from the center of the shaft toe, as shown in Figure 5-10. The normal force at the toe giving rise to the frictional toe resistance equals the sum of the shaft weight, W, and axial dead load applied to the drilled shaft, Q_a, minus the mobilized axial shaft resistance, $R_{s,mob}$. This sum equals the mobilized axial toe resistance, $R_{t,mob}$. The mobilized axial toe resistance can be estimated using the normalized load transfer relationships recommended by O'Neill and Reese (1999). The maximum unit torsional toe resistance (Figure 5-10) can be computed using:

$$\tau_b = \frac{R_{t,mob} \cdot \tan\phi'}{\pi(0.5D)^2} = \frac{4R_{t,mob} \cdot \tan\phi'}{\pi D^2} \qquad (5.12a)$$

for granular soils, assuming that the interface friction angle equals ϕ', or

$$\tau_b = \alpha \cdot s_u \qquad (5.12b)$$

for plastic, fine-grained soils. The torsional toe resistance can be computed following integration of preferred function of unit toe resistance over the surface area of the shaft base to yield:

$$T_t = \frac{1}{4} D \cdot R_{t,mob} \cdot \tan\phi' \text{ assuming the linear distribution} \qquad (5.13a)$$

$$T_t = \frac{1}{3} D \cdot R_{t,mob} \cdot \tan\phi' \text{ assuming the uniform distribution} \qquad (5.13b)$$

for granular soils, or

$$T_t = \frac{\pi}{16} D^3 \cdot \alpha \cdot s_u \text{ assuming the linear distribution} \qquad (5.13c)$$

$$T_t = \frac{\pi}{12} D^3 \cdot \alpha \cdot s_u \text{ assuming the uniform distribution} \qquad (5.13d)$$

for plastic soils. The derivation for Eq. (4.13) can be found in Appendix B.6.

5.5.2 Assessment of Total Torsional Resistance

To evaluate the accuracy of the proposed methodologies, a comparison of the torsional capacities for the available loading test data was conducted. Calculations of torsional toe resistance were performed assuming linear distributions of the unit resistance; the resulting toe resistance is approximately 25% smaller than that computed using a uniform distribution. Only those data where sufficient information was available to reliably compute the unit shaft and toe resistances were selected for comparison. In addition to the capacities observed and computed as part of this work, the full-scale tests conducted by McVay et al. (2014) and the model tests performed in kaolinite by Poulos (1975) help to illustrate the accuracy of the selected methods. (Although other data developed from model tests exist, it is suspected that these are affected by scale effects.) A discussion of the test conditions and data is followed by a comparison of design methodology accuracy.

Poulos (1975) performed a series of axial and torsional loading tests on solid aluminum model piles embedded in kaolinite, ranging in diameter from 1.3 to 38 mm and length from 203 to 527 mm. For each set of two identical piles, one was tested in torsion and the other one was tested in axial loading. The pile-soil adhesion for each type of pile was back-calculated from both torsional and axial tests. For each pile, Poulos (1975) reported the axial adhesion, c_a, and the ratio of c_a and s_u equal to 0.65. Thus, the average s_u over the length of a pile could be computed and used in the evaluation of torsional capacity.

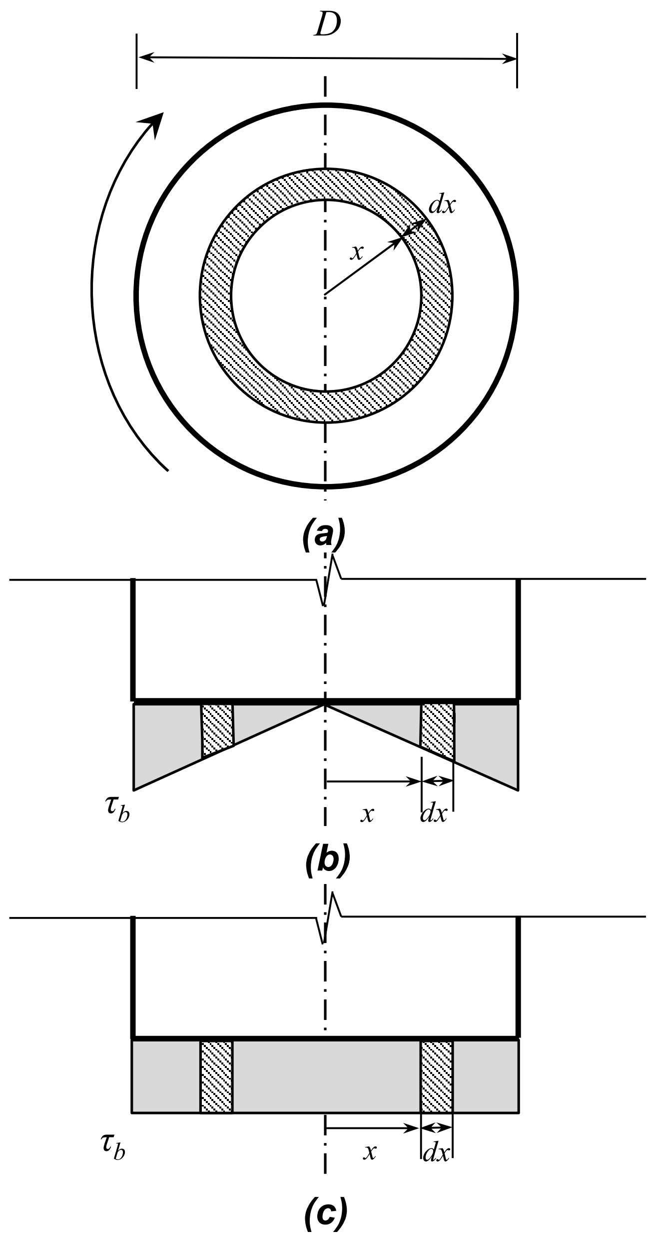

Figure 5-10. Unit torsional toe resistance: (a) developed over the toe bearing area with an assumed (b) linear distribution; (c) uniform distribution for use in the proposed design methodology.

McVay et al. (2014) reported full-scale torsional loading tests on three drilled shafts. One drilled shaft was constructed with a 1.2-m diameter and 3.7-m embedded length (designated TS1), and two with a 1.2-m diameter and 5.5-m embedded length (designated

TS2 and TS3). All of the shafts extended 0.3 m above ground surface, and were axially loaded to 47.6 kN. The water table during the torsional loading test was 3.0 m for TS1 and 1.8 m for TS2 and TS3. The soil profile for TS1 includes a layer of clay (CL) extending from the ground surface to a depth of 0.8 m with average unit weight, γ_{avg}, of 18.1 kN/m^3 and s_u = 30 kPa. This layer was underlain by a layer of poorly graded fine sand with silt (SP-SM) from depths of 0.8 m to the end of the shaft with γ_{avg} = 17.8 kN/m^3, ϕ' = 29°, and SPT N_{60} of 4. There were four soil layers along TS2: from the ground surface, a layer of CL extended to a depth of 0.8 m and was characterized with γ_{avg} = 17.9 kN/m^3 and s_u = 30 kPa. The second layer consisted of fine sand with SP-SM from the depths of 0.8 to 1.8 m and was characterized with γ_{avg} = 18.1 kN/m^3, ϕ' = 31°, and SPT N_{60} of 7. The third layer consisted of fine sand with SP-SM from depths of 1.8 to 3.8 m γ_{avg} = 17.3 kN/m^3, ϕ' = 31°, and SPT N_{60} of 5. This layer was underlain by a layer of fine sand with SP-SM from depths of 3.8 m to the end of the shaft with γ_{avg} = 19.0 kN/m^3, ϕ' = 34°, and SPT N_{60} of 9. For TS3, a CL layer extended from ground surface to a depth of 2.6 m and was characterized with γ_{avg} = 17.8 kN/m^3 and s_u = 30 kPa. Below this layer existed a layer of fine sand with SP-SM to the base of the shaft, characterized with γ_{avg} = 18.2 kN/m^3, ϕ' = 32°, and SPT N_{60} of 7. The unit weight, strength parameters, and SPT N_{60} described above were reported by McVay et al. (2014) and used directly herein.

Tables 4-1 and 4-2 summarize the comparison of torsional capacities computed using the proposed design methodologies to those observed. It can be inferred from the tables that the proposed design approach for plastic soils (i.e., using the α Method for toe and shaft resistance) tends to slightly underpredict the torsional capacity, with a mean sample bias of 1.14 and coefficient of variation (COV) of the sample bias of approximately 20%. For the drilled shafts in layered soil profiles, both β Methods described previously were used for sections of the shafts that were embedded in granular soils. The recommended design approach including the O'Neill and Reese (1999) and Brown et al. (2010) β methods produced mean biases of 1.15 and 0.86, respectively, which indicates that the torsional resistances computed using the Brown et al. (2010) method tend to be larger than those from the O'Neill and Reese (1999) methods for the cases considered. The COV in sample biases were much lower when using the O'Neill and Reese (1999) unit shaft resistance model, but the number of samples enabling the calculation of standard deviation is too small to draw firm conclusions regarding variability in the proposed methodology.

5.5.3 Assessment of Unit Torsional Shaft Resistance

An assessment of ultimate total resistance is of use to those considering the global response of shafts loaded in torsion; however, such comparisons could obscure the actual accuracy of the various components in the design methodology. For example, an underestimation of the resistance in one soil layer could be offset by an overestimation of the resistance in another soil layer. Figure 5-11 shows the comparison of the computed unit shaft resistance profiles for shaft TDS and TDSFB to those developed from the torsional loading tests. Both of the β methods considered here underestimate the unit torsional shaft resistance for the silty sand layer near the toe of TDS as shown in Figure 5-11a from a depth of 2.7 to 3.8 m. The extrapolated ultimate unit shaft resistance for the silty sand layer is 91 kPa, compared to the calculated unit shaft resistance of 49 and 68 kPa using O'Neill and Reese (1999) and Brown et al. (2010) methods, respectively. On the other hand, the unit shaft resistances computed using the α Method alternatively overestimates and underestimates the observed and extrapolated resistances for the two shafts. Further investigation and refinement of design methods for the torsional resistance of drilled shaft foundations seems warranted following the generation of additional full-scale test data.

Table 5-1. Comparison between torsional capacities calculated using the proposed design methodology and test results for piles and shafts in plastic soils.

Tests		D^a (mm)	L^b (mm)	Test Results (N-m)	Calculated	Bias
Poulos (1975) model tests	1A	25.4	254	2.75	2.30	1.20
	1B	12.7	203	0.56	0.50	1.13
	2A	25.4	254	3.53	4.00	0.88
	2B	38.1	229	3.81	6.12	0.62
	3A	25.4	254	2.27	3.24	0.70
	3B	12.7	203	0.77	0.62	1.25
	4A	12.7	203	0.98	0.77	1.27
	4B	12.7	305	1.06	0.85	1.26
	5A	12.7	203	1.10	0.97	1.13
	5B	12.7	305	1.36	1.29	1.05
	6A	25.4	502	1.96	1.91	1.03
	6B	19.1	527	1.35	1.09	1.23
	7A	25.4	502	4.73	4.78	0.99
	7B	19.1	527	2.49	2.91	0.86
	8A	25.4	502	8.41	7.55	1.11
	8B	19.1	527	4.89	4.31	1.13
	9A	12.7	305	0.97	0.63	1.55
	10A	19.1	298	1.23	1.03	1.20
	11A	12.7	305	1.11	0.79	1.40
	11B	12.7	305	0.87	0.62	1.40
	12A	19.1	298	4.45	3.52	1.26
This study	TDSFB	900	4,000	185,000	139,000	1.33
Mean Bias						**1.14**
Coefficient of variation in bias (%)						**19.8**

[a]Diameter of the deep foundation element
[b]Length of the deep foundation element

Table 5-2. Comparison between torsional capacities calculated using the proposed design methodology and test results for selected shafts in layered soils.

Tests		D^a (m)	L^b (m)	Test Results (kN-m)	Recommended β-Method for shafts in granular soils		Global Bias in Proposed Design Approach	
					O'Neill and Reese (1999)	Brown et al. (2010)	O'Neill and Reese (1999)	Brown et al. (2010)
McVay et al. (2014) field tests	TS1	1.2	3.7	95.0	87.1	149	1.09	0.64
	TS2	1.2	5.5	285	234	320	1.22	0.89
	TS3	1.2	5.5	232	209	270	1.11	0.86
This study (kN-m)	TDS	0.9	4.1	251[c]	215	240	1.17	1.05
Mean Bias							**1.15**	**0.86**
Coefficient of variation in bias (%)							**5.0**	**19.6**

[a]Diameter of the drilled shaft
[b]Length of the drilled shaft
[c] Extrapolated torsional capacity (see Figure 5-2)

5.6 Summary and Conclusions

Drilled shafts commonly installed to support mast arm traffic sign and signal structures or the superstructure of skewed bridges must be designed to resist lateral and torsional loads. Although much is known about the lateral load transfer associated with drilled shaft foundations, the same cannot be said of torsional load transfer. To improve the understanding of torsional load transfer, two full-scale, instrumented test shafts designed to meet a state agency standard were constructed and quasi-static monotonic and cyclic loading applied. One drilled shaft was constructed using typical production methods (designated TDS), whereas the other was constructed with a relatively frictionless base (designated TDSFB) to facilitate observation of possible differences in base resistance between the otherwise identical shafts.

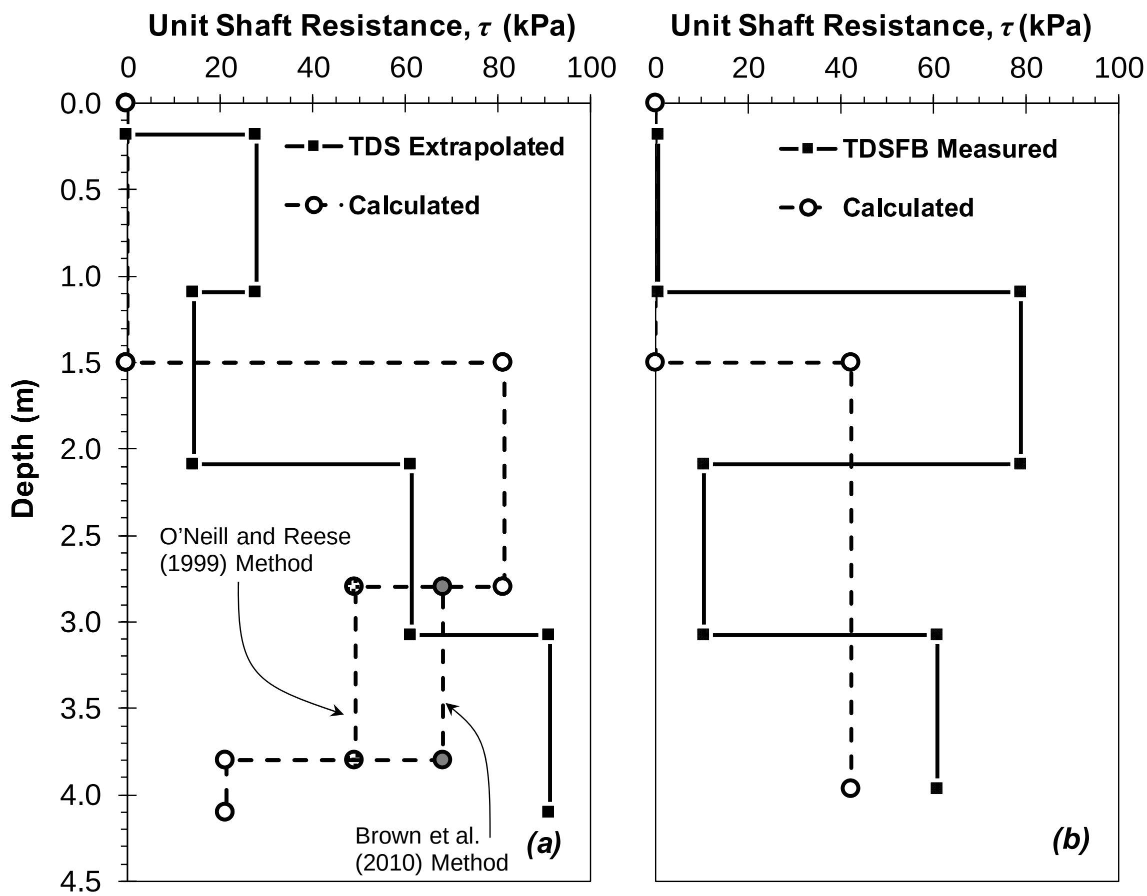

Figure 5-11. Comparison of calculated unit torsional shaft resistance (τ) profiles to (a) extrapolated unit torsional shaft resistance for shaft TDS, and (b) measured unit torsional shaft resistance for shaft TDSFB at 1.75° rotation (compare to Figure 5-4 and Figure 5-5).

Shaft TDSFB was constructed within on relatively uniform layer of overconsolidated clayey silt; however, TDS penetrated a layer of silty sand, and the difference in subsurface conditions yielded significant differences in the observed performance. At the end of monotonic, quasi-static loading, TDSFB had rotated approximately 13°, whereas TDS only rotated 0.14°. Based on the measured torque-rotation response, the torsional resistance of the shaft TDSFB was fully mobilized at 185 kN-m and a rotation of the shaft head of approximately 1.0°. However, the torsional resistance of shaft TDS was not fully mobilized during the test owing to the differences in the soil profiles. Since the measured torque-rotation response of shaft TDSFB was consistent with a hyperbolic relationship, the same was used to estimate the torque-rotation response of shaft TDS at larger rotations. The extrapolated torsional capacity of shaft TDS was 250 kN-m.

The torsional load transfer along the test shafts was evaluated in consideration of the angle of twist and the relationship between unit torsional shaft resistance and rotation to develop τ-θ curves for each tributary area. Based on the back-calculated τ-θ curves of shaft TDSFB, the unit torsional shaft resistances of most of tributary areas were fully mobilized within 1° of rotation. Hyperbolic models were used to extrapolate τ-θ curves for shaft TDS. The observed ultimate unit torsional soil resistance for shaft TDSFB was in the range of 10 to 80 kPa; and the extrapolated ultimate unit torsional soil resistance for shaft TDS was in the range of 18 to 100 kPa. No global degradation of the initial and postyield stiffness with increasing number of cycles was observed for either test shaft during the cyclic loading test.

A rational design methodology for the calculation of torsional capacity of drilled shafts was proposed and its accuracy quantified. Based on the comparison of the estimated and observed torsional capacity for each test conducted in this study, and others available in the literature, the selected design methods appeared to slightly overpredict and underpredict the torsional capacity on average. Although the methods can be used with judgment in the interim, the need for the development of improved design methods remains; such methods would benefit from additional full-scale loading tests similar to those conducted in this study.

5.7 Acknowledgements

This research was funded by Grant SPR 304-701 through the Oregon Department of Transportation. Helpful assistance with the test setup and execution was provided by Xiaomin (Jacky) Chen, Tygh Gianella, Andrew Strahler, John Martin, Jeff Gent, and James Batti. PLI Systems, Inc., of Hillsboro, OR, donated materials, equipment and labor to construct the test shafts. This support is greatly appreciated. We also thank the anonymous reviewers for their helpful comments and suggestions.

5.8 References

ACI Committee 318. (2005) “Building Code Requirements for Structural Concrete (ACI 318-05) and Commentary (318R-05).” American Concrete Institute, Farmington Hills, MI.

Basack, S. and Sen, S. (2014). "Numerical Solution of Single Piles Subjected to Pure Torsion." *J. Geotech. Geoenviron. Eng.*, 140 (1), 74-90.

Basu, P., Loukidis, D., Prezzi, M., and Salgado, R. (2011). “Analysis of shaft resistance of jacked piles in sand.” *Int. J. Numer. Anal. Methods Geomech.*, 35(15), 1605–1635.

Basu, P., Loukidis, D., Prezzi, M., and Salgado, R. (2014). “The mechanics of friction fatigue in jacked piles installed in sand.” *From Soil Behavior Fundamentals to Innovations in Geotechnical Engineering Honoring Roy E. Olson. Geo-Congress 2014*, ASCE, Reston, VA, 546–557.

Bizaliele, M. M. (1992). “Torsional cyclic loading response of a single pile in sand.” Dissertation, Schriftenreihe des Instituts fur Grundbau, Ruhr-Univ., Bochum, Germany.

Broms, B. B. (1964). “Lateral resistance of piles in cohesive soil.” *ASCE Journal for Soil Mechanics and Foundation Division,* 90(2), 27-63.

Brown, D. A., Turner, J. P., and Castelli, R. J. (2010). “Drilled shafts: Construction procedures and LRFD design methods.” *Report No. FHWA-NHI-10-016.* US Department of Transportation, Federal Highway Administration, Washington, D.C.

Chen, Y. J., and Kulhawy, F. H. (1994). “Case history evaluation of the behavior of drilled shafts under axial and lateral loading.” *Final Report, Project 1493-04, EPRI TR-104601*, Geotechnical Group, Cornell University, Ithaca, NY.

Chin, F. K. (1970). “Estimation of the pile Ultimate Load of Piles Not Carried to Failure.” *Proceedings of the 2nd Southern Asian Conference on Soil Engineering*, Singapore, 81-90.

Chin, F. K. (1971). "Discussion of 'Pile test, Arkansas River project.'". *Soil Mech. and Found. Div*., 97(6), 930-932.

Chow, Y. K. (1985). “Torsional response of piles in nonhomogeneous soil.” *J. Geotech. Engrg*., 111(7), 942–947.

Dutt, R. N., and O’Neill, M. W. (1983). “Torsional behavior of model piles in sand.” *Geotechnical Practice in Offshore Engineering*, ASCE, New York, 315-334.

Georgiadis, M. (1987). “Interaction between torsional and axial pile responses.” *Int. J. Numer. Anal. Methods Geomech*., 11, 645–650.

Georgiadis, M., and Saflekou, S. (1990). “Piles under axial and torsional loads.” *Comput. Geotech*., 9, 291–305.

Guo, W. D., and Randolph, M. F. (1996). “Torsional piles in nonhomogeneous media.” *Computers and Geotechnics*, 9(4), 291-305

Guo, W. D., Chow, Y. K., and Randolph, M. F. (2007). “Torsional pile in two-layered nonhomogeneous soil.” *Int. J. Geomech*., 7(6), 410–422.

Hache, R. A. G., and Valsangkar, A. J. (1988). “Torsional resistance of single pile in layered soil.” *J. Geotech. Engrg*., 114(2), 216–220.

Hu, Z. (2003). “Determining the optimum depth of drilled shafts subject to combined torsion and lateral loads in saturated sand from centrifuge testing.” Master’s dissertation, University of Florida, Gainesville, FL.

Huffman, J.C., Strahler, A.W., and Stuedlein, A.W. (2015) “Reliability-based Serviceability Limit State Design for Immediate Settlement of Spread Footings on Clay,” *Soils and Foundations*, August 2015, Vol. 55, No. 4, pp. 798-812.

Huffman, J.C., Martin, J.P., and Stuedlein, A.W. (2016) “Calibration and Assessment of Reliability-based Serviceability Limit State Procedures for Foundation Engineering,” *Georisk: Assessment and Management of Risk for Engineered Systems and Geohazards*, Vol. TBD, No. TBD, pp. TBD; In Press

Kondner, R. L. (1963). “Hyperbolic stress–strain response: Cohesive soils.” *J. Soil Mech. Found. Div*., 89 (1), 115–144Kulhawy, F. H., and Mayne, P. W. (1990). “Manual on Estimating Soil Properties for Foundation Design.” *Report EL-6800.* Prepared for Electric Power Research Institute, Cornell Univ., Ithaca, N.Y

Kulhawy, F. H., and Mayne, P.W. (1990). “Manual on estimating soil properties for foundation design.” *Rep. EL-6800*, Electric Power Research Institute, Cornell Univ., Ithaca, NY.

Laue, J., and Sonntag, T. (1998). “Pile subjected to torsion.” *Proc., Centrifuge ’98*, Balkema, Rotterdam, the Netherlands, 187–192.

McVay, M. C., Herrera, R., and Hu, Z. (2003). “Determine optimum depths of drilled shafts subject to combined torsion and lateral loads using centrifuge testing.” *Report Contract No. BC-354, RPWO #9*. Florida Department of Transportation, Tallahassee, FL.

McVay, M. C., and Hu, Z. (2003). “Determine optimum depths of drilled shafts subject to combined torsion and lateral loads from centrifuge testing (using KB polymer slurry)-supplemental research.” *Report Contract No. BC-545, WO #4*. Florida Department of Transportation, Tallahassee, FL.

McVay, M. C., Bloomquist, D., and Thiyyakkandi, S. (2014). “Field testing of jet-grouted piles and drilled shafts.” *Report BDK75-977-41, 91977.* Florida Department of Transportation, Tallahassee, FL.

Nusairat, J., Liang, R., Engel, R., Hanneman, D., AbuHejleh, N., and Yang, K. (2004). “Drilled shaft design for sound barrier walls, signs, and signals.” *Report No. CDOT-DTD-R-2004-8*, Colorado Department of Transportation, Denver, CO.

Oregon State DOT (ODOT). (2014). *Geotechnical design manual*, Oregon Department of Transportation, Salem, OR

Oregon State DOT (ODOT). (2015). *ODOT Traffic Structures Design Manual*, May 2015 Edition, Oregon Department of Transportation, Salem, OR

O’Neill, M. W., and Reese, L. C. (1999). “Drilled shafts: Construction procedures and design methods.” *Publ. No. FHWA-IF-99-025*, Federal Highway Administration, Office of Implementation, McLean, VA

Poulos, H. G. (1975). “Torsional response of piles.” *Journal of the Geotechnical Engineering Division*, 101(10), 1019-1035.

Randolph, M. F. (1981). “Piles subjected to torsion.” *J. Geotech. Engrg. Div*., 107(8), 1095–1111.

Randolph, M. F. (1983). “Design consideration for offshore piles.” *Geotechnical Practice in Offshore Engineering,* ASCE, New York, 422–439.

Reiter, M. (2008). *December 1–4, 2007 storm events summary*. Prepared for Weyerhaeuser Western Timberlands, Weyerhaeuser Company, Federal Way, WA.

Rollins, K., Clayton, R., Mikesell, R., and Blaise, B. (2005). "Drilled Shaft Side Friction in Gravelly Soils." *J. Geotech. Geoenviron. Eng.*, 131(8), 987-1003.

Stoll, U. W. (1972). “Torque shear test of cylindrical friction piles.” *Civil Engineering*, 42(4), 63-65.

Stuedlein, A.W. and Reddy, S.C. (2014) “Factors Affecting the Reliability of Augered Cast-In-Place Piles in Granular Soils at the Serviceability Limit State,” *J. of the Deep Foundations Institute*, Vol. 7, No. 2, pp. 46-57.

Tawfiq, K. (2000). “Drilled shafts under torsional loading conditions.” *Report Contract No. B-9191*, Florida Department of Transportation, Tallahassee, FL.

White, D. J., and Bolton, M. D. (2004). “Displacement and strain paths during plane strain model pile installation in sand.” *Geotechnique*, 54(6), 375–397.

Zhang, L. (2010). “Nonlinear analysis of torsionally loaded piles in a two layer soil profile.” *Int. J. Geomech*., 10(2), 65–73.

Zhang, L. M., and Kong, L. G. (2006). "Centrifuge modeling of torsional response of piles in sand." *Canadian Geotechnical Journal*, 43(5), 500-515.

6. SIMULATION OF TORSIONALLY-LOADED DEEP FOUNDATIONS CONSIDERING STATE-DEPENDENT LOAD TRANSFER

Authors:

Qiang Li and Armin W. Stuedlein

Journal:

Submitted to: Journal of Geotechnical and Geoenvironmental Engineering

Under second review

6.1 Abstract

Deep foundations may need to resist torsional loads, resulting from wind loading on traffic sign and signal pole structures, or seismic loading on curved or skewed bridges. Although design methods for deep foundations at the ultimate limit states are readily available, no significant effort to quantify the accuracy of existing load transfer-based torsion-rotation methods to predict the full-scale, in-service rotation performance that considers state-dependence of the soil exist. To facilitate the serviceability and ultimate limit state design of geometrically-variable deep foundations constructed in multi-layered soils, a torsional load transfer method is presented using a finite difference model (FDM) framework. Simplified state-dependent load transfer models that relate the unit torsional resistance to the magnitude of relative displacement are developed in consideration of soil-structure interface shear test results. The proposed FDM methodology is validated by comparison to existing analytical solutions and to physical model tests. Parametric studies are conducted to illustrate the role of various design parameters and demonstrate significant effects of nonlinear soil-structure response on the torsional behavior of deep foundations, including the effects of pressure-dependent softening at the soil-structure interface.

6.2 Introduction

Deep foundations must provide sufficient resistance to anticipated loads within specified performance criteria, which can range from the specification of a limiting global displacement or rotation, θ_h, at the head of the foundation (i.e., a serviceability limit state, SLS) to life safety (e.g., ultimate limit states, ULS). Design evaluations for axially- and laterally-loaded deep foundations for the SLS and ULS are routine and numerous methods for the simulation of load transfer exist (e.g., Coyle and Sulaiman 1967; Matlock 1970;

Cox et al. 1974; Reese et al. 1975; Reese and Welch 1975; Vijayvergiya 1977; API 1993; Norris 1986; Ashour et al. 1996; Adami and Stuedlein 2015, Li and Yang 2017). However, deep foundations may also need to resist torsional loads, T_h, which can result from wind loading on traffic sign and signal pole structures, or seismic loading on curved or skewed bridges. Li et al. (2017) proposed design procedures for torsionally-loaded deep foundations for the ULS and quantified their accuracy for selected loading test data. However, the magnitude of rotation associated with the ULS cannot be computed using these design procedures. Additionally, the quantification of the accuracy of existing load transfer-based torsion-rotation SLS methods against full-scale data has not been reported. Accordingly, the selection of a factor of safety or resistance factor suitable for limiting rotations to an acceptable, let alone known, magnitude remains a critical question for the design of torsionally-loaded deep foundations.

Analytical and numerical methods to model the torsional response of deep foundations have been proposed in the framework of linear-elastic or linear-elastic perfectly-plastic soil-structure interaction (SSI; O'Neill 1964; Poulos 1975; Randolph 1981; Chow 1985; Hache and Valsangkar 1988; Zhang 2010; Chen et al. 2016). O'Neill (1964) developed closed-form differential equations for piles in a linear elastic homogenous soil, whereas Poulos (1975) and Randolph (1981) developed a boundary element solution and closed form solution, respectively, for piles in a linear elastic soil with constant or linearly-varying stiffness. Chow (1985) proposed a discrete element approach for piles with varying sections in nonhomogeneous soil. Hache and Valsangkar (1988) provided non-dimensional charts for piles in layered soils using simple mathematical solutions for design purposes. Zhang (2010) developed an analytical method for piles in a two-layer soil profile assuming the shear modulus of soil of each layer varies linearly. An elastic analytical method considering the effect of interaction between torsionally-loaded piles in groups has been developed by Chen et al. (2016).

The consideration of torsional response within nonlinear SSI has received considerably less attention. Combined axial and torsional loading of deep foundations have been explored by Georgiadis and Saflekou (1990) in a study that used nonlinear torsional springs. However, the contribution of torsional resistance by the toe of the foundation was not considered in these models, and the accuracy of the methodology was only evaluated in terms of the axial deformation response of model tests. Guo and Randolph (1996) and Guo et al. (2007) described the use of nonlinear relationships between unit torsional shaft resistance, τ_s, and the local shaft rotation, θ_s, to explore the response of torsionally-loaded deep foundations; however, the toe resistance was also neglected in these analyses. Nonlinearity of the soil was considered by assuming that the normalized shear modulus G/G_{max} decreases linearly with the increasing shear stress. However, the shear modulus degradation may not be linear, especially for soil under static or quasi-static loading (Teachavorasinskun et al. 1991; Lee et al. 2004). None of the load transfer methodologies described above was validated using observed load transfer data.

This study presents a simple nonlinear torsional load transfer method to facilitate the SLS and ULS design of deep foundations loaded in pure torsion. The proposed approach uses a finite difference model (FDM) framework to solve the governing differential equations (GDEs) that describe the performance of a geometrically-variable deep foundation constructed in multi-layered soils. The deep foundation is treated as a linear elastic beam supported by discrete, nonlinear torsional springs along the shaft and at the toe, and may be used to model a driven pile, drilled shaft, or other deep foundation alternative. The FDM allows an iterative solution of the soil reactions based on the relative movement between soil and the foundation at the depth of interest, accounting for internal twist. Simplified state-dependent springs relating the unit torsional resistance to the magnitude of relative displacement are validated using available interface shear tests and the load transfer data from full-scale torsional loading tests. The performance of the proposed modeling methodology is compared against previous analytical solutions to validate the approach and recent full-scale loading test data to validate and evaluate its performance. This study concludes with parametric studies to illustrate the role of various design parameters and the toe resistance on the torsional behavior of deep foundations. The FDM is freely-available for use in academic or professional settings.

6.3 Finite Difference Model

6.3.1 Assumptions and Governing Differential Equations

The well-known FDM approach is used herein within a one-dimensional framework to solve the governing differential equations for a single, circular, torsionally-loaded deep foundation. Model assumptions include that: (1) the deep foundation (Figure 6-1a) can be treated as a beam (Figure 6-1b) with m elements and $2m$+1 nodes, including a node at the toe; (2) the toe of the deep foundation (Figure 6-1c) can be divided into n ring elements with equal radial increments; (3) the foundation properties, in terms of the diameter and the torsional rigidity remain constant within each element, however, these properties may vary between elements along the foundation; (4) the nonlinear relationship between the soil and structure is constant for a given element; (5) the complicated SSI is simplified as a beam interacting with discrete nonlinear torsional springs along the shaft and toe elements; and (6) for each spring, the unit interface shear stress, τ, is a function of the relative circumferential displacement, Δ. The boundary condition for the head of the deep foundation is free, and therefore the model does not consider the rotational stiffness associated with pile groups (e.g., Kong and Zhang 2009). Furthermore, since the mode of relative displacement-induced interface shear is the same for torsional shaft and toe resistance, it is assumed that load transfer models proposed subsequently are equally applicable to the toe and shaft.

The differential equation for a shaft element with a length of dz along the deep foundation and subjected to torsional loading, as shown in Figure 6-2a, is given by:

$$\frac{dT(z)}{dz} = 0.5\pi\tau_s(z)\cdot D(z)^2 \tag{6.1}$$

where $T(z)$ = torque in the shaft at depth z, $D(z)$ = shaft diameter at depth z, and $\tau_s(z)$ = unit torsional shaft resistance provided by the soil at depth z. The internal change in rotation with depth, $d\theta(z)/dz$, as shown in Figure 6-2b, can be expressed by (Gere and Timoshenko 1997):

$$\frac{d\theta(z)}{dz} = \frac{T(z)}{GJ(z)} \tag{6.2}$$

where $GJ(z)$ = torsional rigidity of the shaft at depth z, G = shear modulus of the shaft, and J = polar moment of inertia. The nonlinear torsional springs along the shaft are represented by τ_s-Δ_s curves, where τ_s is the unit torsional shaft or interface shear resistance and Δ_s is the relative circumferential displacement. The rotation of the shaft, $\theta_s(z)$ at depth z, can be determined by:

$$\theta_s(z) = \frac{2\Delta_s(z)}{D(z)} \tag{6.3}$$

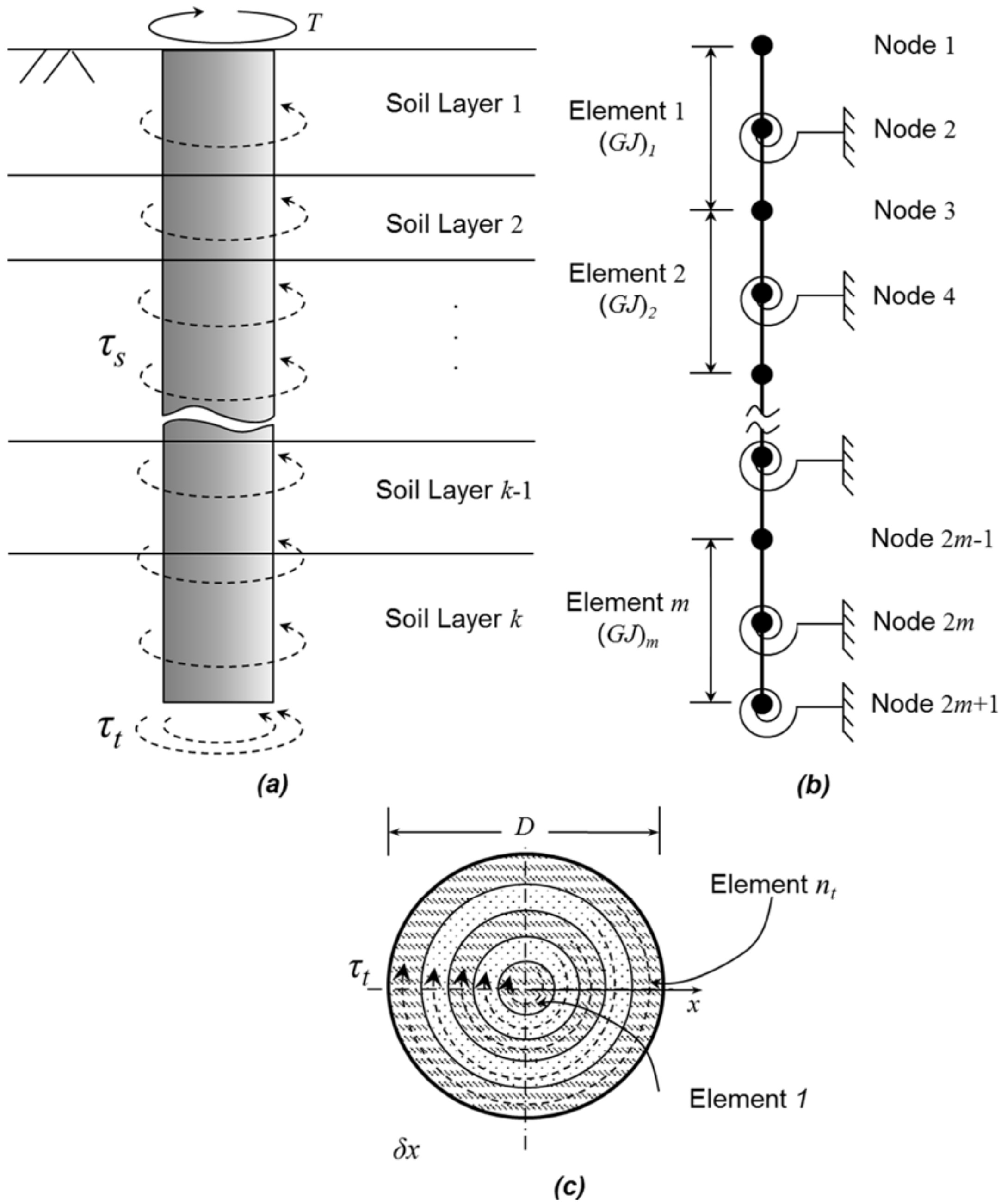

Figure 6-1. Schematic illustration of (a) torsionally-loaded deep foundation, (b) finite difference model with discrete springs along the shaft and base, and (c) discretization of the base of the deep foundation with *n* ring elements; *n* = number of soil layers, and *m* = number of the shaft elements.

The torsional springs at the toe of the deep foundation are represented by τ_t-Δ_t curve, where τ_t and Δ_t are the unit torsional toe or toe interface shear resistance and the relative displacement, respectively. The torsional toe resistance, T_t, at a given rotation can be calculated by evaluating an arbitrary ring element of very small width dx, as shown in Figure 6-2c. The distance from the center of foundation to the mid-point of the annulus is x. The differential area of the element is:

$$dA = \pi(x+\frac{dx}{2})^2 - \pi(x-\frac{dx}{2})^2 = 2\pi x \cdot dx \tag{6.4}$$

With a certain rotation at the toe, θ_t, the whole element undergoes the same relative displacement, $\Delta_t(x) = \theta_t \cdot x$, so that the corresponding torsional unit toe resistance, $\tau_t(x)$ is the same within the differential annulus. This implies that the outermost differential area will achieve a maximum or peak resistance prior to any other interior ring at a given rotation, and that the interface shear mechanism is necessarily progressive in nature. The torsional toe resistance for any given differential ring element is:

$$dT_t(x) = x \cdot \tau_t(x) dA = 2\pi\tau_t(x) \cdot x^2 dx \tag{6.5}$$

which may be integrated over the radius to determine the total mobilized toe resistance, T_t:

$$T_t = 2\pi \int_0^{D/2} \tau_t(x) \cdot x^2 dx \tag{6.6}$$

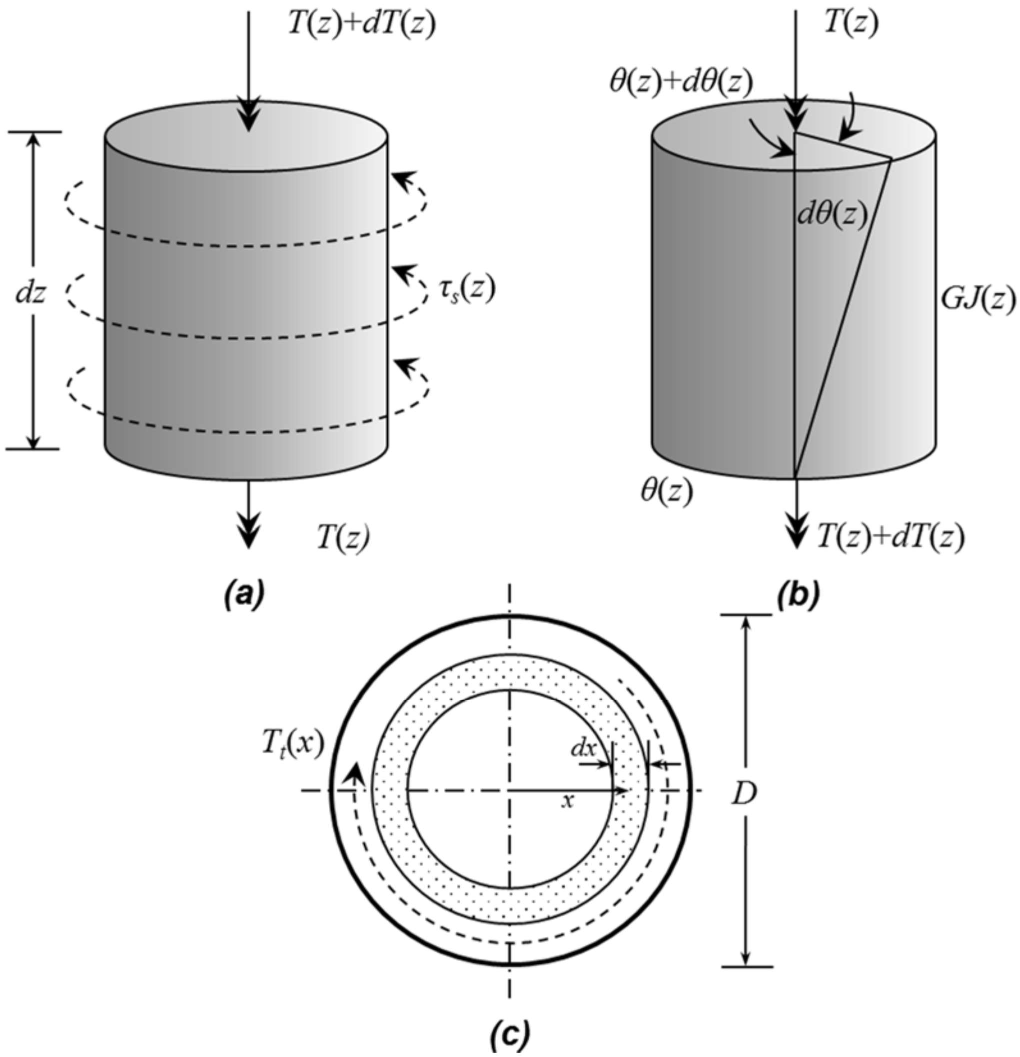

Figure 6-2. Schematic illustration of (a) an element of the torsionally-loaded shaft, (b) the internal twist of a shaft element under torsion, and (c) an element at the foundation base.

6.3.2 Solution of Governing Differential Equations

The central difference scheme is adopted to approximate the continuous derivatives in the GDEs (e.g., Desai and Zaman 2014). For an arbitrary element j, where j = 1, 2,…,m, with a length of $2h$, the change of rotation with depth at node $2j$ can be estimated using:

$$\left(\frac{d\theta}{dz}\right)_{2j} \cong \left(\theta_{2j-1} - \theta_{2j+1}\right)\frac{1}{2h} = \frac{T(2j)}{(GJ)_j} \tag{6.7}$$

where $T(2j)$ = the average torque in the element j, which assumes to be $(T_{2j-1}+T_{2j+1})/2$. For the shaft element j, Eq. (6.1) can be expressed as:

$$T_{2j-1} - T_{2j+1} = \pi D_j^2 \cdot h \cdot \tau_j \tag{6.8}$$

The torsional toe resistance can be determined directly with the summation of the torsional resistance from each toe element. With n_t toe elements, the radial increment is:

$$\delta_x = \frac{D}{2n_t} \tag{6.9}$$

For an arbitrary toe element i, where $i = 1, 2,\ldots, n_t$, the area, $A(i)$, and the distance from the center of toe to the mid-point of the element, $r_t(i)$, are:

$$A(i) = \pi\left\{(i\cdot\delta_x)^2 - \left[(i-1)\delta_x\right]^2\right\} = (2i-1)\pi(\delta_x)^2 \tag{6.10}$$

$$r_t(i) = (i-0.5)\delta_x \tag{6.11}$$

Then, the torsional resistance from the element i is:

$$T_t(i) = \tau_t(i)\cdot A(i)\cdot r_t(i) \tag{6.12}$$

τ_t is a function of Δ_t and can be determined from the proposed τ-Δ models as described subsequently. Therefore, the total torsional toe resistance, T_t, can be determined by:

$$T_t = \sum_{i=1}^{n} T_t(i) \tag{6.13}$$

The determination of the load transfer for the torsionally-loaded deep foundation using the FDM follows a similar procedure proposed by Coyle and Reese (1966) for axially-loaded piles. First, an arbitrarily small toe rotation is applied. Then, equilibrium of torque and compatibility of rotation for each element from is achieved using an iterative solution scheme, which is an unconditionally stable approach, with Eq. (6.7) and (6.8). Therefore, this method is not applicable for a deep foundation with a fully-fixed toe condition.

6.4 Proposed Torsional Load Transfer Curves for Granular Soils

6.4.1 Relevant Soil-Interface Mechanics

Torsional resistance is derived from interface shear between the surface of the deep foundation and the interacting soil. Accordingly, interface shear tests provide the best laboratory-based analog to the actual in-situ interaction. A review of soil-structure interface tests on granular soils reported in the literature (e.g., Clough and Duncan 1971; Gómez et al. 2000a, 2000b; and Iscimen 2004) suggests that two simplified unit torsional resistance-relative displacement relationships, known as τ-Δ curves, are sufficient to describe the interface shear behavior. These include hyperbolic-type displacement-hardening and -softening models for granular soil-structure interfaces categorized as nondilatant (i.e., contractive) and dilatant (Lings and Dietz 2005; Dove and Jarrett 2002), respectively. The tendency for dilation depends on the interface properties, including surface topography and the hardness of the interface and the granular soil properties (e.g., relative density, angularity, and gradation) as observed in the previous studies on soil-structure interfaces (e.g., Kulhawy and Peterson 1979; Uesugi and Kishida 1986; Paikowsky et al. 1995; DeJong and Frost 2002; Dove and Jarrett 2002; Frost et al. 2002; Iscimen 2004; and Lings and Dietz 2005). Since the effects of hardness is not significant for the structure of engineering materials such as steel and concrete (Dove and Frost 1999 and DeJong and Frost 2002), it is not considered herein The structure surface topography may be quantified using the average roughness, R_a, and the maximum roughness, R_{max}. The one-dimensional average roughness of structure, R_a, is defined by:

$$R_a = \frac{1}{L_s}\int_0^L \left|z(\mathrm{x})\right| dx \tag{6.14}$$

where, L_s = sample length, $|z(x)|$ = the absolute height of the profile from the mean (Ward 1982; and DeJong and Frost 2002). The maximum roughness is the maximum absolute vertical relief along the surface profile over a sample length $L_s = d_{50}$, where d_{50} = median particle diameter. The granular soil-structure interface roughness may be evaluated using normalized roughness, $R_n = R_{max}/d_{50}$ (Uesugi and Kishida 1986) or relative roughness, $R_r = R_a/d_{50}$ (Subba Rao et al. 1998).

Based on a series of sand-steel interface tests, Lings and Dietz (2005) categorized the interfaces into three categories: (1) smooth interfaces with $R_r \leq 0.003$ or $R_n \leq 0.02$, (2) rough interfaces with $R_r \geq 0.008$ or $R_n \geq 0.5$, and intermediate interfaces for $0.003 < R_r < 0.008$ or $0.02 < R_n < 0.5$. Lings and Dietz (2005) found that contractive behavior occurred for smooth interfaces, engaging the near-interface particles only, whereas dilatant behavior occurred for intermediate and rough interfaces when the relative density D_r of the soil was larger than the relative density at the soil critical state, $D_{r,cs}$. In this case, the thickness of the sheared soil zone can extend some 5 to $7d_{50}$ (Frost et al. 2004). The selection of the displacement-hardening or –softening τ-Δ curves for use in the proposed FDM may consider the initial state of the granular soil-structure interfaces using (Bolton 1986, Boulanger 2003):

$$D_{r,cs} = \frac{R}{Q - \ln \dfrac{100\sigma_n'}{P_a}} \tag{6.15}$$

where R = empirical constant, which is approximately equal to 1.0, Q = empirical constant, suggested equal to 10 for quartz and feldspar, 8 for limestone, 7 for anthracite, and 5.5 for chalk (Bolton 1986), and P_a = atmospheric pressure. Although Eq. (6.15) is suitable for many granular soils, the effect of particle angularity on the dilative characteristics of granular soil is not well-captured using this approach.

Owing to the need to capture ultimate and serviceability limit state performance, the τ-Δ curve selected for a given soil deposit should be accurate across the range of rotations implied by the interface displacements. An appropriate model should capture the hardening (i.e., contractive) or softening (dilatant) response depending on the in-situ state of the granular soil deposit relative to the critical state and the interface characteristics. The approach incorporated into the proposed FDM consists of determining the tendency for dilation using the relative roughness; smooth interfaces are considered contractive. Eq. (6.15) may then be used to calculate the normal stress-dependent D_r at the critical state. If the in-situ $D_r < D_{r,cs}$, the interface is contractive and modeled as a hardening material (described subsequently). If the in-situ $D_r > D_{r,cs}$, the interface is dilatant and should exhibit softening at large relative displacements. Regardless of the in-situ state, the soil-structure interface response can be sufficiently modeled using a hyperbolic model at small relative displacements prior to the manifestation of softening (Gómez et al. 2000a, 2000b). The details of the selected *τ-Δ* models are described subsequently. The proposed *τ-Δ* models can be used for the springs along the shaft as well the springs at the toe.

6.4.2 Displacement-Hardening Model

The stress-strain and load transfer response of contractive granular soil has been simulated using the hyperbolic model for a variety of applications (e.g., Kondner 1963; Duncan and Chang 1970; and Huffman et al. 2015), and extensively for soil-deep foundation interface analyses (e.g., Chin 1970, 1971; Clemence and Brumund 1975; Wong and Teh 1995; Kim et al. 1999; Cao et al. 2014; Stuedlein and Reddy 2014). Clough and Duncan (1971) extended the hyperbolic model to soil-structure interfaces by incorporating the relative displacement, *Δ*, as given by:

$$\tau = \frac{\Delta}{\dfrac{1}{K_{si}} + \dfrac{\Delta}{\tau_{ult}}} \tag{6.16}$$

where τ_{ult} = asymptotic interface shear stress and K_{si} = initial interface stiffness. The initial interface stiffness is pressure-dependent, and given by:

$$K_{si} = K_I \cdot \gamma_w \cdot \left(\frac{\sigma'_n}{P_a}\right)^{n_j} \tag{6.17}$$

where K_I = dimensionless stiffness number, γ_w = unit weight of water, n_j = dimensionless stiffness exponent. The dimensionless K_I and n_j are determined using the results of interface shear tests. The asymptotic or ultimate interface shear stress is given by:

$$\tau_{ult} = \frac{\tau_f}{R_f} = \frac{\sigma'_n \cdot \tan\delta}{R_f} \tag{6.18}$$

where δ_p = peak interface friction angle, τ_f = the interface shear stress at failure, σ'_n = normal effective stress, and R_f = failure ratio. The displacement-hardening model parameters derived from available interface shear data are summarized in Table 6-1, which can be used to model granular soils in the absence of soil-interface-specific test data. The hyperbolic model parameters in Table 6-1 represent those reported in the literature without the consideration of softening; this is addressed subsequently.

Figure 6-3a shows the characteristic shape of the displacement-hardening model, whereas Figure 6-3b shows an example comparing the hardening model to interface shear tests for medium-dense Density sand against plywood-formed concrete reported by Gómez et al. (2000a) for a variety of normal effective stresses, σ'_n. The hardening response produced by Eq. (6.16) sufficiently captures the interface shear performance.

In the absence of soil-interface-specific test data, τ_{ult} can be determined using the β method for drilled shafts in granular soils, $\tau_{ult} = \beta\ \sigma'_{v0}$, where σ'_{v0} = vertical effective stress at the mid-point of the layer of interest and β = shaft resistance coefficient. O'Neill and Reese (1999), proposed the estimation of β based on the depth, z, and the energy-corrected SPT blow count, N_{60}; and, alternatively, Brown et al. (2010) correlated the coefficient with overconsolidation ratio, OCR, internal friction angle, ϕ', and SPT blow count, N_{60}. Both of these approaches have been summarized and compared to full-scale loading test performance by Li et al. (2017).

An alternative approach can be used to determine the initial shear stiffness K_{si} for 1D springs representing the mobilization of shaft resistance (i.e., τ_s-Δ_s curves) for a torsionally-loaded pile in elastic soil (Randolph 1981):

$$K_{si} = \frac{\tau_s}{\Delta_s} = \frac{2G_s}{r} \tag{6.19}$$

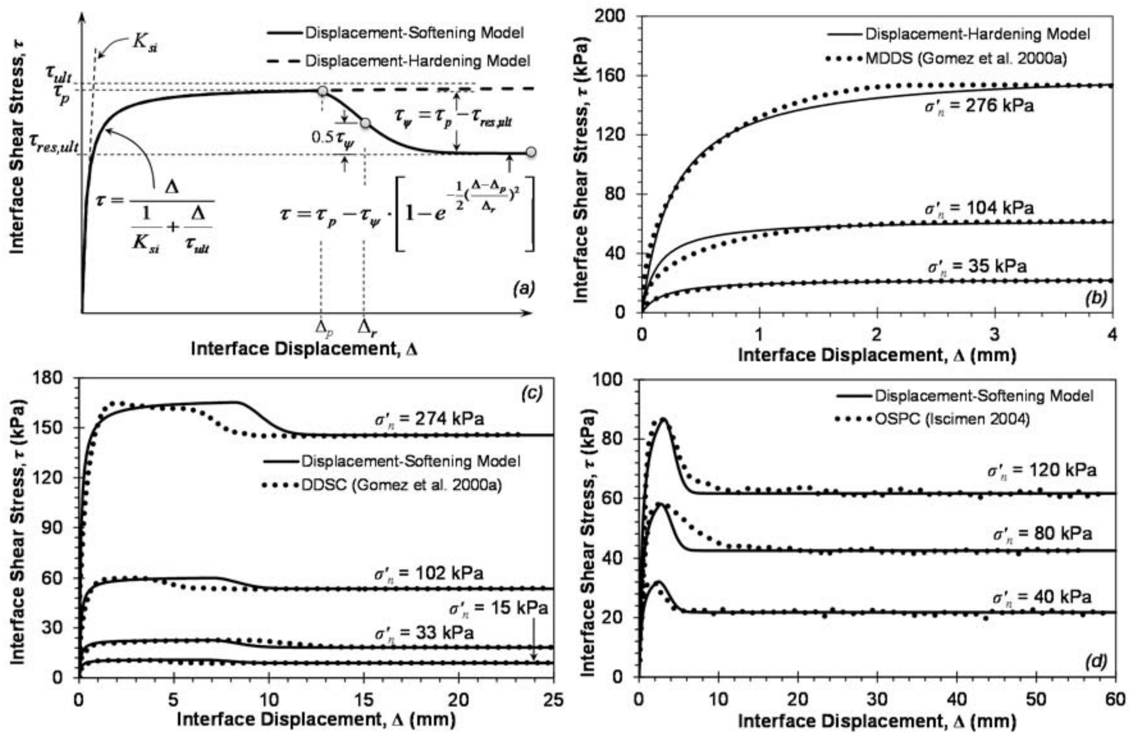

Figure 6-3. Illustration of the proposed displacement displacement-hardening and –softening models for granular soils and proposed for use with the FDM: (a) model formulations, (b) comparison of the displacement-hardening model and the test data for medium-dense Density sand (MDDS) against concrete under different normal stresses, σ_n, and comparison of the displacement-softening model and (c) dense density sand against concrete (DDSC) interfaces, and (d) dense Ottawa sand-packerhead concrete (OSPC) interfaces.

where r = shaft radius and G_s = soil shear modulus. Although not specified by Randolph (1981), the maximum shear modulus, G_{max}, is recommended for use herein. The maximum shear modulus for each layer can be estimated using the average soil shear wave velocity, V_s, and soil density, ρ, using $G_{max} = \rho\,(V_s)^2$. It can also be estimated using the void ratio, e, and the mean effective stress, σ'_m, according to Hardin and Richart (1963) and Hardin (1978):

$$G_{\max} = C_g \cdot P_a^{1-m_g} \frac{(e_g - e)^2}{1+e} \sigma_m'^{\,m_g} \tag{6.20}$$

where C_g, e_g, m_g = regression constants depending solely on the type of soil.

6.4.3 Displacement-Softening Model

In order to account for softening at dilatant interfaces and the consequences thereof, a displacement-softening model is proposed as shown in Figure 6-3a. The hyperbolic model is used to simulate small relative displacements prior to the manifestation of post-peak softening. The relative displacement associated with the onset of softening, Δ_p, corresponds to the peak interface shear stress, τ_p. The same procedures are followed to calibrate the displacement-softening model using interface shear test results as described earlier for the hardening model, except K_{si} and τ_{ult} should be determined by fitting to data where $\tau_s \leq \tau_p$ where $\tau_p = \tau_{ult} \cdot R_f$. Note that the use of R_f here effectively controls the magnitude Δ_p at which τ_p occurs. The post-peak portion of the displacement-softening model is defined by an exponential function to represent the softening behavior, for $\Delta > \Delta_p$, given by:

Table 6-1 Summary of hyperbolic parameters for concrete-sand interface from the literature.

Soil					Concrete Surface & σ'_n (kPa)	K_I	n_j	R_f	δ (deg)
Type	Particle shape	D_r (%)	C_u	d_{50} (mm)					
Uniform sand Clough and Duncan (1971)	Sub-rounded sub-angular	-[a]	1.7	-	Smooth (45-224)	75,000	1.0	0.87	33.0
Chattahoochee River Sand Clemence (1973)	Sub-angular	65	2.5	0.37	Smooth (10-23)	51,000	0.67	0.86	30.4
		65			Rough (10-23)	46,800	0.70	0.86	38.2
		75			Rough (9-27)	54,600	0.66	0.88	42.9
Chattahoochee River Sand Holloway et al. (1975)	Sub-angular	50	2.5	0.37	Mortar	29,400	0.77	0.82	32.3
		75			Mortar (45-224)	36,200	0.77	0.76	33.6
		100			Mortar	46,200	0.77	0.78	33.3
Arkansas River Lock and Dam No. 4 Sand Holloway et al. (1975)	-	0	-	-	Mortar	21,600	1.15	0.87	29.9
		57				27,700	1.15	0.94	31.3
		100				55,700	1.15	0.95	34.6
Jonesville Lock and Dam Sand Holloway et al. (1975)	-	60	-	-	Mortar	51,000	0.81	0.83	34.5
		80			Mortar (96-960)	62,400	0.83	0.80	36.9
		100			Mortar	76,900	0.84	0.72	37.9

[a] Dense. However, the relative density, Dr, was not quantified by the authors

Table 6-1 (continued).

Soil					Concrete Surface & σ'_n (kPa)	K_I	n_j	R_f	δ (deg)
Type	Particle shape	D_r (%)	C_u	d_{50} (mm)					
Uniform sand Peterson (1976)	Subrounded to Well rounded	33	1.7	0.30	Smooth (96-479)	10,200	0.87	0.71	30.0
		62				12,700	0.84	0.62	28.7
		77				8,400	1.17	0.40	31.2
		33	1.7	0.30	Inter-mediate (96-479)	11,000	0.79	0.82	26.9
		62				16,600	0.42	0.71	30.8
		77				8,900	0.85	0.30	33.8
		33	1.7	0.30	Rough (96-479)	10,000	0.83	0.85	31.6
		62				11,900	0.71	0.78	29.8
		77				10,400	0.70	0.41	32.9
Graded Sand Peterson (1976)	Subrounded to rounded	13	4.6	0.84	Smooth (96-479)	12,000	0.83	0.89	30.4
		40				9,200	0.94	0.69	30.7
		73				10,500	1.11	0.75	31.4
		13	4.6	0.84	Inter-mediate (96-479)	9,200	0.66	0.78	32.1
		40				9,200	0.74	0.76	33.6
		73				13,800	0.49	0.60	36.3
		13	4.6	0.84	Rough (96-479)	7,700	0.70	0.78	34.8
		40				13,100	0.67	0.69	32.9
		73				14,800	0.51	0.74	37.0

Table 6-1 (continued).

Soil					Concrete Surface & σ'_n (kPa)	K_I	n_j	R_f	δ (deg)
Type	Particle shape	D_r (%)	C_u	d_{50} (mm)					
Ottawa sand 50-60 (Lee et al. 1989)	Sub-rounded	D[a]	-	-	Smooth (34-207)	19,470	0.35	0.89	26.3
		D[a]			Rough (34-207)	19,240	0.82	0.95	30.4
Blacksburg Sand (Gómez et al. 2000b)	Sub-angular	80	3.0	0.70	Cast against Plywood (38–292)	23,000	0.80	0.76	31.6
Density sand (Gómez et al. 2000a)	Sub-rounded to rounded	49	1.8	0.51	Cast against Plywood (35-276)	26,600	0.83	0.85	31.0
		75			Cast against Plywood (15-274)	21,800	0.71	0.88	29.3
Light Castle Sand (Gómez et al. 2000a)	Sub-angular to angular	80	1.8	0.40	Cast against Plywood (15-276)	20,700	0.79	0.79	33.7
Ottawa Sand 20/30 (Iscimen 2004)	Sub-rounded	80	1.46	0.64	Wet-cast Concrete R_a = 25 µm (40–120)	15,090	0.66	0.68	33.2
					Packerhead Concrete R_a = 55 µm (40–120)	19,750	0.68	0.87	37.1

[a] Dense. However, the relative density, D_r, was not quantified by the authors

$$\tau = \tau_p - \tau_\psi \cdot \left[1 - e^{-\frac{1}{2}\left(\frac{\Delta - \Delta_p}{\Delta_r}\right)^2} \right] \tag{6.21}$$

where τ_ψ = difference between the peak and residual or ultimate (or constant volume) interface shear stress, defined as:

$$\tau_{\psi} = \tau_{p} - \tau_{res,ult} = \sigma_{n}' \cdot (\tan\delta_{p} - \tan\delta_{cv}) \tag{6.22}$$

where $\tau_{res,ult}$ = residual or ultimate interface shear stress, δ_{cv} = residual or ultimate interface friction angle, and Δ_r = relative interface displacement that corresponds to one-half of τ_{ψ}. Based on interface tests reported by Holloway et al. (1975), Gómez et al. (2000a,b) and Iscimen (2004), the average value of Δ_r is approximately 1.0 mm, and this value may be used in the absence of soil-structure interface data. The displacement-softening model sufficiently captures the various rates of softening as shown in Figure 6-3 (c and d) for dense Density sand-concrete (DDSC) interfaces reported by Gómez (2000a) and for the Ottawa sand-packerhead concrete (OSPC) interface reported by Iscimen (2004). Hyperbolic parameters appropriate for use with the displacement-softening model derived from the reported interface shear test data are summarized in Table 6-2.

6.5 Proposed Torsional Load Transfer Curves for Plastic, Fine-Grained Soils

The hyperbolic model may also be used to study the interaction between deep foundations and plastic fine-grained soils (Li et al. 2017). If available, K_{si} and τ_{ult} can be determined directly from interface shear tests or from back-calculated from full-scale loading tests. It is assumed that the parameters K_{si} and τ_{ult} for plastic, fine-grained soils are to be used in transient loading cases (e.g., wind gusts, strong ground motions), will act in an undrained manner, and will not exhibit pressure-dependence. If partially-drained conditions are anticipated, the load transfer models proposed for use with granular soils may be used with appropriate friction angles and the design excess pore pressure field. In the absence of interface shear test data, the initial shear stiffness K_{si} can be calculated using Eq. (6.19) and measurements of V_s. Asymptotic τ_{ult} can be obtained using the α method (e.g., Tomlinson 1980, O'Neill and Reese 1999), $\tau_{ult} = \alpha\, s_u$, where s_u = average undrained shear strength over the depth of interest, and α = an adhesion factor. For deep foundations in plastic, fine-grained soils, the shaft resistance from the ground surface to a depth of 1.5 m or to the depth of seasonal moisture change should be neglected (Li et al. 2017).

The torsional load transfer derived from a full-scale loading test of shaft TDSFB, described by Li et al. (2017), was used to validate the hyperbolic model for plastic, fine-grained soils. The soil properties for TDSFB are summarized in Table 6 3, including the measured maximum unit torsional resistance, τ_m, and the average shaft radius, r, at each layer. Since the torsional shaft resistance on TDSFB was negligible from the ground surface to the depth of 1.1 m, only the portion from the depth of 1.1 m to the bottom of the shaft (4.0 m) was simulated in the comparisons to follow. Measurements of V_s, determined using downhole methods in the footprint of another shaft designated TDS, within 5 m of TDSFB and shown in Figure 6-4 were used to compute G_{max} and K_{si} using Eq. (6.19). Displacement-hardening τ_s-Δ_s curves were constructed for each instrumented tributary area using Eq. (6.16) with K_{si} and $\tau_{ult} = \tau_m$. Described subsequently, these model parameters sufficiently reproduces the observed load transfer and validates the use of the proposed displacement-hardening model for torsionally-loaded deep foundations.

Table 6-2 Summary of displacement-softening model parameters for use with dilatant interfaces.

Type	Particle Shape	D_r (%)	C_u	d_{50} (mm)	Concrete Surface & σ'_n (kPa)	K_I	n_j	R_f
Jonesville Lock and Dam Sand Holloway et al. (1975)	-	80	-	-	Mortar (96-960)	73,420	0.71	0.81
Blacksburg Sand (Gómez et al. 2000b)	Sub-angular	80	3.0	0.70	Cast against Plywood (38–292)	31,630	0.86	0.84
Density sand (Gómez et al. 2000a)	Sub-rounded to rounded	49	1.8	0.51	Cast against Plywood (35-276)	34280	0.76	0.98
		75			Cast against Plywood (15-274)	72,290	0.86	0.99
Light Castle Sand (Gómez et al. 2000a)	Sub-angular to angular	80	1.8	0.40	Cast against Plywood (15–276)	54,220	1.22	0.98
Ottawa Sand 20/30 (Iscimen 2004)	Sub-rounded	80	1.5	0.64	Wet-cast Concrete Ra = 25 µm (40–120)	15,090	0.66	0.68
					Packerhead Concrete Ra = 55 µm (40–120)	19,750	0.68	0.87

Table 6-3 Soil and drilled shaft properties and hyperbolic parameters for instrumented, tributary areas for TDSFB reported by (Li et al. 2017). Note: τ_m = measured ultimate unit torsional shaft resistance and τ_c = calculated resistance using the α method.

Depth (m)	Shaft	Soil							
	r (m)	α	ρ (kg/m^3)	s_u (kPa)	V_s (m/s)	G_{max} (MPa)	τ_c (kPa)	τ_m (kPa)	K_{si} (kPa/mm)
1.1 to 2.1	0.461	0.55	1837	104	189	66	57.2	78.9	285
2.1 to 3.1	0.464	0.55	1837	76	267	131	41.5	10.5	564
3.1 to 4.0	0.494	0.55	1837	55	267	131	30.0	60.9	530

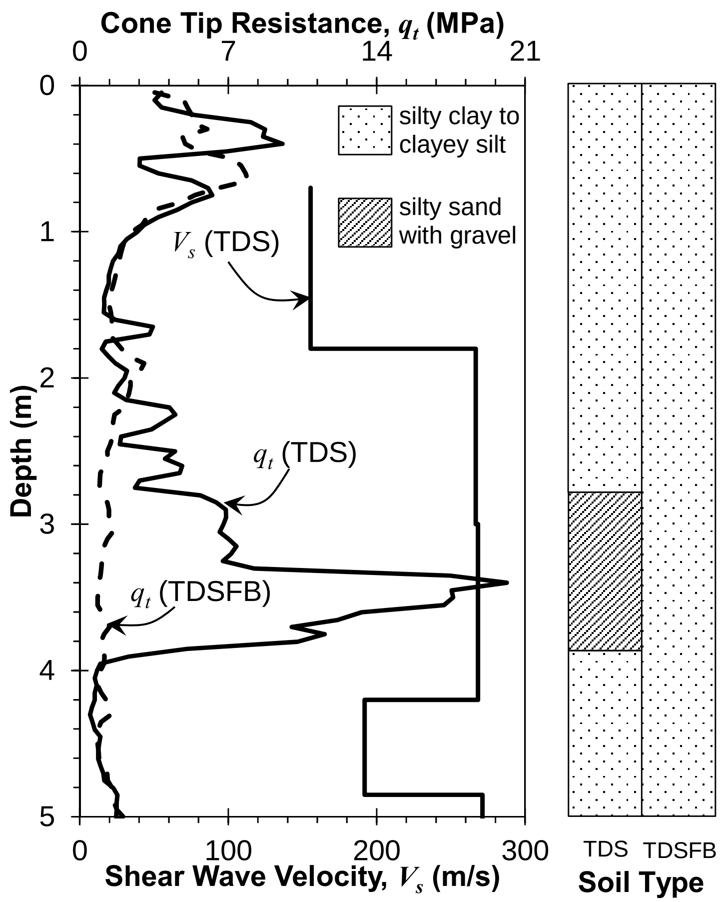

Figure 6-4. Shear wave velocity, V_s, profile at the location of TDS, and corrected cone tip resistance, q_t, profile at the location of TDS and TDSFB with corresponding soil profiles (after Li et al. 2017).

6.6 Validation and Evaluation of the FDM

To validate the proposed FDM, the FDM results are compared to the previous analytical solutions and two series of torsional loading tests, including the centrifuge torsional loading tests conducted by Zhang and Kong (2006) and the full-scale loading tests conducted by Li et al. (2017). Then, the accuracy of the proposed τ-Δ curves calculated using β and α method for granular and plastic, fine-grained soil, respectively, is evaluated by comparing the FDM results with the full-scale test data from Li et al. (2017). Given the similarity in stress path, it is assumed that the proposed displacement-hardening and -softening curves are suitable for both torsional shaft (i.e., τ_s-Δ_s) and toe (i.e., τ_t-Δ_t) responses, despite possible differences due to anisotropic soil fabric.

6.6.1 Validation of the FDM using Previous Analytical Solutions

In a first effort at model validation, the torsional responses of deep foundations using the FDM are compared with previously-reported analytical solutions. Here, the solutions of a pile loaded in torsion proposed by Guo and Randolph (1996) and Guo et al. (2007) are evaluated. As in these studies, the variation of the maximum soil shear modulus of the surrounding soil with depth, z, was modeled using (e.g., Guo and Randolph 1996; Guo et al. 2007):

$$G_{max}(z) = A_g \cdot z^{n_g} \tag{6.23}$$

where A_g = a modulus constant, n_g = depth exponent termed the nonhomogeneity factor. The value of n_g ranges from 0, corresponding to uniform shear modulus, to 1.0, corresponding to a linearly-increasing shear modulus with depth. The shear modulus follows a power law when n_g lies between 0 to 1.0.

In the validation trials, Eq. (6.23) is used to determine the maximum soil shear modulus, G_{max}, at depth, z. Three values of n_g are selected to consider three general types of variations of soil shear modulus with depth (i.e., 0, 0.5, and 1.0). For a deep foundation with constant torsional rigidity, GJ, along the depth, the relationship between the torque at the head of the foundation, T_h, and the corresponding rotation, θ_h, can be expressed as (e.g. Poulos 1975, Hache and Valsangkar 1988, and Guo and Randolph 1996):

$$\theta_h = \frac{I_\theta}{F_\theta} \frac{L}{GJ} T_h \tag{6.24}$$

where L = length of the deep foundation, I_θ = torsional influence factor, which is a function of the relative torsional foundation-soil stiffness ratio, π_t, as presented subsequently, and F_θ equals a correction factor for the effect of nonlinearity in the soil-structural response. In this framework, F_θ is equal to 1.0 for linear elastic soil and structural responses. The dimensionless, relative torsional foundation-soil stiffness ratio, π_t, introduced by Guo and Randolph (1996), is used herein to generalize the validation:

$$\pi_t = \left[\frac{\pi D^2 \cdot A_g}{G \cdot J} \right]^{\frac{1}{2+n_g}} \cdot L^2 \tag{6.25}$$

Figure 6-5 compares the linear elastic torsional responses produced using the FDM and the analytical solutions for a deep foundation in a single layer soil in terms of I_θ and π_t. Toe resistance is not considered here to facilitate a one-to-one comparison of the previous work. Figure 6-5 shows that the FDM reproduces the solutions by Poulos (1975), Hache and Valsangkar (1988), Guo and Randolph (1996), and Zhang (2010).

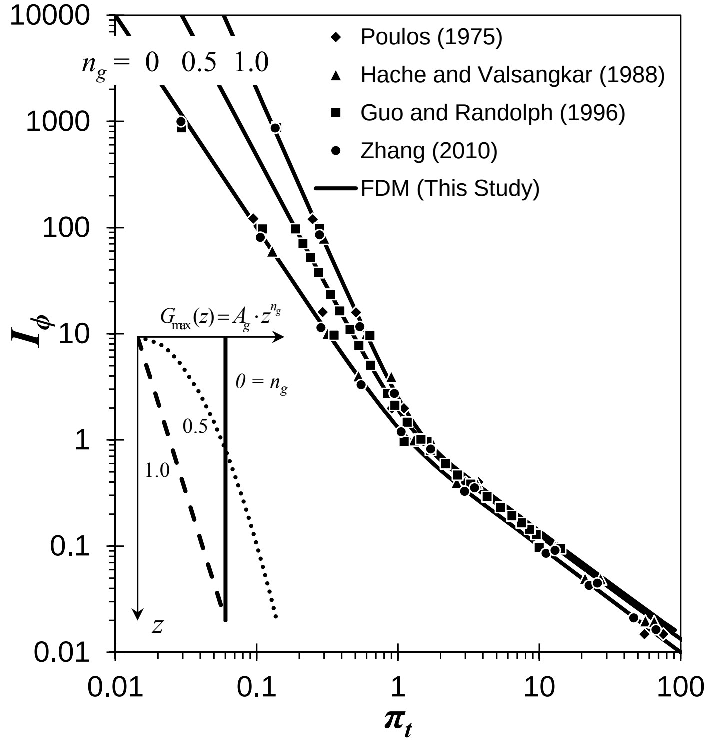

Figure 6-5. Validation of the FDM by comparing the linear elastic responses of a deep foundation in a single layer soil with previous analytical solutions. Inset shows three variations of the maximum soil shear modulus, G_{max}, with depth, z; A_g = a modulus constant, n_g = depth exponent.

To extend the range of validation for the FDM, the linear elastic response of a deep foundation in a two-layer soil profile with upper layer thickness of 0.25L is compared to the analytical solutions from Guo et al. (2007) in Figure 6-6, where L = length of the deep foundation. The relative stiffness ratio of the upper and lower layer is π_{t1} and π_{t2}, respectively. Figure 6-6a shows the relationship between I_ϕ and π_{t1} with π_{t2} = 0.4, 1, 5, and 50; whereas Figure 6-6b shows the relationship between I_ϕ and π_{t2} with π_{t1} = 0.4, 1, 5, and 15. Good agreement between the FDM and previous solutions is observed.

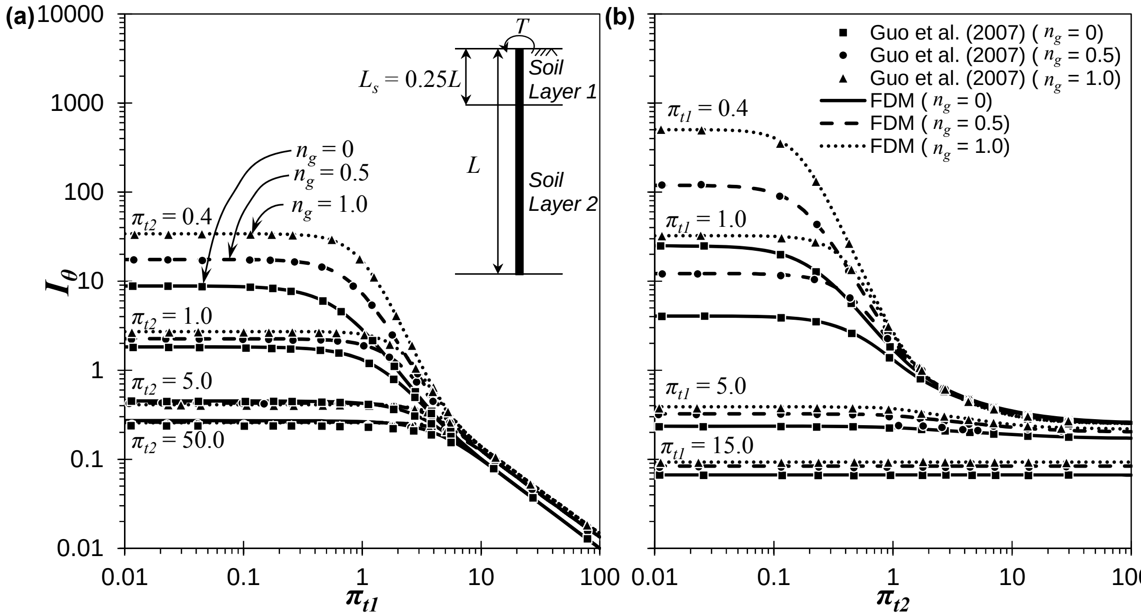

Figure 6-6. Validation of the FDM by comparing the linear elastic responses of a deep foundation in a two-layer soil with the analytical solutions from Guo et al. (2007) for the relationship between (a) I_ϕ and π_{t1} and (b) I_ϕ and π_{t2}.

Linear elastic-perfectly plastic solutions for torsionally-loaded deep foundations in a single layer soil using the FDM are also compared with the analytical solutions from Poulos (1975) and Guo and Randolph (1996). The relationships between the nonlinear correction factor, F_θ, and the ratio of the torque at the head of the deep foundation, T_h, and the ultimate torsional resistance, T_u, with various π_t are shown in Figure 6-7 for deep foundations in soil with constant and linearly varying stiffness. Again, no toe resistance is considered here to facilitate the comparison; the results from the FDM reproduce those of the previous analytical studies.

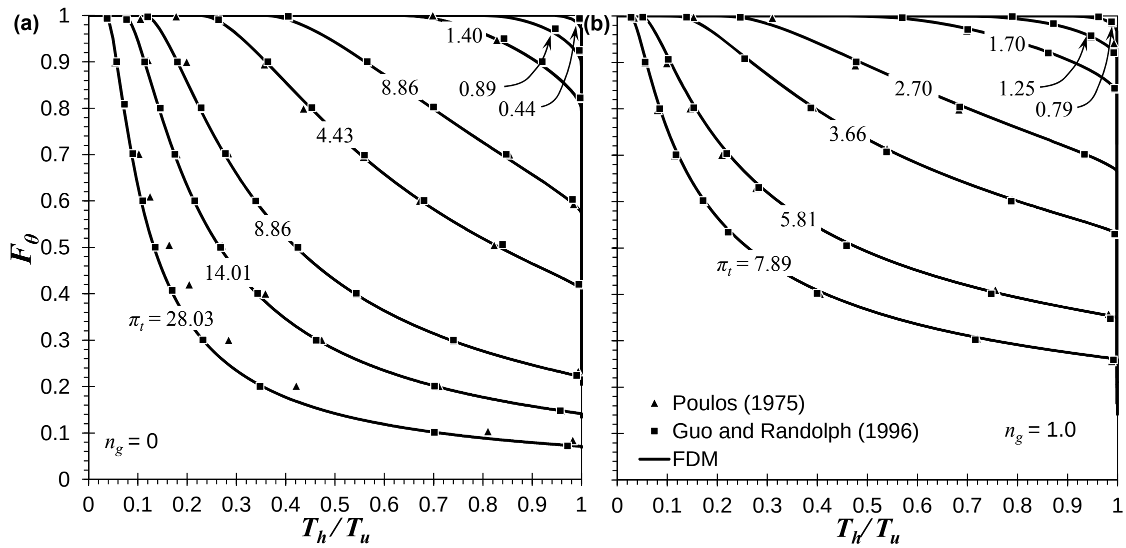

Figure 6-7. Validation of the FDM by comparing the linear elastic-perfectly plastic solutions with previous analytical solutions for deep foundations in the (a) single layer soil with constant stiffness, and (b) single layer soil with linearly-varying stiffness.

6.6.2 Validation of the FDM using Centrifuge Tests

Centrifuge tests by Zhang and Kong (2006) were conducted to study torsional load transfer using aluminum tubes 300 mm in length, 15.7 mm in outside diameter, and 0.9 mm in wall thickness under 40*g* acceleration. The prototype length, outside diameter, and wall thickness for 40*g* equal to 12 m, 628 mm, and 36 mm, respectively, and prototype values are assessed herein. The toe of the pile was conically shaped with a 60° apex angle and 0.6 m length. The pile was jacked into the sand bed following cessation of ground settlement while spinning at 40*g*. The embedded length of the pile was 10.8 m. Six torsional tests were performed with various loading rates (i.e., 0.025, 0.075, and 0.200 deg/s) for each of two relative densities (i.e., 32% and 75%). Load transfer data reported by Zhang and Kong (2006) is shown in Figure 6-8 and Figure 6-9 for loose and dense sand beds. Softening responses were observed at depths above 6.0 m for both loose and dense sand, whereas hardening responses were observed at depths below 6.0 m. Note that τ_{ult} in the loose sand bed is larger than that in the dense sand bed for depths ranging from 1.2 to 3.6 m (Table 6-4), perhaps due to the centrifuge consolidation operation.

In order to validate the FDM, the proposed displacement-hardening and -softening τ_s-Δ_s curves were used to simulate the torsional load transfer by back-calculating the respective model parameters (shown in Table 6-4). In the FDM, the soil was divided into eight layers based on the location of the instruments along the test pile. The overall pile was divided into 90 elements; and the cone shape toe was divided into five elements to account for the change of diameter. The torsional toe resistance was not considered due to the conical shape of the test pile. The τ_s-Δ_s curves using proposed displacement-hardening and softening models represent the observed response accurately for the loose and dense sand, as shown in Figure 6-8a and b, respectively, indicating suitability for use in validating the formulation of the FDM. Figure 6-8c and d show that the global torque-rotation response at the pile heads was accurately captured. The variation in torsional load transfer with depth is shown in Figure 6-9, and indicates that the load transfer is slightly underestimated at small θ_h, but increases in accuracy as the θ_h increases. The FDM formulation sufficiently captures the observed global and depth-dependent response.

6.6.3 Validation and Evaluation of the FDM using Full-Scale Tests

The full-scale loading tests on instrumented drilled shafts TDS and TDSFB reported by Li et al. (2017) are used to validate the formulation of the FDM and evaluate the accuracy of the proposed τ_s-Δ_s curves. Figure 6-10a compares the FDM simulation of TDSFB using the proposed displacement-hardening τ_s-Δ_s model parameters in Table 6.3 to those measured. Here, $\tau_{ult} = \tau_m$ (i.e., the measured resistance) in order to validate the FDM formulation. The torsional resistance is assumed zero at the toe of TDSFB owing to the intentional use of hydrated bentonite at that elevation as discussed by Li et al. (2017). The observed global torque-rotation response at the head of TDSFB is compared to that computed using the FDM in Figure 6-10c and shows that the FDM performs suitably. The profiles of torsional load transfer from the FDM are compared with the observed responses in Figure 6-11a for rotations to 1.75 degrees, further demonstrating the validity of the FDM and ability to simulate the observed, full-scale load transfer.

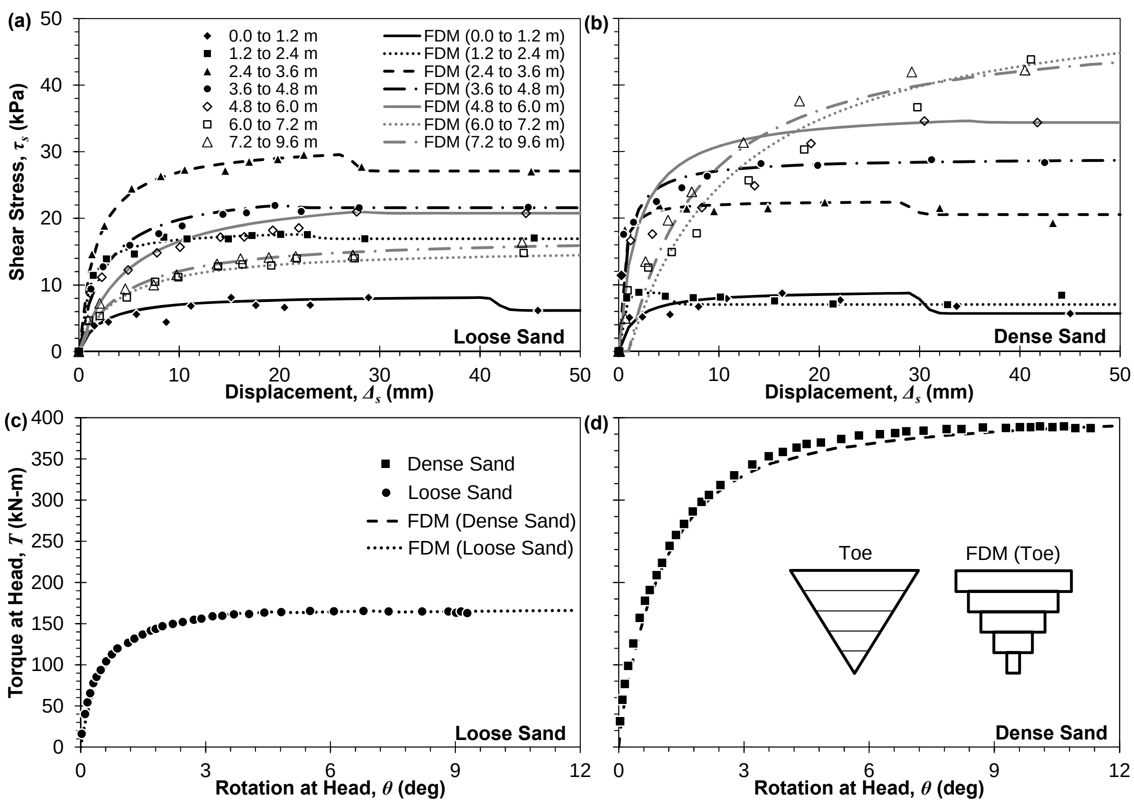

Figure 6-8. Validation of the FDM with the test data from Zhang and Kong (2006) on (a) the τ_s-Δ_s curves for each layer of (a) loose, and (b) dense sand, and global torque-rotation response at the pile head for (a) loose, and (b) dense sand. Inset shows the cone-shaped toe and the model used in the FDM.

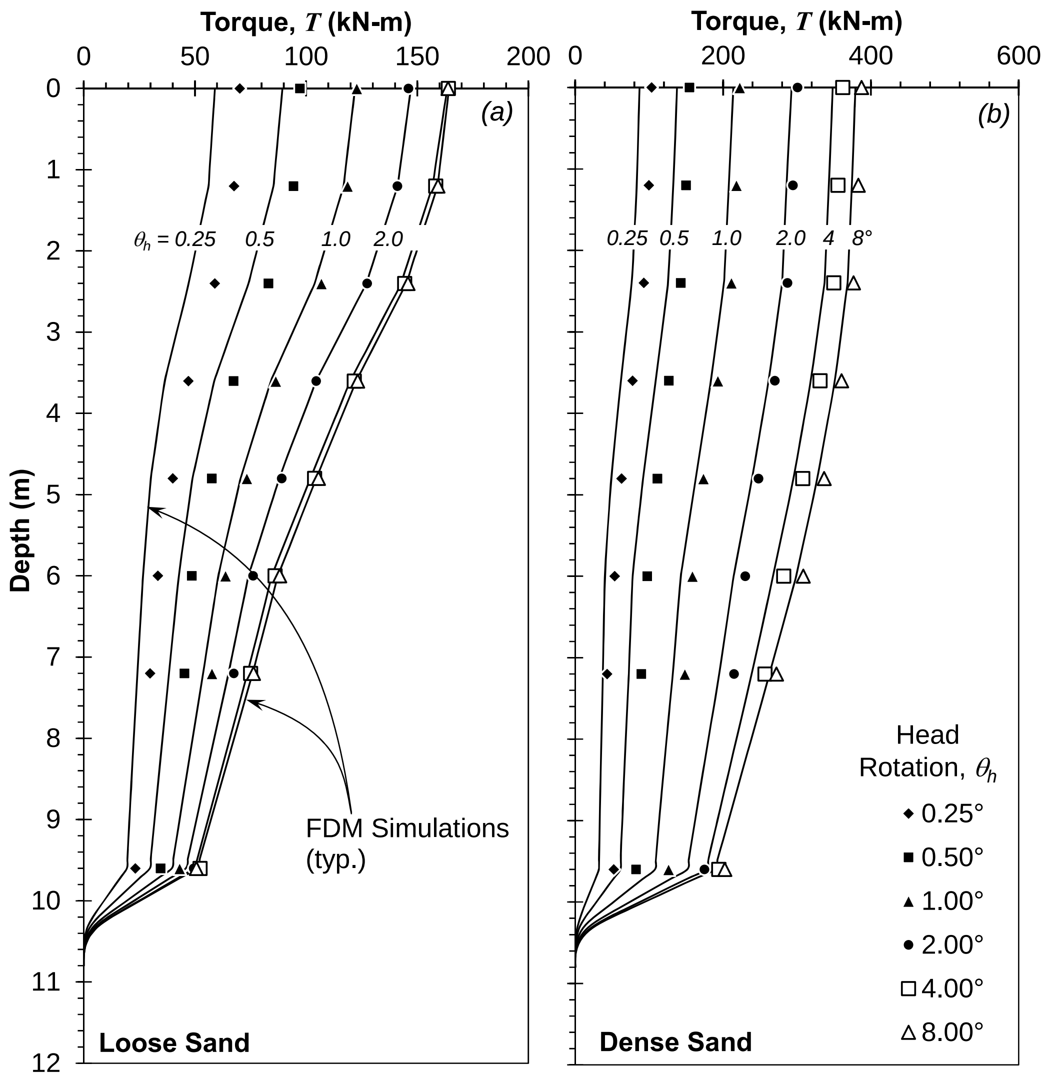

Figure 6-9. Validation of the FDM formulation using the torsional load transfer profiles measured from centrifuge tests by Zhang and Kong (2006) for various head rotations and (a) loose sand, and (b) dense sand.

Table 6-4. Back-calculated model parameters for each instrumented layer in the centrifuge tests conducted by Zhang and Kong (2006)

Depth (m)	K_{si} (kPa/mm)	τ_{ult} (kPa)	τ_p (kPa)	$\tau_{res,ult}$ (kPa)	R_f
Loose Sand					
0.0 to 1.2	4	8.5	8.1	6.2	0.95
1.2 to 2.4	20	18.3	17.6	17.0	0.96
2.4 to 3.6	19	31.5	29.6	27.1	0.94
3.6 to 4.8	10	24.7	22.0	21.6	0.89
4.8 to 6.0	5	24.7	21.0	20.8	0.85
6.0 to 7.2	4	14.8	-	-	0.95
7.2 to 9.6	4	16.4	-	-	0.95
9.6 to 10.8	75	95.2	-	-	0.96
Dense Sand					
0.0 to 1.2	6	9.4	8.8	5.7	0.93
1.2 to 2.4	60	9.3	8.9	7.1	0.96
2.4 to 3.6	80	22.6	22.4	20.6	0.99
3.6 to 4.8	40	29.1	28.8	28.4	0.99
4.8 to 6.0	20	36.4	34.6	34.4	0.95
6.0 to 7.2	5	54.8	-	-	0.80
7.2 to 9.6	7	52.8	-	-	0.80
9.6 to 10.8	182	360.6	-	-	0.88

The accuracy of the proposed τ_s-Δ_s curves is evaluated using the proposed displacement-hardening model with $\tau_{ult} = \tau_c$, where τ_c is calculated using the α method (Table 6.3). The difference between τ_c and τ_m may be partially attributed to the use of s_u estimates from a site-specific correlation to cone tip resistance (Li et al. 2017). Figure 6-10a compares the observed and calculated load-transfer curves, and indicates that the proposed model underestimated the torsional resistance for the depths of 1.1 to 2.1 m and 3.1 to 4.0 m and overestimates the torsional resistance at the depths of 2.1 to 3.1 m. The error in the load transfer curves counteract one another to produce a reasonable, albeit fortuitous, representation of the global torque-rotation response for the shaft head for rotations smaller than 0.1° (Figure 6-10c). Differences exist between the measured response, τ_m, and the response simulated using the α method, τ_c, because of the spatial variability of the soil, measurement error (e.g., q_t), transformation error from measured response to a design value (e.g., s_u), and model error. The over- and under-estimation of the interface shear response for the instrumented tributary areas results in differences between the observed and computed rate of load transfer as shown in Figure 6-11a.

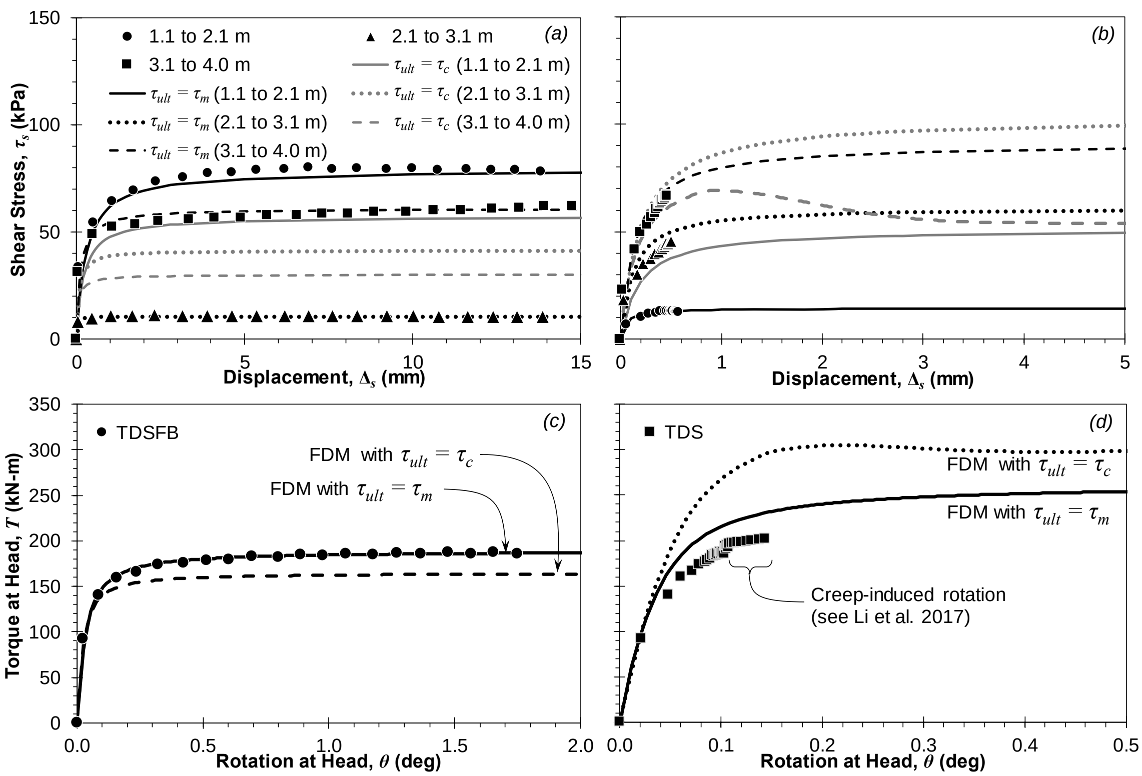

Figure 6-10. Validation and evaluation of the FDM with the test data from Li et al. (2017) on (a) and (b) τ_s-Δ_s curves at each layer for TDSFB and TDS, respectively, and (c) and (d) global torque-rotation response at head for TDSFB and TDS, respectively. Note: τ_m = measured (or extrapolated, for TDS) ultimate unit torsional shaft resistance and τ_c = calculated resistance using the α or β methods.

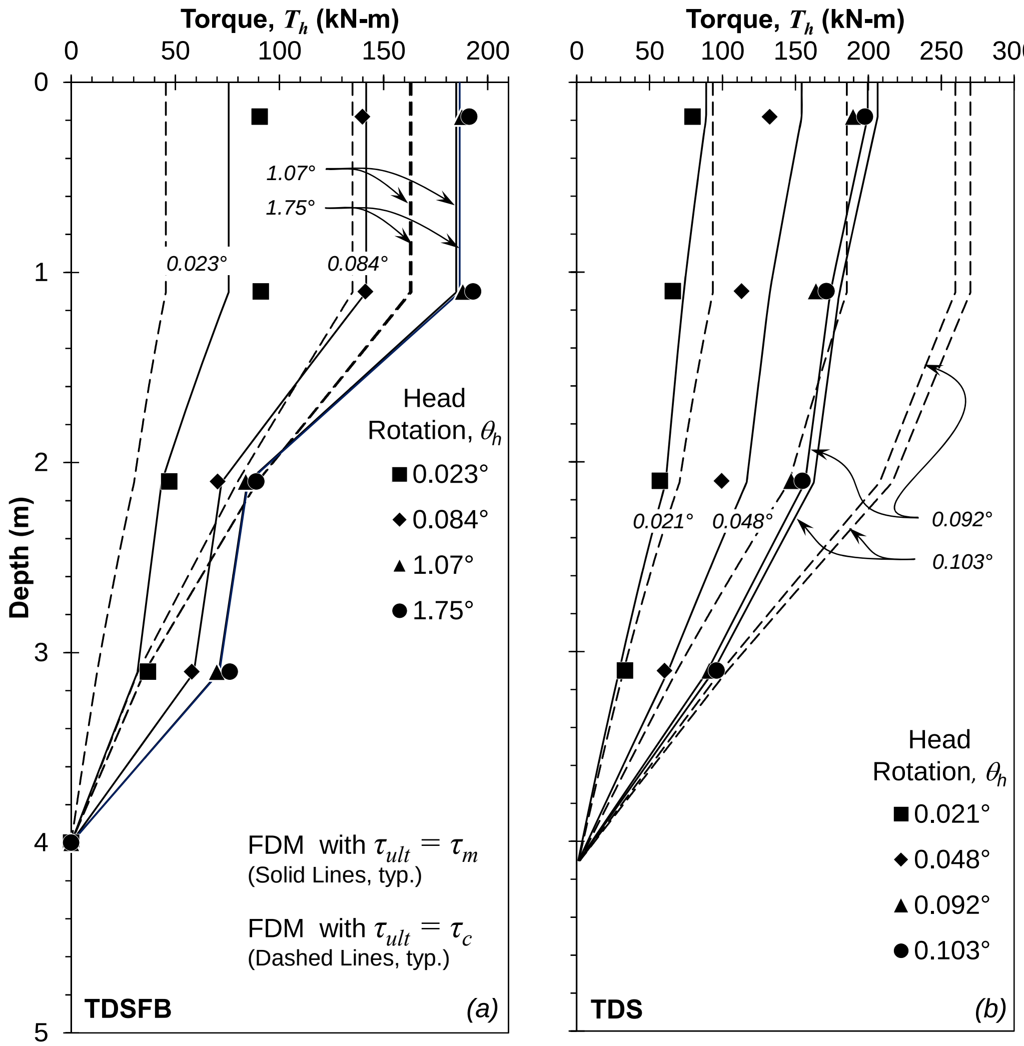

Figure 6-11. Validation of the FDM formulation and evaluation of the proposed τ-Δ models using full-scale torsional loading test data from Li et al. (2017) for load transfer profiles at different shaft head rotations for (a) TDSFB and (b) TDS.

The soil profile for shaft TDS is similar to that of TDSFB except for a lens of silty sand with gravel encountered from the depths of 2.8 to 3.8 m (Figure 6-4). The toe of TDS rests on the silty clay to clayey silt layer (Table 6-5). The unit torsional shaft resistances were not fully mobilized during the test, however, the ultimate unit torsional shaft resistance could be extrapolated using the measurements at each tributary area (Li et al. 2017). For consistency, τ_m is used to differentiate between the FDM validation case, conducted using the extrapolated ultimate unit torsional shaft, from the evaluation case, where τ_c is used to designate the case where the torsional resistance is calculated using the α and β methods for the plastic fine-grained and granular soils, respectively.

The unit shaft resistance model for drilled shafts in granular soils presented in Brown et al. (2010) is used to calculate the shaft resistance coefficient, β, for both the peak and ultimate residual (i.e., constant volume) interface shear resistance. The displacement-softening τ_s-Δ_s curve was selected for this dense sand layer assuming $R_f = 0.85$, $\phi'_p = 40°$, $\phi'_{cv} = 33°$. The torsional resistance for the plastic fine-grained soil from the ground surface to 1.1 m depth was neglected similar to the case for TDSFB. The initial interface stiffness, K_{si}, for each layer was evaluated using Eq. (6.19) and the V_s measurements (Figure 6-4). The τ_t-Δ_t curves for torsional toe resistance was constructed using the displacement-hardening model and the α method, since the toe of TDS was founded in the clayey silt layer.

The soil and drilled shaft properties and the load transfer model parameters for TDS are summarized in Table 6-5. The displacement-hardening and -softening τ_s-Δ_s curves designated with $\tau_{ult} = \tau_m$ in Figure 6-10b were implemented to illustrate the performance of the FDM. Since τ_m was estimated using an extrapolation of the hyperbolic displacement-hardening model, the τ_s-Δ_s curves generated by displacement-hardening model using $\tau_{ult} = \tau_m$ agree well with the measured response. However, the τ_s-Δ_s curves generated by displacement-hardening model using $\tau_{ult} = \tau_c$ over-estimate the unit torsional resistance for the depths of 1.1 to 3.1 m. The calculated displacement-softening τ_s-Δ_s curve (using τ_p and $\tau_{res,ult}$) agrees well with the observed curve, indicating the suitability of the Brown et al. (2010) ULS β method for use in constructing the τ_s-Δ_s curve (Figure 6-10b).

Table 6-5 Summary of parameters used to simulate the torsional response TDS using the FDM. Note: τ_m = measured (extrapolated for TDS) ultimate unit torsional shaft resistance and τ_c = calculated resistance using the α or β methods.

Depth (m)	Shaft		Soil							
	r (m)	ρ (kg/m^3)	s_u (kPa), or ϕ'_p, ϕ'_{cv} (°)	V_s (m/s)	G_{max} (MPa)	α or β	τ_c (kPa)		τ_m (kPa)	K_{si} (kPa/mm)
							τ_{ult}	τ_p, $\tau_{res,ult}$		
0.2 to 1.1	0.470	1,840	274	156	44	$\alpha = 0.00$	0	-	25	285
1.1 to 2.1	0.464	1,840	93	189	66	$\alpha = 0.55$	51	-	13	285
2.1 to 3.1	0.480	1,840	207	267	131	$\alpha = 0.55$	103	-	45	564
3.1 to 4.1	0.506	2,040	40°, 33°	268	147	$\beta_p = 1.40$ $\beta_{res,ult}$=1.09	-	69 54	91	530
Toe	0.506	1,840	34	268	132	-	19	-	-	564

Figure 6-10d compares the FDM results for TDS to the measured global torque-rotation response at the shaft head. Similar to previous comparisons, the FDM formulation sufficiently captures the observed full-scale response when using the extrapolated τ_m, indicating its suitability for forward analyses. The global torsional response using τ_s-Δ_s and τ_t-Δ_t curves calculated from the aforementioned methodologies (α and β methods) overestimate the observed global response at larger rotations, due to differences between the observed and calculated load transfer in the clayey silt soils (α method). However, the computed global response appears reasonable for rotations associated with the SLS (e.g., if using a factor of safety of two or three on the peak resistance).

6.7 Illustrative Parametric Studies

The proposed FDM methodology has been validated using several approaches, and has been shown to reproduce expected and observed behavior. The displacement-hardening and –softening models may be calibrated using available interface shear test data or typical strength parameters (i.e., s_u, ϕ'_p, ϕ'_{cv}).The accuracy of foundation rotations for the SLS and ULS in forward modeling will depend on the accuracy of the proposed interface shear model parameters, and the accuracy of methods used to calibrate τ_s-Δ_s and τ_t-Δ_t model parameters (e.g., α-method, β-method, etc.). Parametric studies are conducted to study the local, soil-structure interface and global response of deep foundations under pure torsion (i.e., with no axial load) to evaluate the effects of nonlinear soil response, including the state-dependent hardening and softening of the soil-structure interface. In light of the low contribution to torsional resistance in soils for deep foundations under pure torsion and to facilitate comparison to previous works (e.g., Poulos 1975 and Guo et al 2007), no toe resistance is considered in the study of the global torsional response. Then, the role of torsional toe resistance in the global response is studied in combination with axial loads, which can produce significant torsional toe resistance as the magnitude of the axial load increases as shown below.

6.7.1 Local Torsional Response of the Soil-Structure Interface

The parametric studies are conducted assuming that the deep foundation is embedded in dry, normally-consolidated Ottawa sand and characterized using the findings reported by Hardin and Richart (1963), Salgado et al. (2000), and Lee et al. (2004) and summarized in Table 6-6. The maximum soil shear modulus at depth z, $G_{max}(z)$, can be estimated using Eq. (6.20). The mean effective stress at depth z, can be obtained by:

$$\sigma'_m(z) = \frac{\sigma'_{v0} + 2\sigma'_{h0}}{3} = \frac{1 + 2K_0(z)}{3}\gamma' \cdot z \tag{6.26}$$

where σ'_{h0} = horizontal effective stress, γ' = effective unit weight of soil, $K_0(z)$ = coefficient of later earth pressure at rest at depth z, computed using (Jaky 1944):

$$K_0(z) = 1 - \sin\phi'_p(z) \tag{6.27}$$

where ϕ'_p is estimated using (Bolton 1986):

$$\phi'_p(z) = \phi'_{cv} + 3I_R(z) \tag{6.28}$$

which is valid for $0 \leq I_R(z) \leq 4$ and $I_R(z)$ = dilatancy index:

$$I_R(z) = D_R \cdot \left[Q + \ln \frac{P_a}{100 \cdot \sigma_m^1(z)} \right] - R \qquad (6.29)$$

where D_R is expressed as a decimal and the empirical constants R and Q are shown in Table 6-6 based on the triaxial tests conducted by Salgado et al. (2000) and Lee et al. (2004).

Table 6-6 The intrinsic soil properties for Ottawa sand (Salgado et al. 2000; Lee et al. 2004)

G_s	C_u	d_{50} *(mm)*	e_{min}	e_{max}	C_g	e_g	m_g	ϕ'_{cv}	Q	R
2.65	1.48	0.39	0.48	0.78	611	2.17	0.44	29.5	9.9	0.86

For each deep foundation element at depth z, the selection of the τ_s-Δ_s model parameters depends on the initial stiffness, K_{si}, and state, $I_R(z)$. The initial stiffness of a given τ_s-Δ_s curve (or τ_t-Δ_t for that matter) depends on G_{max} and D [Eq. (6.19)]; thus, the proposed state-dependent curves are sensitive to scale as illustrated in Figure 6-12. If $I_R(z)$ is negative, the soil is contractive so that $\phi'_p = \phi'_{cv}$ and the displacement-hardening model may be used assuming $\delta = \phi'_{cv}$ (i.e., a rough interface). Then, the Brown et al. (2010) method is used to compute $\tau_{ult}(z)$ using ϕ'_{cv}. Otherwise, if the initial value of $I_R(z)$ is positive, the interface is dilatant and modeled using displacement-softening model. In this case, $\tau_p(z)$ and $\tau_{res,ult}(z)$ are calculated using ϕ'_p and ϕ'_{cv} using the Brown et al. (2010) method.

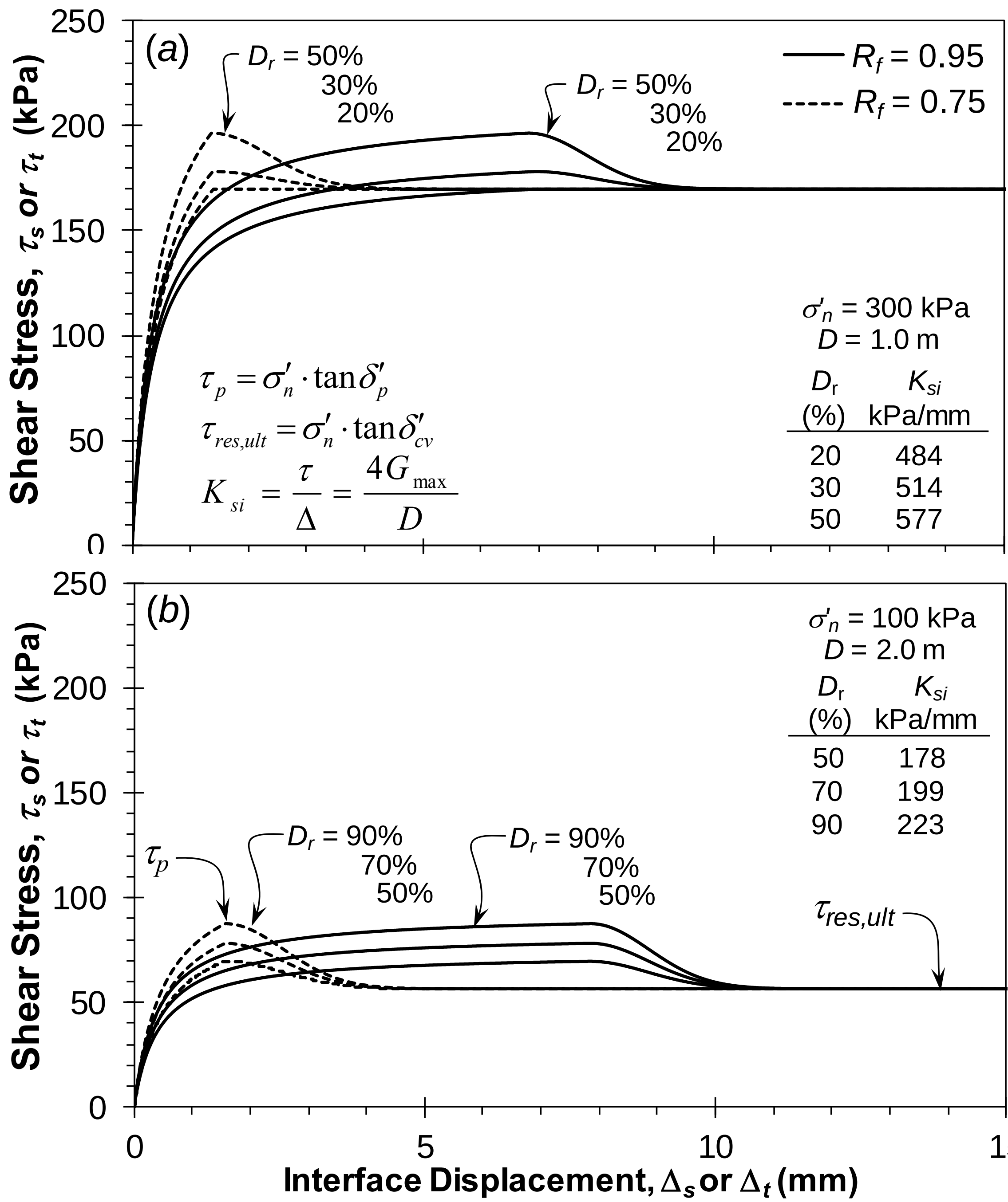

Figure 6-12. Sensitivity of state-dependent τ-Δ curves to failure ratio, R_f, maximum shear modulus, G_{max}, diameter, D, normal effective stress, σ'_n, and relative density, D_r.

Figure 6-12 presents the sensitivity of the state dependent τ-Δ curves to R_f, G_{max}, D, σ'_n, and D_r. Eq. (6.20) was used to compute the state-dependent G_{max}. The small-strain shear modulus, along with D, controls the initial stiffness of the load transfer curves, which necessarily increases with σ'_n, and D_r. Larger interface diameters result in a less stiff interface response (Randolph 1981). For a given σ'_n, and D_r, the peak and residual ultimate shear stress, τ_p and $\tau_{res,ult}$, are the same. However, the displacement at which these shear stresses occurs is controlled by the failure ratio; as R_f increases the transitional displacement, Δ_p, increases. The critical state load transfer methodology proposed here captures pertinent soil behavior and may be calibrated using pile design procedures or the tabulated interface shear model parameters given in Table 6-1 and Table 6-2.

6.7.2 Global Torsional Response of Deep Foundations

The parametric investigation is continued assuming that the selected deep foundation behaves linearly elastic under torsion with G_p = 12 GPa and L = 10 m. Figure 6-13a shows how the state-dependent τ_s-Δ_s curves vary along the shaft with depth for the selected Ottawa sand with D_r = 10% and 90%. To facilitate comparison to previous works, the nonlinearity correction factor, F_θ, implemented by Poulos (1975), Hache and Valsangkar (1988), and Guo and Randolph (1996) is used to indicate the effects of hardening or softening of the interface on the global system response. As described in Section 6.6.1, an F_θ = 1.0 indicates a purely linear-elastic system response, whereas decreasing F_θ indicates increasing system nonlinearity. The general trends described herein using F_θ hold for differing magnitudes of L and G_p.

To evaluate the effect of D_r on the global torsional foundation response, T_h, simulations were performed with D_r ranging from 10% to 100% within a uniform granular soil deposit. The effects of failure ratio, R_f, are also evaluated by varying it from 0.70 to 0.95. Figure

6-13b shows the variation of F_θ with R_f when D_r = 45% and 90%. As expected, the change in R_f does not affect the ratio of maximum, $T_{h,max}$, and residual or ultimate torsional resistance, $T_{res,ult}$, at the foundation head. However, F_θ decreases with increasing R_f for a given ratio of $T_h/T_{res,ult}$, indicating that the relative torsional stiffness decreases with increasing R_f . The variation of F_θ with D_r when R_f = 0.80 is shown in Figure 6-13c. The maximum torsional resistance increases with increasing D_r due to the increase in ϕ'_p with increasing D_r. As shown in Figure 6-13a, the governing soil properties (i.e., G_{max}, ϕ'_p, ϕ'_{cv}) vary with depth. Therefore, in order to exclude the influence of the variation in soil properties in the investigation of the effects of slenderness ratio L/D, D was varied with constant L = 10 m, as shown in Figure 6-13d, when D_r = 45% and R_f = 0.80. The nonlinear correction factor, F_θ, transitions from a relatively linear response at short, relatively rigid piles, to a highly-nonlinear response for slender, flexible piles. Figure 6-13 indicates numerous cases where $T_{h,max}/T_{res,ult}$ > 1.0; this indicates that the shaft experiences a maximum global torsional resistance prior to softening to the constant volume interface response along the entirety of the foundation – a critical consideration in view of wind gust or seismic design.

6.7.3 Torsional Toe Resistance of Deep Foundations

Depending on the function of the deep foundation, the pile or shaft toe resistance to torsion may be small and negligible (e.g., traffic sign and signal pole foundations) or be significant (e.g., stiff foundations supporting heavy superstructures that transfer axial loads to the toe). Thus, it is of interest to evaluate the parametric performance of the proposed methodologies in view of possible toe resistances. Li et al. (2017) demonstrated that the peak and ultimate residual torsional unit toe resistance, τ_{tp} and $\tau_{tres,ult}$, respectively, depends on the mobilized axial toe resistance, $R_{t,mob}$, and can be estimated by:

$$\tau_{tp} = \frac{4R_{t,mob} \cdot \tan(\phi'_p)}{\pi D^2} \tag{6.30}$$

$$\tau_{tres,ult} = \frac{4R_{t,mob} \cdot \tan(\phi'_{cv})}{\pi D^2} \tag{6.31}$$

respectively. The mobilized axial toe resistance is a function of the ultimate unit axial shaft resistance, r_s, and axial toe resistance, r_t, and can be estimated using the normalized load transfer relationships from O'Neill and Reese (1999). It is assumed that the ultimate unit axial shaft resistance, r_s, is equal to the ultimate unit torsional shaft resistance, τ_{ult} or $\tau_{res,ult}$ for hardening or softening response, respectively. This assumption must be confirmed in future studies. The total axial toe resistance, R_t, for drilled shaft foundations are given by (Brown et al. 2010):

$$R_t = \frac{\pi D^2}{4} \cdot r_t = \frac{\pi D^2}{4} \cdot 57.5 N_{60} \text{ with } r_t \leq 2{,}900 \text{ kPa} \tag{6.32}$$

For normally consolidated sands, the SPT blow count, N_{60} can be estimated by (Kulhawy and Mayne 1990):

$$N_{60} = \left[60 + 25\log(d_{50})\right] \cdot D_r^{\,2} \tag{6.33}$$

as used in this parametric study.

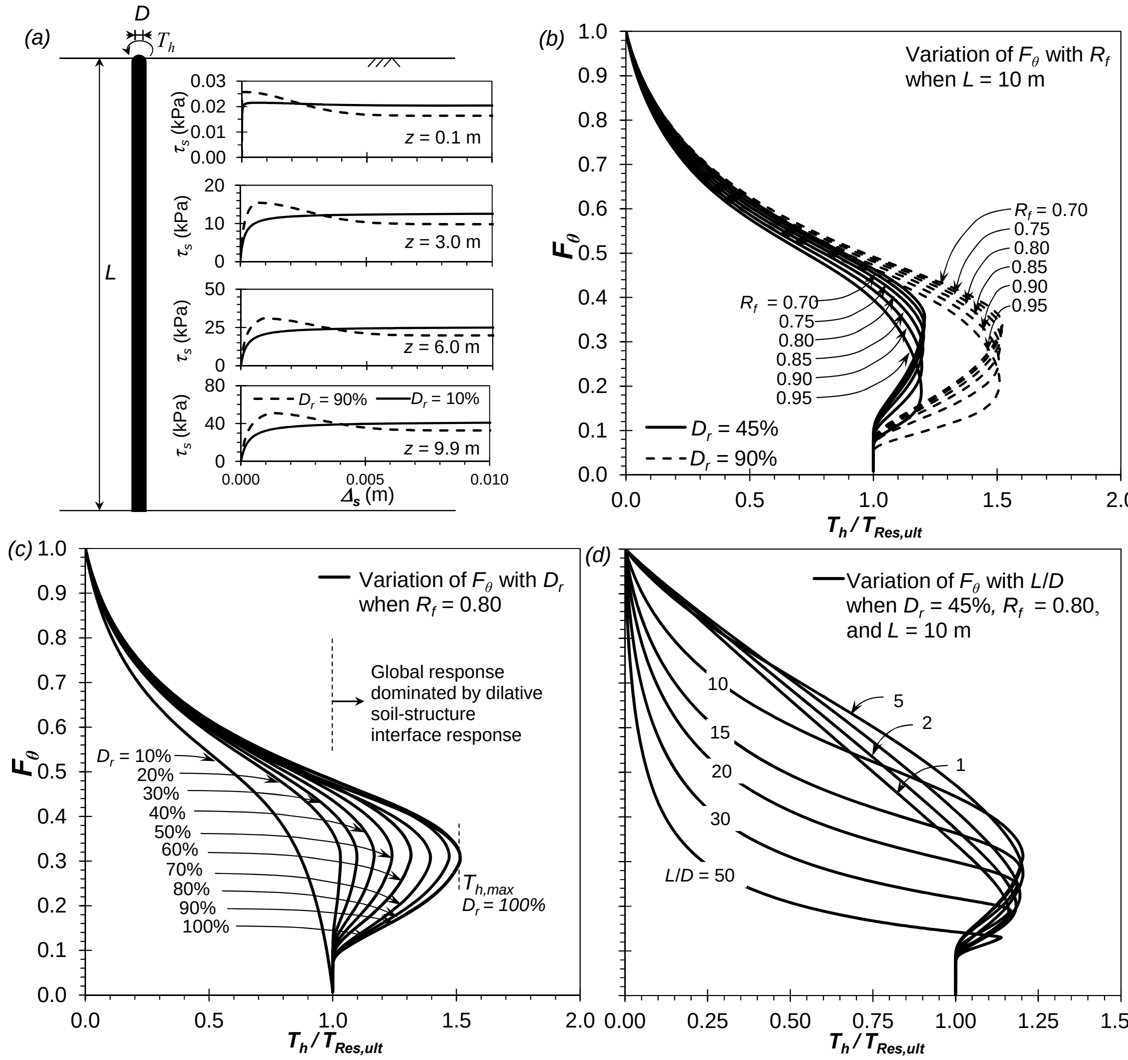

Figure 6-13. Parametric study of a torsionally-loaded deep foundation in Ottawa sand: (a) prescribed pressure-dependent τ_s-Δ_s curves as a function of depth, and the variation of nonlinearity correction factor, F_θ, with (b) failure ratio, R_f, (c) relative density, D_r, and (d) slenderness ratio, L/D.

The parametric study investigated the number of elements, n_t, used to model the toe of the foundation (Figure 6-14a), the position of the toe ring element within the toe (Figure 6-14b), the slenderness ratio, L/D, (Figure 6-14c), and the effect of D_r and $R_{t,mob}$ on the torsional response (Figure 6-14d). The effect of the number of ring elements, n_t, on the torsional toe resistance is evaluated by varying n_t, L/D, and D_r to determine the minimum

n_t that can produce a reliable magnitude of toe resistance for L = 10 m and R_f = 0.8 (Figure 6-14a). Since the torsional toe resistance depends on D and $R_{t,mob}$, a dimensionless normalized torsional toe resistance, T_{nor}, is used to illustrate the effect of n_t, and is defined as:

$$T_{nor} = \frac{T_t}{R_{t,mob} \cdot D} \tag{6.34}$$

For the purposes of demonstration, it is assumed that pure torsion is applied (i.e., there is no axial load, Q_a) to the deep foundation and the unit weight of the foundation is 24 kN/m^3. In order to capture the appropriate normal stress acting on the toe, the mobilized toe bearing resistance was set equal to the self-weight of the shaft minus the upward acting shaft resistance determined using the axial load transfer method prescribed by O'Neill and Reese (1999; refer to Li et al. 2017 for details). Figure 6-14a indicates that L/D and D_r have no effect on the relationship between T_{nor} and n_t. The possible optimum number of n_t appears to be 50 because further increases in n_t produce little effect on the torsional toe resistance. Therefore, n_t = 50 is used in the remaining analyses forming the parametric study. Note that the use of R_f = 0.8 does not affect τ_{tp} and $\tau_{tres,ult}$, only the displacement at which the transition from hardening to softening occurs.

Figure 6-14b shows the mobilization of unit torsional toe resistance, τ_t, with toe rotation, θ_t for selected toe elements when L = 10 m, D = 1 m, D_r = 90%, Q_a = 0, and R_f = 0.8. The toe element is numbered starting from the center (i.e., Element 1 and 50 are the innermost and outermost elements, respectively). Although the specified τ_t-Δ_t curves are identical for all of the toe elements, the τ_t-θ_t curves vary significantly as a function of radial position.

The outermost element achieves the peak resistance prior to other interior elements at a given rotation, since radial displacement is proportional to the distance of the element from the center of the toe.

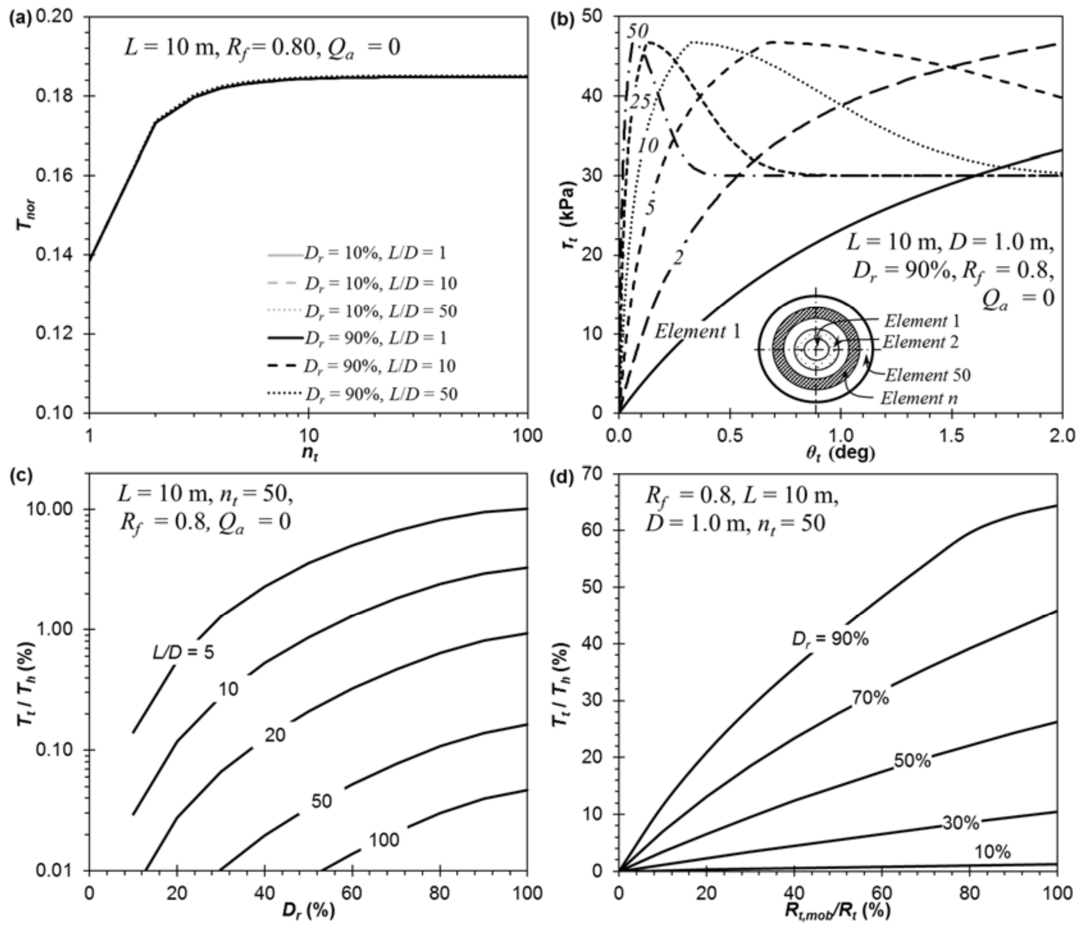

Figure 6-14. Parametric study of the torsional toe resistance, including (a) determination of the optimum number of toe elements, n_t, (b) the progressive mobilization of toe resistance as a function of radial position, and the variation of the proportion of torsional resistance resisted by the toe, T_t/T_h, with (c) relative density, D_r, and slenderness ratio, L/D and (d) relative density, D_r, and the level of mobilized axial toe resistance, $R_{t,mob}$ = R_t.

Figure 6-14c shows the effects of L/D and D_r on the proportion of torque mobilized at the toe, T_t/T_h, at the residual or ultimate state when L = 10 m, Q_a = 0, and R_f = 0.8. It appears that the T_t/T_h decreases as D_r decreases or L/D increases. When no axial load is applied and for a foundation of $L/D = 5$ in soil of $D_r = 100\%$, 10% of the mobilized global resistance can be attributed to the response of the toe. Figure 6-14d illustrates the role of axial loading on toe resistance by demonstrating the effect of $R_{t,mob}$ and D_r on T_t/T_h when $L = 10$ m, $D = 1$ m, and $R_f = 0.8$. Figure 6-14d shows that T_t/T_h increases with increases in $R_{t,mob}$ or D_r. It appears that the proportion of torque taken by toe can be as high as 64% when the axial toe resistance is fully mobilized ($R_{t,mob} = R_t$) and $D_r = 90\%$, producing significant torsional resistance.

6.7.4 Nonlinear Structural Response of Deep Foundation

Shear cracks may develop within a drilled shaft foundation undergoing large torsional loads if insufficient transverse reinforcement is specified (Li et al. 2017). For a column in torsion, the torque-rotation response becomes nonlinear after cracking, as observed by Hsu and Wang (2000), and the torsional rigidity, defined as the ratio of T and θ/L, may reduce at large rotations (Mondal and Prakash 2015). The FDM proposed here may be used to evaluate the influence of nonlinear torsional rigidity on the torsional response of deep foundations. For this investigation, the measured torque (T)-internal twist/length (θ/L) relationship for a structural column reported by Mondal and Prakash (2015) is used as the prototype; the column was constructed with a diameter of 0.61 m and 1.32% transverse steel ratio as shown in Figure 6-15a. The torsional rigidity exhibited distinct nonlinearity with small rotations, as well as softening following the peak torque of 327.5 kN-m.

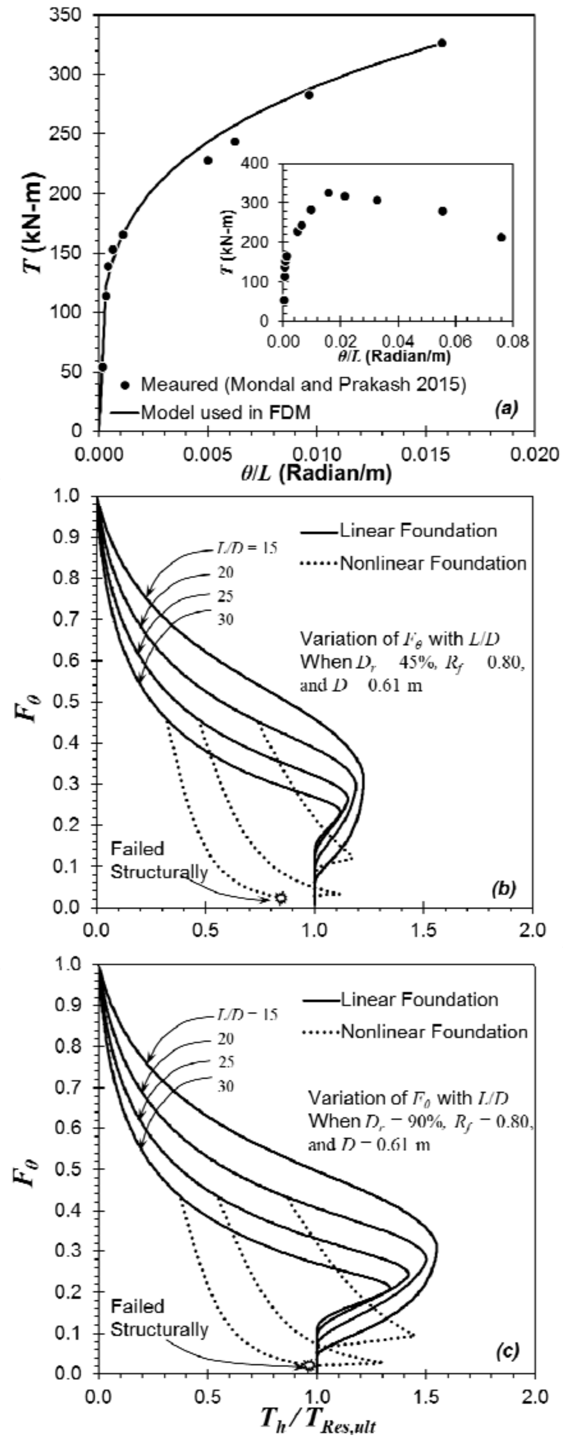

Figure 6-15 Parametric study of a torsionally loaded deep foundation in Ottawa sand with nonlinear structural response using (a) a measured torque (*T*)-internal twist/length (*θ*/*L*) response from Mondal and Prakash (2015) and (b) and (c) the comparison between the linear and nonlinear foundations with different slenderness ratio, *L*/*D* for relative density D_r = 45% and 90%, respectively.

When unembedded columns soften and form a plastic hinge, no additional torsional resistance can be mobilized within the soil; rather, the supported structure will simply undergo continued rotation. Therefore, for the purposes of the parametric investigation of the effect of nonlinear torsional rigidity on the soil-structure interaction of deep foundations, only the pre-peak or hardening portion of the reported torsional response is evaluated. The investigation assumes a linear response for $T \leq 125$ kN-m with a constant torsional rigidity $(GJ)_{max} = 4\times10^5$ kN-m^2; thereafter a power law of the form:

$$T = c_1 \cdot \left(\frac{\theta}{L}\right)^{c_2} \tag{6.35}$$

is used to replicate the experimental data, where c_1 and c_2 = 940 and 0.255, respectively, determined using the least squares method.

It is assumed that the deep foundation is embedded in the same Ottawa sand (Table 6-6) with D_r = 45% and 90%. For comparison purpose, a deep foundation with linear response $[GJ = (GJ)_{max}]$ is also considered. For the nonlinear deep foundation, the initial $(GJ)_{max}$ is used to calculate F_θ since GJ varies along the deep foundation due to the variation of internal rotation. Figure 6-15(b and c) show the comparison of the torsional response between the deep foundations with linear and nonlinear structural response with D_r = 45% and 90%, respectively. The linear and nonlinear foundations have the same response for L/D = 15 and D_r = 45% and 90% because the maximum internal torque remains smaller than the elastic limit of 125 kN-m. However, for larger L/D ratios, the response of the linear and nonlinear foundations diverge for $F_\theta > 0.44$ as the maximum internal torque exceed 125 kN-m, and where the linear elastic foundation remains stiffer than the nonlinear foundation. For L/D = 30 the nonlinear foundation does not mobilize its maximum soil resistance before structural failure when the torque at the head is equal to 327.5 kN-m. Accordingly, structural nonlinearity reduces the foundations global torsional stiffness, and the estimation of the global torsional capacity of a deep foundation may be unconservative if estimating capacity without due consideration of nonlinear structural response.

6.8 Summary and Conclusions

This chapter presents a numerical torsional load transfer method to facilitate the serviceability and ultimate limit state design of circular, torsionally-loaded deep foundations. The finite difference model (FDM) framework was selected to solve the governing differential equations that describe the performance of a circular, geometrically-variable deep foundation constructed in multi-layered state-dependent granular and plastic, fine-grained soils. In this approach, the deep foundation is treated as a beam, and the complicated soil-structure interaction is simplified to a beam interacting with discrete nonlinear torsional springs along the shaft and toe elements. Two simplified load transfer models relating the unit torsional resistance to the magnitude of relative displacement, including a displacement-hardening model and displacement-softening model are developed based on the available interface shear tests reported in the literature and on observed torsional load transfer. The tendency for dilation can be determined based on the interface roughness, normal effective stress, and the granular soil properties (i.e., relative density and grain type).

The displacement-hardening and -softening load transfer models are validated against the experimental interface shear data and the load transfer data from Li et al. (2017). The proposed FDM methodology is validated by comparing the torsional responses from FDM with previous analytical solutions and torsional loading tests. Based on the evaluation of the proposed load transfer curves calculated using the α and β methods, it appears that the accuracy of foundation rotations for the serviceability and ultimate limit states in forward modeling depends on the accuracy of the proposed interface shear model parameters, and the accuracy of methods used to calibrate interface model parameters. Parametric studies illustrate the significant effect of nonlinear-hardening and -softening soil responses and nonlinear structural response on the torsional behavior of deep foundations. In the study of toe resistance, the progressive and differential mobilization of toe resistance is observed along the radial position of toe ring elements with shared τ_t-Δ_t. The contribution of toe resistance in the global response for a foundation subject to pure torsion is small (not greater than 10% of the applied torsion) based on the parametric study. However, increases in axial load results in an increase in the mobilized axial toe resistance, which leads to a corresponding increase in the torsional toe resistance, which can be as great as approximately two-thirds of the total torsional response when bearing into very dense sands. The consideration of structural nonlinearity results in a smaller global torsional stiffness and capacity than that expected assuming a linear elastic structural section.

This work represents a simple, 1D nonlinear approach to the question of torsional response. Significant work remains to address combined loadings. However, the theoretically sound, critical state soil mechanics-consistent approach proposed herein should prove useful to the profession until such time that improved multi-dimensional methods are developed. The FDM is made free and available on request to the senior author.

6.9 Acknowledgements

This research was funded by Grant SPR 304-701 and DTRT13-G-UTC4O through the Oregon Department of Transportation and Pacific Northwest Transportation Consortium, respectively, for which the authors are grateful. The authors wish to thank Professor Andre Barbosa of Oregon State University for helpful discussions regarding the structural response to torsion.

6.10 References

Adami, N., and Stuedlein, A.W. (2015). “Region-Specific Load Transfer Model for ACIP Piles in Granular Soils.” *IFCEE 2015*, 712-722.

American Petroleum Institute (API). (1993*). Recommended practice for planning, design, and constructing fixed offshore platforms*, API RP 2A–WSD, 20th Ed., API, Washington, D.C.

Ashour. M., Pilling, P., Norris, G., and Perez, H. (1996). “Development of strain wedge model program for pile group interference and pile cap contribution effects.” *CCEER Rep. No. 96-4*, Civil Engrg. Dept., University of Nevada, Reno, Nevada

Bolton, M. D. (1986). “The strength and dilatancy of sands.” *Geotechnique*, 36(1), 65–78.

Boulanger, R. (2003). “Relating Kα to Relative State Parameter Index.” *J. Geotech. Geoenviron. Eng*., 129(8), 770-773.

Brown, D. A., Turner, J. P., and Castelli, R. J. (2010). “Drilled shafts: Construction procedures and LRFD design methods.” *Report No. FHWA-NHI-10-016*. US Department of Transportation, Federal Highway Administration, Washington, D.C.

Cao, W., Chen, Y., and Wolfe, W. E. (2014). “New load transfer hyperbolic model for pile-soil interface and negative skin friction on single piles embedded in soft soils*.” Int. J. Geomech*., 14(1), 92–100

Chen, S.L., Kong, L.G., and Zhang, L.M. (2016). “Analysis of pile groups subjected to torsional loading.” *Computers and Geotechnics*, 71, 115-123.

Chin, F. K. (1970). “Estimation of the pile Ultimate Load of Piles Not Carried to Failure.” *Proceedings of the 2nd Southern Asian Conference on Soil Engineering*, Singapore, 81-90.

Chin, F. K. (1971). “Discussion of 'Pile test, Arkansas River project.”. *Soil Mech. and Found. Div*., 97(6), 930-932.

Chow, Y. K. (1985). “Torsional response of piles in nonhomogeneous soil.” *J. Geotech. Engrg*., 111(7), 942–947.

Clemence, S. P. (1973). “The development of instrumentation and model testing for the load distribution in a drilled pier.” *Ph.D. Dissertation*, Georgia Institute of Technology, Atlanta, GA.

Clemence, S. P., and Brumund, W. F. (1975). “Large-scale model test of drilled pier in sand.” *J. Geotech. Engrg. Div*., 101(6), 537–550.

Clough, G. W., and Duncan, J. M. (1971). “Finite element analyses of retaining wall behavior.” *J. Soil Mech. Found. Div.,* ASCE, 97(12), 1657–1673.

Cox, W.R., Reese, L.C., Grubbs B.R. (1974). “Field testing of laterally loaded piles in sand.” *Proc. 6th Offshore Technology Conf.,* OTC , Houston, TX, 459-472.

Coyle, H. M., and Reese, L. C. (1966). “Load Transfer for Axially Loaded Piles In Clay.” *J. of Soil Mech. and Found. Engrg. Div.* 92(2), 1-26.

Coyle, H. M., and Sulaiman, I. (1967). ‘‘Skin friction for steel piles in sand.’’ *J. Soil Mech. Found. Div*., 93(6), 261–270.

DeJong, J. T., Frost, J. D. (2002), “A Multisleeve Friction Attachment For The Cone Penetrometer,*” Geotech. Test. J.,* 25(2), 111–127.

Desai, C. S., and Zaman, M. (2014). *Advanced geotechnical engineering soil–structure interaction using computer and material models* , CRC Press, Taylor & Francis Group, Boca Baton, FL.

Dove, J. E. and Frost, J. D., (1999). “Peak Friction Behavior of Smooth Geomembrane-Particle Interfaces,” *Journal of Geotechnical and Geoenvironmental Engineering*, ASCE, 125 (7), 544–555.

Dove, J. E., and Jarrett, J. B. (2002). “Behavior of dilative sand interfaces in a geotribology framework.” *J. Geotech. Geoenviron. Eng*., 128(1), 25–37.

Duncan, J. M., and Chang, C.-Y. (1970). “Nonlinear analysis of stress and strain of soil.” *J. Soil Mech. and Found*. Div., 96(5), 1629–1653.

Frost, J. D., DeJong, J. T., Recalde, M. (2002). “Shear failure behavior of granular-continuum interfaces”, *Engineering Fracture Mechanics*, 69(17), 2029-2048.

Frost, J.D., Hebeler, G.L., Evans, T.M., and DeJong, J.T. (2004). “Interface Behavior of Granular Soils,” *9th Biennial Int. Conf. Engrg., Constr., and Oper. in Challeng. Env., ASCE*, Reston, VA, 8 pp.

Georgiadis, M., and Saflekou, S. (1990). “Piles under axial and torsional loads.” *Comput. Geotech*., 9, 291–305.

Gere, J.M., and Timoshenko, S.P. (1997). *Mechanics of Materials*, PWS Pub.Co., Boston.

Gómez, J. E., Filz, G. M., and Ebeling, R. M. (2000a). ‘‘Development of an improved numerical model for concrete-to-soil interfaces in soil-structure interaction analyses.’’ *Technical Rep. ITL-99-1*, U.S. Army Engineer Research and Development Center, Vicksburg, Miss.

Gómez, J. E., Filz, G. M., and Ebeling, R. M. (2000b). ‘‘Extended load/unload/reload hyperbolic model for interfaces: Parameter values and model performance for the contact between concrete and coarse sand.’’ *ERDC/ITL TR-00-7*, U.S. Army Engineer Research and Development Center, Vicksburg, Miss.

Guo, W. D., Chow, Y. K., and Randolph, M. F. (2007). “Torsional pile in two-layered nonhomogeneous soil.” *Int. J. Geomech.,* 7(6), 410–422.

Guo, W. D., and Randolph, M. F. (1996). “Torsional piles in nonhomogeneous media.” *Comput. Struct.*, 19(4), 265–287.

Hache, R. A. G., and Valsangkar, A. J. (1988). “Torsional resistance of single pile in layered soil.” *J. Geotech. Engrg.*, 114(2), 216–220.

Hardin, B. O. (1978). ‘‘The nature of stress-strain behavior of soils.’’ *Proc., ASCE Geotech. Engrg. Div.., Spec. Conf.*, Vol. 1, ASCE, New York, 3–90.

Hardin, B. O., and Richart, F. E., Jr. (1963). ‘‘Elastic wave velocities in granular soils.’’ *J. Soil Mech. Found. Div.*, ASCE, 89(1), 33–65.

Holloway, D. M., Clough, G. W., and Vesic, A. S. (1975). “Mechanics of pile-soil interaction in cohesionless soil.” *Contract Report S-75-5, U. S. Army Wtrways. Exper. Sta*., Vicksburg, Mississippi.

Hsu, H. L., and Wang, C. L. (2000). “Flexural-torsional behavior of steel reinforced concrete members subjected to repeated loading.” *Earthquake Eng. Struct. Dyn.*, 29(5), 667–682.

Huffman, J.C., Strahler, A.W., and Stuedlein, A.W. (2015) “Reliability-based serviceability limit state design for immediate settlement of spread footings on clay,” *Soils and Foundations*, 55(4), 798-812.

Iscimen, M. (2004). “Shearing Behavior of Curved Interfaces.” Master’s thesis, Georgia Institute of Technology, Atlanta, GA.

Jaky, J. (1944). “The coefficient of earth pressure at-rest.” *J. Soc. Hung. Archit. Eng.*, 78(22), 355–358.

Kim, S., Jeong, S., Cho, S., and Park, I. (1999). “Shear load transfer characteristics of drilled shafts in weathered rocks.” *J. Geotech. Geoenviron. Eng.*, 125(11), 999–1010.

Kondner, R. L. (1963). “Hyperbolic stress–strain response: Cohesive soils.” *J. Soil Mech. Found. Div.* , 89 (1), 115–143.93q

Kulhawy, F. H., Peterson, M. S., (1979), “Behavior of Sand-Concrete Interfaces”, Proceedings, *Sixth Pan American Conference On Soil Mechanics And Foundation Engineering*, Vol. 2, Lima, Peru, 225-236.

Kulhawy, F. H., and Mayne, P.W. (1990). “Manual on estimating soil properties for foundation design.” *Rep. EL-6800*, Electric Power Research Institute, Cornell Univ., Ithaca, NY.

Lee, P. A., Kane, W. F., Drumm, E. C., and Bennett, R. M. (1989). “Investigation and modeling of soil-structure interface properties.” *Foundation engineering: Current* *principles and practice,* ASCE Geotechnical Special Publication 22, New York, 580–587.

Lee, J., Salgado, R., and Carraro, J. A. H. (2004). "Stiffness degradation and shear strength of silty sands." *Can. Geotech. J.*, 41(5), 831–843.

Li, Q., and Yang, Z. (2017). "*P–y* approach for laterally loaded piles in frozen silt." *J. Geotech. Geoenviron. Eng.*, 143(5), http://dx.doi.org/10.1061/(ASCE)GT.1943-606.0001556

Li, Q., Stuedlein, A.W., Barbosa, A. R. (2017). "Torsional load transfer of drilled shaft foundations." *J. Geotech. Geoenviron. Eng.*, 143(8), http://dx.doi.org/10.1061/(ASCE)GT.1943-5606.0001701.

Lings, M. L., and Dietz, M. S. (2005). "The peak strength of sand-steel interfaces and the role of dilation." *Soils Found.*, 45(6), 1–14.

Matlock, H. (1970). "Correlations for Design of Laterally Loaded Piles in Soft Clay." *Proc., 2nd Annual Offshore Technology Conf.,* OTC 1204, Houston, TX, 577-594.

Mondal, T. G., and Prakash, S. S. (2015). "Nonlinear finite-element analysis of RC bridge columns under torsion with and without axial compression." *J. Bridge Eng.*, 10.1061/(ASCE)BE.1943-5592.0000798, 04015037.

Norris, G. M. (1986). "Theoretically based BEF laterally loaded pile analysis." *Proc., Third Int. Conf. on Numerical Methods in Offshore Piling*, Editions Technip, Paris. France, 361-386.

O'Neill, M. W. (1964). "Determination of the pile-head torque-twist relationship for a circular pile embedded in a clay soil." *Master's thesis*, The Univ. of Texas at Austin, TX.

O'Neill, M. W., and Reese, L. C. (1999). "Drilled shafts: Construction procedures and design methods." *Publ. No. FHWA-IF-99-025*, Federal Highway Administration, Office of Implementation, McLean, VA

Paikowsky, S. G., Player, C. M., and Connors, P. J. (1995). "A dual interface apparatus for testing unrestricted friction of a soil along solid surfaces." *Geotech. Test. J.*, 18(2), 168–193.

Peterson, M. S., (1976), "Stress deformation behavior of soil concrete interfaces." Master's thesis, Syracuse University, Syracuse, NY.

Poulos, H. G. (1975). "Torsional response of piles." *J. Geotech. Engrg. Div.*,101(10), 1019–1035.

Randolph, M. F. (1981). "Piles subjected to torsion." *J. Geotech. Engrg. Div.,* 107(8), 1095–1111.

Reese, L. C., Cox, W. R., and Koop, F. D. (1975). "Field testing and analysis of laterally loaded piles in stiff clay." *Proc., 7th Offshore Technology Conf.*, SPE, Richardson, TX, 671-690.

Reese, L., Welch, R. (1975), “Lateral loading of deep foundations in stiff clay.” *Journal of Geotechnical Engineering Div*., ASCE, 101(GT7), 633-649.

Salgado, R., Bandini, P., and Karim, K. (2000). “Shear strength and stiffness of silty sand.” *J. Geotech. Geoenviron. Eng*., 126(5), 451–462.

Stuedlein, A. W. and Reddy, S. C. (2014). “Factors affecting the reliability of augered cast-in-place piles in granular soils at the serviceability limit state,” *J. of the Deep Foundations Institute*, 7(2), 46-57.

Subba Rao, K. S., Allam, M. M., and Robinson, R. G. (1998). “Interfacial friction between sands and solid surfaces.” *Geotech. Eng.*, 131, 75–82.

Teachavorasinskun, S., Shibuya, S., and Tatsuoka, F. (1991). “Stiffness of sands in monotonic and cyclic torsional simple shear.” *In Proceedings of Geotechnical Engineering Congress*, Boulder, Colo., 10–12 June 1991. *Edited by* F.G. McLean, D.A. Campbell, and D.W. Harris. ASCE Geotechnical Special Publication 27, Vol. 1, pp. 863–878.

Tomlinson, M.J. (1980). *Foundation Design and Construction*, Fourth Edition. Pitman Advanced Publishing Program, Boston, MA, 793 p.

Uesugi, M., and Kishida, H. (1986). “Frictional resistance at yield between dry sand and mild steel.” *Soils Found*., 26(4), 139–149.

Vijayvergiya, V. N. (1977). “Load-movement characteristics of piles.” *Proc., Ports '77: 4th Annual Symposium of the Waterway, Port, Coastal, and Ocean Division., ASCE*, New York, 269-284

Ward, H. C. (1982). *Profile characterization, chapter 4, in rough surfaces*, Thomas, T. R. (ed.), Longman, London, UK.

Wong, K. S., and Teh, C. I. (1995). “Negative skin friction on piles in layered deposits.” *J. Geotech. Engrg.,* 121(6), 457–465.

Zhang, L. (2010). “Nonlinear analysis of torsionally loaded piles in a two layer soil profile.” *Int. J. Geomech.*, 10(2), 65–73.

Zhang, L.M., and Kong, L.G. (2006). “Centrifuge modeling of torsional response of piles in sand.” *Canadian Geotechnical Journal*, 43(5), 500-515.

7. EXPERIMENTAL PROGRAM FOR AXIAL AND LATERAL LOADING TESTS

To study the impact of steel casing and high-strength steel reinforcement on the axial and lateral performance of drilled shaft foundations and to evaluate the appropriateness of existing load transfer models, four instrumented full-scale drilled shaft were designed and constructed. This chapter introduces the design and construction of the test specimens and describes the various kinds of instrumentation used to observe their performance. The chapter concludes with a discussion of the experimental setup used to load the shafts in axial and lateral loading. Chapters 8, 9, and 10 follow, and present the detailed results of the loading test program and their interpretation and use in forward design analyses.

7.1 Test Shafts Configuration

The four test shafts were designed with an embedded length of 18.3 m (60 ft), and a nominal diameter of 915 mm (36 in); the actual diameter varied, sometimes significantly, as a function of construction sequence and installation method, as described below. All of the test shafts extended 1.5 m (5 ft) above ground surface to facilitate the loading test setup, described subsequently. The uncased shaft with mild (Grade 60) internal reinforcement (designated MIR) represents a typical production shaft. Shaft MIR therefore serves as the baseline for comparison to the three other shafts. The steel reinforcement of MIR consisted of nine No. 14 longitudinal steel bars with 2% longitudinal steel ratio and two No. 5 spirals at a center-to-center spacing of 150 mm (6 in). Table 7-1 summarizes the salient features of MIR, whereas Figure 7-1a presents the typical cross-section, including the information of the internal reinforcement and the locations of the PVC crosshole sonic logging (CSL) access tubes, thermal wires used for thermal integrity profiling (TIP), inclinometer casing, and strain gauges, as described subsequently. To reduce the congestion of the reinforcement cage as compared to MIR and reduce possibility of anomalies associated with poor concrete flowing through the cage, high-strength (Grade 80) reinforcement was used along with hollow threaded bars in shaft HSIR (high strength internal reinforcement). The internal reinforcement for HSIR could be designed with longitudinal steel ratio of 1.5% to achieve the same nominal structural axial resistance as MIR according to Section 5.7.4.4 of the AASHTO provisions (AASHTO 2014). Nine No. 11 bars and two No. 5 spirals at a center-to-center spacing of 200 mm (8 in) were nominally selected to provide the required longitudinal reinforcement. However, as shown in Figure 7-1b, three No. 11 bars were substituted with 73/56 hollow threaded bars which provided the necessary structural requirements in addition to access for cross-hole sonic logging tests (Josef 2011).

The two experimental cased shafts included one with internal reinforcement (designated CIR) and one with no significant internal reinforcement (designated CNIR). Figure 7-1c and Figure 7-1d present the typical cross-sections of CIR and CNIR, both of which had an outside dimeter and steel wall thickness of 940 mm (37 in) and 12.5 mm (1/2 in), respectively (Table 7-1). Grade 50 straight-seam steel casing was used for both the cased shafts, specially made to produce the same nominal concrete area in section as the uncased shafts. The steel reinforcement cage placed within CIR was identical to that of MIR, whereas the cage for CNIR (with 0.15% longitudinal steel) was selected to facilitate delivery of the strain gauges to the required elevations. In practice, shaft CNIR would offer substantially improved constructability of fully-cased shafts should its loading performance exhibit similar characteristics to the CIR due to the lack of internal reinforcement. To compare the effect of subtle construction differences on axial resistance, the auger diameter used for CNIR and CIR was 940 and 915 mm (37 and 36 in), respectively; this subtle difference was found to produce a significant effect on the axial response but little impact on the lateral response. Figure 7-2 show the steel cages for test shafts. It noted that the cages for MIR and CIR were identical so that the cage in Figure 7-2b is used to represent both MIR and CIR.

Table 7-1. Summary of the configuration of the experimental, instrumented test shafts. The total and embedded length of each shaft is 19.8 m (65 ft) and 18.3 m (60 ft), respectively.

Test Shaft and Designation	Nominal Auger Diameter m (in)	Internal Steel Type	External Steel Type	Casing Wall Thickness mm (in)	Internal and External Steel (%)
Mild Internal Steel Reinforcement (MIR)	0.915 (36)	Grade 60	-	0	2.00
High-strength Internal Reinforcement (HSIR)	0.915 (36)	Grade 80	-	0	1.50
Cased, Mild Internal Reinforcement (CIR)	0.915 (36)	Grade 60	Grade 50	12.5 (0.5)	7.20
Cased, No Internal Reinforcement (CNIR)	0.940 (37)	Grade 60*	Grade 50	12.5 (0.5)	5.33

* only 0.15% of longitudinal steel reinforcement was used to deliver strain gages to the necessary elevations

7.2 Construction of the Test Shafts and the Reaction Piles

The test shafts were installed on June 16th and 17th, 2015. The wet construction method was used in the construction of the test shafts by introducing polymer slurry into the dry borehole at an excavation depth of approximately 5.5 m (18 ft) before the borehole was excavated to the final depth of 18.3 m (60 ft). Figure 7-3 shows the construction of the uncased shafts, including drilling a hole, lowering the steel cage into the hole, installing sonotube concrete form, and placing the concrete using the tremie method. Sonotube concrete forms were used to form the shafts above ground surface and were pushed 0.46 m (18 in) below ground. For the cased shaft, Figure 7-4 shows the construction procedure, including drilling a hole, vibrating steel casing into the hole, lowering the steel cage, and placing the concrete.

Because the use of 940 mm (37 in) auger, the installation of the casing for CNIR was much easier than for CIR. The average compressive strength of the concrete on the day of the loading tests of MIR, HSIR, CIR, and CNIR was 69, 72, 65 and 64 MPa (10,500, 10,050, 9,440, and 9,270 psi), respectively. The concrete mix design used for the test shafts is summarized in Table 7-2.

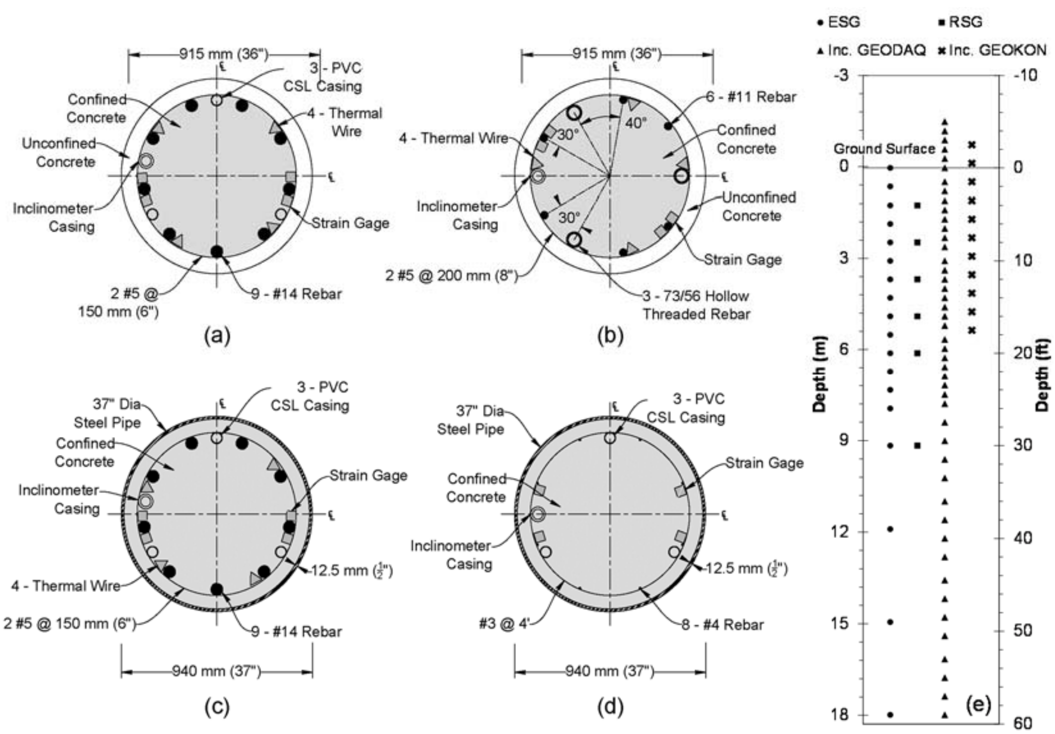

Figure 7-1: Cross-sections of the test shafts: (a) MIR, (b) HSIR, (c) CIR, and (d) CNIR with shaded area indicating the confined concrete used in section analyses, and (e) elevations of the resistance strain gauges (RSG), embedded strain gauges (ESG), GEODAQ in-place inclinometer (Type I Inc.), and GEOKON in-place inclinometer (Type II Inc.).

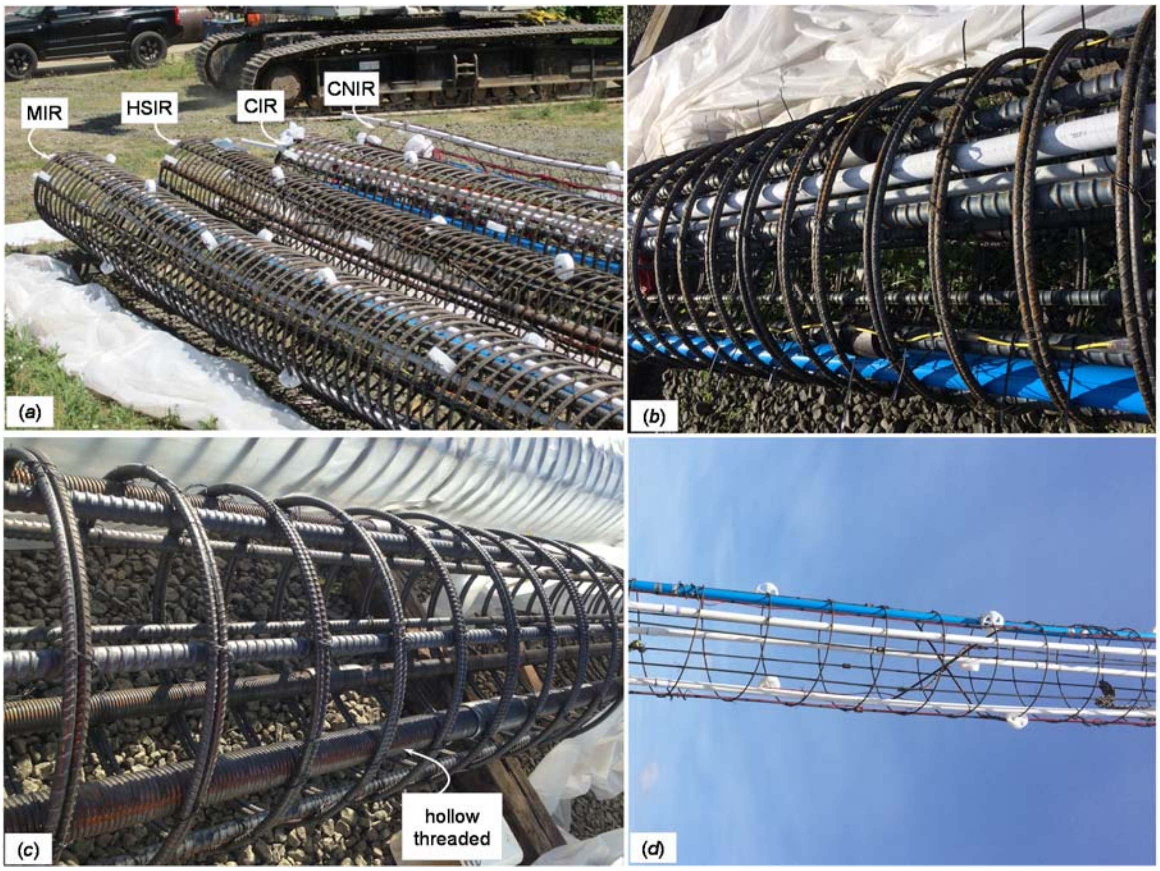

Figure 7-2: Fabricated steel cages of (a) all test shafts, (b) MIR or CIR (*n.b.*, these cages are identical), (c) HSIR, and (d) CNIR.

Figure 7-3: Construction of the uncased shafts: (a) drilling a hole, (b) lowering the steel cage into the hole, (c) installing sonotube concrete form, and (d) placing the concrete.

Figure 7-4: Construction of the cased shafts: (a) drilling a hole, (b) vibrating steel casing into the hole, (c) lowering the steel cage for CNIR, and (d) placing the concrete.

Twelve continuous flight auger piles (Figure 4-9) were installed to serve as reaction shafts (RS) to provide uplift reaction in axial loading tests. On either side of the shaft, there were two 0.76 m (30 in) diameter by 17 m (55 ft) long RS with 63 mm (2¼ in) diameter solid steel thread bars at center of the RS.

Table 7-2 Concrete mix design for the test shafts

Parameters	Value
Comp. Strength 28 days, MPa (psi)	28 (4,000)
Slump, mm (in)	216 ± 38 (8.5 ± 1.5)
Air Content (%)	1.5% ± 1.5%
Plastic Unit Weight, kg/m^3 (pcf)	2,241 (139.9)
Maximum water/cement (w/c) Ratio	0.50
Water Reducer, mL/m^3 (oz/yd^3)	1,880 (49)
Hydration Stabilizer, mL/m^3 (oz/yd^3)	3,760 (97)
Maximum Aggregate	9.5 mm (3/8")

7.3 Instrumentation of the Test Shafts

An instrumentation program was developed to observe the axial and lateral response of the shafts during testing. The shafts were instrumented, as shown in Figure 7-5, using concrete embedment strain gages (ESGs), resistance strain gages (RSGs), load cells, dial gages and string-potentiometers, and in-place inclinometers to observe the axial and lateral response of the shafts during testing. For each shaft, as shown in Figure 7-1e, ESGs were installed at 18 elevations and RSGs were installed at six elevations; two pairs of each strain gauge type were installed at given elevation. The locations of the strain gauges and inclinometers at each elevation of each shaft are shown in Figure 7-1a through Figure 7-1d. The RSGs had a strain limit of 50,000 $\mu\varepsilon$, whereas two types of ESGs were used: a low range (3000 $\mu\varepsilon$ limit) and high range (8000 $\mu\varepsilon$ limit) type, the latter of which was placed where the greatest flexural strains were anticipated during the lateral loading tests.

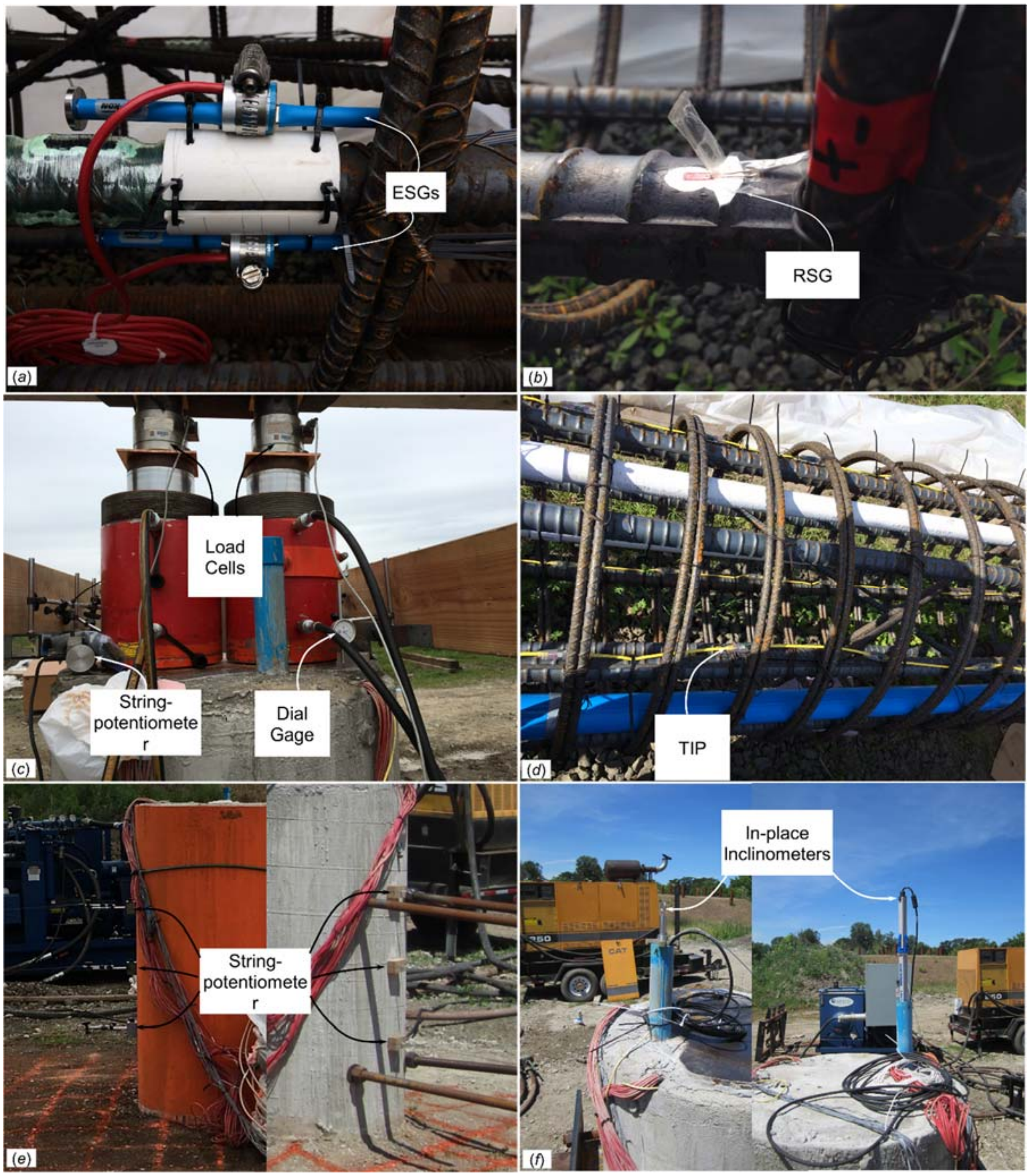

Figure 7-5. Instrumentation of the test shafts, including (a) concrete embedment strain gages (ESGs), (b) resistance strain gages (RSGs), (c) load cells, dial gages and string-potentiometers for axial loading tests, (d) string-potentiometers for lateral loading tests, (e) in-place inclinometers, and thermal wires used for thermal integrity profiling (TIP).

During the axial loading tests, the load applied at the top of each test shaft was measured directly using load cells. Three dial gauges and three string-potentiometers were used to measure displacements. The displacements measured from the dial gauges and string-potentiometers were nearly identical, and the mean value of the six measurements was used to represent the shaft head displacements. During the lateral loading tests, string-potentiometers and load cells were used to measure the applied displacement and corresponding lateral load. Each test shaft was instrumented with three string-potentiometers at different elevations above the ground surface with 0.3 m (1 ft) apart. The middle string-potentiometers were set at the same elevation of the resultant of the actuator-applied load. The displacements measured from the string-potentiometers and inferred from the in-place inclinometers were nearly identical at the point of load application. The measured displacement from the string-potentiometer was used to represent the deflection at the loading point, and the estimated displacement from the inclinometers was used to present the lateral displacement profiles along the shafts.

Given the need for reliable and redundant measurements to be used in the development of the lateral load transfer, inclinometers were used to measure the tilt, or slope, along the test shafts. Two types of in-place inclinometers were used: a GEODAQ model i6 (designated Type I inclinometer) and a GEOKON model 6150 (designated Type II inclinometer). The sensor resolution of Type I and II inclinometers was 0.004° and 0.0006°, respectively. The Type I inclinometer consisted of eight modules, connected together in series, where each module had a length of 2.4 m (8 ft). The top four modules had eight tilt sensors each (spaced 0.3 m or1 ft), whereas the bottom four modules had four tilt sensors per module (spaced 0.6 m or 2 ft). The Type II inclinometer had 11 tilt sensors placed 0.6

m (2 ft) apart starting from the loading point (Figure 7-1e). The Type II inclinometer was used in shafts MIR and CNIR, whereas the Type I inclinometer was used in shafts HSIR and CIR.

7.4 Non-destructive Integrity Tests

To investigate the integrity of the concrete in the test shafts, CSL method was performed on each shaft in accordance with ASTM D6760 (ASTM, 2014a) and the thermal integrity profiling (TIP) method was conducted in accordance with ASTM D7949 (ASTM, 2014b) for MIR, HSIR, and CIR. The TIP method monitors the temperature generated by curing cement (i.e., hydration energy) using a thermal probe that is lowered down an access tube or using thermal wires that are attached to the reinforcement cage (e.g., Mullins, 2010 and Johnson, 2016). The TIP method is able to detect anomalies by the relative differences in the measured thermal signature. In addition, the TIP method can be used to estimate the actual shape of the shaft along its length based on the relationship between the shaft diameter and hydration temperature and can be compared to the field concreting logs to assess the overall quality of the shaft (Mullins, 2010; Mullins, 2013).

The NDT results indicated that the four shafts were constructed without anomalies; the specific test outcomes and comparison of the two NDT methods performed on these four test shafts is described by Stuedlein et al. (2016). Notably, the CSL results, which can be found in Appendix C, showed that the hollow threaded bar produced significantly cleaner *p*-wave velocity signals and improved clarity in the resulting waterfall plots. The profile of measured temperature and inferred shaft radius with depth based on the TIP results, which can be found in Appendix D, is shown in Figure 7-6. The as-built diameter (Figure 7-6b) of the uncased test shafts above the ground surface was known since a sonotube was used;

however, the as-built diameter below the ground surface was generally larger than the auger diameter (915 mm or 36 in). Comparing the average temperature profiles between the cased and uncased shafts (Figure 7-6a), significant differences are observed above a depth of about 8 m (26.5 ft), whereas similarities are noted for depths below 8 m. Of particular note at a depth of about 5 m (16.4 ft) and corresponding to the interface between the first and second (a water bearing) soil layers, the shaft became somewhat belled. The drilling protocols were identical for all shafts and therefore the variation in diameter of the excavation should be similar. However, this is not observed in the temperature profile due to the presence of the casing, which would have been surrounded by flowing groundwater that could act to cool the shaft. The temperature profile indicated the presence of significant gaps between the casing and the sidewalls of the shaft cavity from depths of 3 to 8 m (10 to 26.5 ft). The presence of gaps seemed to be confirmed upon loading (described subsequently). In addition, the temperature-based inference of shaft radius appeared slightly smaller than the actual (and known) radius, perhaps due to the cooling effect of the groundwater.

7.5 Axial Loading Test Setup

Axial loading tests were conducted on April 8th, 15th, 21st, and 26th, 2016 for CNIR, CIR, HSIR, and MIR, respectively, approximately 10 months after the shafts were constructed. Conventional top-down axial compression load tests were conducted by inducing a load into the test shaft using hydraulic jacks and by reacting against a large, 18 MN (4,000 kip) capacity cross beam with two saddle beams tied to reaction piles, as shown in Figure 7-7. Axial displacements were applied to the test shafts using two jacks with the combined capacity of 7,120 kN (1,600 kips) at 70 MPa (10 ksi). Four 63 mm (2¼ in) diameter solid steel thread bars connected the reaction frames to four 0.76 m (30 in) diameter by 17 m (55 ft) long continuous flight auger piles, two on either side of the test shaft, to provide the necessary tiedown resistance to the uplift reaction generated by the jacking force.

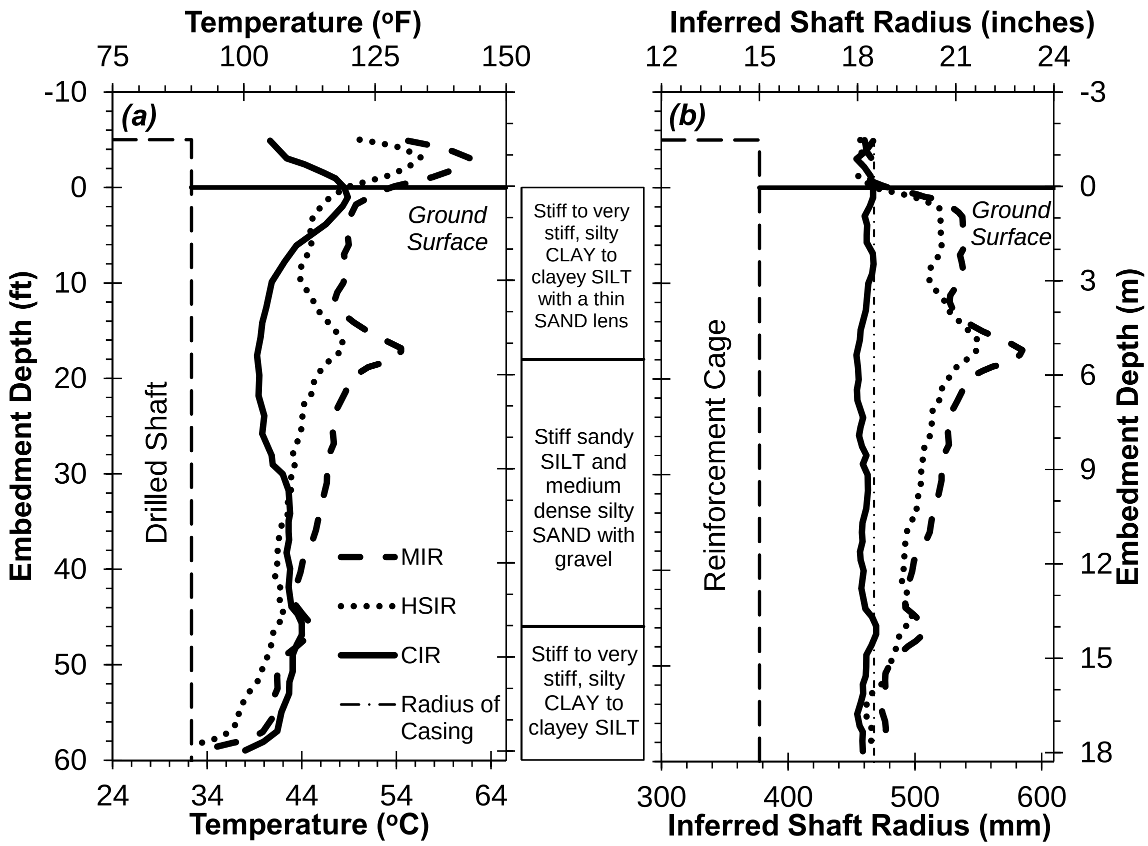

Figure 7-6. Comparison of (a) average temperature-depth profiles, and (b) average radius-depth profiles for shafts MIR, HSIR, and CIR.

Axial loads were applied in increments of 267 kN (60 kips) until failure or until the limit of available pressure with the hydraulic pump was reached. The loading increments were deemed too large for the cased shafts, but were used nonetheless to facilitate the comparison of load-displacement behavior among the test shafts. At each load increment, the applied axial loads were maintained for 10 minutes to allow sufficient sampling of the ESGs, which required 3 seconds/sample.

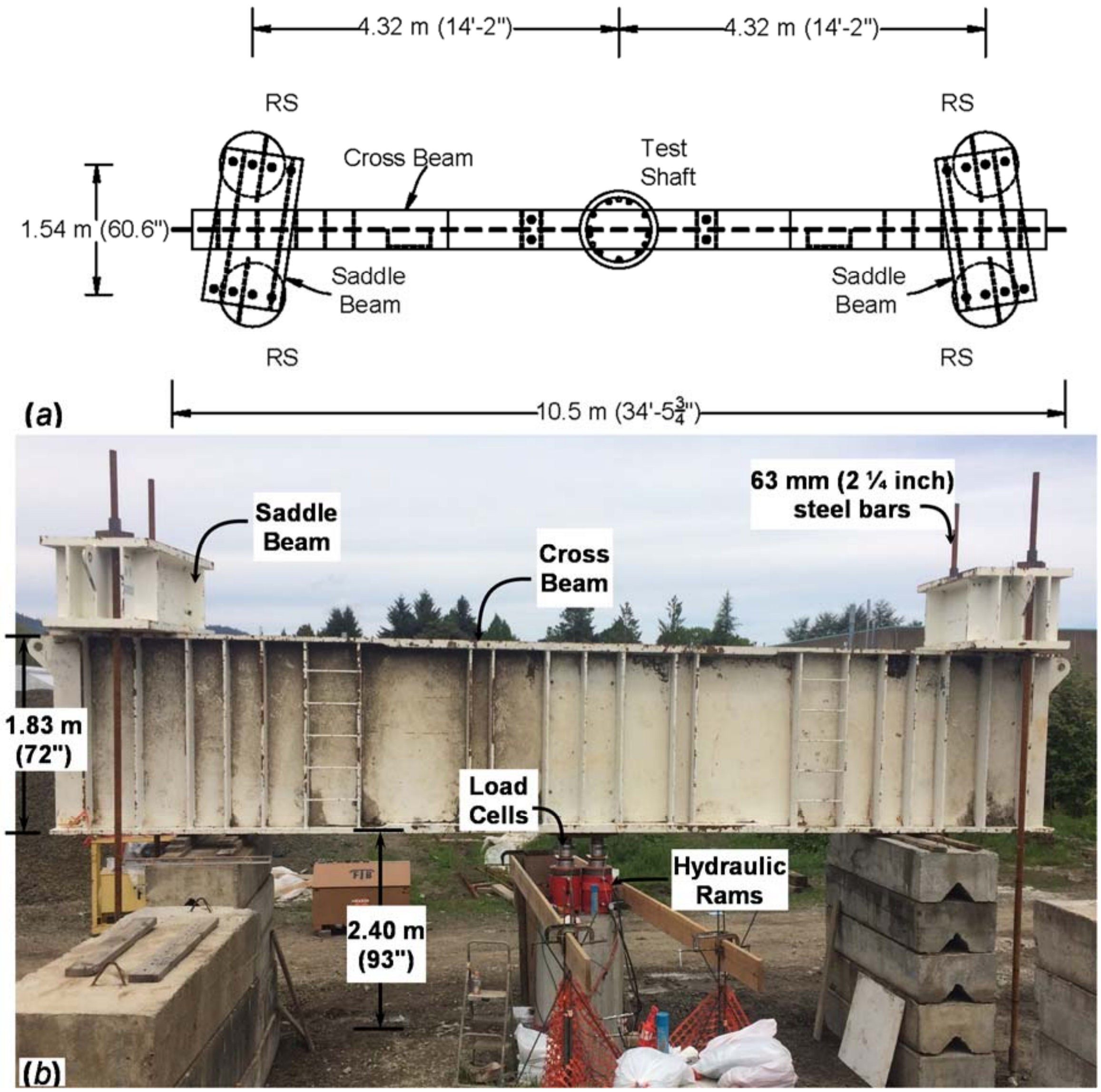

Figure 7-7: Experimental setup for the axial loading tests: (a) top view and (b) plan view.

7.6 Lateral Loading Test Setup

Lateral loading tests were conducted by displacing two test shafts at a resultant point located approximately 760 mm (2.5 ft) above the ground surface using a hydraulic actuator

(Figure 7-8). Owing to the need to displace each shaft to large displacements, the loading tests were paired with shafts of similar flexural rigidity; therefore, shaft MIR provided the reaction for HSIR, whereas CIR provided the reaction for CNIR (and vice versa). Lateral loading tests were conducted on June 4th and 14th, 2016 for uncased and cased shafts, respectively.

Figure 7-8: Lateral loading tests setup for (a) uncased shafts and (b) cased shafts. Note, the photos were taken at the applied displacement of 447, 206, 213, and 205 mm (17.6, 8.11, 8.39, and 8.07 in) for MIR, HSIR, CIR, and CNIR, respectively.

The loading tests commenced with a target of 2.54 mm (0.1 inch) of incremental displacement until the displacement reached 12.7 mm (0.5 inch). The incremental lateral displacement increased to 6.35 mm (0.25 inch) until total displacement of 25.4 mm (1.0 inch). Then, the incremental lateral displacement of 12.7, 25.4, and 50.8 mm (0.5, 1.0, and

2.0 inch) were applied when the total displacement reached at 50.8, 101.6, 304.8 mm (2.0, 4.0, and 12.0 inch), respectively. The displacement recorded at the resultant point of load application at HSIR and CIR was used to control the applied displacements; accordingly, displacements of the reacting shafts were alternately smaller, equal, and larger than the specified displacements due to compliance in the experimental setup and the spatial variability of the soil. Lateral loads, V_h, were held at 18-minute time intervals at each target load to allow sufficient sampling of ESG data. Table 7-3 summarizes the load schedule of applied displacement, y_h, at the loading points. For the cased shafts, the final applied displacement was approximately 203 mm (8 in) due to the limitation of the available pressure possible with the hydraulic actuator.

Table 7-3. Summary of loading protocol and measured lateral displacement, y_h, and lateral shear force, V_h, for the four test shafts.

Increment	Scheduled y_h, mm (inch)	Measured y_h, mm (inch)				Measured V_h, kN (kip)	
		MIR	HSIR	CIR	CNIR	uncased	cased
0	0	0	0	0	0	0	0
1	2.5 (0.1)	2.6 (0.1)	3.3 (0.1)	4.3 (0.2)	3.8 (0.1)	170 (38)	130 (29)
2	5.1 (0.2)	4.3 (0.2)	5.5 (0.2)	8.0 (0.3)	6.4 (0.3)	210 (47)	180 (40)
3	7.6 (0.3)	6.0 (0.2)	8.8 (0.3)	11.7 (0.5)	8.1 (0.3)	260 (58)	225 (50)
4	10.2 (0.4)	7.5 (0.3)	10.8 (0.4)	17.6 (0.7)	11.1 (0.4)	280 (63)	275 (62)
5	12.7 (0.5)	9.7 (0.4)	13.5 (0.5)	20.7 (0.8)	13.1 (0.5)	310 (70)	310 (69)
6	19.1 (0.8)	16.0 (0.6)	19.9 (0.8)	29.0 (1.1)	19.9 (0.8)	370 (83)	415 (93)
7	25.4 (1.0)	20.7 (0.8)	25.7 (1.0)	35.1 (1.4)	25.6 (1.0)	425 (95)	495 (111)

Table 7-3 (continued).

Increment	Scheduled y_h, mm (inch)	Measured y_h, mm (inch)				Measured V_h, kN (kip)	
		MIR	HSIR	CIR	CNIR	uncased	cased
8	38.1 (1.5)	34.5 (1.4)	38.9 (1.5)	50.0 (2.0)	38.9 (1.5)	530 (119)	630 (142)
9	50.8 (2.0)	46.6 (1.8)	51.4 (2.0)	65.2 (2.6)	51.8 (2.0)	605 (137)	745 (167)
10	76.2 (3.0)	68.7 (2.7)	77.1 (3.0)	91.5 (3.6)	77.7 (3.1)	720 (162)	925 (208)
11	102 (4.0)	92.0 (3.6)	103 (4.0)	115 (4.5)	103 (4.0)	800 (179)	1,085 (244)
12	152 (6.0)	183 (7.2)	151 (6.0)	164 (6.5)	155 (6.1)	860 (194)	1,350 (304)
13	203 (8.0)	446 (17.5)	206 (8.1)	213 (8.4)	205 (8.1)	885 (199)	1,540 (346)
14	254 (10.0)	477 (18.8)	255 (10.0)	-	-	910 (204)	-
15	305 (12.0)	523 (20.6)	305 (12.0)	-	-	920 (207)	-

7.7 References

AASHTO (2014). *LRFD Bridge Design Specifications*. 7th edition, American Association of State Highway and Transportation Officials, Washington, D.C.

ASTM (2014a) "Standard Test Method for Integrity Testing of Concrete Deep Foundations by Ultrasonic Crosshole Testing," *ASTM D 6760*, ASTM International, West Conshohocken, PA, 7 pp.

ASTM. (2014b). "Standard Test Methods for Thermal Integrity Profiling of Concrete Deep Foundations," *ASTM D7949*, ASTM International, West Conshohocken, PA, 2014, www.astm.org.

Josef, K.A. (2011). "Hollow threaded rebar for cross hole sonic logging access tubes combined with longitudinal concrete reinforcing in drilled shafts." *DFI Journal: The Journal of the Deep Foundations Institute*, 5(2). 16-22.

Johnson, K.R. (2016) "Analyzing thermal integrity profiling data for drilled shaft evaluation.", *DFI Journal: The Journal of the Deep Foundations Institute*, 10(1), 25-33

Mullins, G. (2010) "Thermal Integrity Profiling of Drilled Shafts," *DFI Journal: The Journal of the Deep Foundations Institute*, 4(2), 54 – 64.

Mullins, G. (2013). “Advancements in drilled shaft construction, design, and quality assurance: the value of research.” *International Journal of Pavement Research and Technology*, 6(2), 93–99.

Stuedlein, A.W., Li, Q., Zammataro, J., Belardo, D., Hertlein, B., and Marinucci, A. (2016) “Comparison of Non-Destructive Integrity Tests on Experimental Drilled Shafts,” *Proceedings, 41st Annual Meeting of the Deep Foundations Institute*, New York, NY. 10 pp.

8. AXIAL LOAD TRANSFER OF DRILLED SHAFT FOUNDATIONS WITH AND WITHOUT STEEL CASING

Authors:

Qiang Li , Armin W. Stuedlein , and Antonio Marinucci

Journal:

Journal of the Deep Foundations Institute

https://doi.org/10.1080/19375247.2017.1403074

8.1 Abstract

Steel casing is commonly used in drilled shaft construction to maintain the integrity of the borehole during drilling; however, little guidance regarding the effect of the casing on axial load transfer exists in the literature. To address this aspect of drilled shaft design and construction, this chapter presents a study of axial load transfer of drilled shaft foundations using four, full-scale, instrumented drilled shafts: two uncased and two cased drilled shafts, reinforced with either mild or high strength steel reinforcement. Axial loading tests were performed and used to compare various performance metrics between the cased and uncased shafts, including the axial load-displacement curves, load transfer distributions, and back-calculated unit shaft resistance-relative displacement relationships (*t-z* curves) and unit toe resistance-toe displacement relationships (*q-z* curves). The uncased test shafts exhibited significantly greater axial shaft resistance compared to the cased test shafts, and data from thermal integrity profiler (TIP) sensors allowed interpretation of the differences in soil-shaft contact conditions and the resulting load transfer. Although the ultimate axial resistance of the uncased test shafts could not be mobilized, sufficient data was developed to allow comparison to the cased test shafts and extrapolation to anticipated ultimate resistance conditions. The back-calculated *t-z* curves of the uncased test shafts were modeled and used, along with the *q-z* curves from the cased shafts, to estimate the anticipated large deformation response. Selected axial load transfer models were evaluated and modified to produce region-specific *t-z* and *q-z* curve models to aid the design of drilled shaft bridge foundations in Oregon. Based on observations in this study and those previously reported, the effects of permanent casing on axial load transfer are summarized

to provide an up-to-date reference on the reductions expected based on construction sequencing and installation methods.

8.2 Introduction

Drilled shaft foundations are commonly selected to support highway bridges and heavily loaded superstructures owing to their suitability for transmitting large axial, lateral, and torsional loads to the subsurface. Steel casing is frequently used in drilled shaft construction, either for temporary support of the borehole during construction or for permanent resistance to anticipated lateral loads. In some instances, steel casing, which was intended for temporary support, is difficult to withdraw during construction (Owens and Reese, 1982), and it becomes a permanent feature of the foundation. In these cases, a reassessment of load transfer is required in the cased portion, where the new section may exhibit less axial and torsional resistance, and greater flexural resistance. Owing to the significant differences in stiffness (and therefore natural frequency) between cased and uncased shafts, ignoring the contribution of the permanent casing to the seismic response of substructures can lead to substantial errors. The assessment of load transfer of steel cased drilled shafts requires the evaluation of certain considerations that differ from uncased shafts. Steel casing provides significant flexural resistance and confinement to the infill concrete, which leads to an increase of inelastic deformation and flexural capacity (Roeder et al. 1999; Roeder et al. 2010; and Roeder and Lehman 2012). Common terms for this type of deep foundation include Cast-In-Steel-Shell (CISS) pile and concrete-filled tubes (CFT), and are frequently used by the Washington, California, and Alaska Departments of Transportation (e.g., Gebman et al., 2006; Roeder and Lehman, 2012; Li and Yang, 2017; and Yang et al., 2017). However, depending on the method of construction, steel casing may result in reduced axial load transfer to the surrounding soil. Geotechnical design models for axial resistance of drilled shafts with permanent steel casing are not well established, and the understanding of the magnitude and nature of the reduced axial load transfer can be improved.

In general, axial loads applied to deep foundations are supported by a combination of shaft and toe resistance. A number of procedures to calculate the static axial capacity of deep foundations have been established that consider the stress history, in-situ lateral stresses, undrained shear strength (within a total stress adhesion approach), and drained strength (within an effective stress approach) of the soil (e.g., O'Neill and Reese, 1978; Reese and O'Neill, 1988; Poulos, 1989; Kulhawy, 1991; Mayne and Harris, 1993; Chen and Kulhawy, 1994; O'Neill and Reese, 1999; Chen and Kulhawy, 2002; Jamiolkowski, 2003; Kulhawy, 2004; Kulhawy and Chen, 2007; and Brown et al., 2010). The axial capacity of a deep foundation can also be estimated directly by scaling up cone penetration test (CPT) measurements, including corrected cone tip resistance, q_t, sleeve resistance, f_s, pore water pressure, u_2, and shear wave velocity, V_s (e.g., Bustamante and Gianeselli, 1982; Alsamman, 1995; Fioravante et al., 1995; Eslami and Fellenius, 1997; Takesue et al., 1998).

Each of the aforementioned methods is useful for estimating the static axial capacity of a drilled shaft in the respective geologic formation(s); however, the methods do not provide information regarding the magnitude of displacement required to achieve a given axial resistance, as is possible using a load transfer approach. With this approach, the soil reaction around the shaft and at the toe can be represented by discrete nonlinear springs distributed along the shaft (t-z curves) and at the toe of the shaft (q-z curves), where t = unit axial shaft resistance, z = is relative displacement, and q = unit toe resistance. The approach used to develop load-transfer curves includes empirical procedures that are based on experimental data (e.g., Coyle and Reese, 1966; Coyle and Sulaiman, 1967; Holmquist and Matlock, 1976; and Grosch and Reese, 1980), on numerical techniques (e.g., Poulos and Davis, 1968; and Butterfield and Banerjee, 1971), and on theoretical methods (e.g., Chin, 1970; Kraft et al., 1981; Chow, 1986; McVay et al., 1989; Randolph, 1994; and Poulos, 2001).

Reductions in axial capacity should be considered for permanently cased drilled shafts (e.g., AASHTO, 2014; and Brown et al., 2010). A limited amount of axial loading tests reported in the published literature was used to assess the reduction in axial load transfer associated with the use of casing, and guidance on the magnitude of the reduction is scarce. Owens and Reese (1982) detailed a comparative study of cased and uncased shafts using full-scale loading tests at several sites and reported that, in some cases, the ratio of unit shaft resistance of cased to uncased shafts could be as low as 9%. Camp et al. (2002) reported the findings of axial loading tests of three partially cased drilled shafts where the ratio of unit shaft resistance of the cased portion to the uncased portion was in the range of 20 to 58%. However, AASHTO (2014) states that casing reduction factors of 0.5 to 0.75 are commonly used, which is not consistent with the published field studies. Hence, improvement of design guidance could benefit from additional full-scale observations.

Among several global objectives of this study on drilled shafts constructed with high-strength reinforcement bars and/or steel casing, this chapter describes the comparison of axial load transfer between uncased and cased shafts to improve the understanding of the magnitude and nature of axial load transfer and to evaluate the suitability of existing load transfer models. Four instrumented test shafts with nominal diameters of 0.9 m (36 in) and embedded lengths of 18.3 m (60 ft) were constructed at the geotechnical engineering field research site (GEFRS) on the Oregon State University (OSU) campus in Corvallis, Oregon. Two of the test shafts were constructed without steel casing and designated hereinafter as the test shafts with mild internal reinforcement (MIR) and high-strength internal reinforcement (HSIR). The other two test shafts were constructed with permanent steel casing, including the cased test shaft with internal reinforcement (designated CIR) and nominally without internal reinforcement (designated CNIR). The results of the loading tests are presented, including the axial load-displacement curves, the axial load transfer distributions, and the back-calculated *t-z* and *q-z* curves. Then, selected axial load transfer models are evaluated and modified to produce region-specific axial load transfer models for uncased drilled shafts. Finally, the effect of permanent casing on the axial response is discussed, and recommendations for axial shaft reduction with casing are developed based on available test data, soil conditions, and construction sequencing.

8.3 Experimental Program

Four test shafts and 12 reaction piles were installed at the GEFRS in Corvallis, Oregon. Chapter 4 presents the geotechnical explorations, stratigraphy, and corresponding subsurface conditions for the site, and specifically the location of the test shafts (Figure 4-11). The test site layout, including test shafts and exploration plan, is shown in Figure 4-9.

The axial loading test setup, as well as the test shafts configuration and instrumentation, is discussed in Chapter 7.

8.4 Interpretation of Measured Axial Strains

At the same elevation, the concrete embedment strain gauges (ESGs) and resistance strain gauges (RSGs) recorded similar values of axial strain. Therefore, only the axial strains measured using the ESGs, which were installed at more elevations, were used to interpret the axial load transfer. The axial load, Q, at a depth, z, was evaluated using:

$$Q(z) = E_s(z) \cdot A(z) \cdot \varepsilon(z) \tag{8.1}$$

where $E_s(z)$ = composite secant modulus of the shaft, $A(z)$ = cross-sectional area of the shaft, and $\varepsilon(z)$ = recorded axial strain. The cross-sectional area of the shaft at each depth of interest was estimated using the inferred shaft radius back-calculated using the TIP results (Figure 7-6b). The secant modulus of the shaft is a function of strain level; therefore, the secant modulus varies along the length of the shafts during loading and varies according to the applied load and resulting strain even at the same elevation. The relationship between E_s and ε was evaluated for each shaft using the method presented by Fellenius (1989, 2017). First, the tangent modulus, E_t, for different strain levels was estimated using the applied loads and strains at the ground level, where shaft resistance is the smallest, using:

$$E_t(\varepsilon) = \frac{\Delta Q(\varepsilon)}{A \cdot \Delta\varepsilon} \tag{8.2}$$

where $\Delta Q(\varepsilon)$ and $\Delta\varepsilon$ = change of load and strain, respectively, from one load increment to the subsequent increment. The linear relationship between tangent modulus and corresponding strain was obtained using the ordinary least squares (OLS) method, and is expressed by:

$$E_t(\varepsilon) = a \cdot \varepsilon + b \tag{8.3}$$

where a = slope of the tangent modulus line and b = initial tangent modulus. An example of the evaluation of the strain-dependence of tangent modulus using the data from MIR is shown in Figure 8-1. Then, the secant modulus was obtained by (Fellenius 2017):

$$E_s = 0.5a \cdot \varepsilon + b \tag{8.4}$$

The axial load, Q, at the depth z, was then be computed as a function of strain:

$$Q(z) = \left[0.5a \cdot \varepsilon(z) + b\right] \cdot A(z) \cdot \varepsilon(z) \tag{8.5}$$

The small slope shown in Figure 8-1 is representative of large diameter, axially stiff shafts; smaller, more slender elements, such as augercast piles, exhibit significantly greater variation in tangent modulus with strain level (Stuedlein et al., 2012).

8.5 Load and Displacement Observed at Shaft Head

The measured load-displacement response at the top of the shaft is shown in Figure 8-2 for each test shaft. The axial resistance of the cased test shafts CIR and CNIR was fully mobilized (i.e., achieved an ultimate resistance) since plunging was observed at final displacements of 84 and 74 mm (3.3 and 2.9 in) at maximum applied load of approximately 1,960 kN (440 kips) and 1,330 kN (300 kips), respectively, prior to termination of the tests. The subtle change in auger diameter between CIR and CNIR (915 vs. 940 mm, respectively) resulted in about 47% greater axial resistance for CIR. Shafts MIR and HSIR could not be loaded to an ultimate axial resistance, as the available hydraulic pressure capacity of the hydraulic pump limited the application of higher loads (specifically, the pressure was limited to 65 MPa or 9,500 psi for safety purposes).

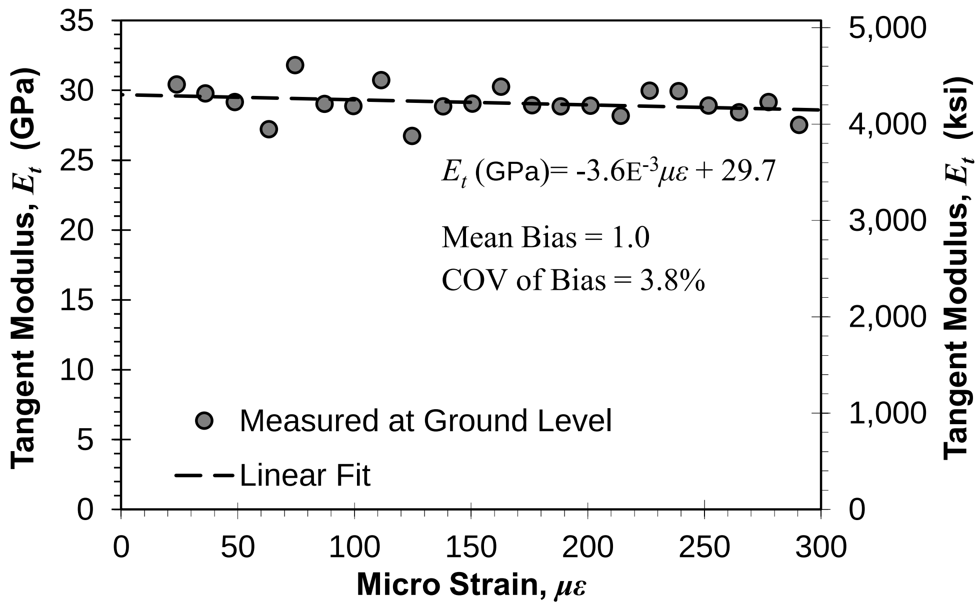

Figure 8-1. Example of evaluation of the strain-dependence of tangent modulus for MIR.

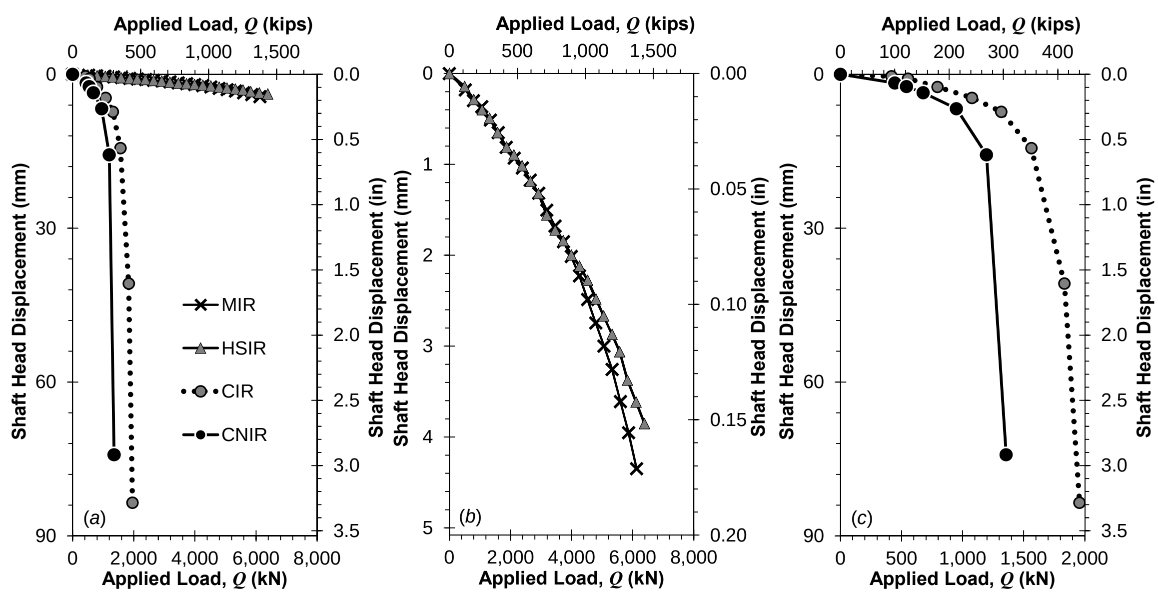

Figure 8-2. Relationship between the measured load and displacement for (a) each of the test shaft, (b) uncased shafts, and (c) cased shafts.

The load-displacement response at the top of the uncased shafts was nearly identical to one another, as shown in Figure 8-2. The maximum load applied to MIR and HSIR was 6,125 kN (1,377 kip) and 6,380 kN (1,435 kip), respectively, with corresponding displacements of 4.3 mm (0.17 in) and 3.8 mm (0.15 in), or about one order of magnitude smaller than for the cased test shafts. For example, although the axial resistance of MIR was not fully mobilized by the end of the test, MIR still exhibited about 210% greater resistance compared to the fully-mobilized axial resistance of CIR. The resulting improvement in axial load transfer is due to the rougher soil-concrete interface and larger as-built diameter of the uncased test shafts, and to the presence of gaps between the soil and casing for the cased shafts. In a production setting, the TIP data could have been used to establish a basis for remedial grouting at the soil-shaft interface to ensure intimate contact between the soil and the casing to improve its load transfer characteristics.

8.6 Axial Load Transfer

Load transfer distributions for the test shafts at selected load increments and for the cased test shafts for all of the load increments are shown in Figure 8-3. Each of the test shafts exhibited bending during axial loading, which may have resulted from the following: (1) differences in shaft geometry and resistance with azimuthal direction and depth, (2) differences in the axial load applied by the two jacks (arising from differences in surface topography of the shaft head and energy losses in the hydraulic lines), (3) imperfect alignment of the reaction frame, and/or (4) differential mobilization of uplift load transfer among the four reaction piles (observed from optical survey). In view of the observed bending, the load transfer data were interpreted following fitting of the observed load transfer to the continuous function:

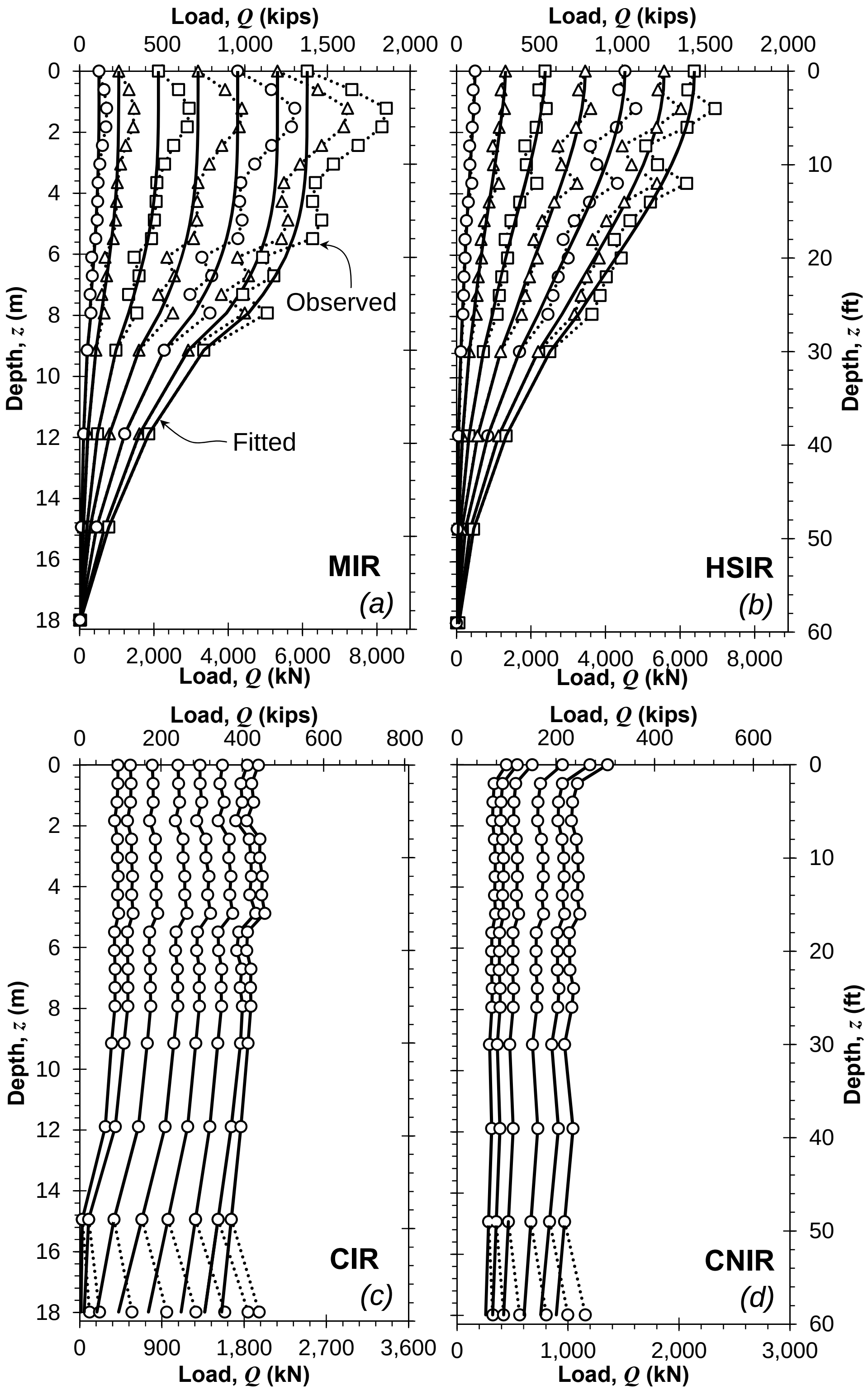

Figure 8-3: Measured and fitted load transfer distributions of shafts (a) MIR and (b) HSIR (c) CIR, and (d) CNIR.

$$Q = \frac{a_1}{\cosh\left[(z/a_2)^n\right]} + a_3 \tag{8.6}$$

where a_1, a_2, a_3 and n = fitting parameters, determined using OLS regression. The constraint applied in curve fitting was that load at the shaft head equaled the load measured using the load cells. In addition, the measured data from the depths of 0.6 to 3.0 m (2 to 10 ft) for MIR were omitted in the curve fitting due to the significant influence of bending at this section along the shaft. Since the bending effects were negligibly small at deeper portions of the test shafts, the measured loads at the depths below 9.1 m (30 ft) were used for all further analyses of load transfer. The measured and fitted load distribution for the two uncased test shafts, MIR and HSIR, is shown in Figure 8-3(a and b), respectively. The soil provided relatively small shaft resistance near the ground surface to depths of 3.0 m (10 ft) and 1.2 m (4 ft) for MIR and HSIR, respectively. Low shaft resistance in near-surface soils is typical in plastic soils owing to the seasonal moisture changes that occur and result in shrinkage (contraction) of soil away from the shaft (Brown et al. 2010). For MIR, the relatively small shaft resistance observed from the ground surface to the depth of 3.0 m (10 ft) may have also resulted from bending effects in addition to seasonal moisture changes. The toe resistances of the uncased test shafts were not mobilized significantly during the loading tests.

For the two cased test shafts, the loads observed at a depth of 18.0 m (59 ft) were not consistent with the loads recorded above this location, perhaps due to misalignment of the gauges during installation and construction. The tip resistance determined using SCPT2 (Figure 4-9) was very similar from a depth of about 11.9 to 18.0 m (39 to 59 ft); therefore, it was assumed that the mobilized unit shaft resistance at depths from 11.9 to 14.9 m (39 to 49 ft) for each load increment was the same as that at depths from 14.9 to 18.0 m (49 to 59 ft). However, it was reasonably assumed that the first two load increments applied to CIR produced unit resistances at the bottom of the shaft that were approximately half of those observed for the tributary area immediately above the base of the shaft. Furthermore, it appears that the shaft resistance was very small from the ground surface to the depth of about 7.9 m (26 ft) and/or mobilized with very little relative displacement, which may be attributed, in part, to the gaps that formed between the casing and the soil.

8.6.1 Unit Shaft Resistance-Relative Displacement Relationships (t-z curves)

To generalize the results of the two loading tests of the uncased shafts specifically for similar soils in the Willamette Valley, and to evaluate various design models, unit shaft resistance-relative displacement relationships were developed. The unit shaft resistance, t, was computed by considering the representative tributary area for each portion of the instrumented shaft using the following approach:

$$t = \frac{\Delta Q}{\pi D \cdot \Delta L} \tag{8.7}$$

where ΔQ =the change of axial load along the tributary area, D = the average as-built diameter along the tributary area, and ΔL = the height of tributary area. The relative displacement was calculated by subtracting compression of the shaft at the depth of interest due to axial loading from the displacement induced in the shaft at the depth of the section above. The axial compression of the shaft, δ, was estimated by:

$$\delta = \frac{Q \cdot \Delta L}{A \cdot E_s} \tag{8.8}$$

where Q = the average axial load along the tributary area and A = the average area of the cross-section along the tributary area. The relationship between unit shaft resistance and relative displacement, known as a *t-z* curve, was thus constructed to represent the mobilization of shaft resistance along a unit tributary area of a deep foundation element. Since the axial load transfer data for MIR from depths of 0.6 to 3.0 m (2 to 10 ft) were omitted in the curve fitting, the unit shaft resistance was calculated considering this portion of the shaft as one tributary area. For comparison purposes, one *t-z* curve from depths of 0.6 to 3.0 m (2 to 10 ft) was also calculated for HSIR. The *t-z* responses for the cased test shafts were evaluated at those elevations from where a gap between the casing and soil was not suspected (i.e., from depths of 7.9 to 18.0 m).

The *t-z* curves for the various tributary depths are shown in Figure 8-4 for each test shaft. It appears that the maximum unit shaft resistance of the uncased test shafts ranged from 6 to 300 kPa (120 to 6,200 psf), whereas the maximum unit shaft resistance for the cased test shafts ranged from 8 to 35 kPa (175 to 700 psf). Shaft CIR exhibited greater unit shaft resistances than CNIR below a depth of about 12 m (39 ft), a result stemming from the use of the smaller auger. As relative displacement increased, the interface of CIR softened to reduce to a residual resistance that corresponded to the ultimate resistances observed for CNIR, equal to 12 to 17 kPa (240 to 360 psf).

The back-calculated *t-z* curves for MIR and HSIR are compared in Figure 8-5 through Figure 8-7 to those obtained by fitting to a hyperbolic model using OLS and those computed from a model proposed below. Relatively large differences in the *t-z* responses of MIR and HSIR were observed from the ground surface to a depth of about 6.7 m (22 ft); however, below a depth of 6.7 m (22 ft), similar *t-z* responses were observed. The difference in the upper portion (to a depth of about 4.3 m) may be attributed to bending effects, differences in the as-built shaft geometry, and different water contents in the soil near the ground surface. Based on data from a weather station at the test site, a rain event with an accumulated rainfall of 21 mm (0.84 in) was observed seven days prior to testing HSIR. During testing of HSIR, the groundwater table was located at a depth of 1.8 m (5.9 ft). However, a four-day rain event ended two days prior to testing MIR, which produced an accumulated rainfall of 37 mm (1.47 in) and resulted in the groundwater rising to a depth of 1.6 m (5.2 ft). Thus, changes in water content and effective stresses in the near-surface vadose zone were likely between the time that MIR and HSIR were tested.

For the uncased test shafts, the distribution of the measured peak and extrapolated ultimate unit shaft resistance, $r_{s,m}$ and $r_{s,ult}$, respectively, are shown in Figure 8-8. The hyperbolic model (Kondner 1963) was used to simulate the *t-z* curves for each tributary area of the uncased shafts since they did not exhibit plunging. The model was then used to estimate the ultimate unit shaft resistance, which was assumed equal to the asymptotic, extrapolated resistance. On average, $r_{s,ult}$ determined from extrapolation was 21% larger than $r_{s,m}$. Note: these figures also present the results of a proposed model, described in detail in the sections that follow.

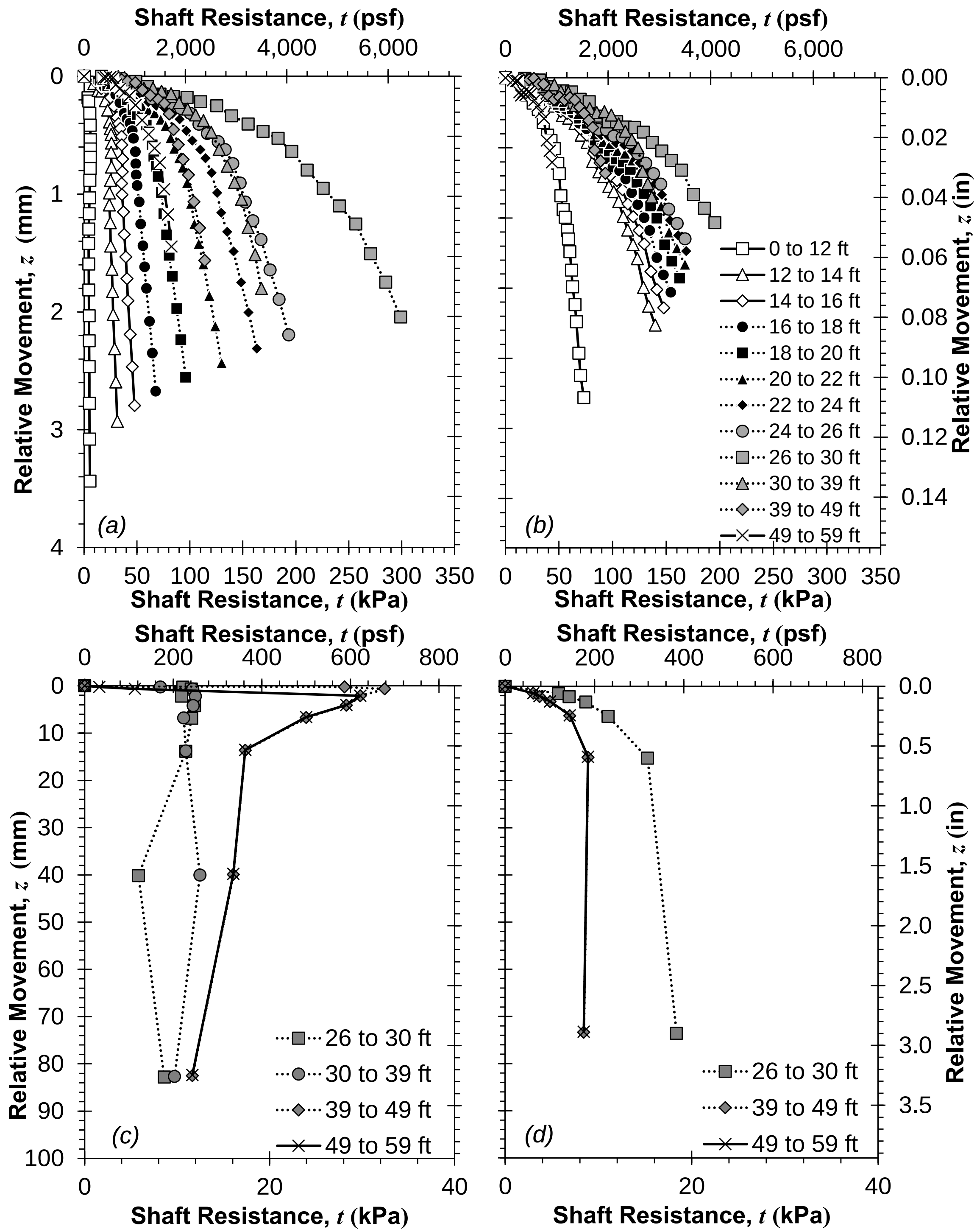

Figure 8-4: Measured *t-z* responses for (a) MIR, (b) HSIR, (c) CIR, and (d) CNIR at different depths.

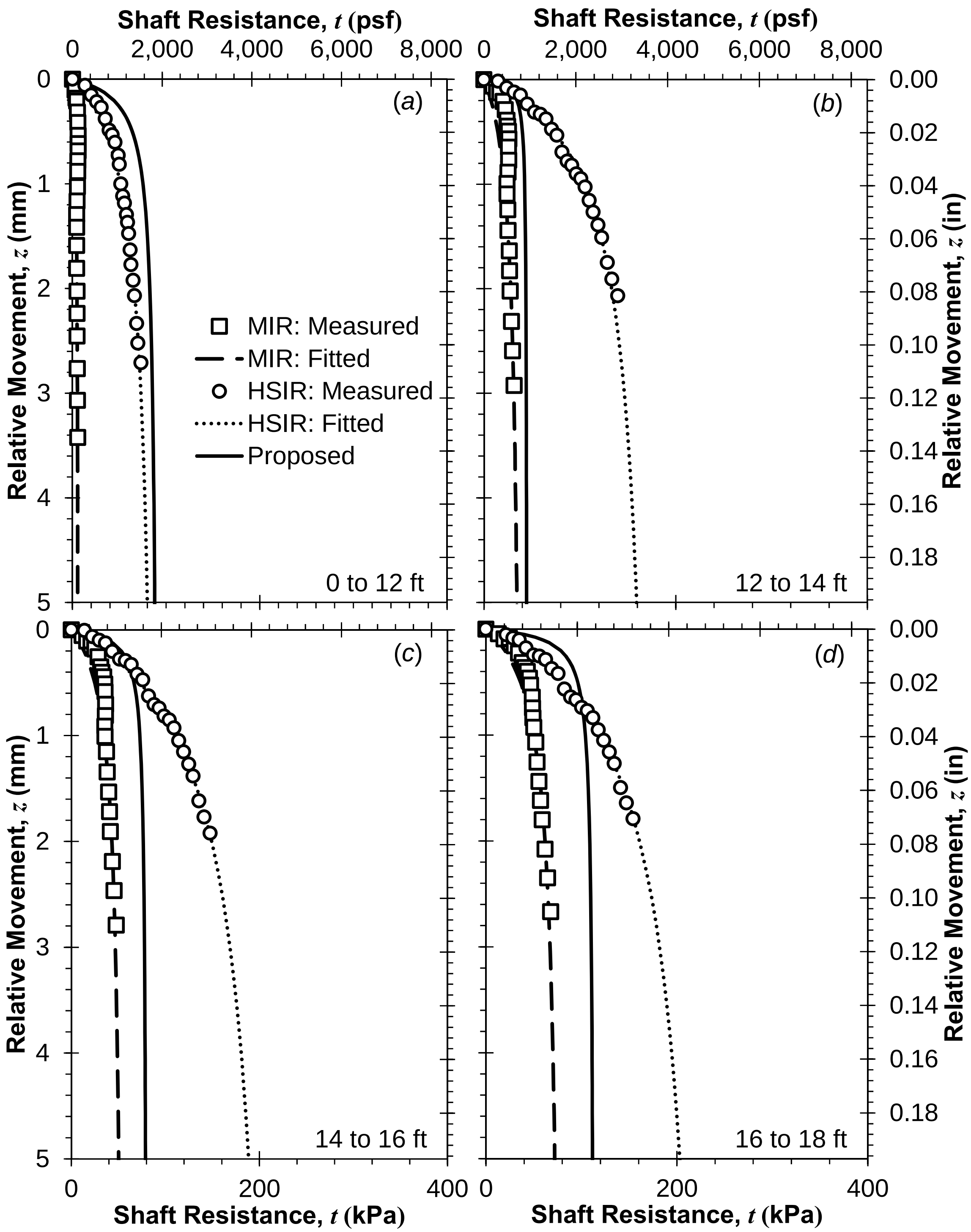

Figure 8-5: Measured, fitted, and proposed *t-z* responses at each tributary area for the two uncased test shafts for load increments from 0 to 5.5 m (0 to 18 ft).

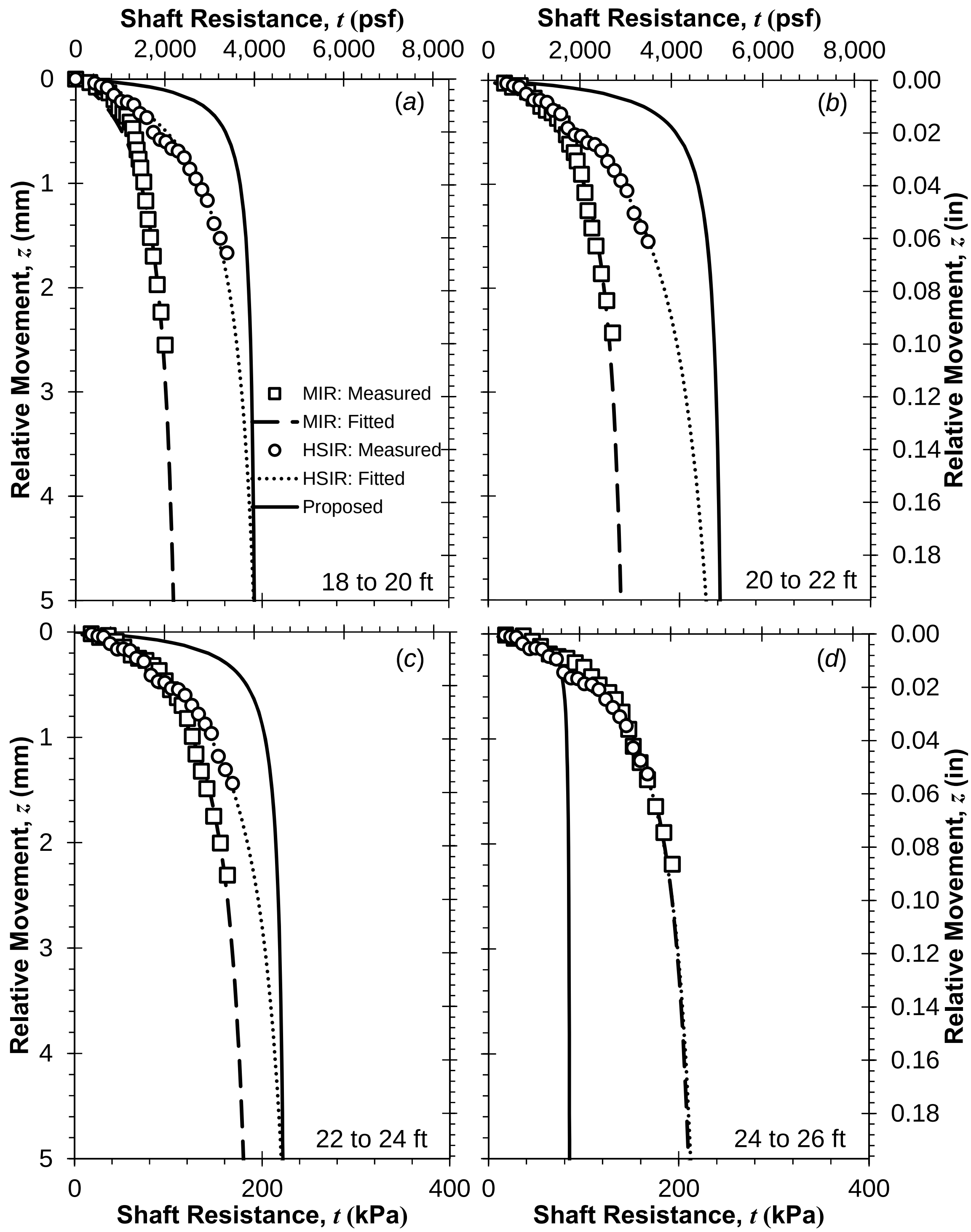

Figure 8-6: Measured, fitted, and proposed *t-z* responses at each tributary area for the two uncased test shafts for load increments from 5.5 to 7.9 m (18 to 26 ft).

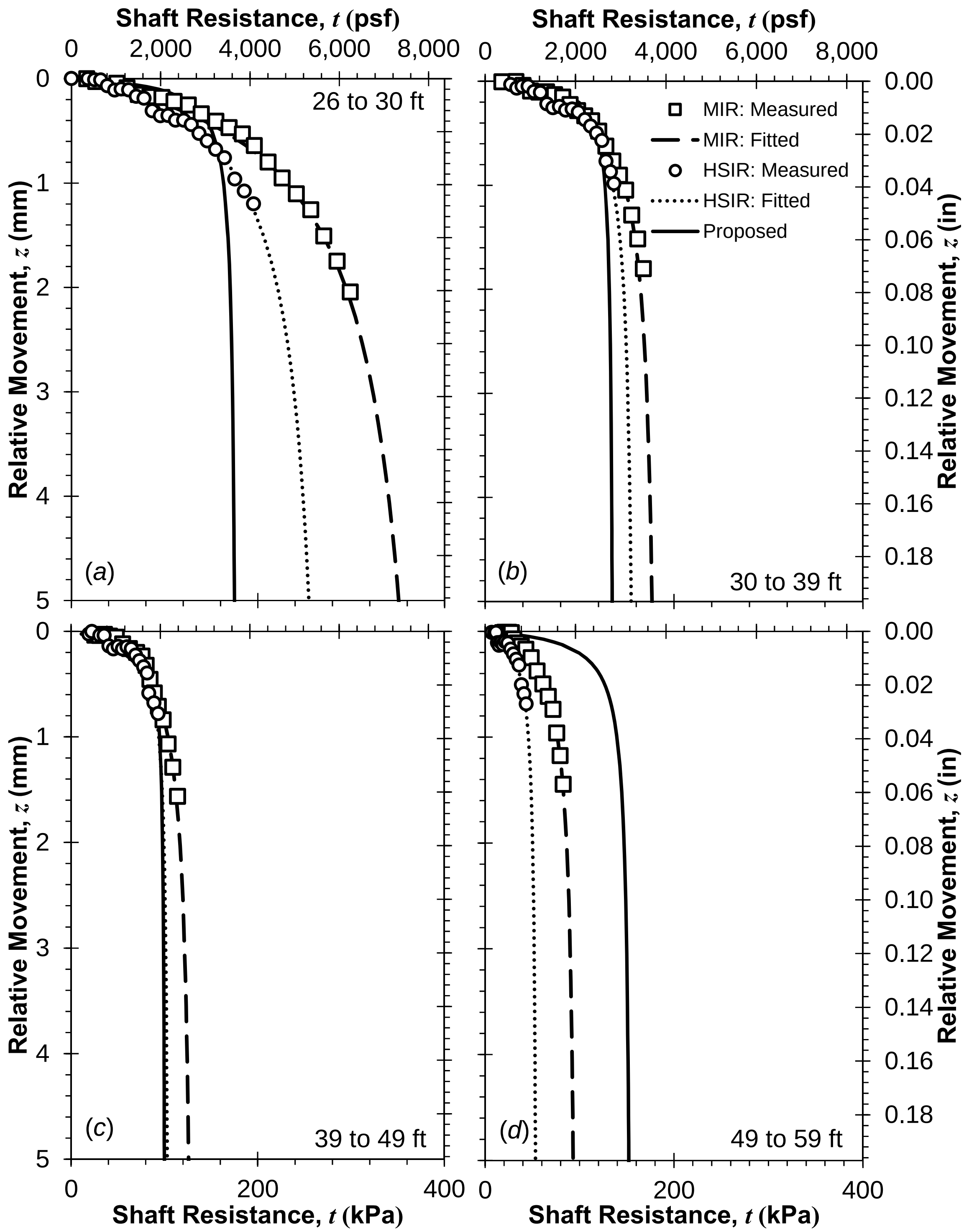

Figure 8-7: Measured, fitted, and proposed *t-z* responses at each tributary area for the two uncased test shafts for load increments from 7.9 to 18.0 m (26 to 59 ft).

8.6.2 Unit Toe Resistance-Toe Displacement Relationships (q-z curves)

The load-displacement curves in Figure 8-3 imply that the toe resistance of the uncased test shafts was not significantly mobilized during the loading tests. However, the cased test shafts did demonstrate an ultimate toe resistance was mobilized during the testing. Therefore, the unit toe resistance and toe displacement relationships (i.e., *q-z* curves) could be evaluated, as shown in Figure 8-9, and used to interpret the ultimate resistance of the uncased shafts. The toe resistance for the cased shafts essentially became fully-mobilized at displacements ranging from 20 to 40 mm (0.8 to 1.5 in), or about 2 to 4% of the shaft diameter. The measured peak unit toe resistance, $r_{t,m}$, for CIR and CNIR was 2,240 and 1,290 kPa (47 and 27 ksf), respectively (note, a model proposed to estimate the toe resistance in similar soils is also shown in Figure 8-9, and is described in detail in subsequent sections.

The hyperbolic model was used to fit the *q-z* curves for CIR and CNIR to extrapolate the ultimate unit toe resistance, $r_{t,ult}$, for each shaft, which was 2,550 and 1,380 kPa (53 and 29 ksf), respectively. The difference between the *q-z* response of CIR and CNIR may be due to the differences in drilling protocols used to construct the two shafts. In general, an auger will bore a hole larger than the tool's outside diameter due to various factors such as flexure of the Kelly bar, misalignment of the drill string upon reentry into the hole, and inclination (causing a deviation in verticality) of the Kelly bar. Therefore, the use of an auger diameter equal to the outside diameter of the casing likely resulted in over-drilling or enlarging the diameter of shaft CNIR sufficiently to allow groundwater to flow between the casing and the borehole downward to the toe of the shaft, possibly resulting in a swelling and softening of the near-toe soils before the concrete cured.

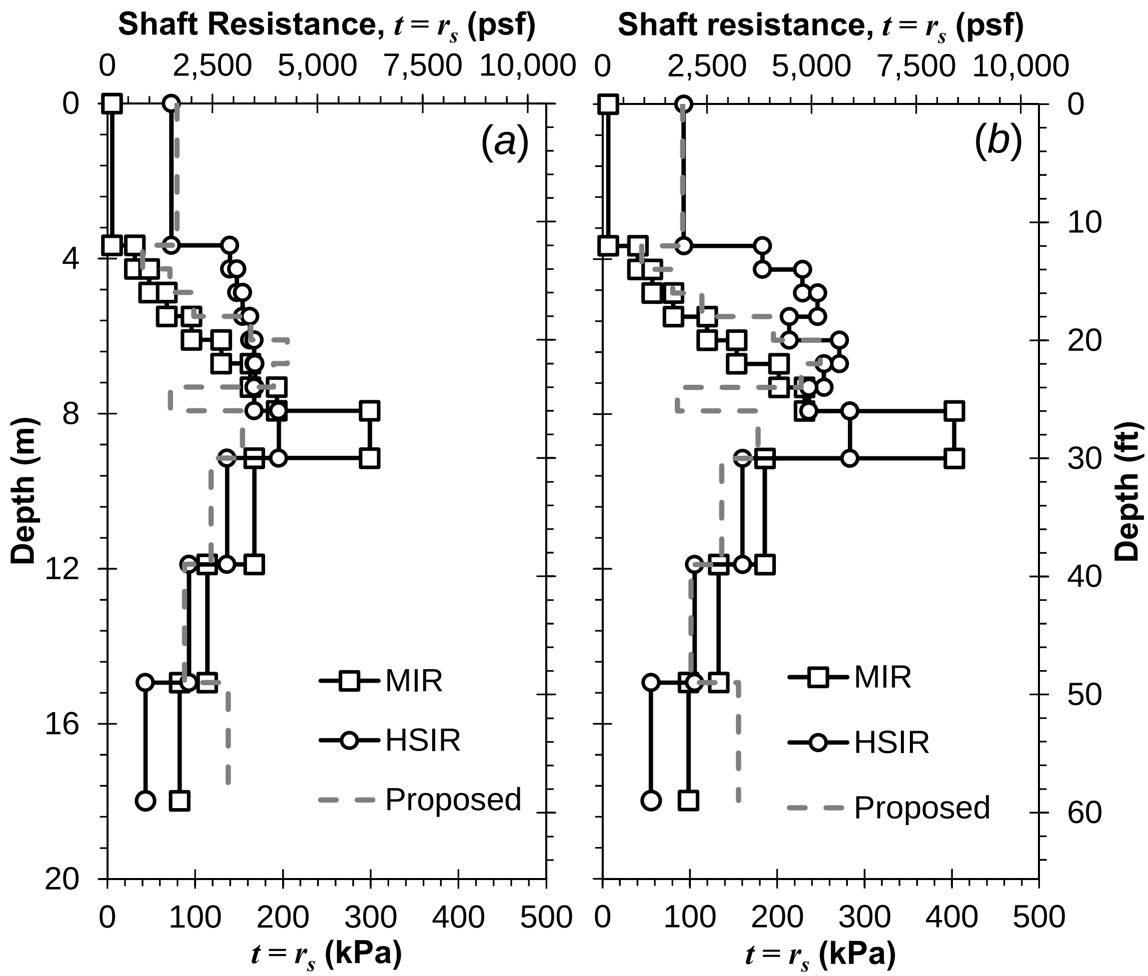

Figure 8-8: Shaft resistance profile of (a) measured peak shaft resistance, $r_{s,pm}$, and corresponding proposed model and (b) extrapolated ultimate shaft resistance, $r_{s,pult}$, and corresponding proposed model.

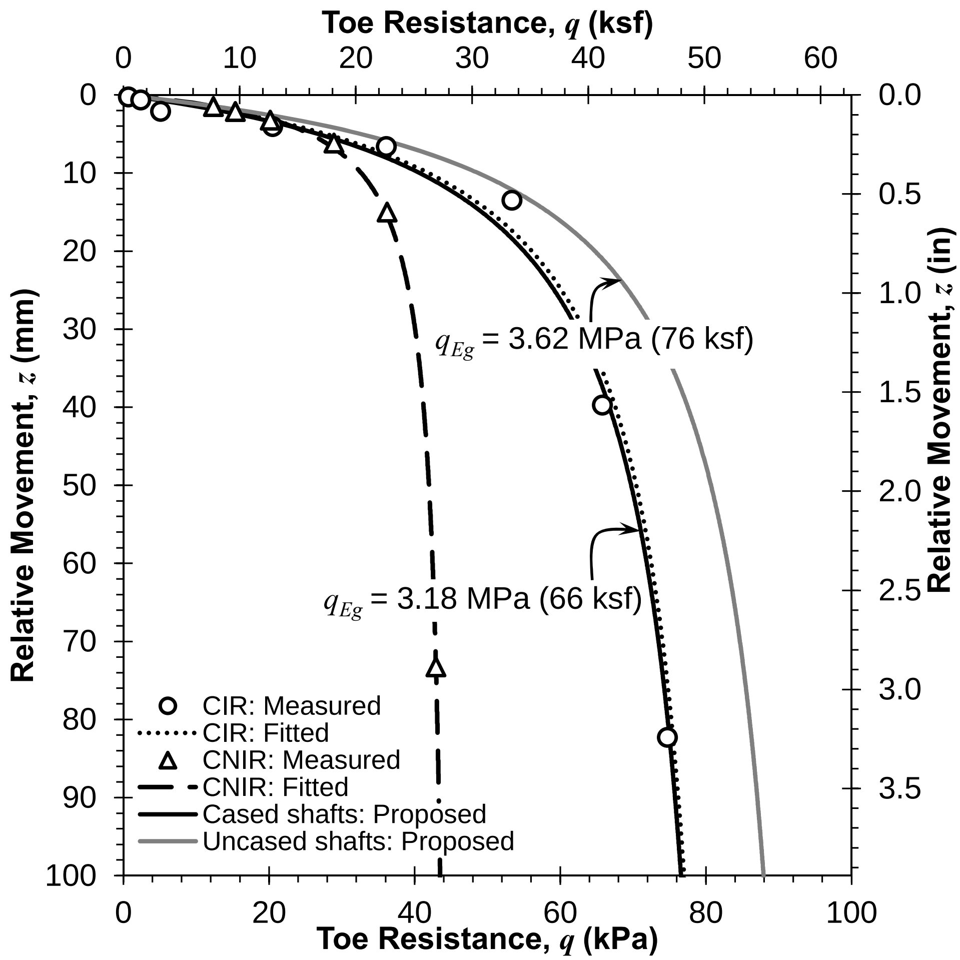

Figure 8-9: The measured, fitted, and proposed *q*-*z* responses for the test shafts.

8.7 Proposed Axial Load Transfer Model

To aid in the design of bridge foundations in the Willamette Valley, region-specific *t*-*z* and *q*-*z* curve models were developed for the uncased drilled shafts for use in similar soils. The hyperbolic model was selected as the appropriate functional form for the proposed load transfer models given its conservative and asymptotic nature. The hyperbolic model was implemented using direct SCPT measurements, specifically q_t, f_s, u_2, and V_s, from the test site. The proposed model was then used to simulate the axial load transfer for the uncased test shafts at large displacements.

8.7.1 Proposed t-z Curve Model

The hyperbolic model has been used to simulate the stress-strain and load transfer response for a variety of engineering applications (e.g., Kondner, 1963; Duncan and Chang, 1970; and Huffman et al., 2015) and has been used extensively for soil-structure interface analyses (e.g., Chin, 1970, 1971; Clemence and Brumund, 1975; Wong and teh 1995; Kim et al., 1999; Cao et al., 2014; Stuedlein and Reddy, 2014; Li et al., 2017; and Li and Stuedlein, 2017). The hyperbolic model proposed by Clough and Duncan (1971) for soil-structure interfaces, adapted herein for constructing the *t-z* curves, is given by:

$$t = \frac{z}{\dfrac{1}{K_{t,si}} + \dfrac{z}{t_{ult}}} \tag{8.9}$$

where $K_{t,si}$ = initial stiffness of a given *t-z* curve and t_{ult}= asymptotic unit shaft resistance of the hyperbola. The asymptotic unit shaft resistance, t_{ult}, can be estimated from CPT measurements, as described below.

8.7.2 Evaluation of the Asymptotic Unit Shaft Resistance

Although the axial resistance of the uncased test shafts was not fully mobilized (Figure 8-2), the measured peak resistance can be considered representative of a lower-bound capacity (Eslami and Fellenius, 1997). Therefore, both the measured peak ($r_{s,m}$) and the extrapolated ultimate values ($r_{s,ult}$) of unit shaft resistance were correlated to the CPT data to construct separate region-specific models. The direct CPT method was initially developed by Eslami and Fellenius (1997) based on 102 axial loading tests of mostly driven pile foundations. Niazi (2014) extended the direct CPT method for all deep foundations using a combined database 153 driven, jacked and bored or augered piles. According to

Eslami and Fellenius (1997), the unit shaft resistance, r_s, can be correlated to the effective cone resistance, $q_E = q_t - u_2$:

$$r_s = C_s \cdot q_E \tag{8.10}$$

where C_s = shaft coefficient that is estimated using the CPT-based soil classification chart proposed by Eslami and Fellenius (1997) or using the soil behavior type (SBT) classification index, I_c (Niazi, 2014):

$$\log\left(C_s\right) = 0.732 I_c - 3.681 \tag{8.11}$$

where the SBT classification index I_c is calculated following the procedure by Robertson (2009).

Using this concept, a region-specific linear relationship between I_c and the log-transformed values of C_s was generated by back-calculating C_s for each tributary area of the uncased test shafts. To provide reasonable lower- and upper-bound estimations of unit shaft resistance, $r_{s,m}$ and $r_{s,ult}$ were used to back-calculate C_s, as shown in Figure 8-10. Since the experimental data from the ground surface to a depth of about 3.7 m (12 ft) was significantly affected by bending, these data were excluded in the development of the models. The shaft coefficient for soils with $2.00 \leq I_c \leq 2.67$ can be expressed as:

$$\log\left(C_{s,m}\right) = 0.98 I_c - 3.88 \qquad \text{for } r_{s,m} \tag{8.12}$$

$$\log\left(C_{s,ult}\right) = 0.95 I_c - 3.69 \qquad \text{for } r_{s,ult} \tag{8.13}$$

where $C_{s,m}$ and $C_{s,ult}$ = shaft coefficient back-calculated using measured peak and extrapolated ultimate values of unit shaft resistance, respectively. Therefore, according to

Eq. (8.10), the lower- and upper-bound unit shaft resistances, $r_{s,pm}$ and $r_{s,pult}$, respectively, proposed for use in similar Willamette Valley soils can be estimated using:

$$r_{s,pm} = C_{s,m} \cdot q_E \tag{8.14}$$

$$r_{s,pult} = C_{s,ult} \cdot q_E \tag{8.15}$$

The profile of the proposed unit shaft resistances, $r_{s,pm}$ and $r_{s,pult}$, is shown in Figure 8-8a and Figure 8-8b, respectively. The mean bias ($r_{s,m}/r_{s,pm}$) for the proposed lower-bound model is 1.28 and the coefficient of variation (COV) of the sample bias is 62%, whereas the mean bias ($r_{s,ult}/r_{s,pult}$) and the COV are 1.33 and 70%, respectively, for the proposed upper-bound model. These performance statistics indicate that the proposed models under-predict the unit shaft resistances, on average, and exhibit a high degree of variability. Both $r_{s,pm}$ and $r_{s,pult}$ can be used as the asymptotic unit shaft resistance t_{ult} in Eq. (8.9) to estimate axial load transfer. However, $r_{s,pult}$ is used subsequently to extrapolate the global axial response of the uncased test shafts at larger displacements.

8.7.3 Evaluation of the Initial t-z Stiffness

The initial stiffness, $K_{t,si}$, of a given *t-z* curve can be estimated using the analytical solution developed by Randolph and Wroth (1978) for axially-loaded deep foundations in linear elastic soil, which is given by:

$$K_{t,si} = \frac{\xi \cdot G_s}{r} \tag{8.16}$$

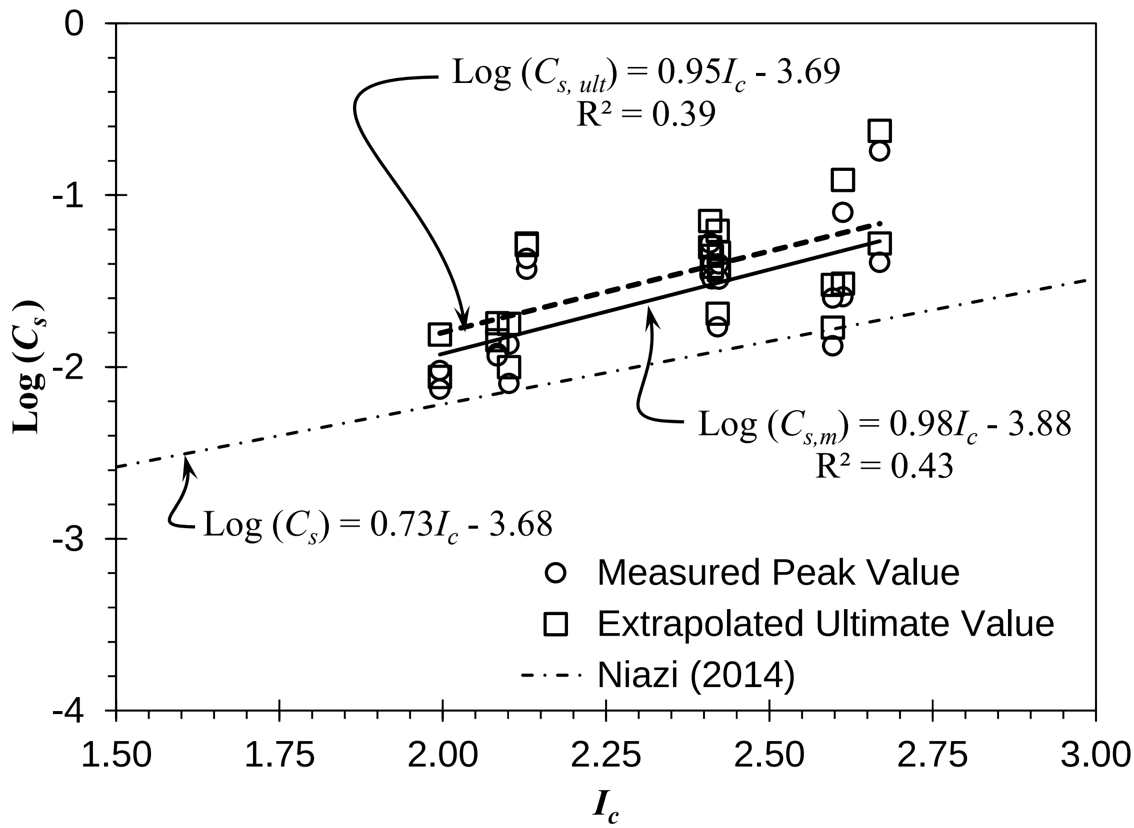

Figure 8-10: Relationship between the SBT classification index I_c and the shaft correlation coefficient $C_{s,m}$ and $C_{s,ult}$ back-calculated using the measured peak and extrapolated ultimate values, respectively.

where G_s = shear modulus of the soil, r = radius of the shaft, and ξ = a function related to the geometry of the deep foundation and to the decay of shear strains away from the shaft interface:

$$\xi = \ln\left(\frac{r_m}{r}\right) \tag{8.17}$$

where r_m = radial distance from the center of the foundation at which shear stresses in the soil become negligible. Although Randolph and Wroth (1978) did not specify the type of shear modulus, G_s, to be used, the maximum shear modulus, G_{max}, is recommended for use herein. Given the general availability of these measurements at bridge sites in the seismically-active Oregon region, G_{max} can be evaluated using shear wave velocity measurements, V_s, and soil density, ρ:

$$G_{\max} = \rho \cdot V_s^2 \tag{8.18}$$

The radial distance, r_m, can be estimated by (Randolph and Wroth, 1978):

$$r_m = 2.5L \cdot \eta \cdot (1 - \nu_{avg}) \tag{8.19}$$

where ν = Poisson's ratio of the soil around the deep foundation, L = length of the deep foundation, and η = inhomogeneity factor:

$$\eta = \frac{G_{\max}(0.5\mathrm{L})}{G_{\max}(L)} \tag{8.20}$$

where $G_{max}(0.5L)$ and $G_{max}(L)$ = maximum shear modulus of the soil at the foundation mid-depth and at the base, respectively. For layered soils, the radial distance $r_m(i)$ at soil layer i can be estimated by (Lee, 1991; and Zhang et al., 2010):

$$r_m(i) = 2.5L \cdot \eta(i) \cdot \left[1 - \nu(i)\right] \tag{8.21}$$

where $\nu(i)$ = Poisson's ratio of the soil around the foundation and $\eta(i)$ = inhomogeneity factor at soil layer i. It was assumed that the $\nu(i)$ was equal to 0.2 for predominantly sandy soils with drained conditions and to 0.5 for predominantly clayey soils with undrained conditions, as suggested by Niazi (2014). The inhomogeneity factor, $\eta(i)$, can be estimated by (Lee, 1991; and Zhang et al. 2010):

$$\eta_i = \frac{G_{\max}(i) \cdot L(i)}{G_{\max}(\max) \cdot L} \tag{8.22}$$

where $G_{max}(max)$ = the largest maximum shear modulus among the soil layers along the length of the deep foundation, $G_{max}(i)$ = maximum shear modulus of soil layer i, and $L(i)$ = length of the deep foundation in layer i.

Table 8-1 summarizes the soil parameters used to model the uncased test shafts as developed from SCPT-3, as well as the hyperbolic parameters $t_{ult} = r_{s,pult}$ and $K_{t,si}$ for each tributary area. Figure 8-5 through Figure 8-7 compare the measured *t-z* curves to those predicted using the proposed CPT-and shear wave velocity-based hyperbolic model. Discrepancies between the proposed and measured *t-z* curves are due to the differences observed between the proposed unit shaft resistance model and the extrapolated ultimate shaft resistance (Figure 8-8b) and due to the discrepancy between the actual and estimated initial stiffness.

8.7.4 Proposed q-z Curve Model

Based on the observed *q-z* response of the cased shafts, a hyperbolic *q-z* curve was used to model the response of the toe resistance. To estimate the response of the uncased shafts at large displacements, the observed toe response of shaft CIR was the most appropriate and representative of actual conditions. The hyperbolic *q-z* curve can be expressed as:

$$q = \frac{z}{\dfrac{1}{K_{q,si}} + \dfrac{z}{q_{ult}}} \tag{8.23}$$

where $K_{q,si}$ = initial stiffness of the q-z curve, and q_{ult} = asymptotic unit toe resistance that can be computed directly from CPT measurements.

Table 8-1: Soil properties and *t-z* model parameters for the uncased test shafts based on SCPT-3.

Depth, m (ft)	I_c	q_E kPa (ksf)	$t_{ult} = r_{s,pult}$ kPa (psf)	ρ kg/m^3 (lb/ft^3)	V_s m/s (ft/s)	G_{max} MPa (ksf)	$K_{t,si}$ kPa/mm (ksf/in)
0 to 3.7 (0 to 12)	2.40	4839 (101)	92 (1915)	1987 (124)	180 (591)	65 (1349)	421 (223)
3.7 to 4.3 (12 to 14)	2.67	772 (16)	45 (941)	1722 (108)	260 (852)	116 (2427)	737 (391)
4.3 to 4.9 (14 to 16)	2.61	1863 (39)	81 (1683)	1893 (118)	260 (852)	128 (2669)	778 (413)
4.9 to 5.5 (16 to 18)	2.42	3964 (83)	114 (2374)	1991 (124)	325 (1065)	210 (4383)	1243 (659)
2.5 to 6.1 (18 to 20)	2.10	11984 (250)	196 (4088)	2175 (136)	341 (1119)	253 (5284)	1764 (936)
6.1 to 6.7 (20 to 22)	2.00	17535 (366)	249 (5203)	2184 (136)	341 (1119)	254 (5306)	1835 (973)
6.7 to 7.3 (22 to 24)	2.08	14079 (294)	227 (4751)	2169 (135)	345 (1130)	257 (5376)	1888 (1002)
7.3 to 7.9 (24 to 26)	2.13	4521 (94)	86 (1795)	2093 (131)	348 (1140)	253 (5286)	1877 (996)
7.9 to 9.1 (26 to 30)	2.41	5684 (119)	178 (3718)	2145 (134)	348 (1140)	259 (5417)	1941 (1030)
9.1 to 11.9 (30 to 39)	2.41	4190 (88)	137 (2852)	2097 (131)	333 (1091)	232 (4850)	1789 (949)
11.9 to 14.9 (39 to 49)	2.42	2867 (60)	101 (2117)	2034 (127)	302 (989)	185 (3861)	1476 (783)
14.9 to 18.0 (49 to 59)	2.60	3278 (68)	156 (3250)	2044 (128)	302 (989)	186 (3879)	1350 (716)

8.7.5 Evaluation of the Ultimate Unit Toe Resistance

Eslami and Fellenius (1997) suggested that the unit toe resistance, r_t, could be estimated by:

$$r_t = C_t \cdot q_{Eg} \tag{8.24}$$

where C_t = toe correlation coefficient and q_{Eg} = geometric average of the effective cone tip resistance over the influence zone around the toe. Eslami and Fellenius (1997) defined the influence zone as from a depth of 4*D* (where *D* = diameter of the deep foundation) below the toe of the deep foundation up to a depth of 8*D* above the toe when the foundation is installed through a weak soil into a dense soil and up to a depth of 2*D* above the toe when the foundation is installed through a dense soil into a weak soil. Fellenius (2017) suggested that the toe correlation coefficient C_t is equal to unity for foundation diameters smaller than 0.4 m (16 in) and equal to 1/(3*D*) for diameters equal to or greater than 0.4 m, where *D* is in meters (or 12/*D* when *D* is measured in inches). Niazi (2014) proposed a linear relationship between the geometric average of the SBT classification index, I_{cg}, in the influence zone and log-transformed values of C_t, when $1.69 \leq I_{cg} \leq 3.77$, as given by:

$$\log\left(C_t\right) = 0.325 I_{cg} - 1.218 \tag{8.25}$$

Eq. (8.25) does not account for the larger displacements required to mobilize larger diameter piles and shafts, which may need to be adjusted for scale effects at the toe.

Since these shafts were not intended to bear on any particular soil layer, the cone tip resistance of the closest CPT (SCPT-2 in Figure 4-11) was used to back-calculate C_t, where the zone of influence was defined as the distance of 4*D* above and below the shaft tip. The corresponding back-calculated lower- and upper-bound toe coefficients for CIR are $C_{t,m}$ = 0.70 and $C_{t,ult}$ = 0.80 for the measured peak, $r_{t,m}$, and extrapolated ultimate, $r_{t,ult}$, toe resistance, respectively, with I_{cg} = 2.66 and q_{Eg} = 3,180 kPa (66 ksf). These toe correlation coefficients may be used to construct the lower- and upper-bound estimates of unit toe resistance using Eq. (8.24) and CPT measurements, as well as the *q-z* curve given by Eq. (8.23). Given the similarity between I_{cg} for the various CPTs at the toe elevation of the test shafts, $C_{t,ult}$ was approximately equal to 0.80, which was used to evaluate the axial load response for the uncased test shafts at large displacements.

8.7.6 Evaluation of the Initial Stiffness

The initial stiffness of a *q-z* curve, $K_{q,si}$, can be estimated assuming that the toe of a deep foundation acts as a rigid punch being forced into an elastic half-space (Randolph and Wroth, 1978; and Guo, 2000), resulting in:

$$K_{q,si} = \frac{4G_{sg}}{\pi r \cdot (1 - \nu_{sg}) \cdot \omega} \tag{8.26}$$

where G_{sg} and ν_{sg} = geometric average of the shear modulus and Poisson's ratio of the soil over the influence zone around the toe, respectively, and ω = base load transfer factor. The use of the maximum shear modulus, G_{maxg}, is recommended in Eq. (8.26), where G_{sg} = G_{maxg}. Guo and Randolph (1998) suggested that ω = 1.0; however, the back-calculated ω was approximately equal to 4.0 (from CIR), which can be attributed to the possible softening effects caused by drilling to compensate the use of G_{maxg}, which was measured without disturbance caused by construction. The *q-z* curves computed using Eq. (8.26) are shown in Figure 8-9. The CPT measurements and model parameters q_{ult} and $K_{q,si}$ are provided in Table 8-2.

Table 8-2: Soil properties and *q-z* model parameters the test shafts.

Test Shafts	I_{cg}	q_{Eg}, kPa (ksf)	$q_{ult} = r_{t,pult}$, kPa (psf)	ρ_g, kg/m^3 (lb/ft^3)	V_{sg}, m/s (ft/s)	G_{maxg}, MPa (ksf)	$K_{q,si}$ kPa/mm (ksf/in)
Cased Shafts	2.66	3,180 (66)	2,550 (53)	2,040 (128)	290 (953)	170 (3607)	230 (124)
Uncased Shafts	2.66	3,620 (76)	2,900 (61)	2,060 (128)	330 (1068)	220 (4558)	295 (156)

Note: ρ_g, V_{sg} = geometric average soil density and shear velocity, respectively, in the influence zone.

8.8 Prediction of Axial Load Response of the Uncased test Shafts

Using the commercially available software package TZPile (Reese et al. 2014) and the as-built diameter computed from TIP measurements (see Section 7.4), the fitted and proposed *t-z* curves were used to simulate and compare the axial response of shafts MIR and HSIR at large displacements. The proposed *t-z* curves were developed based on the extrapolated ultimate shaft resistance (Figure 8-8b). Since no *q-z* curves were developed directly from the uncased shafts, the proposed *q-z* curves (Figure 8-9) were used to model the toe resistance.

To evaluate the performance of the proposed axial load transfer models, the proposed *t-z* and *q-z* curves were used to calculate the axial response of MIR and HSIR, shown in Figure 8-11 and Figure 8-12. The simulated global axial load-displacement responses for

HSIR and MIR at the shaft head are shown in Figure 8-11. Excellent agreement between the test data and the responses extrapolated using the fitted *t-z* curves is observed in Figure 8-11. The axial resistance for the uncased test shafts at a displacement of 25 mm (1.0 in) would be approximately equal to 7,650 and 8,810 kN (1,720 and 1,980 kips) for MIR and HSIR, respectively, when using *t-z* curves fitted to the observed load transfer characteristics (i.e., “extrapolated”). The load transfer distribution at select head displacements are shown in Figure 8-12, where good agreement with the test data can be observed.

The differences in the axial response between HSIR and MIR in Figure 8-11 and Figure 8-12 are largely due to the variation in the shaft diameter and the resulting composite secant modulus. The deviation between the axial load profiles determined using the proposed model and the profiles determined using the measurements could be attributed to the over- and under-estimation of the *t-z* response for the tributary areas. The proposed *t-z* and *q-z* models sufficiently approximate the test data, with apparent offsetting of error at various depths (see Figure 8-5 through Figure 8-7). At a displacement of 25 mm (1.0 in) and using the proposed model, the predicted axial resistances for the uncased shafts are equal to approximately 8,830 and 8,670 kN (1,985 and 1,950 kips) for MIR and HSIR, respectively.

8.9 Evaluation of FHWA Method (O’Neill and Reese 1999)

The load-displacement response at the head of the drilled shaft can also be estimated using normalized load transfer relations presented by O’Neill and Reese (1999), which is referred as FHWA method herein. Figure 8-13 shows the normalized shaft and toe load transfer for drilled shafts in plastic and granular soils

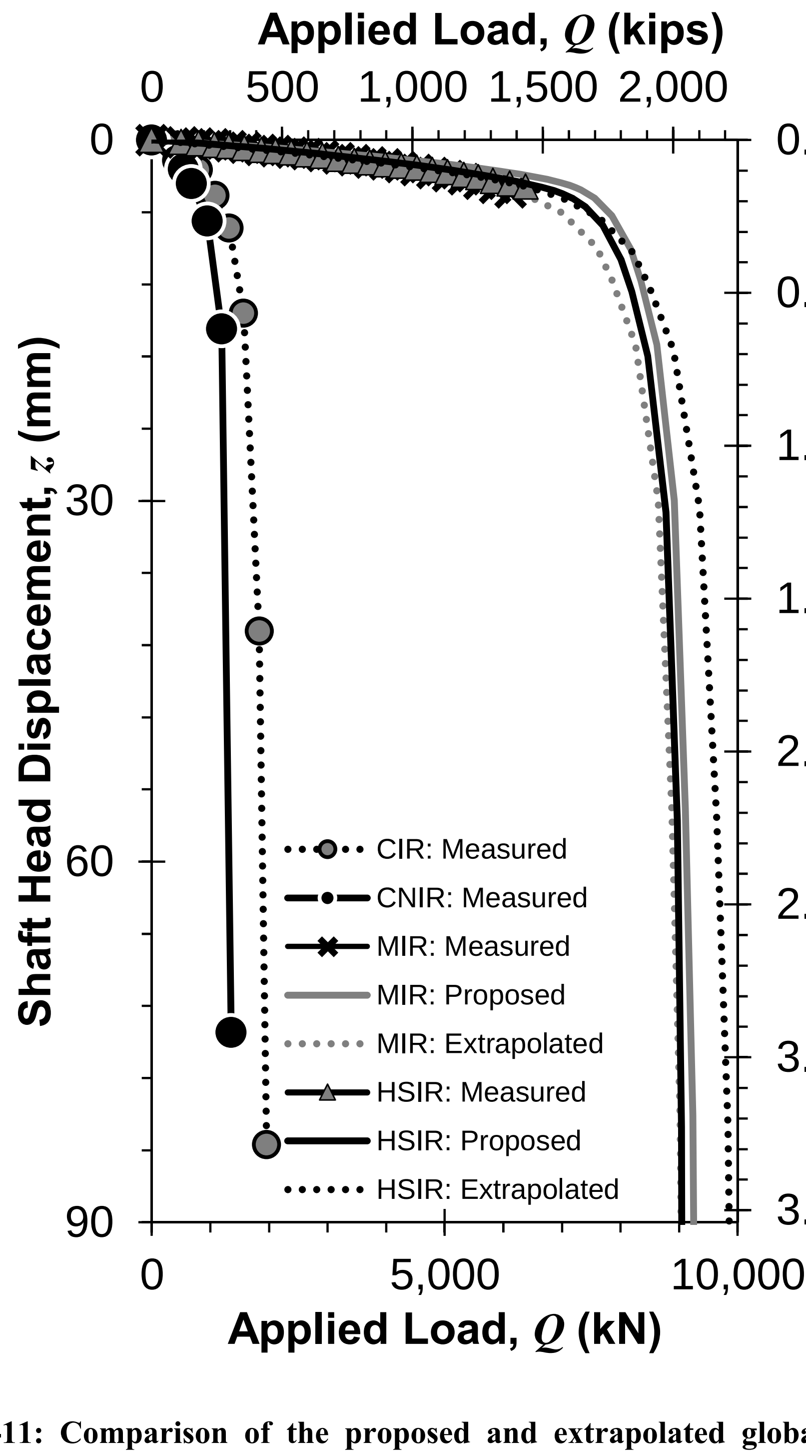

Figure 8-11: Comparison of the proposed and extrapolated global axial load-displacement relationship using proposed and fitted *t-z* curves, respectively, and the measured responses of all test shafts. Note, the proposed *q-z* curves were used in both proposed and extrapolated responses.

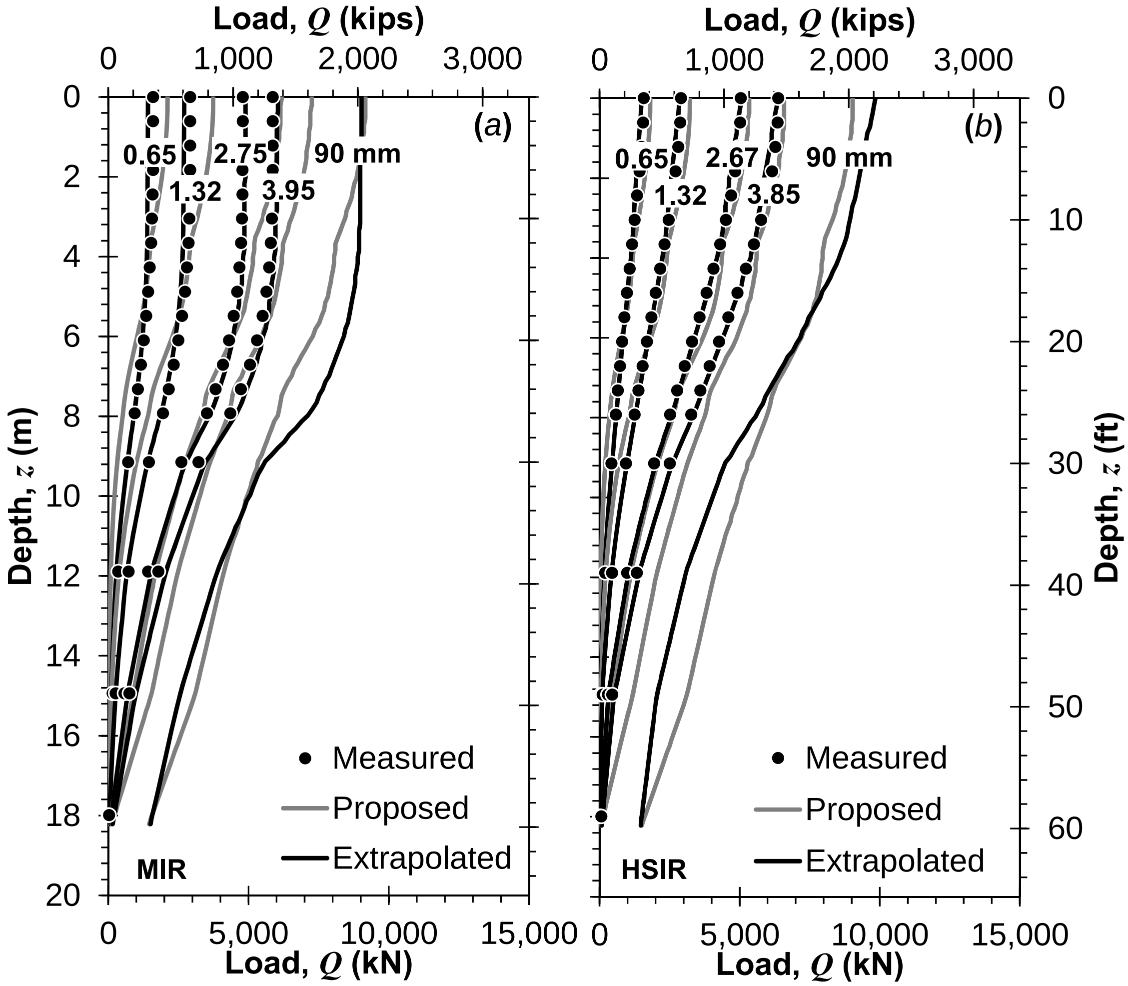

Figure 8-12: Comparison of the proposed and extrapolated axial load profile using proposed and fitted *t-z* curves, respectively, with the measured data of (a) MIR and (b) HSIR. Note, the proposed *q-z* curves were used in both proposed and extrapolated responses.

Table 8-3 and Table 8-4 summarize the soil and drilled shaft properties for the uncased and cased test shafts, respectively. The average shaft diameter of uncased shafts for each soil layer was estimated based on Figure 7-6. The effective unit weight, γ', of each soil layer was obtained based on the laboratory results described by Dickenson and Haines. (2006) and Nimityongskul (2010). The undrained shear strength, s_u, for the plastic soil layers was correlated to CPT cone-tip resistance, q_c, (Figure 4-11) using (e.g., Kulhawy and Mayne 1990):

$$s_u = \frac{q_c - \sigma_{vo}}{N_k} \tag{8.27}$$

where σ_{vo} = total overburden stress and N_k = cone factor. The N_k, which varies from 15 when the groundwater table is at its highest (e.g., 0.6 m or 2 ft) in the spring and about 23 when the groundwater table is at its lowest (e.g., 2.5 m or 8 ft), generally in the fall, based on s_u back-calculated from footing loading and consolidated undrained triaxial tests (Martin 2018). The friction angle, ϕ', of the granular soil layers was estimated using correlations to CPT cone-tip resistance (Kulhawy and Mayne 1990). Explorations SCPT-2, SCPT-3, CPT-4, and SCPT-5 were used to estimate the necessary soil parameters.

The shaft resistance was estimated using α and β method for plastic, fine-grained and granular soil, respectively. The unit shaft resistance, r_s, in plastic soil can be estimated by (O'Neill and Reese 1999; and Brown et al. 2010):

$$r_s = \alpha \cdot s_u \tag{8.28}$$

where α = adhesion factor, which is a function of the average s_u for the stratum of interest:

$$\alpha = 0.55 \qquad \text{for} \qquad \frac{s_u}{P_a} \leq 1.5 \tag{8.29a}$$

$$\alpha = 0.55 - 0.1\left(\frac{s_u}{P_a} - 1.5\right) \qquad \text{for} \qquad 1.5 \leq \frac{s_u}{P_a} \leq 2.5 \tag{8.29b}$$

$$\alpha = 0.45 \qquad \text{for} \qquad \frac{s_u}{P_a} > 2.5 \tag{8.29c}$$

where P_a = atmospheric pressure. The unit shaft resistance, r_s, in granular soil was estimated using:

$$r_s = \beta \cdot \sigma'_{v0} \tag{8.30}$$

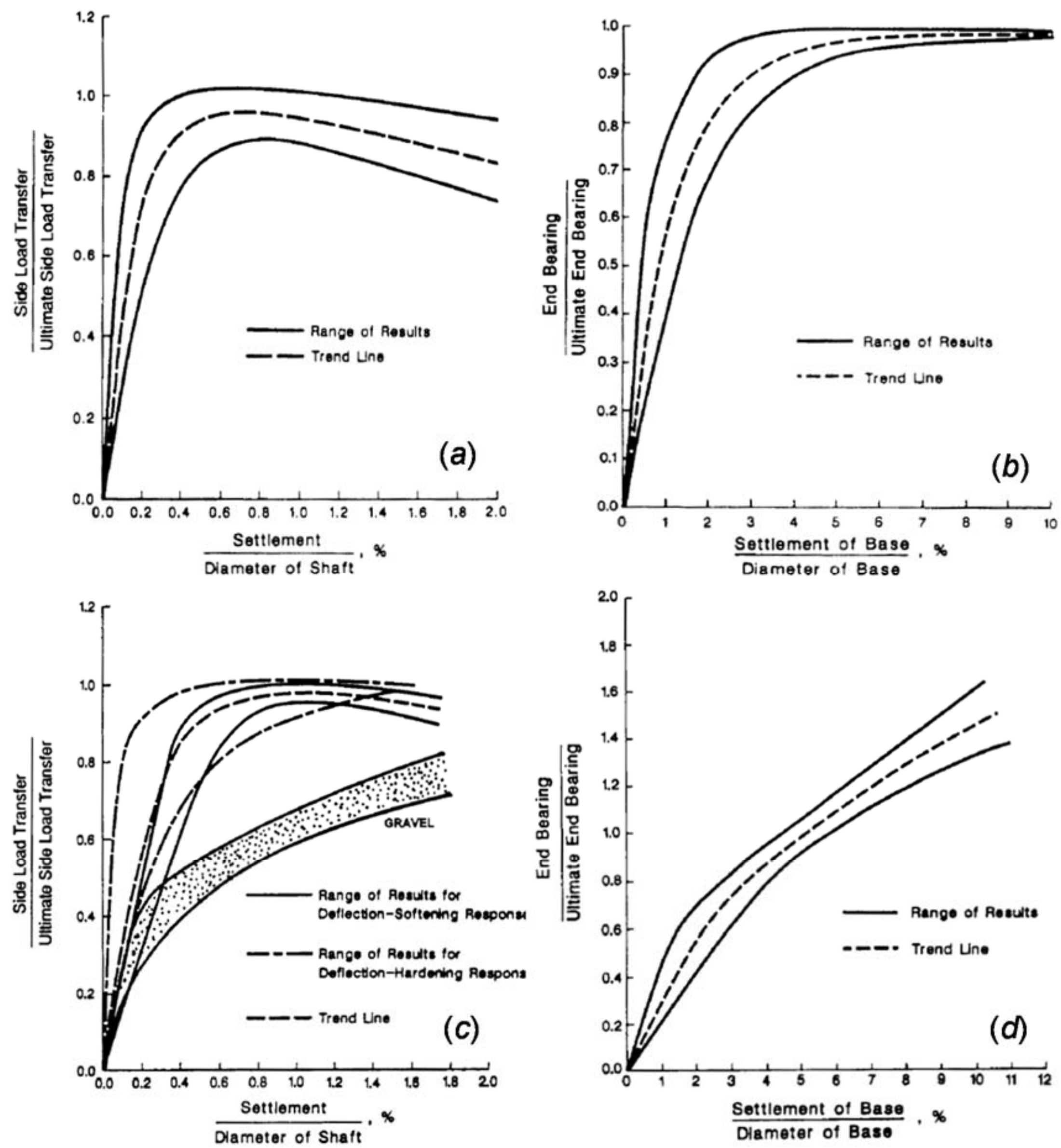

Figure 8-13: Normalized load transfer for drilled shaft for (a) shaft resistance and (b) base resistance in plastic soil, and (c) shaft resistance and (d) base resistance in granular soil (O'Neill and Reese 1999)

where σ'_{v0} = vertical effective stress at the mid-point of the layer of interest and β = shaft resistance coefficient. The β-coefficient was determined using the method recommend by Brown et al. (2010):

$$\beta = (1-\sin\phi')\cdot \mathrm{OCR}^{\sin\phi'} \tan\phi' \le K_p \tan\phi' \tag{8.31}$$

where OCR = overconsolidation ratio, computed using an empirical estimate of the normalized vertical effective preconsolidation stress, σ'_p :

$$\frac{\sigma'_p}{P_a} = 0.47\cdot\left(N_{60}\right)^m \tag{8.32}$$

where N_{60} = energy-corrected SPT blow count. The coefficients α and β for different soil layers are summarized in Table 8-3 and Table 8-4. The reduction factor of 0.5 and 0.6 were used for cased shafts in granular and plastic soil, respectively, with the lower bound as recommend by Brown et al. (2010). Since the toe of each test shaft was in plastic soil, the unit toe resistance was estimated by (Brown et al. 2010):

$$r_t = N_c \cdot s_u \tag{8.33}$$

where N_c = bearing capacity factor, which was assumed to be 9.0 with s_u > 95 kN (2000 psf). Table 8-3 and Table 8-4 summarize the estimated shaft, R_s, and toe resistance, R_t. The estimated applied load was calculated by:

$$Q = R_{ult} - W = R_s + R_t - W \tag{8.34}$$

where R_{ult} = ultimate axial resistance and W = shaft weight.

The trend lines for the mobilization of shaft and toe resistance shown in Figure 8-13 were used to evaluate the axial response of each shaft. Since the cased shafts have the same diameter, the axial response for each cased shaft is the same. Figure 8-14 compares the measured and estimated load-displacement response at the head of the drilled shafts. The difference between MIR and HSIR in the estimated response is due to the variation in diameter between the two shafts. To facilitate the evaluation of the FHWA method, the bias in axial load (i.e., the ratio of the observed and computed load at the shaft head) at each displacement was calculated for displacements smaller than or equal to a diameter-normalized displacement of 2% (See Figure 8-13) which is summarized in Table 8-5.

It appears that the FHWA method under-predicts the axial load for the uncased shafts and overpredicts that the axial load for the cased shafts. The FHWA method was developed in consideration of numerous tests on uncased production shafts, which were likely tested shortly (within several weeks) following construction. Owing to the short soil "recovery" period near the soil-shaft interface, the observed shaft resistance was likely smaller than a long-term shaft resistance. The lower-bound casing reduction factor of 0.5 and 0.6 for cased shafts in granular and plastic soil, respectively, appears unconservative; this is explored in greater detail below. The effect of casing reduction factors is addressed subsequently. The FHWA Method suggested that fully-mobilized resistance for MIR and HSIR was equal to approximately of 5,800 and 5,600 kN (1,300 and 1,250 kip), respectively. However, MIR and HSIR were not full-mobilized with the maximum load of 6,125 and 6,380 kN (1,377 and 1,435 kip), respectively, as measured during the loading tests.

Table 8-3: Soil and drilled shaft properties for the uncased test shafts and the calculation of the axial resistance.

Depth m (ft)	Soil Type	MIR D, m (in)	HSIR D, m (in)	γ' kN/m^3(pcf)	s_u kPa (psf)	ϕ' deg	a or β or N_c	MIR R_s, kN (kip)	HSIR R_s, kN (kip)
0 to 1.9 (0 to 6.3)	Silty CLAY to Clayey SILT	1.04 (41.1)	1.02 (40.2)	18.1 (115)	110 (2,275)	-	$a = 0.55$	79 (18)	78 (17)
1.9 to 3.4 (6.3 to 11.0)	Silty CLAY to Clayey SILT	1.07 (42.3)	1.03 (40.7)	8.3 (52.6)	65 (1,315)	-	$a = 0.55$	181 (41)	174 (39)
3.4 to 3.7 (11.0 to 12.0)	SAND	1.06 (41.6)	1.05 (41.2)	10.6 (67.6)	-	39	$\beta = 1.86$	89 (20)	88 (20)
3.7 to 5.0 (12.0 to 16.5)	Silty CLAY to Clayey SILT	1.10 (43.4)	1.08 (42.4)	8.3 (52.6)	60 (1,225)	-	$a = 0.55$	149 (33)	145 (33)
5.0 to 12.2 (16.5 to 40)	Silty SAND	1.07 (42.1)	1.02 (40.3)	10.6 (67.6)	-	38	$\beta = 1.26$	3,021 (679)	2,892 (650)
12.2 to 18.3 (40.0 to 60.0)	Silty CLAY to Clayey SILT	0.98 (38.5)	0.96 (37.9)	7.5 (47.6)	290 (5,990)	-	$a = 0.42$	2,283 (513)	2,247 (505)
Toe	Silty CLAY to Clayey SILT	0.98 (38.5)	0.96 (37.9)	7.5 (47.6)	290 (5,990)	-		1,960 (441)	1900 (427)
R_{ult}								7762 (1,745)	7524 (1,691)

Table 8-4: Soil and drilled shaft properties for the cased test shafts and the calculation of the axial resistance.

Depth, m (ft)	Soil Model	D, m (in)	γ' kN/m3 (pcf)	s_u kPa (psf)	ϕ' deg	a or β or N_c	R_s kN (kip)
0 to2.0 (0 to 6.6)	Silty CLAY to Clayey SILT	0.94 (37)	18.1 (115)	85 (1,800)	-	$a = 0.55$	34 (8)
0 to 3.5 (6.6 to 11.5)	Silty CLAY to Clayey SILT	0.94 (37)	8.3 (52.6)	75 (1515)	-	$a = 0.55$	91 (20)
3.5 to 3.8 (11.5 to 12.5)	SAND	0.94 (37)	10.6 (67.6)	-	40	$\beta = 1.98$	54 (12)
3.8 to 5.5 (12.5 to 18.0)	Silty CLAY to Clayey SILT	0.94 (37)	8.3 (52.6)	70 (1,420)	-	$a = 0.55$	95 (21)
5.5 to 18.3 (18.0 to 40)	Silty SAND	0.94 (37)	10.6 (67.6)	-	39	$\beta = 1.39$	1674 (376)
12.2 to 18.3 (40.0 to 60.0)	Silty CLAY to Clayey SILT	0.94 (37)	7.5 (47.6)	285 (5,930)	-	$a = 0.42$	1075 (242)
Toe	Silty CLAY to Clayey SILT	0.94 (37)	7.5 (47.6)	285 (5,930)	-	$N_p = 9$	1779 (400)
R_{ult}							4801 (1,079)

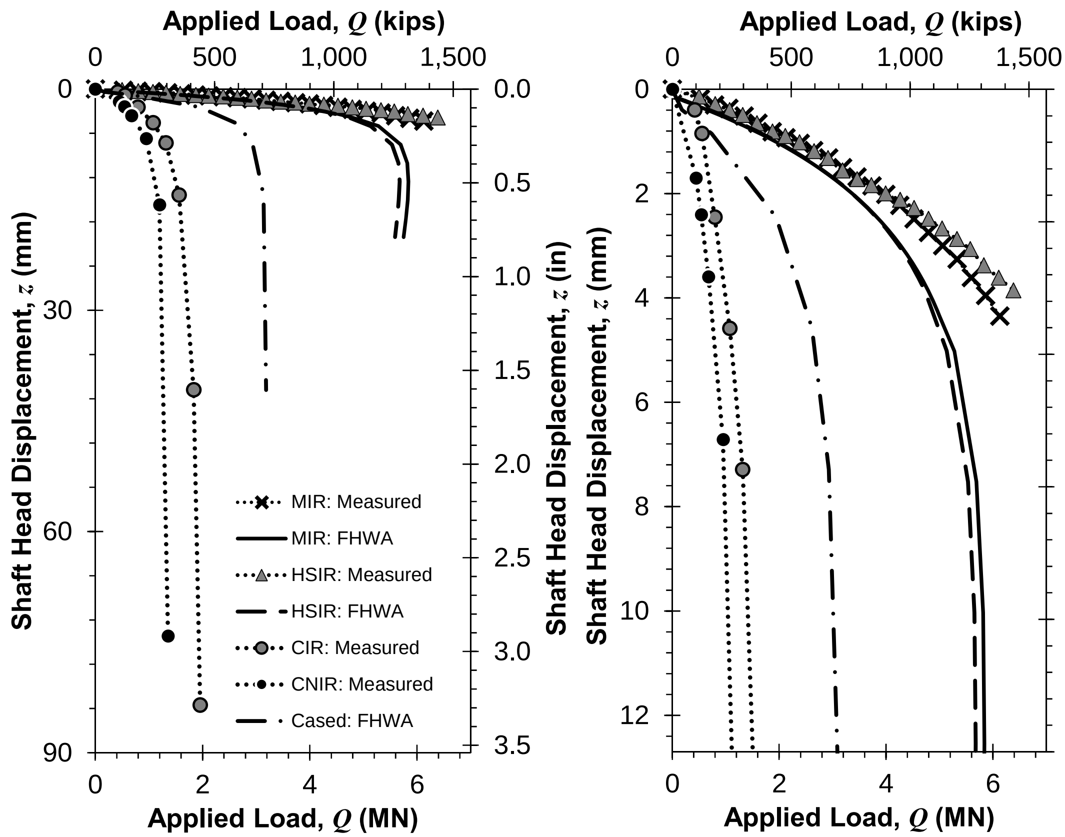

Figure 8-14: Comparison of the predicted global axial load-displacement relationship using FHWA method, and the measured responses of all test shafts for at (a) large range of scale and (b) for the initial response with displacement up to 12.7 mm (0.5 in).

Table 8-5: Comparison of the measured axial load-displacement responses of the test shafts to the calculated responses using FHWA method for diameter-normalized displacementless than or equal to 2%.

Test Shaft	Maximum z considered mm (in)	FHWA	
		Mean Bias	COV (%)
MIR	0 to 4 (0 to 0.17)	1.27	16%
HSIR	0 to 4 (0 to 0.15)	1.28	13%
CIR	0 to 14 (0 to 0.57)	0.81	94%
CNIR	0 to 16 (0 to 0.62)	0.31	13%

8.10 Effect of Permanent Casing on Axial Load Response

The effect of permanent casing on axial load transfer is compared in Figure 8-15 using the *t-z* curves for different tributary areas for the cased and uncased shafts. The uncased shafts exhibited significantly larger unit shaft resistances than did the cased shafts. The differences, which were more pronounced at shallower depths, were attributed to the enhanced load transfer characteristics at the soil-concrete interface. The comparison between the fitted ultimate unit shaft resistance for the uncased test shafts and the measured resistance for the cased shafts is at relative soil-shaft movements of 2 and 12.5 mm are summarized in Table 8-6 using the shaft resistance ratio, defined as the ratio of unit shaft resistance for the cased shafts and that of the uncased shafts at given relative soil-shaft movements. Since the shaft resistance ratio depends on the specific installation procedure, it assigned the variable of $R_{d\text{-}vc,d}$ to represent construction sequence in the ratio: ratio of a shaft that was drilled and casing vibro-installed, to that of a drilled, uncased shaft. At small relative soil-shaft movements, CIR exhibited $R_{d\text{-}vc,d}$ ranging from 4 to 44%, and then decreased as the interface softened to produce $R_{d\text{-}vc,d}$ ranging from 3 to 23% at 12.5 mm. Shaft CNIR exhibited hardening, but with substantially smaller $R_{d\text{-}vc,d}$ given the use of the slightly larger auger, with $R_{d\text{-}vc,d}$ ranging from 3 to 5% and 4 to 11% for relative movements of 2 and 12.5 mm, respectively. The subtle difference in auger diameter (0.91 vs. 0.94 m, or 36 vs. 37 in) produced significantly different shaft load transfer characteristics.

The unit shaft resistance ratios from full-scale tests conducted by Owens and Reese (1982), Camp et al. (2002), and this study are summarized in Table 8-7. Owens and Reese (1982) studied the effects of casing on shaft resistance at a site in Galveston, Texas where the test shafts were designated G-1 and G-3, and at a site in eastern Texas where the shafts were designated E-1 and E-2. The diameter and length of the steel casing used in shaft G-3 was 0.91 m (36 in) and 18.3 (60 ft), respectively. After the borehole was drilled to a depth of 10.7 m (35 ft) using a 0.91 m (36 in) diameter auger, the steel casing was installed to a depth of 12.2 m (40 ft) using the torque and crowd supplied by the drill rig. Then, a 0.86 m (34 in) diameter auger was used to drill the borehole to a depth of 18.3 m (60 ft). The diameter and length of test shaft G-1 was 1.21 m (48 in) and 18.3 m (60 ft), respectively. Prior to drilling, a steel casing 1.21 m (48 in) in diameter was vibrated to a depth of 15.8 m (52 ft); a 1.17 m (46 in) diameter auger was used to drill the borehole the final depth of 18.3 m. The effect of casing installation methods on the unit shaft resistance was substantial. The unit shaft resistance for G-3 (drill then twist in casing) compared to G-1 (vibrate casing then drill) reduced by an amount ranging from $R_{d\text{-}tc,vc\text{-}d}$ = 9 to 30%, with the largest variability occurring in the sand deposits and with very little variability in the plastic, fine-grained soils (Table 8-7). The reduction of the unit shaft resistance was greater in the loose, saturated sands (average $R_{d\text{-}tc,vc\text{-}d}$ = 13%) than in the dense to very dense sands (average $R_{d\text{-}tc,vc\text{-}d}$ = 23%). On the other hand, on average, the unit shaft resistance of the vibro-cased portion of G-1 within the soft clay layer from a depth of 12.8 to 15.9 m (42 to 52 ft) was about 89% of the unit shaft resistance for the uncased portion of G-3. Vibro-installation of steel casing results in densification and in an increase in unit shaft resistance if the casing is installed prior to drilling as compared to drill-then-install casing in sandy soil, whereas the vibro-installation of casing prior to drilling in the deep, soft clay layer resulted in a reduction in unit shaft resistance compared to that of an uncased shaft.

The diameter and length of the shafts E-1 and E-2 were 0.91 m (36 in) and 18.3 m (60 ft), respectively. Prior to drilling, the casing for shaft E-1 was vibrated to a depth of only

12.2 m (40 ft) because densification of the very loose to medium dense sand prevented further penetration. To reduce shaft resistance on the inside of the casing, the soil was excavated to the same depth as the tip of the casing; the casing was then advanced to 18.3 m using a vibratory hammer. On the other hand, shaft E-2 was constructed using a temporary casing that was vibrated to the full depth, the soil inside of the casing was excavated, and then the casing was extracted during placement of the concrete. Considering the densification of the sand that resulted from the vibratory installation of the permanent steel casing to 10.7 m depth for shaft E-1, $R_{vc\text{-}d\text{-}cr,dc}$ was about 33% on average. On the other hand, considering depths of 13.8 to 18.3 m, where the comparison relates a vibro-cased and drilled and cast shaft interface to a vibro-cased, drilled, and the casing removed, $R_{vc\text{-}d,vc\text{-}d\text{-}cr,}$ indicating the benefit of a concrete-soil interface, the reduction in shaft resistance averaged 14%.

Table 8-6: Comparison of shaft resistance ratios, $R_{d\text{-}vc,d}$, between the cased and uncased shafts.

Depth m (ft)	Predominant Soil Type	Shaft Resistance Ratio at 2 mm (0.1 in)		Shaft Resistance Ratio at 12.5 mm (0.5 in)	
		CIR	CNIR	CIR	CNIR
7.9 to 9.1 (26 to 30)	Stiff sandy silt	4%	3%	3%	4%
9.1 to 11.9 (30 to 39)	Dense silty sand	8%	-	6%	-
11.9 to 14.9 (39 to 49)	Stiff sandy, clayey silt	28%	3%	15%	7%
14.9 to 18.0 (49 to 59)	Stiff sandy, clayey silt	44%	5%	23%	11%

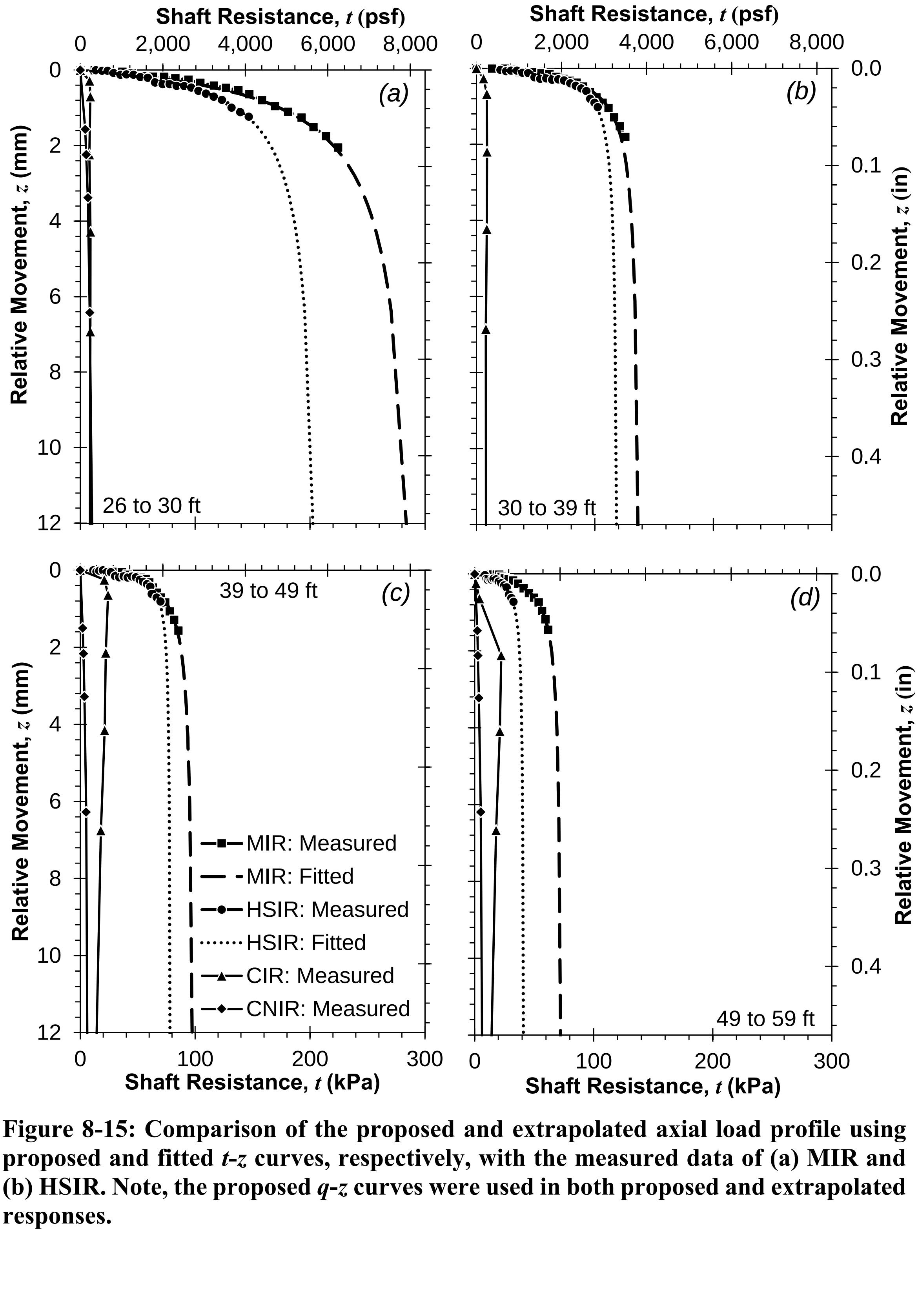

Figure 8-15: Comparison of the proposed and extrapolated axial load profile using proposed and fitted *t-z* curves, respectively, with the measured data of (a) MIR and (b) HSIR. Note, the proposed *q-z* curves were used in both proposed and extrapolated responses.

Table 8-7: Reduction in unit shaft resistance as a function of construction sequencing.

Reference	Definition of Shaft Resistance Ratio	Range in Depths m (ft)	Shaft Resistance Ratio	Soil Type	Range in Displacements mm (in)	Shaft resistance ratio, R_r	
						Range	Average
Owens and Reese (1982)	Shaft G-3 (drilled to a depth of 35 ft then twist-cased to a depth of 40 ft) to G-1 (vibro-cased to a depth of 52 ft then drilled to a depth of 60 ft, followed by casing removal).	0 to 6.4 (0 to 21)	$R_{d\text{-}tc,vc\text{-}d}$[1]	Loose to medium dense silty fine sand	23 to 45 (0.90 to 1.75)	9.0 to 17%	13%
		6.4 to 7.9 (21 to 26)	$R_{d\text{-}tc,vc\text{-}d}$	Very soft to medium stiff clay	23 to 45 (0.90 to 1.75)	17 to 18%	17%
		7.9 to 10.7 (26 to 35)	$R_{d\text{-}tc,vc\text{-}d}$	Dense to very dense silty fine sand	23 to 45 (0.90 to 1.75)	18 to 30%	23%
Owens and Reese (1982)	Shaft G-1 (vibro-cased then drilled) to G-3 (uncased, drilled from a depth of 40 to 60 ft).	12.8 to 15.9 (42 to 52)	$R_{vc\text{-}d,d}$[2]	Soft clay with thin lenses of silty sand	23 to 45 (0.90 to 1.75)	85 to 100%	89%
Owens and Reese (1982)	Shaft E-2 (vibro-cased to a depth of ~57 ft prior to drilling inside the casing then vibro-cased to a depth of 60 ft, followed by casing removal) to E-1 (vibro-cased to a depth of 40 ft prior to drilling inside the casing, then vibro-cased to a depth of 60 ft).	0 to 10.7 (0 to 35)	$R_{vc\text{-}d\text{-}cr,dc}$[3]	Very loose to medium dense sand	23 to 38 (0.9 to 1.5)	21 to 70%	33%

Notes: [1] $R_{d\text{-}tc,vc\text{-}d}$ = drilled then twist-installation of casing compared to vibro-cased then drilled; [2] $R_{vc\text{-}d,d}$ = vibro-cased then drilled compared to drilled; [3] $R_{vc\text{-}d\text{-}cr,dc}$ = vibro-cased then drilled and cast followed by removal of casing to driven casing;[4] $R_{vc\text{-}d,vc\text{-}d\text{-}cr}$ = vibro-cased then drilled to vibro-cased then drilled and cast following removal of casing;[5] $R_{d\text{-}vc,d}$ = drilled then vibro-cased to drilled.

Table 8-7 **(continued)**

Reference	Definition of Shaft Resistance Ratio	Range in Depths m (ft)	Shaft Resistance Ratio	Soil Type	Range in Displacements mm (in)	Shaft resistance ratio, R_r	
						Range	Average
Owens and Reese (1982)	Shaft E-1 (vibro-cased from a depth of 40 to 60 ft then drilled inside the casing) to E-2 (vibro-cased then drilled, followed by casing removal)	13.8 to 18.3 (45 to 60)	$R_{vc\text{-}d,vc\text{-}d\text{-}cr}$[4]	Very loose to loose sand	23 to 38 (0.9 to 1.5)	8.2 to 20%	14%
Camp et al. (2002)	Vibro-cased portion to uncased portion of shafts (vibro-cased then drilled)	(various)	$R_{vc\text{-}d,d}$	Cooper Marl	$\lesssim$ 12.5 ($\lesssim$ 0.5)	20 to 58%	34%
This Study	Cased shafts (drilled then vibro-cased) to uncased shafts	7.9 to 14.9 (26 to 49)	$R_{d\text{-}vc,d}$[5]	Stiff sandy silt and dense silty sand	12.5 (0.5)	3% to 15%	7%
This Study	Cased shafts (drilled then vibro-cased) to uncased shafts	14.9 to 18.3 (49 to 60)	$R_{d\text{-}vc,d}$	Stiff sandy clayey silt	12.5 (0.5)	11% to 23%	17%

Notes: [1] $R_{d\text{-}tc,vc\text{-}d}$ = drilled then twist-installation of casing compared to vibro-cased then drilled; [2] $R_{vc\text{-}d,d}$ = vibro-cased then drilled compared to drilled; [3] $R_{vc\text{-}d\text{-}cr,dc}$ = vibro-cased then drilled and cast followed by removal of casing to driven casing;[4] $R_{vc\text{-}d,vc\text{-}d\text{-}cr}$ = vibro-cased then drilled to vibro-cased then drilled and cast following removal of casing;[5] $R_{d\text{-}vc,d}$ = drilled then vibro-cased to drilled.

Camp et al. (2002) reported results from loading test of three partially-cased drilled shafts that incorporated permanent casing through weak sediments overlying Cooper Marl, within which the shafts were founded. The steel casing for each shaft was vibrated into place prior to the excavation of the shafts, allowing for a comparison of the effect of casing in the Cooper Marl. Load transfer data obtained during the bidirectional loading tests indicated that the unit shaft resistance was fully mobilized at relative soil-shaft displacements generally less than about 12.5 mm ($\lesssim$ 0.5 in; Camp 2017). The shaft resistance ratio, $R_{vc\text{-}d,d}$, defined in this ratio of vibro-cased and drilled to the uncased shaft resistance, ranged from about 20 to 58%, with an average of about 34%.

Clearly, construction procedures and sequencing, as well as the type of soil conditions, control the magnitude of shaft resistance reduction that is possible. Table 8-7 may be used as a reference to aid practitioners in estimating possible reductions.

8.11 Summary and Conclusions

Four full-scale, instrumented drilled shafts were constructed as part of a study to evaluate various performance characteristics of cased and uncased shafts, with and without internal reinforcement consisting of either Grade 60 or Grade 80 steel reinforcement bars. This chapter explored the effects of the steel casing and the effects of auger diameter (relative to the casing diameter) on the axial load transfer characteristics of the cased shafts relative to the uncased shafts. For the shafts incorporating permanent casing, the shafts were drilled to depth using slurry, and then the casing was vibrated into place. The thermal integrity profiling (TIP) method using thermal wires was used as part of the nondestructive testing (NDT) program to provide an estimate of the actual shape of the shaft. For the cased shafts, the results from the TIP profiling indicated that potential gaps existed between the steel casing and the sidewall of the drilled borehole. As deduced from the results of the NDT and load testing, the use of thermal wires with shafts that incorporate steel casing can prove helpful in determining whether voids are present between the steel casing and the sidewalls of the shaft.

Despite similar depth of embedment and nominally similar as-constructed diameter, comparison of the load-displacement curves for the cased and uncased shafts indicated significant differences in their axial response. The load transfer curves developed from the results of the load tests confirmed that the use of steel casing and the method used to install the casing resulted in substantial differences in the load transfer behavior between the cased and uncased shafts. In addition, the shafts constructed with an auger that was nominally the same diameter as the casing resulted in less effective load transfer characteristics as compared to shafts constructed with an auger that was slightly smaller in diameter than the casing.

Empirical *t-z* (shaft resistance) and *q-z* (toe resistance) curves were developed based on the results of the load tests. A direct CPT-based method for estimating load transfer curves for uncased shafts in similar soils was proposed and used to extend the results of the load test program. Finally, to provide a useful reference for practitioners considering the use of casing in drilled shaft foundations the effect of casing on axial load transfer characteristics was evaluated based on load test data reported in the literature as well as with the load testing results from this study.

8.12 Acknowledgements

The authors wish to acknowledge the many agencies, firms, and individuals who have contributed to the ongoing research effort. The authors are grateful for support from the

Oregon Department of Transportation through Grant SPR 765 and from the Pacific Northwest Transportation Consortium (PacTrans) through grant DTRT12-UTC10. The West Coast Chapter (WCC) of the ADSC contributed funds to help offset material costs associated with the construction of the test shafts, with critical coordination efforts and guidance provided by John Starcevich (Malcolm Drilling, Inc.), Becky Patterson (WCC ADSC), and Rick Walsh (Hayward Baker, Inc.). Malcolm Drilling, Inc. constructed the test shafts; Pacific Foundation, Inc. installed the reaction piles; and Ralph's Concrete donated the concrete pumping services. The Grade 80 solid and hollow steel reinforcement bars were donated by ConTech Systems, whereas the Grade 60 steel reinforcement bars and all cage fabrication was donated by PJ's Rebar. The permanent steel casing was donated by Skyline Steel, and the Grade 150 steel reinforcement bars for the reaction anchors were contributed by Williams Form, Inc. Spacers and bar boots were provided by Foundation Technologies. Crosshole sonic logging services was donated by GEI Consultants; and Thermal Integrity Profiling Thermal Wires® and logging services were provided by Pile Dynamics, Inc.

8.13 References

AASHTO (2014). *LRFD Bridge Design Specifications*. 7th edition, American Association of State Highway and Transportation Officials, Washington, D.C.

Alsamman, O.M. (1995). "The use of CPT for calculating axial capacity of drilled shafts." *Ph.D. Dissertation*, University of Illinois at Urbana-Champaign, IL.

ASTM (2014a) "Standard Test Method for Integrity Testing of Concrete Deep Foundations by Ultrasonic Crosshole Testing," *ASTM D 6760*, ASTM International, West Conshohocken, PA, 7 pp.

ASTM. (2014b). "Standard Test Methods for Thermal Integrity Profiling of Concrete Deep Foundations," *ASTM D7949*, ASTM International, West Conshohocken, PA, 2014, www.astm.org.

Brown, D.A., Turner, J.P., and Castelli, R.J. (2010). “Drilled shafts: Construction procedures and LRFD design methods.” *Report No. FHWA-NHI-10-016.* US Department of Transportation, Federal Highway Administration, Washington, D.C.

Bustamante, M. and Gianeselli, L. (1982). “Pile bearing capacity prediction by means of static penetrometer.” *Proc., European Symp. on Penetration Testing*. A. A. Balkema. Rotterdam, The Netherlands, 493-500.

Butterfield, R., and Banerjee, P.K. (1971). “The elastic analysis of compressible piles and pile groups.” *Geotechnique*, London, England, 21(1), 43-60.

Camp, W.M., Brown, D.A., and Mayne, P.W. (2002). “Construction methods effects on drilled shaft axial performance.” *Deep foundations 2002*, Geotechnical Special Publication No. 116, M.W. O’Neil and F.C. Townsend, eds., ASCE, Reston, VA. 193-208.

Camp, W.M. (2017). *Personal Communication*, 28 June 2017.

Cao, W., Chen, Y., and Wolfe, W.E. (2014). “New load transfer hyperbolic model for pile-soil interface and negative skin friction on single piles embedded in soft soils.” *Int. J. Geomech.*, 14(1), 92–100

Chen, Y.J. and Kulhawy, F.H. (1994). “Case history evaluation of the behavior of drilled shafts under axial and lateral loading.” *Electric Power Research Institute TR-104601, ResearchProject*, *1493– 04*, Palo Alto.

Chen, Y.J. and Kulhawy, F.H. (2002). “Evaluation of drained axial capacity for drilled shafts.” *Proc., Deep Foundations 2002, Geotech. Spec. Publication No. 116*, ASCE, Reston, Va., 2, 1200–1214.

Chin, F. K. (1970). “Estimation of the pile Ultimate Load of Piles Not Carried to Failure.” *Proceedings of the 2nd Southern Asian Conference on Soil Engineering*, Singapore, 81-90.

Chin, F. K. (1971). “Discussion of pile test, Arkansas River project.”. *Soil Mech. and Found. Div*., 97(6), 930-932.

Chow, Y.K. (1986). "Analysis of vertically loaded pile groups." *International Journal for Numerical and Analytical Methods in Geomechanics*, 10, 59-72.

Clemence, S.P., and Brumund, W.F. (1975). “Large-scale model test of drilled pier in sand.” *J. Geotech. Engrg. Div*., 101(6), 537–550.

Clough, G. W., and Duncan, J. M. (1971). “Finite element analyses of retaining wall behavior.” *J. Soil Mech. Found. Div.,* ASCE, 97(12), 1657–1673.

Coyle, H. M., and Reese, L. C. (1966). “Load transfer for axially loaded piles in clay.” *Journal of Soil Mechanics and Foundations Div*, 92(SM2), 1-26.

Coyle, H.M., and I.H. Sulaiman. (1967). “Skin friction for steel piles in sand.” *Journal of the Soil Mechanics and Foundation Division*, 93(SM6), 261-278.

Dickenson, S.E. and Haines, B.Z. (2006). *Characterization of the geotechnical engineering field research site at Oregon State University*, 3rd Ed., Oregon State Univ., Corvallis, OR.

Duncan, J. M., and Chang, C.-Y. (1970). “Nonlinear analysis of stress and strain of soil.” *J. Soil Mech. and Found*. Div., 96(5), 1629–1653.

Eslami, A., and Fellenius, B. H. (1997). “Pile capacity by direct CPT and CPTu methods applied to 102 case histories.” *Canadian Geotechnical Journal*, *34*(6), 886-904.

Fellenius, B. H. (1989). “Tangent modulus of piles determined from strain data.” Proc., 1989 Found. Congr., Spec. Tech. Publ. No. SPT 22, F. H. Kulhawy, ed., Vol. 1, ASCE, Reston, Va., 500–510.

Fellenius, B. H. (2017). Basics of foundation design. Electronic Edition. <www.Fellenius.net>.

Fioravante, V., Ghionna, V.N., Jamiolkowski, M., and Pedroni, S. (1995). “Load carrying capacity of large diameter bored piles in sand and gravel.” In *Proceedings of 10th Asian regional conference on soil mechanics and foundation engineering, Beijing*, 2, 3-15.

Gebman, M., Ashford, S. A, and Restrepo, J. I. (2006). “Axial force transfer mechanisms within cast-in-steel-shell piles”. *Report No. SSRP-94/10*, Department of Structural Engineering, University of California at San Diego, La Jolla, CA.

Grosch, J., and Reese, L. (1980). “Field tests of small-scale pile segments in a soft clay deposit under repeated axial loading.” *Rep. Prepared for Am. Petro. Inst., Austin, Tex.*

Guo, W. D. (2000). “Vertically loaded single piles in Gibson soil.” *J. Geotech. Geoenviron. Eng*., 126(2), 189–193.

Guo, W. D., and Randolph, M. F. (1998). ‘‘Rationality of load transfer approach for pile analysis.’’ *Comp. and Geotechnics*, 23(1–2), 85–112.

Holmquist, D.V. and Matlock, H. (1976). “Resistance-displacements relationships for axially loaded piles in soft clay.” *Proceedings, 8th offshore Technology Conference*, Houston, TX, Vol. 1, pp. 553-569

Huffman, J.C., Strahler, A.W., and Stuedlein, A.W. (2015) “Reliability-based serviceability limit state design for immediate settlement of spread footings on clay,” *Soils and Foundations*, 55(4), 798-812.

Jamiolkowski, M. (2003). “Deep foundations on bored and auger piles.” *Proc. 4th Intern.Geotechnical Seminar on Deep Foundations on Bored and Auger Piles*, Ghent: 83–100.

Kim, S., Jeong, S., Cho, S., and Park, I. (1999). “Shear load transfer characteristics of drilled shafts in weathered rocks.” J. Geotech. Geoenviron. Eng., 125(11), 999–1010.

Kondner, R.L. (1963). “Hyperbolic stress–strain response: cohesive soils.” *J. Soil Mech. Found. Div.* 89 (1), 115–143.

Kraft, L.M., Kagawa, T., and Ray, R.P. (1981). “Theoretical *t-z* curves.” *Journal of the Geotechnical Engineering Division*, 107(11), 1543-1561.

Kulhawy, F. H., and Mayne, P.W. (1990). “Manual on estimating soil properties for foundation design.” *Rep. EL-6800*, Electric Power Research Institute, Cornell Univ., Ithaca, NY.

Kulhawy, F. H. (1991). Drilled shaft foundations.” *Foundation engineering handbook*, 2nd Ed., H. Y. Fang, ed., Van Nostrand-Reinhold, New York.

Kulhawy, F. H. (2004). “On the axial behavior of drilled foundations.” *Proc., GeoSupport 2004: Drilled Shafts, Micropiling, Deep Mixing, Remedial Methods, and Specialty Foundation Systems, GSP 124*, J. P. Turner and P. W. Mayne, eds., ASCE, Reston, Va., 34–51.

Kulhawy, F.H. and Chen, J.-R. (2007). “Discussion of ‘Drilled Shaft Side Resistance in Gravelly Soils’ by Kyle M. Rollins, Robert J. Clayton, Rodney C. Mikesell, and Bradford C. Blaise,” *Journal of Geotechnical and Geoenvironmental Engineering*, ASCE, 133(10), 1325-1328.

Lee, C.Y. (1991) “Discrete layer analysis of axially loaded piles and pile groups.” *Comput Geotech*; 11(4):295–313.

Li, Q., Stuedlein, A.W., Barbosa, A. R. (2017). “Torsional load transfer of drilled shaft foundations.” *J. Geotech. Geoenviron. Eng.*, 143(8), http://dx.doi.org/10.1061/(ASCE)GT.1943-5606.0001701.

Li, Q., and Stuedlein, A.W. (2017). “Simulation of torsionally-loaded deep foundations considering state-dependent load transfer.” *J. Geotech. Geoenviron. Eng.*, in review.

Li, Q., and Yang, Z. (2017). “*P–y* approach for laterally loaded piles in frozen silt.” *J. Geotech. Geoenviron. Eng.*, 143(5), http://dx.doi.org/10.1061/(ASCE)GT.1943-606.0001556

Martin, J.P. (2018). “Full-Scale Loading Tests of Shallow Foundations on Aggregate Pier-reinforced Clayey Silt,” *MS Thesis*, Oregon State University, *Under Development*

Mayne, P.W., and Harris, D.E. (1993). “Axial Load-Displacement Behavior of Drilled Shaft Foundations in Piedmont Residuum,” *FHWA Reference Number 41-30-2175*, Georgia Tech Research Corporation, Atlanta, GA.

McVay, M.C., F.C. Townsend, D.G. Bloomquist, M.O. O'Brien, and J.A. Caliendo. (1989). "Numerical analysis of vertically loaded pile groups." *Proceedings, Foundation Engineering Congress: Current Principles and Practices*, Evanston, IL, 675-690.

Niazi, F.S. (2014). “Static axial pile foundation response using seismic piezocone data.” *PhD thesis*, Georgia Institute of Technology, Atlanta, GA.

Nimityongskul, N. (2010). “Effects of soil slope on lateral capacity of piles in cohesive soils.” *Ph.D. Dissertation*, Civil and Construction Engineering Department, Oregon State University, Corvallis, OR.

O'Neill, M.W., and Reese, L.C. (1978). “Load transfer in a slender drilled pier in sand” *, Preprint 3141, Spring Convention and Exposition,* Pittsburgh, PA.

O'Neill, M.W., and Reese, L.C. (1999). "Drilled shafts: Construction procedures and design methods." *Publ. No. FHWA-IF-99-025*, Federal Highway Administration, Office of Implementation, McLean, VA

Owens, M.J., and Reese, L.C. (1982). "The influence of a steel casing on the axial capacity of a drilled shaft." *Report No. 255-1F*. Texas State Department of Highways and Public Transportation Center for Transportation Research, Bureau of Engineering Research, The University of Texas at Austin, Austin, TX.

Poulos, H.G., and Davis, E.H. (1968). "The settlement behaviour of single axially loaded incompressible piles and piers." *Geotechnique*, London, England, 18(3), 351-371.

Poulos, H.G. (1989). "Pile behaviour—theory and application." *Géotechnique,* London, England, 39 (3), 365–415.

Poulos, H.G. (2001). "Pile foundations." In *Geotechnical and Geoenvironmental Engineering Handbook*, Edited R.K. Rowe, Kluwer Academic Press.

Randolph, M.F. and Wroth, C.P. (1978). "Analysis of deformation of vertically-loaded piles." ASCE *Journal of the Geotechnical Engineering Division*, 104(GT12): 1465 – 1488.

Randolph, M.F. (1994). "Design methods for pile groups and pile drafts." *Proceedings, XIII ICSMFE*, New Delhi, India , 61-82.

Reese, L.C., and O'Neill, M.W. (1988). "Drilled shafts: Construction procedures and design methods." *Pub. No. FHWA-HI-88-042*, U.S. Dept. of Transportation, Washington, D.C., 564–564.

Reese, L. C., Wang, S. T. and Arrellage, J., (2014), "Analysis of load versus settlement for an axially loaded deep foundation", *TZPILE v2014 Technical Manual*, ENSOFT, INC., Austin, TX.

Robertson, P.K., (2009), "Interpretation of cone penetration tests – a unified approach", *Canadian Geotechnical Journal*, 46(11), 1337–1355.

Roeder, C. W., Cameron, B., and Brown, C. B. (1999). "Composite action in concrete-filled tubes." *J. Struct. Eng.,* 125(5), 477–484.

Roeder, C. W., Lehman, D. E., and Bishop, E. (2010). "Strength and stiffness of circular concrete filled tubes." J. *Struct. Eng.,* 136(12), 1545–1553.

Roeder, C., and Lehman, D. (2012). "Initial Investigation of Reinforced Concrete Filled Tubes for Use in Bridge Foundations." *Report No. WA-RD 776.1*. The State of Washington Department of Transportation, Olympia, Washington.

Stuedlein, A.W. and Reddy, S.C. (2014) "Factors Affecting the Reliability of Augered Cast-In-Place Piles in Granular Soils at the Serviceability Limit State," *J. of the Deep Foundations Institute*, Vol. 7, No. 2, pp. 46-57.

Stuedlein, A.W., Neely, W.J., and Gurtowski, T.G. (2012) "Reliability-based Design of Augered Cast-In-Place Piles in Granular Soils," *Journal of Geotechnical and Geoenvironmental Engineering*, 138(6), 709-717.

Takesue, K., Sasao, H., and Matsumoto, T. (1998). "Correlation between ultimate pile skin friction and CPT data." *Geotechnical Site Characterization*, 2, 1177-1182.

Wong, K. S., and Teh, C. I. (1995). "Negative skin friction on piles in layered deposits." *J. Geotech. Engrg.,* 121(6), 457–465.

Yang, Z., Li, Q., Horazdovsky, J., Hulsey, J. L., and Marx, E. E. (2017). "Performance and design of laterally loaded piles in frozen ground." *Journal of Geotechnical and Geoenvironmental Engineering*, 143 (5),http://dx.doi.org/10.1061/(ASCE)GT.1943-5606.0001642, 06016031.

Zhang, Q-Q., Zhang, Z-M., and He, J-Y. (2010). "A simplified approach for settlement analysis of single pile and pile groups considering interaction between identical piles in multilayered soils." *Computers and Geotechnics.* 37(7-8): 969–976.

9. LATERAL LOAD TRANSFER OF DRILLED SHAFT FOUNDATIONS WITH AND WITHOUT STEEL CASING AND HIGH-STRENGTH REINFORCEMENT

Authors:

Qiang Li , Armin W. Stuedlein , and Antonio Marinucci

Journal:

To be submitted to: Journal of Geotechnical and Geoenvironmental Engineering

9.1 Abstract

The amount of steel reinforcement in drilled shaft foundations has increased over the past several decades to account for anticipated lateral loads and the associated seismically-induced flexural demands. Increased reinforcement may lead to increased possibilities of anomalies within shafts due to the increased difficulty for concrete to flow through reduced clearance between the reinforcement. High-strength steel reinforcement and permanent steel casing may be used to mitigate the concreting concern. However, the comparison of lateral load transfer between drilled shafts with and without permanent steel casing and high-strength reinforcement has not been previously investigated, raising questions regarding the suitability of existing analytical approaches for the evaluation of lateral load transfer. This study presents the full-scale lateral response of drilled shaft foundations constructed with and without steel casing, and with high strength reinforcement. The lateral loading performance of cased shaft without internal reinforcement exhibited similar characteristics to the cased shaft with internal reinforcement. Similar lateral loading performance between the uncased shafts with mild and high-strength reinforcement was also observed. It indicates that the high-strength reinforcement can be used without detriment to the lateral performance of drilled shafts. Significant differences between the soil reaction-displacement (*p*-*y*) curves back-calculated for the cased and uncased shafts with the same nominal diameter were observed, indicating non-negligible effects of soil-foundation interface and diameter on the back-calculated *p*-*y* curves.

9.2 Introduction

Drilled shaft foundations provide significant structural and geotechnical resistance for support of bridges, buildings, and other civil infrastructure subjected to lateral loads.

Owing to the improved understanding of seismic hazards, the amount of steel reinforcement used in drilled shaft construction has increased over the past several decades. However, the greater steel area can result in reduced clearance between longitudinal and transverse reinforcement such that concrete has increased difficulty in flowing through the reinforcement cage and therefore increased likelihood for voids and defects within the shaft. The use of high-strength reinforcement steel, including multi-functional hollow bar, can reduce the congestion of the reinforcement cage and mitigate some of the concreting concerns associated with reinforced concrete (RC). Moreover, the use of permanent steel casing can provide significant increase of deformation and flexural capacity of the foundation element (Roeder et al. 1999; Roeder et al. 2010; and Roeder and Lehman 2012), which can lead to a decrease in the amount, or the outright elimination, of internal reinforcement. Due to their beneficial characteristics, drilled shafts with permanent steel casing, which are also known as reinforced concrete-filled steel-pipe piles and concrete-filled tubes (CFT), have been used by the Washington, California, and Alaska Departments of Transportation (e.g., Gebman et al. 2006; Roeder et al. 2010; Li and Yang 2017; and Yang et al. 2017).

The yield strength, f_y, of steel generally used for the internal reinforcement of drilled shafts ranges from 280 MPa to 420 MPa (40 to 60 ksi; Brown et al. 2010). ACI 318-14 (ACI 2014) generally limits f_y to 550 MPa (80 ksi) and 690 MPa (100 ksi) for the longitudinal and transverse reinforcement, respectively. It is noted that ACI (2014) limits the magnitude of f_y, used in design only; it does not exclude the use of higher grades of steel. These design limits were developed in consideration of the strain developed in the concrete and to limit crack development and width under service loads. For a beam or column, use of high-strength rebar may increase the structural performance. Hassan et al. (2008) conducted tests on six large-size reinforced concrete beams with Grade 60 (f_y = 420 MPa) and high-strength steel microcomposite multistructural formable (MMFX) steel (f_y = 827 MPa) under the three-point bending configuration. Hassan et al. (2008) found that the beams with high-strength steel exhibited up to 80% greater shear strength with 40% less area of higher-strength steel. Trejo et al. (2014) and Barbosa et al. (2015) studied the seismic performance of 0.6-m (24-inch) diameter circular reinforced concrete bridge columns and found that columns using Grade 80 reinforcement exhibited similar resistance and displacement ductility compared to those using Grade 60. However, similar tests of drilled shaft foundations constructed with high-strength internal reinforcement have not been performed and questions regarding the ductility of these members remain.

A number of lateral load transfer studies have been conducted on drilled shafts with or without permanent casing (e.g., Welch and Reese 1972; Bierschwale et al. 1981; Mayne et al. 1992; Wallace et al. 2001; Yang et al. 2012; Khalili-Tehrani et al. 2014). However, the comparison of lateral load transfer between the drilled shafts with and without permanent casing at the same site and soil conditions have not been previously reported in the literature.

The objective of this chapter is to study the effect of high-strength steel reinforcement, permanent steel casing, and steel casing without internal reinforcement on the lateral performance of full-scale drilled shaft foundations and to evaluate the appropriateness of existing load transfer models. Four instrumented drilled shafts with 0.9 m (36 in) nominal diameter and 18.3 m (60 ft) embedded length were constructed at the geotechnical engineering field research site (GEFRS) on the Oregon State University (OSU) campus in

Corvallis, Oregon. Two of the test shafts were constructed without steel casing, and two test shafts were constructed with full-length permanent steel casing. First, the subsurface conditions at the test site and the experimental setup, including the instrumentation program, are described. Then, the results of the lateral loading tests, including the performance at the head of the shaft, the lateral displacement profiles, and the back-calculated curvature, moment, and soil reaction-displacement (*p*-*y*) curves, are compared. Back-calculated *p*-*y* curves for each shaft are compared and used, along with widely-available *p*-*y* curve models, to simulate the lateral response of each shaft to form a basis for the evaluation of model suitability and differences in interface friction.

9.3 Overview of the Lateral Loading Tests

The geotechnical explorations, stratigraphy, and corresponding subsurface conditions for the test site, and specifically the location of the test shafts are presented in Chapter 4. Figure 4-9 shows the test site with exploration plan and four test shafts. The lateral loading test setup, including the test shafts configuration and instrumentation and loading protocol, is discussed in Chapter 7.

During the loading tests, gaps developed behind the shafts and the soil at the ground surface heaved and cracked in front of the shafts to form a radial cracking pattern in front of the shafts that indicated the formation of passive wedges. Figure 9-1 and Figure 9-2 show the cracks, gaps, and ground heaving at the end of the loading tests for uncased and cased shafts, respectively, which may be interpreted using the 0.3 m (1 ft) by 0.3 m (1 ft) spaced grid. Table 9-1 summarizes the displacement at ground level, y_{gl}, the approximate maximum gap width, w_{gap}, the maximum distance of cracking emanating from the front and edges of the shaft, $d_{c,f}$ and $d_{c,s}$, respectively, and y_h. Comparison of y_{gl} from the inclinometers to w_{gap} indicates similarity in magnitudes. Based on the distance of crack propagation, CIR appeared mobilized a larger volume of soil during the loading test as compared to the uncased shafts, attributed to deeper extent of load transfer; this is confirmed in the lateral displacement profiles described subsequently. Owing to the use of a slightly larger auger and the development of larger gaps between the shaft from depths of 3 to 8 m (9.8 to 26.5 ft) (see Chapter 7), CNIR produced less surface expression of mobilized soil volume as compared to CIR.

Table 9-1. Comparison of the displacement at ground level, y_{gl}, the approximate maximum gap width, w_{gap}, the maximum distance of cracking emanating from the front and edges of the shaft, $d_{c,f}$ and $d_{c,s}$, respectively, for lateral head displacement, y_h, of about 200 mm (8 in).

Test Shaft	y_h mm (in)	y_{gl} mm (in)	Approximate w_{gap}, mm (in)	$d_{c,f}$ m (ft)	$d_{c,s}$ m (ft)
MIR	183 (7.2)	142 (5.6)	150 (6.0)	1.5 (5)	1.2 (4)
HSIR	205 (8.1)	152 (6.0)	165 (6.5)	1.8 (6)	1.2 (4)
CIR	213 (8.4)	183 (7.2)	190 (7.5)	3.4 (11)	1.5 (5)
CNIR	205 (8.1)	186 (7.3)	190 (7.5)	1.8 (6)	1.5 (5)

Figure 9-1: Photos at the end of the loading tests showing: (a) crack patterns, (b) gap behind the shaft, and (c) side view of the shaft for MIR with applied displacement of 523 mm (20.6 in), and (d) crack patterns, (e) gap behind the shaft, and (f) side view of the shaft for HSIR with applied displacement of 305 mm (12.0 in).

Figure 9-2: Photos at the end of the loading tests for (a) crack patterns, (b) gap behind the shaft, and (c) side view of the shaft for CIR with applied displacement of 213 mm (8.4 in),, and (d) crack patterns, (e) gap behind the shaft, and (f) side view of the shaft for CNIR with applied displacement of 205 mm (8.1 in).

9.4 Section Analyses for the Test Shafts

In order to estimate the bending moment, M, distribution along the test shafts based on the measured section curvature, ϕ, through strain gages and inclinometers, section analyses, described by Stuedlein et al. (2015), were conducted to evaluate the moment-curvature (M-ϕ) relationship for each test shaft. Both the finite element platform OpenSees (McKenna et al. 2010) and the finite difference platform LPILE (Isenhower and Wang 2015) were used to perform section analyses and compare to the response observed during the loading tests.

For the OpenSees model, the steel material was simulated using the uniaxial bilinear material model, *Steel01* (Mazzoni et al. 2006), considering strain hardening and assuming similar tensile and compressive stress-strain responses (Figure 9-3a). The initial stiffness, E_{steel}, and strain-hardening ratio, b, were assumed equal to be 200 GPa (29,000 ksi) and 0.01, respectively. The actual geometry of the hollow bars were modeled directly in the OpenSees model. The concrete was simulated using the modified Kent and Park (Kent and Park 1971; Yassin 1994; Mazzoni et al. 2006) material model, *Concrete02*, considering linear tension softening. As shown in Figure 9-3b, the compressive strength of concrete, f_c, is calculated as:

$$f_c = f'_c \cdot \left[2\frac{\varepsilon_c}{\varepsilon_{c0}} - \left(\frac{\varepsilon_c}{\varepsilon_{c0}} \right)^2 \right] \text{ for } 0 \leq |\varepsilon_c| \leq |\varepsilon_{c0}| \tag{9.1a}$$

$$f_c = \frac{\left(\varepsilon_c - \varepsilon_{c0}\right) \cdot \left(f_{cu} - f'_c\right)}{\varepsilon_{cu} - \varepsilon_{c0}} + f'_c \text{ for } |\varepsilon_{c0}| \leq |\varepsilon_c| \leq |\varepsilon_{cu}| \tag{9.1b}$$

$$f_c = f_{cu} \text{ for } |\varepsilon_c| \geq |\varepsilon_{cu}| \tag{9.1c}$$

where f'_c = compressive strength, ε_c and ε_{c0} = compressive strain and strain at the maximum compressive strength, f_{cu} = crushing strength, and ε_{cu} = strain at crushing strength. The effect of confinement on the concrete in the cased shafts and the core concrete within the transverse reinforcement of the uncased shafts, as indicated by the shaded area in Figure 7-1a to Figure 7-1d, was incorporated into section analyses following the approach of Mander et al. (1988). The compressive strength, f'_c, of the unconfined concrete was determined on the day of each loading test as described above. The modulus of elasticity of concrete, E_c, was estimated through $4{,}700\sqrt{f'_c}$ (MPa) based on ACI 318-14 (ACI 2014). The ε_{c0} of unconfined concrete was assumed to be $2f'_c/E_c$ in the modified Kent and Park material model. The parameters of f_{cu}, and ε_{cu} were assumed to equal $0.85f'_c$ and 0.38%, respectively, for unconfined concrete (Hognestad 1951). For the confined concrete, the parameters f'_c, ε_{c0}, f_{cu} and ε_{cu} were determined using Mander et al. (1988). The tensile strength, f_t, for both confined and unconfined concrete, was assumed equal to $0.33\sqrt{f'_c}$ (MPa) (e.g., Vecchio and Collins 1986). The tension softening stiffness, E_{ts}, for both the confined and unconfined concrete was assumed equal to f_t/ε_{c0} (e.g., Barbosa 2011; Elgamal et al. 2014). However, the use of $E_{ts} = 10f_t/\varepsilon_{c0}$ appears to better capture the measured M-ϕ relationships (Figure 9-4b), particularly for the uncased shafts at larger curvature. The concrete parameters used in the OpenSees model are summarized in Table 9-2.

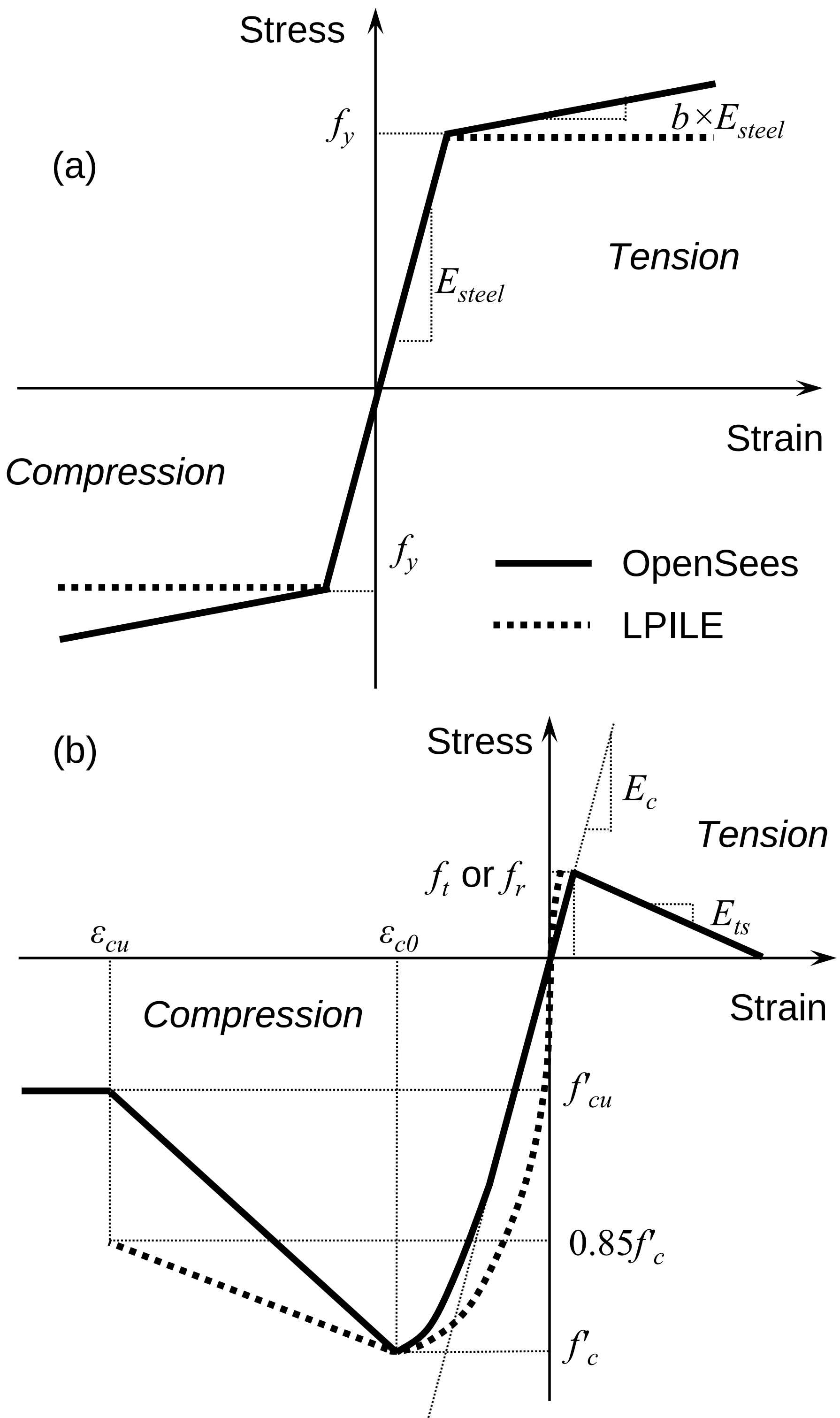

Figure 9-3: Stress-strain relationship of (a) concrete and (b) steel used in the OpenSees and LPILE models.

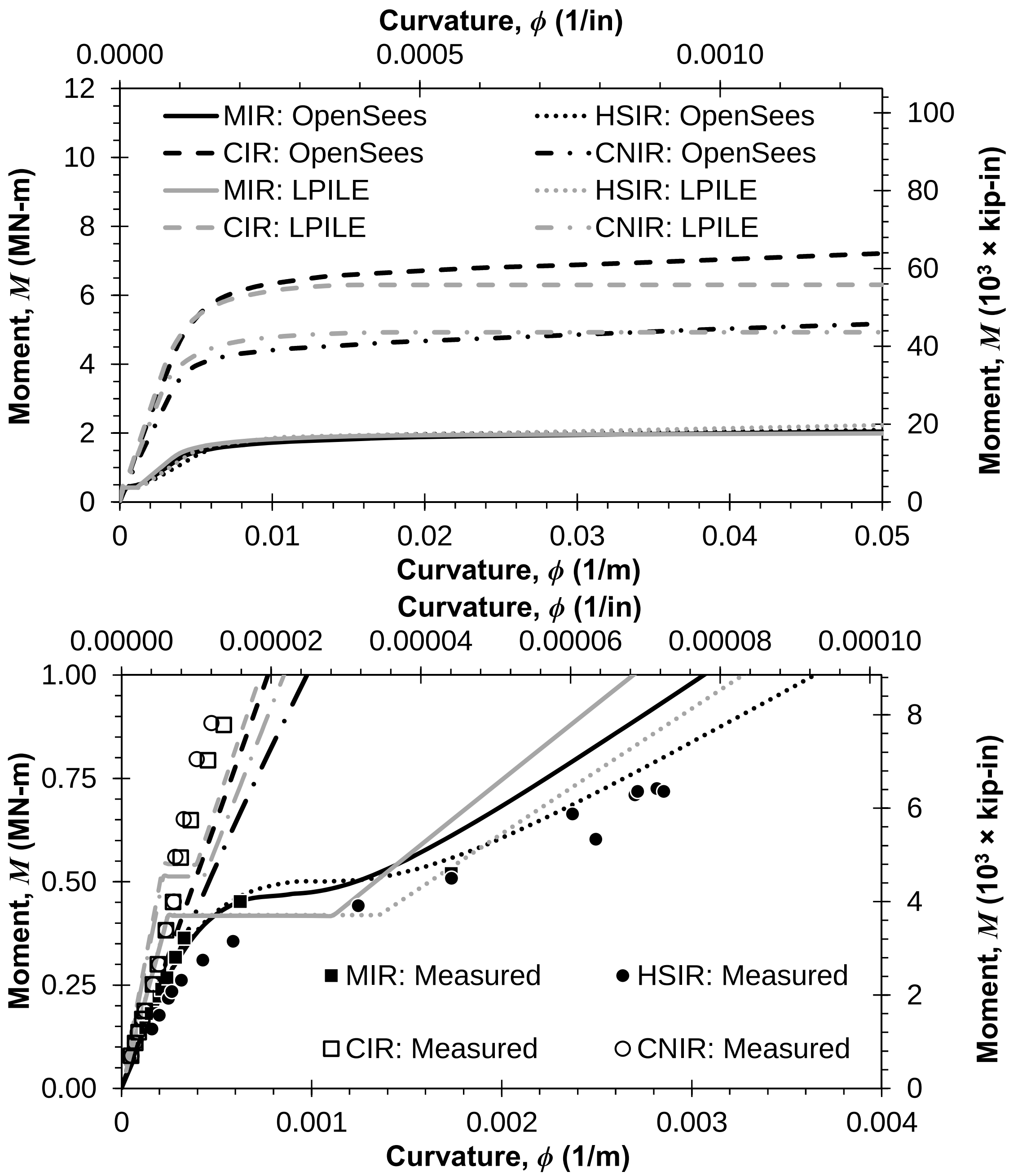

Figure 9-4: Moment-curvature relationships for the test shafts section at the ground level, including (a) the comparison of calculated relationships using OpenSees and LPILE, and (b) comparison of the calculated and measured relationships.

The stress-strain model of concrete and steel implemented in LPILE is slightly different to the OpenSees *Concrete02* model. The LPILE model assumes an elastic-perfectly plastic constitutive response for steel (Figure 9-3a). Since the hollow bars in HSIR could not be modeled in LPILE, solid bars with similar steel area were used, which reduces the local moment of inertia and corresponding flexural rigidity. The concrete stress-strain relationship used in LPILE is shown in Figure 9-3b, and can be calculated through Eqs. (9.1a) and (9.1b) assuming $\varepsilon_{c0} = 1.7f'_c/E_c$, $\varepsilon_{cu} = 0.38\%$, $f_{cu} = 0.85f'_c$, and $f_c = 0$ when $|\varepsilon_c| \geq |\varepsilon_{cu}|$. The modulus of rupture, f_r, was assumed to equal $0.62\sqrt{f'_c}$ (MPa) with the corresponding tensile strain, ε_t, calculated by:

$$\varepsilon_t = -\varepsilon_{c0}\left(1-\sqrt{1+\frac{f_r}{f'_c}}\right) \tag{9.2}$$

The concrete model in LPILE specifies a larger initial compressive stiffness for a given f'_c through the use of $\varepsilon_{c0} = 1.7f'_c/E_c$ as compared to $\varepsilon_{c0} = 2f'_c/E_c$ for OpenSees model. In addition, $f_r = 0.62\sqrt{f'_c}$ (MPa) is used in the LPILE model, which is larger than $f_t = 0.33\sqrt{f'_c}$ (MPa) used in the OpenSees model. The tension softening and the effect of confinement on the concrete are not considered in LPILE.

Table 9-2 Concrete model parameters used to simulate the test shafts in OpenSees.

Test Shaft	Confinement	f'_c, MPa (ksi)	ε_{c0}, %	f_{cu}, MPa (ksi)	ε_{cu}, %	f_t, MPa (ksi)	E_{ts}, GPa (ksi)
MIR	Unconfined, Cover	68.9 (10.1)	0.354	59 (8.5)	0.380	2.76 (0.40)	0.78 (113)
	Confined, Core	86.7 (12.6)	0.807	82.9 (12.0)	1.354	2.76 (0.40)	0.78 (113)
HSIR	Unconfined, Cover	72.1 (10.5)	0.361	61.3 (8.9)	0.380	2.82 (0.77)	0.78 (113)
	Confined, Core	88.9 (12.9)	0.782	84.7 (12.3)	1.314	2.82 (0.77)	0.78 (113)
CIR	Confined	88.1 (12.8)	0.952	72.9 (10.6)	3.407	2.68 (0.39)	0.78 (113)
CNIR	Confined	87.0 (12.6)	0.953	71.9 (10.4)	3.443	2.66 (0.39)	0.78 (113)

Figure 9-4 shows the calculated and measured M-ϕ relationships of the test shafts at the ground surface, corresponding to the location where measuring the M-ϕ relationship directly was possible. The general section performance of MIR and HSIR is similar for the initial and large-curvature responses of the shafts. However, the flexural rigidity of MIR was slightly larger than that of HSIR for the transition from the pre-cracking to post-initial cracking regime, stemming from the larger steel area used with MIR as compared to HSIR. The initial measured M-ϕ response for both the uncased and cased shafts agree quite well with the results estimated using OpenSees (e.g., $\phi \lesssim 2.5\text{E}^{-4}\ \text{m}^{-1}$), whereas the LPILE models over-estimate the flexural stiffness. The OpenSees model accurately captured the smooth M-ϕ transition following initial concrete cracking for MIR, but did not appear to model the transition for HSIR as accurately. However, at larger curvatures, the effect of smaller steel area for HSIR was compensated by the higher yield strength, the use of hollow bars (with larger moment of inertia), and the slightly higher compressive concrete strength.

No evidence for concrete cracking was observed in the cased shafts during testing, nor was it computed in the OpenSees model. Rather, the cased shafts appear to remain elastic or slightly harden for the range in curvature induced during the loading tests. Both the OpenSees and LPILE models indicate the significant increase in flexural rigidity and moment capacity for the cased shafts as compared to the uncased shafts, owing to the greater steel area with the use of steel casing and greater confinement of the concrete (Roeder et al. 1999; Roeder et al. 2010; Roeder and Lehman 2012) as considered in OpenSees model. The moment capacity of CIR is approximately 40% larger than that of CNIR due to the use of internal reinforcement based on the OpenSees model. Using MIR as a baseline for comparison, the increase in moment capacity for HISR, CNIR, and CIR is approximately 2, 150, and 250%, respectively, at a curvature of 0.05 m^{-1} (0.00127 in^{-1}) based on the OpenSees model.

In general, the M-ϕ relationships computed using LPILE are similar to those from OpenSees; however, the initial response for each shaft from LPILE are larger than that from the OpenSees models, which is attributed to the larger initial compressive stiffness and tensile strength of the LPILE concrete model. The effect of initial concrete cracking calculated from LPILE is significant for each shaft, a result of neglecting the tension softening of the concrete. Again, no cracking was observed in the cased shafts for curvatures induced, suggesting room for improvement in the concrete models available in LPILE. The slight differences between the LPILE and OpenSees models at large curvatures is mainly caused by differences in the stress-strain relationships assumed for the steel reinforcements; LPILE does not consider strain hardening.

Since the M-ϕ relationship obtained using OpenSees exhibited better agreement with the measured responses as compared to the LPILE models, the OpenSees models were used to estimate the moment profiles for each shaft, as described subsequently. To account for the effect of the variation of the as-built diameter along the uncased shafts (Figure 7-6b) on the back-calculated moment and p-y relationships, a series of section analyses were conducted using the as-built diameter at each instrumented elevation. Then, the depth-specific M-ϕ relationship based on the OpenSees model was used to estimate the moment at each instrumented elevation from the curvature obtained from the ESGs or inclinometers, as appropriate at a given strain level.

9.5 Load-Displacement Response at the Shaft Head

The global lateral response at each shaft head was measured using load cells and string-potentiometers at the resultant loading point (Figure 7-8). Table 7-3 summarizes the imposed and measured displacements, y_h, and shear force, V_h, at the head of each test shaft. At the end of the lateral loading tests, the maximum displacement for MIR and HSIR was 523 and 305 mm (20.6 and 12.0 in), respectively, with a developed shear force, V_h, of 920 kN (207 kip). In comparison, the V_h for CIR and CNIR was 1,540 kN (346 kip) with corresponding y_h of just 213 and 205 mm (8.4 and 8.1 in), respectively.

Figure 9-5 shows the measured lateral load-lateral displacement response at the head of the shaft. The lateral system resistance of the uncased shafts was fully-mobilized at an applied load of approximately 890 kN (200 kips) and at applied displacement of approximately 150 mm (6 in). The shafts exhibited a similar lateral response to applied displacements of approximately 190 mm (7.5 in), with slight differences at small displacements. The initial response for MIR was slightly stiffer than HSIR, consistent with its slightly larger diameter (Figure 7-8) and stiffer M-ϕ relationship described previously. Towards the end of the loading test (discussed below), MIR exhibited larger lateral displacement than HSIR at a given lateral load, possibly due to: (1) the slightly higher moment capacity of HSIR for $\phi \geq 0.2$ m^{-1}(Figure 9-4a), and (2) inherent variability of the soil stiffness and strength.

The lateral resistance of the cased shafts was not fully–mobilized during the loading tests. Although the moment capacity of CIR was approximately 40% larger than that of CNIR, the differences in capacity was inconsequential for the displacements imposed. Further, CNIR appeared slightly stiffer than CIR, perhaps due to variability in the soil layer thicknesses and consistency, or due to measurement error. However, the differences are minor and the exhibited responses can be assumed equal for practical purposes.

9.6 Lateral Displacement Profiles

In order to understand the lateral load transfer for test shafts, the lateral responses, including the profiles of lateral displacement, moment, and soil reaction, were investigated. The distribution of lateral displacement and soil reaction along the shafts were also used to evaluate the lateral soil reaction-displacement relationships (p-y curves) at various depths.

For HSIR and CIR, the lateral displacements, $y(z)$, were calculated by integrating the slope, $s(z)$, along the shaft and obtained directly using the GEODAQ data acquisition system. For MIR and CNIR using the Type II inclinometer, the $s(z)$ was recorded by tilt sensors from the loading point to the depth of 5.3 m (17.5 ft). A seventh order polynomial was fit to the discrete slope measurements along the shaft. Since the Type II inclinometer did not provide measurements below 5.3 m (17.5 ft; Figure 7-1e), it was assumed that the slope was zero based on the zero curvature measured from the ESGs. Then, the displacement profiles for MIR and CNIR were computed by integration of the rotation polynomial function along the shaft using:

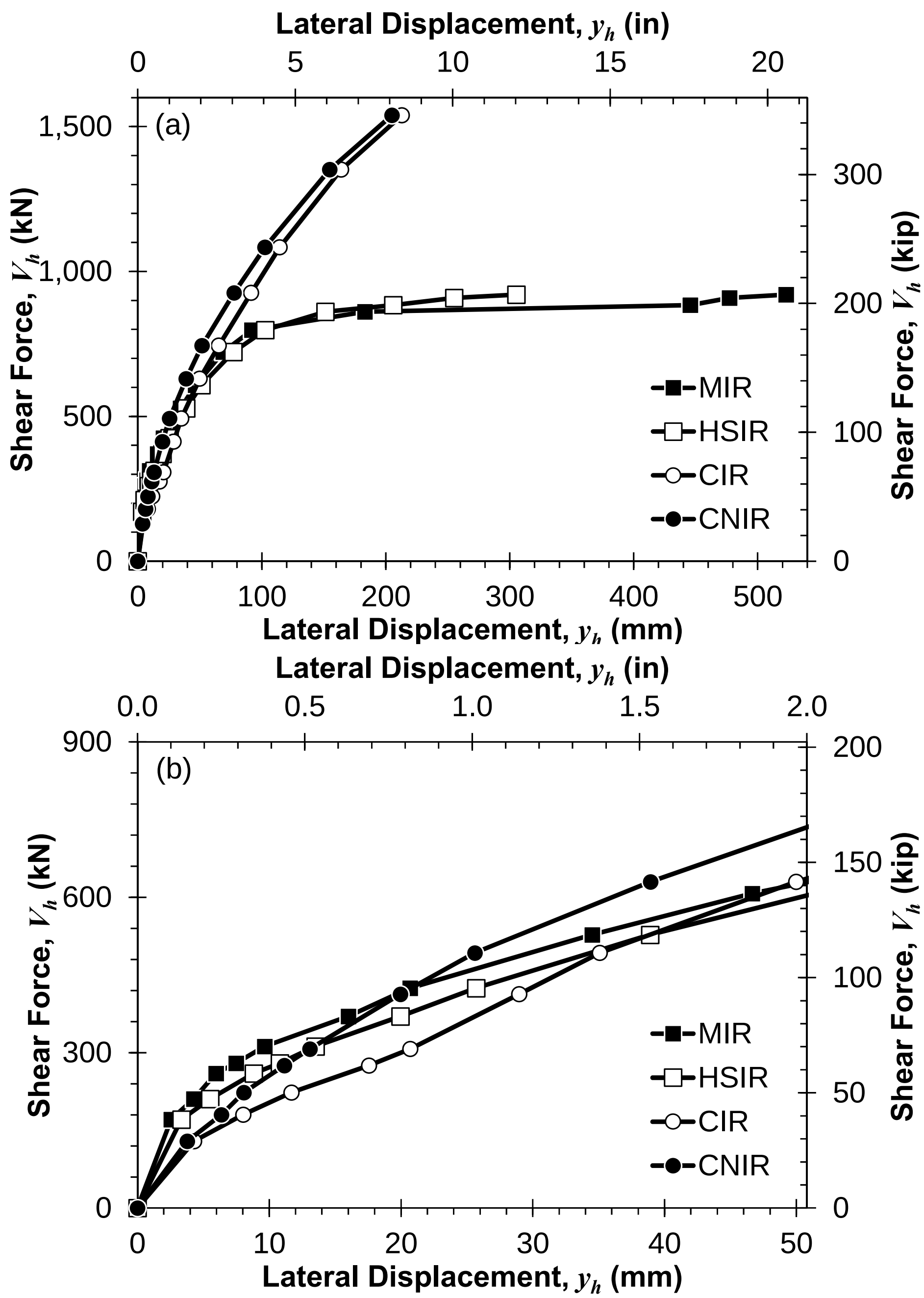

Figure 9-5: Load-displacement response at the shaft head for the test shafts (a) during the loading tests and (b) with lateral displacement up to 50 mm.

$$y(z) = \int s(z)\,\mathrm{d}\,z \tag{9.3}$$

Figure 9-6 presents the lateral displacement profile for each test shaft at similar lateral load magnitudes to aid comparison between shafts of similar and different flexural rigidities. The lateral displacement profile for each shaft was similar for relatively small lateral loads (e.g., 275 to 280 kN, or 62 to 63 kips). However, differences between the shafts emerged with increases in lateral load. For example, for V_h = 920 to 925 kN (approximately 208 kips) the displacement at the ground surface for MIR, HSIR, CIR, and CNIR was approximately 411, 229, 79, and 75 mm (16.2, 9.0, 3.1, and 2.9 in), respectively.

The maximum depth of the mobilized soil-foundation displacement for the cased shafts at the highest load is approximately 9.0 m (30 ft), or $10D_n$ (D_n = nominal diameter), whereas it is approximately 3.7 m (12 ft), or $4D_n$, for the uncased shafts. The significant differences in the depth of soil-foundation displacement are due to the differences in the flexural rigidity of the shafts; the significantly larger flexural rigidity of the cased shafts allows deeper soils to participate in the system response.

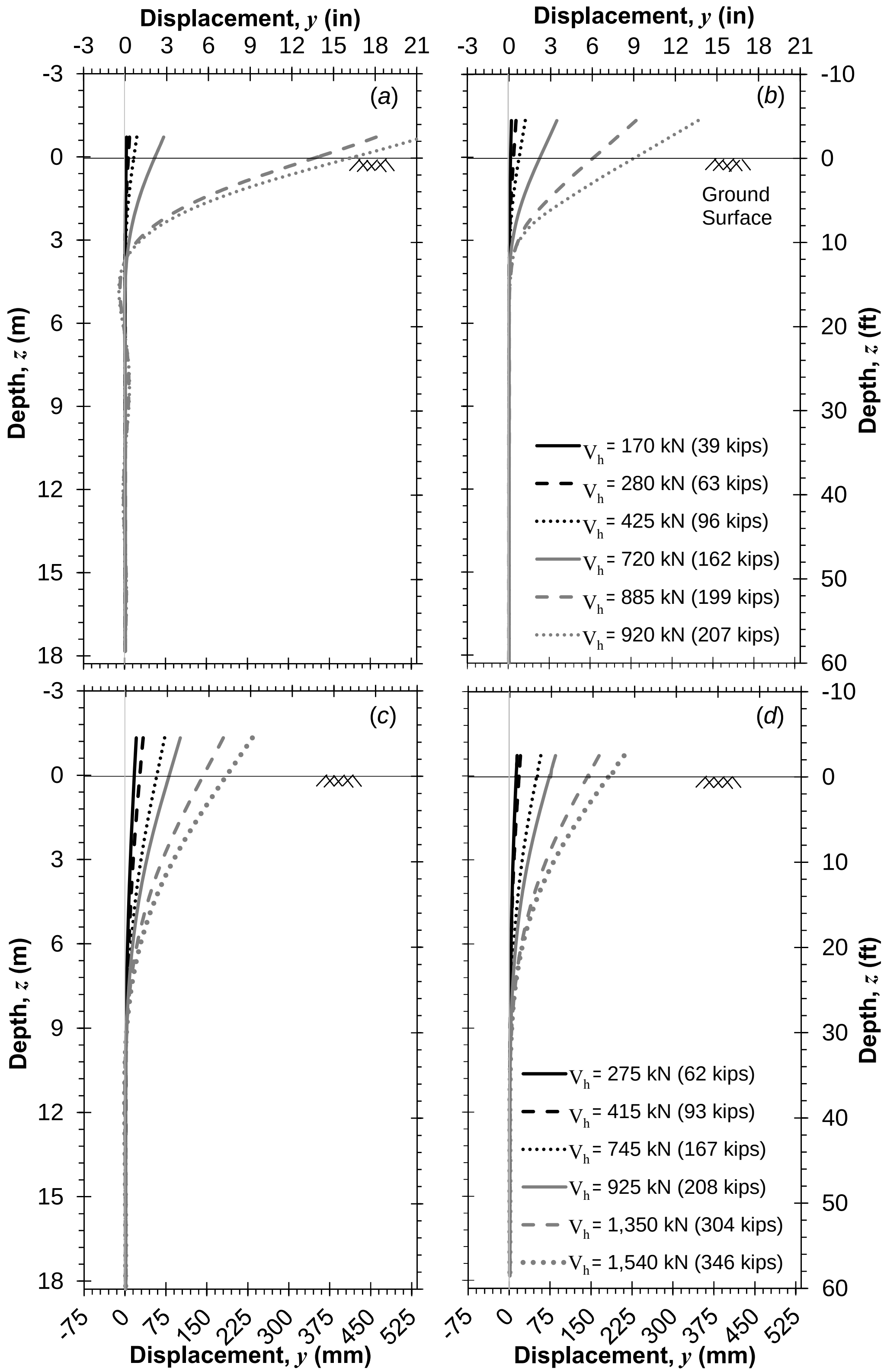

Figure 9-6: Selected lateral deflection profiles for (a) MIR, (b) HSIR, (c) CIR, and (d) CNIR.

9.7 Lateral Soil Reaction-Displacement Relationships (*p-y* curves)

The lateral displacement, $y(z)$, as shown in Figure 9-6, were used to directly construct the lateral resistance-lateral displacement, or p-y, curves. The lateral soil reaction, $p(z)$, was back-calculated using beam theory by double differentiating the bending moment, $M(z)$, along the test shafts with respect to depth, z, using:

$$p(z) = \frac{d^2}{dz^2} M(z) \tag{9.4}$$

The bending moment at depth z, $M(z)$, is a function of section curvature, $\phi(z)$, and nonlinear flexural rigidity, EI, given by:

$$M(z) = EI \cdot \phi(z) \tag{9.5}$$

The moment profile was obtained based on the nonlinear M-ϕ relationship, as shown in Figure 9-4. The variation of the as-built diameter along the uncased shafts (Figure 7-6) was considered in the development of the depth-dependent M-ϕ relationship. Then, a sixth order polynomial function was used to fit the discrete M at the instrumented level for each test shaft.

The $\phi(z)$ was computed using the measured axial strain, $\varepsilon(z)$, from the ESGs by:

$$\phi(z) = \frac{\varepsilon_T(z) - \varepsilon_C(z)}{h} \tag{9.6}$$

or the slope, $s(z)$, from inclinometers by:

$$\phi(z) = \frac{d}{dz} s(z) \tag{9.7}$$

where $\varepsilon_T(z)$ and $\varepsilon_C(z)$ = measured tensile and compressive strain at depth z, h = horizontal distance between the strain gauges. Seventh order polynomial functions were used to fit the measured slope along the test shafts to perform the numerical differentiation.

The evaluation of $p(z)$ is sensitive to the quality (and quantity) of the discrete measurements along the shaft because of the use of curve fitting techniques and numerical differentiation. The Type II inclinometers (used with MIR and CNIR) provided $s(z)$ from the loading point to the depth of 5.3 m (17.5 ft) and spaced at 0.6 m (2 ft), producing a total of 11 measurements. Thus, the quality of the fitting and numerical differentiation may lead to unreasonable estimation of $p(z)$. Therefore, only the measurements from the ESGs were used to estimate $\phi(z)$ and $p(z)$ for MIR and CNIR, whereas both the measurements from the ESGs and Type I inclinometer were used for HSIR and CIR.

The $\phi(z)$ calculated from the ESGs were considered more reliable than those calculated from the inclinometer measurements for the initial stages of loading. However, as the loading and displacement increased, the ESG measurements became unreliable as the strains in the concrete either exceeded the strain range of the gage or the concrete began to crack in proximity to the gage from the induced flexural strains. Taking CIR as an example as shown in Figure 9-7, the profiles of curvature, displacement, moment, and soil reaction at selected lateral loads are compared. When the loads were smaller than 415 kN (93 kips), the profiles of obtained using the ESG and inclinometer measurements agree fairly well. Measurements of $\phi(z)$ from ESGs (Figure 9-7b) became increasingly unreliable for the estimation of $p(z)$ with increasing loads. The $\phi(z)$ measured from ESGs below a depth of about 14.9 m (49 ft) was negligible throughout the loading tests, as expected, whereas considerable fluctuations in the derived $\phi(z)$ were produced by the fit to the inclinometer-based slope. Therefore, the comparisons that follow below use the $p(z)$ based on the ESGs to construct *p*-*y* curves at small lateral displacements and when considered reliable at a given depth, whereas the $p(z)$ derived from the high resolution inclinometer was used for large lateral displacements. Curvature derived from the ESG measurements were used to construct $p(z)$ for all of the near-zero, deeper instrumented sections.

Figure 9-8 compares the *p*-*y* curves at selected depths for the uncased and cased shafts from the ground surface to a depth of $3D_n$ (i.e., 2.7 m or 9 ft) and 7 D_n (i.e., 6.4 m or 21 ft), respectively. The *p*-*y* curves for the two cased shafts are similar to one another, as are those for the uncased shafts at each depth. However, the soil reaction for the uncased shafts are significantly larger than those for cased shafts at a given soil displacement, as shown in the Figure 9-8a through Figure 9-8d. This may be attributed to: (1) the improved roughness of the soil-concrete interface associated with the uncased shafts as compared to the soil-steel interface (Lam and Martin 1986), which provides a larger counteracting moment in the direction of load due to axial shaft resistance, and (2) the as-built diameter of the uncased shafts are significantly larger than those of the cased shafts (Figure 7-6b), which also leads to a larger unit soil resistance (Lam and Martin 1986; Lam 2013). Furthermore, the uncased shafts exhibit a significantly large initial stiffness in the *p*-*y* response, demonstrating excellent coupling with the adjacent soil, perhaps in part due to the stiffening of the surrounding soil during water migration associated with the hydration of the concrete.

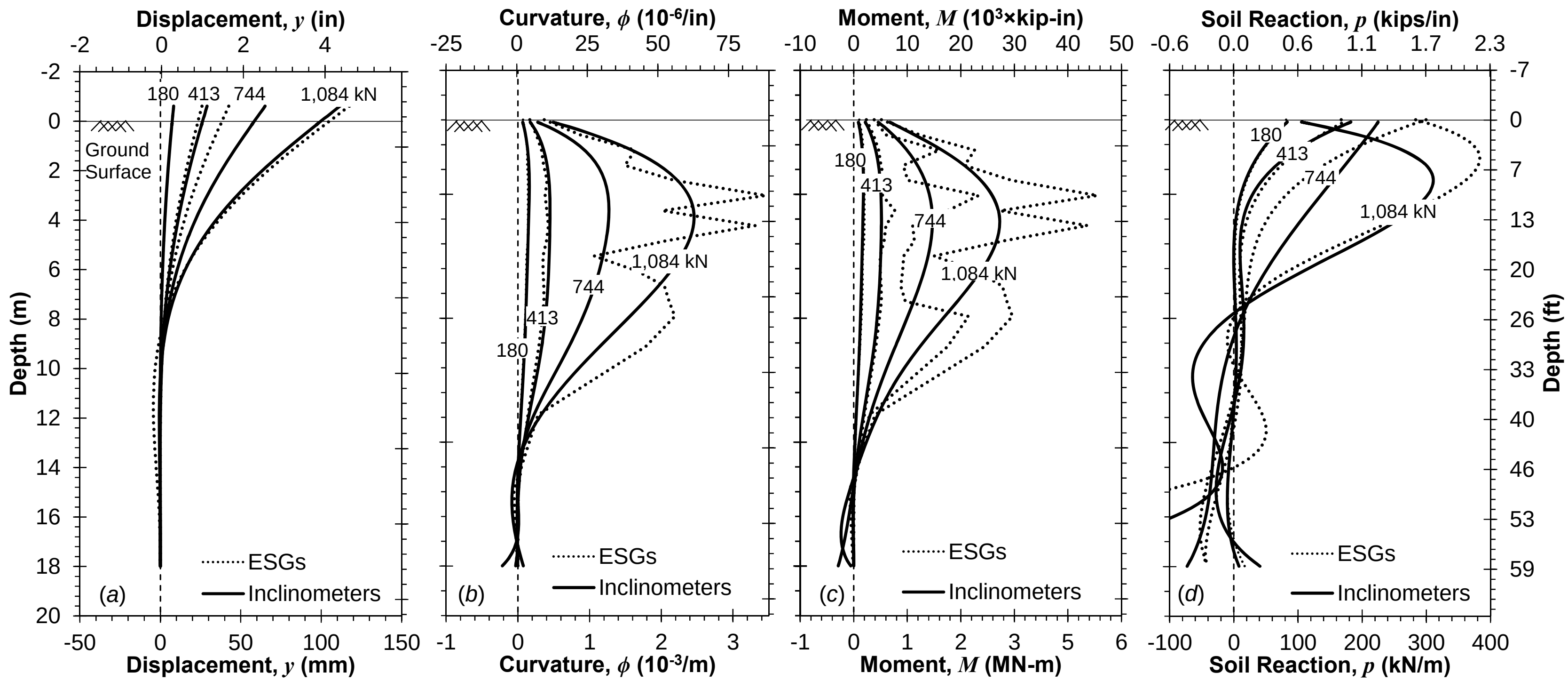

Figure 9-7: Comparison of selected profiles of (a) displacement, (b) curvature, (c) moment, and (d) soil reaction obtained using the measurements from ESGs and the GEODAQ in-place inclinometer for CIR. Note: markers indicates the directly measured data at certain depths, which were not derived using numerical integration or differentiation.

Softening in the near-surface *p-y* curves was noted, similar to the *p-y* curves obtained by Nimityongskul (2010), derived from piling tested 30 m (98 ft) away from the present test site, as well as from loading tests on plastic soils reported by others (e.g., Matlock 1970; Reese and Welch 1975). For the cased shafts, the initial stiffness of the *p-y* curves were similar to one another above the depths of 1.2 m (6 ft). However, the initial response transition to a concave-up shape from the depths of 2.7 to 6.4 m (9 to 21 ft), due to the loss of soil-casing coupling and gaps that had formed as observed in Figure 7-6b and in the axial loading response of these shafts described in Chapter 8.

9.8 Assessment of Back-Calculated *p-y* Curves

The site-specific *p-y* curves back-calculated for each shaft were used to compare with the commonly-available (termed "general", herein) *p-y* curve models, which may not be universally suitable for deep foundations with different diameters, installation methods (e.g., drilled shafts versus driven piles) or types of soil-structure interface (e.g., cased versus uncased drilled shafts). In addition, the sufficiency of a selected, commonly-available software package LPILE (Isenhower and Wang 2015) was evaluated using the back-calculated *p-y* curves and the M-ϕ response provided by the section analysis available in LPILE to predict the lateral response of each test shaft. An effort was also made to compare the test results to the lateral responses simulated using LPILE with the back-calculated and the general *p-y* curve models available in LPILE.

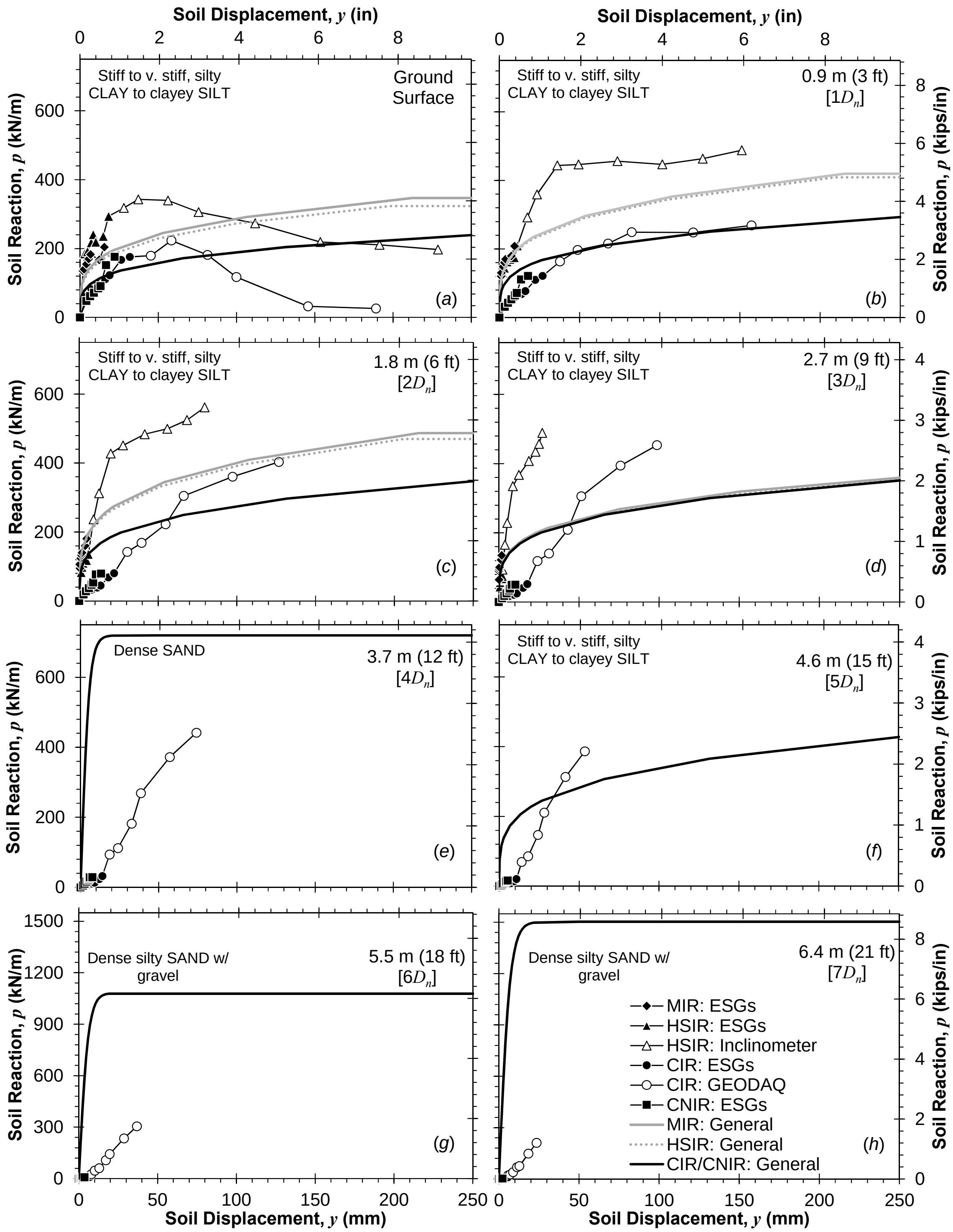

Figure 9-8: Back-calculated *p-y* curves for all of the test shafts at (a) ground surface, (b) 0.9 m (3 ft), (c) 1.8 m (6 ft), and (d) 2.7 m (9 ft), and for only the cased test shafts at (e) 3.7 m (12 ft), (f) 4.6 m (15 ft), (g) 5.5 m (18 ft), and (h) 6.4 m (21 ft).

9.8.1 Comparison of the Back-Calculated and the General p-y Curves

The *stiff clay without free water* (Welch and Reese 1972; Reese and Welch 1975) and *API Sand* models (Reese et al. 1974; API 2010) have been proposed and are generally used for plastic and granular soils, respectively. To evaluate the suitability of these general *p*-*y* curve models for the cased and uncased shafts, comparisons were made between the back-calculated and the general *p*-*y* curves.

The *p*-*y* curve models used for the uncased and cased shafts are summarized in Table 9-3 and Table 9-4, respectively. The effective unit weight, γ', of each soil layer was obtained based on the laboratory results described by Dickenson and Haines. (2006) and Nimityongskul (2010). The undrained shear strength, s_u, for the plastic soil layers was correlated to CPT cone-tip resistance, q_c, using Eq. (8.27). The friction angle of the granular soil layers was estimated using correlations to CPT cone-tip resistance (Kulhawy and Mayne 1990). Explorations SCPT-2, SCPT-3, CPT-4, and SCPT-5 were used to estimate the necessary soil parameters for the available *p*-*y* curve models. Exploration CPT-4 and SCPT-5 were performed to a depth of approximately 12 m (40 ft) in between the test shafts one day after the loading tests in zone of soil not likely to be affected by the loading. Explorations SCPT-2 and -3 were conducted five months prior to the loading tests and were used for depths below 12 m (40 ft). Other parameters, including the strain corresponding to a stress of 50% of the peak soil strength of plastic soils, ε_{50}, and the coefficient of subgrade reaction, k, were selected based on recommendations provided in Isenhower and Wang (2015).

Table 9-3 Summary of selected soil models and corresponding *p-y* curve parameters used to simulate the uncased shafts in LPILE.

Soil Model	Depth m (ft)	γ' kN/m^3(pcf)	s_u kPa (psf)	ε_{50}	ϕ' deg	k, MN/m^3(pci)
Stiff Clay w/o Free Water	0 to 1.9 (0 to 6.3)	18.1 (115)	110 (2,275)	0.005	-	-
Stiff Clay w/o Free Water	1.9 to 3.4 (6.3 to 11.0)	8.3 (52.6)	65 (1,315)	0.007	-	-
API Sand	3.4 to 3.7 (11.0 to 12.0)	10.6 (67.6)	-	-	39	40 (150)
Stiff Clay w/o Free Water	3.7 to 5.0 (12.0 to 16.5)	8.3 (52.6)	60 (1,225)	0.007	-	-
API Sand	5.0 to 12.2 (16.5 to 40)	10.6 (67.6)	-	-	38	33 (120)
Stiff Clay w/o Free Water	12.2 to 18.3 (40.0 to 60.0)	7.5 (47.6)	290 (5,990)	0.004	-	-

Note: γ' = effective unit weight, s_u = undrained shear strength, ε_{50} = strain corresponding to a stress of 50% of the peak soil strength, ϕ'= friction angle, and k = coefficient of subgrade reaction.

Table 9-4 Summary of selected soil models and corresponding *p-y* curve parameters used to simulate the cased shafts in LPILE

Soil Model	Depth, m (ft)	γ' kN/m3 (pcf)	s_u kPa (psf)	ε_{50}	ϕ' deg	k, MN/m3 (pci)
Stiff Clay w/o Free Water	0 to2.0 (0 to 6.6)	18.1 (115)	85 (1,800)	0.007	-	-
Stiff Clay w/o Free Water	0 to 3.5 (6.6 to 11.5)	8.3 (52.6)	75 (1,515)	0.007	-	-
API Sand	3.5 to 3.8 (11.5 to 12.5)	10.6 (67.6)	-	-	40	42 (155)
Stiff Clay w/o Free Water	3.8 to 5.5 (12.5 to 18.0)	8.3 (52.6)	70 (1,420)	0.007	-	-
API Sand	5.5 to 18.3 (18.0 to 40)	10.6 (67.6)	-	-	39	40 (150)
Stiff Clay w/o Free Water	12.2 to 18.3 (40.0 to 60.0)	7.5 (47.6)	285 (5,930)	0.004	-	-

Figure 9-8 shows the comparison of the back-calculated and the general *p-y* curves at selected depths for the test shafts. The slight difference between the general *p-y* curves for MIR and HSIR are due to the variation of the diameter profile (Figure 7-6). Since the back-calculated *p-y* curves for MIR and HSIR are similar to one another, as are those for CIR and CNIR, the comparison was made quantitatively for HSIR and CIR. The mean bias (i.e., the ratio of the back-calculated and the general soil reaction, *p*) calculated at measured soil displacements at each instrumented depth, and the coefficient of variation (COV), of the sample biases are summarized in Table 9-5. The range of mean bias and COV for HSIR are 1.11 to 1.42 and 20% to 42%, respectively, for depths ranging from the ground surface to 2.7 m (9 ft), whereas for CIR these are 0.04 to 0.86 and 37% to 132%, respectively, for the depths ranging from the ground surface to 6.4 m (21 ft). The differences between the back-calculated and the general *p-y* curves stem from the different deep foundation diameters, installation methods, and types of soil-structure interface. For example, the stiff clay model without free water (Welch and Reese 1972; Reese and Welch 1975) was derived based on a 0.9-m (3-ft) diameter drilled shaft, which may not be appropriate for driven piles or cased drilled shafts.

Table 9-5 Accuracy of the general *p-y* curves at selected depths as compared to the observed *p-y* curves

Depth m (ft)	HSIR		CIR	
	Mean Bias	COV (%)	Mean Bias	COV (%)
0	1.32	29%	0.86	45%
0.9 (3)	1.25	20%	0.75	37%
1.8 (6)	1.11	38%	0.64	71%
2.7 (9)	1.42	54%	0.60	95%
3.7 (12)	-	-	0.17	122%
4.6 (15)	-	-	0.39	121%
5.5 (18)	-	-	0.07	132%
6.4 (21)	-	-	0.04	118%

9.8.2 Load-Displacement Response at the Shaft Head

The back-calculated and general *p-y* curve models were used to simulate the lateral responses of the shafts using LPILE in order to validated the LPILE model framework (by using the back-calculated *p-y* curves) and to evaluate the response when assuming that the generally-available curves are appropriate. For the case of validation, the *p-y* curves back-calculated from ground surface to the depth of $10D_n$ was used for the cased shafts, whereas the back-calculated *p-y* curves from ground surface to the depth of $4D_n$ was used for the uncased shafts, given the negligible response observed below $4\ D_n$. The general *p-y* curve models shown in Table 9-3 and Table 9-4 were used for the soil below these depths. It is noted here that the soil below these depths has little effect on the lateral response given the respective flexural rigidity and moment capacity of each shaft. The as-built diameter of the uncased shafts (Figure 7-6b) was accounted for the purposes of this comparison. Due to the lack of reliability of the inclinometer measurements and corresponding smaller range in displacement for the back-calculated *p-y* curves for MIR and CNIR (Figure 9-8), small lateral displacements were applied to the head of MIR and CNIR up to 35 and 19 mm (1.4 and 0.8 in), respectively, in the LPILE model using the back-calculated *p-y* curves for MIR and CNIR, respectively. To simulate the lateral response of MIR and CNIR at large lateral displacements with the LPILE model using the back-calculated *p-y* curves, the back-calculated *p-y* curves for HSIR and CIR with larger displacement range were used, respectively.

The lateral responses of each test shaft was also simulated using only general *p-y* curve models (Table 9-3 and Table 9-4) to evaluate the sufficiency of the general *p-y* curves available in LPILE. Comparisons of the measured and simulated lateral responses were made.

Figure 9-9 compares the measured load-displacement response at the head of each test shaft to those calculated using LPILE using the general and back-calculated *p-y* curves. The responses of the uncased shafts simulated using the back-calculated *p-y* curves agree well with the measured response at the lateral displacements up to about 25 mm (1 in). The simulation of the uncased shafts then diverges from the measured response to over-estimate the applied shear force, which may have resulted from the limitation of the polynomial fitting method used for the back-calculation following plastic hinging in the shaft. As shown in Figure 9-10e, the inclinometer-based slope measurements could not capture the large curvature at depths near the plastic hinge upon section yielding. The response of the cased shafts simulated using the back-calculated *p-y* curves agree well with the measured load-displacement response across all of the displacements simulated, indicating that LPILE can reproduce the observed response when providing back-calculated *p-y* curves. The under-prediction of the initial stiffness may be caused by the slight under-prediction of the M-ϕ relationships with OpenSees model (Figure 9-4), which were used to back-calculate the *p-y* curves.

The responses of the uncased shafts simulated using the general *p-y* curves agree well with the measured responses at the lateral displacements up to about 100 mm (4 in). At larger displacement, the simulation using general *p-y* curves over-predicts the shear force. For CIR, the general *p-y* curves over-predict the shear force at shaft head at given applied displacements. The simulated responses for CNIR using general *p-y* curves agree well with the observed responses at the lateral displacements up to about 150 mm (6 in). The general *p-y* curves appear to under-predict the lateral resistance of CNIR at larger displacement.

To facilitate the evaluation of the back-calculated and the general *p-y* curves, the bias of lateral load (i.e., the ratio of the observed and computed shear force at the shaft head) at each applied displacement was calculated and is summarized in Table 9-6. It indicates that both the back-calculated and the general *p-y* curves over-predict the lateral resistance at given displacements within the range of y_h considered. For the cased shafts, the back-calculated *p-y* curves under-predict the lateral resistance at given displacements within the range of y_h considered, whereas the general *p-y* curves over-predict the lateral resistance.

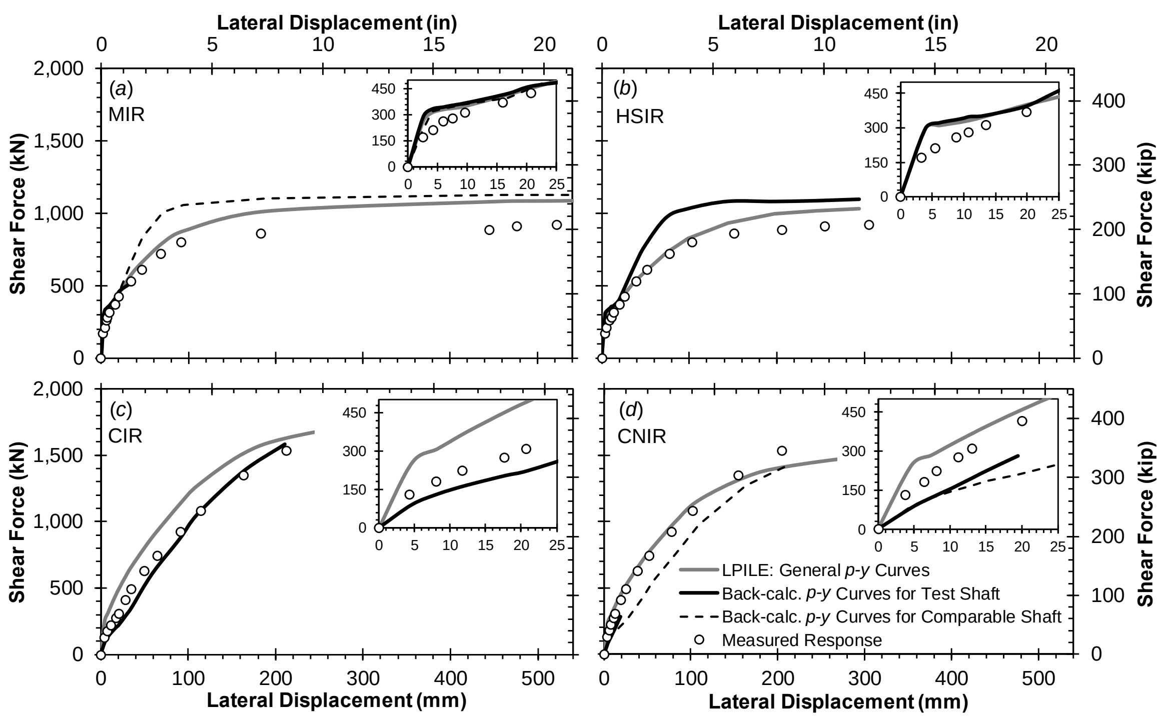

Figure 9-9: Comparison between the measured load-displacement response for the test shafts to the calculated response from LPILE model using general *p-y* curve models and back-calculated *p-y* curves for (a) MIR, (b) HSIR, (c) CIR, and (d) CNIR.

Table 9-6 Comparison of the measured load-displacement responses of the test shafts to the calculated responses using general and back-calculated *p-y* curves.

Test Shaft	Max. y_h considered, mm (in)	General *p-y* curves		Back-calculated *p-y* curves	
		Mean Bias	COV (%)	Mean Bias	COV (%)
MIR	0 to 35 (0 to 1.4)	0.82	13%	0.80	17%
HSIR	0 to 294 (0 to 11.6)	0.88	14%	0.79	12%
CIR	0 to 211 (0 to 8.3)	0.73	19%	1.24	14%
CNIR	0 to 19 (0 to 0.8)	0.72	19%	1.44	5%

9.8.3 Lateral Responses along the Shafts

Figure 9-10 and Figure 9-11 compare the measured and simulated responses of the tests shafts in terms of the depth-varying displacement, curvature, and moment to help evaluate the lateral load transfer simulated using the general and the back-calculated *p-y* curves. These figures present profiles for V_h = 170, 425, 884, and 920 kN (39, 96, 199, and 207 kip) for the uncased shafts, and V_h = 275, 415, 925, and 1,540 kN (62, 93, 208, and 346 kip) for the cased shafts. The corresponding measured y_h for each shaft is indicated in each figure and summarized in Table 7-3 and Table 9-7 through Table 9-10. To facilitate comparison between the two LIPLE simulation cases and the measured data, the comparisons are made at the same magnitude of lateral displacement at the head of the shaft. Therefore, differences between the applied and calculated V_h may be noted in Table 9-7 through Table 9-10.

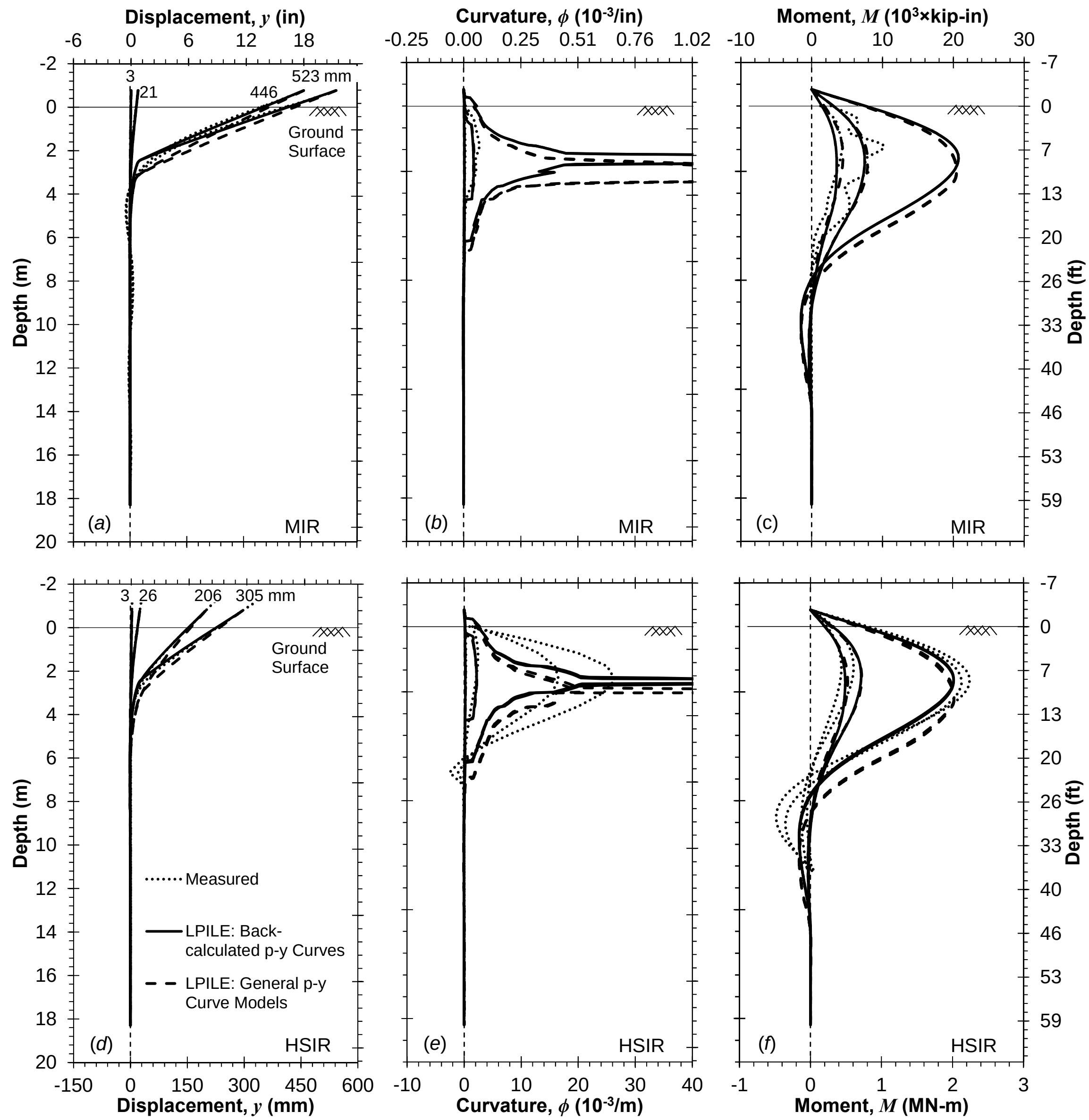

Figure 9-10: Comparison between the measured data and the LPILE model using general *p-y* curve models and back-calculated *p-y* curves on the selected profiles of (a) displacement, (b) curvature, and (c) moment for MIR, and (d) displacement, (e) curvature, and (f) moment for HSIR.

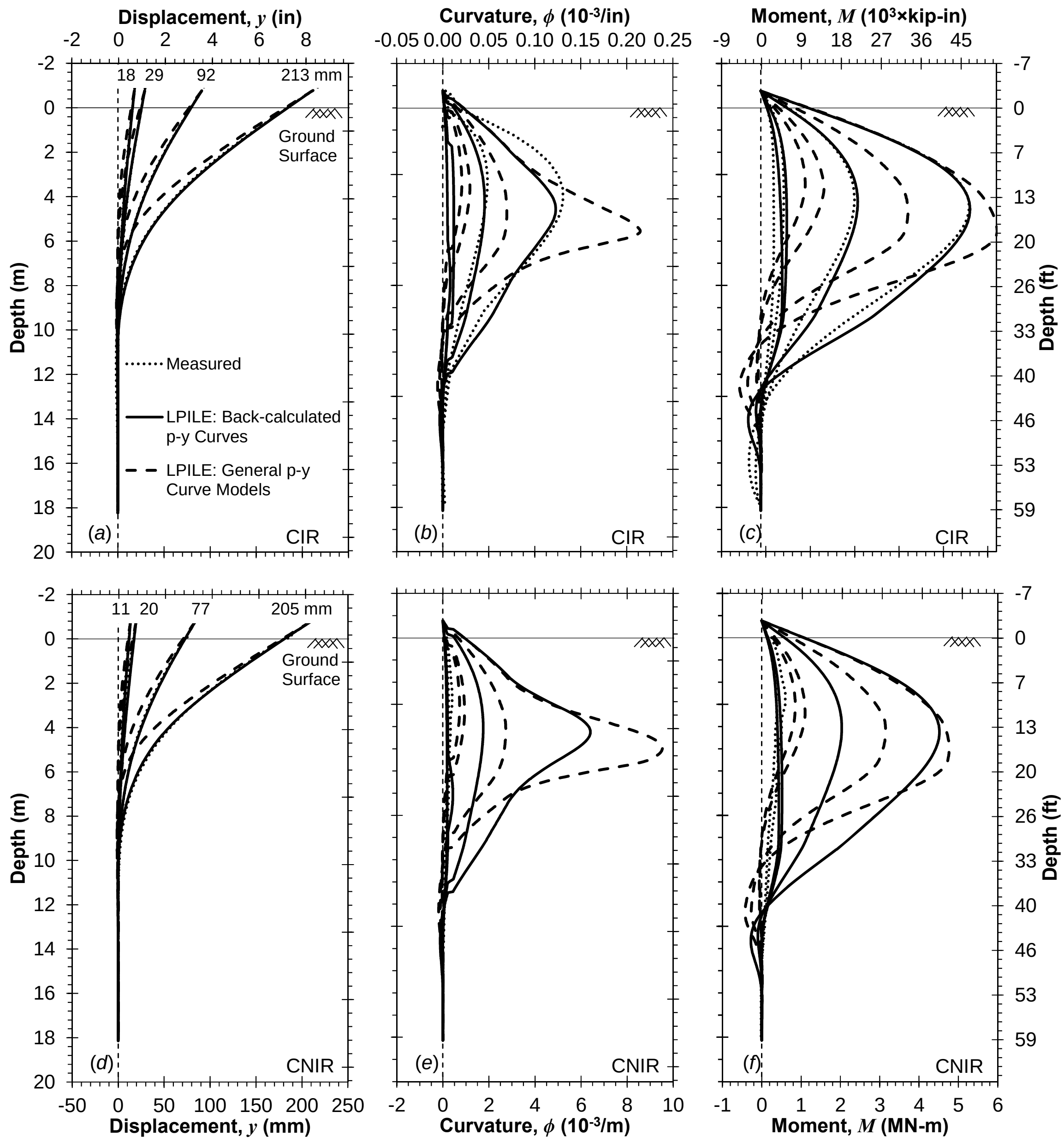

Figure 9-11: Comparison between the measured data and the LPILE model using general *p-y* curve models and back-calculated *p-y* curves on the selected profiles of (a) displacement, (b) curvature, and (c) moment for CIR, and (d) displacement, (e) curvature, and (f) moment for CNIR.

The comparisons in Figure 9-10 and Figure 9-11use the lateral displacement profiles measured using the in-place inclinometers. The profiles of curvature and moment, for CIR and HSIR, were based on the Type I inclinometers measurements, whereas, for MIR and CNIR, those profiles were based on the ESGs measurement at small lateral load. Figure 9-10b, Figure 9-10c, Figure 9-11d and Figure 9-11e only show the measured profiles of curvature and moment with V_h = 170 and 425kN (39 and 96kip) and V_h = 275 and 415kN (62 and 93 kip) for MIR and CNIR, respectively, due to the lack of reliability of the Type II inclinometer and ESGs measurements at large applied displacements. Table 9-7 through Table 9-10 present a quantitative comparison of the lateral responses of the test shafts in terms of the percent difference between observed and computed shear force at the shaft head, V_h, maximum bending moment, M_{max}, and depth-to-maximum bending moment, H_{Mmax}.

For the uncased shafts, the back-calculated *p-y* curves naturally produce better agreement with the lateral displacement profiles than those computed using the general *p-y* curve models. The general shapes and trends of the moment profiles from both LPILE simulations follow those of the test data. In general, the ranges in percent difference between the observed M_{max} and those simulated using the back-calculated and general *p-y* curves are 5 to 30%, and 0.3 to 25%, respectively. The ranges in percent difference between the observed H_{Mmax} and those simulated using the back-calculated and general *p-y* curves are 2 to 39%, and 24 to 34%, respectively. For the comparison of V_h, the ranges in percent difference between the observed and the simulated using the back-calculated and general *p-y* curves are 8 to 54%, and 2 to 55%, respectively. Generally, both simulation cases exhibit similar accuracy for the uncased shafts at small displacements, but the accuracy for

H_{Mmax} with the general *p-y* curves is smaller than the back-calculated *p-y* curves, in some cases significantly, as the applied displacement increases.

For the cased shafts, the profiles of displacement, curvature, and moment computed using the back-calculated *p-y* curves agree quite well with the observed profiles. The ranges in percent difference between the observed M_{max} and those simulated using the back-calculated and general *p-y* curves are 0.4 to 49%, and 13 to 109%, respectively. The ranges in percent difference between the observed H_{Mmax} and those simulated using the back-calculated and general *p-y* curves are 2 to 86%, and 6 to 79%, respectively. For the comparison of V_h, the ranges in percent difference between the observed and the simulated using the back-calculated and general *p-y* curves are 3 to 38%, and 6 to 49%, respectively. Generally, the accuracy for the cased shafts using back-calculated *p-y* curves is greater than the general *p-y* curves across all of the displacements simulated. This indicates that the general models are naturally less suitable than the site-specific models. This may be attributed to the use of stiff clay model without free water (Welch and Reese 1972; Reese and Welch 1975), which may not be suitable for cased shafts.

9.9 Summary and Conclusions

Drilled shaft foundations have been commonly used to provide significant structural and geotechnical resistance to support bridges, buildings, and other civil infrastructure subjected to lateral loads. In order to account for the seismic demands, the amount of steel reinforcement in drilled shaft foundations has increased over the past several decades. However, the increase of reinforcing steel bar area reduces the clearance between the longitudinal and transverse reinforcement, which may increase the difficulty of concrete flowing through the spacing of reinforcement and increase the likelihood for voids and defects within the foundations. Moreover, the use of permanent steel casing can also lead to a decrease in the amount, or the outright elimination, of internal reinforcement since the steel casing is able to provide significant increase of inelastic deformation and flexural capacity of the foundation. However, no literature has reported the study of lateral load transfer between the drilled shafts with and without permanent steel casing and high-strength reinforcement at the same site and soil conditions.

Table 9-7 Comparison of the measured lateral response for MIR with the LPILE simulations

y_h, mm (in)	Model	V_h, kN (kip)	M_{max}, kN-m (kip-in)	H_{Mmax}, m (ft)
3 (0.1)	Measured	171 (38)	497 (4,397)	1.8 (6.0)
	LPILE w/ back-calculated *p-y* curves	289 (65)	400 (3,540)	2.7 (8.9)
	Difference	51%	22%	39%
	LPILE w/general *p-y* curves	265 (60)	498 (4,409)	2 (7.6)
	Difference	43%	0%	24%
21 (0.8)	Measured	425 (95)	1,149 (10,170)	1.8 (6.0)
	LPILE w/ back-calculated *p-y* curves	466 (105)	846 (7,492)	2.5 (8.3)
	Difference	9%	30%	32%
	LPILE w/general *p-y* curves	459 (103)	893 (7,908)	2.6 (8.5)
	Difference	8%	25%	34%

Table 9-8 Comparison of the measured lateral response for HSIR with the LPILE simulations

y_h, mm (in)	Model	V_h, kN (kip)	M_{max}, kN-m (kip-in)	H_{Mmax}, m (ft)
3 (0.1)	Measured	171 (38)	491 (4,345)	1.8 (6.0)
	LPILE w/ back-calculated *p-y* curves	299 (67)	553 (4,890)	2.6 (8.4)
	Difference	54%	12%	33%
	LPILE w/general *p-y* curves	300 (67)	591 (5,230)	2.6 (8.4)
	Difference	55%	18%	33%
26 (1.0)	Measured	425 (95)	686 (6,068)	1.8 (6.0)
	LPILE w/ back-calculated *p-y* curves	460 (103)	806 (7,138)	2.2 (7.4)
	Difference	8%	16%	20%
	LPILE w/general *p-y* curves	434 (98)	815 (7,213)	2.4 (7.8)
	Difference	2%	17%	25%
206 (8.1)	Measured	884 (199)	2403 (21,266)	2.5 (8.3)
	LPILE w/ back-calculated *p-y* curves	1,078 (242)	2279 (20,168)	2.5 (8.1)
	Difference	20%	5%	2%
	LPILE w/general *p-y* curves	997 (224)	2,284 (20,217)	3.4 (11)
	Difference	12%	5%	29%
305 (12.0)	Measured	920 (207)	2,532 (22,408)	2.4 (8.0)
	LPILE w/ back-calculated *p-y* curves	1,093 (246)	2,278 (20,164)	2.4 (7.9)
	Difference	17%	11%	1.56%
	LPILE w/general *p-y* curves	1,033 (232)	2,285 (20,221)	3.2 (10.6)
	Difference	12%	10%	28%

Table 9-9 Comparison of the measured lateral response for CIR with the LPILE simulations

y_h, mm (in)	Model	V_h, kN (kip)	M_{max}, kN-m (kip-in)	H_{Mmax}, m (ft)
18 (0.7)	Measured	275 (62)	332 (2,937)	5.7 (18.8)
	LPILE w/ back-calculated *p-y* curves	204 (46)	546 (4,834)	7.8 (25.6)
	Difference	30%	49%	31%
	LPILE w/general *p-y* curves	454 (102)	1,132 (10,020)	3.4 (11.3)
	Difference	49%	109%	50%
29 (1.1)	Measured	413 (93)	584 (5,170)	3.8 (12.6)
	LPILE w/ back-calculated *p-y* curves	294 (66)	661 (5,849)	5.1 (16.8)
	Difference	33%	12%	29%
	LPILE w/general *p-y* curves	593 (133)	1,611 (14,260)	3.6 (11.9)
	Difference	36%	94%	6%
92 (3.6)	Measured	926 (208)	2,384 (21,098)	4.1 (13.6)
	LPILE w/ back-calculated *p-y* curves	872 (196)	2,467 (21,835)	4.2 (13.9)
	Difference	6%	3%	2%
	LPILE w/general *p-y* curves	1,134 (255)	3,747 (33,160)	4.7 (15.4)
	Difference	20%	44%	12%
213 (8.4)	Measured	1,539 (346)	5,303 (46,938)	4.4 (14.6)
	LPILE w/ back-calculated *p-y* curves	1,582 (356)	5,325 (47,134)	4.6 (15.0)
	Difference	3%	0.4%	3%
	LPILE w/general *p-y* curves	1,627 (366)	6,018 (53,261)	5.5 (18.2)
	Difference	6%	13%	22%

Table 9-10 Comparison of the measured lateral response for CNIR with the LPILE simulations

y_h, mm (in)	Model	V_h, kN (kip)	M_{max}, kN-m (kip-in)	H_{Mmax}, m (ft)
11 (0.4)	Measured	275 (62)	377 (3,337)	3.0 (10.0)
	LPILE w/ back-calculated *p-y* curves	200 (45)	437 (3,863)	7.7 (25.2)
	Difference	32%	15%	86%
	LPILE w/general *p-y* curves	370 (83)	517 (4,576)	7.1 (23.2)
	Difference	29%	31%	79%
20 (0.8)	Measured	413 (93)	602 (5,326)	2.4 (8.0)
	LPILE w/ back-calculated *p-y* curves	282 (63)	852 (7,545)	3.1 (10)
	Difference	38%	34%	22%
	LPILE w/general *p-y* curves	450 (101)	1,102 (9,758)	3.4 (11.0)
	Difference	9%	59%	32%

To help address this gap in knowledge, four full-scale drilled shafts were constructed to improve the understanding of the lateral load transfer of cased and uncased shafts, with and without internal reinforcement consisting of either Grade 60 or Grade 80 reinforcing steel bars. With the comparisons of various performance metrics between the test shafts, including the performance at the head of the shafts, the lateral displacement, curvature and moment profiles, and the back-calculated soil reaction-displacement (*p-y*) curves, test results of the cased and uncased shafts indicated significant differences in their lateral responses. The cased test shafts exhibited significantly greater lateral resistance as compared to the uncased shafts. The shaft HSIR showed a similar lateral response at shaft head as MIR at small displacements. As the lateral resistance was getting fully mobilized, HSIR exhibited less lateral displacements as compared to MIR with the same lateral loads. The comparison of the *p-y* curves for each test shaft shows that the rougher soil-foundation interface and larger diameter lead to larger unit soil resistances at given soil displacements.

Back-calculated *p-y* curves for each shaft were compared and used, along with widely-available *p-y* curve models, to evaluate the sufficiency of the commonly used software package LPILE and the use of general *p-y* curves for a specific site condition; and it shows that the general models are naturally less suitable than the site-specific models.

9.10 References

ACI (American Concrete Institute). (2014). "Building code requirements for structural concrete (ACI 318-14) and commentary (318R-14)."*ACI Committee 318*, Farmington Hills, MI.

API (2010). *Recommended Practice for Planning, Designing and Constructing Fixed Offshore Platforms - Working Stress Design, API RP 2A-WSD*, 21st Edition, Errata and Supplement, American Petroleum Institute, Washington, DC.

Barbosa, A.R. (2011). "Simplified vector-valued probabilistic seismic hazard analysis and probabilistic seismic demand analysis: Application to the 13-story NEHRP reinforced concrete frame-wall building design example." *Ph.D. thesis*, Dept. of Structural Engineering, Univ. of California, San Diego.

Barbosa, A. R., Link, T., and Trejo, D. (2015). "Seismic Performance of High-Strength Steel RC Bridge Columns." *ASCE J. Bridge Eng*., 10.1061/(ASCE)BE.1943-5592.0000769, http://ascelibrary.org/doi/abs/10.1061/(ASCE)BE.1943-5592.0000769

Bierschwale, M. W. Coyle, H. M., and Bartoskewitz, R. E. (1981). "Lateral load tests on drilled shafts founded in clay." *Drilled piers and caissons*, M. W. O'Neill, ed., ASCE, New York, N.Y., 98-113.

Brown, D. A., Turner, J. P., and Castelli, R. J. (2010). "Drilled shafts: Construction procedures and LRFD design methods." *Report No. FHWA-NHI-10-016.* US Department of Transportation, Federal Highway Administration, Washington, D.C.

Dickenson, S.E. and Haines, B.Z. (2006). *Characterization of the geotechnical engineering field research site at Oregon State University*, 3rd Ed., Oregon State Univ., Corvallis, OR.

Elgamal, A., Lu, J., and Mackie, K. (2014). "MSBridge: OpenSees Pushover and Earthquake Analysis of Multi-span Bridges-User Manual." *Rep.No. SSRP–14/04*, California Department of Transportation (Caltrans) Sacramento, CA.

Gebman, M., Ashford, S. A, and Restrepo, J. I. (2006). “Axial force transfer mechanisms within cast-in-steel-shell piles”. *Report No. SSRP-94/10*, Department of Structural Engineering, University of California at San Diego, La Jolla, CA.

Hassan, T.K., Seliem, H.M., Dwairi, H., Rizkalla, S.H., and Zia, P. (2008). “Shear Behavior of Large Concrete Beams Reinforced with High-Strength Steel,” *ACI Structural Journal*,105(2), 173–179.

Hognestad, E. (1951). “A study on combined bending and axial load in reinforced concrete members.” *University of Illinois Engineering Experiment Station*, Univ. of Illinois, Urbana-Champaign, IL, 43–46.

Isenhower, W. M. and Wang, S. T. (2015). *Technical Manual for LPile 2015*, Ensoft, Inc., Austin, TX.

Kent, D.C., and Park, R. (1971). “Flexural members with confined concrete.” *Journal of the Structural Division*. 97(7): 51-93

Khalili-Tehrani, P., Ahlberg, E.R., Rha, C., Lemnitzer, A., Stewart, J.P., Taciroglu, E. and Wallace, J.W. (2014). “Nonlinear load-deflection behavior of reinforced concrete drilled piles in stiff clay.” *J. Geotech. Geoenviron. Eng.*, 140(3), 04013022.

Kulhawy, F. H., and Mayne, P.W. (1990). “Manual on estimating soil properties for foundation design.” *Rep. EL-6800*, Electric Power Research Institute, Cornell Univ., Ithaca, NY.

Lam, I.P.O. (2013) “Diameter Effects on p-y Curves.” *38th Annual Meeting of the Deep Foundations Institute*, Phoenix, AZ.

Lam, I., and Martin, G. (1986). “Seismic design of highway bridge foundations.” *Rep. No. FHWA/RD-86/102*, Federal Highway Administration, Washington, D.C.

Li, Q., and Yang, Z. (2017). “*P–y* approach for laterally loaded piles in frozen silt.” *J. Geotech. Geoenviron. Eng.*, 143(5), http://dx.doi.org/10.1061/(ASCE)GT.1943-606.0001556

Mander, J.B., Priestley, M.J.N, Park R. (1988). “Theoretical stress-strain model for confined concrete.” *Journal of the Structural Division*, 114(8):1804-1826.

Matlock, H. (1970). Correlations for Design of Laterally Loaded Piles in Soft Clay. *Proc., 2nd Annual Offshore Technology Conf.,* OTC 1204, Houston, Vol. 1, 577-594.

Martin, J.P. (2018). “Full-Scale Loading Tests of Shallow Foundations on Aggregate Pier-reinforced Clayey Silt,” *MS Thesis*, Oregon State University, *Under Development*

Mayne, P.W., Kulhawy, F.H., and Trautmann, C.H. (1992). “An experimental study of the behavior of drilled shaft foundations under static and cyclic lateral and moment loading.” *Rep. TR-lO0221*, Electric Power Res. Inst., Palo Alto, CA

Mazzoni, S., McKenna, F., and Fenves, G.L. (2006). *Open System for Earthquake Engineering Simulation User Manual*. Pacific Earthquake Engineering Research Center, University of California, Berkeley. http://opensees.berkeley.edu

McKenna, F., Scott, M.H., and Fenves, G.L. (2010). "Nonlinear finite-element analysis software architecture using object composition." *Journal of Computing in Civil Engineering*, 24(1), 95-107.

Nimityongskul, N. (2010). "Effects of soil slope on lateral capacity of piles in cohesive soils." *Ph.D. Dissertation*, Civil and Construction Engineering Department, Oregon State University, Corvallis, OR.

Reese, L.C., Cox, W.R., and Koop, F.D. (1974). "Analysis of laterally loaded piles in sand." *Proc. 6th Offshore Technology Conference, Paper 2080*, Houston, Texas, 473-483.

Reese, L.C. and Welch, R.C. (1975), "Lateral loading of deep foundations in stiff clay." *Journal of Geotechnical Engineering Division,* 101(7), 633-649.

Roeder, C. W., Cameron, B., and Brown, C. B. (1999). "Composite action in concrete-filled tubes." *J. Struct. Eng.,* 125(5), 477–484.

Roeder, C. W., Lehman, D. E., and Bishop, E. (2010). "Strength and stiffness of circular concrete filled tubes." J. *Struct. Eng.,* 136(12), 1545–1553.

Roeder, C., and Lehman, D. (2012). "Initial Investigation of Reinforced Concrete Filled Tubes for Use in Bridge Foundations." *Report No. WA-RD 776.1*. The State of Washington Department of Transportation, Olympia, Washington.

Stuedlein, A.W., Li, Q., Arduino, P., Ganji, A. (2015) "Behavior of drilled shafts with high-strength reinforcement and casing." *Rep. 2013-M-OSU-0024*, Pacific Northwest Transportation Consortium University Transportation Center, Seattle, WA.

Trejo, D., Barbosa, A.R., and Link, T. (2014). "Seismic Performance of Circular Reinforced Concrete Bridge Columns Constructed with Grade 80 Reinforcement". *Research SRS 500-610*. Oregon State University, Corvallis, OR.

Vecchio, F.J., and Collins, M.P. (1986). "Modified compression-field theory for reinforced concrete elements subjected to shear." *ACI Journal*, 83(2), 219–231.

Wallace, J. W., Fox, P. J., Stewart, J. P., Janoyan, K., Qiu, T., and Lermitte, S. (2001). "Cyclic large deflection testing of shaft bridges: Part I-Background and field test results." *Report to California Department of Transportation*, University of California, Los Angeles, CA

Welch, R. C., and Reese, L. C. (1972). "Lateral load behavior of drilled shafts." *Res. Rep. 89-10*, Center for Highway Research, The University of Texas at Austin, Tex

Yang, Z., Li, Q., Horazdovsky, J., Hulsey, J.L., and Marx, E. (2012). "Analysis of Laterally Loaded Piles in Frozen Soils." *In Proceedings of the GeoCongress 2012: State of the Art and Practice in Geotechnical Engineering.* Geotechnical Special Publication (225). ASCE, Reston, Va. 215-224.

Yang, Z., Li, Q., Horazdovsky, J., Hulsey, J. L., and Marx, E. E. (2017). "Performance and design of laterally loaded piles in frozen ground." *Journal of Geotechnical and Geoenvironmental Engineering*, 143 (5), http://dx.doi.org/10.1061/(ASCE)GT.1943-5606.0001642, 06016031.

Yassin, M. (1994). “Nonlinear analysis of prestressed concrete structures under monotonic and cycling loads.” *PhD dissertation*, University of California, Berkeley, CA.

10. PROPOSED *p-y* CURVE MODEL FOR WILLAMETTE SILT CONSIDERING SCALE EFFECTS

10.1 Basis for Development of the Region-specific Lateral Load Transfer Model

To aid in the design of bridge foundations in the Willamette Valley, region-specific *p-y* curve models were developed for deep foundations under lateral loading based on consideration of the widely-used *stiff clay without free water* model (Welch and Reese 1972; Reese and Welch 1975) available in commonly-used software (e.g., LPile, (Isenhower and Wang 2015). Chapter 7 described the identification of possible gaps between the steel casing and the surrounding soil, with confirmation of poor axial interface response in Chapter 8. Chapter 9 showed that the gaps between the steel casing and surrounding soil affected the back-calculated *p-y* curves for the cased shafts. In light of these observations, the back-calculated *p-y* curves for uncased shafts were used to propose the region-specific *p-y* curve model for Willamette Silt. The *p-y* curves back-calculated from the ground surface to a depth of 2.7 m (9 ft) for HSIR, which extend to large displacements, were selected for development of the Willamette Silt-specific lateral load transfer model. The comparison between HSIR and CIR was used to study the interface (i.e., concrete-soil versus steel-soil interface) and installation effects, which caused the formation of gap between casing and soil. Owing to the availability of *p-y* curves back-calculated for a 325 mm (12.75 in) diameter driven pipe pile (designated DPP) and extending from the ground surface to a depth of 2.1 m (7 ft), tested at the same site and reported by Nimityongskul (2010), an assessment of the Willamette Silt *p-y* curves could be made with regard to possible scale (i.e., diameter) effects.

10.2 Comparison of *p-y* Curves for Small- and Large-Diameter Foundations in Willamette Silt

Figure 10-1 compares the back-calculated *p-y* curves for the larger diameter drilled shaft, HSIR and CIR, and the smaller-diameter driven steel pile, DPP, for shallow depths that correspond to the source of significant lateral resistance. Several important observations may be drawn from the comparison:

1. The initial stiffness of individual p-y curves increases with depth, regardless of foundation type or diameter;
2. The "concave up" shape of the initial response for the deeper *p-y* curves for CIR was caused by the presence of gaps between the casing and shaft borehole (), as discussed in Chapters 7, 8 and 9;
3. The *p-y* curves transition from a softening-type response to a hardening-type response with increasing depth, indicative of an over-consolidated plastic soil response, regardless of foundation type or diameter;
4. The peak lateral soil resistance of the shafts HSIR and CIR increases with depth, whereas the peak lateral soil resistance for DPP increases with depth to a depth of about 3 to 4 pile diameters, whereupon it decreases slightly with depth; and,
5. The stiffness and peak lateral soil resistance is significantly larger for the larger diameter drilled shafts than the smaller diameter driven pile, indicative of scale (or diameter) effects, and interface characteristics in comparison of HSIR and DPP.

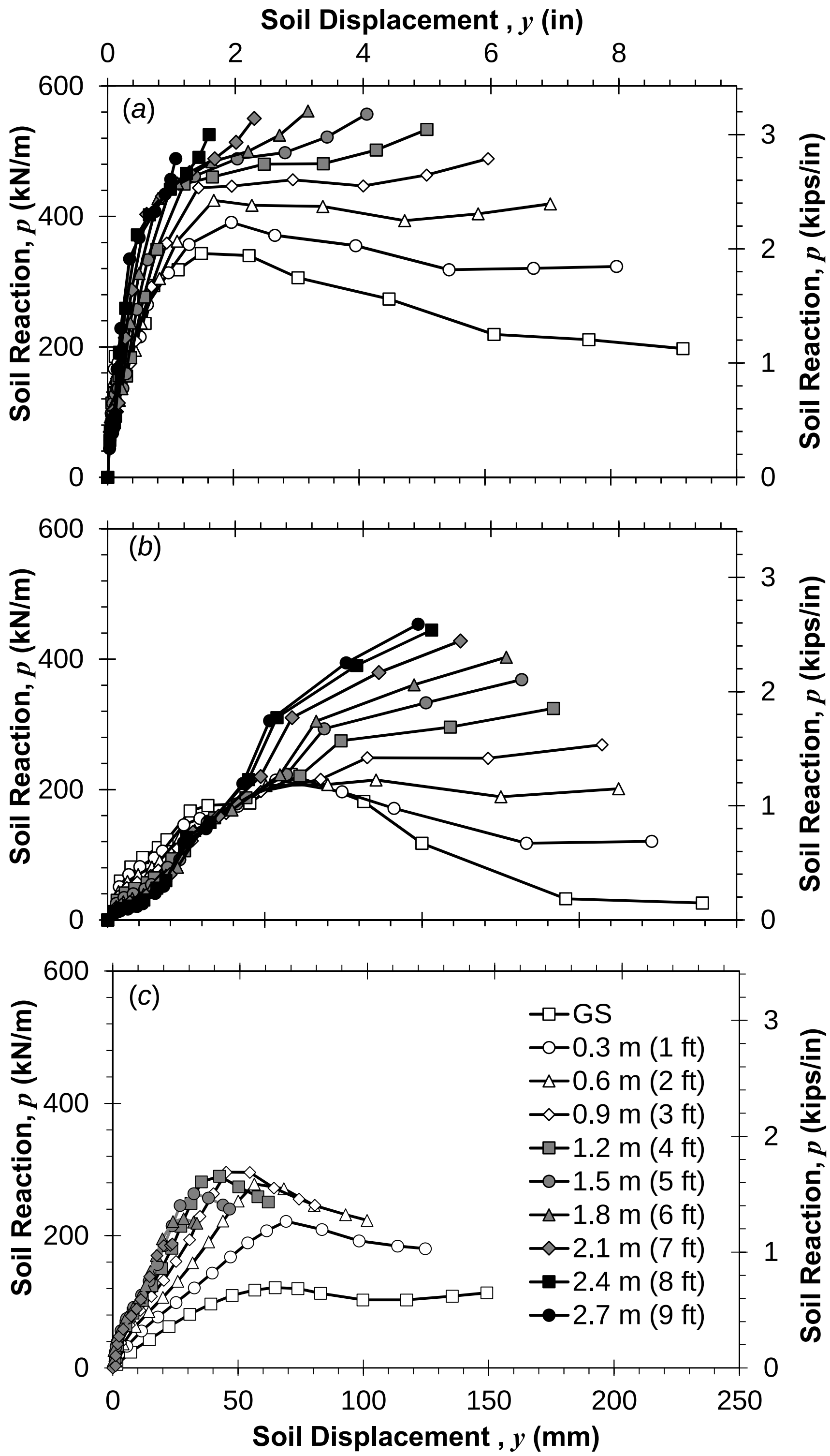

Figure 10-1 Back-calculated *p-y* curves for (a) HSIR and (b) CIR from ground surface to the depth of 2.7 m (9 ft) and (c) DPP from ground surface to the depth of 2.1 m (7 ft)

These observations are fully-consistent with established principles of soil-structure interaction. Accordingly, the development of a region-specific model would adhere to the full-scale observations as well as other soil-structure interaction principles established over decades of experience.

10.3 Development of the Region-Specific Lateral Load Transfer Model Considering Scale Effects

The development of a lateral load transfer model for the Willamette Valley region, and specifically the Willamette Silt deposit, requires an assessment of the ultimate lateral soil resistance, the initial stiffness or displacement-dependent response, and the general shape of the *p-y* curves themselves. In the discussion that follows, the analytical methodologies established for stiff plastic soils are assessed for suitability in modeling the deep foundations considered herein and are modified based on the observations to produce improvements in accuracy.

The ultimate lateral soil resistance, p_u, for deep foundations in plastic soils at depth z can be calculated as follows (e.g., Matlock 1970; Welch and Reese 1972; Reese and Welch 1975; Reese et al. 1975):

$$p_u(z) = N_p(z) \cdot s_u(z) \cdot D(z) \tag{10.1}$$

where $N_p(z)$ = depth-dependent ultimate lateral resistance coefficient, which depends on the geometry of the failure mechanism (e.g., shallow, 3D passive wedge mechanism, versus the deep, 2D, flow failure mechanism), size of deep foundations, and soil properties, $s_u(z)$ = depth-dependent undrained shear strength, and $D(z)$ = the depth-dependent diameter. Reese et al. (1975) proposed that the depth-dependent change from the shallow to the deep failure mechanism in stiff clay can be facilitated through $N_p(z)$, by setting the ultimate lateral resistance coefficient to the smaller of:

$$N_p(z) = 2 + \frac{\gamma'_{avg} \cdot D(z) \cdot z}{s_u(z)} + \frac{2.83z}{D(z)} \tag{10.2}$$

$$N_p(z) = 11 \tag{10.3}$$

where γ'_{avg} = average effective unit weight from the ground surface to depth z.

The ultimate lateral resistance coefficient, N_p, associated with the full-scale data that was presented in Figure 10-1 was estimated for each *p-y* curve for HSIR and DPP. The s_u corresponding to HSIR and DPP at each depth was estimated using the site-specific N_K factor in Eq. (8.27) with explorations CPT-4 (Figure 4-9, Appendix A.7) and 1997 CPT-1 (Appendix A.11), which is the exploration nearest to DPP. The ultimate lateral resistance coefficient was back-calculated for each depth by assuming that the representative p_u was equal to the observed peak or extrapolated asymptotic value, depending if the soil resistance was partially-mobilized (typically associated with hardening behavior) or if the soil resistance was fully-mobilized and subsequently exhibited post-peak softening behavior. If the lateral resistance was not fully-mobilized, the hyperbolic model was used to fit to the empirical *p-y* curves to extrapolate to the asymptotic p_u. Extrapolation to asymptotic quantities has been shown in numerous geotechnical applications that the extrapolated quantities represent relatively conservative (i.e., less than the likely) quantity estimates (Stuedlein 2008; and Huffman and Stuedlein 2014).

Figure 10-2 shows the variation of N_p with normalized depth *z/D*, which indicates that the back-calculated N_p for HSIR, CIR, and DPP share a similar trend from the ground surface to $z/D \approxeq 3$. Figure 10-2 also compares the back-calculated N_p to that derived from the stiff clay model from Reese et al. (1975) for a range in z/D. The minor differences between the estimates of N_p computed using the Reese et al. (1975) model for each foundation are due to differences in the soil properties (i.e., s_u and γ'_{avg}) and foundation diameters at each z/D, as indicated by the second and third terms in Eq. (10.2). The stiff clay model under-estimated N_p by approximately 30%, as the mean bias (i.e., the ratio of the observed and calculated N_p) was determined equal to 1.3.

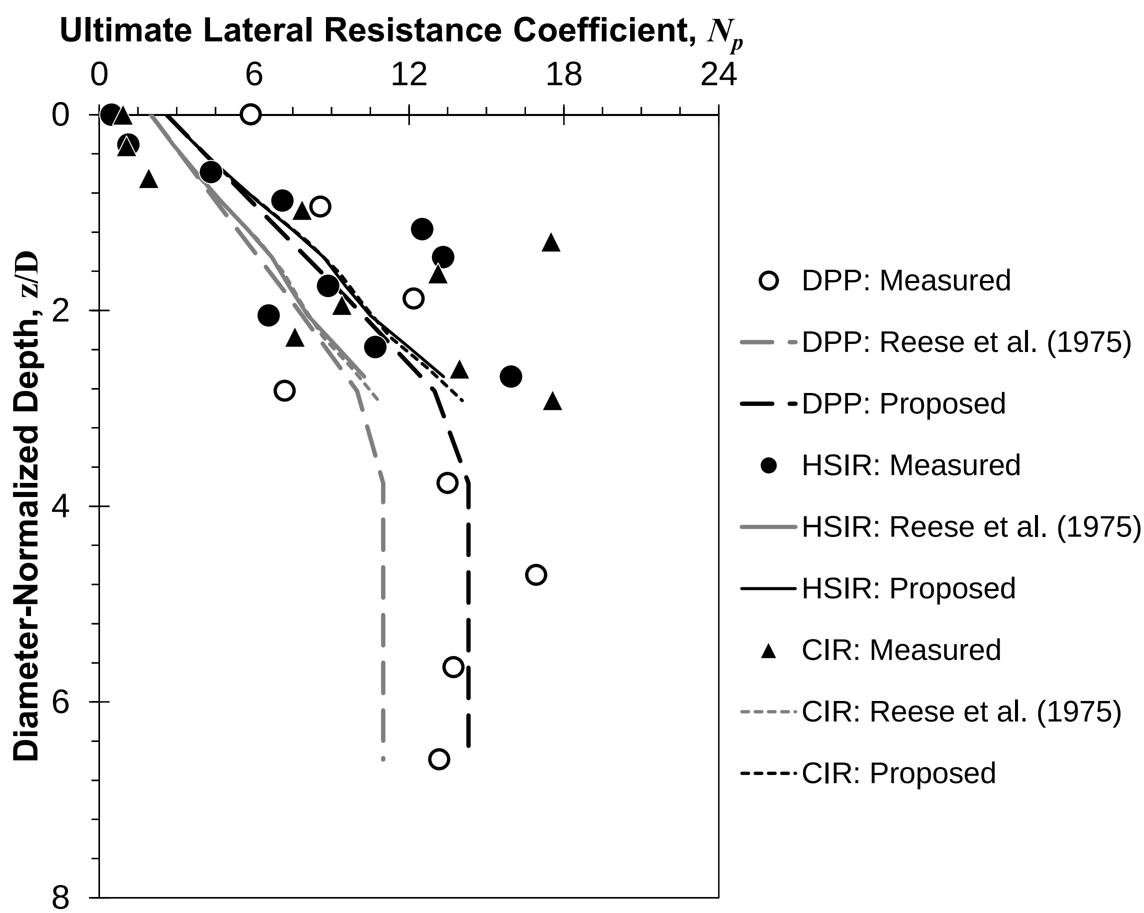

Figure 10-2 Comparison of measured ultimate lateral resistance coefficient, N_p, to the model from Reese et al. (1975) for stiff clay and the corresponding proposed model for Willamette silt

Based on the full-scale observations reported herein, adjustments to the ultimate soil resistance appear warranted. In order to improve the performance of the Reese et al. (1975) model, it is proposed to modify p_u computed using Eqs. (10.2) and (10.3) using a model factor of 1.3 as follows:

$$p_u(z) = 2.6s_u(z)\cdot D(z) + 1.3\gamma'_{avg}\cdot D(z)\cdot z + 3.7s_u(z)\cdot z \tag{10.4}$$

$$p_u(z) = 14.3s_u(z)\cdot D(z) \tag{10.5}$$

where Eqs. (10.4) and (10.5) are formulated to compute p_u directly, rather than coefficient N_p, for ease of incorporation into software.

In the *stiff clay without free water* model (Welch and Reese 1972; Reese and Welch 1975), *p*-*y* curves are presented in displacement- and resistance-normalized terms. The displacement equal to that corresponding to one-half of p_u, termed, y_{50}, is used to normalize the lateral soil displacement, y, in the *p*-*y* model. In this approach, y_{50}, is termed the characteristic displacement, and is used to relate the strain within soil to the displacement of the soil-pile or soil-shaft interface. The *stiff clay without free water* model specifies that the characteristic displacement y_{50} be computed using:

$$y_{50} = 2.5\varepsilon_{50}\cdot D \tag{10.6}$$

where ε_{50} = the strain corresponding to a shear stress equal to 50 percent of the shear strength. In the model proposed herein, the concept of a characteristic displacement was also used, though in a slightly different manner. A characteristic displacement, y_c, was defined in consideration of Eq. (10.6):

$$y_c = 2.5\varepsilon_{50} \cdot D \tag{10.7}$$

However, as described subsequently, y_c may not correspond to the displacement at one-half of the p_u. The p-y data back-calculated for HSIR and DPP at different depths were normalized by p_u and y_c, as shown in Figure 10-3. The normalized p-y data for HSIR exhibit significantly less variability than the normalized p-y data associated with CIR and DPP. When y/y_c = 1, the measured $p/p_u \approxeq 0.5$ for HSIR, indicating the y_c is approximately the displacement at one-half of the p_u, whereas $p/p_u \approxeq 0.05$ to 0.4 for CIR and $p/p_u \approxeq 0.1$ to 0.3 for DPP. The differences between the stiffer HSIR and softer CIR response are caused by the differences in installation (i.e., gap) effects, whereas the difference HSIR and DPP indicates the scale effects. Furthermore, differences between HSIR and the cased shaft and driven pile exist due to differences in the soil-pile interface (i.e., soil-concrete vs. soil-steel interfaces).

It appears that the normalized p-y data in Figure 10-3 could be modeled by a hyperbolic model for the range in displacements that are typically considered for serviceability and strength limit states. The hyperbolic model has been used extensively for soil-deep foundation interface analyses (e.g. Chin 1970, 1971; Clough and Duncan 1971; Clemence and Brumund 1975; Wong and Teh 1995; Kim et al. 1999; Cao et al. 2014; Stuedlein and Reddy 2014). The hyperbolic model is selected herein to represent and simulate the lateral load transfer response of deep foundations in Willamette Silt deposits. The functional form of the proposed region-specific normalized p-y curves is given by:

$$\frac{p}{p_u} = \frac{y / y_c}{\frac{1}{K} + \frac{y / y_c}{\left(p / p_u\right)_{ult}}} \tag{10.8}$$

where K = the diameter-dependent initial stiffness, and $(p/p_u)_{ult}$ = normalized ultimate soil resistance. Since the maximum value of p/p_u is equal to one, the ratio $(p/p_u)_{ult}$ is also equal to 1.0. The initial stiffness, K_{HSIR}, for HSIR was obtained through fitting to the back-calculated, normalized *p*-*y* data using the ordinary least squares (OLS) method. The value of initial stiffness thus determined is $K_{HSIR} \approxeq 1.5$. It is noted that the estimated K_{HSIR} is only suitable for HSIR and other 1,025 mm (40 in) uncased drilled shafts in Willamette Silt; the effects of scale (or diameter) on the initial stiffness for deep foundations with other diameters should be accounted for, as described subsequently. As shown in Figure 10-3, the hyperbolic model sufficiently captures the trend of the observed normalized *p*-*y* data for HSIR. The mean bias (i.e., the ratio of the observed and calculated p/p_u) and COV of the observed normalized *p*-*y* curves and the fitted hyperbolic model for HSIR were 1.1 and 18%, respectively.

Studies by Carter (1984) and Ling (1988) proposed that the initial stiffness is proportional to the foundation diameter (Pender 1993; Lam 2013). Therefore, to account for the diameter effects, the initial stiffness of DPP can be modeled using:

$$K_{Design} = K_{ref} \cdot \frac{D_{Design}}{D_{ref}} \tag{10.9}$$

where D_{Design} = the diameter of the foundation under design consideration, K_{ref} = the initial stiffness used as a reference (in this case 1.5) and D_{ref} = the diameter used as a reference (in this case 1,025 mm or 40 in). It is noted that the use of Eq. (10.9) is typically considered as a y-multiplier for normalized p-y data. Since D_{DPP} = 325 mm (12.75 in) and D_{HSIR} = 1,025 mm (40 in) over depths ranging from the ground surface to 2.7 m (9 ft), K_{DPP} was estimated using Eq. (10.9) (where $K_{DPP} = K_{Design}$) and was equal to 0.48. Figure 10-3a compares the observed normalized p-y curves for DPP and the hyperbolic model using K_{DPP} = 0.48. The hyperbolic model appears suitable to represent the observed normalized p-y curves for DPP. The mean bias and COV of the observed normalized p-y curves and the fitted hyperbolic model for DPP were 0.96 and 36%, respectively. Thus, Eq. (10.9) is sufficiently suitable for accounting for scale effects and where HSIR serves as the reference shaft and diameter. However, this study is based on the test data from two deep foundations with average diameter of 325 and 1,025 mm (12.75 and 40 in) in Willamette Silt. Use of Eq. (10.9) for deep foundations larger than 1,025 mm (40 in) should be done cautiously, but will be consistent with previously-reported efforts (Carter 1984; Ling 1988; Pender 1993; and Lam 2013).

If only scale effects were considered for CIR with D_{CIR} = 940 mm (37 in), the initial stiffness $K_{CIR,scale}$ = 1.4 according to Eq. (10.9). The hyperbolic model using Eq. (10.9) for CIR is shown in Figure 10-3b with mean bias and COV of the observed normalized p-y data and the fitted hyperbolic model of 0.48 and 63%, respectively. It appears that the consideration of *only* scale effects over-predicts the p/p_u by two times for a given y/y_c. To investigate the combined effect of installation and interface roughness, the fitted initial stiffness, $K_{CIR,}$ was obtained and determined equal 0.3. The ratio of $K_{CIR}/K_{CIR,scale}$ can be considered as a representation of the combined installation and interface effects, appropriate for the use with permanent steel casing when vibrated into an excavated drilled shaft borehole. Therefore, for a cased drilled shaft installed in the same manner as CIR and exhibiting similar borehole-casing gapping, the initial stiffness may be estimated by the following:

$$K_{cased} = \frac{K_{CIR}}{K_{CIR,scale}} K_{uncased} = \frac{0.3}{1.4} K_{uncased} \cong 0.2 K_{uncased} \tag{10.10}$$

Based on the comparison of HSIR and DPP, it is likely that had remedial, post-construction grouting of the gaps between the casing and the soil been conducted, that no casing reduction factor to the initial *p-y* curve stiffness, *K*, would be necessary. This speculation should be confirmed in future research efforts.

10.4 Parametric Study of Scale Effects on the Willamette Silt *p-y* Curves

A comparison of *p-y* curves for various foundation diameters was conducted to study the role of scale effects using the proposed *p-y* curve model [Eq. (10.9)]. The diameters investigated ranged from 0.3 to 1.2 m (12 to 48 in) at depths ranging from ground surface to 2.4 m (8 ft). It was assumed that the foundations were installed in a uniform deposit of Willamette Silt with s_u = 100 kPa (2,100 psf), γ'_{avg} = 17 kN/m^3 (100 pcf), and ε_{50} = 0.005. The diameter-dependent initial stiffness, *K*, was determined using HSIR as reference with K_{ref} = 1.5. Table 10-1 summarizes the foundation diameters, *D*, and depths with estimated y_c and p_u, computed using Eqs. (10.7) and (10.4) or (10.5), respectively. The characteristic displacement, y_c, is independent of depth for a soil deposit with uniform s_u, and ranges from 3.8 to 15.2 mm (0.15 to 0.60 in) for diameters ranging from 0.3 to 1.2 m (12 to 48 in). The ultimate lateral soil resistance, p_u, depends on both depth and diameter, as discussed above. It is noted that as the failure mode changes from the 3D passive wedge failure mechanism to the 2D flow failure mechanism, the p_u reaches the maximum value as indicated by Eq. (10.5). For example, for D = 0.3 m (12 in), the transition depth from passive wedge to flow failure mechanism was at approximately 0.9 m or 3 ft (3D).

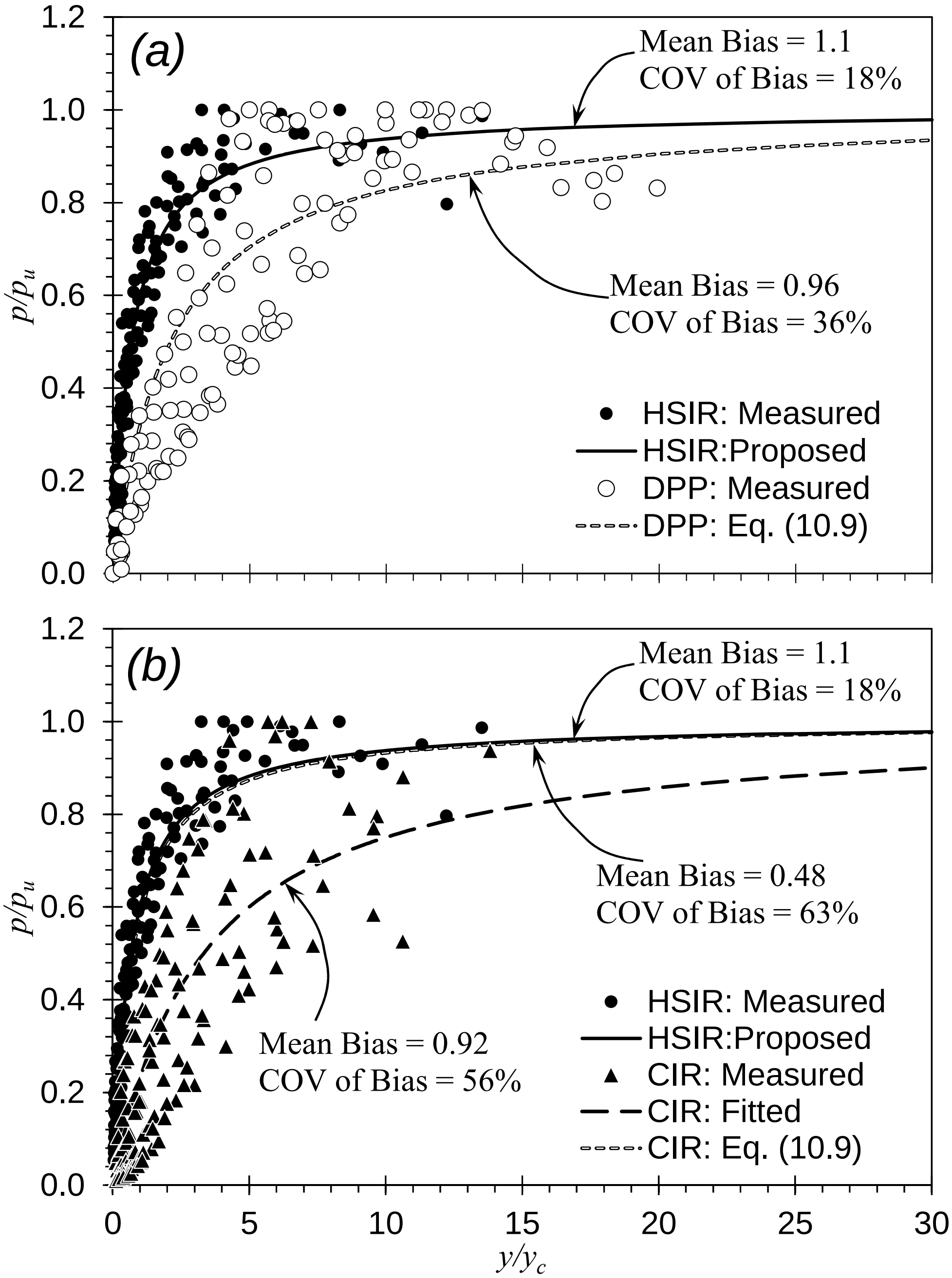

Figure 10-3 Comparison of normalized *p-y* curves for (a) HSIR and DPP, and (b) HSIR and CIR, and the corresponding models proposed for Willamette Valley Silt and adjusted for scale, where appropriate.

Figure 10-4 compares the *p-y* curves at selected depths for foundations with various diameters. It appears that at each depth the initial stiffness of the *p-y* curves increases with the increase of diameter as indicated by Eq. (10.9). At shallow depths, the initial stiffness and ultimate lateral soil resistance for a given foundation diameter increases with increases in depth, indicative of the passive wedge failure mechanism. As depths increase, and as the flow failure mechanism controls (e.g., compare *p-y* curves for the 0.3 m diameter foundation at depths of 1.2 and 2.4 m), the *p-y* curve becomes independent of depth.

10.5 Summary and Conclusions

The experimentally-derived lateral load transfer data was used to explore the differences between a widely-accepted *p-y* curve model, and differences between three different types of instrumented foundations tested at full-scale a the GEFRS at Oregon State University. The three foundations included the 1,025 mm (40 in) diameter drilled shaft HSIR, the 940 mm (37 in) diameter cased shaft CIR, and the 325 mm (12.75 in) diameter driven steel pipe pile DPP. Significant differences in the observed *p-y* curves was noted between these various deep foundations, however, they all shared similar trends in the ultimate lateral soil resistance. The trends in ultimate lateral soil resistance also differed from that computed using the widely-accepted *p-y* curve model, indicating that the region-specific model for ultimate lateral soil resistance proposed herein will be more suitable for various types of deep foundations constructed in this region.

A methodology to scale the initial stiffness of the region-specific *p-y* curves determined using the proposed model was also developed, based on consideration of previously-reported efforts, to account for differences in foundation diameter. The scaling approach was found to suitably predict the response of the small-diameter driven pipe pile when using the larger diameter HSIR as a reference. Permanently-cased drilled shafts, constructed using the same approach as for CIR, can also be evaluated using the proposed region-specific *p-y* curve model when adding a scale factor to account for the interface roughness and installation effects. Although this option is now available for designers, it is recommended that any suspected anomalies (e.g., gaps) between the casing and drilled shaft borehole be post-grouted to ensure good coupling between the shaft and the soil and to improve the load transfer characteristics.

Table 10-1: Summary of foundation diameters, *D*, and depths with estimated y_c and p_u using proposed model

Depth	y_c and p_u	D = 0.3 m (12 in)	D = 0.6 m (24 in)	D = 0.9 m (36 in)	D = 1.2 m (48 in)
Ground Surface	y_c, mm (in)	3.8 (0.15)	7.6 (0.30)	11.4 (0.45)	15.2 (0.60)
	p_u, kN/m (kips/in)	85 (0.49)	171 (0.97)	256 (1.46)	341 (1.95)
0.6 m (2 ft)	y_c, mm (in)	3.8 (0.15)	7.6 (0.30)	11.4 (0.45)	15.2 (0.60)
	p_u, kN/m (kips/in)	331 (1.89)	421 (2.40)	511 (2.92)	601 (3.43)
1.2 m (4 ft)	y_c, mm (in)	3.8 (0.15)	7.6 (0.30)	11.4 (0.45)	15.2 (0.60)
	p_u, kN/m (kips/in)	469 (2.68)	671 (3.83)	766 (4.37)	860 (4.91)
2.4 m (8 ft)	y_c, mm (in)	3.8 (0.15)	7.6 (0.30)	11.4 (0.45)	15.2 (0.60)
	p_u, kN/m (kips/in)	469 (2.68)	939 (5.36)	1259 (7.19)	1362 (7.78)

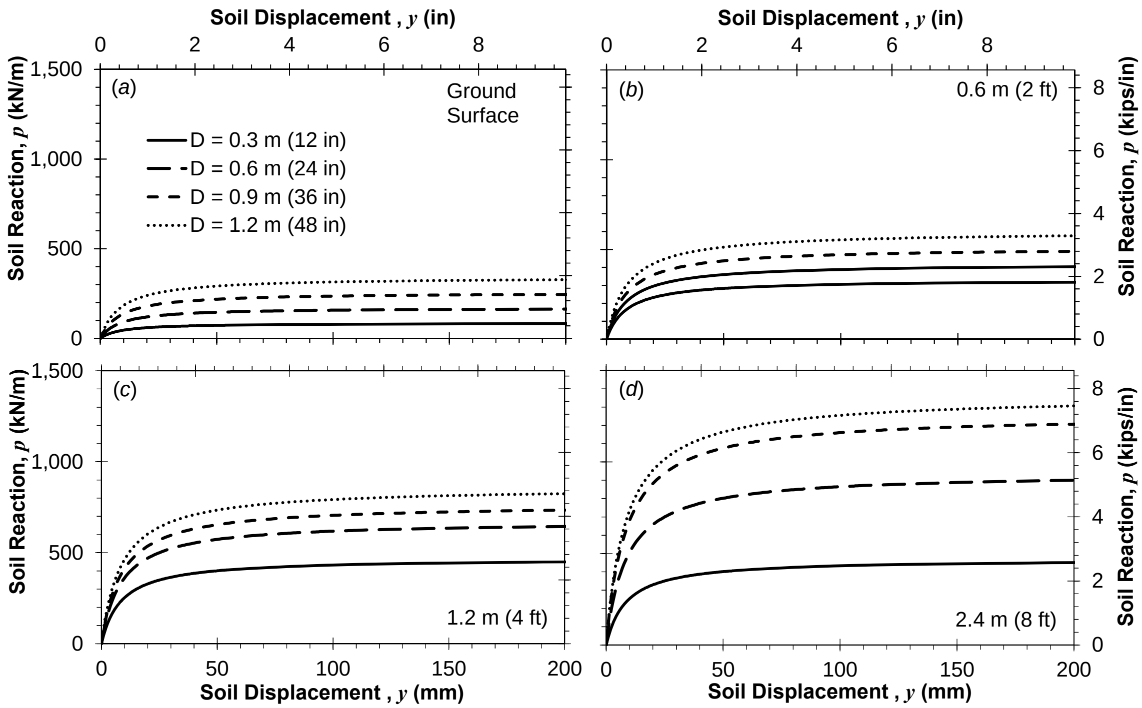

Figure 10-4 Comparison of *p-y* curves derived from the proposed Willamette Valley Silt model at selected depths for deep foundations with various diameters

10.6 References

Cao, W., Chen, Y., and Wolfe, W.E. (2014). "New load transfer hyperbolic model for pile-soil interface and negative skin friction on single piles embedded in soft soils." *Int. J. Geomech.*, 14(1), 92–100

Carter, D. P. (1984). "A non-linear soil model for predicting lateral pile response." *Rep. No. 359*, Civil Engineering Dept., Univ. of Auckland, New Zealand.

Chin, T. K. (1970). "Estimation of the ultimate load of piles from tests not carried at failure." *Proc., Second South East Asian Conf. Soil Mech. Found. Engrg.*, Singapore.

Chin, F. K. (1971). "Discussion of pile test, Arkansas River project*." Soil Mech. and Found. Div.*, 97(6), 930-932.

Clemence, S. P., and Brumund, W. F. (1975). "Large-scale model test of drilled pier in sand." *J. Geotech. Engrg. Div.*, 101(6), 537–550.

Clough, G. W., and Duncan, J. M. (1971). "Finite element analyses of retaining wall behavior." *J. Soil Mech. Found. Div.*, ASCE, 97(12), 1657–1673.

Huffman, J. C., and Stuedlein, A. W. (2014). "Reliability-Based Serviceability Limit State Design of Spread Footings on Aggregate Pier Reinforced Clay." *J. Geotech. Geoenviron. Eng.*, 10.1061/(ASCE)GT.1943-5606.0001156, 04014055.

Isenhower, W. M. and Wang, S. T. (2015). *Technical Manual for LPile 2015*, Ensoft, Inc., Austin, TX.

Kim, S., Jeong, S., Cho, S., and Park, I. (1999). “Shear load transfer characteristics of drilled shafts in weathered rocks.” *J. Geotech. Geoenviron. Eng.*, 125(11), 999–1010.

Matlock, H. (1970). “Correlations for design of laterally loaded piles in soft clay.” *Proc., 2nd Annual Offshore Technology Conf.*, OTC 1204, Houston, 577–594.

Nimityongskul, N. (2010). “Effects of soil slope on lateral capacity of piles in cohesive soils.” *Ph.D. Dissertation*, Civil and Construction Engineering Department, Oregon State University, Corvallis, OR.

Lam, I.P.O. (2013) “Diameter Effects on p-y Curves.” *38th Annual Meeting of the Deep Foundations Institute*, Phoenix, AZ.

Ling, L. (1988). “Back Analysis of Lateral Load Tests on Piles,” *M.E. Thesis*, Civil Engineering Department, University of Auckland.

Pender, M. J. (1993). “Aseismic pile foundation design analysis.” *Bull. NZ Nat. Soc. Earthquake Eng*., 26(1), 49–160.

Reese, L., Cox, W., and Koop, F. (1975). “Field Testing and Analysis of Laterally Loaded Piles in Stiff Clay.” *Proc. 7th Offshore Technology Conf.*, OTC 2312, Houston, 2, 671-690.

Reese, L., Welch, R. (1975). “Lateral loading of deep foundations in stiff clay.” *Journal of Geotechnical Engineering Div.*, ASCE, 101(GT7), 633-649.

Stuedlein, A. W. (2008). “Bearing capacity and displacement of spread footings on aggregate pier reinforced clay.” *Ph.D. thesis*, Univ. of Washington, Seattle.

Welch, R. C., and Reese, L. C. (1972). "Lateral load behavior of drilled shafts," *Res. Rep. 89-10*, Center for Highway Research, The University of Texas at Austin, Tex

Wong, K. S., and Teh, C. I. (1995). “Negative skin friction on piles in layered deposits.” *J. Geotech. Engrg*., 121(6), 457–465.

11. SUMMARY AND CONCLUSION

The main objective of this dissertation is to improve the understanding of load transfer of drilled shaft foundations under axial, lateral, and torsional loading at full-scale and using various composite cross-sections. To accomplish this objective, six full-scale test shafts were instrumented and installed at the Oregon State University (OSU) Geotechnical Engineering Field Research Site (GEFRS).

To investigate the torsional load transfer of drilled shaft foundations, two uncased shafts, including one constructed using typical production methods (designated TDS) and the other constructed with a relatively frictionless base (designated TDSFB), were used to address the complete lack of full-scale torsional load transfer measurements in the literature. Quasi-static, monotonic and cyclic torsional loading tests were conducted on these two shafts. Empirical τ-θ curves were developed for each of the instrumented tributary areas of the shafts, including both granular soils and plastic, fine-grained soils. A numerical framework for the simulation of torsionally-loaded, geometrically-variable deep foundations in multi-layered soils was developed, including both the numerical architecture and two specific τ-Δ curves that can be calibrated with commonly available soil design parameters.

To study the axial and lateral load transfer of drilled shaft foundations, two uncased shafts were constructed, one using mild steel and one using high strength steel reinforcement, designated MIR and HSIR, respectively, and two shafts with steel casing and with and without internal mild steel reinforcement, designated CIR and CNIR, respectively. The comparison of the cased and uncased shafts was intended to determine differences in axial load transfer. Owing to limited anticipated differences in the axial loading of the two cased shafts if constructed using the same auger diameter, an additional construction variable, that of the auger diameter, was investigated to compare differences in axial load transfer that would result. Accordingly, shaft CNIR was drilled with a 940 mm (37 in) diameter auger (i.e., the same size diameter as that of the casing), whereas CIR was drilled with a slightly smaller, 915 mm (36 in) diameter auger. The comparison of uncased shafts MIR and HSIR was intended to determine if differences in longitudinal steel area (due to the use of high strength bar) would significantly affect the flexural response during lateral loading. The comparison of cased shafts CIR and CNIR was intended to determine whether the presence of internal steel would significantly affect the flexural response during lateral loading. This chapter identifies specific conclusions stemming from the comparison of performance, separated into performance in axial and lateral loading.

11.1 Torsional Load Transfer

The quasi-static monotonic and cyclic torsional loading tests were conducted with the results, including applied torsion-shaft head rotation curves, shear strain, torsion, and unit torsional shaft resistance distributions along the length of the shafts, back-calculated unit torsional shaft resistance-local rotation relationships (τ-θ curves), and results of the cyclic loading tests. The ultimate resistance computed using proposed design methods were compared against that observed from the loading tests as well as other loading test data available in the literature to provide a preliminary baseline of design method accuracy and variability. The significant findings include:

1. At the end of monotonic, quasi-static loading, TDSFB had rotated approximately 13°, whereas TDS only rotated 0.14° due to a silty sand layer was encountered near the toe of TDS.

2. The torsional resistance of the shaft TDSFB was fully-mobilized at 185 kN-m and a rotation of the shaft head of about 1.0°.
3. The torsional resistance of shaft TDS was not fully mobilized during the test due to the differences in the soil profiles.
4. Empirical τ–θ curves were developed based on the results of the load tests, appropriate for use in similar soils in the Willamette Valley.
5. No global degradation of the initial and post-yield stiffness with increasing number of cycles was observed for either test shaft during the cyclic loading test.
6. A rational design methodology for the calculation of torsional capacity of drilled shafts was proposed and its accuracy quantified.

11.2 Simulation of Torsionally-Loaded Deep Foundations

A torsional load transfer method was presented using a finite difference model (FDM) framework; and simplified state-dependent spring models, relating the unit torsional resistance to the magnitude of relative displacement, were developed. With the developed model, parametric study was conducted to study the effect of various design variables on torsional resistance The main findings of this study are provided as following:

1. The proposed hardening and softening load transfer models for drilled shafts loaded in torsion were suitable for capture observed interface shear behavior based on the comparisons with experimental interface shear data and the full-scale load transfer data presented in Chapter 4.5.
2. The accuracy of foundation rotations for the serviceability and ultimate limit states in forward modeling depended on the accuracy of the proposed interface shear

model parameters, and the accuracy of methods used to calibrate interface model parameters

3. Parametric studies illustrated the significant effect of nonlinear-hardening and -softening soil responses on the torsional behavior of deep foundations.
4. The contribution of toe resistance in the global response for a foundation subject to pure torsion was small (not greater than 10% of the applied torsion) based on the parametric study. However, increases in axial load results would lead to a corresponding increase in the torsional toe resistance, which could be as great as approximately two-thirds of the total torsional response when bearing into very dense sands.

11.3 Axial Load Transfer

The axial loading tests were used to compare various performance metrics between the cased and uncased shafts, including the axial load-displacement curves, load transfer distributions, and back-calculated unit shaft resistance-relative displacement relationships (*t-z* curves) and unit toe resistance-toe displacement relationships (*q-z* curves). Specific conclusions include:

1. The effect, of using augers of slightly different diameter was shown to greatly impact the axial resistance of the cased shafts. Shaft CIR, constructed with the smaller, 915 mm (36 in) diameter auger for the 940 mm (37 in) diameter casing, exhibited approximately 45% greater axial resistance than the shaft with the larger diameter. Therefore, when constructing permanently cased drilled shafts, field engineers must confirm that the auger diameter specified for use is actually used prior to commencing the excavation of the borehole.

2. The axial resistance of shafts CIR and CNIR was fully-mobilized at the applied load of approximately 1,960 kN (440 kips) and 1,330 kN (300 kips), respectively. These shafts plunged to final displacements of 84 and 74 mm (3.3 and 2.9 in) prior to termination of the tests.
3. The axial resistance of the uncased shafts was not fully-mobilized during the loading tests. The load applied to shafts MIR and HISR was 6,125 kN (1377 kip) and 6,380 kN (1,435 kip) with corresponding displacement of 4.3 mm (0.17 in) and 3.8 mm (0.15 in). These shafts, constructed with the same nominal (i.e., auger) diameter as CIR, produced significantly better axial performance than the cased shafts.
4. The uncased shafts exhibited significantly greater axial shaft resistance as compared to the cased shafts due to the rougher soil-concrete interface and larger as-built diameter of the uncased test shafts, and to the presence of gaps between the soil and casing for the cased shafts. For, example, although axial resistance of shaft MIR was not fully mobilized at end of the axial loading test, it still exhibited 210% more axial resistance comparing to the fully-mobilized axial resistance of shaft CIR.
5. Empirical *t-z* (shaft resistance) and *q-z* (toe resistance) curves were developed based on the results of the load tests, appropriate for use in similar soils in the Willamette Valley.
6. A direct CPT-based method for estimating the axial load transfer curves for uncased shafts in similar soils was proposed and can be used to extend the results of the load test program to design of bridge foundations in the Willamette Valley.

7. The effect of casing on axial load transfer characteristics was evaluated based on load test data reported in the literature as well as with the load testing results from this study. The effect of installation method and construction sequence was found to play a critical role in the quality and quantity of axial load transfer. Table 8-7 should be referred to for guidance in determining appropriate casing reduction factors.

11.4 Lateral Load Transfer

The results of the lateral loading tests, including the performance at the head of the shaft, the lateral displacement profiles, and the back-calculated curvature, moment, and soil reaction-displacement (*p*-*y*) curves were compared to form the following findings:

1. The lateral resistance of the uncased shafts was fully-mobilized at the applied load of approximately 890 kN (200 kips) and at applied displacement of approximately 150 mm (6 in).
2. The uncased shafts exhibited a similar lateral response to applied displacements of approximately 190 mm (7.5 in), with minor differences at small displacements.
3. Towards the end of the lateral loading test, MIR exhibited larger lateral displacement than HSIR, possibly due to: (1) the slightly higher moment capacity of HSIR for $\phi \geq 0.2\ \mathrm{m}^{-1}$, and (2) inherent variability of the soil stiffness and strength. Both test shafts exhibited plastic hinging at large displacements, indicating loss of flexural resistance.
4. Based on the results of the loading test program, it appears that there is no evidence to suggest that the use of high-strength (Grade 80) reinforcement will result in

detrimental or poorer lateral performance as compared to a shaft constructed to the same axial and flexural capacity with Grade 60 steel.

5. Due to the significantly greater flexural resistance, the cased shafts transferred load to significantly greater depths than the uncased shafts. The maximum depth of the mobilized soil-foundation displacement for the cased shafts at the highest load is approximately 9.0 m (30 ft), or $10D_n$ (D_n = nominal diameter), whereas it is approximately 3.7 m (12 ft), or $4D_n$, for the uncased shafts.
6. The lateral resistance of the cased shafts was not fully-mobilized during the loading tests, despite reaching significantly greater loads than the uncased shafts. The maximum load applied to shafts CIR and CNIR was 1,540 kN (346 kip) with corresponding displacement of 213 and 205 mm (8.4 and 8.1 in), respectively. Cased shafts will respond in a more resilient manner than uncased shafts at the same nominal diameter due to their significantly greater flexural rigidity.
7. Although the moment capacity of CIR was approximately 40% larger than that of CNIR, the differences in capacity did not result in significant differences in performance for the displacements imposed.
8. Owing to the optimal placement of steel casing at the “extreme fiber” location of the drilled shaft, permanently and fully-cased shafts may be constructed without internal reinforcement except where tying into the superstructure. Permanently and partially-cased shafts will likely require some internal reinforcement to account for flexural and shear demands at soil layer contacts and in sloping ground. The specification of a sacrificial thickness of structural steel to account for corrosion may be warranted for permanently-cased shafts.

9. The results of the lateral loading test program were used to develop empirical soil reaction-displacement (*p-y*) curves appropriate for use in Willamette Silt soils.
10. The comparison of the *p-y* curves for each test shaft shows that the rougher soil-foundation interface and larger diameter lead to larger unit soil resistances at given soil displacements.
11. A *p-y* curve model suitable for Willamette Silt was proposed and can be readily implemented into commonly used software.
12. Recommendations to account for pseudo-scale effects due to the increasing contribution of shaft resistance to lateral resistance with increased diameter were proposed. The recommendations can be seamlessly incorporated into the proposed *p-y* curve model for Willamette Silt. The scaling relationship is appropriate for foundations with diameters ranging from 325 mm to 1,025 mm, but should be used cautiously for larger diameters until data from larger diameter foundations can be obtained.

11.5 Suggestions for Further Study

The results of this study can be used as a basis for understanding of load transfer of drilled shaft foundations under axial, lateral, and torsional loading. However, several new questions arose over the course of this research. Suggestions for further study include:

1. The investigation on the effect of installation method, for example dry, mineral slurry-, or polymeric slurry-supported shaft cavity construction, on load transfer and the τ–θ curves.
2. The investigation on the impact of the cracking of concrete in torsion on the response of drilled shafts. This study could improve our understanding on the

concrete shear modulus to be used to estimate stiffness and strength of concrete core of the drilled shafts in torsion.

3. The investigation of the performance of drilled shafts with Grade 97 bar to further open the reinforcement cage and reduce the rate of suspected anomalies. Such a study could identify the limiting yield stress that would cause a significant softening of the moment-curvature relationship and result in less desirable displacement performance of test shafts.
4. The investigation of casing reduction factors for shaft resistance that focuses on the effect of construction sequence and installation method at the GEFRS site. Examples include vibro-installation followed by shaft excavation, impact driven-installation followed by excavation, and oscillation-installation followed by excavation. These additional three studies would complete the picture regarding method and sequence of installation on the magnitude of shaft resistance along soil-steel interfaces.
5. The investigation of the lateral response of larger diameter shafts to improve the empirical basis for the scaling law recommended herein. To augment the data derived from the 325 mm (12.75 in), 940 mm (37 in) and 1025 mm (40 in) diameter foundations studied herein, instrumented shafts with diameters of 1,830 mm (72 in) and 3,660 (144 in) could be constructed and tested laterally as done herein and corresponding *p-y* curves determined. The scaling relationship could then be evaluated and adjusted as necessary.
6. Sophisticated three-dimensional (3D) numerical models could be developed by calibrating to the model response to the full-scale data developed as part of this

research and then used to investigate the scale effects on the lateral load responses of drilled shafts until larger diameter shafts become available for testing.

Appendix A CONE PENETRATION TEST (CPT) AND SEISMIC CONE PENETRATION TEST (SCPTS) RESULTS

This appendix presents the CPT and SCPT results used in this study.

A.1 CPT-1 for Lateral Loading Tests

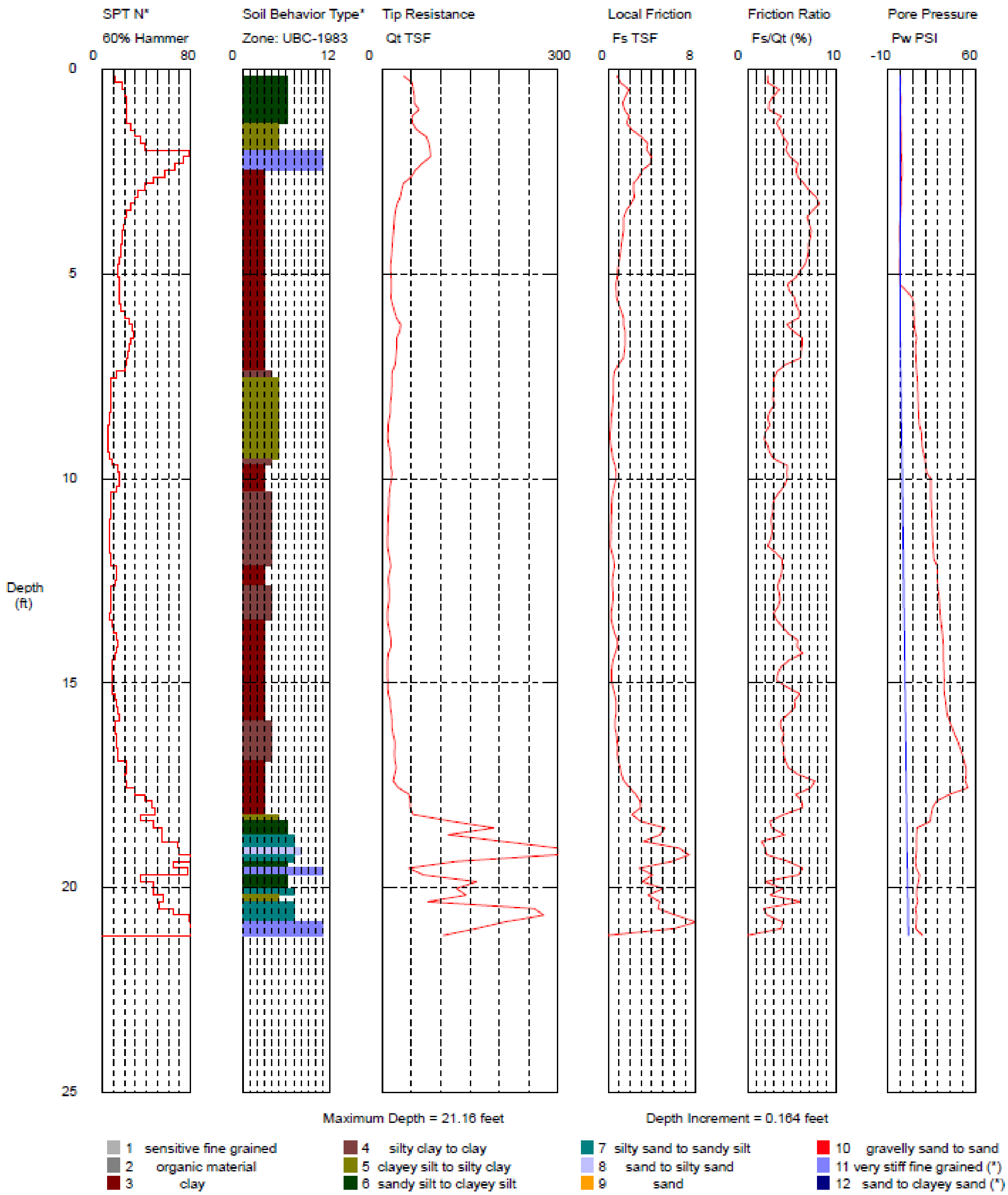

A.2 SCPT-2 for Lateral Loading Tests

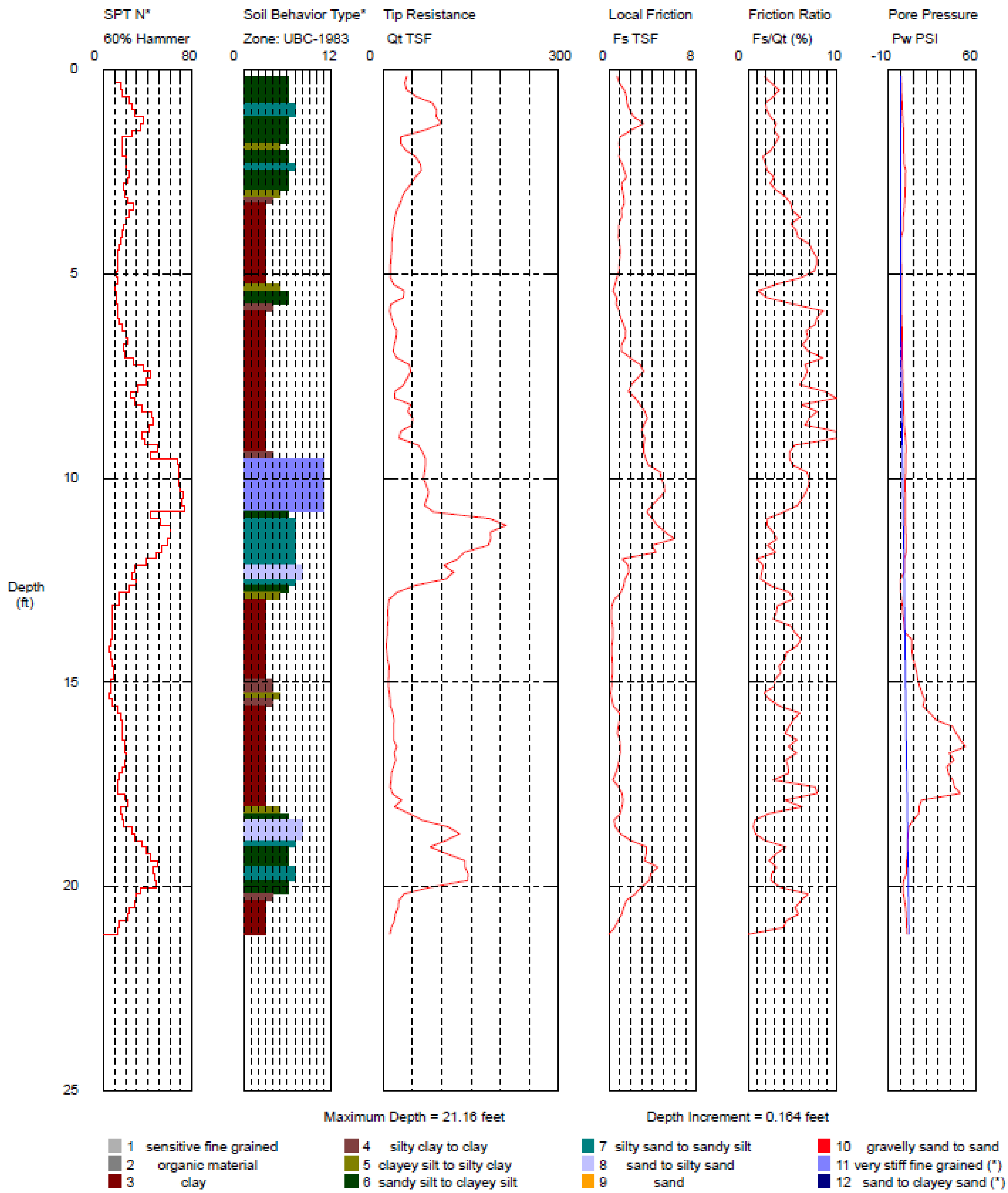

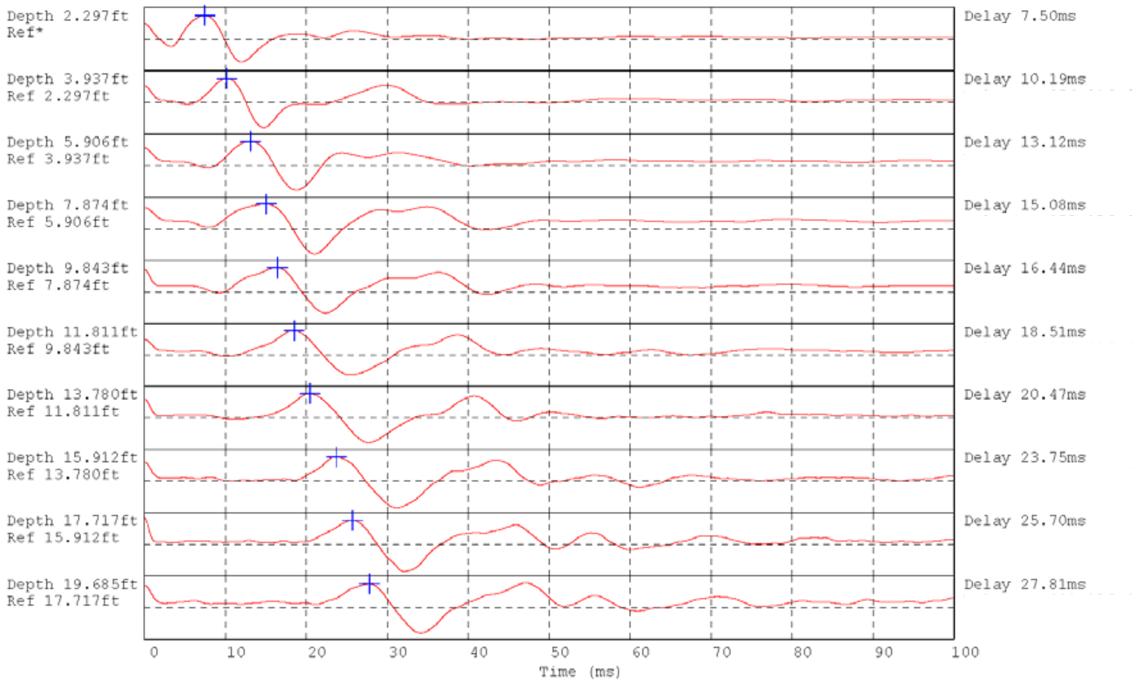

Hammer to Rod String Distance 1.3 (m)
* = Not Determined

A.3 CPT-3 for Lateral Loading Tests

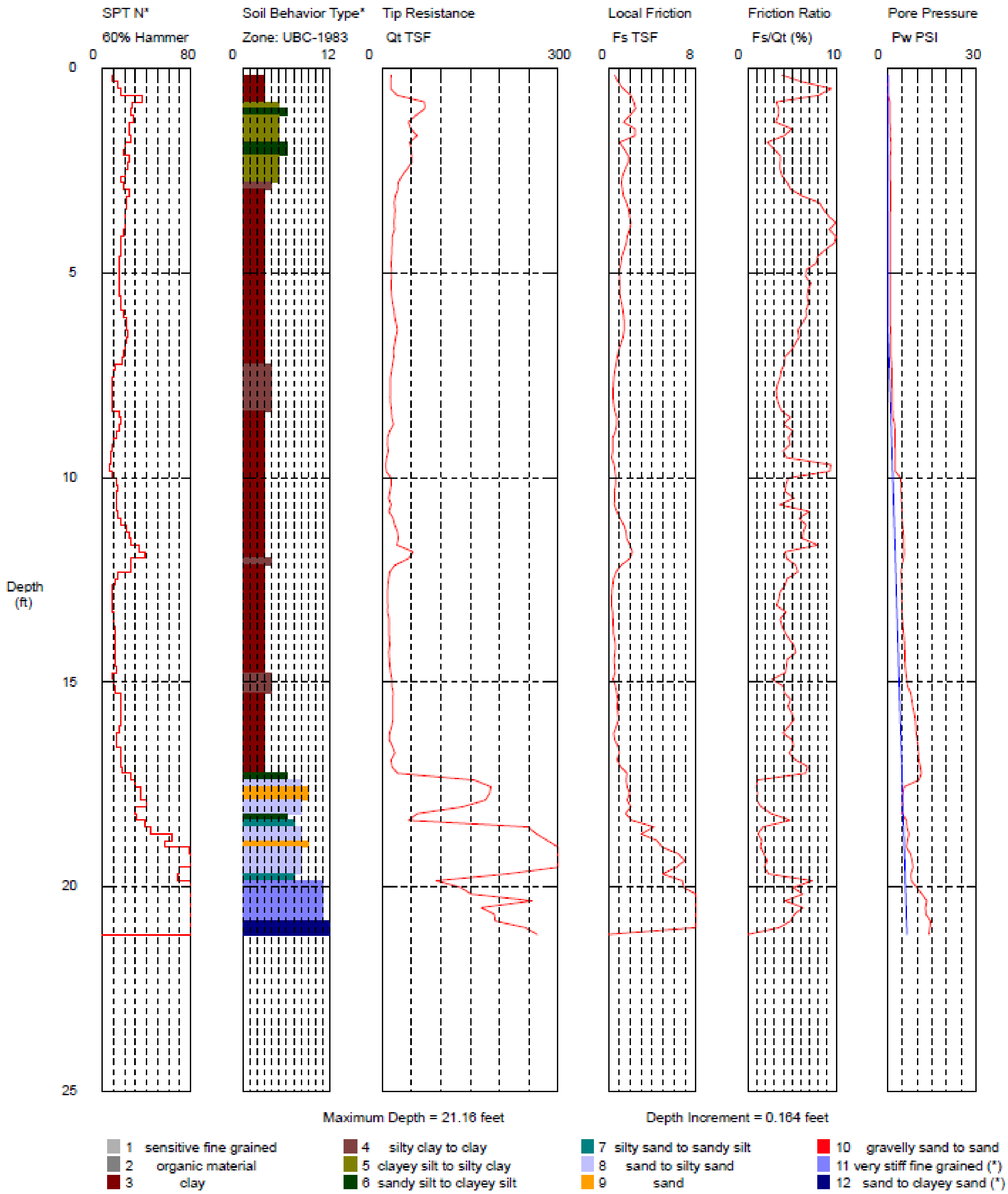

A.4 SCPT-1 for Axial and Lateral Loading Tests

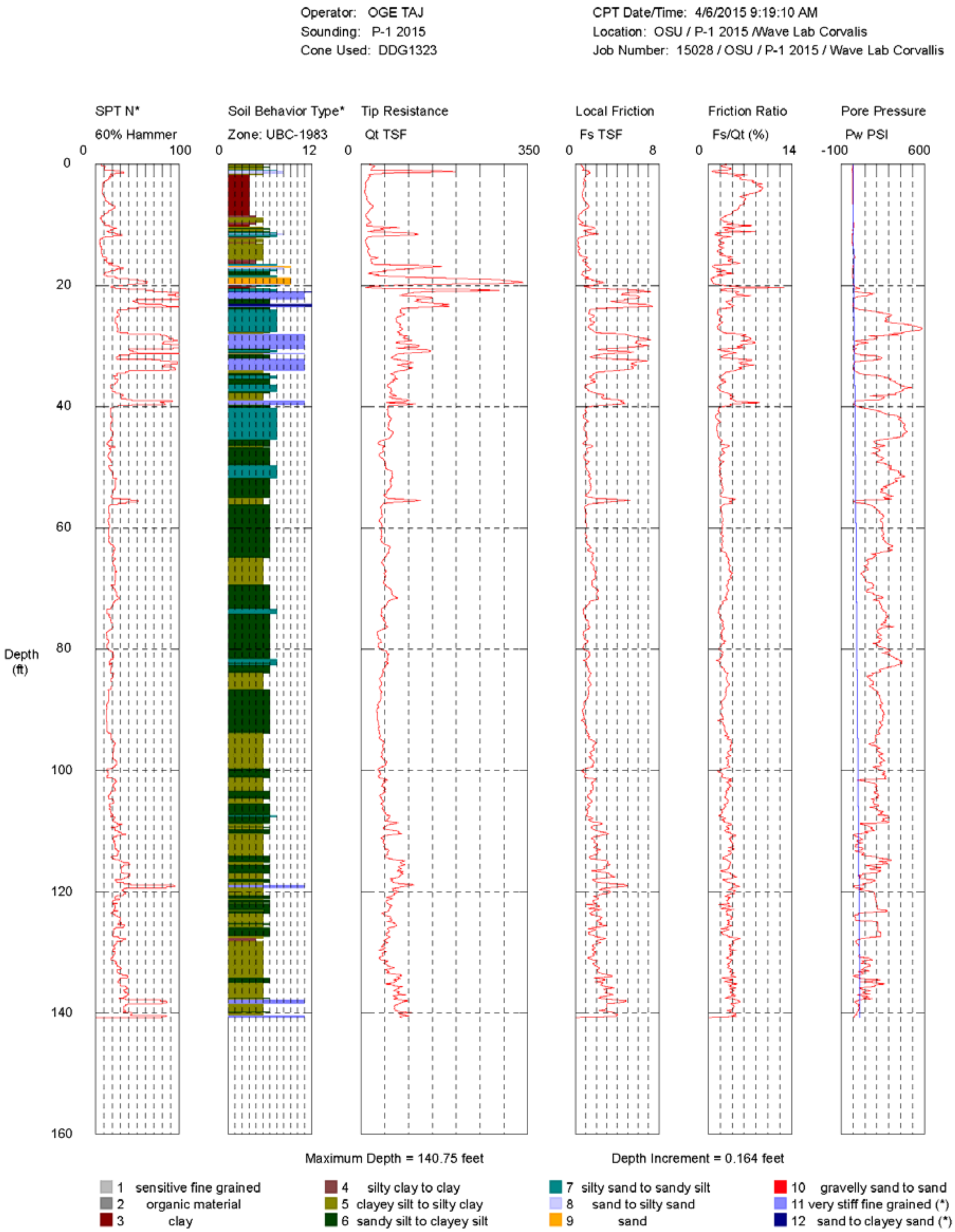

Soil behavior type and SPT based on data from UBC-1983

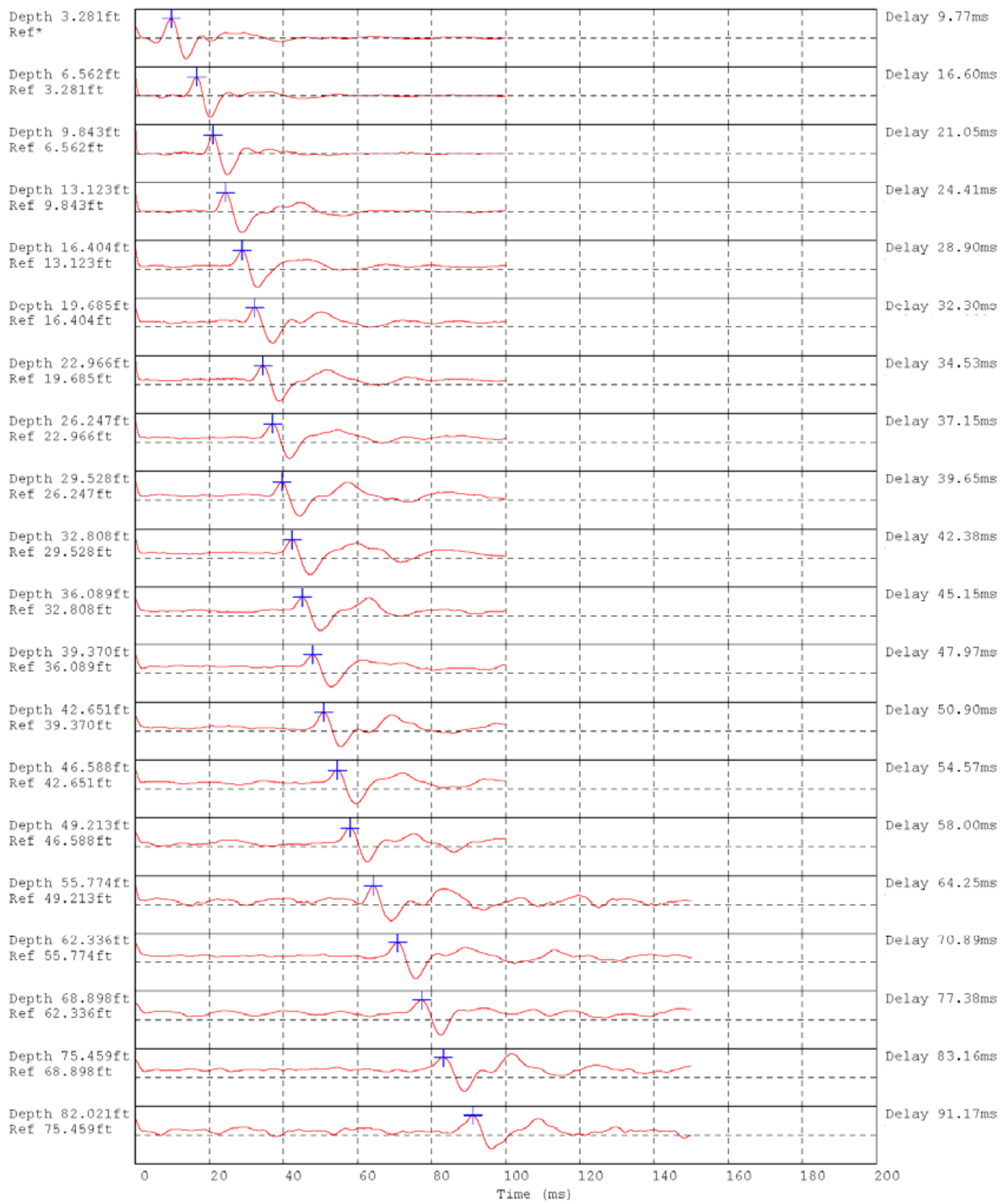

Hammer to Rod String Distance 1.3(m)
* = Not Determined

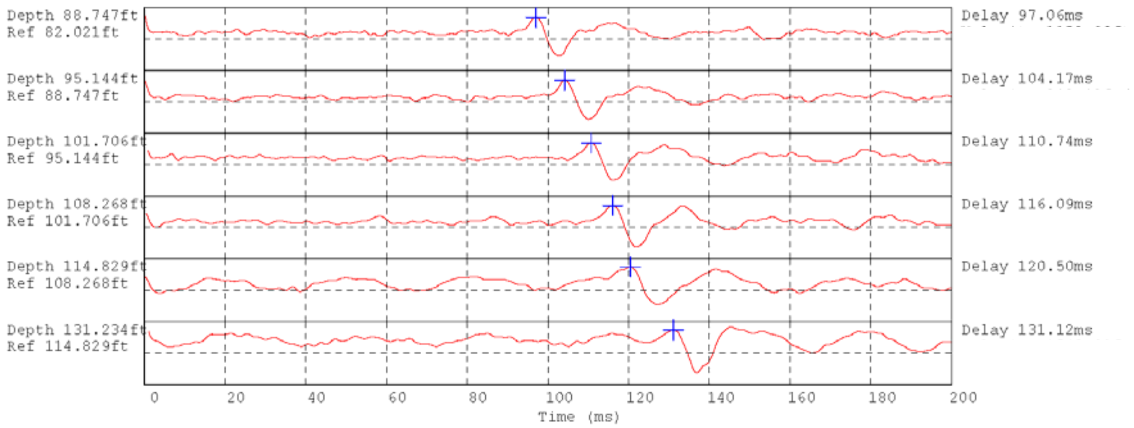

Hammer to Rod String Distance 1.3 (m)
* = Not Determined

A.5 SCPT-2 for Axial and Lateral Loading Tests

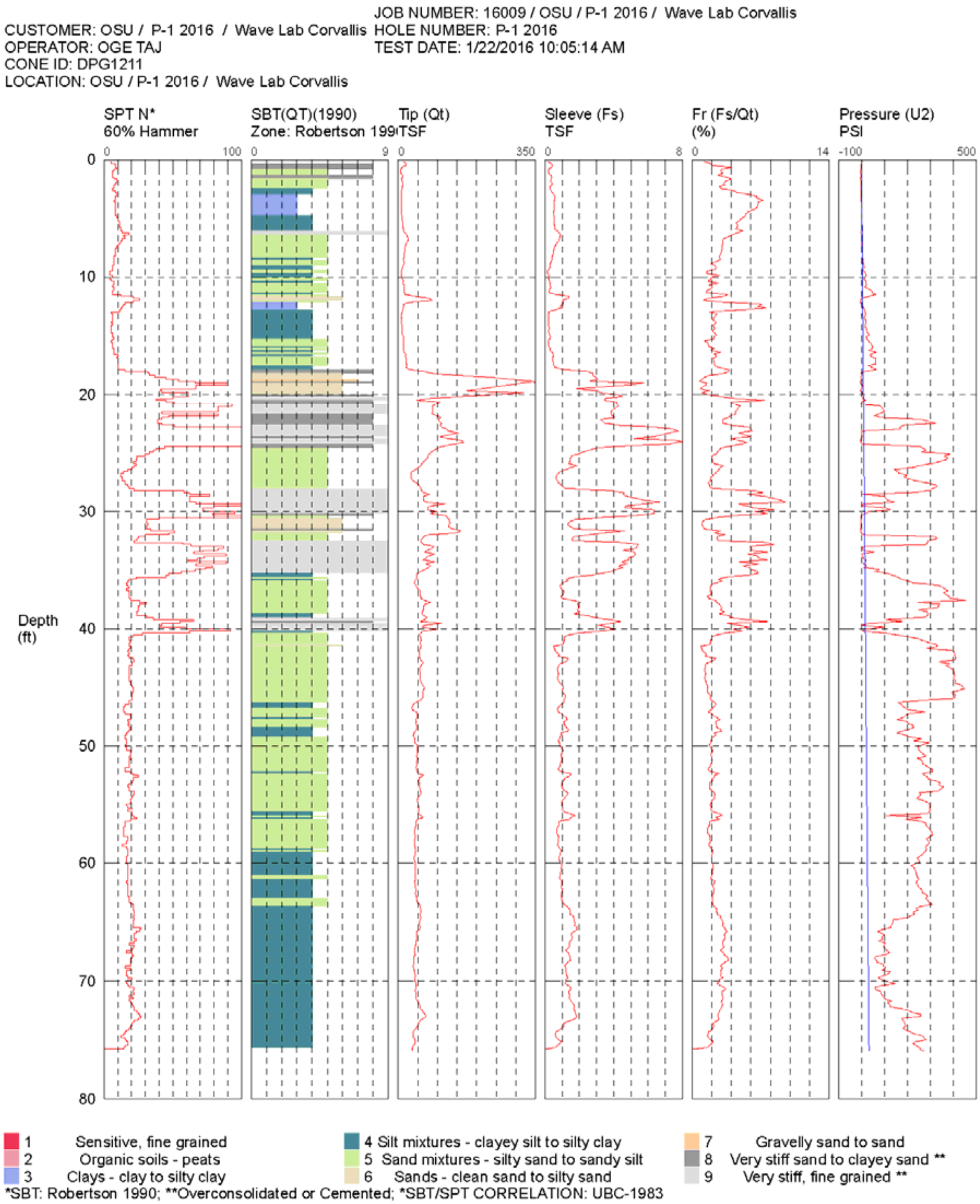

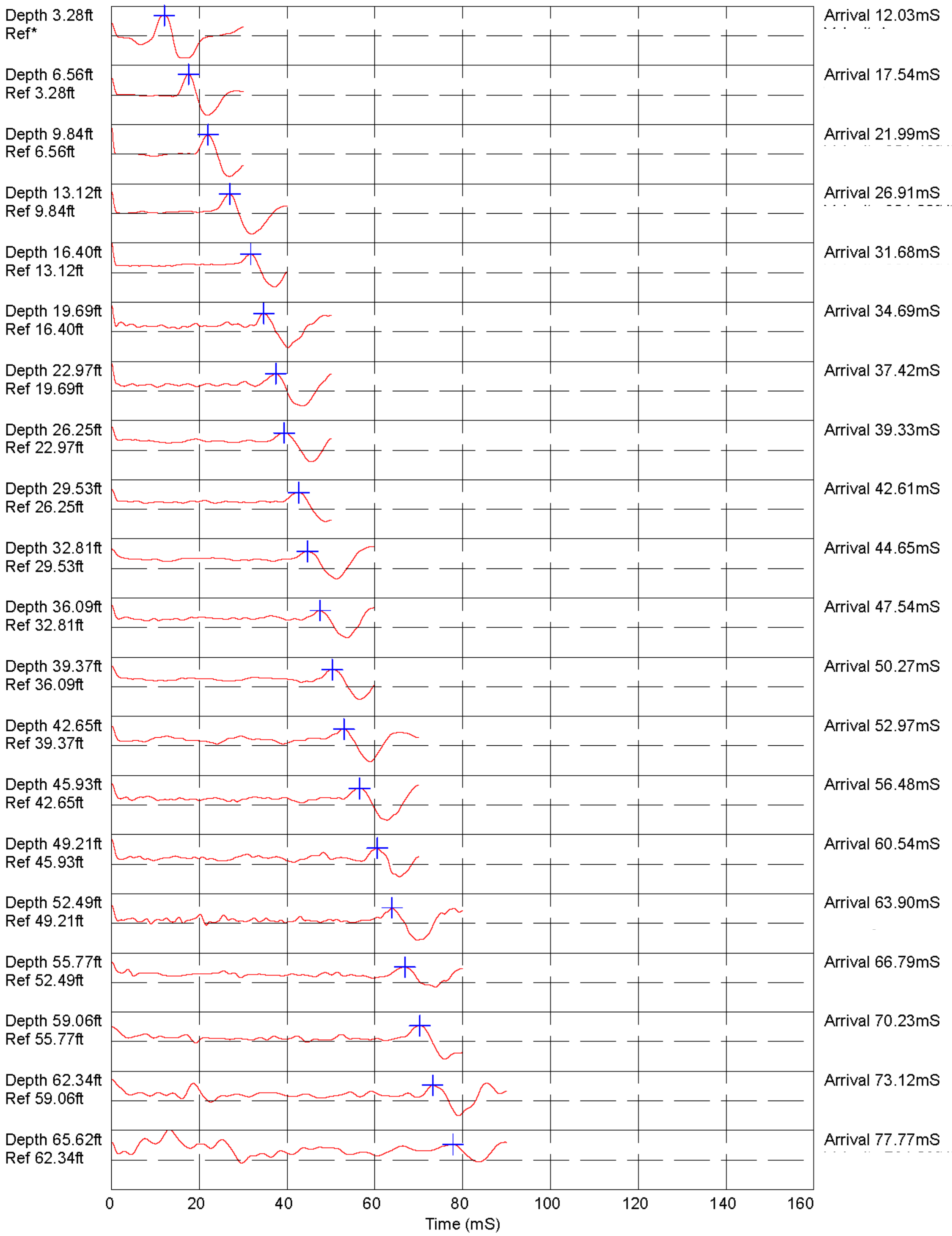
Depth 3.28ft
Ref*
Arrival 12.03mS
Depth 6.56ft
Ref 3.28ft
Arrival 17.54mS
Depth 9.84ft
Ref 6.56ft
Arrival 21.99mS
Depth 13.12ft
Ref 9.84ft
Arrival 26.91mS
Depth 16.40ft
Ref 13.12ft
Arrival 31.68mS
Depth 19.69ft
Ref 16.40ft
Arrival 34.69mS
Depth 22.97ft
Ref 19.69ft
Arrival 37.42mS
Depth 26.25ft
Ref 22.97ft
Arrival 39.33mS
Depth 29.53ft
Ref 26.25ft
Arrival 42.61mS
Depth 32.81ft
Ref 29.53ft
Arrival 44.65mS
Depth 36.09ft
Ref 32.81ft
Arrival 47.54mS
Depth 39.37ft
Ref 36.09ft
Arrival 50.27mS
Depth 42.65ft
Ref 39.37ft
Arrival 52.97mS
Depth 45.93ft
Ref 42.65ft
Arrival 56.48mS
Depth 49.21ft
Ref 45.93ft
Arrival 60.54mS
Depth 52.49ft
Ref 49.21ft
Arrival 63.90mS
Depth 55.77ft
Ref 52.49ft
Arrival 66.79mS
Depth 59.06ft
Ref 55.77ft
Arrival 70.23mS
Depth 62.34ft
Ref 59.06ft
Arrival 73.12mS
Depth 65.62ft
Ref 62.34ft
Arrival 77.77mS
0
20
40
60
80
100
120
140
160
Time (mS)

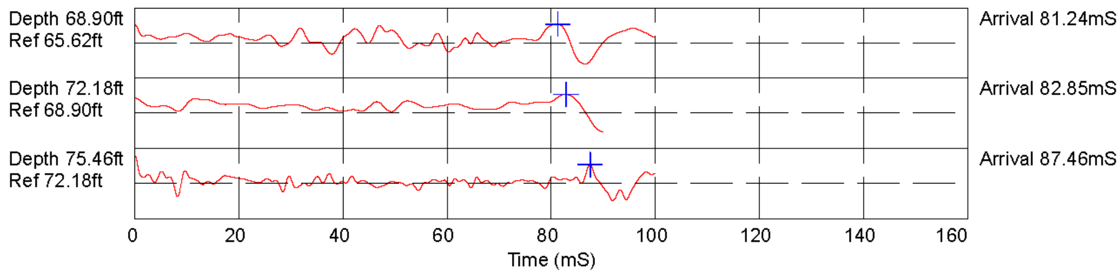

Hammer to Rod String Distance (ft): 4.27
* = Not Determined

JOB NUMBER: 16009 / OSU / P-1 2016 / Wave Lab Corvallis

A.6 SCPT-3 for Axial and Lateral Loading Tests

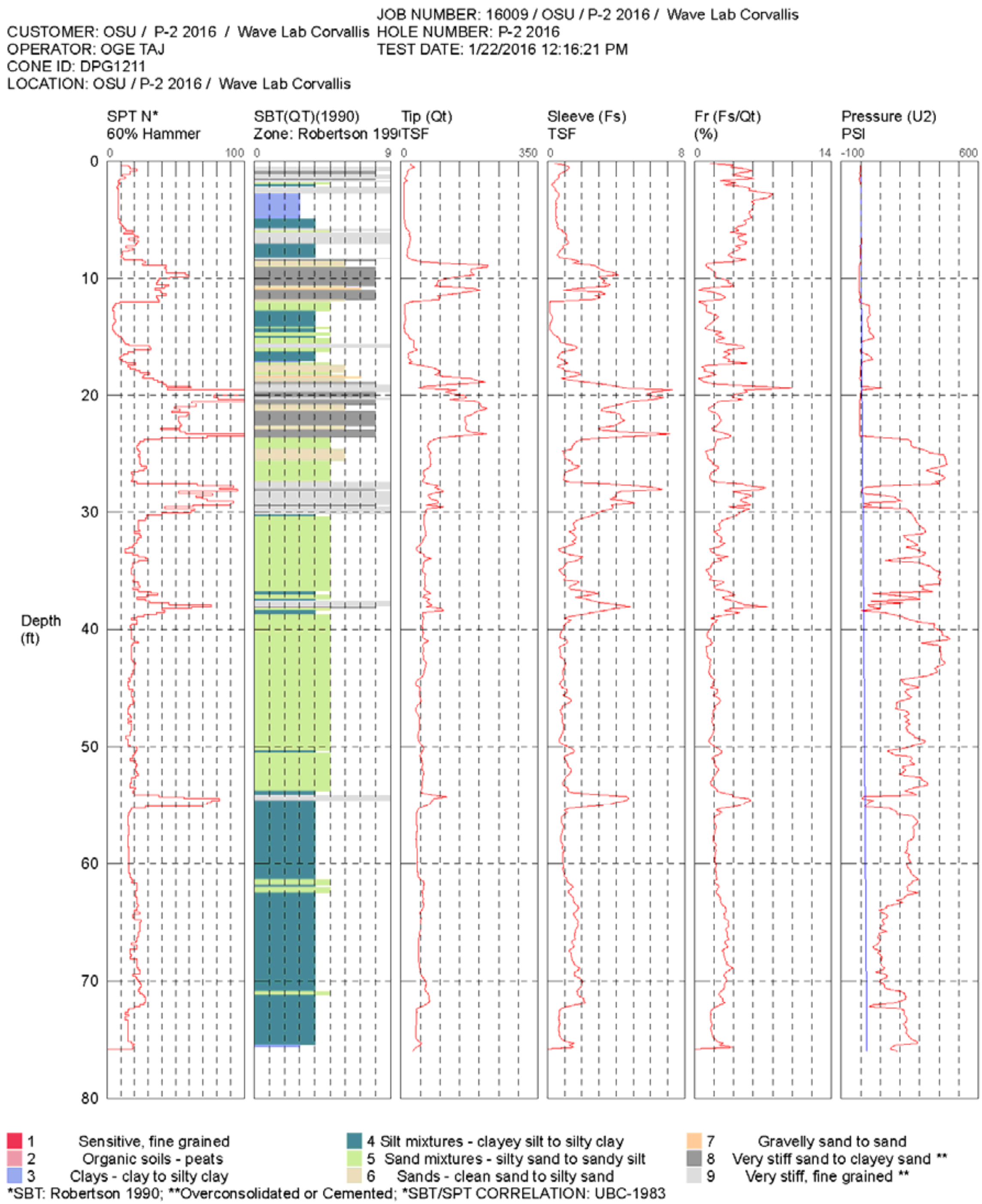

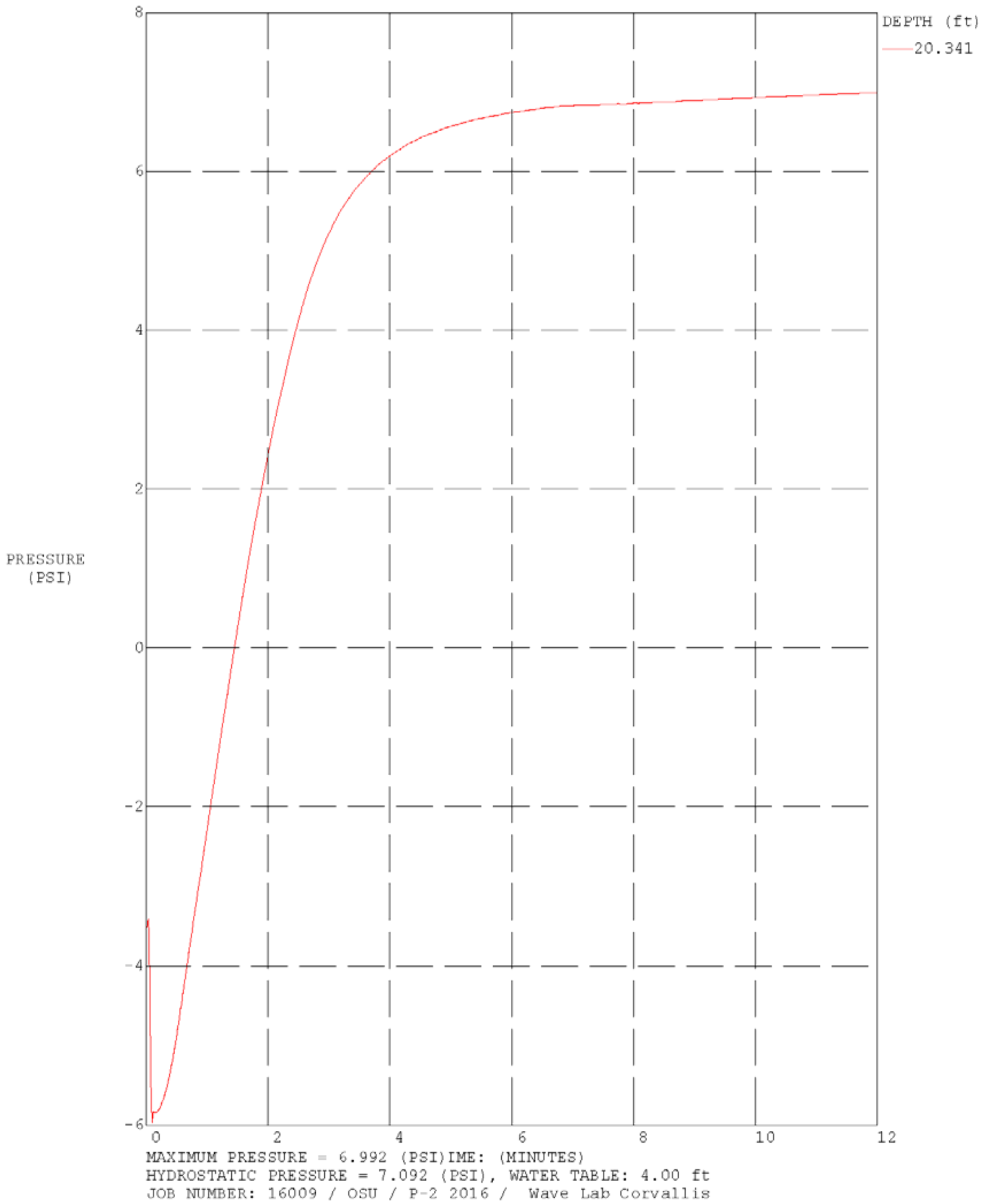

DEPTH (ft)
20.341
PRESSURE
(PSI)
8
6
4
2
0
-2
-4
-6
0
2
4
6
8
10
12
MAXIMUM PRESSURE = 6.992 (PSI)IME: (MINUTES)
HYDROSTATIC PRESSURE = 7.092 (PSI), WATER TABLE: 4.00 ft
JOB NUMBER: 16009 / OSU / P-2 2016 / Wave Lab Corvallis

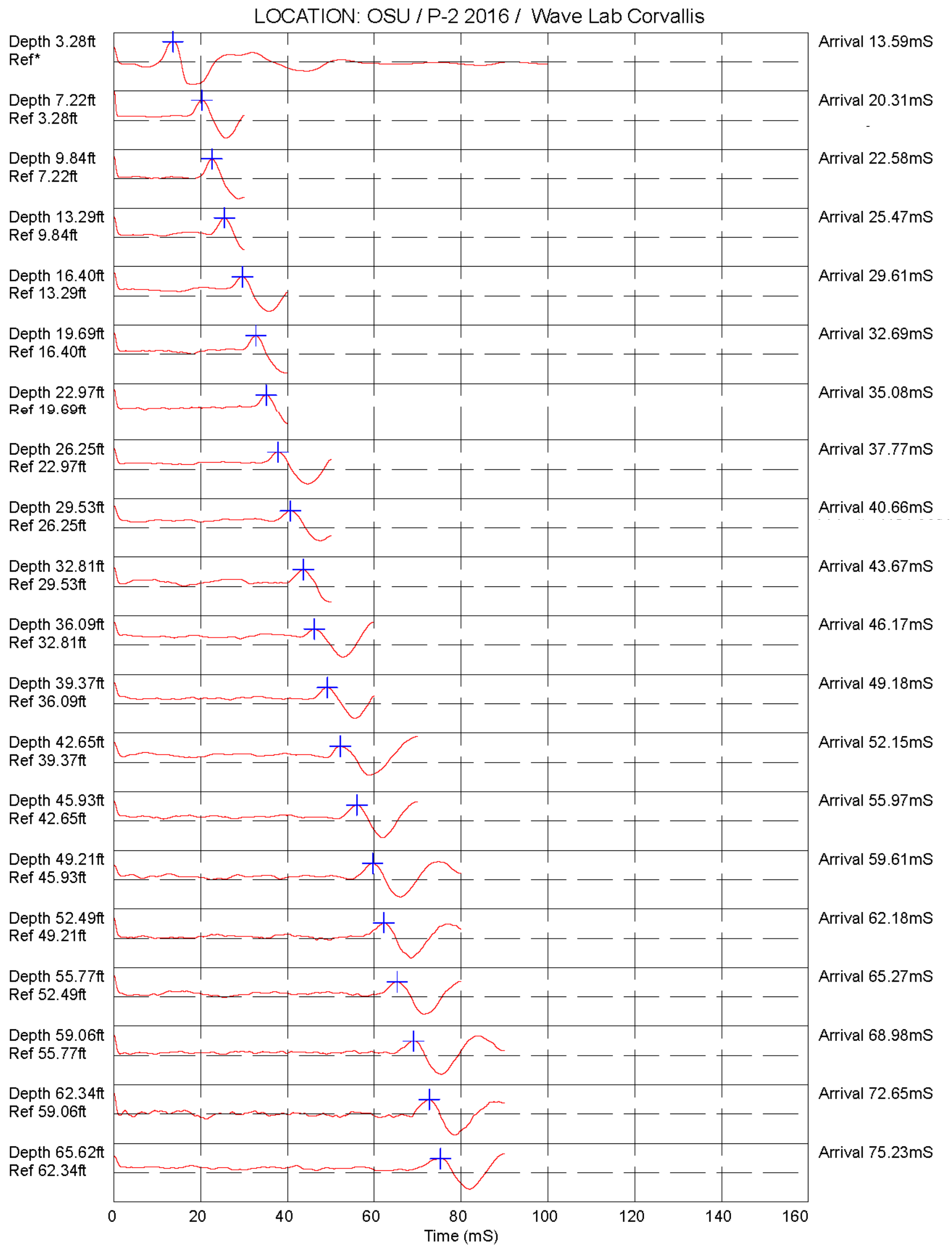
LOCATION: OSU / P-2 2016 / Wave Lab Corvallis
Depth 3.28ft
Ref*
Arrival 13.59mS
Depth 7.22ft
Ref 3.28ft
Arrival 20.31mS
Depth 9.84ft
Ref 7.22ft
Arrival 22.58mS
Depth 13.29ft
Ref 9.84ft
Arrival 25.47mS
Depth 16.40ft
Ref 13.29ft
Arrival 29.61mS
Depth 19.69ft
Ref 16.40ft
Arrival 32.69mS
Depth 22.97ft
Ref 19.69ft
Arrival 35.08mS
Depth 26.25ft
Ref 22.97ft
Arrival 37.77mS
Depth 29.53ft
Ref 26.25ft
Arrival 40.66mS
Depth 32.81ft
Ref 29.53ft
Arrival 43.67mS
Depth 36.09ft
Ref 32.81ft
Arrival 46.17mS
Depth 39.37ft
Ref 36.09ft
Arrival 49.18mS
Depth 42.65ft
Ref 39.37ft
Arrival 52.15mS
Depth 45.93ft
Ref 42.65ft
Arrival 55.97mS
Depth 49.21ft
Ref 45.93ft
Arrival 59.61mS
Depth 52.49ft
Ref 49.21ft
Arrival 62.18mS
Depth 55.77ft
Ref 52.49ft
Arrival 65.27mS
Depth 59.06ft
Ref 55.77ft
Arrival 68.98mS
Depth 62.34ft
Ref 59.06ft
Arrival 72.65mS
Depth 65.62ft
Ref 62.34ft
Arrival 75.23mS
0
20
40
60
80
100
120
140
160
Time (mS)

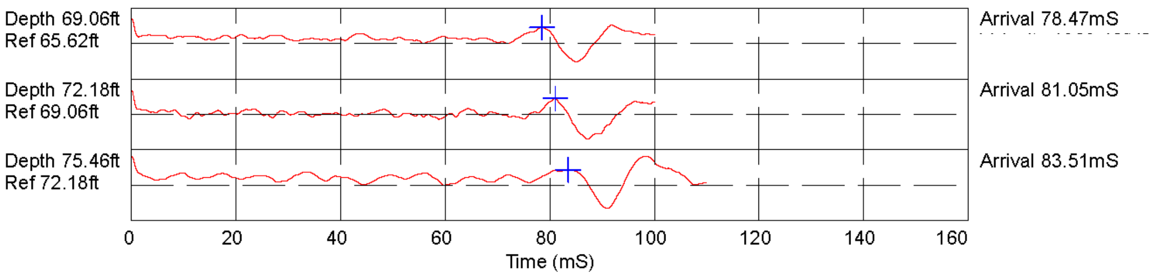

Hammer to Rod String Distance (ft): 4.27
* = Not Determined

A.7 CPT-4 for Axial and Lateral Loading Tests

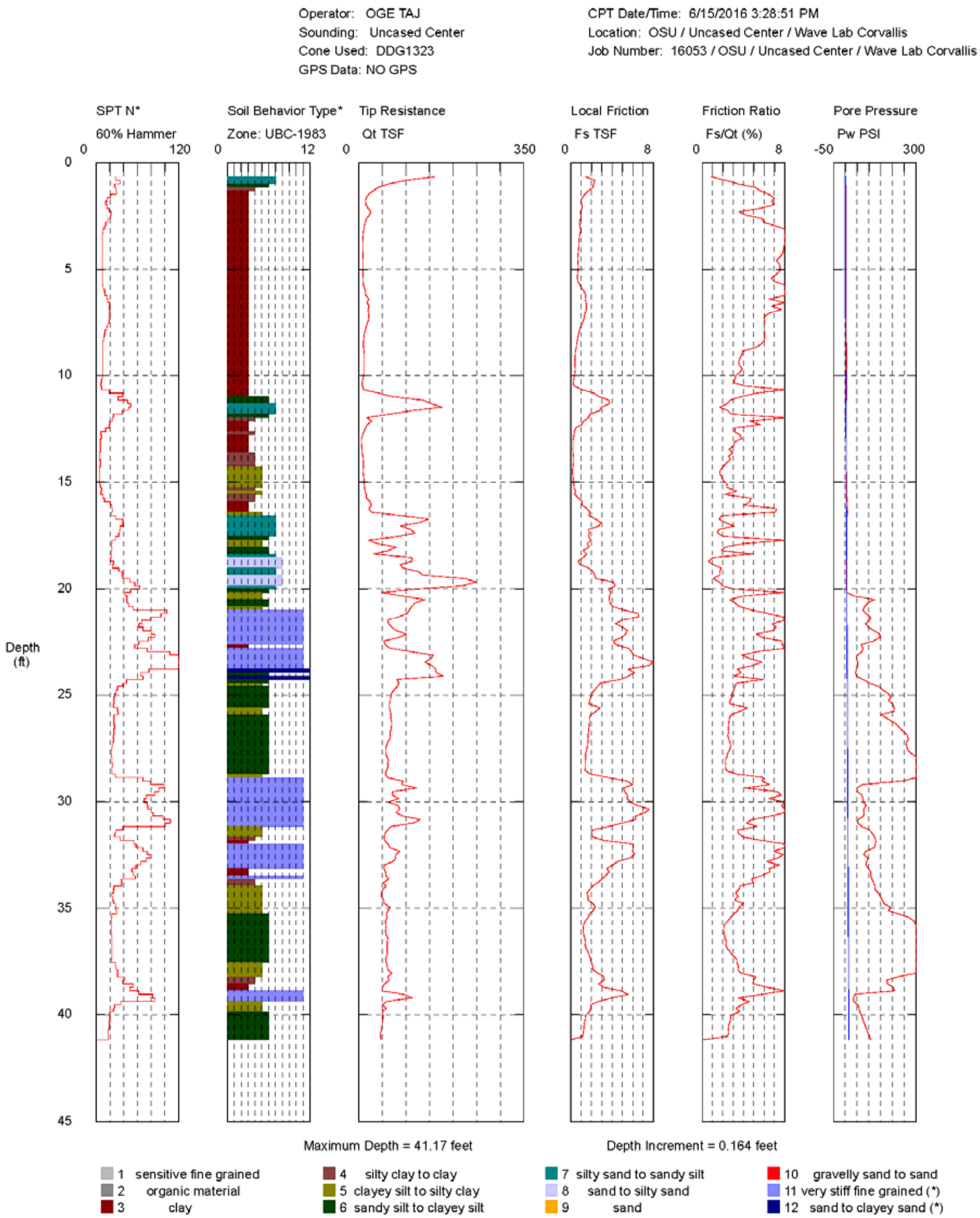

A.8 SCPT-5 for Axial and Lateral Loading Tests

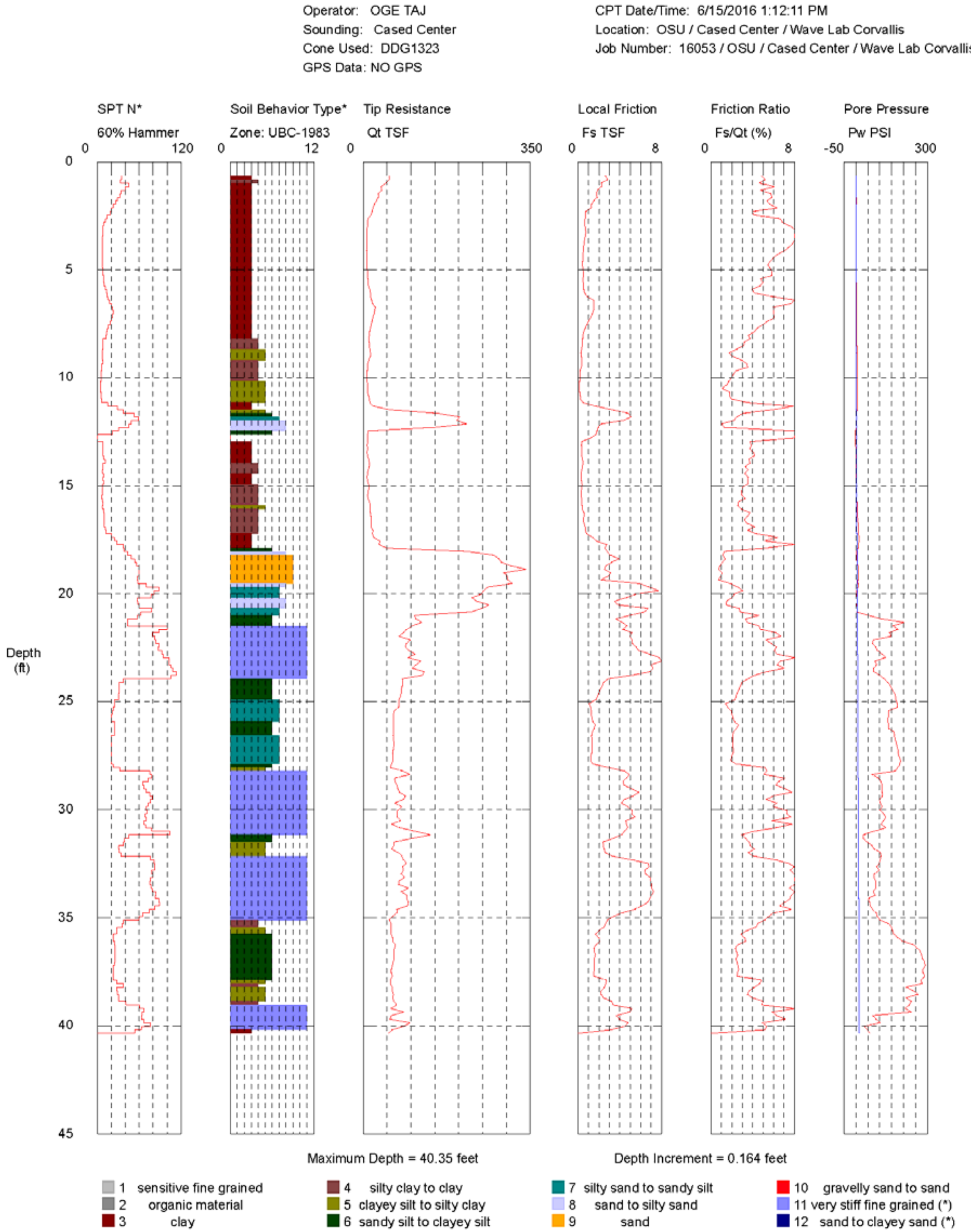

*Soil behavior type and SPT based on data from UBC-1983

A.9 SCPT-6 for Axial and Lateral Loading Tests

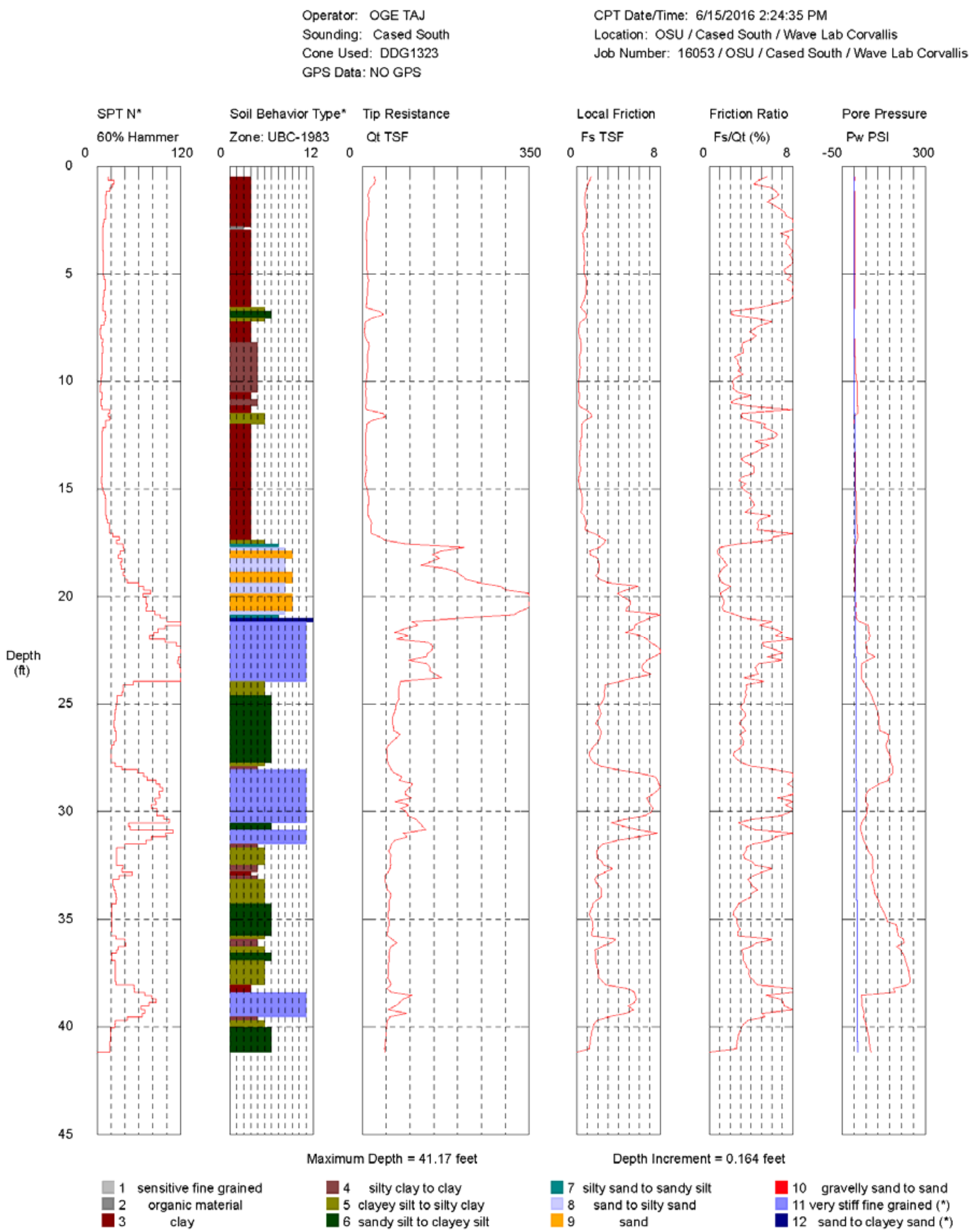

*Soil behavior type and SPT based on data from UBC-1983

A.10 SCPT-7 for Axial and Lateral Loading Tests

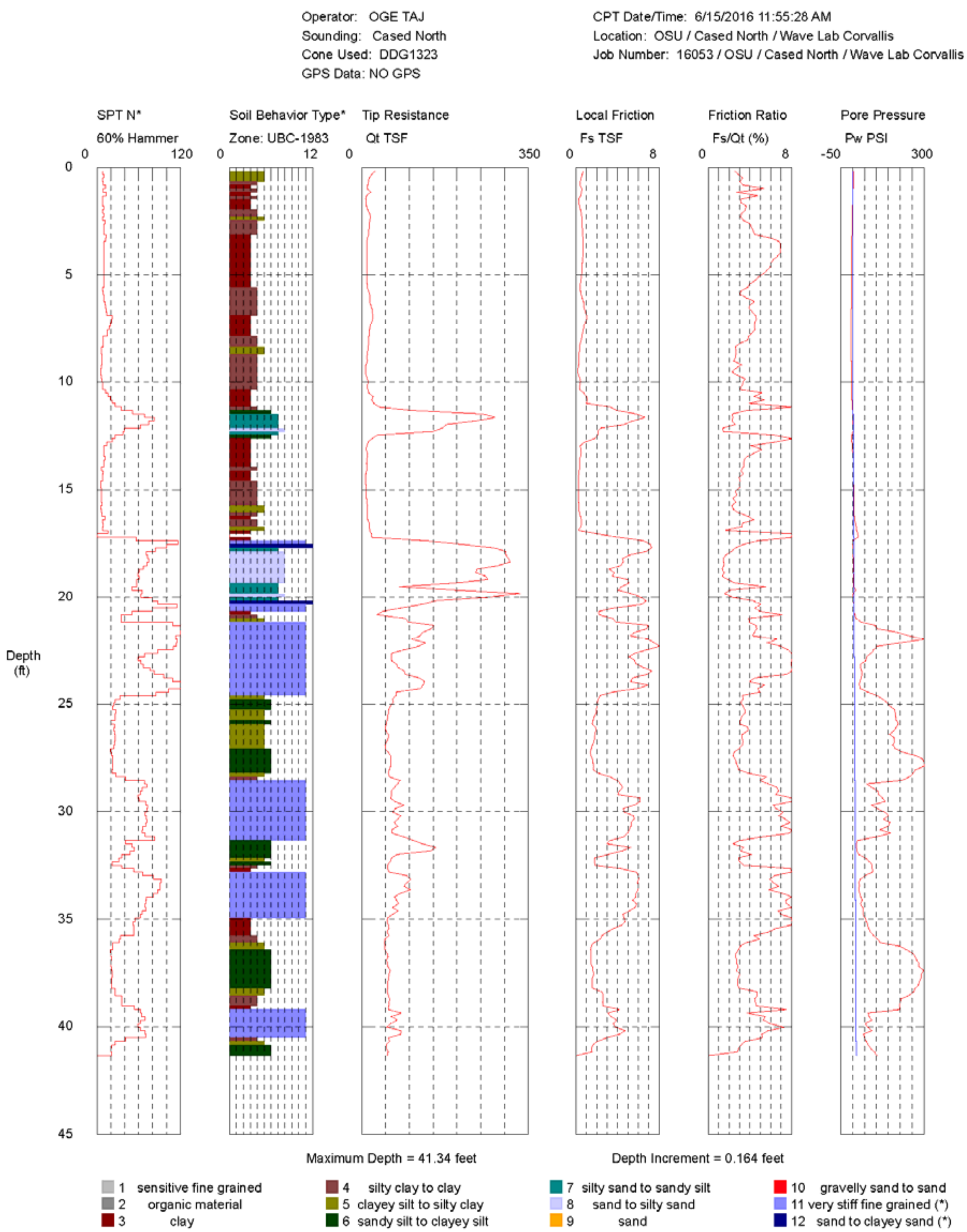

*Soil behavior type and SPT based on data from UBC-1983

A.11 1997 CPT-1

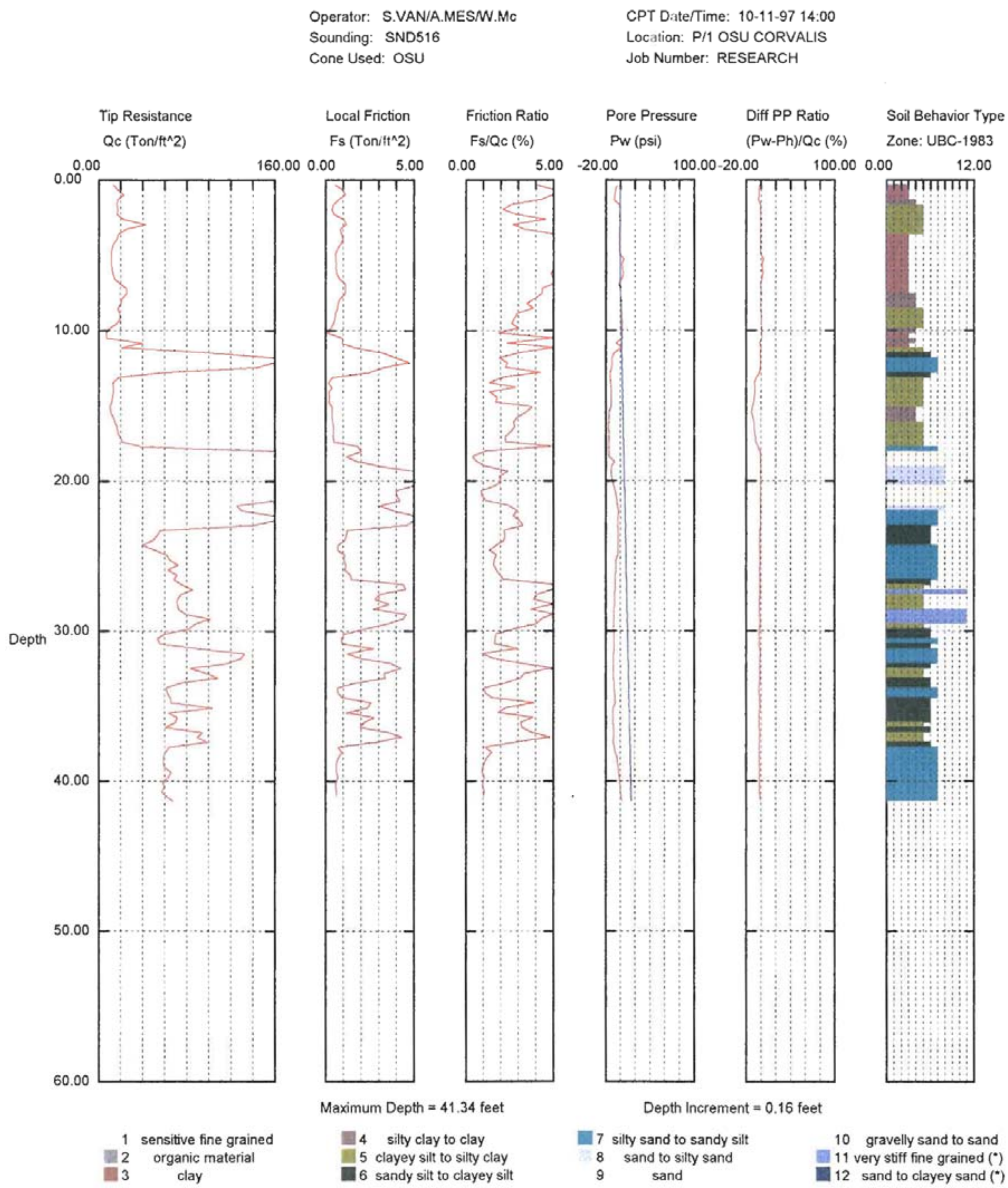

Appendix B DATA ANALYSES FOR TORSIONAL LOADING TESTS

This appendix presents the detailed data analyses used for torsional loading tests.

B.1 Data Smoothing of String-Potentiometer Data

The observed string potentiometer displacements were smoothed prior to analysis using a weighted smoothing function, that is given by:

$$S_j = \frac{1}{16}\left(Y_{j-3} + 2Y_{j-2} + 3Y_{j-1} + 4Y_j + 3Y_{j+1} + 2Y_{j+2} + Y_{j+3}\right) \tag{B.1}$$

where S_j = the j^{th} point in the smoothed data, Y_j = the j^{th} point in the original data, j = 4 to n - 3, and n is the total number of points in the recorded data.

B.2 Interpretation of Measured Torsional Shear Strains

The methodology for processing the torsional shear strains was derived from mechanical shafts subjected to torsion, as shown in Figure B-1a (Gere and Timoshenko 1997). For the shaft in Figure B-1a, the stress element *abcd* is in a state of pure shear (Figure B-1b) with magnitude τ. Since the strain gages installed in the shaft were inclined 45° from the longitudinal axis, a wedge-shaped element with a 45° inclination taken by cutting stress element *abcd*, as shown in Figure B-1c, was used to form the representative element for analysis. Due to force equilibrium on the wedge-shaped element, the stresses ($\tau_{45°}$ and $\sigma_{45°}$) on the inclined face are given by:

$$\tau_{45^o} = 0, \quad \sigma_{45^o} = \tau \tag{B.2}$$

Similarly, the stresses $\tau_{-45°}$ and $\sigma_{-45°}$ can also be obtained:

$$\tau_{-45^o} = 0, \quad \sigma_{-45^o} = \tau \tag{B.3}$$

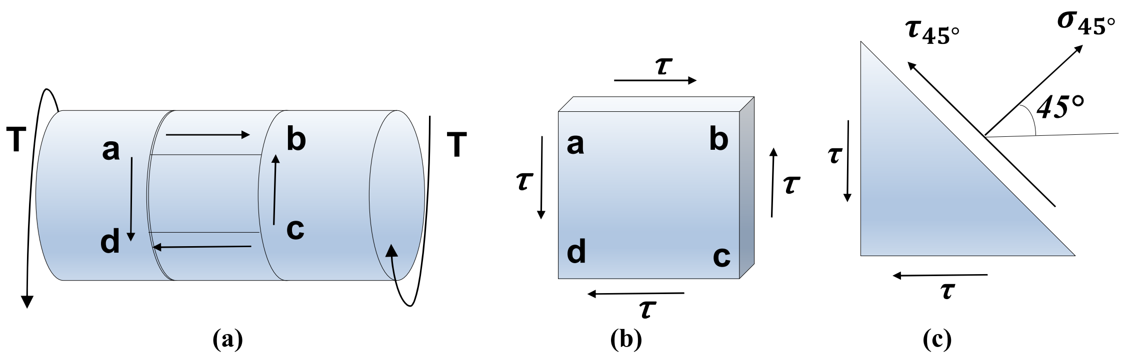

Figure B-1. Analytical model for the assessment of torsionally-induced shear strains: (a) a shaft subjected to torsion, (b) a representative stress element, and (c) a wedge-shaped element (modified from Gere and Timoshenko 1997).

For an element inclined at 45° (Figure B-2), the relationship between the strains ($\varepsilon_{45°}$ and $\varepsilon_{-45°}$) and shear stresses ($\sigma_{45°}$ and $\sigma_{-45°}$), is given by:

$$\varepsilon_{45^o} = \frac{\sigma_{45^o}}{E} - \frac{\nu \cdot \sigma_{-45^o}}{E} = \frac{\tau}{E} + \frac{\nu \cdot \tau}{E} = \frac{\tau}{E}(1+\nu) \tag{B.4}$$

$$\varepsilon_{-45^o} = -\varepsilon_{45^o} = -\frac{\tau}{E}(1+\nu) \tag{B.5}$$

where ν = Poisson's ratio and E = the Young's modulus, which was estimated based on the ACI 318-05 model (ACI 318 2005) using the concrete strength at the test day. In this element, the strain $\varepsilon_{45°}$ and $\varepsilon_{-45°}$ are equal to the strains measured using the ESGs. Therefore, the shear stresses at the location of ESGs can be obtained by:

$$\tau = \frac{E \cdot \varepsilon_{45^o}}{(1+\nu)} \tag{B.6}$$

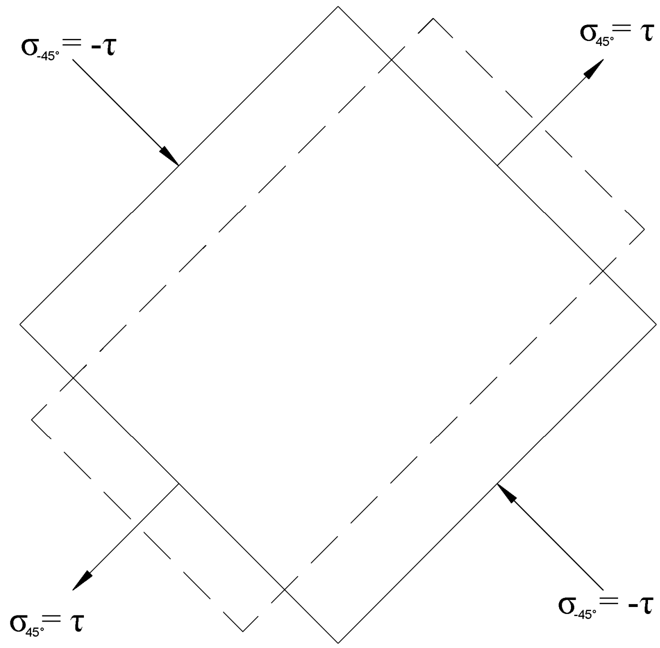

Figure B-2. Model element inclined 45° (modified from Gere and Timoshenko 1997).

Because the embedded strain gages were attached to the hoop reinforcements (Figure B-3), which were 76 mm (3 in) from the surface of the shaft, the strain directly at the soil-shaft interface was not measured. It was assumed that the shear stresses were distributed linearly with distance away from the center of the section, as shown in Figure B-3, as is commonly assumed in structural mechanics applications (Hibbeler 2013). The maximum shear stress at the shaft surface is given by:

$$\tau_{max} = \frac{r}{\rho}\tau \qquad \text{(B.7)}$$

where r = radius of shaft = 0.45 m (17.5 in), ρ = the distance from shaft center to strain gages = 0.38 m (15 in), τ = the shear stresses at the location of ESGs estimated using Eq. (B.3). The internal torque at the location of each ESG can then be computed by:

$$T = \frac{\tau_{\max} J}{r} \tag{B.8}$$

where J = polar moment of inertia, which is given by

$$J = \frac{\pi r^4}{2} \tag{B.9}$$

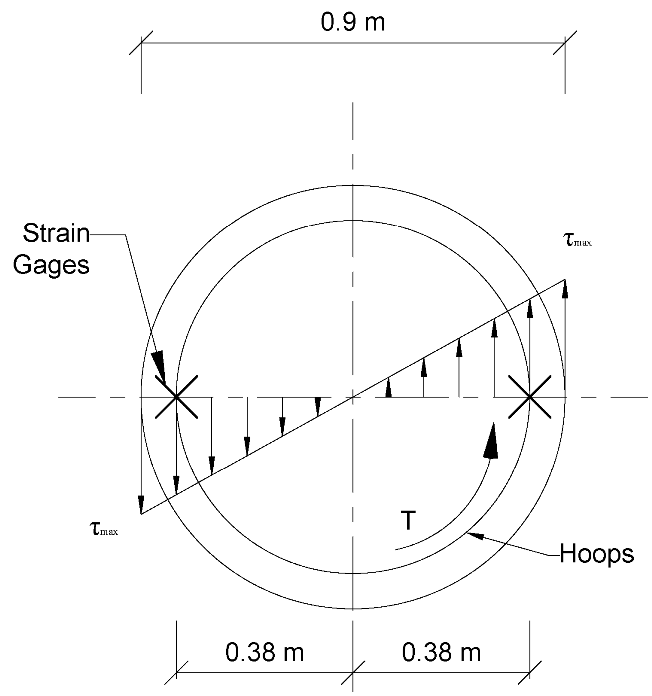

Figure B-3. Shear stress distribution at the cross section of the shaft subjected to torsion. Note: 0.9 m = 36 in and 0.38 m = 15 in.

B.3 Hyperbolic Models for Torque-Rotation Response

Figure B-4 and Figure B-5 compare the available torque-rotation data of shaft TDSFB and TDS, respectively, in hyperbolic space to a fitted line and show the comparison between the measured and predicted response using the hyperbolic model. This data corresponds to the rotation imposed at the shaft head and the corresponding torque developed in response to rotation.

B.4 Angle of Twist and Implication for Load Transfer

In order to compute the true rotation at each instrumented elevation of the shaft and back-calculate accurate τ–θ curves, the variation of the angle of twist with depth must be computed. Based on the diameter profile and the torque recorded at each level for the shaft, the angle of twist can be estimated using:

$$\varphi = \frac{T \cdot \Delta L}{G \cdot J} \tag{B.10}$$

where G = shear modulus of test shafts. Owing to the unreliable gages at the base of the shafts, and the possible uncertainty in the assumed toe resistance, the shaft head was chosen as the reference point for the computation of the angle of twist, and is therefore set equal to zero in Figure B-6, which shows the angle of internal twist profiles corresponding to 1.75° of rotation of TDSFB (corresponding to a rotation of 0.1° for TDS). The non-zero angle of twist at the shaft base does not imply true fixity at the base; rather the angle of twist is presented as a negative value to indicate that it is a subtractive quantity for computing the "true rotation" for each section of shaft, which is the relative rotation between the specific section of the shaft and the surrounding soils. The true rotation of each section along the shaft was computed by subtracting the rotation at the shaft head and the angle of twist at that section.

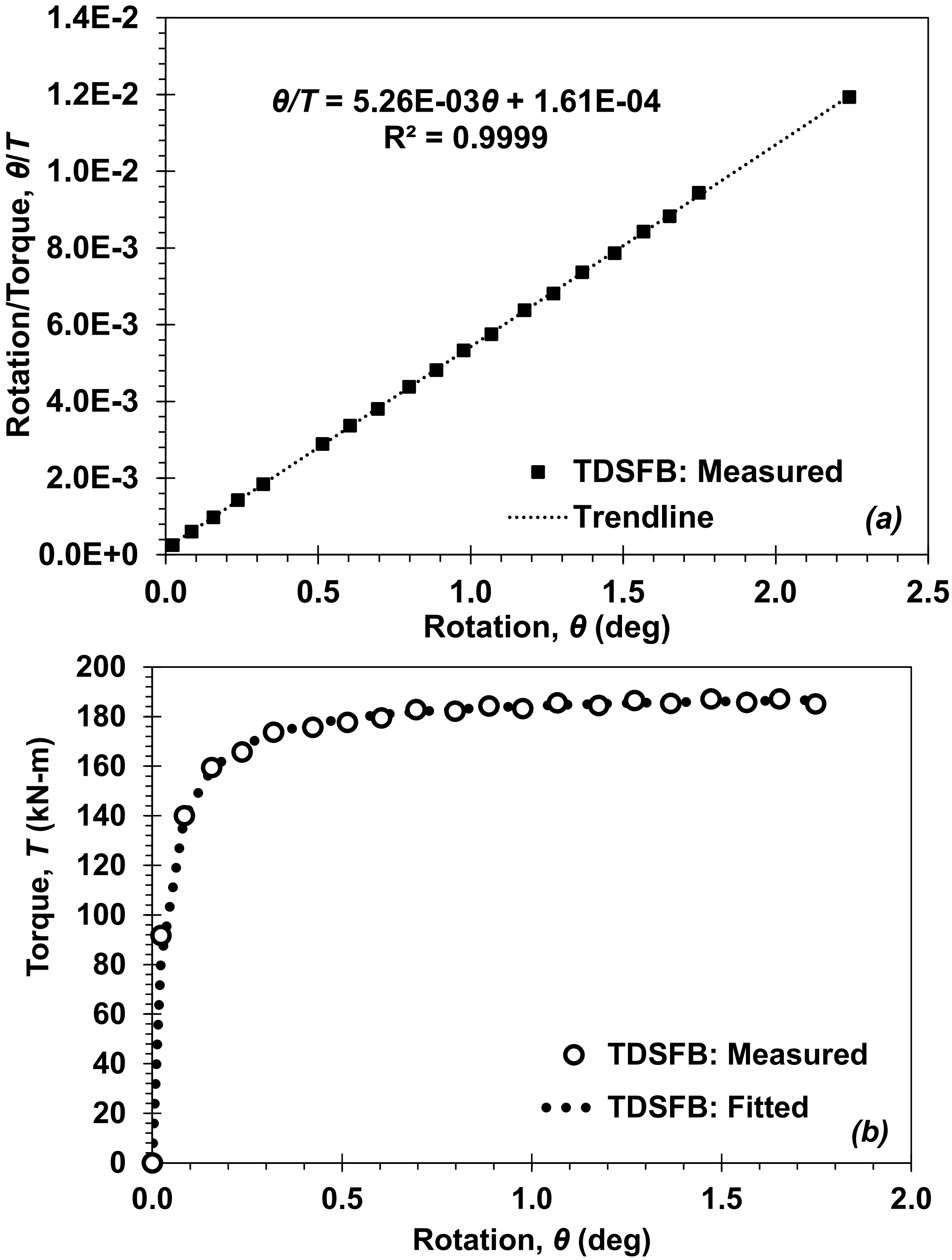

Figure B-4. Hyperbolic model for TDSFB: (a) observed torque-rotation response in hyperbolic space and fitted hyperbolic model and (b) comparison between predicted and measured response.

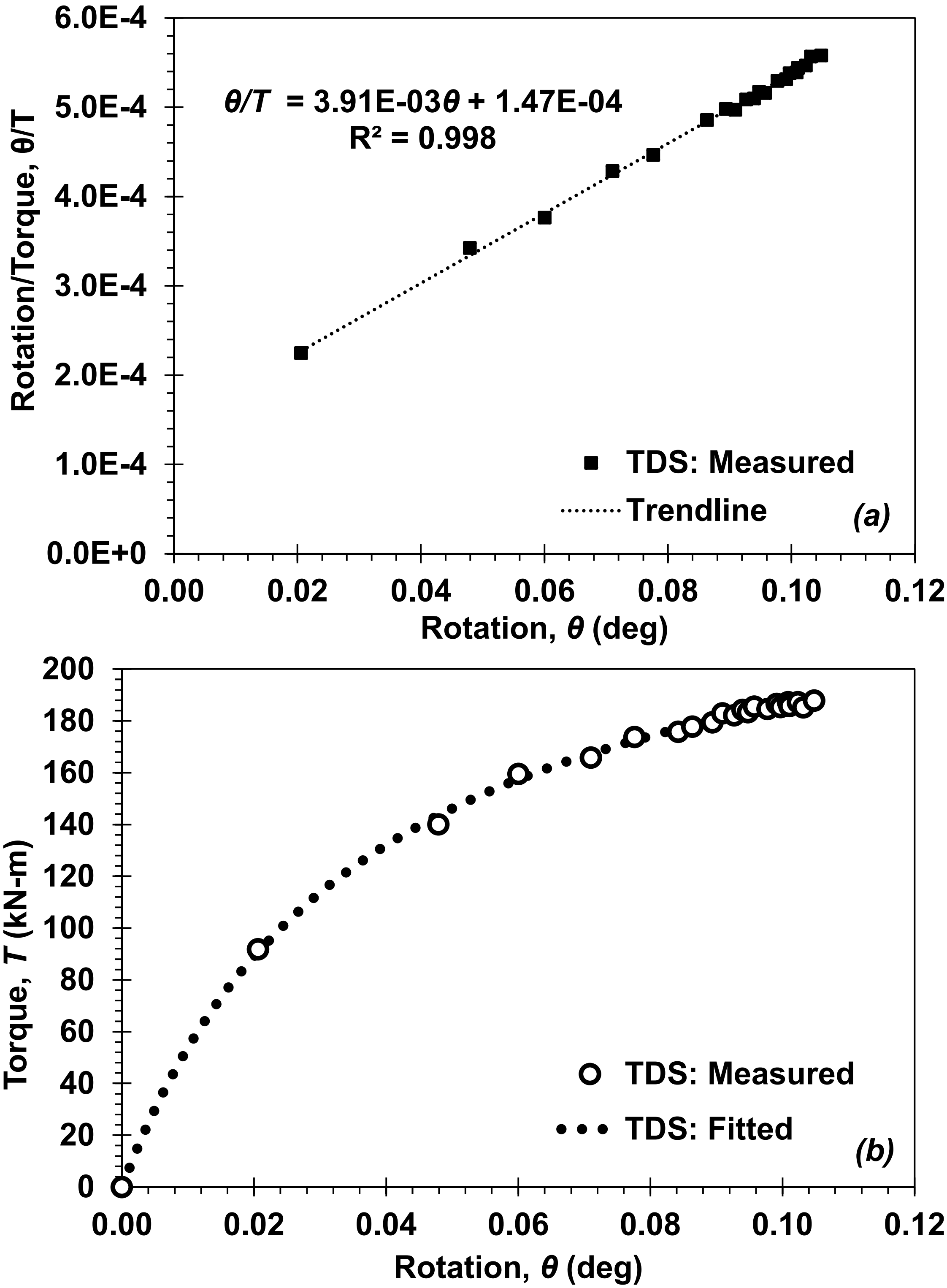

Figure B-5. Hyperbolic model for TDS (a) observed torque-rotation response in hyperbolic space and fitted hyperbolic model and (b) comparison between predicted and measured response.

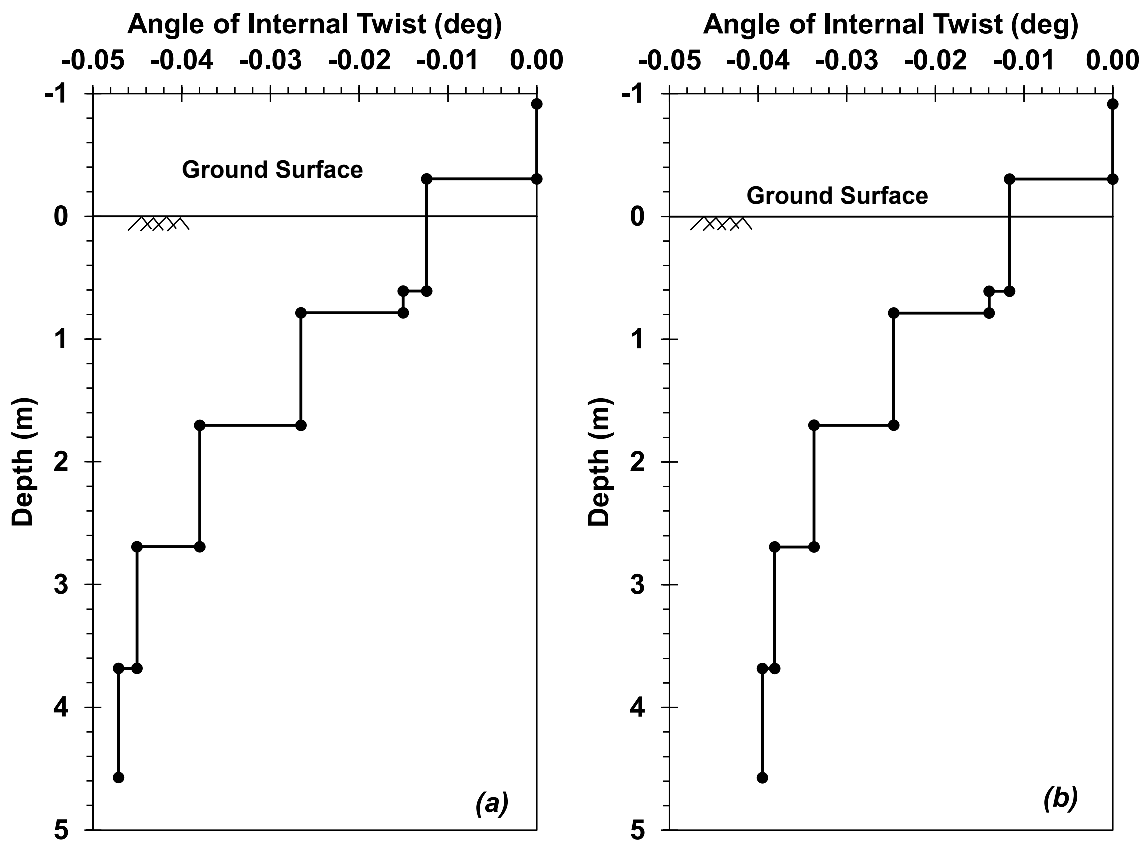

Figure B-6. Angle of twist profile for (a) TDS and (b) TDSFB at 1.75° of TDSFB head rotation.

B.5 Hyperbolic Models for τ–θ Relationship for Shaft TDS

Figure B-7 through Figure B-10 show the observed τ–θ curves in hyperbolic space and fitted hyperbolic models and comparisons between fitted and measured response at different tributary area from the depths of 0.18 m (7 in) to the toe of the shaft. In some instances, the first τ–θ data pairs were omitted from the hyperbolic curve fitting algorithm.

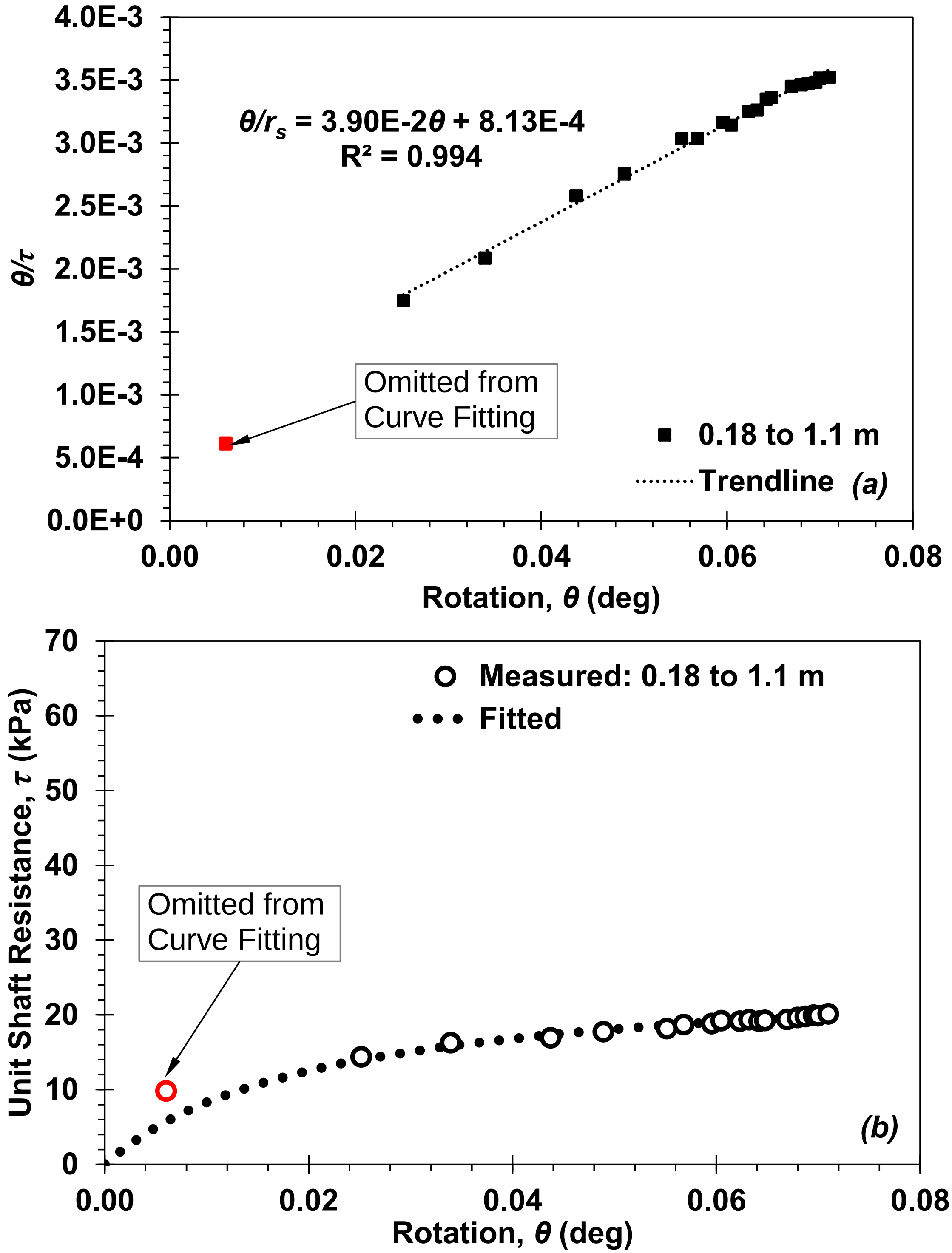

Figure B-7. Hyperbolic model for TDS (a) observed τ–θ curve in hyperbolic space and fitted hyperbolic model and (b) comparison between fitted and measured response at depth from 0.18 to 1.1 m (7 to 49 in).

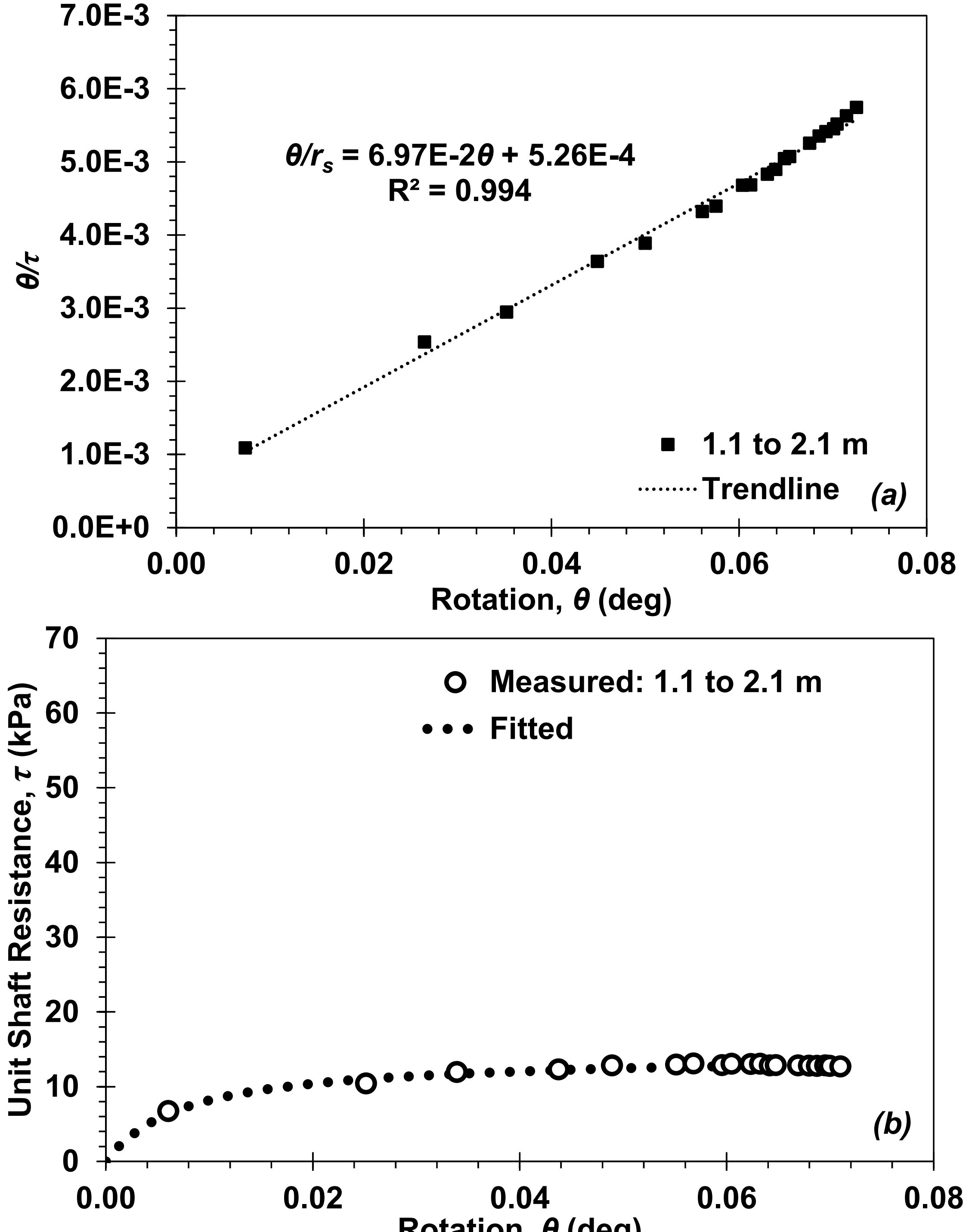

Figure B-8. Hyperbolic model for TDS (a) observed τ–θ curve in hyperbolic space and fitted hyperbolic model and (b) comparison between fitted and measured response at depth from 1.1 to 2.1 m (49 to 82 in).

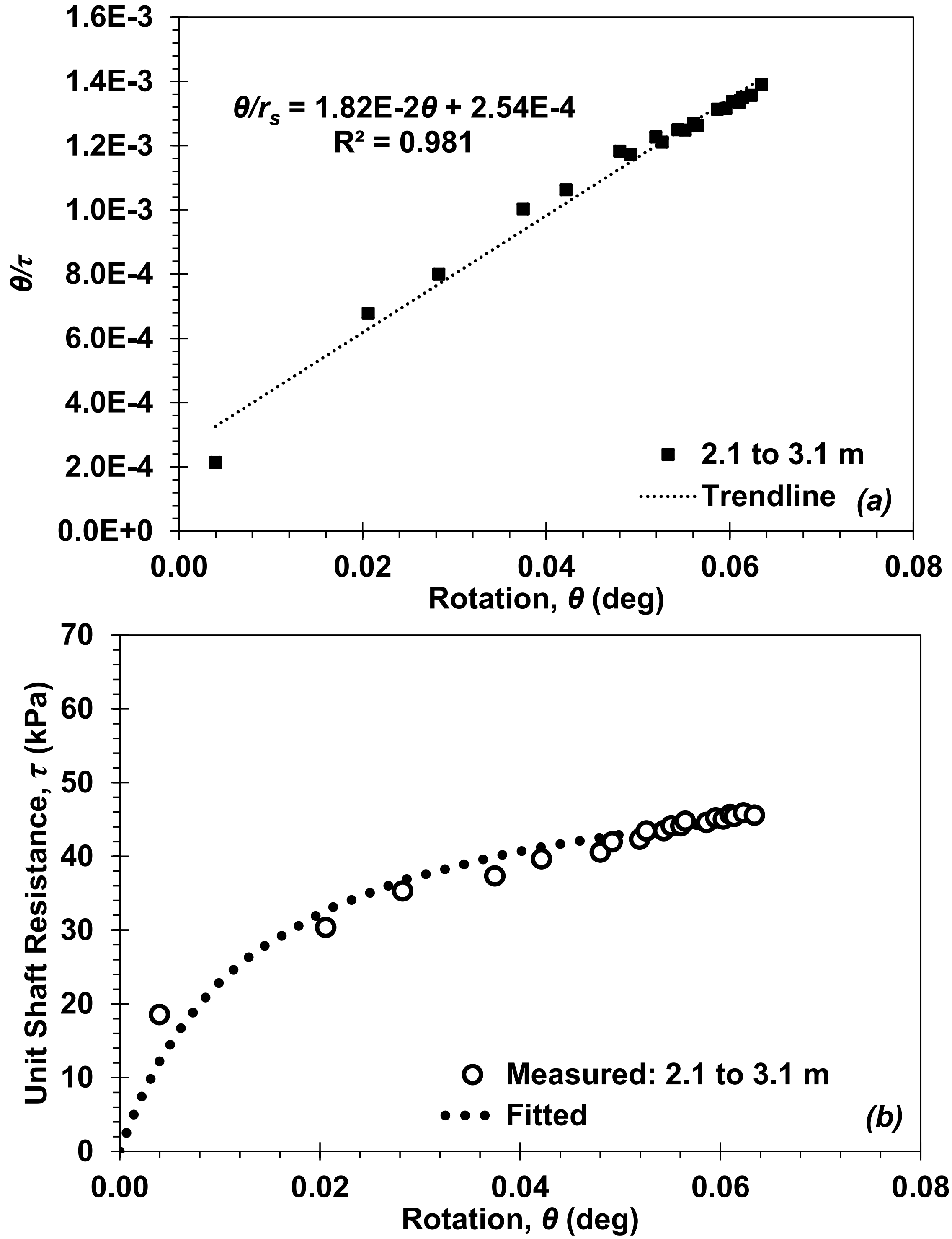

Figure B-9. Hyperbolic model for TDS (a) observed τ–θ curve in hyperbolic space and fitted hyperbolic model and (b) comparison between fitted and measured response at depth from 2.1 to 3.1 m (82 to 121 in).

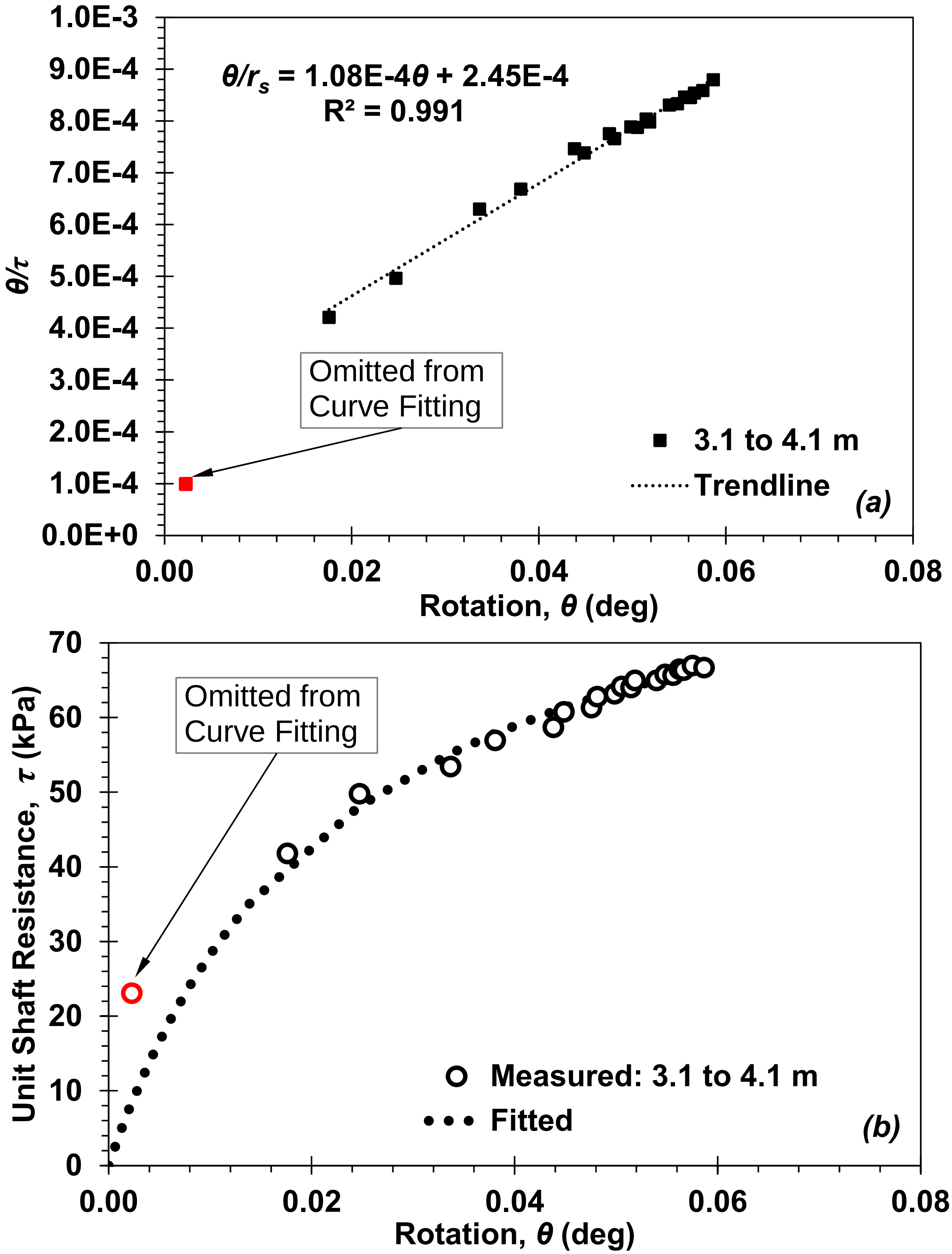

Figure B-10. Hyperbolic model for TDS (a) observed τ–θ curve in hyperbolic space and fitted hyperbolic model and (b) comparison between fitted and measured response at depth from 3.1 to 4.1 m (121 to 156 in).

B.6 Toe Resistance Calculation Scheme

Figure 5-10 illustrates the assumed unit torsional toe resistance distribution, which varies linearly with distance away from the center of the toe. The normal force at the toe is equal to the mobilized axial toe resistance, $R_{t,mob}$. The maximum unit torsional toe resistance at the edge of the bottom can be computed using:

$$\tau_b = \frac{R_{t,mob} \tan \phi^{'}}{\pi (0.5D)^2} = \frac{4R_{t,mob} \tan \phi^{'}}{\pi D^2} \tag{B.11a}$$

$$\tau_b = \alpha s_u \tag{B.11b}$$

for granular and plastic soils, respectively.

For an arbitrary ring with inner radius of x and width of dx, as shown in Figure B-11, the area, dA, of the ring is given by:

$$dA = \pi (x + dx)^2 - \pi x^2 = 2\pi x dx \tag{B.12}$$

by ignoring the square of differentials, $(dx)^2$. The torsional resistance generated by the ring is:

$$dT_t = \tau_x dA = 2\pi \tau_x x dx \tag{B.13}$$

where τ_x = the unit torsional toe resistance on the ring, which is:

$$\tau_x = \frac{2x}{D} \tau_b \tag{B.14}$$

Equation (B.14) can be substituted into Equation (B.13) to obtain:

$$dT_t = \tau_x x dA = \frac{4\pi}{D}\tau_x x^3 dx \tag{B.15}$$

Then, the toe resistance can be estimated by integrating Equation (B.15) for *x* from zero to *D/2*.

$$T_t = \int_0^{D/2} \frac{4\pi}{D}\tau_x x^3 dx = \frac{\pi}{16}D^3\tau_b \tag{B.16}$$

Substituting Equation (S.11) into Equation (S.16), the toe resistance is:

$$T_t = \frac{1}{4}DR_{t,mob}\tan\phi' \tag{B.17a}$$

$$T_t = \frac{\pi}{16}D^3\alpha s_u \tag{B.17b}$$

for granular and plastic soils, respectively.

B.7 References

ACI Committee 318. (2005) *Building Code Requirements for Structural Concrete (ACI 318-05) and Commentary (318R-05),* American Concrete Institute, Farmington Hills, MI.

Gere, J.M., and Timoshenko, S.P. (1997). *Mechanics of Materials*, PWS Pub.Co., Boston.

Hibbeler, R.C. (2013) *Mechanics of Materials*. 9th Edition. Upper Saddle River (NJ): Pearson Prentice Hall, 181-243

Appendix C CROSSHOLE SONIC LOG (CSL) INTEGRITY TEST

This appendix presents the report of integrity testing of drilled foundation shafts using Crosshole Sonic Log (CSL) integrity test.

GEI Consultants

Consulting
Engineers and
Scientists

November 13, 2015
GEI/OSU Research Project

VIA EMAIL: armin.stuedlein@oregonstate.edu

Professor Armin Stuedlein, PhD, P.E.
School of Civil and Construction Engineering
Oregon State University
101 Kearney Hall
Corvallis, OR 97331

RE: Nondestructive Testing of Drilled Shafts at OSU Earthquake Research Site, Corvallis, Oregon.

Dear Dr. Stuedlein:

Following the integrity testing of four drilled-shaft foundations at the OSU Earthquake research site in Corvallis, Oregon during our site visit on July 6, 2015, we are pleased to submit herewith a summary of the test results and our interpretation of them.

The shafts tested were designated CIR, CNIR, HSIR and MIR. Shafts CIR and CNIR have permanent casing. Shafts HSIR and MIR are uncased, and the above-grade portions were formed using cylindrical cardboard "Sonotube" forms. Some minor localized variations were observed in the test data for each shaft, but there were no significant anomalies or indications of potential defects.

The attached report contains the test results together with our analyses and conclusions.

We appreciate this opportunity to provide support to your research work project, and remain available to provide any other information that you may require concerning this project.

Sincerely,

GEI CONSULTANTS, INC.

Bernard H. Hertlein, FACI, M.ASCE, M.GI.
Senior Consultant

Robert W. Acker, P.E.
Vice President

BHH:nls

GEI Consultants

Consulting
Engineers and
Scientists

Integrity Testing of Drilled Foundation Shafts

Corvallis, Oregon

Submitted to:
School of Civil & Construction Engineering
Oregon State University
101 Kearney Hall
Corvallis, OR 97331

Submitted by:
GEI Consultants, Inc.
400 N. Lakeview Parkway, Suite 140
Vernon Hills, IL 60061
847-984-3401

November 13, 2015

GEI Research Project

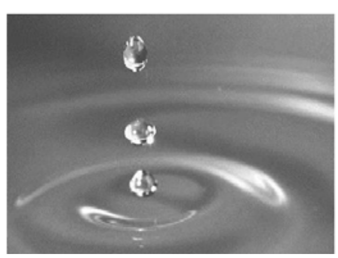

Bernard H. Hertlein, FACI,
M.ASCE, M.GI
Senior Consultant

Table of Contents

Appendix

1. Introduction

Professor Armin Stuedlein at Oregon State University (OSU) is Principal Investigator for a research program on drilled shaft capacity sponsored by the Association of Drilled Shaft Contractors (ADSC-IAFD). Four drilled shaft foundations were constructed for this program at the OSU Earthquake Engineering Laboratory in Corvallis, Oregon.

One of the requirements of the research project is that the integrity of the foundation shafts be verified by the Crosshole Sonic Log (CSL) integrity test. GEI Consultants, Inc. volunteered to perform the integrity testing. CSL testing of the four shafts that are the subject of this report was completed in a visit to the site in Corvallis on July 6, 2015. This report presents copies of the test results, together with our analyses, interpretations and conclusions.

2. Site Description and Purpose of Testing

The shafts are placed in a rectangular group, as shown in Figure 3 of the Appendix to this report. The shafts are each three feet in diameter, and approximately 65 feet long. The shafts all extended approximately five feet above grade. Two shafts had full-length permanent steel casing, and two shafts were formed above grade using cylindrical cardboard "Sonotube" forms. Concrete was placed in the shafts up to design cut-off level by the tremie method. The shafts were designated as follows:

CIR = Cased shaft with internal reinforcement.

CNIR = Cased shaft with light internal reinforcement.

HSIR = Uncased shaft with high-strength reinforcement.

MIR = Uncased baseline shaft with mild reinforcement.

Shafts CIR, CNIR and MIR each contained three full-depth PVC access tubes attached to the interior of the reinforcing cage. Shaft HSIR contained three all-thread high-strength steel hollow anchor bars instead of the PVC tubes. The hollow bars were 73 mm (3 in) OD, 55 mm (2 in) ID. The length of each shaft that was accessible for testing was checked by using a weighted tape measure inside the CSL access tubes to measure the tube length, and then outside the tube to measure the length of tube above surface of the concrete. The shaft length from top of concrete down to the base of the CSL tubes varied by a few inches, most likely due to movement of the tubes when the reinforcing cage was picked and placed in the shaft excavation.

Shafts HSIR and MIR also each contained two pairs of horizontal PVC pipes at about 18 inches and 45 inches below the top of concrete to provide full-width penetrations for the installation of anchor rods for lateral load tests – see Appendix Photographs 1 and 2.

CSL tests were performed between all vertical tube-pair combinations, to provide three profiles for each shaft. The CSL tests fulfilled two purposes:

1. To verify shaft condition and integrity to aid in validating the load test data.
2. To evaluate the effectiveness of the high-strength anchor bars as CSL access tubes.

3. Test Method Description

The Cross-hole Sonic Log (CSL) method is a down-hole Ultrasonic Pulse Velocity (UPV) test, recognized by the American Society for Testing and Materials (ASTM) in ASTM D6760, Standard Test Method for Integrity Testing of Concrete Deep Foundations by Ultrasonic Crosshole Testing. The UPV through concrete is a function of the density and modulus of the material, and can therefore be used to assess material quality. When a series of measurements are made at uniform spacing and over a uniform path length, they can be plotted graphically to permit a rapid visual assessment of material uniformity.

The CSL tests for this project were performed in general conformance with ASTM D6760. Transmitter and receiver probes are placed in tubes or boreholes within the concrete to be tested. The probes are connected to a control unit containing a timer, pulse generator, and signal amplifier. The data output is stored on a portable PC. The cables to the probes pass over a measurement winch that is connected to the control unit. As the cables are withdrawn, pulling the probes up the access tubes, the winch emits a series of impulses that cause the transmitter probe to emit an ultrasonic pulse at predetermined intervals vertically. The timer circuit measures the time between pulse emission and detection by the receiver. The depth of the probes is known by the cable length withdrawn over the measurement winch. A continuous series of measurements is made for each profile, and all data is stored on the PC.

For display, the pulse waveform is modulated to give a line of data where each positive peak in the pulse is shown as a dash, and each negative peak is shown as a blank space. The lines of data are printed as a stacked graph to build up a vertical profile of the pulse propagation time through the concrete [Figure 1]. In a sound, uniform material, the stacked profile will show a series of straight parallel lines. Where pulse velocity is reduced by anomalies such as missing or low modulus material, the pulse propagation time will show an increase, and the profile lines will show a deflection proportional to the increase in propagation time, which is commonly referred to as First Arrival Time (FAT).

In some cases, defects can significantly reduce pulse amplitude, causing an apparent loss of received signal. However, poor mechanical bond between the access tubes and the concrete, or lack of water in the tubes can also cause loss of signal. In addition, the pulse is refracted at the interface between the tubes and the water, and the concrete and the tubes. This creates focal points in both the receiver and transmitter tubes which are slightly behind the center axis of the tube with regard to the direction of propagation. Since the probes are freely suspended, they can move about laterally, passing in and out of the focal points as they are withdrawn, causing variation in transmitted pulse strength and received signal amplitude. Similarly, in normal, sound concrete, the received amplitude of an ultrasonic pulse can vary, depending on aggregate shape and orientation, and minor local changes in aggregate distribution.

In addition, the access tubes can sometimes move relative to each other as the reinforcing steel cage is picked and placed, and may not be truly parallel once the cage is installed in the shaft. Tube to tube distance, particularly around the perimeter of the shaft, is therefore only known with certainty at the top of the shaft, where it can be physically measured. Velocities calculated from FAT and the measured tube spacing at the top of the shaft must therefore be considered as approximations.

Evaluation of concrete quality is, therefore, primarily based on the uniformity of the pulse FAT, or computed average velocity. Where an apparent loss of signal is shown, the raw data for each pulse in that zone are examined to evaluate signal amplitude, or strength, which may have fallen below the digital detection threshold, and so appear as a signal loss or delay on the normal profile.

4. Test Results

Copies of the recorded CSL profiles are given in the Appendix to this report. The CSL tubes are numbered sequentially in a clockwise direction around the shaft, with Tube No. 1 being the northernmost tube. Each profile is identified by the numbers of the pair of tubes between which the profile was developed.

4.1 Shaft CIR

The CSL profiles for Shaft CIR show some minor variation in pulse first arrival time (FAT) and pulse energy between about 2 feet and 4.5 feet below the top of concrete. There was also some random signal disturbance appearing as horizontal streaks that was attributed to local electrical noise on profile 1-2. Other than the foregoing observations, there is no evidence of any significant anomalies in Shaft CIR. Typical CSL pulse velocity was about 12,830 ft/s.

4.2 Shaft CNIR

In shaft CNIR there is a thin zone about 3.5 feet below the top of concrete where both pulse energy and velocity are reduced by up to 50 percent. There are similar small zones at 10-foot intervals all the way down the shaft, but they show progressively less reduction with depth. We believe that they are most likely localized zones of partial segregation or lack of consolidation associated with tube fixings or couplers. Some electrical interference is apparent as horizontal streaks in profile No. 2-3. The shaft is otherwise proven to be sound and continuous. Typical CSL pulse velocity was about 12,770 ft/s.

4.3 Shaft HSIR

Shaft HSIR also shows thin zones of reduced pulse amplitude and velocity at about 10 foot-intervals, starting at five feet below top of concrete, but no evidence of any significant anomalies. Typical CSL pulse velocity was about 12,360 ft/s.

4.4 Shaft MIR

Shaft MIR shows two thin zones of reduced pulse energy and velocity on all three profiles at about four feet and fourteen feet below the top of the concrete. Profiles 1-2 and 1-3 also show some reduction in velocity and energy at about two feet and 3.5 feet below top of concrete, which are most likely due to the horizontal PVC pipes. The pulse amplitude fell below the detection threshold; therefore, the reduction in velocity could not be estimated. Some electrical interference is apparent as horizontal streaks in the lower portions of profile Nos. 1-2 and 1-3. Typical CSL pulse velocity was about 12,320 ft/s.

4.5 Observations

It is noteworthy that the received CSL pulses in the PVC tubes appear complex and “fuzzy”, whereas the pulses in the hollow bars are crisp and clean, producing more sharply defined CSL profiles – examples are shown below.

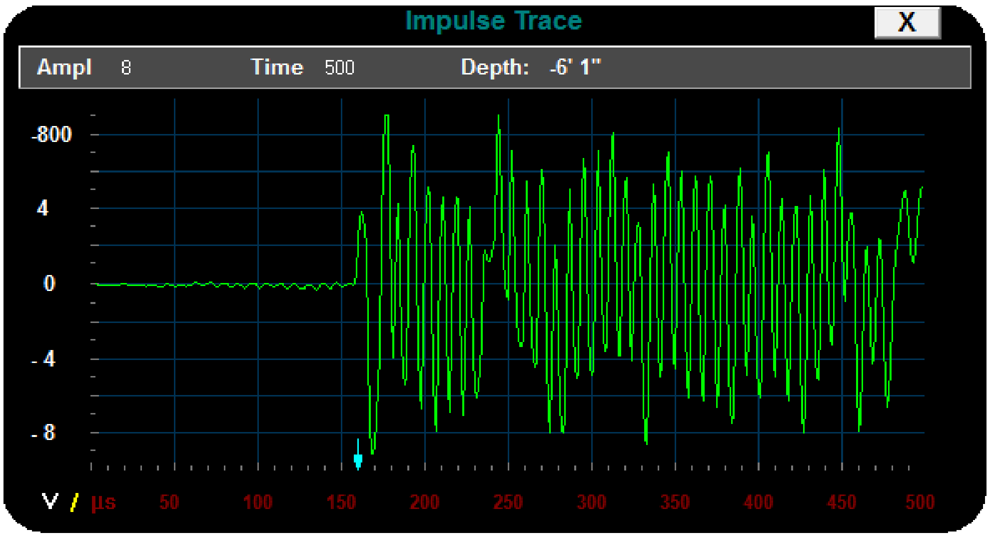

Pulse example from Shaft CIR, PVC access tubes

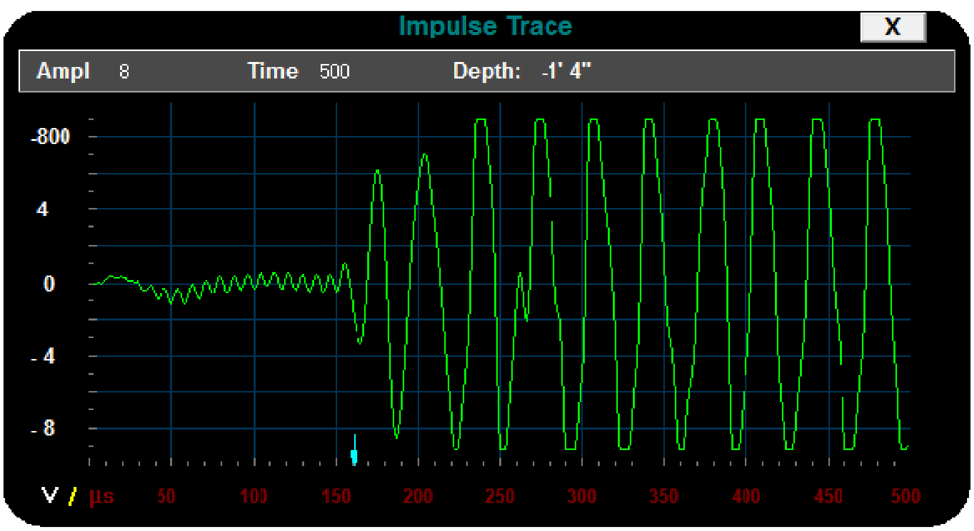

Pulse example from Shaft HSIR, Steel Hollow Bar access tubes

5. Conclusions

The CSL profiles for Shafts CIR, CNIR, HSIR and MIR show some minor increases in FAT, but no evidence of any significant anomalies that are considered likely to adversely affect shaft capacity. Therefore, all four shafts are considered to be sound and continuous.

The CSL profiles for the shafts containing PVC access tubes show complex signals, most likely as a result of refraction at the tube/concrete interface, that appear to have reduced the resolution of small anomalies like the horizontal PVC tubes. The shaft containing the hollow bar access tubes produced cleaner, less complex signals. We conclude that the hollow bars perform satisfactorily as CSL access tubes, and therefore have the potential to aid designers in reducing reinforcing steel congestion in heavily reinforced shafts.

Appendix

Figure 1: CSL Data Processing

Figure 2: CSL Access Tube Numbering Plan

Figure 3: Site Layout Diagram

Photograph No. 1: Shaft HSIR

Photograph No. 2: Shaft MIR

Integrity Test Results

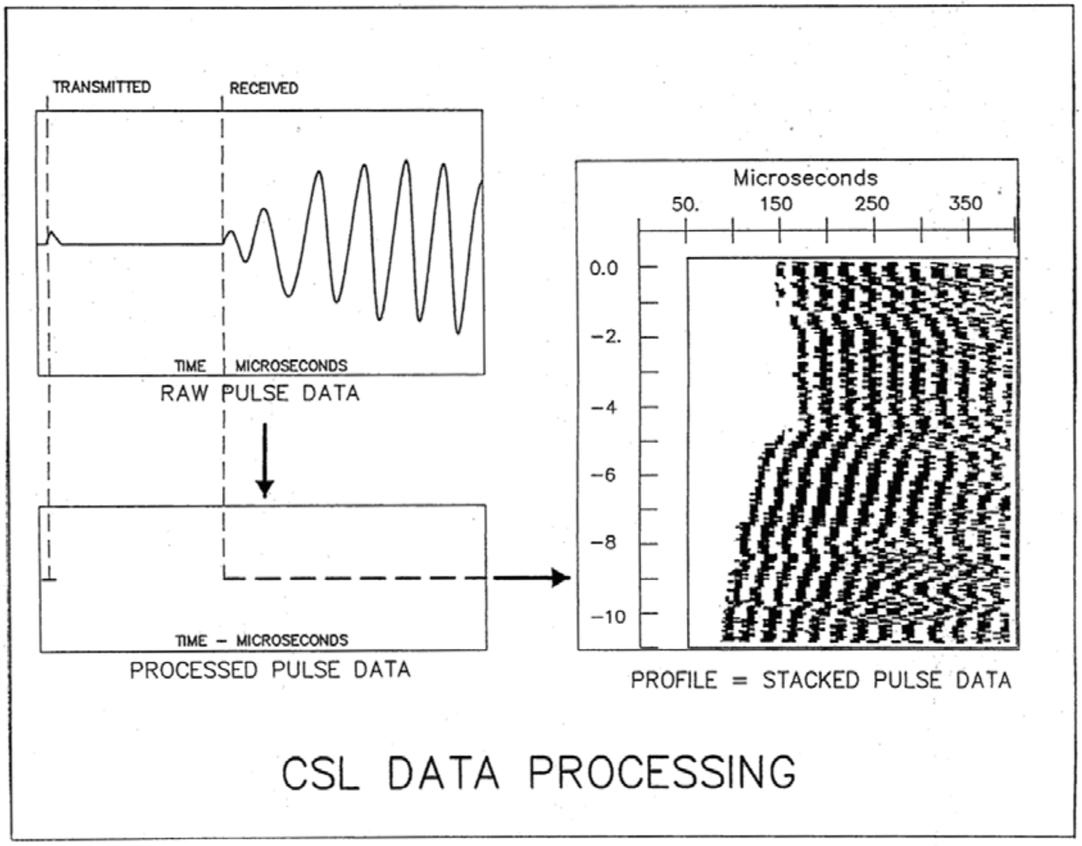
TRANSMITTED
RECEIVED
TIME
MICROSECONDS
RAW PULSE DATA
TIME – MICROSECONDS
PROCESSED PULSE DATA
Microseconds
50.
150
250
350
0.0
-2.
-4
-6
-8
-10
PROFILE = STACKED PULSE DATA
CSL DATA PROCESSING

Figure 1

Integrity Testing of Drilled Foundation Shafts
Corvallis, Oregon
November 13, 2015

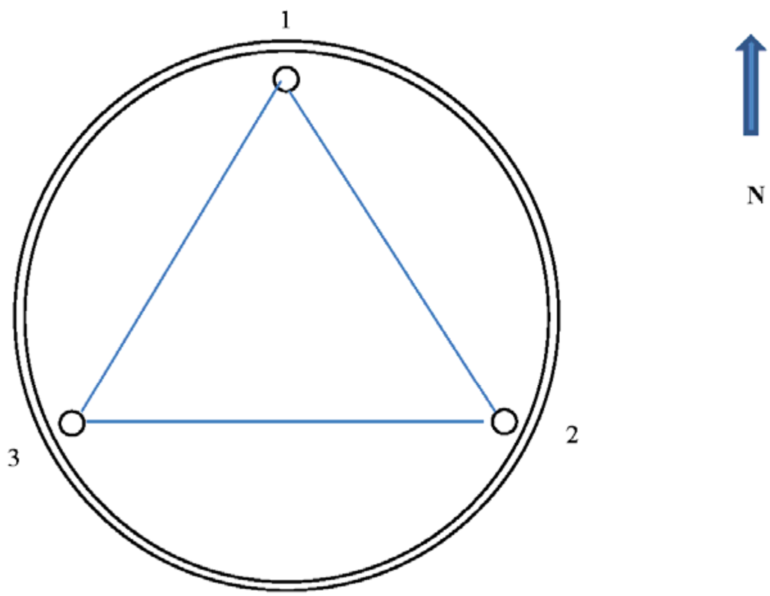

Figure 2 – CSL Tube Numbering Plan

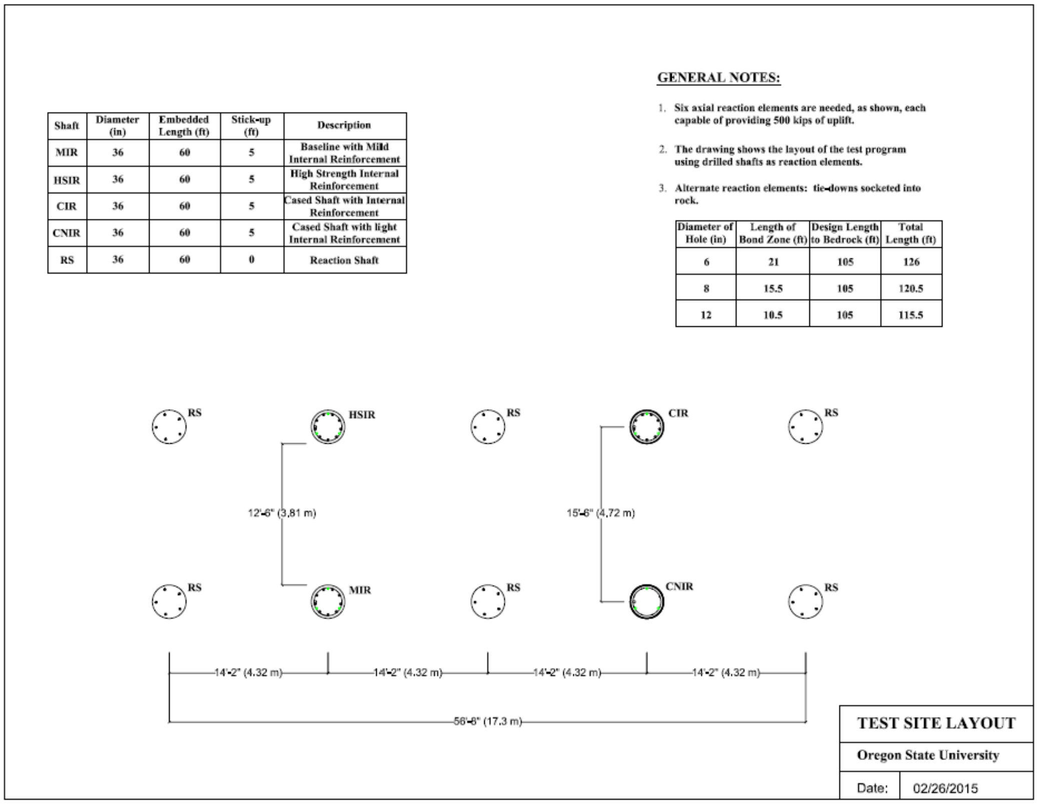

Figure 3: Site Layout Diagram

Photograph 1: Shaft HSIR

Integrity Testing of Drilled Foundation Shafts
Corvallis, Oregon
November 13, 2015

Photograph No. 2: Shaft MIR

Sonic Logging Profile : OSU Corvallis

Client	OSU	Pile Diameter	3' 0"
Pile No.	CIR	Foundation Type	Drilled Shaft
Date tested	7/6/2015	Date cast	6/15/2015
Operator	BHH		

Profile: 1 - 2 (63' 3") **Profile: 1 - 3 (63' 2")** **Profile: 2 - 3 (63' 3")**

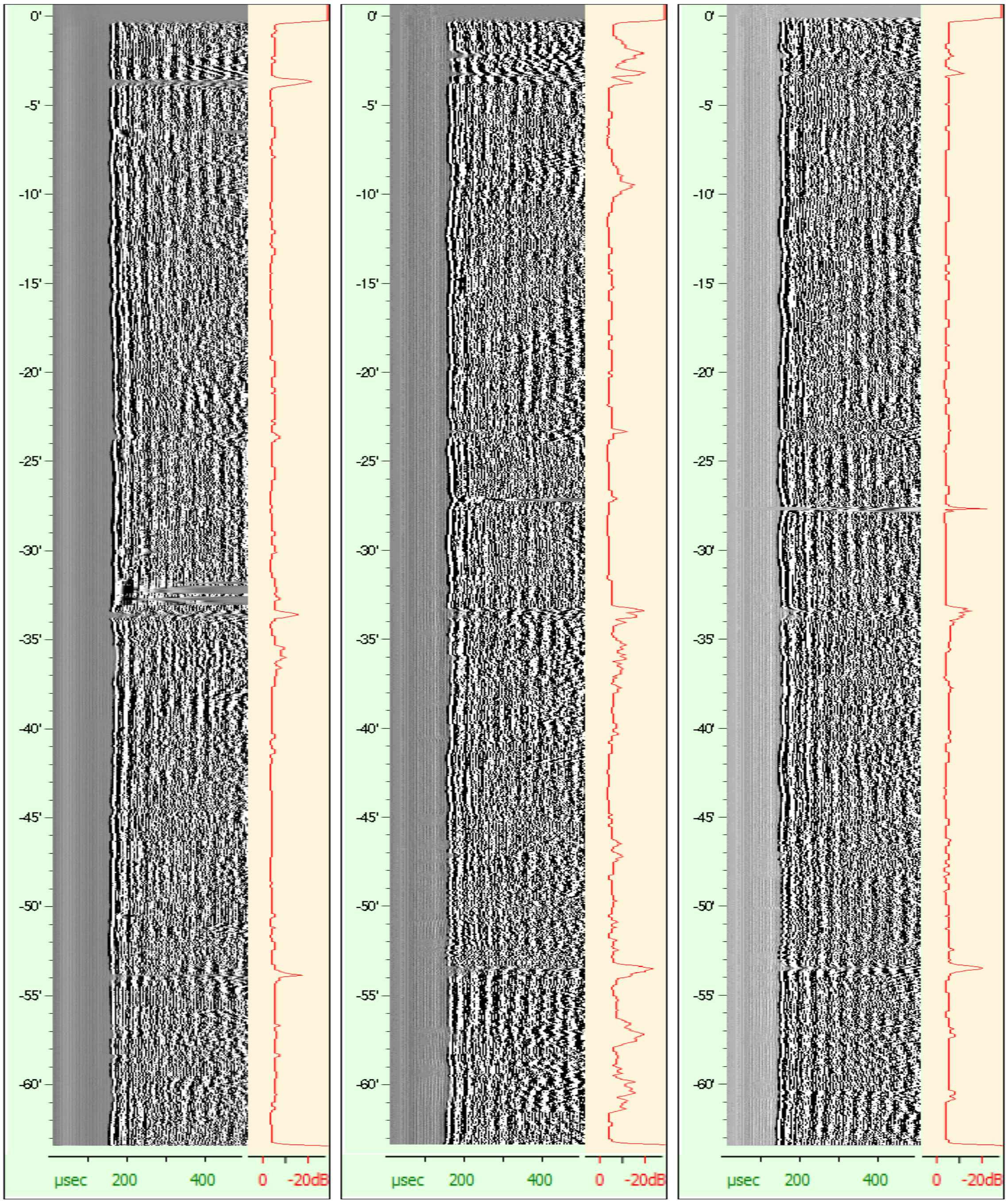

Sonic Logging Profile : OSU Corvallis

Client	OSU	Pile Diameter	3' 0"
Pile No.	CNIR	Foundation Type	Drilled Shaft
Date tested	7/6/2015	Date cast	6/14/2015
Operator	BHH		

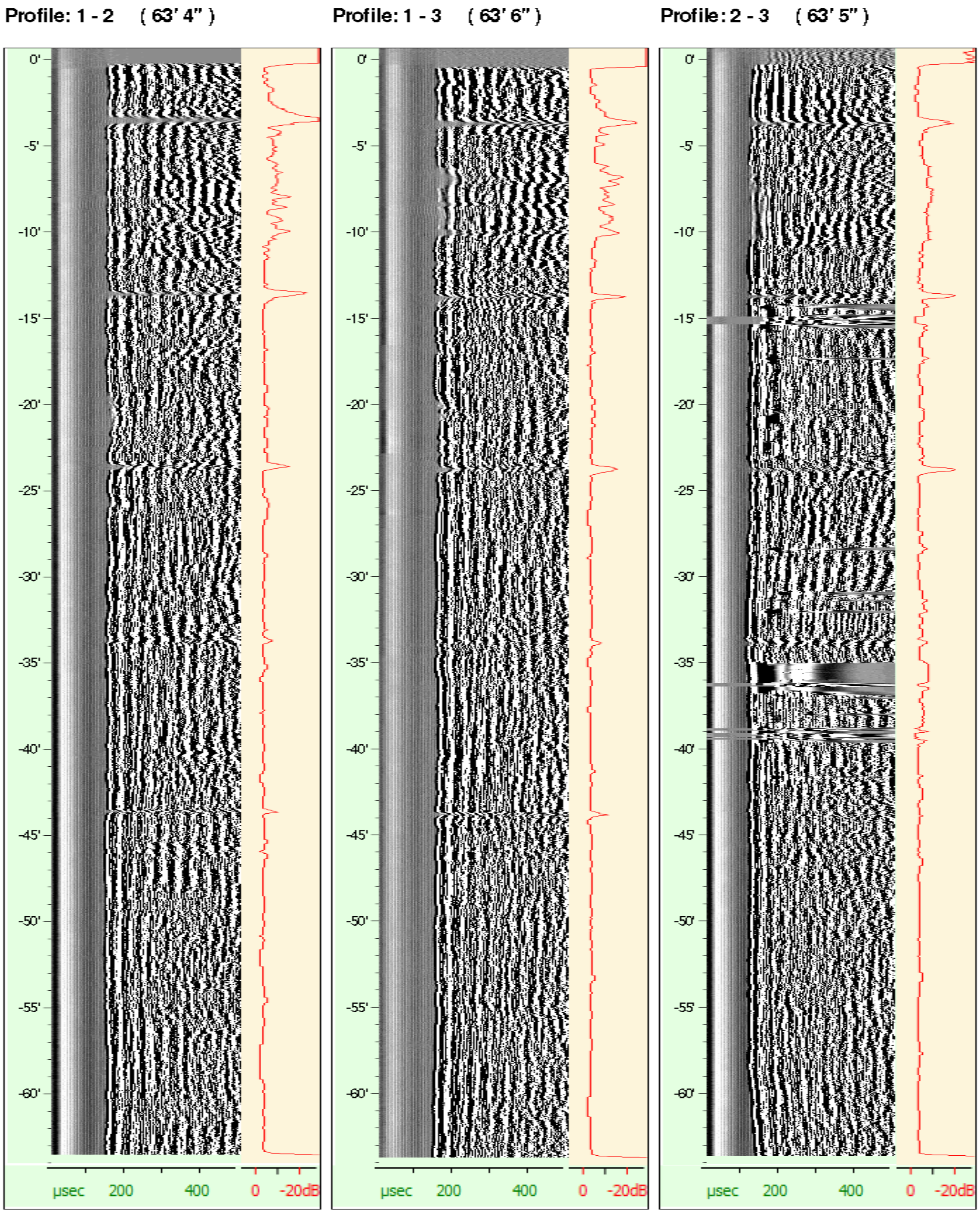

Sonic Logging Profile : OSU Corvallis

Client	OSU	Pile Diameter	3' 0"
Pile No.	HSIR	Foundation Type	Drilled Shaft
Date tested	7/6/2015	Date cast	6/15/2015
Operator	BHH		

Profile: 1 - 2 (63' 8") **Profile: 1 - 3 (63' 8")** **Profile: 2 - 3 (64' 0")**

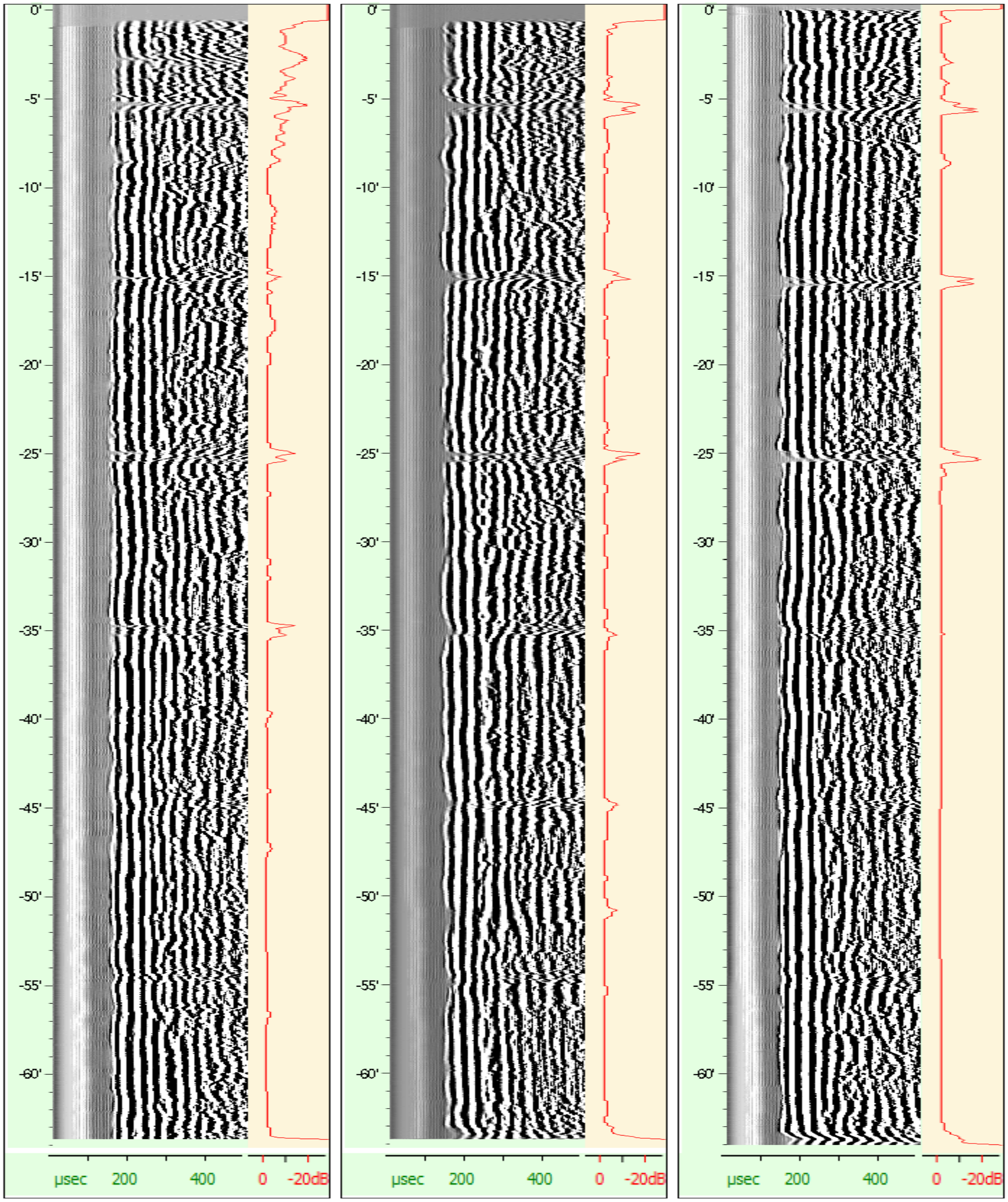

Sonic Logging Profile : OSU Corvallis

Client	OSU	Pile Diameter	3' 0"
Pile No.	MIR	Foundation Type	Drilled Shaft
Date tested	7/6/2015	Date cast	6/14/2015
Operator	BHH		

Profile: 1 - 2 (63' 4") **Profile: 1 - 3 (63' 4")** **Profile: 2 - 3 (63' 3")**

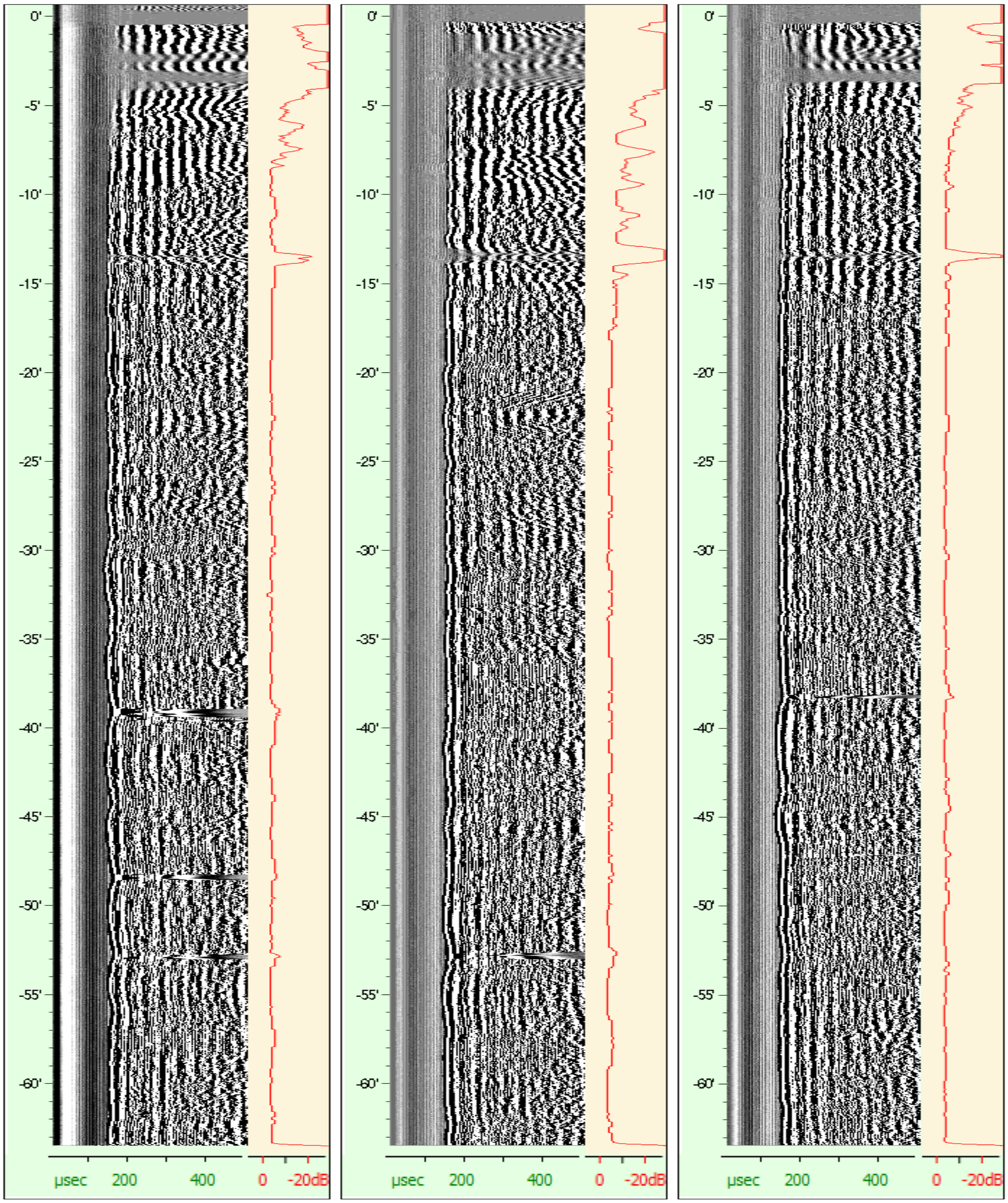

Appendix D THERMAL INTEGRITY PROFILING (TIP)

This appendix presents the report of integrity testing of drilled foundation shafts using Thermal Integrity Profiling (TIP) Thermal Wire method.

Quality Assurance for Deep Foundations

Pile Dynamics, Inc.

December 19, 2017

Armin Stuedlein
Associate Professor
Oregon State University
101 Kearney Hall
Corvallis, OR 97331

Re: Thermal Integrity Profiling for NDT Comparison on OSU Test Shafts

Shafts: MIR, CIR & HSIR

The enclosed data presents the results Thermal Integrity Profiling (TIP) using Thermal Wires for the above-referenced project. The objective of TIP testing was to demonstrate the use of the TIP integrity testing method. The TIP data for MIR and HSIR was recorded beginning on June 16th and ending June 22nd, 2015. The TIP data for CIR was recorded beginning on June 17th and ending June 22nd, 2015.

THERMAL INTEGRITY PROFILING – INSTRUMENTATION AND ANALYSIS

Thermal Integrity Profiler (TIP) testing was performed by means of Thermal Wire® cables and Thermal Acquisition Ports (TAPs). The TIP system, manufactured by Pile Dynamics, Inc (PDI) in association with FGE, reads concrete temperatures during curing using cables embedded in the concrete.

The Thermal Wire cables consist of temperature sensors spaced every one foot along the length of a wire. For each of these shafts, four Thermal Wires were attached symmetrically along the full length of each reinforcement cage prior to cage placement.

Once the cage was set and concrete placed, a TAP box was attached to each wire, and data acquisition began.

During curing of the concrete, the hydrating cement generates heat, increasing the temperature in the shaft. Every 15 minutes the TAP units automatically record the measured temperature at each sensor location along the length of the wire, generating a profile of temperature versus depth at each increment of time. After the concrete peak temperature has been achieved, each TAP was connected to a TIP processing unit and the data was downloaded for further interpretation in the office.

The TIP results may be evaluated for shaft shape and integrity, concrete quality, and for location of the reinforcing cage. The overall average temperature for all Thermal Wire readings over the embedded depths can be directly related to the overall volume of concrete installed. Shaft integrity may be assessed based on the average temperature measurements from each Thermal Wire at each depth increment. If the measured average temperature versus depth is consistent, the shaft is considered to be uniform in shape and quality. Bulges can be identified as localized increases in average temperature, while insufficient concrete quality or section reductions can be identified as localized decreases in average temperature. Anomalies present over more than ten percent of the effective cross-sectional area are normally seen in multiple Thermal Wires at the same depth. Because soil and/or slurry pockets produce no heat, areas of soil intrusion or inclusion are indicated by lower local temperatures.

Reinforcement cage location can be estimated based on the relative temperature difference between an individual Thermal Wire and the average of all wires. Higher individual Thermal Wire temperatures indicate the wire is closer to the center of the shaft, or near a local bulge, while lower individual Thermal Wire temperatures indicate the wire is closer to the soil-shaft interface, or a local defect. By viewing diametrically opposite Thermal Wires, instances where a lateral shift of the reinforcing cage has occurred can be determined, if one wire temperature is higher than average and the diametrically opposite wire temperature is lower than average.

SHAFT DETAILS

Shaft details were obtained through field measurements and information provided to PDI. Typically, relevant borings, installation records, concrete records, and the completed Thermal Field Log are provided along with the TIP data in order to perform an analysis. The reported shaft lengths and shaft details are summarized in Table C-1.

Table C-1. Reported Shaft Installation Details

Foundation Unit	Concrete Placement Date	Shaft Diameter (in.)	Reinforcing Cage Diameter (in.)	Reported Shaft Length (ft.)	Theoretical Concrete Volume (yd^3)	Reported Concrete Volume Placed (yd^3)
MIR	6/16/2015	36	30	65	17.0	21.0
HSIR	6/16/2015	36	30	65	17.0	20.0
CIR	6/17/2015	36	30	65	17.0	17.4

RESULTS

TIP results include the measured temperature and calculated shaft radius versus depth. The radius calculations were based on the measured Thermal Profile in conjunction with the reported shaft length and the reported concrete volume summarized in the above table. Given sufficient thermal measurement points, the calculated radius can be interpolated to obtain a 3-D shaft profile. The generated 3-D profiles are based on the four cables attached to the reinforcing cage, while Thermal Profiles present the measured temperature versus depth for each active sensor at the selected time interval.

The optimal time for the 3-D shaft profile generally occurs between one half the time to peak temperature and the time of peak temperature. Shafts MIR, HSIR, and CIR reached peak temperature approximately 46, 49, and 46 hours after placement, respectively.

In general, temperature variations of +/- 4 degrees Fahrenheit are within normal range for TIP results due to variations in the cable location and unavoidable shifting or movement of reinforcing cage during installation in the shaft excavation. Anomalies would be indicated by abrupt reductions in temperature at a particular depth.

The thermal results are presented in Figures C-1 through Figure C-6. Figures C-1, C-3, and C-5 present the measured Temperature (degrees Fahrenheit) vs. Depth (feet) on the left plot, and the Estimated Radius (inches) *vs*. Depth (feet) on the right of the plot. Temperature roll-off at the top of a shaft is caused by heat loss due to the concrete/air interface. Temperature roll-off at the bottom of a shaft is caused by heat loss due to the concrete/soil interface at the shaft base.

A 3-D interpretation of each shaft is presented in Figures C-2, C-4 and C-6. The reinforcing cage is displayed as a 2-D color spectrum with an overlay of projected shaft exterior surface on the left side of these figures. The spectrum identifies the average concrete cover at each plotted location based on the temperature at each node. A 3D interpretation with the reported soil information and ground water location is displayed on the right side of these figures.

ANALYSIS

MIR

The average calculated radius is generally consistent and slightly above the design shaft radius of 18 inches. Thermal results indicate the reinforcing cage is slightly shifted over the instrumented length of the shaft. The shifting is such that Wire 1 is nearer the shaft center and Wire 3 is nearer the soil interface. The top sensor was positioned approximately 2 to 3 feet below the top of concrete. The top of shaft roll-off was observed approximately 5 feet below the top of shaft. The bottom temperature roll-off begins approximately 5 feet up from the shaft base. No major anomalies were indicated in the base of the shaft.

As noted above, the computed average radius is generally consistent with the design shaft radius. An increase in temperature was observed in the top 5 feet of data. An increase in temperature is typically an indication of an increase in shaft radius. The observed increase in temperature appears to be the result of a 36 inch sonotube concrete form positioned around the top 5 feet of the shaft. The cardboard sonotube form acts as an insulator resulting in increased temperature readings. Hyperbolic adjustments were applied to account for this insulating effect.

The overall thermal signature in the Temperature (degrees Fahrenheit) vs. Depth (feet) graph indicates the shaft is continuous with no abrupt reductions in temperature indicative of major anomalies over the tested length (Figure C-1).

HSIR

The average calculated radius is generally consistent and slightly above the design shaft radius of 18 inches. Thermal results indicate the reinforcing cage is relatively centralized over the tested length. The top sensor was positioned approximately 2 to 3 feet below the top of concrete. The top of shaft roll-off was observed approximately 5 feet below the top of shaft. The bottom temperature roll-off begins approximately 5 feet up from the shaft base. No major anomalies were indicated in the base of the shaft.

As noted above, the computed average radius is generally consistent and slightly above the design shaft radius. An increase in temperature was observed in the top 5 feet of data. An increase in temperature is typically an indication of an increase in shaft radius. The observed increase in temperature appears to be the result of a 36 inch sonotube concrete form positioned around the top 5 feet of the shaft. The cardboard sonotube form acts an insulator resulting increase temperature readings. Hyperbolic adjustments were applied to account for this insulating effect.

The overall thermal signature in the Temperature (degrees Fahrenheit) vs. Depth (feet) graph indicates the shaft is continuous with no abrupt reductions in temperature indicative of major anomalies over the tested length (Figure C-3).

CIR

Shaft CIR reportedly contained a full length temporary steel casing. The average calculated radius is generally consistent with the design shaft radius of 18 inches. Thermal results indicate the reinforcing cage is relatively centralized over the tested length. The top sensor was positioned approximately 2 to 3 feet below the top of concrete. Only a partial top of shaft roll-off was observed in the top 2 feet of data. The bottom temperature roll-off begins approximately 5 feet up from the shaft base. No major anomalies were indicated in the base of the shaft.

As noted above, the computed average radius is generally consistent with the design shaft radius. An increase in temperature was observed near the top of the data from a depth of 2 to 10 feet. An increase in temperature is typically an indication of an increase in shaft radius. This increase in temperature appears to be the result of an air gap located outside the permanent casing acting as an insulator. This increase in temperature outside the casing appears to terminate near the reported depth of ground water. Hyperbolic adjustments were applied to account for this insulating effect.

The overall thermal signature in the Temperature (degrees Fahrenheit) vs. Depth (feet) graph indicates the shaft is continuous with no abrupt reductions in temperature indicative of major anomalies over the tested length (Figure C-5).

ADDITIONAL CONSIDERATIONS

Uncertainties in the interpreted TIP results include calculated corrections for shaft top and bottom shape which depend on the air and the annual average soil temperature, respectively. Other factors include variations in the thermal diffusivity of the soil around the shaft and the reinforcing cage which may have undergone movement during concrete placement. Furthermore, inaccuracies in the observed, installed concrete volumes may cause errors in calculated radii and 3-D shaft shape interpretations. These factors limit the direct, unquestioned use of the results presented in these results for shaft suitability. We recommend that the responsible engineer(s) use TIP results in conjunction with the soil borings, shaft construction/inspection records, and foundation loading information to determine foundation acceptability with respect to design requirements. Please note that the TIP results for shafts MIR, HSIR, and CIR are for demonstration use only.

We appreciate the opportunity to be of assistance to you on this project. Please contact us if you have any questions regarding these results, or if we may be of further assistance.

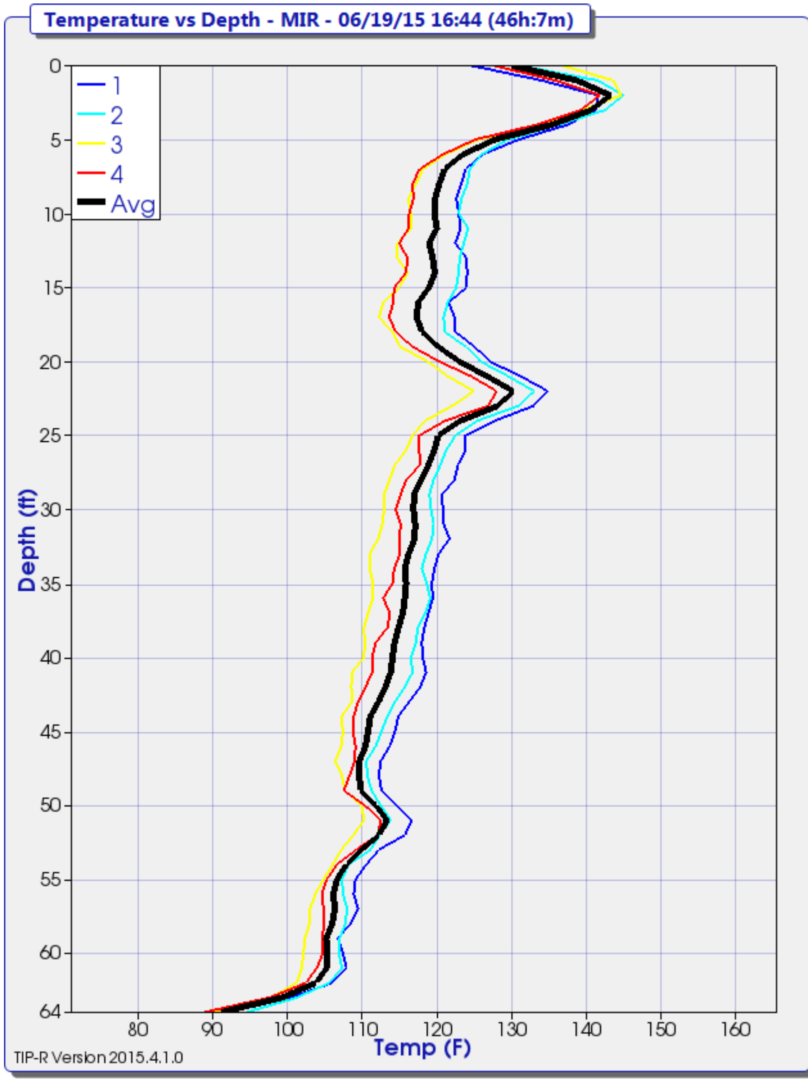

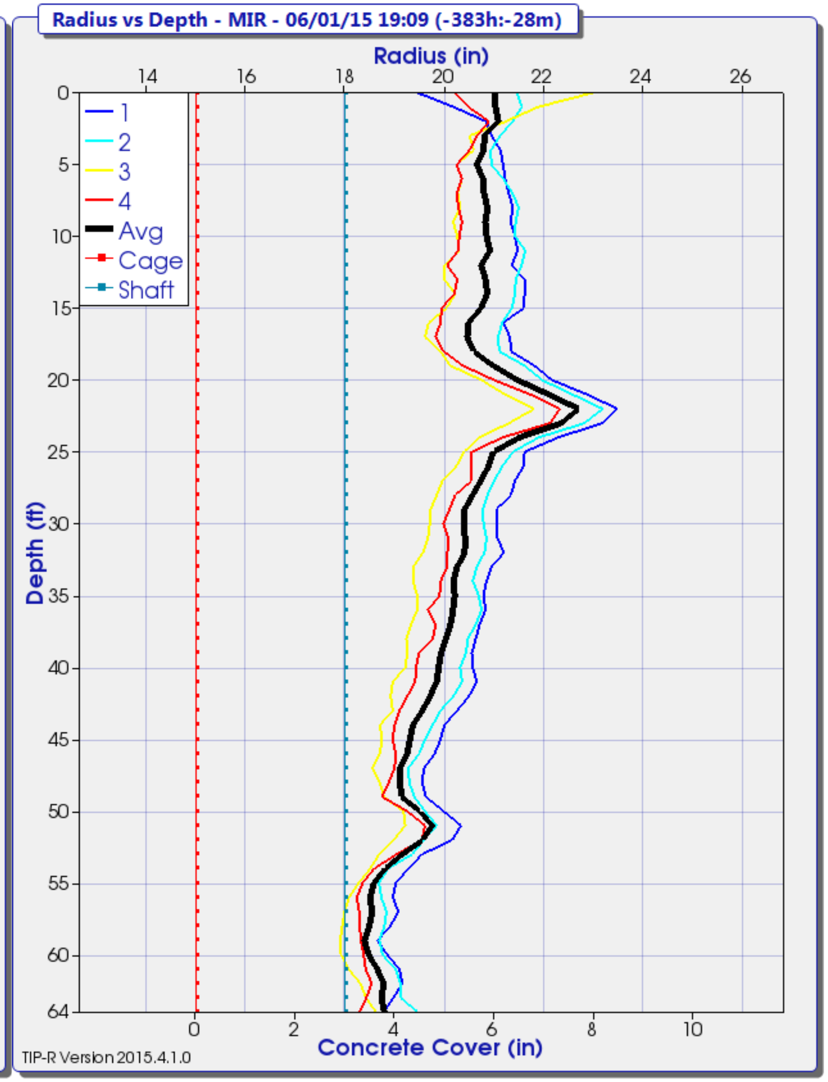

Figure C-1: Measured Temperature vs. Depth and Estimated Radius vs. Depth: MIR

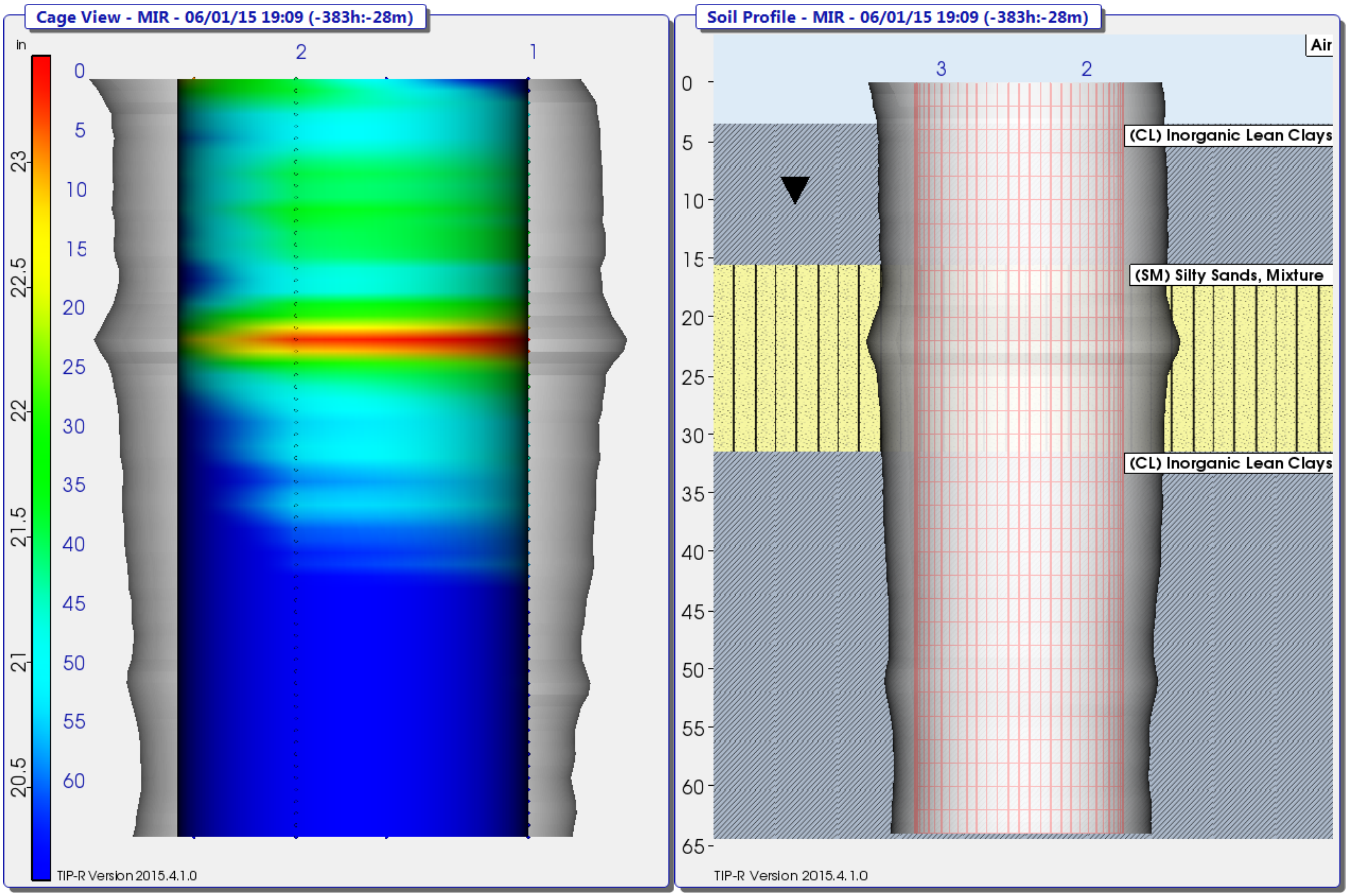

Figure C-2: 3-D Cage View and 3-D Interpretation with Soil Information: MIR

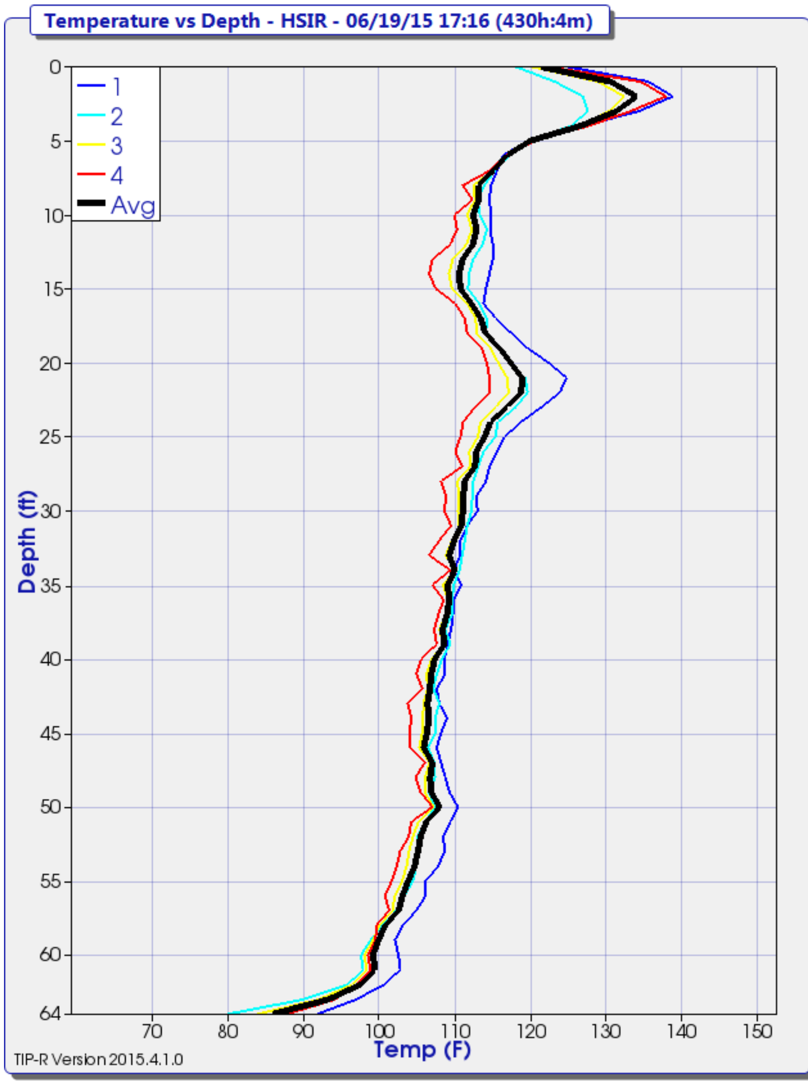

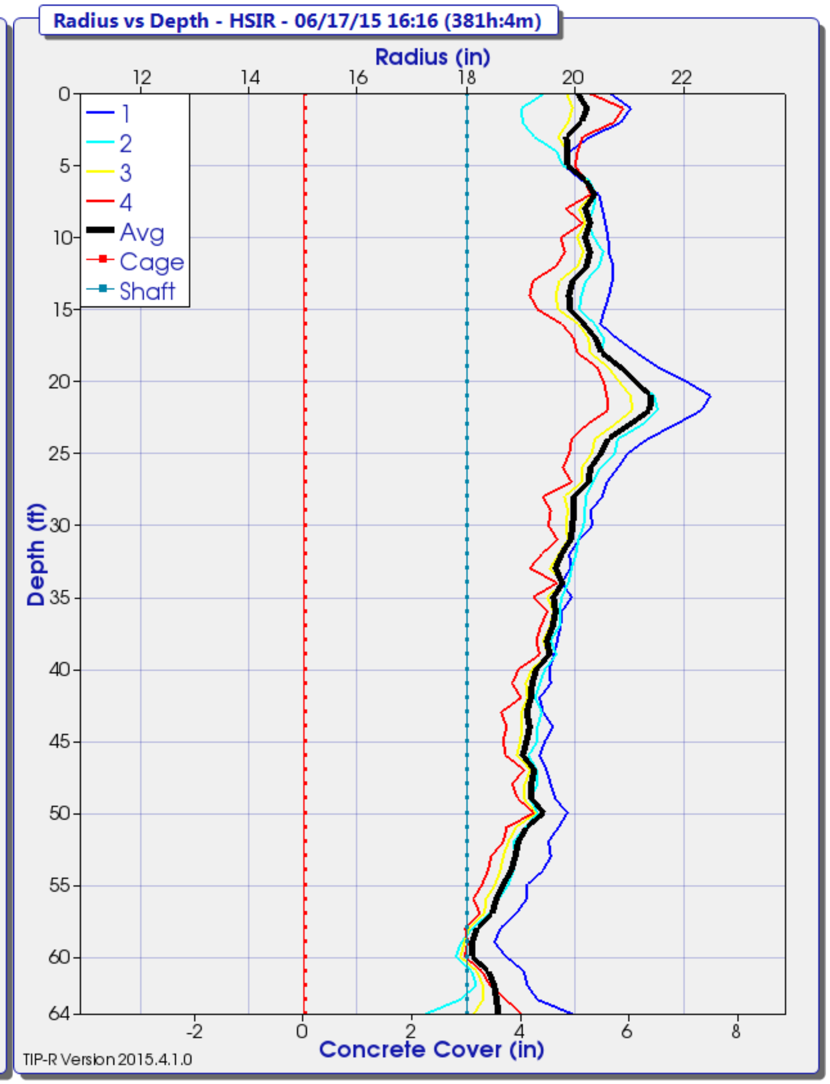

Figure C-3: Measured Temperature vs. Depth and Estimated Radius vs. Depth: HSIR

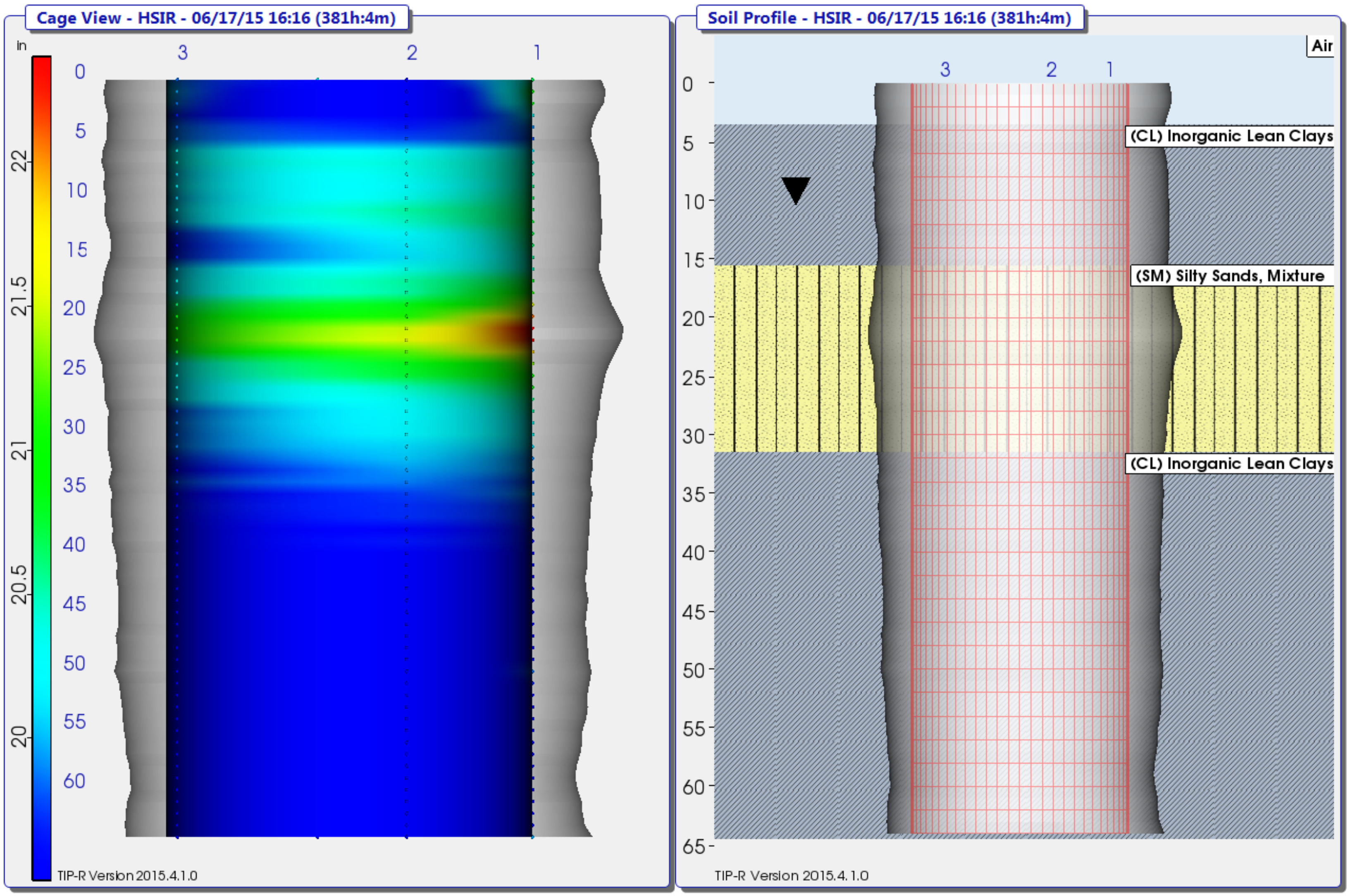

Figure C-4: 3-D Cage View and 3-D Interpretation with Soil Information: HSIR

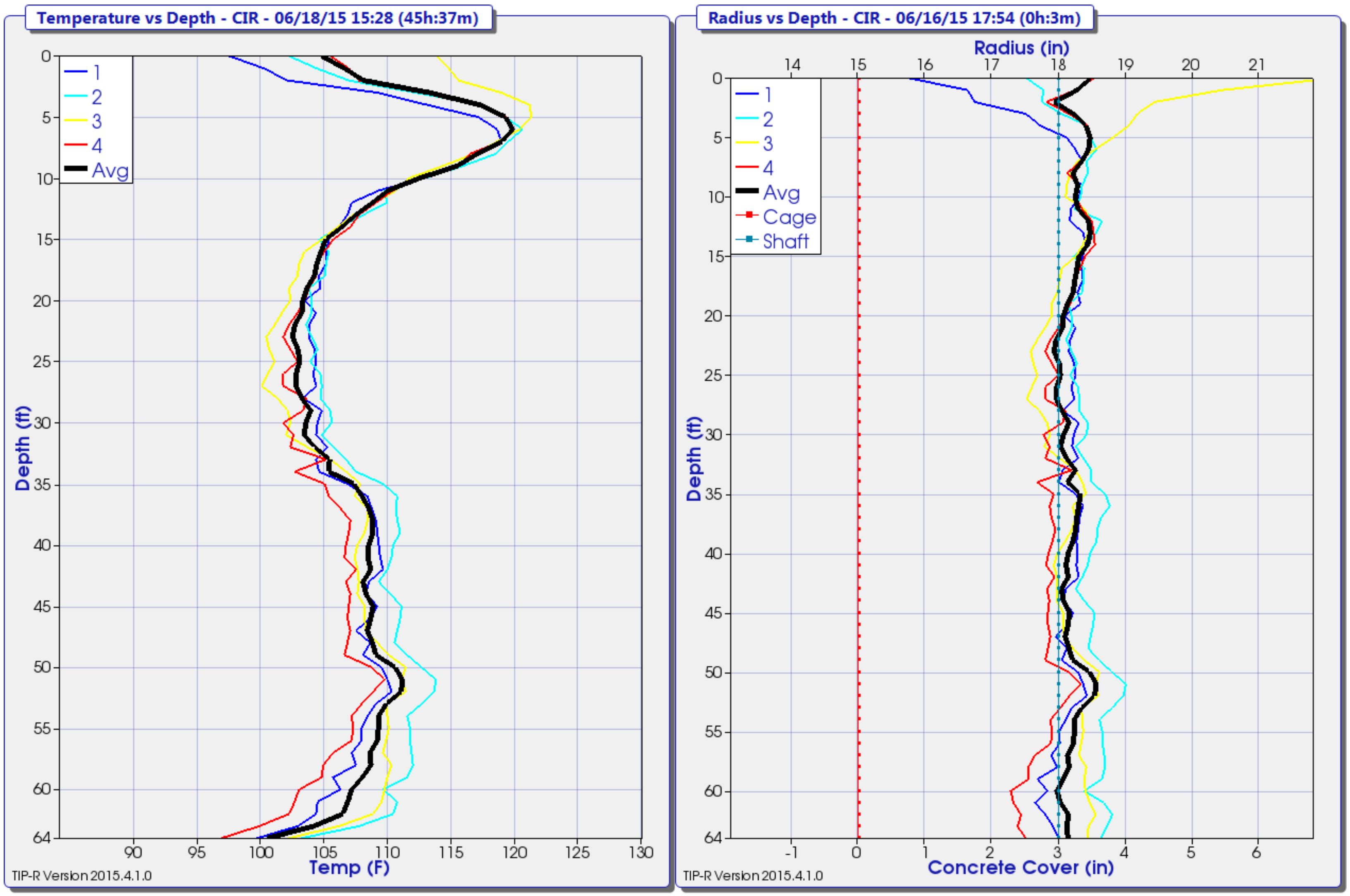

Figure C-5: Measured Temperature vs. Depth and Estimated Radius vs. Depth: CIR

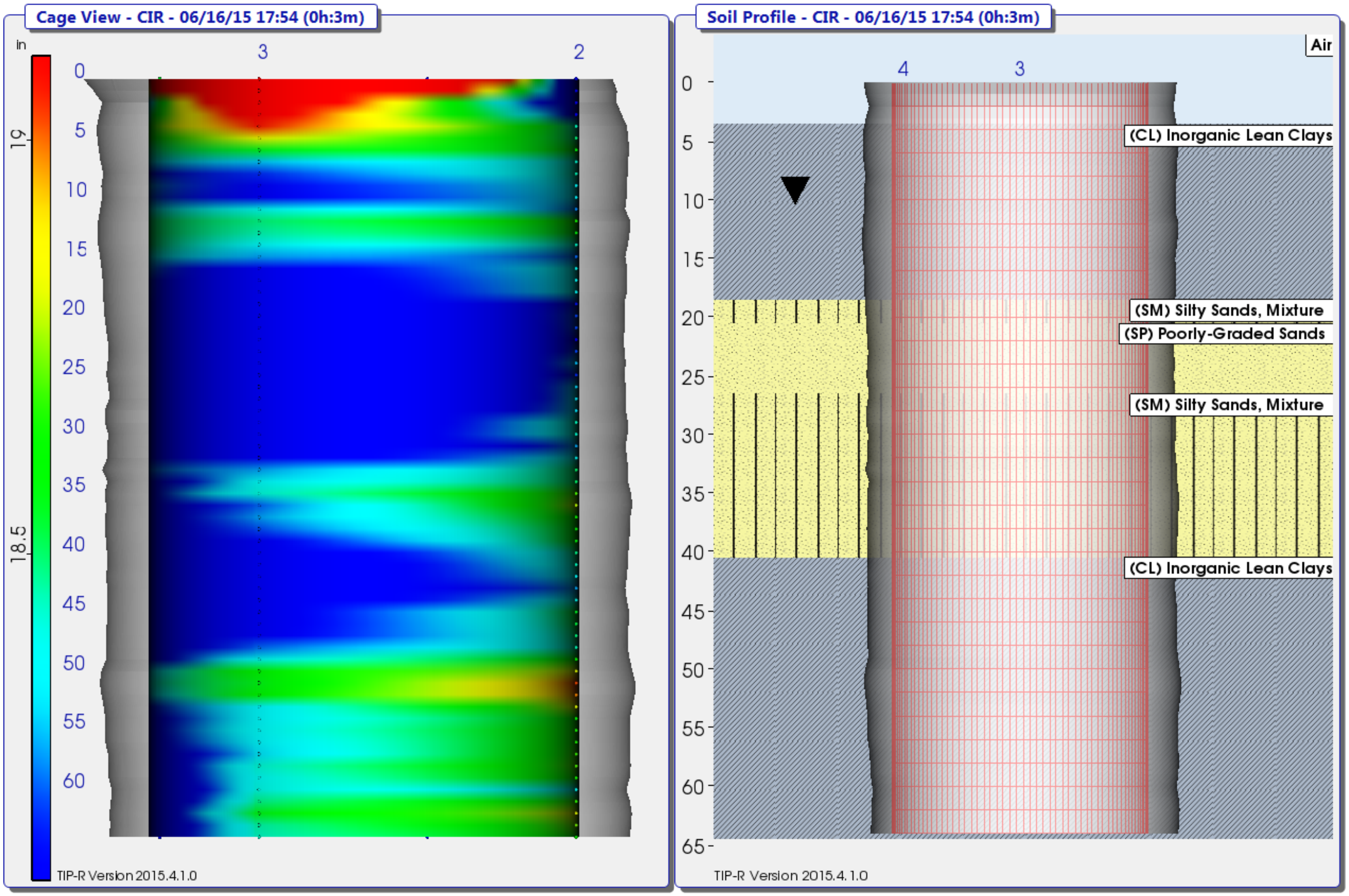

Figure C-6: 3-D Cage View and 3-D Interpretation with Soil Information: CIR